

**Ovipositing the Prostate**  
**Wasp-Inspired Needles for Prostate Laser Ablation**

Bloemberg, J.

**DOI**

[10.4233/uuid:2ec9dfaf-b9d6-46a5-9438-69c0fdd0a6b0](https://doi.org/10.4233/uuid:2ec9dfaf-b9d6-46a5-9438-69c0fdd0a6b0)

**Publication date**

2025

**Document Version**

Final published version

**Citation (APA)**

Bloemberg, J. (2025). *Ovipositing the Prostate: Wasp-Inspired Needles for Prostate Laser Ablation*. [Dissertation (TU Delft), Delft University of Technology]. <https://doi.org/10.4233/uuid:2ec9dfaf-b9d6-46a5-9438-69c0fdd0a6b0>

**Important note**

To cite this publication, please use the final published version (if applicable).  
Please check the document version above.

**Copyright**

Other than for strictly personal use, it is not permitted to download, forward or distribute the text or part of it, without the consent of the author(s) and/or copyright holder(s), unless the work is under an open content license such as Creative Commons.

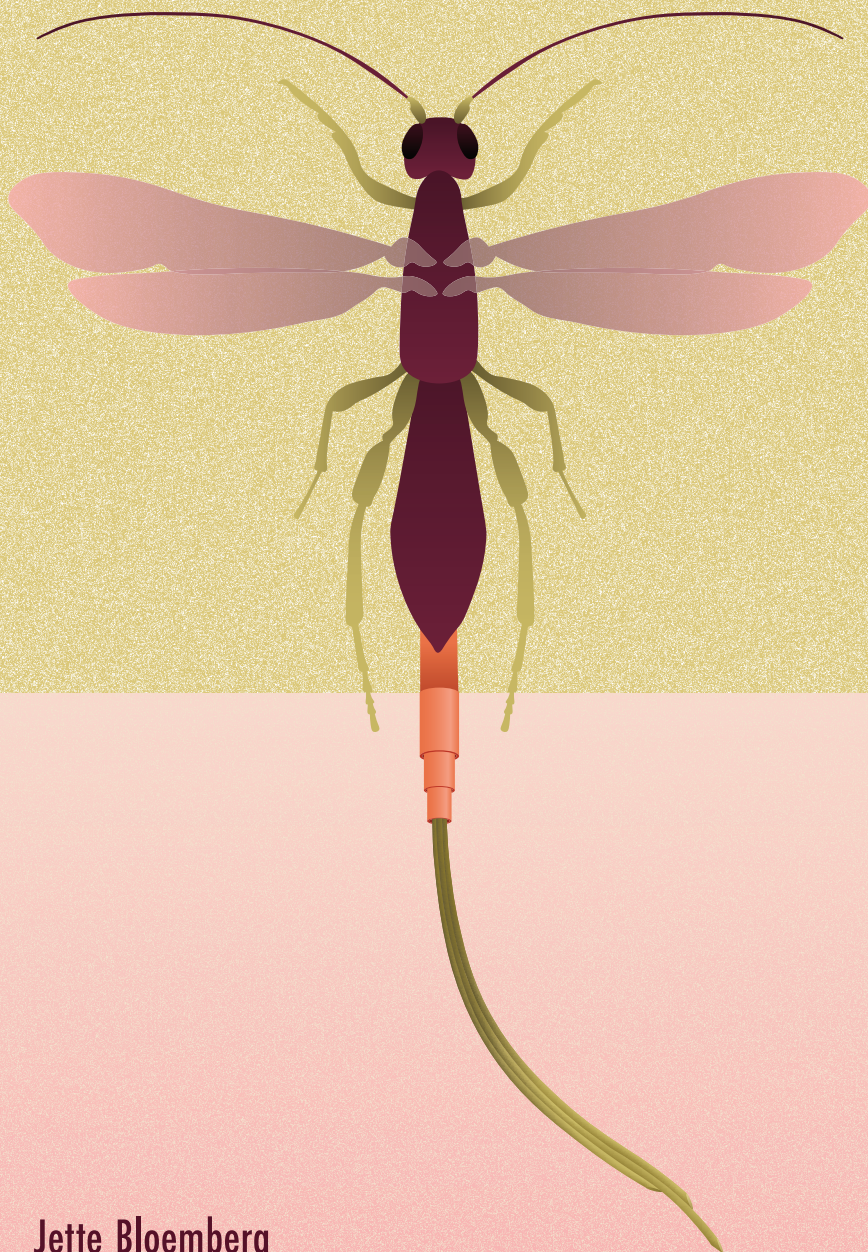
**Takedown policy**

Please contact us and provide details if you believe this document breaches copyrights.  
We will remove access to the work immediately and investigate your claim.



# OVIPOSITING the PROSTATE

Wasp-Inspired Needles for Prostate Laser Ablation



Jette Bloemberg







# **OVIPOSITING THE PROSTATE**

Wasp-Inspired Needles for Prostate Laser Ablation

## **Dissertation**

for the purpose of obtaining the degree of doctor  
at Delft University of Technology  
by the authority of the Rector Magnificus Prof. dr. ir. T.H.J.J. van der Hagen,  
chair of the Board for Doctorates  
to be defended publicly on  
Tuesday 30 September at 10:00 o'clock

by

**Jette BLOEMBERG**

Master of Science in Mechanical Engineering,  
Delft University of Technology, the Netherlands.



This dissertation has been approved by the promotor.

Composition of the doctoral committee:

Rector Magnificus  
Prof. dr. ir. P. Breedveld  
Dr. ir. A. Sakes

Chairperson  
Delft University of Technology, promotor  
Delft University of Technology, promotor

*Independent members:*

Prof. dr. J. Dankelman  
Prof. dr. ir. J.L. Herder  
Prof. dr. ir. F.T. Muijres  
Dr. S. Graziosi  
Dr. D.M. de Bruin

Delft University of Technology  
Delft University of Technology  
Wageningen University & Research  
Politecnico di Milano, Italy  
Amsterdam UMC



This research was supported by the Netherlands Organisation for Scientific Research (Nederlandse Organisatie voor Wetenschappelijk Onderzoek, NWO), domain Applied and Engineering Sciences (Toegepaste en Technische Wetenschappen, TTW), project number P18-26 Project 4: Novel Trans-Perineal Laser Ablation (TPLA) platform for accurate treatment of prostate tumours under MRI.

Research data supporting the findings described in this thesis are available at 4TU.ResearchData doi: 10.4121/43f41c07-65bb-42d5-bb60-e28a3d3f9954.

Printed by: Ridderprint, [www.ridderprint.nl](http://www.ridderprint.nl)  
Cover designed by: J. Bloemberg

Copyright © 2025 by J. Bloemberg  
ISBN: 978-94-6522-601-9

An electronic version of this dissertation is available at: <https://repository.tudelft.nl/>



# Table of Contents

- Summary..... ix
- Samenvatting ..... xi
- 1. Introduction ..... 1
  - 1.1 Prostate cancer treatment ..... 3
  - 1.2 Local treatment: TransPerineal Laser Ablation (TPLA). .... 3
  - 1.3 Biological inspiration for needle path control: The wasp ovipositor ..... 5
  - 1.4 Thesis goal. .... 7
  - 1.5 Thesis outline ..... 8
- Part 1. Background ..... 13
- 2. A Literature Review of Needle Positioning Hazards ..... 15
  - 2.1 Introduction ..... 17
    - 2.1.1 Background ..... 17
    - 2.1.2 Hazards in needle positioning ..... 17
  - 2.2 Methods. .... 19
    - 2.2.1 Literature search ..... 19
    - 2.2.2 Eligibility criteria ..... 19
    - 2.2.3 Literature search results. .... 20
  - 2.3 Results ..... 21
    - 2.3.1 Quantification of hazards ..... 21
    - 2.3.2 Clinical guidelines ..... 27
  - 2.4 Discussion. .... 31
    - 2.4.1 Main findings ..... 31
    - 2.4.2 Limitations. .... 31
    - 2.4.3 Solution strategies. .... 32
    - 2.4.4 Five-year view ..... 35
  - 2.5. Conclusion. .... 35
- 3. A Literature Review of Bioinspired Needles ..... 43
  - 3.1 Introduction ..... 45
    - 3.1.1 Background ..... 45
    - 3.1.2 Problem definition ..... 46
    - 3.1.3 Goal and structure ..... 47
  - 3.2 Methods. .... 47

3.2.1 Literature search . . . . .	47
3.2.2 Eligibility criteria . . . . .	47
3.2.3 Literature search results . . . . .	48
3.2.4 Classification of bioinspired needles . . . . .	48
3.3 Interacting. . . . .	50
3.3.1 Reducing grip . . . . .	50
3.3.2 Enlarging grip . . . . .	54
3.4 Propelling . . . . .	61
3.4.1 External . . . . .	61
3.4.2 Internal . . . . .	63
3.5 Discussion. . . . .	65
3.5.1 Comparative analysis . . . . .	65
3.5.2 Limitations and recommendations . . . . .	68
3.5.3 Temporal distribution and future perspective . . . . .	70
3.6 Conclusion . . . . .	70
<b>4. A Patent Review of Focal Therapy Instruments . . . . .</b>	<b>79</b>
4.1 Introduction . . . . .	81
4.1.1 Background . . . . .	81
4.1.2 Problem definition . . . . .	81
4.1.3 Goal and structure . . . . .	82
4.2 Methods. . . . .	82
4.2.1 Patent search . . . . .	82
4.2.2 Eligibility criteria . . . . .	84
4.2.3 Patent search results . . . . .	84
4.2.4 Classification of focal therapy instruments. . . . .	84
4.3 Destroy cancer cells on a cell level. . . . .	85
4.3.1 Destroy cell structure . . . . .	85
4.3.2 Disable cell function. . . . .	91
4.4 Destroy cancer cells on a network level . . . . .	93
4.4.1 Destroy network structure . . . . .	93
4.4.2 Disable network function . . . . .	95
4.5 Commercially available instruments. . . . .	96
4.6 Discussion. . . . .	98
4.6.1 Main findings . . . . .	98
4.6.2 Design suitability for medical purposes . . . . .	101
4.6.3 Further research . . . . .	101
4.6.4 Five-year view . . . . .	102
4.7 Conclusion . . . . .	103



## **Part 2. Needle Design - Propulsion, Transport & Steering** **115**

<b>5. From Ovipositor to Self-Propelled Transport Needle</b> .....	<b>117</b>
5.1 Introduction .....	119
5.1.1 Pancreatic tissue sampling .....	119
5.1.2 Bio-inspiration: Ovipositor-based tools for MIS .....	119
5.1.3 Combining self-propulsion and tissue transport .....	123
5.1.4 Goal of this study .....	124
5.2 Design .....	124
5.2.1 Needle .....	124
5.2.2 Actuation .....	126
5.2.3 Prototype .....	128
5.3 Evaluation .....	129
5.3.1 Experimental goal .....	129
5.3.2 Experiment 1: Core-transport capability .....	130
5.3.3 Experiment 2: Self-propulsion capability .....	134
5.3.4 Proof-of-principle sequential functioning .....	136
5.4 Discussion .....	137
5.4.1 Main findings .....	137
5.4.2 Limitations and future research .....	138
5.5 Conclusion .....	139
<b>6. From Ovipositor to Self-Propelled Steerable Needle</b> .....	<b>145</b>
6.1 Introduction .....	147
6.2 Design .....	150
6.2.1 Needle .....	150
6.2.2 Prototype .....	152
6.3 Evaluation .....	153
6.3.1 Experimental goal .....	153
6.3.2 Experimental facility .....	154
6.3.3 Experimental procedure .....	157
6.3.4 Data analysis .....	157
6.3.5 Results .....	157
6.3.6 Explorative experiments .....	161
6.4 Discussion and conclusion .....	162
Appendix 6.A Needle propulsion efficiency .....	169

## **Part 3. Actuation Design - From Experimental Facility to MRI Compatibility** **175**

<b>7. Exploring Wasp-Inspired Manual Actuation</b> .....	<b>177</b>
7.1 Introduction .....	179

7.1.1 Focal laser ablation. . . . .	179
7.1.2 State-of-the-art in self-propelled needles . . . . .	179
7.1.3 Goal of this study . . . . .	181
7.2 Design . . . . .	181
7.2.1 Design requirements . . . . .	181
7.2.2 Overall system design . . . . .	182
7.2.3 Prototype . . . . .	186
7.3 Evaluation . . . . .	189
7.3.1 Experimental goal. . . . .	189
7.3.2 Experimental facility . . . . .	189
7.3.3 Experimental procedure . . . . .	191
7.3.4 Results . . . . .	191
7.4 Discussion. . . . .	193
7.4.1 Needle performance. . . . .	193
7.4.2 Limitations. . . . .	193
7.4.3 Future work . . . . .	194
7.5 Conclusion . . . . .	196
<b>8. Enabling Wasp-Inspired Actuation for Steering. . . . .</b>	<b>201</b>
8.1 Introduction . . . . .	203
8.2 Materials and methods . . . . .	204
8.2.1 Wasp-inspired needle design . . . . .	204
8.2.2 Experimental goal and variables. . . . .	206
8.2.3 Experimental facility and procedure . . . . .	206
8.3 Results . . . . .	207
8.4 Discussion and conclusion . . . . .	209
Appendix 8.A Optical fiber evaluation . . . . .	213
<b>9. Fusing Wasp-Inspired Actuation with Pneumatics . . . . .</b>	<b>217</b>
9.1 Introduction . . . . .	219
9.1.1 Transperineal laser ablation . . . . .	219
9.1.2 MRI-compatible needles . . . . .	219
9.1.3 Wasp-inspired needles . . . . .	220
9.1.4 Goal of this study . . . . .	222
9.2 Design . . . . .	223
9.2.1 Needle . . . . .	223
9.2.2 Actuation unit . . . . .	223
9.2.3 Control unit . . . . .	225
9.2.4 Prototype . . . . .	225
9.3 Evaluation . . . . .	226

9.3.1 Experimental goal . . . . .	226
9.3.2 Experimental variables . . . . .	227
9.3.3 Experimental facility . . . . .	227
9.3.4 Experimental procedure . . . . .	229
9.3.5 Data analysis . . . . .	229
9.3.6 Results . . . . .	229
9.3.7 Additional MRI experiment . . . . .	231
9.4 Discussion. . . . .	233
9.4.1 Main findings . . . . .	233
9.4.2 Limitations. . . . .	233
9.4.3 Recommendations and future research. . . . .	234
9.5 Conclusion . . . . .	235

## **Part 4. Actuation Design - From Needle Holder to Universal Actuator 241**

<b>10. A Telescopic Actuator for a Self-Propelled Needle . . . . .</b>	<b>243</b>
10.1 Introduction . . . . .	245
10.1.1 Wasp-inspired needles. . . . .	245
10.1.2 Problem definition . . . . .	246
10.1.3 Goal of this study . . . . .	248
10.2 Design . . . . .	248
10.2.1 Needle . . . . .	248
10.2.2 Actuation system . . . . .	248
10.2.3 Final design . . . . .	251
10.2.4 Prototype. . . . .	251
10.3 Evaluation. . . . .	253
10.3.1 Experimental goal and variables . . . . .	253
10.3.2 Experimental facility and procedure . . . . .	254
10.3.3 Results . . . . .	256
10.4 Discussion. . . . .	257
10.4.1 Main findings . . . . .	257
10.4.2 Buckling prevention. . . . .	257
10.4.3 Limitations . . . . .	258
10.4.4 Recommendations and future research. . . . .	259
10.5 Conclusion . . . . .	260
<b>11. A Universal Actuator for a Self-Propelled Needle . . . . .</b>	<b>263</b>
11.1 Introduction . . . . .	265
11.2 Design . . . . .	266
11.2.1 Needle . . . . .	266
11.2.2 Actuation system . . . . .	267



11.2.3 Final design . . . . .	271
11.2.4 Prototype . . . . .	273
11.3 Evaluation . . . . .	275
11.3.1 Experimental goal . . . . .	275
11.3.2 Experimental facility . . . . .	275
11.3.3 Experimental variables . . . . .	277
11.3.4 Experimental procedure . . . . .	277
11.3.5 Results . . . . .	277
11.4 Discussion . . . . .	278
11.4.1 Main findings . . . . .	278
11.4.2 Limitations . . . . .	281
11.4.3 Recommendations and future research . . . . .	281
11.5 Conclusion . . . . .	284
<b>12. Discussion . . . . .</b>	<b>287</b>
12.1 Findings of this thesis . . . . .	289
12.2 Needle and actuation: Toward clinical implementation . . . . .	292
12.3 Nature and engineering: A future outlook . . . . .	297
12.4 Conclusions . . . . .	300
<b>Acknowledgements . . . . .</b>	<b>305</b>
<b>Curriculum Vitae . . . . .</b>	<b>309</b>
<b>List of Publications . . . . .</b>	<b>310</b>
<b>PhD Portfolio . . . . .</b>	<b>312</b>

# Summary

Prostate cancer is one of the most common types of cancer in men, especially as they get older. The primary treatments involve radical prostatectomy or radiotherapy, which target the entire prostate gland but often lead to side effects that impair urinary, sexual, or bowel function. The good news is that prostate cancer usually grows slowly and is often detected at an early stage, opening the door for more localized treatments with fewer side effects, such as TransPerineal Laser Ablation (TPLA). TPLA is based on light-tissue interaction. The tissue absorbs the light and converts it into heat, which induces irreversible thermal damage to the tissue, resulting in local cell death. The light is delivered via a laser fiber inside a needle positioned near the tumor under ultrasound guidance. In the future, Magnetic Resonance Imaging (MRI) is expected to replace ultrasound as the preferred imaging guidance option.

For TPLA, control of the needle path is of utmost importance to accurately reach the target region. Commonly used needles are rigid and bound to straight trajectories, which might lead to restricted access because of Pubic Arch Interference (PAI) or targeting errors because of needle deflection caused by needle-tissue interaction. Therefore, using current needles makes it hard to control the needle trajectory and reach the target region.

In nature, needle-like structures exist that allow for trajectory control. Specifically, certain species of parasitic wasps possess a slender and steerable needle-like structure called the ovipositor, of which they can control the trajectory. These wasps not only advance their ovipositors through often stiff substrates without suffering damage by using a so-called self-propelled motion, but they can also steer their ovipositors in order to reach their desired targets. Wasp-inspired mechanisms might address current challenges in TPLA needles. Therefore, the main purpose of this thesis is to present and evaluate innovative wasp-inspired needle designs developed to enhance needle trajectory control for TPLA treatment.

In **Part 1, Chapter 2** reviews challenges in needle positioning for therapeutic prostate cancer interventions, including (1) access restrictions to the prostate gland caused by the pubic arch, known as PAI, and (2) needle positioning errors. Current clinical guidelines addressing PAI and needle positioning errors are ambiguous, and clinical compliance varies, complicating the assessment of acceptable levels of PAI and needle positioning errors.

**Chapter 3** reviews the state-of-the-art in bioinspired medical needles, categorizing the strategies for needle-tissue interaction (i.e., reduce or enlarge grip) and propulsion (i.e., external or internal strategies) of the needle.

To identify future directions of the technologies applied by instruments for localized cancer treatment, **Chapter 4** reviews the patent literature on minimally- and non-invasive focal therapy instruments to treat localized cancer, categorizing the patented instruments based on their treatment target, treatment purpose, and treatment means.

**Part 2** presents two designs of wasp-inspired needles. Parasitic wasps can self-propel their ovipositors and transport eggs through them. **Chapter 5** combines these mechanisms into a 3-mm outer diameter needle comprising six parallel nitinol rods interconnected by an internal ring. The prototype demonstrated self-propulsion through and transport of tissue-mimicking phantoms.

In addition to self-propulsion and transport, the parasitic wasp can curve and steer its ovipositor to reach the desired target location. **Chapter 6** presents the design of a steerable self-propelled 0.89-mm outer diameter needle containing a central needle segment with a bevel-shaped prebent tip. The prototype was able to self-propel and steer in tissue-mimicking phantoms without buckling.

**Part 3** explores novel actuation mechanisms for wasp-inspired needles, enabling MRI guidance. **Chapter 7** presents a manual MRI-compatible actuation system for a 0.84-mm outer diameter self-propelled needle. The manual actuation system was inspired by the click pen and solely consists of MR-safe 3D-printed parts. The evaluation showed that the needle was visible in MR images and self-propelled through *ex vivo* human prostate tissue. **Chapter 8** enhances this system by integrating a steering mechanism into the actuation system and accommodating an optical fiber for TPLA procedures, enabling discrete bevel-shaped tip steering in tissue-mimicking phantoms.

**Chapter 9** investigates MRI-compatible pneumatic actuation for wasp-inspired needles, which alleviates the need for urologists to operate the needle manually within the confined space of the MRI bore. The prototype demonstrated that it was able to actuate the self-propelled needle in *ex vivo* porcine liver tissue under MRI guidance.

In addition to MRI compatibility, TPLA requires decoupling the needle from the actuation system, which is explored in **Part 4**. **Chapter 10** presents a user-friendly design, allowing the actuation system to be stationary as it drives the needle forward in a self-propelled sequence. In this design, the low-friction ball spline facilitates needle propulsion into tissue while preventing buckling, which was exemplified in experiments in tissue-mimicking phantoms.

**Chapter 11** explores a modular actuation system that enables a theoretically infinite needle length inspired by mechanical pencils. By clamping, advancing, and releasing the needle segments sequentially, the needle achieved self-propulsion through tissue-mimicking phantoms and fruits with differing stiffnesses and inhomogeneous anatomies.

This thesis shows the value of translating biological into engineering mechanisms to tackle design challenges in medical instruments. The needle and actuation system designs presented in this thesis contribute to a new generation of needles that enhance needle trajectory control for TPLA treatment. The proposed wasp-inspired needle designs and actuation systems pave the way for improving percutaneous interventions, particularly TPLA for prostate cancer treatment.



# Samenvatting

Prostaatkanker is een veelvoorkomende ziekte bij mannen, vooral op latere leeftijd. Gebruikelijke behandelingen, zoals het operatief verwijderen van de prostaat of bestraling, kunnen vervelende bijwerkingen veroorzaken die invloed hebben op het plassen, de seksualiteit en de stoelgang. Bemoedigend is dat prostaatkanker meestal langzaam groeit en vaak vroeg wordt ontdekt, waardoor minder ingrijpende behandelingen, zoals TransPerineale Laser Ablatie (TPLA), mogelijk zijn. Bij TPLA wordt laserlicht gebruikt om de kanker te behandelen. Een dunne laservezel wordt via een naald dicht bij de tumor geplaatst onder echogeleiding. In de toekomst wordt verwacht dat Magnetic Resonance Imaging (MRI) echografie zal vervangen, omdat je op een MRI beeld beter onderscheid tussen tumor en gezond weefsel kunt maken en de temperatuur van het weefsel tijdens de behandeling kunt meten.

Bij TPLA moet de naald precies op de juiste plek komen. Momenteel gebruiken artsen vaak rechte rigide naalden. Dit kan leiden tot beperkte toegankelijkheid van tumorlocaties vanwege interferentie met de schaamboom of tot plaatsingsfouten doordat de naald afbuigt door interactie met het weefsel. In de natuur bestaan er echter naaldachtige structuren, zoals de legboor van sluipwespen, waarvan de plaatsing heel nauwkeurig gecontroleerd kan worden. De wesp kan haar legboor door een vaste ondergrond bewegen zonder schade. Daarnaast is de legboor bestuurbaar om gericht het doel te bereiken. Door inspiratie te halen uit de slimme mechanismen in de legboor, kunnen oplossingen bedacht worden voor de huidige problemen met naalden. Het hoofddoel van dit proefschrift is daarom het presenteren en evalueren van innovatieve wespeïnspireerde naaldontwerpen die de controle over het naaldtraject verbeteren voor TPLA-behandelingen.

In **Deel 1, Hoofdstuk 2**, worden de problemen bij het positioneren van naalden voor prostaatkankerbehandelingen besproken, waaronder (1) botten die in de weg zitten en (2) fouten in naaldplaatsing. Huidige klinische richtlijnen voor deze problemen zijn onduidelijk en de naleving verschilt per ziekenhuis. Dit bemoeilijkt het beoordelen van een acceptabel niveau van botinterferentie en fouten in naaldplaatsing.

**Hoofdstuk 3** bespreekt de huidige technieken in naalden geïnspireerd op de natuur. De naaldontwerpen werden gecategoriseerd op basis van de strategieën voor naald-weefselinteractie en naaldvoortstuwing.

Om toekomstige richtingen in technologieën voor lokale kankerbehandeling te identificeren, behandelt **Hoofdstuk 4** de octrooiliteratuur over minimaal- en niet-invasieve focale therapie-instrumenten. De gevonden instrumenten werden gecategoriseerd op basis van hun behandel doelwit, behandel doel en behandel middel.

**Deel 2** presenteert twee ontwerpen van naalden geïnspireerd op de sluipwesp. Sluipwespen kunnen eitjes transporteren door de legboor en hun legboor voortstuwten in bomen zonder de legboor te duwen en zonder dat de legboor knikt. **Hoofdstuk 5** combineert deze mechanismen in een naald met een buitendiameter van 3 mm bestaande uit zes nitinol stokjes verbonden door een interne ring. Het prototype van de naald was in staat om zichzelf voort te bewegen door fantoomweefsel en het weefsel door zichzelf te transporteren.

Naast voortstuwing en transport, kan de sluipwesp haar legboor buigen en sturen om de gewenste locatie te bereiken. **Hoofdstuk 6** presenteert het ontwerp van een stuurbare naald met buitendiameter van 0,89 mm. Het prototype kan zichzelf voortbewegen en sturen in fantoomweefsels zonder te knikken.

**Deel 3** verkent nieuwe aandrijftechnieken voor wespgeïnspireerde naalden die in een MRI-scanner gebuikt kunnen worden. **Hoofdstuk 7** introduceert een handmatige, MR-veilige aandrijving voor een voortstuwende naald geïnspireerd door een het klikmechanisme in een balpen. Deze aandrijving bestaat uitsluitend uit MR-veilige 3D-geprinte onderdelen. De evaluatie liet zien dat de naald zichtbaar was in MRI-scans en voortbewoog door *ex vivo* menselijk prostaatweefsel. **Hoofdstuk 8** borduurt voort op deze handmatige aandrijving door een stuurmechanisme en een laservezel voor TPLA te integreren in het aandrijfsysteem.

**Hoofdstuk 9** onderzoekt MR-veilige pneumatische aandrijving voor wespgeïnspireerde naalden, waardoor de arts niet in de beperkte ruimte van de MRI-tunnel hoeft te werken. Het prototype kon de naald voortstuwten in *ex vivo* varkensleverweefsel in een MRI scanner.

Naast MR-veiligheid, vereist TPLA dat de naald losgekoppeld is van het aandrijfsysteem, wat wordt onderzocht in **Deel 4**. **Hoofdstuk 10** beschrijft een gebruiksvriendelijk ontwerp waarin het aandrijfsysteem stationair blijft, terwijl de naald wordt aangedreven met een voortstuwende beweging. In dit ontwerp zorgt de verbinding met rollagers voor een lage wrijvingskracht voor de voortstuwing in weefselfantomen.

**Hoofdstuk 11** onderzoekt een modulair aandrijfsysteem dat een theoretisch oneindige naaldlengte mogelijk maakt gebaseerd op mechanische vulpotloden. Doormiddel van achtereenvolgens de naaldsegmenten vast te klemmen, naar voren te bewegen en los te laten, stuwde de naald zichzelf en een TPLA-laservezel voort door weefselfantomen en fruit.

Dit proefschrift toont aan dat we technische ontwerpuitdagingen in medische instrumenten aan kunnen pakken door inspiratie uit de natuur te halen. De ontwerpen gepresenteerd in dit proefschrift dragen bij aan een nieuwe generatie naalden die de controle over het naaldtraject voor TPLA-behandelingen verbeterd. De gepresenteerde naaldontwerpen geïnspireerd op de legboor van de sluipwesp en de bijbehorende aandrijfsystemen zijn veelbelovend voor de verbetering van medische toepassingen met naalden, met name TPLA voor de behandeling van prostaatkanker.



## **Introduction**



## 1.1 Prostate cancer treatment

Prostate cancer is one of the most common types of cancer in men, especially as they get older. In 2020, it was the second most common cancer diagnosed in men and the fifth leading cause of cancer-related deaths for men worldwide [1]. Prostate cancer occurs when cancerous cells form in the tissues of the prostate gland.

The prostate gland is a vital component of the male reproductive system, as it produces a part of the semen that plays a role in activating sperm [2, 3]. All male mammals have a prostate gland. The size of the human prostate approximates that of a walnut. The location of the prostate is in the pelvis, directly below the bladder, surrounding the urethra (Figure 1.1) [2]. When looking at the type of tissue, the prostate gland consists of approximately 40 tubuloalveolar glands embedded in smooth muscle and dense connective tissue, enclosed by a connective tissue capsule [2].

Anatomically, the prostate gland is divided into three zones: the central zone, the transition zone, and the peripheral zone [4]. All three zones have different embryologic origins and can be distinguished by histology or medical imaging techniques such as Magnetic Resonance Imaging (MRI) [5]. Moreover, these zones have different susceptibilities to pathological conditions. The prostate is a gland that typically keeps growing throughout life, which can cause benign prostate enlargement that may affect urination. Benign conditions arise in the transition zone and are not cancerous. Prostate cancer occurs when cancerous cells form in the tissues of the prostate gland. Cancerous cells predominantly arise in the peripheral zone, accounting for 70% of all cases [5].

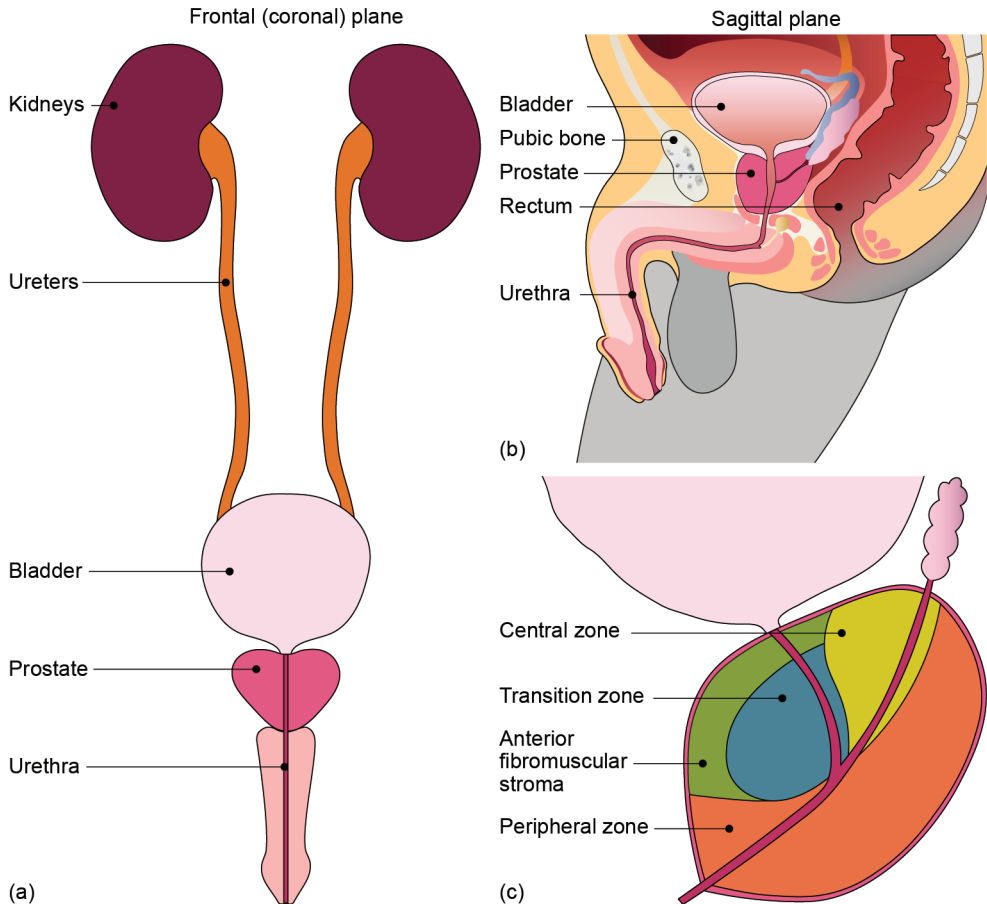
The current gold standard for prostate cancer treatment is a radical prostate treatment, i.e., radical prostatectomy or radiotherapy. During a radical prostatectomy, the entire prostate gland is surgically removed. Radiotherapy can be applied using external beam radiation therapy or brachytherapy. However, radical prostate treatments targeted at the prostate as a whole often come with side effects that impair urinary, sexual, or bowel function [6-8].

The good news is that prostate cancer usually grows slowly and is often detected at an early stage. Patients who are diagnosed with prostate cancer at an early stage can be eligible for focal therapy instead of a radical treatment [9]. Focal therapy is a local treatment type that can result in an oncological cure while preserving the functional anatomy and minimizing side effects by preserving noncancerous tissue [10, 11]. Several focal therapy modalities are being studied, such as high-intensity focused ultrasound, cryotherapy, photodynamic therapy, irreversible electroporation, and focal laser ablation [11]. These modalities have already shown promising oncological outcomes and fewer side effects as compared to radical treatments [12-16].

## 1.2 Local treatment: TransPerineal Laser Ablation (TPLA)

An appealing focal therapy modality to treat prostate cancer is TransPerineal Laser Ablation (TPLA). TPLA is a focal therapy technique based on light-tissue interaction, where light is

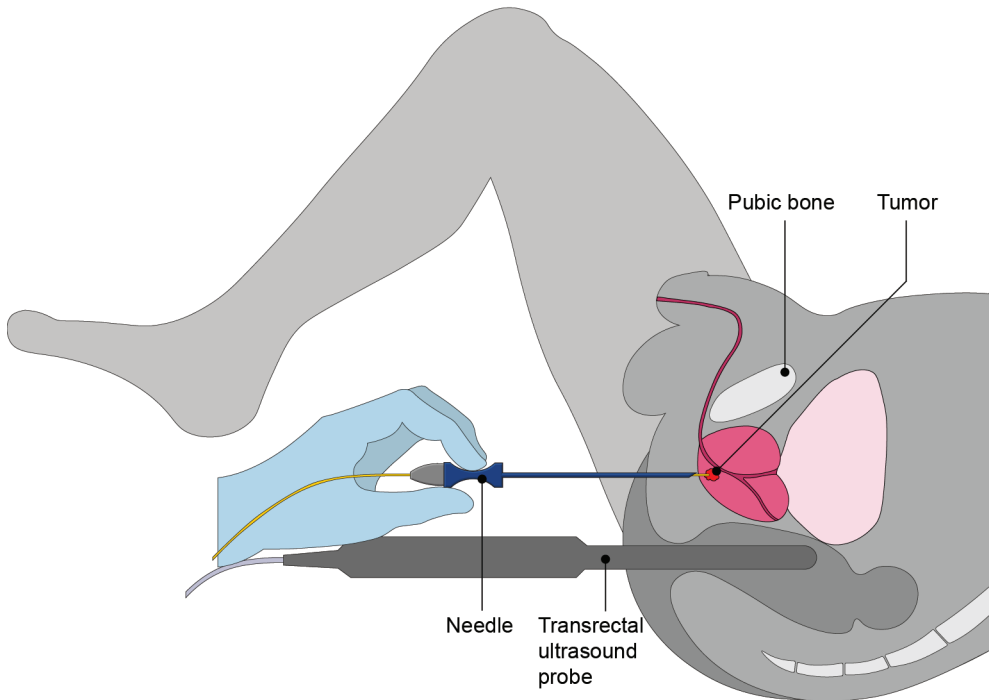




**Figure 1.1. Schematic visualization of the male urinary and reproductive system** in the frontal (coronal) plane (a) showing the kidneys, ureters, bladder, prostate, and urethra, and in the sagittal plane (b) showing the bladder, pubic bone, prostate, rectum, and urethra. The sagittal section view of the prostate (c) shows how the prostate gland is divided into three main zones: the central zone, the transition zone, and the peripheral zone. Besides the zones, there is the anterior fibromuscular stroma, the most anterior part of the prostate, consisting of muscle cells and dense connective tissue without glandular tissue. Illustration adapted from Servier Medical Art under CC attribution license 3.0.

absorbed by the tissue and converted into heat [17]. This conversion induces irreversible thermal damage to the tissue, resulting in local cell death [18]. The light is delivered by a laser fiber positioned near the tumor using a 21-gauge (i.e.,  $\sim 0.8$  mm outer diameter) needle under ultrasound guidance [13] (Figure 1.2). TPLA leads to homogeneous tissue necrosis caused by one or multiple laser fibers and does not appear to alter the sexual and urinary function of the patient [19]. Furthermore, the ablation can be performed under local anesthesia combined with conscious sedation in an operating or intervention room [20, 21], thereby strongly reducing the operating time and costs compared to radical treatments.

During TPLA, the laser fibers are placed centrally into the prostate tumor under ul-



**Figure 1.2. Typical setup for TransPerineal Laser Ablation (TPLA) of the prostate.** The patient is positioned in the lithotomy position (i.e., lying on their back with their legs raised and spread apart). The setup includes a transrectal ultrasound probe and a laser fiber needle inserted into the tumor. During needle insertion, the arch of the pubic bone might cause access restriction.

trasound guidance using a transrectal ultrasound probe. In the future, MRI is expected to replace ultrasound as the preferred imaging guidance option. MRI provides advantages over ultrasound, including the ability to differentiate between tumor and healthy tissue and to monitor temperature increase in the ablated area [22-24]. The latter allows for the evaluation of tissue necrosis during the TPLA procedure [22-24].

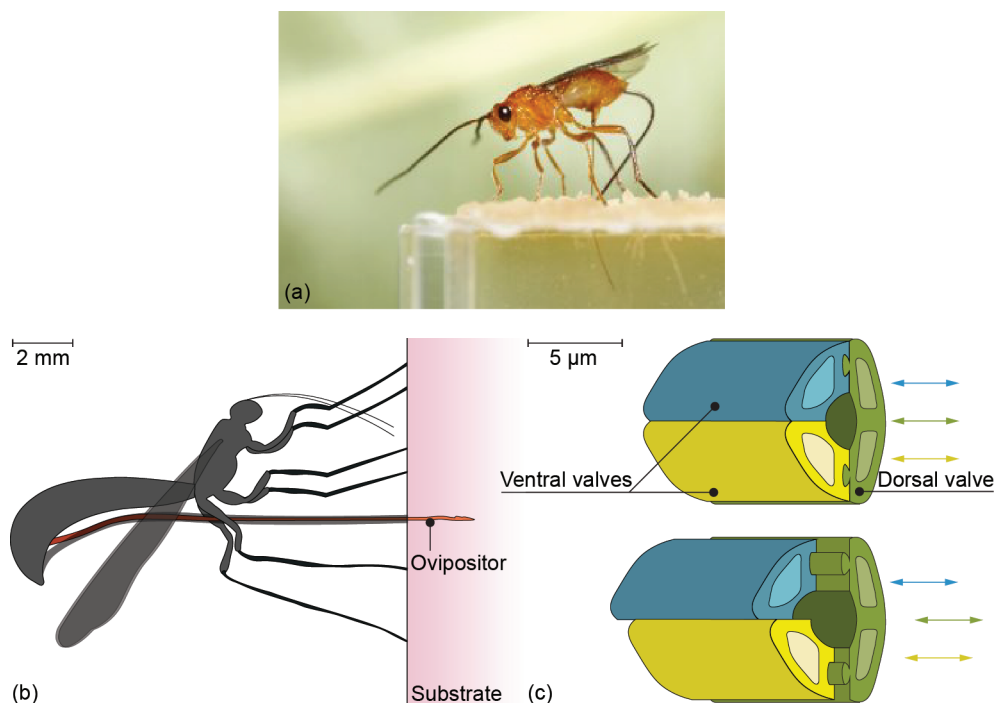
For local treatments such as TPLA, control of the needle path is of utmost importance to accurately reach the target region. In order to reach the prostate, the needle is inserted transperineally, i.e., through the skin between the anus and the scrotum. Commonly used needles are rigid and bound to straight trajectories, which might lead to restricted access because of pubic arch interference or targeting errors because of needle deflection caused by needle-tissue interaction. Therefore, using current needles makes it hard to control the needle trajectory.

### 1.3 Biological inspiration for needle path control: The wasp ovipositor

In nature, needle-like structures exist that allow for trajectory control. Specifically, certain species of parasitic wasps possess a slender and steerable needle-like structure called the

ovipositor, of which they can control the trajectory (Figure 1.3). Female parasitic wasps use their ovipositor, which literally means egg-placer, to lay their eggs inside host organisms deep within substrates such as fruits and wood [25, 26]. These wasps not only advance their ovipositors through often stiff substrates without suffering damage, but they can also steer their ovipositors in order to reach their desired targets [27]. For TPLA applications, wasp-inspired needles are particularly interesting due to their ability to advance without buckling, transport, and steer, allowing for trajectory adjustments.

The ovipositor is a very slender organ shaped like a flexible, hollow needle, typically measuring several tens to hundreds of micrometers in diameter and extending to several centimeters in length. The highest length-to-diameter ratios are found in wasp species that need to probe deeply, such as the wood-probing *Megarhyssa atrata* Fabricius (Hymenoptera: Ichneumonidae), which has an ovipositor length-to-diameter ratio of 260 [26] and an ovipositor length of up to 142 mm [26]. The ovipositor consists of three parallel segments, called “valves,” which are connected by a tongue-and-groove (i.e., olistheter) mechanism [28]. This mechanism joins two surfaces with a groove along one side and a corresponding ridge, the tongue, along the opposite side. The tongue of one valve fits into the groove of the adjacent valve, allowing the valves to slide relative to each other while preventing their separation [28].



**Figure 1.3. The ovipositor of a parasitic wasp.** (a) The parasitic wasp *Diachasmimorpha longicaudata* Ashmead (Hymenoptera: Braconidae) ovipositing into an agar gelatin substrate (from [33]). (b) Schematic illustration of a parasitic wasp using its ovipositor to lay eggs inside a substrate. (c) The ovipositor consists of three parallel valves (green, yellow, and blue) that can move reciprocally (based on [27]).

Although the exact mechanisms female parasitic wasps use for ovipositor insertion and buckling prevention are still being studied, two main methods of ovipositor insertion have been identified in the scientific literature [27]: (1) pushing the ovipositor as a whole into the substrate, which was observed only in soft substrates, and (2) inserting with alternating valve movements, which was observed in both soft and solid substrates. In this second insertion method, the wasp moves the valves alternately to achieve a so-called “self-propelled motion” [27, 29]. First, one of the valves advances deeper into the tissue, whereas the other valves remain stationary [29, 30]. The friction forces of the stationary valves in contact with the surrounding substrate counteract the friction and cutting forces of the advanced valve in contact with the surrounding substrate because of the difference in surface area between the stationary and advanced valves [30]. The wasp alternates the advancing movements between the valves to propel the ovipositor through the substrate incrementally. This alternating valve mechanism allows for ovipositor insertion while avoiding net push forces and axial loads that would otherwise result in the wasp being pushed away from the substrate, given the wasp’s small mass, and bending, buckling, or breaking of the ovipositor [27, 29].

In addition to the self-propelled motion, the wasp can steer the ovipositor and transport eggs through an internal channel within the ovipositor [27, 31, 32]. The remarkable mechanisms of the wasp to transport eggs, advance, and steer inside solid substrates without buckling inspired us to design needles and their actuation mechanisms.

Inspired by the wasp ovipositor, needles have been developed in the scientific literature embodying different wasp-inspired capabilities [34-38]. Research has shown that using a multisegmented, wasp-inspired probe with a 4-mm diameter, actuated with an advancing-retraction motion, reduces tissue motion and damage in the needle’s vicinity [34, 35, 39]. This effect is observed when compared to pushing the needle as a whole through *ex vivo* porcine brain tissue and gelatin-based tissue-mimicking phantoms [34, 35, 39]. Moreover, Paritotokkaporn *et al.* [40] presented 2D samples with an ovipositor-inspired directional friction pattern actuated with a reciprocal motion, which could move *ex vivo* porcine muscle tissue and tissue-mimicking phantoms along the sample surface without applying an external push force to the tissue (phantom). In order to miniaturize the needle diameter to submillimeter dimensions, Scali *et al.* [36-38] replaced the complex-shaped interlocking groove-and-tongue mechanism inspired by the ovipositor with nitinol rods devoid of serrations and bundled by a shrinking tube, resulting in a needle that can self-propel using the reciprocal motion and steer by inducing an offset between the needle segments, creating a discrete bevel-shaped tip [37]. Early *ex vivo* experiments demonstrated the self-propelled motion of the wasp-inspired needle in tissue [41], although the achieved steering curvatures were low and a clinical application was still lacking.

## 1.4 Thesis goal

TPLA is a localized prostate cancer treatment that requires needle trajectory control. Wasp-in-

spired needles have the potential to enhance needle trajectory control in TPLA treatment. **The main goal of this thesis is, therefore, to present and evaluate innovative wasp-inspired needle designs developed to enhance needle trajectory control for TPLA treatment.** In order to achieve this goal, this thesis focuses on the following four research objectives:

- First, we aim to identify challenges in designing needles that can enhance trajectory control. This means identifying hazards associated with needle positioning in prostate cancer treatment that result in limited needle trajectory control. Additionally, we will review the state-of-the-art in bioinspired needle designs developed to enhance needle trajectory control, as well as current and emerging needle-like instruments for local cancer treatment described in the patent literature.
- Second, we will explore design strategies for ovipositor-inspired needles that can be used during TPLA treatment. Specifically, we will explore new design pathways to apply wasp-inspired self-propulsion, steerability, and transport capabilities in needle designs at clinically applicable dimensions.
- Third, we will challenge issues in needle actuation for their use during TPLA treatment. While ultrasound currently provides image guidance during TPLA, future treatments are expected to use MRI. Consequently, our goal is to go beyond the state-of-the-art and to develop MRI-compatible actuation systems, which do not comprise metallic, magnetic, or conductive materials [42].
- Fourth, to ensure the needle reaches its target location within the patient, we will tackle possibilities to decouple the actuation system from the needle. This involves exploring design strategies toward a universal actuator capable of actuating needle segments and functional elements, such as a laser fiber for TPLA treatment, over unlimited insertion lengths.

## 1.5 Thesis outline

The schematic illustration in Figure 1.4 shows the outline of this thesis.

The first, **Background**, part of the thesis starts in **Chapter 2** with a literature review of hazards in needle positioning for therapeutic prostate cancer interventions. This leads to an analysis of the causes of needle positioning hazards, as well as insights into design opportunities to mitigate these hazards, such as steerable needles. **Chapter 3** reviews and classifies bioinspired needle designs based on their strategies for needle-tissue interaction and propulsion of the needle. **Chapter 4** investigates patents on instrument designs for focal therapy to treat localized cancer, which provides insights into the future directions of the technologies applied by the instruments described in the patents.

The second, **Needle Design – Propulsion, Transport & Steering**, part of the thesis describes the design and evaluation of wasp-inspired needles. Female parasitic wasps have demonstrated the ability to self-propel their ovipositors, transport eggs through them, and steer to reach their desired target location. **Chapter 5** explores using the wasp-inspired self-propulsion mechanism to combine needle propulsion and tissue transport into a single



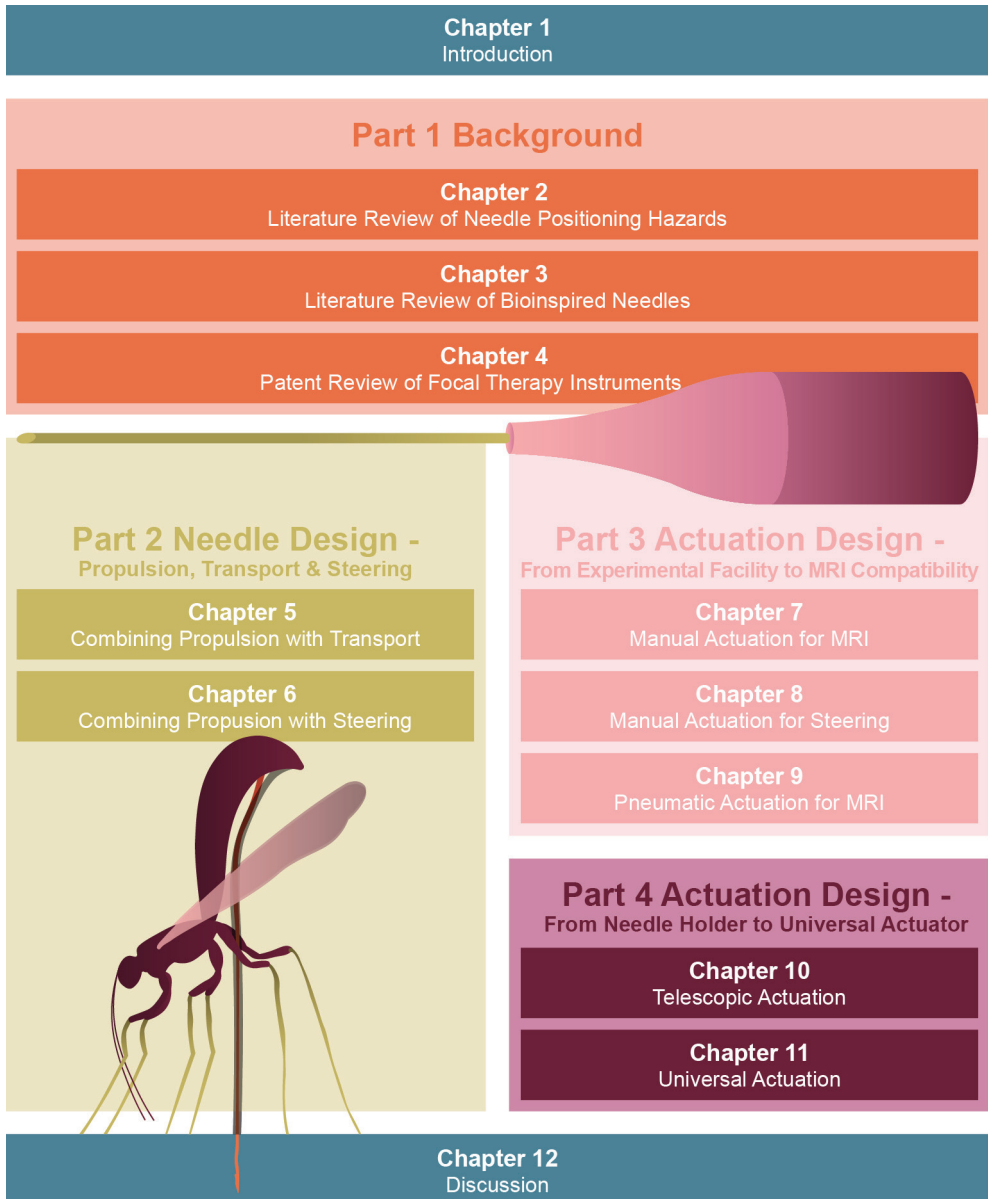


Figure 1.4. Visual outline of this thesis.

transport needle. **Chapter 6** addresses the challenge of integrating wasp-inspired steering strategies in a multi-segmented self-propelled needle to achieve steering curvatures comparable to those of parasitic wasp ovipositors.

The third, **Actuation Design – From Experimental Facility to MRI Compatibility**, part of the thesis explores developing and evaluating novel actuation mechanisms for wasp-inspired

needles enabling MRI compatibility. **Chapter 7** presents the first manual and MRI-compatible actuation system of a wasp-inspired self-propelled needle evaluated in *ex vivo* human prostate tissue within an MR system. **Chapter 8** enhances this manual MRI-compatible actuation system by integrating an omnidirectional needle steering mechanism. **Chapter 9** investigates MRI-compatible pneumatic actuation, which alleviates the need for urologists to operate the needle manually within the confined space of the MRI bore. We introduce a novel pneumatic actuation system of a wasp-inspired self-propelled needle and its evaluation in *ex vivo* porcine liver tissue within an MR system.

In addition to MRI compatibility, TPLA applications require decoupling the needle from the actuation system, which is explored in the fourth, **Actuation Design – From Needle Holder to Universal Actuator**, part of the thesis. **Chapter 10** explores a novel user-friendly design allowing the actuation system to be stationary as it drives the needle forward at a self-propelled sequence. **Chapter 11** goes beyond the parasitic wasp and explores a modular actuation system that enables a theoretically infinite needle length.

Finally, **Chapter 12** couples the four parts and discusses the main findings of this thesis, addressing the next steps for future research.

## References

1. Sung H, Ferlay J, Siegel RL, Laversanne M, Soerjomataram I, Jemal A, et al. Global cancer statistics 2020: GLOBOCAN estimates of incidence and mortality worldwide for 36 cancers in 185 countries. *CA: a cancer journal for clinicians*. 2021;71(3):209-49. doi: 10.3322/caac.21660.
2. Marieb EN, Hoehn K. Human anatomy & physiology. Tenth edition ed: Pearson education; 2016.
3. Verze P, Cai T, Lorenzetti S. The role of the prostate in male fertility, health and disease. *Nature Reviews Urology*. 2016;13(7):379. doi: 10.1038/nrurol.2016.89.
4. Ali A, Du Feu A, Oliveira P, Choudhury A, Bristow RG, Baena E. Prostate zones and cancer: lost in transition? *Nature Reviews Urology*. 2022;19(2):101-15. doi: 10.1038/s41585-021-00524-7.
5. Lee CH, Akin-Olugbade O, Kirschenbaum A. Overview of prostate anatomy, histology, and pathology. *Endocrinology and Metabolism Clinics*. 2011;40(3):565-75. doi: 10.1016/j.ecl.2011.05.012.
6. Sanda MG, Dunn RL, Michalski J, Sandler HM, Northouse L, Hembroff L, et al. Quality of life and satisfaction with outcome among prostate-cancer survivors. *New England Journal of Medicine*. 2008;358(12):1250-61. doi: 10.1056/NEJMoa074311.
7. Potosky AL, Davis WW, Hoffman RM, Stanford JL, Stephenson RA, Penson DE, et al. Five-year outcomes after prostatectomy or radiotherapy for prostate cancer: the prostate cancer outcomes study. *Journal of the National Cancer Institute*. 2004;96(18):1358-67. doi: 10.1093/jnci/djh259.
8. Hamdy FC, Donovan JL, Lane J, Mason M, Metcalfe C, Holding P, et al. 10-year outcomes after monitoring, surgery, or radiotherapy for localized prostate cancer. *N Engl J Med*. 2016;375:1415-24. doi: 10.1056/NEJMoa1606220.
9. Ghoreifi A, Gomella L, Hu JC, Konety B, Lunelli L, Rastinehad AR, et al. Identifying the best candidate for focal therapy: a comprehensive review. *Prostate Cancer and Prostatic Diseases*. 2024;1-9. doi: 10.1038/s41391-024-00907-y.
10. Lindner U, Lawrentschuk N, Trachtenberg J. Focal laser ablation for localized prostate cancer. *Journal of Endourology*. 2010;24(5):791-7. doi: 10.1089/end.2009.0440.
11. Lodeizen O, de Bruin M, Eggener S, Crouzet S, Ghai S, Varkarakis I, et al. Ablation energies for focal treatment of prostate cancer. *World journal of urology*. 2019;37(3):409-18. doi: 10.1007/

s00345-018-2364-x.

12. Van Luijcklaar A, Greenwood BM, Ahmed HU, Barqawi AB, Barret E, Bomers JG, et al. Focal laser ablation as clinical treatment of prostate cancer: report from a Delphi consensus project. *World journal of urology*. 2019;37(10):2147-53. doi: 10.1007/s00345-019-02636-7.
13. van Riel LA, van Kollenburg RA, Vis AN, van Leeuwen PJ, de Reijke TM, de Bruin DM, et al. Safety and feasibility of Soractelite transperineal focal laser ablation for prostate cancer and short-term quality of life analysis from a multicenter pilot study. *European urology open science*. 2022;39:48-54. doi: 10.1016/j.euros.2022.02.012.
14. Ganzer R, Hadaschik B, Pahernik S, Koch D, Baumunk D, Kuru T, et al. Prospective multicenter phase II study on focal therapy (hemiblation) of the prostate with high intensity focused ultrasound. *The Journal of urology*. 2018;199(4):983-9. doi: 10.1016/j.juro.2017.10.033.
15. Shah TT, Ahmed H, Kanthabalan A, Lau B, Ghei M, Maraj B, et al. Focal cryotherapy of localized prostate cancer: a systematic review of the literature. *Expert review of anticancer therapy*. 2014;14(11):1337-47. doi: 10.1586/14737140.2014.965687.
16. Blazeviski A, Scheltema MJ, Yuen B, Masand N, Nguyen TV, Delprado W, et al. Oncological and quality-of-life outcomes following focal irreversible electroporation as primary treatment for localised prostate cancer: a biopsy-monitored prospective cohort. *European urology oncology*. 2020;3(3):283-90. doi: 10.1016/j.euo.2019.04.008.
17. van Riel LA, van Kollenburg RA, Freund JE, Almasian M, Jager A, Engelbrecht MR, et al. Reliable Visualization of the Treatment Effect of Transperineal Focal Laser Ablation in Prostate Cancer Patients by Magnetic Resonance Imaging and Contrast-enhanced Ultrasound Imaging. *European urology open science*. 2023;54:72-9. doi: 10.1016/j.euros.2023.06.002.
18. Pacella CM, Breschi L, Bottacci D, Masotti L. Physical principles of laser ablation. *Image-guided Laser Ablation*. 2020:7-18. doi: 10.1007/978-3-030-21748-8\_2.
19. Oto A, Sethi I, Karczmar G, McNichols R, Ivancevic MK, Stadler WM, et al. MR imaging-guided focal laser ablation for prostate cancer: phase I trial. *Radiology*. 2013;267(3):932-40. doi: 10.1148/radiol.13121652.
20. de Rienzo G, Lorusso A, Minafra P, Zingarelli M, Papapicco G, Lucarelli G, et al. Transperineal interstitial laser ablation of the prostate, a novel option for minimally invasive treatment of benign prostatic obstruction. *European Urology*. 2021;80(1):95-103. doi: 10.1016/j.eururo.2020.08.018.
21. Manenti G, Nezzo M, Ryan CP, Fraioli FR, Carreri B, Gigliotti PE, et al. Transperineal laser ablation (TPLA) with ultrasound/MRI fusion guidance in the treatment of localized radiotherapy-resistant prostate cancer. *BJR| Open*. 2023;5(1):20230042. doi: 10.1259/bjro.20230042.
22. Vogl TJ, Naguib NN, Lehnert T, Nour-Eldin N-EA. Radiofrequency, microwave and laser ablation of pulmonary neoplasms: clinical studies and technical considerations. *European journal of radiology*. 2011;77(2):346-57. doi: 10.1016/j.ejrad.2009.07.034.
23. Lindner U, Lawrentschuk N, Weersink RA, Davidson SR, Raz O, Hlasny E, et al. Focal laser ablation for prostate cancer followed by radical prostatectomy: validation of focal therapy and imaging accuracy. *European urology*. 2010;57(6):1111-4. doi: 10.1016/j.eururo.2010.03.008.
24. Stafford RJ, Shetty A, Elliott AM, Klumpp SA, McNichols RJ, Gowda A, et al. Magnetic resonance guided, focal laser induced interstitial thermal therapy in a canine prostate model. *The Journal of urology*. 2010;184(4):1514-20. doi: 10.1016/j.juro.2010.05.091.
25. Ghara M, Kundanati L, Borges RM. Nature's Swiss Army knives: ovipositor structure mirrors ecology in a multitrophic fig wasp community. *PLoS One*. 2011;6(8):e23642. doi: 10.1371/journal.pone.0023642.
26. Le Lannic J, N  non J-P. Functional morphology of the ovipositor in *Megarhyssa atrata* (Hymenoptera, Ichneumonidae) and its penetration into wood. *Zoomorphology*. 1999;119(2):73-9. doi: 10.1007/s004350050082.
27. Cerkvenik U, Van de Straat B, Gussekloo SW, Van Leeuwen JL. Mechanisms of ovipositor insertion and steering of a parasitic wasp. *Proceedings of the National Academy of Sciences*.

- 2017;114(37):E7822-E31. doi: 10.1073/pnas.1706162114.
28. Quicke D, Fitton M, Tunstead J, Ingram S, Gaitens P. Ovipositor structure and relationships within the Hymenoptera, with special reference to the Ichneumonoidea. *Journal of Natural History*. 1994;28(3):635-82. doi: 10.1080/00222939400770301.
29. Vincent J, King M. The mechanism of drilling by wood wasp ovipositors. *Biomimetics (USA)*. 1995.
30. Cerkvenik U, Dodou D, van Leeuwen JL, Gussekloo SW. Functional principles of steerable multi-element probes in insects. *Biological Reviews*. 2019;94(2):555-74. doi: 10.1111/brv.12467.
31. Ahmed T, Zhang T-t, He K-l, Bai S-x, Wang Z-y. Sense organs on the ovipositor of *Macrocentrus cingulum* Brischke (Hymenoptera: Braconidae): their probable role in stinging, oviposition and host selection process. *Journal of Asia-Pacific Entomology*. 2013;16(3):343-8. doi: 10.1016/j.aspen.2013.04.015.
32. Austin A, Browning T. A mechanism for movement of eggs along insect ovipositors. *International Journal of Insect Morphology and Embryology*. 1981;10(2):93-108. doi: 10.1016/S0020-7322(81)80015-3.
33. Cerkvenik U, Gussekloo SWS, van Leeuwen J. WUR Spotlight. 2018. [Available from: <https://weblog.wur.eu/spotlight/parasitic-wasp-inspires-advancements-in-surgery/>].
34. Frasson L, Ko S, Turner A, Parittotokkaporn T, Vincent JF, Rodriguez y Baena F. STING: a soft-tissue intervention and neurosurgical guide to access deep brain lesions through curved trajectories. *Proceedings of the Institution of Mechanical Engineers, Part H: Journal of Engineering in Medicine*. 2010;224(6):775-88. doi: 10.1243/09544119JEM663.
35. Leibinger A, Oldfield MJ, Rodriguez y Baena F. Minimally disruptive needle insertion: a biologically inspired solution. *Interface focus*. 2016;6(3):20150107. doi: 10.1098/rsfs.2015.0107.
36. Scali M, Kreeft D, Breedveld P, Dodou D. Design and evaluation of a wasp-inspired steerable needle. *Proceedings of SPIE; Portland, Oregon, United States: International Society for Optics and Photonics*; 2017. p. 1016207.
37. Scali M, Breedveld P, Dodou D. Experimental evaluation of a self-propelling bio-inspired needle in single-and multi-layered phantoms. *Scientific reports*. 2019;9(1):1-13. doi: 10.1038/s41598-019-56403-0.
38. Scali M, Pusch T, Breedveld P, Dodou D. Ovipositor-inspired steerable needle: design and preliminary experimental evaluation. *Bioinspiration & Biomimetics*. 2017;13(1):016006. doi: 10.1088/1748-3190/aa92b9.
39. Oldfield MJ, Leibinger A, Seah TET, y Baena FR. Method to reduce target motion through needle-tissue interactions. *Annals of biomedical engineering*. 2015;43(11):2794-803. doi: 10.1007/s10439-015-1329-0.
40. Parittotokkaporn T, Frasson L, Schneider A, Huq SE, Davies BL, Degenaar P, et al. Soft tissue traversal with zero net force: Feasibility study of a biologically inspired design based on reciprocal motion. *2008 IEEE International Conference on Robotics and Biomimetics*; 2009: IEEE. doi: 10.1109/ROBIO.2009.4912983.
41. Scali M. Self-propelling needles: From biological inspiration to percutaneous interventions: Delft University of Technology; 2020. doi: 10.4233/uuid:523e3e5f-08f0-4acb-ab45-abaa7ace3967.
42. ASTM. F2503. Standard practice for marking medical devices and other items for safety in the magnetic resonance environment. *ASTM International, West Conshohocken, PA*; 2013.

---

# PART 1.

## BACKGROUND





# 2

## **A Literature Review of Needle Positioning Hazards**

Published as:

Bloemberg J.\*, de Vries M.\*, van Riel L., de Reijke T., Sakes A., Breedveld P., van den Dobbelsteen J. (2024). Therapeutic prostate cancer interventions: a systematic review on pubic arch interference and needle positioning errors. *Expert Reviews on Medical Devices*, 21(7):625-641. doi: 10.1080/17434440.2024.2374761 (\*these authors have contributed equally to this work).





## **Abstract**

This study focuses on the quantification of and current guidelines on the hazards related to needle positioning in prostate cancer treatment: (1) access restrictions to the prostate gland by the pubic arch, so-called Pubic Arch Interference (PAI) and (2) needle positioning errors. Next, we propose solution strategies to mitigate these hazards. The literature search was executed in the Embase, Medline ALL, Web of Science Core Collection\*, and Cochrane Central Register of Controlled Trials databases. The literature search resulted in 50 included articles. PAI was reported in patients with various prostate volumes. The level of reported PAI varied between 0 and 22.3 mm, depending on the patient's position and the measuring method. Low-Dose-Rate Brachytherapy induced the largest reported misplacement errors, especially in the cranio-caudal direction (up to 10 mm) and the largest displacement errors were reported for High-Dose-Rate Brachytherapy in the cranio-caudal direction (up to 47 mm), generally increasing over time. Current clinical guidelines related to prostate volume, needle positioning accuracy, and maximum allowable PAI are ambiguous, and compliance in the clinical setting differs between institutions. Solutions, such as steerable needles, assist in mitigating the hazards and potentially allow the physician to proceed with the procedure.

## 2.1 Introduction

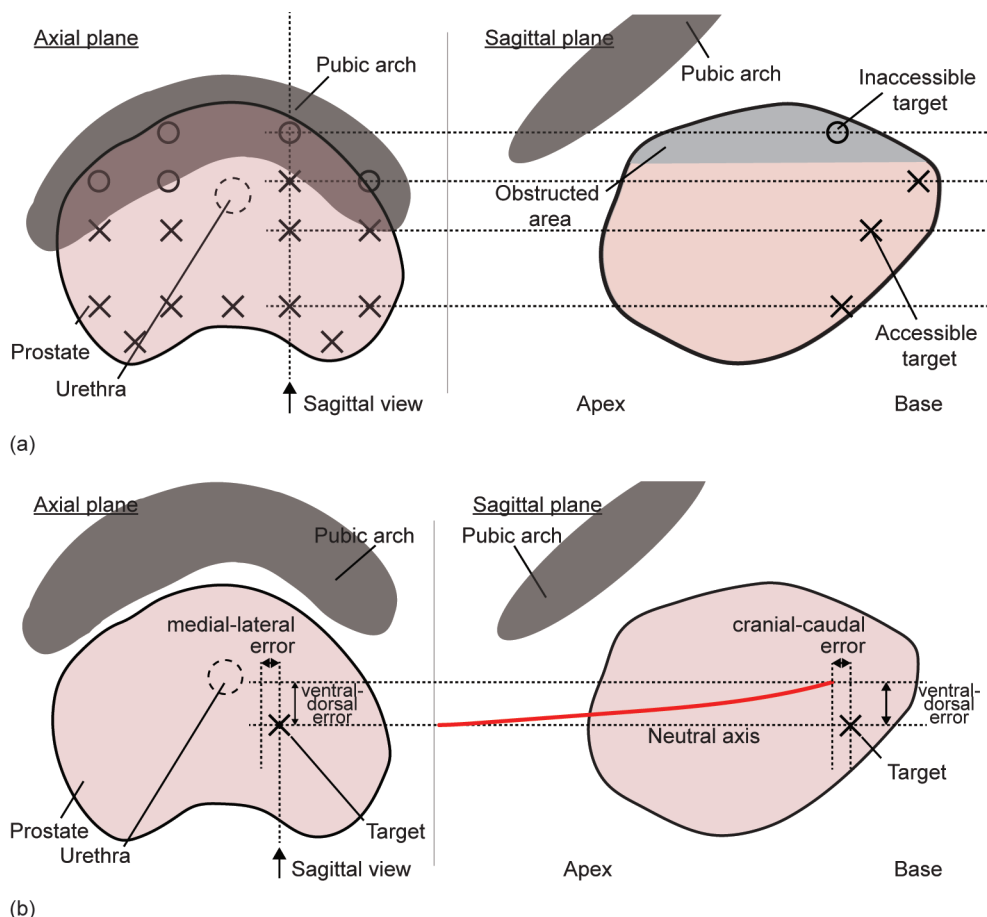
### 2.1.1 Background

Prostate cancer was the second most-diagnosed cancer in men and the fifth leading cause of cancer-related deaths worldwide in 2020 [1]. In the United States, prostate cancer was estimated to be the most-diagnosed cancer in men and the second leading cause of cancer-related deaths in 2023 [2]. When detected in an early and localized stage, treatments such as radical prostatectomy [3], external beam radiation therapy [4], or brachytherapy [5] can be performed. These are whole-gland treatment modalities and provide high rates of oncological control. This is at risk of negative side effects for the patient, such as irritative micturition, urinary incontinence, erectile dysfunction, and rectal toxicity, thereby lowering the Quality of Life (QoL) [6, 7].

Over the past decade, a trend toward focal (boost) therapies has been observed that can potentially minimize negative side effects [6-8]. For example, brachytherapy is often used as a whole-gland monotherapy, but it can be used as a focal (boost) therapy as well. Brachytherapy modalities include Low-Dose-Rate Brachytherapy (LDR BT), High-Dose-Rate Brachytherapy (HDR BT), and Pulsed-Dose-Rate Brachytherapy (PDR BT), in which radioactive sources or catheters loaded with radioactive sources are placed in the prostate for irradiation. In LDR BT, the implanted radioactive sources are left permanently within the prostate. Whereas in HDR BT and PDR BT, the radioactive sources are temporarily placed into the prostate via needles or catheters. Focal boost therapies such as brachytherapy treat the tumor with high dosages of, for example, radiation, whilst the remainder of the prostate gland is treated with a lower dose. Focal therapy is a shift from whole-gland treatment to targeting the tumor, while sparing the surrounding healthy tissue, thereby preserving genitourinary and gastrointestinal function [9]. Focal treatment modalities include e.g., brachytherapy, Focal Laser Ablation (FLA), irreversible electroporation, cryotherapy, high-intensity focused ultrasound, and photodynamic therapy. These are percutaneous procedures in which needles are guided through the perineal skin to reach the target volume for treatment. However, potential perturbations while passing intermediate structures may cause hazardous situations. This chapter provides an overview of the quantification of these hazards and the associated current guidelines, and solution strategies to mitigate these hazards.

### 2.1.2 Hazards in needle positioning

Two hazards widely reported in the literature can hamper adequate needle positioning. First, the pubic arch can restrict access to the ventrolateral part of the prostate. This affects the total needle geometry (i.e., the spatial composition of all inserted needles) in the target volume [10], as depicted in Figure 2.1a, assuming currently available rigid needles are inserted parallel to each other in the horizontal direction. This phenomenon is known as Pubic Arch Interference (PAI). Accessibility of all regions inside the target volume is a requirement in focal (boost) therapies and brachytherapy as whole-gland monotherapy to obtain homogeneity of the total



**Figure 2.1. Hazards in needle positioning.** (a) Schematic of total needle geometry in patients with Pubic Arch Interference (PAI). The planned total needle geometry, indicated in the axial plane, is based on the needle geometry of Mate *et al.* [101]. The pubic arch obstructs parts of the prostate resulting in a non-conformal total needle geometry, indicated by the light gray area in the sagittal plane, making accessible targets (X) inaccessible (O) using the transperineal approach with parallel horizontal needle trajectories (i.e., perpendicular to the transperineal template) using straight needle insertion. (b) Schematic of individual needle positioning errors in the prostate. The directions of the positioning error of the needle (red line) are shown in the axial and sagittal planes. The needle deviated from the neutral axis and did not reach the target (X).

needle geometry and to ensure an effective treatment [11]. The level of PAI indicates to what extent a homogeneous needle distribution can be achieved.

Secondly, needle positioning errors can arise from misplacement (i.e., the needle is positioned in a location different from the planned location due to unwanted needle deflections [12]) or needle displacement (i.e., the needle is shifted to a different location after positioning). Erroneous individual needle positioning induces treatment of unintended areas (Figure 2.1b), which might lead to undertreatment of tumor tissue or overtreatment of healthy tissue (e.g., urethra, bladder, rectum, and neurovascular bundle), leading to similar side effects as documented for whole-gland treatment modalities, such as irritative micturition, urinary

incontinence, erectile dysfunction, and rectal toxicity, thereby lowering the QoL [6, 7].

In this study, the term ‘hazard’ is used to refer to potential sources of harm related to transperineal needle positioning. These hazards are, in particular, (1) access restrictions to the prostate gland, i.e., PAI, and (2) needle positioning errors. Insight into the quantification of these hazards and solution strategies to mitigate them can provide information about the impact of different hazards and may give clues about how to minimize these hazards. To our knowledge, a systematic overview of the scientific literature on the quantification of the hazards related to transperineal needle positioning in prostate cancer treatments and their corresponding guidelines is not yet available. Here, we intend to fill this gap by providing a systematic overview of the quantification of these hazards. Furthermore, we propose solution strategies to mitigate these hazards.

## 2.2 Methods

### 2.2.1 Literature search

This systematic review was performed in accordance with the PRISMA guidelines. The review was registered at Protocols.io (doi: 10.17504/protocols.io.6qpvr89eplmk/v1). The literature search was executed using the Embase, Medline ALL, Web of Science Core Collection\*, and Cochrane Central Register of Controlled Trials databases and included journal articles and conference abstracts in the English language. We used tailored search terms for each database using thesaurus terms (MeSH). The search keywords of the queries were organized into three categories: (1) therapy (e.g., brachytherapy, ablation therapy, laser ablation), (2) target (e.g., prostate, prostate tumor), and (3) needles and challenges or hazards (e.g., needle, catheter, probe, pubic). The Supplementary material shows the entire search queries for the used databases in this systematic review. The publication year for the conference abstracts was limited to 2019 – 2023.

### 2.2.2 Eligibility criteria

Throughout this review, the needle is defined as the device used to puncture tissues and position the energy or radiation source in the target volume. Only interventions were included with which prostate cancer can be treated locally via the transperineal pathway without resecting the prostate, excluding articles on diagnostics, treatment of benign tumors, (partial) resection of the prostate, and prostate volume determination. Regarding the study conditions, only clinical studies were accepted, whereas pre-clinical, phantom, animal, and simulation studies were excluded. Furthermore, only studies focused on the quantitative assessment of needle positioning were accepted, excluding studies solely focused on needle design, planning, patient selection, physician learning curve, automated needle detection, functional or biological outcomes, hospitalization time, and costs. Hazards unrelated to needle positioning were excluded, such as prostate movement due to bladder filling, brachytherapy seed migration, and inter-observer variability.

### 2.2.3 Literature search results

The search yielded 3309 articles (last update December 2023). Based on the eligibility criteria, two researchers (M.V. and J.B.) independently checked the titles, abstracts, and full texts subsequently in order to avoid bias. After full-text inspection, 50 articles were identified fulfilling all eligibility criteria (Figure 2.2). To our knowledge, no validated tool exists for assessing the risk of bias in studies on the quantification of PAI and needle positioning errors. Therefore, we created a series of six parameters that can be used to orient the readers in making a judgment about the quality of the included studies (see Supplementary material). The following data of the included articles were extracted: (a) author name and year of publication, (b) treatment type, (c) number of patients, (d) imaging modality, (e) patient position during imaging, (f) prostate volume, (g) PAI or needle positioning errors measured, and (h) time between implantation and error measurement.

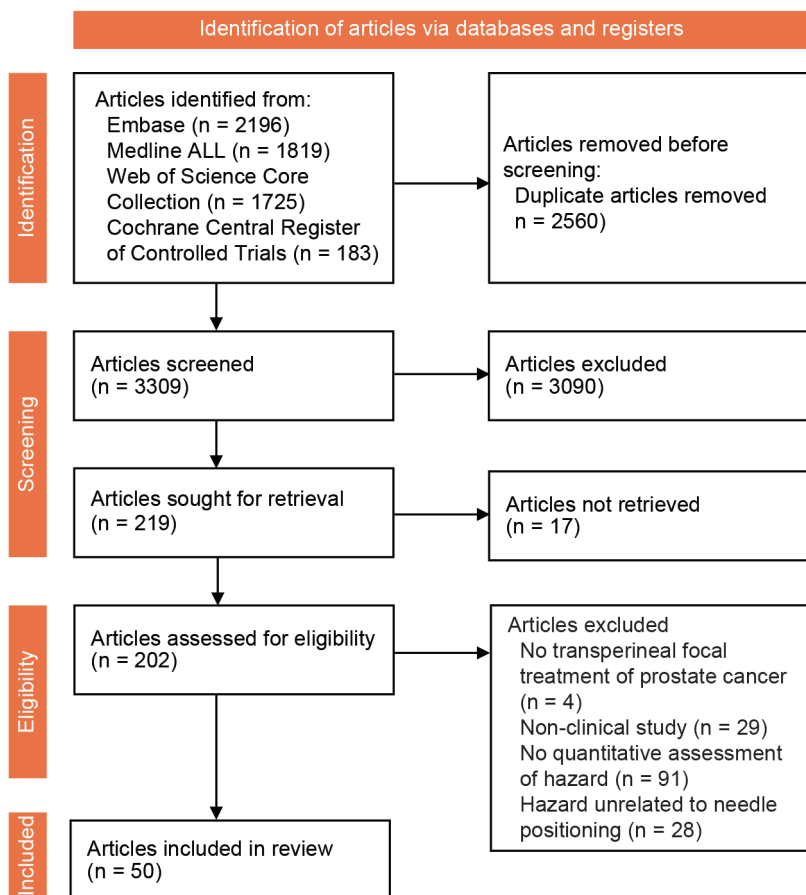


Figure 2.2. PRISMA flow diagram of the literature selection method.

## 2.3 Results

### 2.3.1 Quantification of hazards

#### *Pubic arch interference*

PAI has been assessed in fifteen included studies, as shown in Table 2.1. Eleven studies described the level of prostate obstruction by the pubic arch and fifteen studies reported the incidence of PAI for various prostate volumes. Sejpal *et al.* [13] researched the largest patient population, with 243 patients, and reported that 47 patients (19.3%) showed PAI during needle insertion.

PAI quantification is generally performed on TransRectal UltraSound (TRUS)-Computed Tomography (CT) fusion imaging or Magnetic Resonance Imaging (MRI) scans, with the patient in supine position, whereas needle implantation is performed under TRUS guidance with the patient in dorsal lithotomy position. Solely CT is less commonly used in clinical practice, due to its poor soft tissue contrast. The patient's position significantly influenced the level of observed PAI, ranging from 0 mm, if total clearance between the pubic arch and the prostate was observed, to 22.3 mm [13]. Tincher *et al.* [10] studied the level of PAI for seven patients after CT scans in both lithotomy and supine position. The authors reported that the patient's posture change from supine to lithotomy position decreased the level of PAI by 5 mm [10]. Next to posture change, the used imaging modality also induced discrepancies. Martin *et al.* [14] assessed PAI on TRUS, CT, and MRI scans. They found a linear correlation between PAI on the CT and MRI scans with the patient in supine position, whereas 75% of patients had larger values for PAI on CT compared to MRI. They reported PAI on CT and MRI of  $2.9 \pm 0.6$  mm and  $2.0 \pm 0.6$  mm (average  $\pm$  standard error), respectively. PAI on the TRUS scans with the patient in lithotomy position was  $0.6 \pm 0.5$  mm, which was different from both CT and MRI ( $p < 0.06$ ). Strang *et al.* [15] reported that nine patients appeared to have PAI on CT, whereas only four of these nine patients had PAI on TRUS. The change in patients' posture from supine to lithotomy position and imaging modality reduced obstruction by the pubic arch by 11.8 mm on average. In contrast, Wallner *et al.* [16] showed a decrease of only 0.4 mm.

#### *Needle positioning error*

Thirty-five included studies documented quantitative needle positioning errors. Tables 2.2 and 2.3 show the reported misplacement and displacement errors, respectively. The majority of the studies (80%, 28/35) documented the error for an HDR BT treatment, 11% (4/35) for an LDR BT treatment, 6% (2/35) for a PDR BT treatment, and 3% (1/35) for an FLA treatment. The included studies reported needle misplacement and displacement assessed on anatomical images of the patient but used different procedures and methodologies, such as (1) whether to change patient posture to allow for a specific imaging method and (2) varying imaging modalities, time intervals, and reference markers.

Table 2.1. Overview of studies that evaluated Pubic Arch Interference (PAI).

Level of PAI [mm]	Number of patients	Patients with PAI [%]	Imaging modality	Patient position	Prostate volume [cc]	Treatment	Reference
$\bar{x} = 9.5 \pm 6.9$ (0 – 22.3)	27	85.2	MRI	Supine	$\bar{x} = 92.3 \pm 38.0$ (48.0 – 178.9)	HDR BT	de Vries <i>et al.</i> [86]
(0 – 15.1)	40	25	MRI	Supine	$\bar{x} = 63.8 \pm 18.4$	LDR BT	Zheng <i>et al.</i> [38]
$\bar{x} = 2.0 \pm 0.6$ (0 – 12.5)	41	80.5	MRI	Supine			
$\bar{x} = 2.9 \pm 0.6$ (0 – 12.5)	41	82.9	CT	Supine		LDR BT	Martin <i>et al.</i> [14]
$\bar{x} = 0.6 \pm 0.5$ (0 – 4)	41	46.3	TRUS (5 mm)	Lithotomy	$\bar{x} = 32.6 \pm 2.3$		
(0 – > 5)	21	14.3	TRUS (5 mm)	Lithotomy	$\bar{x} = 28.5$ $\bar{x} = 28.1$ (17.6 – 42.2)		
(0 – > 5)	21	28.6	CT (3 mm)	Lithotomy		LDR BT	Fukada <i>et al.</i> [41]
(0 – > 5)	21	23.8	CT + TRUS fusion	Lithotomy	$\bar{x} = 29.5$ $\bar{x} = 28.8$ (19.0 – 39.9)		
(0 – 10)	5	100	TRUS (5 mm)	Lithotomy	< 50	LDR BT	Ryu <i>et al.</i> [42]
n/a	145	5.5	TRUS (7.5 MHz)	Lithotomy	$\bar{x} = 40.0$ (33.8 – 86.0)	LDR BT	Gibbons <i>et al.</i> [35]
$\bar{x} = 6$ (0 – 10)	243	19.3	CT (5 mm)	Supine			
	243		TRUS (5 mm)	Lithotomy	$\bar{x} = 44.7 \pm 11.1^*$	LDR BT	Sejpal <i>et al.</i> [13]
n/a	40	40	CT (5 mm)	n/a	$\bar{x} = 56 \pm 17$	LDR/HDR BT	Nickers <i>et al.</i> [87]
n/a	50	6	TRUS (7.5 MHz, 5 mm)	Lithotomy	$\bar{x} = 32$ (17 – 52)	LDR BT	Henderson <i>et al.</i> [40]
$\bar{x} = 12.2 \pm 3.4$ (8 – 20)	9	100	CT	Supine	$\bar{x} = 30.9 \pm 9.8$		
$\bar{x} = 0.4 \pm 3.6$ (0 – 7)	14	28.6	TRUS (7 MHz, 5 mm)	Lithotomy	$\bar{x} = 39.0 \pm 18.1$	LDR BT	Strang <i>et al.</i> [15]
$\bar{x} = 12.7$ (10 – 21)	7	100	CT (5 mm)	Supine	$\bar{x} = 34.6 \pm 11.4$ (17 – 48)		
$\bar{x} = 7.8$ (6 – 12)	7	100	CT (5 mm)	Lithotomy		BT	Tincher <i>et al.</i> [10]
(0 – 13)*	21	71.4*	CT (5 mm)	Supine			
	33	n/a	TRUS (6 MHz, 5 mm)	Lithotomy	$\bar{x} = 57^*$ (50 – 95)*	LDR BT	Wang <i>et al.</i> [88]
$\bar{x} = 0$ (0 – 20)	97	46.4*	CT (5 mm)	Supine			
	97		TRUS (6 MHz)	Lithotomy	$\bar{x} = 36$ (15 – 131)	LDR BT	Bellon <i>et al.</i> [39]
$\bar{x} = 2.2 \pm 3.5^*$ (0 – 10)	16	62.5	CT (5 mm)	Supine			
$\bar{x} = 1.8 \pm 4.1^*$ (0 – 10)	16	50	TRUS (6 MHz)	Lithotomy	$\bar{x} = 36$ (22 – 55)	LDR BT	Wallner <i>et al.</i> [16]
n/a	54	5.6	TRUS (4 or 5 MHz)	Lithotomy	$\leq 60$	HDR BT	Borghede <i>et al.</i> [52]

For each study, the following information is reported: the level of PAI [mm], number of patients, percentage of patients with PAI [%], imaging modality and patient position used for the assessment of prostate volume, prostate volume [cc], treatment, and reference. Clearance between the pubic arch and the prostate is reported as 0 mm PAI.  $\bar{x}$  = median,  $\bar{x}$  = average  $\pm$  standard deviation, and (..) = range.

BT = Brachytherapy, CT = Computed Tomography, HDR BT = High-Dose-Rate Brachytherapy, LDR BT = Low-Dose-Rate Brachytherapy, MRI = Magnetic Resonance Imaging, n/a = not available, TRUS = Transrectal Ultrasound,

\* If not specified in the manuscript, a best approximation was made based on the information in the graphs.

Table 2.2. Overview of studies that evaluated needle misplacement in transperineal prostate interventions.

Needle misplacement $\pm$ SD (range) [mm] (measurement method)								
Cranio-caudal	Ventral-dorsal	Medial-lateral	Number of patients	Imaging modality	Treatment	Patient posture change (pre-, intra-, postoperative)	Time [h]	Reference
$\bar{x} = 3.8 \pm 0.2$ (AM)	$\bar{x} = 1.5 \pm 0.1$ (AM)	$\bar{x} = 1.3 \pm 0.1$ (AM)	15	TRUS (6 MHz)	LDR BT	No change	n/a	Jamaluddin <i>et al.</i> [89]
$\bar{x} = 1.1$ (AM)	$\bar{x} = 1.8$ (AM)	$\bar{x} = 0^a$ (AM)	10	MRI (1.5T)	FLA, robotic implantation	No change	0.15	Cepek <i>et al.</i> [23]
n/a	> 2 (MF)	> 4 (MF)	5	TRUS (6.5 MHz), X-ray	LDR BT, robotic implantation	n/a	1	Fichtinger <i>et al.</i> [51]
n/a	$\bar{x} = 1.8 \pm 0.6^b$ (AM)	$\bar{x} = 1.8 \pm 0.6^b$ (AM)	30	TRUS (1 mm)	HDR BT	n/a	n/a	Szlag <i>et al.</i> [90]
n/a	$\bar{x} = 3$ (0 – 10) <sup>b</sup> (AM)	$\bar{x} = 3$ (0 – 10) <sup>b</sup> (AM)	10	MRI (0.5T)	LDR BT	No change	0.08 – 0.17	Cormack <i>et al.</i> [91]
$\bar{x} = 4.5$ (IOF)	$\bar{x} = 2.2$ (IOF)	$\bar{x} = 2.0$ (IOF)	10	X-ray	LDR BT	n/a – lithotomy – supine	72	Taschereau <i>et al.</i> [92]

For each study, the following information is reported: needle misplacement divided into cranio-caudal, ventral-dorsal, and medial-lateral directions, number of patients, imaging modality used for the assessment of misplacement, treatment, patient position pre-, intra-, and postoperatively, time between implantation and error measurement, and reference.  $\bar{x}$  = median,  $\bar{x}$  = average  $\pm$  standard deviation, and (..) = range.

MF = Marker Frames attached to needle guide, AM = Anatomical Marker (e.g., bone, urethra, ventral rectal wall, urethra, prostate base), FM = Fiducial Marker (e.g., gold marker), IOF = Isocentric Orthogonal Films, CT = Computed Tomography, FLA = Focal Laser Ablation, HDR BT = High-Dose-Rate Brachytherapy, LDR BT = Low-Dose-Rate Brachytherapy, MRI = Magnetic Resonance Imaging, n/a = not available or not applicable, TRUS = Transrectal Ultrasound, US = Ultrasound, <sup>a</sup>No statistically significant misplacement, <sup>b</sup>Ventral-dorsal and medial-lateral errors were measured together as a single error.

Table 2.3. Overview of studies that evaluated needle displacement in transperineal prostate interventions.

Needle displacement $\pm$ SD (range) [mm] (measurement method)										
Cranio-caudal			Ventral-dorsal	Medial-lateral	Number of patients	Imaging modality	Treatment (number of fractions)	Patient posture change	Time [h]	Reference
<1 fraction	1-2 fraction	> 2 fractions	<1 fraction	<1 fraction						
$\bar{x} = 0.9 \pm 0.4$ (FM)	n/a	n/a	n/a	n/a	20	TRUS	HDR BT (1)	n/a	n/a	David <i>et al.</i> [93]
n/a	n/a	n/a	$\bar{x} = 1.0$ (-1.7 – 1.8) (AM)	$\bar{x} = 0.9$ (-0.9 – 1.5) (AM)	10	TRUS	HDR BT (1)	n/a	0.18	Wu <i>et al.</i> [94]
n/a	$\bar{x} = 2.2 \pm 1.8$ (IM)	$\bar{x} = 5.0 \pm 3.0^f$ (IM)	n/a	n/a	24	MRI (1.5T)	HDR BT (2)	Supine – lithotomy – supine	1 – 3	Buus <i>et al.</i> [24]
$\bar{x} = 3.8 \pm 3.2$ (FM)	n/a	n/a	n/a	$\bar{x} = 1.6 \pm 2.1$ (FM)	2	X-ray	HDR BT (2)	No change	0.25	Smith <i>et al.</i> [28]
n/a	$\bar{x} = 0.9$ (0 – 5.5) (during fraction) (AM)	n/a	$\bar{x} = 0.5$ (0 – 2.1) (during fraction) (AM)	$0.6$ (0 – 2.9) (during fraction) (AM)	17	MRI (1.5T)	HDR BT, self-an-choring catheter (1)	No change	n/a	Maenhout <i>et al.</i> [33]

continued on next page



Table 2.3. Continued.

Needle displacement $\pm$ SD (range) [mm] (measurement method)										
Cranio-caudal			Ventral-dorsal	Medial-lateral	Number of patients	Imaging modality	Treatment (number of fractions)	Patient posture change	Time [h]	Reference
<1 fraction	1-2 fraction	> 2 fractions	<1 fraction	<1 fraction						
n/a	n/a	n/a	$\bar{x} = 0.8 \pm 0.9$ (AM)	$\bar{x} = 0.0 \pm 1.8$ (AM)	7	TRUS (1 mm)	HDR BT (2)	No change	1 – 2	Carrara <i>et al.</i> [22]
n/a	(0-18) <sup>c</sup> (FM)		n/a	n/a	162	X-ray	HDR BT (4)	n/a	0 – 36	Aluwini <i>et al.</i> [46]
n/a	$\bar{x} = 8.7 \pm 3.3$ ( $2.7 \pm 1.1 - 14.7 \pm 1.7$ ) (FM)		n/a	n/a	20	CT (2 mm)	HDR BT (4)	n/a – lithotomy – supine	0 – 24	Reynés-Llompart <i>et al.</i> [21]
n/a	$\bar{x} = 0.97 \pm 0.76^c$ (FM)	n/a	$\bar{x} = 0.97 \pm 0.76^c$ (1 – 2 fraction) (FM)	$\bar{x} = 0.97 \pm 0.76^c$ (1 – 2 fraction) (FM)	33	CT (1 mm)	HDR BT (2)	n/a	6	Peddada <i>et al.</i> [95]
n/a	$\bar{x} = -0.22 \pm 0.2^c$ (FM)		$\bar{x} = -0.02 \pm 0.06^c$ (>1 fraction) (FM)	$\bar{x} = 0.01 \pm 0.04^c$ (>1 fraction) (FM)	23	CT (2 mm)	PDR BT, self-anchoring catheter (24)	n/a	2.2 – 48	Dinkla <i>et al.</i> [96]
$\bar{x} = 6 \pm 4$ (FM)	$\bar{x} = 12 \pm 6$ (FM)	$\bar{x} = 12 \pm 6$ (FM)	n/a	n/a	30	CT (1.25 mm)	HDR BT (5)	n/a	6 – 54	Kawakami <i>et al.</i> [97]
n/a	$\bar{x} = 5.8 \pm 1.9$ (-13 – 12) (FM, AM)	n/a	n/a	n/a	13	CT (2 mm)	HDR BT (3,4)	n/a – lithotomy – supine	0 – 48	Huang <i>et al.</i> [17]
n/a	$\bar{x} = 3.5$ (-14 – 13) (AM method) $\bar{x} = 2.3$ (-18 – 9) (FM method)	n/a	n/a	n/a	26	CT (1.25 mm)	HDR BT (1,2)	n/a – lithotomy – supine	36 – 672	Kovalchuk <i>et al.</i> [20]
n/a	$\bar{x} = 4.3 \pm 2.7$ (0.3 – 10) (FM)	$\bar{x} = 5.9 \pm 3.6$ (-2.3 – 12.9) (FM)	n/a	n/a	30	CT (3 mm)	HDR BT (7)	n/a	21 – 69	Takenaka <i>et al.</i> [53]
n/a	$\bar{x} = 5.1$ (1.9 – 10.1) (FM)	n/a	n/a	n/a	15	CT (3 mm)	HDR BT (2)	n/a	24	Foster <i>et al.</i> [98]
n/a	$\bar{x} = 12.6$ (0.6 – 24.6) (FM)	n/a	n/a	n/a	22	CT, X-ray	HDR BT (2)	n/a	24	Fox <i>et al.</i> [31]
$\bar{x} = 11.1 \pm 7.6$ (FM)	n/a	n/a	n/a	n/a	20	CT (3 mm, 1.5-mm interval), X-ray	HDR BT (1)	n/a – lithotomy – supine	2 – 3	Holly <i>et al.</i> [19]
0 – 0.5 (AM)	0 – 0.4 (AM)	n/a	0 – 1.3 <sup>b</sup> , 0 – 1.0 <sup>b</sup> (1-2 fraction) (AM)	0 – 1.3 <sup>b</sup> , 0 – 1.0 <sup>b</sup> (1-2 fraction) (AM)	25	TRUS	HDR BT (1)	n/a	0.83 – 1.2	Milickov <i>et al.</i> [99]
$\bar{x} = 7.5$ (-2.9 – 23.9) (FM)	n/a	n/a	n/a	n/a	25	CT (3 mm), X-ray	HDR BT (2)	n/a – lithotomy – supine	1.4 – 6.1	Whitaker <i>et al.</i> [18]

continued on next page

Table 2.3. Continued.

Needle displacement $\pm$ SD (range) [mm] (measurement method)										
Cranio-caudal			Ventral-dorsal	Medial-lateral	Number of patients	Imaging modality	Treatment (number of fractions)	Patient posture change	Time [h]	Reference
<1 fraction	1-2 fraction	> 2 fractions	<1 fraction	<1 fraction						
$\bar{x} = 4.5 \pm 1.7$ (FM)	$\bar{x} = 5.6 \pm 3.6$ (FM)	$\bar{x} = 6.4 \pm 4.2$ (FM)	n/a	n/a	91	CT (3 mm), X-ray	HDR BT (3)	n/a	0 – 48	Tiong <i>et al.</i> [47]
n/a	$\bar{x} = 7$	(-14 – 24) (FM)	n/a	n/a	64	CT (3 mm)	HDR BT (4,7,9)	n/a	72 – 120	Yoshida <i>et al.</i> [100]
n/a	$\bar{x} = 7.9$ (0 – 21) (AM)	$\bar{x} = 3.8$ (0 – 25.5) (AM)	n/a	n/a	20	CT (3 mm)	HDR BT (3)	n/a	21 – 28	Simnor <i>et al.</i> [54]
n/a	$\bar{x} = 2.7$ (-6.0 – 13.5) (AM) $\bar{x} = 5.4$ (-3.75 – 18.0) (FM)	n/a	n/a	n/a	10	CT (3 mm)	HDR BT (2)	n/a	24	Kim <i>et al.</i> [60]
$\bar{x} = 1.0$ (0-6) (day 2), $\bar{x} = 1.2$ (0-6) (day 3) (FM)	n/a	n/a	n/a	n/a	43	CT (2 mm)	PDR BT, self-anchoring catheter (46)	n/a	24 – 48	Pieters <i>et al.</i> [30]
n/a	$\bar{x} = 2$ (0 – 4) (FM, AM)	$\bar{x} = 10$ (5 – 23) (FM, AM)	n/a	n/a	50	CT (2 & 5 mm)	HDR BT (4)	n/a – lithotomy – frog-leg	3 – 28	Mullokandov <i>et al.</i> [25]
n/a	$\bar{x} = 11.5$ (0 – 47) (IM)	n/a	n/a	n/a	20	CT (5 mm)	HDR BT (2)	n/a	18 – 24	Hoskin <i>et al.</i> [32]
n/a	$\bar{x} = 16 \pm 6$ , $\bar{x} = 18$ (AM) $\bar{x} = 15 \pm 4$ , $\bar{x} = 12$ (FM)	n/a	n/a	n/a	47	X-ray	HDR BT (4)	n/a	2 – 48	Pellizzon <i>et al.</i> [27]
n/a	$\bar{x} = 20$ (FM, AM)	$\bar{x} = 4$ (FM, AM)	n/a	n/a	10	TRUS (7.5 MHz, 5 mm), X-ray	HDR BT (4)	No change	6 – 36	Martinez <i>et al.</i> [29]
n/a	$\bar{x} = 6.8$ (0 – 31.4) (FM), $\bar{x} = 8.3$ (0 – 25.6) (AM)	$\bar{x} = 3.9$ (0 – 10.4) (FM) $\bar{x} = 4.2$ (0 – 9.1) (AM)	n/a	n/a	96	X-ray	HDR BT (4)	n/a	5 – 40	Damore <i>et al.</i> [26]

For each study, the following information is reported: needle displacement in cranio-caudal direction before the first fraction, between the first and second fraction, and after the second fraction, needle displacement in ventral-dorsal and medial-lateral direction before the first fraction unless otherwise indicated, number of patients imaging modality, treatment, patient position pre-, intra-, and postoperatively, time between implantation and error measurement, reference.  $\bar{x}$  = median,  $\bar{x}$  = average or mean, SD = Standard Deviation, and (..) = range.

AM = Anatomical Marker (e.g., bone, urethra, ventral rectal wall, urethra, prostate base), FM = Fiducial Marker (e.g., gold maker), IM = Ink Markers on the patient's skin or measurement of the needle outside the patient's body, CT = Computed Tomography, HDR BT = High-Dose-Rate Brachytherapy, MRI = Magnetic Resonance Imaging, n/a = not available or not applicable, PDR BT = Pulsed-Dose-Rate Brachytherapy, SD = Standard Deviation, TRUS = Transrectal Ultrasound, <sup>a</sup>No statistically significant displacement, <sup>b</sup>Ventral-dorsal and medial-lateral errors were measured together as a single error, <sup>c</sup>Cranio-caudal, ventral-dorsal, and medial-lateral errors were measured together as a single error, <sup>d</sup>Cranio-caudal and medial-lateral errors were measured together as a single error, <sup>e</sup>Total error between all fractions was documented, <sup>f</sup>Total error between 1st and 3rd fractions were documented.

The patient's position regularly changed between the preoperative, intraoperative, and postoperative procedure [17-21], potentially influencing needle misplacement and displacement. Both Carrara *et al.* [22] and Cepek *et al.* [23] reported a single position (i.e., lithotomy position) for the entire duration of the procedure to minimize movement of the prostate and the tumor, and Cepek *et al.* [23] documented misplacement errors after needle insertions with symmetrical bevel-tip needles during FLA procedures of 1.1 mm, 1.8 mm, and 0 mm in the cranio-caudal, ventral-dorsal, and medial-lateral directions, respectively. They discussed that the error was caused mainly by needle deflection due to the initial skin puncture and the heterogeneity of tissue [23]. Carrara *et al.* [22] documented mean needle displacement of 0.8 mm and 0.0 mm in the ventral-dorsal and medial-lateral directions, respectively. In contrast, in the study by Buus *et al.* [24], patients were placed in supine position for the first MRI scan, in lithotomy position during implantation phase, and again in supine position for the second MRI scan to measure the error prior to treatment. The authors reported mean cranio-caudal needle displacements of 2.2 mm and 5.0 mm between the first and second HDR BT fractions and after the second HDR BT fraction, respectively. Another patient position transition was described by Mullokandov *et al.* [25]. In their study, the patients were taken out of the lithotomy position and placed in a frog-leg position (i.e., flexing the hips and abducting the legs) after implantation. The authors reported mean cranio-caudal needle displacements of 2 and 10 mm between the first and second HDR BT fraction and after the second HDR BT fraction, respectively.

Quantification of the error was performed using different imaging modalities, time intervals, and reference markers such as metal markers, bone anatomy, or other implanted needles [26, 27]. Solely Smith *et al.* [28] measured the error along the entire needle length, whereas in other studies the end position of the distal tip was evaluated. Most studies used CT to measure the error (54%, 19/35), whereas some studies used X-ray (29%, 10/35), TRUS (20%, 7/35), MRI (11%, 4/35), or a combination of multiple imaging modalities (14%, 5/35). The time between the reference image and imaging after implantation ranged from nine minutes to four weeks.

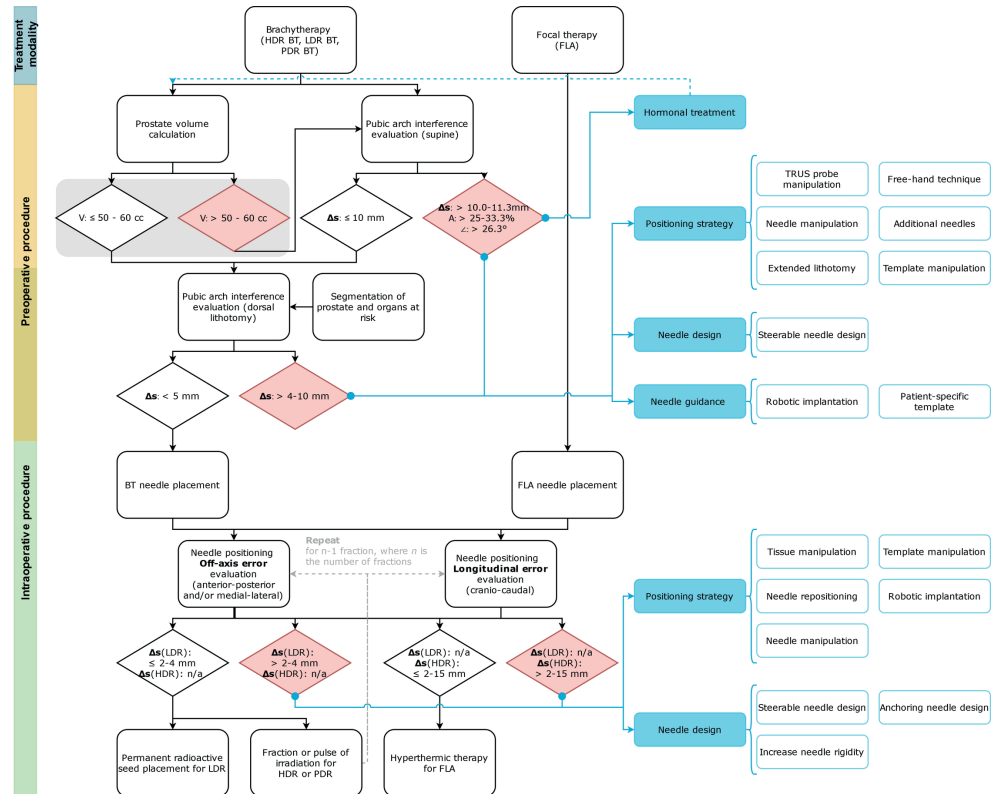
Displacement errors were only reported for HDR BT and PDR BT. Most studies documented displacement in the cranio-caudal direction (i.e., 93%, 27/29), of which the largest average error of 20 mm was documented by Martinez *et al.* [29], who used 1.9-mm diameter flexible plastic needles with metal stylets during HDR BT. The authors stated that despite the needles being attached to the template, which was sutured to the perineal skin, the needles displaced up to 31 mm in the caudal direction [29]. They stated that the elasticity of perineal tissues was most likely the cause of needle displacement [29].

Pieters *et al.* [30] developed unique PDR BT catheters with an umbrella anchoring mechanism at the tip to fixate the catheter inside the prostate gland. The authors stated that self-anchoring catheters showed an absolute mean displacement of 1 mm [30] compared to mean displacements of 11 to 13 mm in HDR BT of conventional needles [19, 31, 32]. The

self-anchoring catheters were also used for HDR BT by Maenhout *et al.* [33], who reported an average three-dimensional (3D) error of 1.3 mm.

### 2.3.2 Clinical guidelines

Figure 2.3 provides a proposed decision-making process integrated into the current clinical workflow so that physicians can decide on the continuation of the procedure. This process includes published clinical guidelines retrieved from the included studies related to prostate volume, PAI, and needle positioning errors. Exceeding a limit may result in patient exclusion or requires a solution to make the patient eligible again. In case of experiencing PAI during HDR or PDR BT treatment, one solution is to optimize the radiation dose by considering the actual positions of the implanted BT catheters. The radiation dose is determined by the dwell



**Figure 2.3. Decision tree for conformity to treatment plan including clinical guidelines.** Rounded rectangle shapes indicate procedural steps. Diamond shapes indicate the limits. Exceeding a limit (red diamond shape) requires a solution (blue rectangle shape). Blue rectangle shapes indicate solutions for the procedural steps that the blue line with the dot grasps, the blue-outlined rectangle shapes indicate examples of the solutions. Note that the preoperative procedure (indicated in yellow) and the intraoperative procedure (indicated in green) partially overlap as the approaches differ between institutions.  $V$  = prostate volume,  $\Delta s$  = orthogonal distance from the inner surface of the pubic arch to the ventral border of the prostate in mm,  $A$  = obstructed area by the pubic arch compared to total prostate cross-section in %,  $\angle$  = angle between the pubic symphysis and ventral border of the prostate. The gray block overlaid on the limits for prostate volume indicates that the guideline for prostate volume is superfluous according to new brachytherapy guidelines.

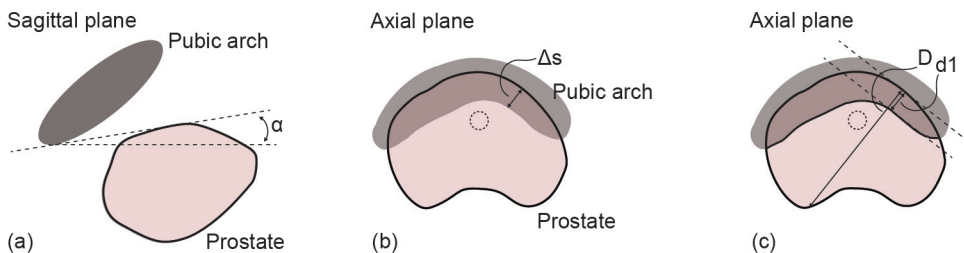
positions, i.e., the specific locations along the catheter where the radioactive sources reside, and the corresponding dwell times, i.e., the amount of time the radioactive sources reside at their dwell positions [34]. By increasing the dwell times of the catheters inserted as ventrally as possible and thus increasing the extension of the 100% isodose line, which defines the region where the radiation dose is equal to the prescribed dose, toward the ventral prostate areas, it becomes feasible to sufficiently irradiate the entire prostate also in case of PAI occurrence. However, a drawback is the potential creation of high-dose areas, which could impact nearby healthy Organs At Risk (OARs).

#### Prostate volume

Prostate volume is traditionally used as an indicator for the occurrence of PAI and is calculated on preoperative scans using the elliptical approximation: Prostate volume =  $\pi / 6$  (height x width x length) of the prostate [35]. The American Brachytherapy Society (ABS) guidelines state that focal (boost) treatment of a prostate volume of > 60 cc is technically more challenging as PAI is more prevalent in enlarged prostates. Thus, the ABS reported a prostate volume of > 60 cc as a relative contraindication for prostate brachytherapy [36]. In contrast, the revised Groupe Européen de Curiethérapie and the European Society for Radiotherapy & Oncology (GEC-ESTRO) Advisory Committee for Radiation Oncology Practice (ACROP) prostate brachytherapy guidelines, published in 2022, state that a prostate gland of > 50 – 60 cc is no longer a contraindication for prostate brachytherapy as larger prostates can be successfully implanted if there is minimal PAI [37]. In some institutions, borderline cases with a prostate volume of 55 to 60 cc are generally better examined in accordance with the GEC-ESTRO ACROP guidelines. The prostate and the OARs are segmented on MRI or CT and digitally rotated to estimate the level of PAI in lithotomy position as described by de Vries *et al.* [13]. However, no guidelines are reported for adequate rotation related to posture change from supine to lithotomy position.

#### Pubic arch interference

Prior to needle implantation, the level of PAI is measured on an MRI or CT scan with the patient in supine position to estimate the risk of obstruction during needle implantation with the patient in lithotomy position. Figure 2.4 indicates various methods to quantify PAI.



**Figure 2.4. Measuring methods of Pubic Arch Interference (PAI).** (a) Angle ( $\alpha$ ) between pubic symphysis and ventral border of prostate, (b) Orthogonal distance ( $\Delta s$ ) from inner surface of pubic arch to ventral border of the prostate and (c) Prostate diameter blockage ( $d1$ ) by the pubic arch compared to total prostate diameter ( $D$ ).

Firstly, the angle of PAI can be calculated in the sagittal plane by drawing two lines on the scan; one horizontal line through the pubic symphysis and one line connecting the most ventral point of the prostate with the most dorsal point of the pubic arch at the pubic symphysis (Figure 2.4a). Angle  $\alpha$  between the pubic symphysis and ventral border of the prostate is the angle that can be related to a boundary value above which PAI is likely to occur. Zheng *et al.* [38] retrospectively analyzed MRI scans of 40 prostate cancer patients and suggested a boundary value of  $\alpha = 26.3^\circ$  to predict the occurrence of PAI in lithotomy position. They reported that the angle  $\alpha$  of PAI was statistically correlated with the occurrence of PAI ( $p < 0.01$ ).

Secondly, besides the angle of PAI, the distance of the obstruction between pubic arch and prostate can be assessed (Figure 2.4b). Multiple studies reported a threshold of 10.0 mm obstruction in supine position, assessed by overlaying the narrowest part of the pubic arch over the largest contour of the prostate in the axial plane and measured from the point of the prostate, which was at the greatest perpendicular distance from the caudal edge of the pubic arch [13, 39]. Zheng *et al.* [38] suggested the boundary value of 11.3 mm as a reliable predictor of intraoperative PAI. They calculated PAI by using two parallel lines in sagittal plane through the pubic symphysis and reported a statistical correlation between distance and PAI ( $p < 0.01$ ). When the distance exceeded 11.3 mm PAI was reported to be excessive.

Lastly, Bellon *et al.* [39] and Henderson *et al.* [40] overlaid the largest prostate cross-section on the narrowest portion of the pubic arch. The percentage of overlapping prostate diameter indicates PAI (Figure 2.4c). Bellon *et al.* [39] and Henderson *et al.* [40] considered 25% and 33% obstruction of the prostate diameter in the axial plane as an indication of excessive PAI, respectively. These approximations were not based on a rigorous study. Some studies assessed PAI based on TRUS visualizations with the patient in lithotomy position. This position is associated with less PAI and larger accessibility of the prostate due to pelvic rotation than supine position [10]. Strang *et al.* [15] excluded patients with  $> 4$  mm PAI, whereas Fukada *et al.* [41] expected excessive PAI if  $> 5$  mm obstruction was shown, and Ryu *et al.* [42] excluded patients with  $> 10$  mm PAI.

#### *Needle positioning error*

Needle misplacement errors are affected by the needle-tissue interaction forces [43], needle design [44], and the implantation procedure [45]. On the other hand, needle displacement errors depend on the duration of treatment and perturbations between the needle positioning and treatment phase [31]. In HDR BT and PDR BT, the patient receives multiple treatment fractions, whereas, in LDR BT and FLA, the patient receives a single dose. Multiple treatment fractions increase the time between needle positioning and treatment, which is associated with an increase in positioning error.

Several studies described correction of the needle position after the detection of misplacement or displacement. Aluwini *et al.* [46] reported that 43.8% of the HDR BT patients required at least one correction of the needle position of more than 3 mm, mostly in the cranial direction. Whitaker *et al.* [18] showed that 67% of the needles had a displacement in

the cranio-caudal direction of at least 5 mm that required correction, and Tiong *et al.* [47] stated that up to three needles had to be corrected in cranio-caudal direction per fraction in HDR BT to lower the percentage of fractions from 82.3% to 12.2% in which displacements over 3 mm occurred. Buus *et al.* [24] reported that needle displacements of 3 and 5 mm introduced a decrease of 5 and 10% in target coverage for HDR BT, respectively. The authors proposed a 3D-positioning error threshold of 3 mm, calculated between HDR BT fractions, from the needle tip position relative to the corresponding transperineal template opening. For a single-fraction treatment with a dose of  $\geq 15$  Gy, they stated that displacement should be less than 2 mm due to the absence of the averaging dose effect of multiple fractions. Kolkman-Deurloo *et al.* [48] and Tiong *et al.* [47] analyzed the effect of needle displacements in HDR BT on X-ray scans along the longitudinal axis in simulation studies and recommended corrections of needles with an error exceeding 3 mm. It should be noted that the location of the needles in the transperineal template dictated the impact of the error on the OARs, as the needles in the dorsal rows were close to the rectum and the needles in the ventral rows were close to the urethra. Kolkman-Deurloo *et al.* [48] discussed that needles in the second and third dorsal rows of the transperineal template generally have larger impact on the dose coverage than needles in the ventral rows of the template because of the higher dwell weights (i.e., the relative contribution of a needle to the total administered dose in brachytherapy). Ventral rows of the template are less critical due to the lower dwell weights provided such that the dose to the urethra is not too high.

Poder *et al.* [49] reported that 3D-source positioning errors in HDR BT plans could be up to 2 to 5 mm while avoiding significant ( $> 10\%$ ) changes in the dose volume histogram of the prostate. Similarly, Mason *et al.* [50] investigated needle positioning errors and reported a threshold of approximately 2 – 3 mm based on a minimum value required for error detection and avoiding unnecessary countermeasures assessed by a physician. Nevertheless, the effect of the needle error still depended on the location of the needle in the target volume, the direction of the positioning error, and the weights of the dwells. Poder *et al.* [49] found that displacement of heavily weighted catheters, mainly around the urethra, resulted in under-treatment of the central region. Regarding the direction of the error, they stated that errors of 3 mm in the cranial-caudal direction (i.e., longitudinal errors) were more sensitive than the off-axis errors, lateral errors were more sensitive than medial errors, and cranial errors had more impact on the dose plan compared to caudal errors. For off-axis errors, Fichtinger *et al.* [51] reported a limit of 2 mm, whereas Borghede *et al.* [52] reported a limit of 3-4 mm, both for LDR BT procedures. For longitudinal errors, limits were reported for HDR BT procedures, ranging from 2 mm [24] to 15 mm [53], whilst most studies reported a limit of 3 mm [17, 46, 47] or 5 mm [18, 26, 27, 54]. This shows that reported limits for needle positioning errors depend, amongst others, on the location of the needle and the direction of the needle positioning error.

## 2.4 Discussion

### 2.4.1 Main findings

This work provided an overview of the quantification of hazards related to needle positioning in transperineal treatment procedures of localized prostate cancer. We distinguished between the total needle geometry required in the target volume and the individual needle positioning. Firstly, access restrictions to the prostate gland by the pubic arch affect the total needle geometry as the ventrolateral part of the prostate cannot be reached considering the conventional linear trajectories. Obstructions of the prostate up to 22.3 mm were reported for various prostate volumes.

Secondly, individual needle positioning non-conformal to the treatment plan can potentially affect the treatment efficacy. Needle positioning errors were subdivided into mis- and displacement. Needle misplacement was reported for LDR BT, HDR BT, and FLA procedures, in which for LDR BT largest errors were reported, especially in the cranio-caudal direction. Needle displacement was only reported for HDR BT and PDR BT as these techniques involve fractionated doses, whereas LDR BT and FLA are single-dose treatments. Displacements were reported in all directions. The largest displacement was measured in the cranio-caudal direction, and generally increased over time.

Reported clinical guidelines indicate limits regarding prostate volume, PAI, and needle positioning error that, when exceeded, demand for patient exclusion from the procedure or solutions to minimize the impact on the treatment. However, these guidelines are general and ambiguous, and compliance in the clinical setting differs between institutions.

### 2.4.2 Limitations

The evaluation of the needle position and the level of PAI depend on (1) patient posture change, (2) imaging modality and specifications, (3) moment of assessment, (4) implemented assessment method, and (5) the assessor. Firstly, patient posture change from supine to lithotomy position introduces discrepancies, and the use of multiple imaging modalities can introduce imaging co-registration inaccuracies [39]. Buus *et al.* [24] reported that their average MRI-US co-registration error was 0.52 mm with a maximum of 0.95 mm. They stated that organ motion induced by patient posture change affected the outcomes. This is substantiated by Yamoah *et al.* [55], who revealed that preoperative planning for LDR BT resulted in poorer biochemical control and higher urinary toxicity compared to interventions with intraoperative planning using solely TRUS in lithotomy position.

Secondly, the imaging modality and specifications contribute to uncertainties in the quantitative measurements. CT slice thickness introduces an uncertainty of the needle position because of partial volume artifacts. Kovalchuk *et al.* [20] considered uncertainty in needle tip determination of 0.63 mm as this was half the slice thickness of their CT slices. Kim *et al.* [56] reported that an increased CT slice thickness increased the obtained dose error after simulations with random shifting of HDR BT catheters. The mean dose error was 0.7% for



2-mm slices, 1.1% for 3-mm slices, and 1.7% for 5-mm slices. Regarding MRI, Ballester *et al.* [57] described that the voxel size can change delineation due to blurring [57]. Concerning TRUS, Fedorov *et al.* [58] described that TRUS images have poor contrast at the apex and base of the prostate and can affect the image due to the TRUS probe compressing the prostate gland. Furthermore, ultrasound has a resolution of 200  $\mu\text{m}$ , resulting in the lack of tumor visualization because of limited sensitivity [59].

Thirdly, time can be a confounding factor as the observed error depends on the moment of evaluation. Kim *et al.* [60] described that maximum catheter displacement occurred in the 12 hours after the first fraction for HDR BT, whereas Taschereau *et al.* [12] reported misplacement of the needles 72 hours after positioning, which makes these measurements potentially, to a greater extent, subjected to the influence of edema and organ motion.

Fourthly, the assessment method influences the analysis. For example, PAI quantification can be performed by three different methods, and needle positioning errors can be assessed using bone anatomy, metal markers, or other implanted needles as reference markers. Kim *et al.* [60] reported an average discrepancy of 2.7 mm in needle displacement between measurements using the ischial bone or two gold markers as reference markers.

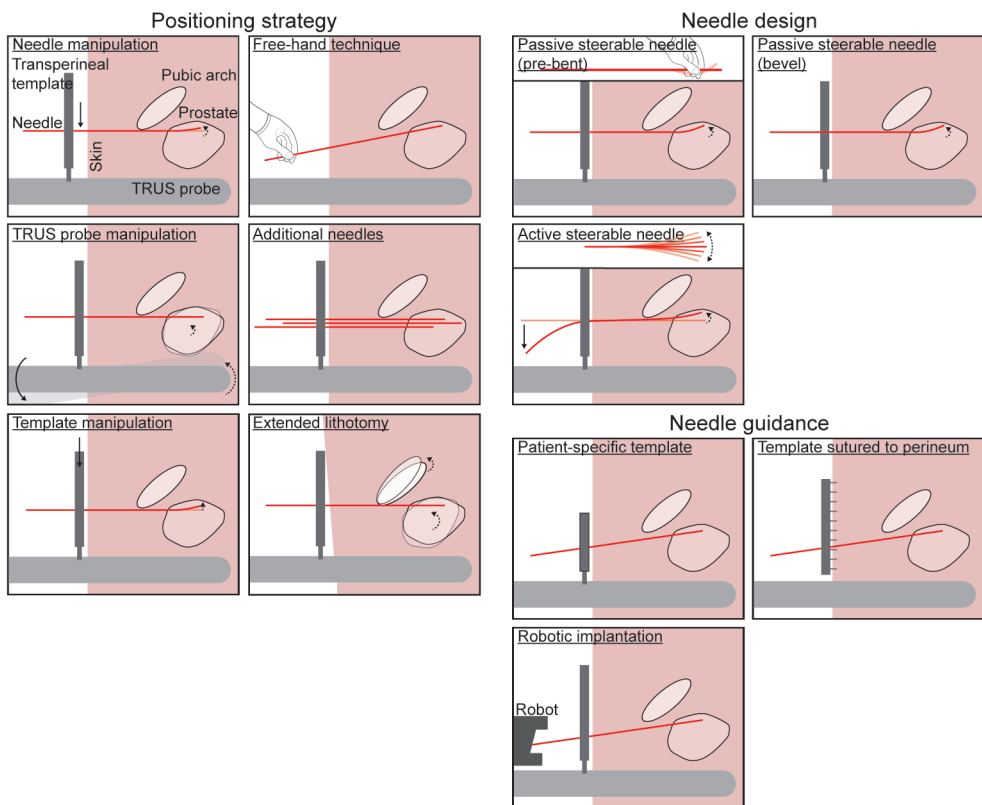
Lastly, inter-observer variability plays a role in the assessment. Kim *et al.* [60] reported a difference in displacement error detection of  $1.0 \pm 0.9$  mm with a maximum difference of 5.0 mm between two observers. Therefore, the error threshold should be large enough to be detected, considering all the above-stated inaccuracies, and low enough to avoid a significant impact on the treatment plan.

### 2.4.3 Solution strategies

To operate below the upper limit of the guidelines for needle positioning, countermeasures can be implemented to enable continuation in line with the treatment plan (Figure 2.3). Minimizing PAI can be achieved in several ways, subdivided into four pillars: (1) neo-adjuvant hormonal therapy, (2) positioning strategy, (3) needle design, and (4) needle guidance. Improving needle positioning accuracy can be related to (1) positioning strategy and (2) needle design.

Clinical institutions often use hormonal therapy, such as Androgen Deprivation Therapy (ADT), to downsize the prostate gland and reduce the risk of PAI. For example, Kucway *et al.* [61] showed a volume reduction of the prostate of 33% after 3 - 4 months of ADT. Traditionally, this therapy is performed prior to the brachytherapy treatment in patients with prostate volumes of 50 - 60 cc or with observed excessive PAI [13, 40, 61]. Sejpal *et al.* [13] reported that 27% of the patients received ADT due to an enlarged prostate or PAI > 10 mm. On the other hand, this therapy can induce severe side effects for the patient, such as erectile dysfunction, hot flushes, increased cardiovascular morbidity, and consequently a lower QoL [62-65]. The ABS, therefore, concluded that ADT is only recommended in patients with observed PAI, as no benefit was shown from adding ADT to prostate brachytherapy for low-risk and favorable intermediate-risk patients without PAI [66].

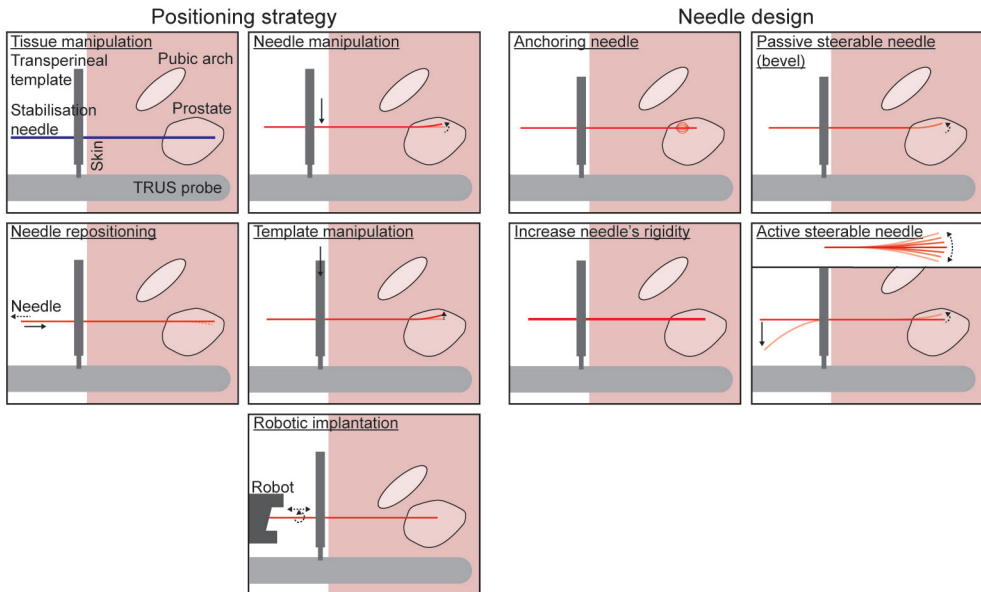
Despite preoperative PAI assessment and the use of ADT in many patients, PAI can still occur during needle implantation. Recently, intraoperative imaging techniques with the patient in the lithotomy position (i.e., needle insertion position), such as intraoperative on-site Cone-Beam CT (CBCT) [67, 68] and mobile CT [69], have gained importance in adaptive brachytherapy. Figure 2.5 shows techniques to obtain a conformal total needle geometry if PAI occurs [15]. Regarding positioning strategies, the patient's lithotomy position can be extended, the TRUS probe, the transperineal template or the needle can be manipulated [70], and the needles can be positioned using a free-hand technique without the use of a transperineal template or guide [35, 71]. However, the free-hand technique is reported to be difficult and requires experience from the physician, as buckling of the needle can occur due to the absence of the transperineal template for guidance [35]. Concerning needle guidance strategies, the needles can be obliquely positioned using a robotic device for angulated ap-



**Figure 2.5. Overview of solution strategies to improve total needle geometry in prostate with Pubic Arch Interference (PAI).** The positioning strategy can be altered by needle manipulation, a free-hand positioning technique, Transrectal Ultrasound (TRUS) probe manipulation, additional needles, template manipulation, or positioning the patient in the extended lithotomy position. The needle design can be changed by developing a passive steerable needle (e.g., with a pre-bent or a bevel-shaped tip) or an active steerable needle. The needle guidance can be adapted by using a patient-specific template, a template sutured to the patient's perineum instead of attached to the TRUS probe, or robotic implantation of the needle.

proaches [72], a template sutured to the patient's perineum instead of attached to the TRUS probe, or a patient-specific template [24]. For needle design-related solutions, a needle with an asymmetric tip can be steered using the asymmetric needle-tissue force distribution on the needle tip [44], whereas occasionally the distal tip of a needle is bent in an adequate angle by the physician to circumvent the pubic arch. On the other hand, asymmetric needle tip steering depends on needle-tissue interaction forces, making needle control challenging, and a substantial on-site modification in the design of the medical device potentially increases the risk of a needle positioning error. Such designs are referred to as passive steerable needles [73]. De Vries *et al.* [74] proposed using steerable needles with tip control, known as active steerable needles, to overcome PAI and optimize the dose distribution. Podder *et al.* [75] described that steerable needles could create curvatures conform the prostate geometry while reducing the total number of needles required, thereby minimizing edema and potentially improving treatment outcomes.

Needle positioning accuracy can be improved by changing the needle design or altering the positioning strategy, as indicated in Figure 2.6. Off-axis errors can be minimized by means of steerable needles that counteract perturbations or robotic devices that minimize insertion or friction forces, thus theoretically reducing needle deflection. Bloemberg *et al.* [76] described a wasp-inspired, self-propelling, steerable needle that could incorporate an optical fiber for FLA. To reduce longitudinal needle displacement errors, the prostate can be



**Figure 2.6. Overview of solution strategies to improve transperineal needle positioning accuracy.** The needle positioning accuracy can be improved by altering the positioning strategy or changing the needle design. The positioning strategy can be altered by tissue manipulation, needle manipulation, needle repositioning, template manipulation, or robotic implantation. The needle design can be changed by developing an anchoring needle, a passive steerable needle (e.g., with a bevel-shaped tip), or an active steerable needle.

stabilized, the needle can be anchored in the transperineal template sutured to the perineal skin, or the needle design can be adjusted to accomplish needle anchoring once they are inside the prostate [30]. Taschereau *et al.* [12] used two additional stabilization needles but observed no significant influence on needle displacement. Self-anchoring catheters were described by Pieters *et al.* [30] and Maenhout *et al.* [33], with which external fixation in the transperineal template became unnecessary and needle displacement was minimized.

An overarching solution for needle misplacement and displacement errors is repositioning the needles by advancing or retracting them or completely re-implanting them; however, this induces additional tissue trauma [77-79]. In current clinical practice, imaging is often performed after a treatment fraction to evaluate the longitudinal error of the needles, after which displaced needles are advanced again. Keyes *et al.* [78] described seven patients in which the needles for LDR BT were re-implanted to ensure coverage of the underdosed areas of the prostate. All patients had excellent dosimetry after the re-implantation procedure [78]. Hughes *et al.* [79] stated that re-implantation increased the prostate dose metrics D90 (i.e., the minimum dose received by 90% of the target volume) and V100 (the percentage of the target volume that received at least 100% of the prescription dose [80]) from 49 Gy to 201 Gy and from 46% to 98%, respectively. Noteworthy is the absence of studies related to needle positioning in ablative therapies compared to brachytherapy, which could be explained by the fact that these relatively new ablative therapies are often still in the clinical trial phase [81]. In contrast, brachytherapy has been performed since the early twentieth century [82, 83].

#### 2.4.4 Five-year view

Future research should be conducted to better relate hazards of needle positioning in transperineal treatment procedures of localized prostate cancer and clinical outcomes. With this, congruent and adequate guidelines related to PAI and needle positioning errors can be implemented. We expect a trend toward novel devices with which challenges in needle positioning can be mitigated, including (1) robotically controlled needles that can be obliquely inserted to improve the accessibility of the target volume while providing very stable and accurate needle guidance [72] and (2) active steerable needles that allow for positioning along curved trajectories to optimize total needle geometry with high positioning accuracy. These solutions should be combined with high-resolution imaging methods like MRI for precise target volume identification and needle guidance. In the scientific literature, steerable needles and brachytherapy robots compatible with MRI are already upcoming; however, these are not common in clinical practice yet [84, 85].

## 2.5. Conclusion

This systematic review of the scientific literature examines the hazards and guidelines associated with needle positioning during transperineal prostate procedures. Current clinical guidelines regarding prostate volume, needle positioning accuracy, and maximum allowable

PAI are ambiguous. Thus, a case-specific approach is recommended to avoid a suboptimal procedure or patient exclusion. Steerable needles can offer intraoperative flexibility in needle placement and allow for the correction of perturbations while overcoming PAI to ensure an optimized treatment.

## Supplementary material

The appendices underlying this study are available at doi: 10.1080/17434440.2024.2374761.

## Acknowledgements

The authors wish to thank Wichor M. Bramer from the Erasmus MC Medical Library for developing and updating the search strategies.

## References

1. Sung H, Ferlay J, Siegel RL et al. Global cancer statistics 2020: GLOBOCAN estimates of incidence and mortality worldwide for 36 cancers in 185 countries. *CA: a cancer journal for clinicians*. 2021;71(3):209-249. doi: 10.3322/caac.21660.
2. Siegel RL, Miller KD, Wagle NS, Jemal A. Cancer statistics, 2023. *Ca Cancer J Clin*. 2023;73(1):17-48. doi: 10.3322/caac.21763.
3. Wilt TJ, Brawer MK, Jones KM et al. Radical prostatectomy versus observation for localized prostate cancer. *New England Journal of Medicine*. 2012;367(3):203-213. doi: 10.1056/NEJMoa1113162.
4. Zhu Z, Zhang J, Liu Y, Chen M, Guo P, Li K. Efficacy and toxicity of external-beam radiation therapy for localised prostate cancer: a network meta-analysis. *British journal of cancer*. 2014;110(10):2396-2404. doi:10.1038/bjc.2014.197.
5. Martin JM, Handorf EA, Kutikov A et al. The rise and fall of prostate brachytherapy: use of brachytherapy for the treatment of localized prostate cancer in the National Cancer Data Base. *Cancer*. 2014;120(14):2114-2121. doi: 10.1002/cncr.28697.
6. Jain A, Deguet A, Iordachita I et al. Intra-operative 3D guidance and edema detection in prostate brachytherapy using a non-isocentric C-arm. *Med Image Anal*. 2012;16(3):731-743. doi: 10.1016/j.media.2010.07.011.
7. Frank SJ, Pisters LL, Davis J, Lee AK, Bassett R, Kuban DA. An assessment of quality of life following radical prostatectomy, high dose external beam radiation therapy and brachytherapy iodine implantation as monotherapies for localized prostate cancer. *The Journal of urology*. 2007;177(6):2151-2156. doi:10.1016/j.juro.2007.01.134.
8. Lodeizen O, de Bruin M, Eggen S et al. Ablation energies for focal treatment of prostate cancer. *World journal of urology*. 2019;37(3):409-418. doi: 10.1007/s00345-018-2364-x.
9. De La Rosette J, Ahmed H, Barentsz J et al. Focal therapy in prostate cancer-report from a consensus panel. *J Endourol*. 2010;24(5):775-780. doi: 10.1089/end.2009.0596.
10. Tincher SA, Kim RY, Ezekiel MP et al. Effects of pelvic rotation and needle angle on pubic arch interference during transperineal prostate implants. *Int J Radiat Oncol Biol Phys*. 2000;47(2):361-363. doi: 10.1016/S0360-3016(00)00434-X.
11. Jamema SV, Saju S, Shetty UM, Pallad S, Deshpande D, Shrivastava S. Dosimetric comparison of inverse optimization with geometric optimization in combination with graphical optimization for HDR prostate implants. *Journal of Medical Physics/Association of Medical Physicists of India*. 2006;31(2):89. doi: 10.4103/0971-6203.26694.
12. Taschereau R, Pouliot J, Roy J, Tremblay D. Seed misplacement and stabilizing needles in

- transperineal permanent prostate implants. *Radiother Oncol.* 2000;55(1):59-63. doi: 10.1016/S0167-8140(00)00162-6.
13. Sejpal SV, Sathiaseelan V, Helenowski IB et al. Intra-operative pubic arch interference during prostate seed brachytherapy in patients with CT-based pubic arch interference of  $\leq 1$  cm. *Radiother Oncol.* 2009;91(2):249-254. doi: 10.1016/j.radonc.2009.02.006.
  14. Martin GV, Pugh TJ, Mahmood U et al. Permanent prostate brachytherapy pubic arch evaluation with diagnostic magnetic resonance imaging. *Brachytherapy.* 2017;16(4):728-733. doi: 10.1016/j.brachy.2017.02.001.
  15. Strang JG, Rubens DJ, Brasacchio RA, Yu Y, Messing EM. Real-time US versus CT determination of pubic arch interference for brachytherapy. *Radiology.* 2001;219(2):387-393. doi: 10.1148/radiology.219.2.r01ma37387.
  16. Wallner K, Ellis W, Russell K, Cavanagh W, Blasko J. Use of TRUS to predict pubic arch interference of prostate brachytherapy. *Int J Radiat Oncol Biol Phys.* 1999;43:583-585. doi: 10.1016/S0360-3016(98)00459-3.
  17. Huang Y, Miller B, Doemer A et al. Online correction of catheter movement using CT in high-dose-rate prostate brachytherapy. *Brachytherapy.* 2013;12(3):260-266. doi: 10.1016/j.brachy.2012.08.008.
  18. Whitaker M, Hruba G, Lovett A, Patanjali N. Prostate HDR brachytherapy catheter displacement between planning and treatment delivery. *Radiother Oncol.* 2011;101:490-494. doi: 10.1016/j.radonc.2011.08.004.
  19. Holly R, Morton GC, Sankrecha R et al. Use of cone-beam imaging to correct for catheter displacement in high dose-rate prostate brachytherapy. *Brachytherapy.* 2011;10(4):299-305. doi: 10.1016/j.brachy.2010.11.007.
  20. Kovalchuk N, Furutani KM, MacDonald OK, Pisansky TM. Dosimetric effect of interfractional needle displacement in prostate high-dose-rate brachytherapy. *Brachytherapy.* 2012;11, 111-118. doi: 10.1016/j.brachy.2011.05.006.
  21. Reynés-Llompart G, Pino F, Modolell I et al. Impact of prostate catheter displacement in inverse planning-simulated annealing and geometric optimization. *Brachytherapy.* 2016;15(2):112-117. doi: 10.1016/j.brachy.2015.10.003.
  22. Carrara M, Tenconi C, Mazzeo D et al. Study of the correlation between rectal wall in vivo dosimetry performed with MOSkins and implant modification during TRUS-guided HDR prostate brachytherapy. *Radiation Measurements.* 2017;106:385-390. doi: 10.1016/j.radmeas.2017.03.016.
  23. Cepek J, Lindner U, Ghai S et al. Mechatronic system for in-bore MRI-guided insertion of needles to the prostate: An in vivo needle guidance accuracy study. *J Magn Reson Imaging.* 2015;42(1):48-55. doi: 10.1002/jmri.24742.
  24. Buus S, Lizondo M, Hokland S et al. Needle migration and dosimetric impact in high-dose-rate brachytherapy for prostate cancer evaluated by repeated MRI. *Brachytherapy.* 2018;17(1):50-58. doi: 10.1016/j.brachy.2017.08.005.
  25. Mullokandov E, Gejerman G. Analysis of serial CT scans to assess template and catheter movement in prostate HDR brachytherapy. *Int J Radiat Oncol Biol Phys.* 2004;58(4):1063-1071. doi: 10.1016/j.ijrobp.2003.08.020.
  26. Damore SJ, Syed AMN, Puthawala AA, Sharma A. Needle displacement during HDR brachytherapy in the treatment of prostate cancer. *Int J Radiat Oncol Biol Phys.* 2000;46(5):1205-1211. doi: 10.1016/S0360-3016(99)00477-0.
  27. Pellizzon ACA, Salvajoli JV, Novaes PERS, Maia MAC, Ferigno R, Fogaroli RC. Needle displacement during high-dose-rate afterloading brachytherapy boost and conventional external beam radiation therapy for initial and local advanced prostate cancer. *Urol Int.* 2003;70(3):200-204. doi: 10.1159/000068775.
  28. Smith RL, Hanlon M, Panettieri V et al. An integrated system for clinical treatment verification of HDR prostate brachytherapy combining source tracking with pretreatment imaging. *Brachytherapy.* 2018;17(1):111-121. doi: 10.1016/j.brachy.2017.08.004.

29. Martinez AA, Pataki I, Edmundson G, Sebastian E, Brabbins D, Gustafson G. Phase II prospective study of the use of conformal high-dose-rate brachytherapy as monotherapy for the treatment of favorable stage prostate cancer: A feasibility report. *Int J Radiat Oncol Biol Phys.* 2001;49(1):61-69. doi: 10.1016/S0360-3016(00)01463-2.
30. Pieters BR, van der Grient JNB, Blank LECM, Koedooder K, Hulshof MCCM, de Reijke TM. Minimal displacement of novel self-anchoring catheters suitable for temporary prostate implants. *Radiother Oncol.* 2006;80(1):69-72. doi: 10.1016/j.radonc.2006.06.014.
31. Fox CD, Kron T, Leahy M et al. Interfraction patient motion and implant displacement in prostate high dose rate brachytherapy. *Med Phys.* 2011;38(11):5838-5843. doi: 10.1118/1.3641865.
32. Hoskin PJ, Bownes PJ, Ostler P, Walker K, Bryant L. High dose rate afterloading brachytherapy for prostate cancer: Catheter and gland movement between fractions. *Radiother Oncol.* 2003;68(3):285-288. doi: 10.1016/S0167-8140(03)00203-2.
33. Maenhout M, van der Voort van Zyp JRN, Borot de Battisti M et al. The effect of catheter displacement and anatomical variations on the dose distribution in MRI-guided focal HDR brachytherapy for prostate cancer. *Brachytherapy.* 2018;17(1):24-30 (2018). doi: 10.1016/j.brachy.2017.04.239.
34. Dickhoff LR, Kerkhof EM, Deuzeman HH, Creutzberg CL, Alderliesten T, Bosman PA. Adaptive objective configuration in bi-objective evolutionary optimization for cervical cancer brachytherapy treatment planning. In: *Proceedings of the Genetic and Evolutionary Computation Conference.* 2022;1173-1181.
35. Gibbons EP, Smith RP, Beriwal S, Krishna K, Benoit RM. Overcoming pubic arch interference with free-hand needle placement in men undergoing prostate brachytherapy. *Brachytherapy.* 2009;8(1):74-78.
36. Davis BJ, Horwitz EM, Lee WR et al. American Brachytherapy Society consensus guidelines for transrectal ultrasound-guided permanent prostate brachytherapy. *Brachytherapy.* 2012;11(1):6-19. doi: 10.1016/j.brachy.2011.07.005.
37. Henry A, Pieters BR, Siebert FA, Hoskin P. GEC-ESTRO ACROP prostate brachytherapy guidelines. *Radiotherapy and Oncology.* 2022;167:244-251. doi: 10.1016/j.radonc.2021.12.047.
38. Zheng Y, Wu J, Chen S, Liu Y, Zhang G. Predicting pubic arch interference in permanent prostate brachytherapy based on the specific parameters derived from nuclear magnetic resonance imaging. *J Contemp Brachytherapy.* 2018;10(5):405-410. doi: 10.5114/jcb.2018.79247.
39. Bellon J, Wallner K, Ellis W, Russell K, Cavanagh W, Blasko J. Use of pelvic CT scanning to evaluate pubic arch interference of transperineal prostate brachytherapy. *Int J Radiat Oncol Biol Phys.* 1999;43(3):579-581. doi: 10.1016/S0360-3016(98)00466-0.
40. Henderson A, Laing RW, Langley SEM. Identification of pubic arch interference in prostate brachytherapy: Simplifying the transrectal ultrasound technique. *Brachytherapy.* 2003;2(4):240-245. doi: 10.1016/j.brachy.2003.11.001.
41. Fukada J, Shigematsu N, Nakashima J, Ohashi T, Kawaguchi O, Oya M. Predicting pubic arch interference in prostate brachytherapy on transrectal ultrasonography-computed tomography fusion images. *J Radiat Res.* 2012;53(5):753-759. doi: 10.1093/jrr/rrs020.
42. Ryu B, Bax J, Edirisinge C et al. Prostate brachytherapy with oblique needles to treat large glands and overcome pubic arch interference. *Int J Radiat Oncol Biol Phys.* 2012;83:1463-1472. doi: 10.1016/j.ijrobp.2011.10.012.
43. van Gerwen DJ, Dankelman J, van den Dobbelsteen JJ. Needle-tissue interaction forces—A survey of experimental data. *Medical engineering & physics.* 2012;34(6):665-680. doi: 10.1016/j.medengphy.2012.04.007.
44. Misra S, Reed KB, Douglas AS, Ramesh K, Okamura AM. Needle-tissue interaction forces for bevel-tip steerable needles. In: *2008 2nd IEEE RAS & EMBS International Conference on Biomedical Robotics and Biomechatronics.* IEEE. 2008. 224-231.
45. Wan G, Wei Z, Gardi L, Downey DB, Fenster A. Brachytherapy needle deflection evaluation and correction. *Med Phys.* 2005;32:902-909. doi: 10.1118/1.1871372.



46. Aluwini S, Busser WMH, Baartman LEA et al. Fractionated high-dose-rate brachytherapy as monotherapy in prostate cancer: Does implant displacement and its correction influence acute and late toxicity? *Brachytherapy*. 2016;15(6):707-713. doi: 10.1016/j.brachy.2016.05.008.
47. Tiong A, Bydder S, Ebert M et al. A Small Tolerance for Catheter Displacement in High-Dose Rate Prostate Brachytherapy is Necessary and Feasible. *Int J Radiat Oncol Biol Phys*. 2010;76(4):1066-1072. doi: 10.1016/j.ijrobp.2009.03.052.
48. Kolkman-Deurloo IKK, Roos MA, Aluwini S. HDR monotherapy for prostate cancer: A simulation study to determine the effect of catheter displacement on target coverage and normal tissue irradiation. *Radiother Oncol*. 2011;98:192-197. doi: 10.1016/j.radonc.2010.12.009.
49. Poder J, Carrara M, Howie A, Cutajar D, Bucci J, Rosenfeld A. Derivation of in vivo source tracking error thresholds for TRUS-based HDR prostate brachytherapy through simulation of source positioning errors. *Brachytherapy*. 2019;18(5):711-719. doi: 10.1016/j.brachy.2019.05.001.
50. Mason J, Henry A, Bownes P. Error detection thresholds for routine real time in vivo dosimetry in HDR prostate brachytherapy. *Radiother Oncol*. 2020;149:38-43. doi:10.1016/j.radonc.2020.04.058.
51. Fichtinger G, Fiene JP, Kennedy CW et al. Robotic assistance for ultrasound-guided prostate brachytherapy. *Med Image Anal*. 2008;12:535-545. doi: 10.1016/j.media.2008.06.002.
52. Borghede G, Hedelin H, Holmäng S, Johansson KA, Sernbo G, Mercke C. Irradiation of localized prostatic carcinoma with a combination of high dose rate iridium-192 brachytherapy and external beam radiotherapy with three target definitions and dose levels inside the prostate gland. *Radiother Oncol*. 1997;44:245-250. doi: 10.1016/S0167-8140(97)00122-9.
53. Takenaka T, Yoshida K, Ueda M et al. Assessment of daily needle applicator displacement during high-dose-rate interstitial brachytherapy for prostate cancer using daily CT examinations. *J Rad Res*. 2012;53:469-474. doi: 10.1269/jrr.11168.
54. Simnor T, Li S, Lowe G et al. Justification for inter-fraction correction of catheter movement in fractionated high dose-rate brachytherapy treatment of prostate cancer. *Radiother Oncol*. 2009;93(2):253-258. doi: 10.1016/j.radonc.2009.09.015.
55. Yamoah K, Eldredge-Hindy HB, Zaorsky NG et al. Large prostate gland size is not a contraindication to low-dose-rate brachytherapy for prostate adenocarcinoma. *Brachytherapy*. 2014;13(5):456-464. doi: 10.1016/j.brachy.2014.04.003.
56. Kim Y, Hsu IC, Lessard E, Vujic J, Pouliot J. Dosimetric impact of prostate volume change between CT-based HDR brachytherapy fractions. *Int J Radiat Oncol Biol Phys*. 59, 1208-1216 (2004).
57. Ballester MAG, Zisserman AP, Brady M. Estimation of the partial volume effect in MRI. *Medical Image Analysis*. 2002;6(4):389-405. doi: 10.1016/S1361-8415(02)00061-0.
58. Fedorov A, Khallaghi S, Sánchez CA et al. Open-source image registration for MRI-TRUS fusion-guided prostate interventions. *International journal of computer assisted radiology and surgery*. 2015;10(6):925-934. doi: 10.1007/s11548-015-1180-7.
59. Klotz CL. Can high resolution micro-ultrasound replace MRI in the diagnosis of prostate cancer? *European urology focus*. 2020;6(2):419-423. doi: 10.1016/j.euf.2019.11.006.
60. Kim Y, Hsu IC, Pouliot J. Measurement of craniocaudal catheter displacement between fractions in computed tomography-based high dose rate brachytherapy of prostate cancer. *J Appl Clin Med Phys*. 2007;8(4):1-13. doi: 10.1120/jacmp.v8i4.2415.
61. Kucway R, Vicini F, Huang R, Stromberg J, Gonzalez J, Martinez A. Prostate volume reduction with androgen deprivation therapy before interstitial brachytherapy. *J Urol*. 2002;167(6):2443-2447. doi: 10.1016/S0022-5347(05)65001-X.
62. Press RH, Morgan TM, Cutrell PK et al. Patient-reported health-related quality of life outcomes after HDR brachytherapy treatment from small (<60 cc) and large (≥60 cc) prostate glands. *Brachytherapy*. 2019;18:13-21. doi: 10.1016/j.brachy.2018.08.009.
63. Kopp RP, Marshall LM, Wang PY et al. The burden of urinary incontinence and urinary bother among elderly prostate cancer survivors. *European Urology*. 2013;64(4):672-679 (2013). doi: 10.1016/j.eururo.2013.03.041.



64. Saigal CS, Gore JL, Krupski TL, Hanley J, Schonlau M, Litwin MS. Androgen deprivation therapy increases cardiovascular morbidity in men with prostate cancer. *Cancer: Interdisciplinary International Journal of the American Cancer Society*. 2007;110(7):1493-1500. doi:10.1002/cncr.22933.
65. Basaria S, Lieb J, Tang AM et al. Long-term effects of androgen deprivation therapy in prostate cancer patients. *Clinical endocrinology*. 2002;56(6):779-786. doi: 10.1046/j.1365-2265.2002.01551.x.
66. Keyes M, Merrick G, Frank SJ, Grimm P, Zelefsky MJ. Use of Androgen Deprivation Therapy with Prostate Brachytherapy, A Systematic Literature Review. *Brachytherapy*. 2017;16(2):245. doi: 10.1016/j.brachy.2016.11.017.
67. Karius A, Strnad V, Lotter M, Kreppner S, Bert C. First clinical experience with a novel, mobile cone-beam CT system for treatment quality assurance in brachytherapy. *Strahlentherapie und Onkologie*. 2022;198(6):573-581. doi: 10.1007/s00066-022-01912-7.
68. Karius A, Karolczak M, Strnad V, Bert C. Technical evaluation of the cone-beam computed tomography imaging performance of a novel, mobile, gantry-based X-ray system for brachytherapy. *Journal of Applied Clinical Medical Physics*. 2022;23(2):e13501. doi: 10.1002/acm2.13501.
69. Chernavsky NE, Morcos M, Wu P, Viswanathan AN, Siewerdsen JH. Technical assessment of a mobile CT scanner for image-guided brachytherapy. *Journal of applied clinical medical physics*. 2019;20(10):187-200. doi: 10.1002/acm2.12738.
70. Stone NN, Stock RG. Prostate brachytherapy in patients with prostate volumes  $\geq 50$  cm<sup>3</sup>: Dosimetric analysis of implant quality. *Int J Radiat Oncol Biol Phys*. 2000;46:1199-1204. doi: 10.1016/S0360-3016(99)00516-7.
71. Roy JN, Wallner KE, Chiu-Tsao ST, Anderson LL, Ling CC. CT-based optimized planning for transperineal prostate implant with customized template. *Int J Radiat Oncol Biol Phys*. 1991; 21(2):483-489. doi: 10.1016/0360-3016(91)90800-J.
72. Kettenbach J, Kronreif G. Robotic systems for percutaneous needle-guided interventions. *Minimally Invasive Therapy & Allied Technologies*. 2015;24(1):45-53. doi:10.3109/13645706.2014.977299.
73. van de Berg NJ, Dankelman J, van den Dobbelsteen JJ. Design of an actively controlled steerable needle with tendon actuation and FBG-based shape sensing. *Medical Engineering & Physics*. 2015;37(6):617-622. doi: 10.1016/j.medengphy.2015.03.016.
74. de Vries M, Sikorski J, Misra S, van den Dobbelsteen J. Axially rigid steerable needle with compliant active tip control. *PLoS ONE*. 2021;16(12):e0261089. doi:10.1371/journal.pone.0261089
75. Podder TK, Dicker AP, Hutapea P, Darvish K, Yu Y. A novel curvilinear approach for prostate seed implantation. *Med Phys*. 2012;39(4):1887-1892. doi: 10.1118/1.3694110.
76. Bloemberg J, Trauzettel F, Coolen B, Dodou D, Breedveld P. Design and evaluation of an MRI-ready, self-propelled needle for prostate interventions. *PLoS ONE*. 2022;17(9):e0274063. doi:10.1371/journal.pone.0274063.
77. Marcu LG, Lawson JM. Technical and dosimetric aspects of iodine-125 seed reimplantation in suboptimal prostate implants. *Br J Radiol*. 2013;86(1026):20130058. doi: 10.1259/bjr.20130058.
78. Keyes M, Pickles T, Agranovich A, Kwan W, Morris WJ. 125I reimplantation in patients with poor initial dosimetry after prostate brachytherapy. *Int J Radiat Oncol Biol Phys*. 2004;60(1):40-50. doi: 10.1016/j.ijrobp.2004.02.011.
79. Hughes L, Waterman FM, Dicker AP. Salvage of suboptimal prostate seed implantation: Re-implantation of underdosed region of prostate base. *Brachytherapy*. 2005;4(2):163-170. doi: 10.1016/j.brachy.2005.03.002.
80. Morris WJ, Spadinger I, Keyes M, Hamm J, McKenzie M, Pickles T. Whole prostate D90 and V100: A dose-response analysis of 2000 consecutive 125I monotherapy patients. *Brachytherapy*. 2014;13(1):32-41. doi: 10.1016/j.brachy.2013.08.006.
81. Natarajan S, Raman S, Priester AM et al. Focal Laser Ablation of Prostate Cancer: Phase I Clinical Trial. *J Urol*. 2016;196:68-75. doi: 10.1016/j.juro.2015.12.083.
82. Skowronek J. Current status of brachytherapy in cancer treatment-short overview. *Journal of*

- contemporary brachytherapy. 2017;9(6):581–589. doi: 10.5114/jcb.2017.72607.
83. Devlin PM, Holloway CL, Stewart AJ. Brachytherapy: applications and techniques. New York: Springer Publishing Company; 2015.
  84. Fischer GS, Iordachita I, Csoma C et al. MRI-compatible pneumatic robot for transperineal prostate needle placement. IEEE-ASME Transactions on Mechatronics. 2008;13(3):295–305. doi: 10.1109/TMECH.2008.924044.
  85. Siepel FJ, Maris B, Welleweerd MK, Groenhuis V, Fiorini P, Stramigioli S. Needle and biopsy robots: A review. Current Robotics Reports. 2021;2(1):73–84. doi: 10.1007/s43154-020-00042-1.
  86. de Vries M, Wilby S, Palmer AL et al. Overcoming pubic arch interference in prostate brachytherapy using steerable needles. Journal of Contemporary Brachytherapy. 2022;14(5):495–500. doi: 10.5114/jcb.2022.121562.
  87. Nickers P, Thissen B, Jansen N, Deneufbourg JM. 192Ir or 125I prostate brachytherapy as a boost to external beam radiotherapy in locally advanced prostatic cancer: A dosimetric point of view. Radiother Oncol. 2006;78(1):47–52. doi: 10.1016/j.radonc.2005.09.002.
  88. Wang H, Wallner K, Sutlief S, Blasko J, Russell K, Ellis W. Transperineal brachytherapy in patients with large prostate glands. Int J Cancer. 2000;90(4):199–205. doi: 10.1002/1097-0215(20000820)90:4<199:AID-IJC3>3.0.CO;2-C.
  89. Jamaluddin MF, Ghosh S, Waine MP et al. Quantifying 125I placement accuracy in prostate brachytherapy using postimplant transrectal ultrasound images. Brachytherapy. 2017;16(2):306–312. doi: 10.1016/j.brachy.2016.11.015.
  90. Szlag M, Ślosarek K, Rembielak A, Białas B, Fijałkowski M, Bystrzycka J. Real-time brachytherapy for prostate cancer - Implant analysis. Rep Pract Oncol Radiother. 2008;13(1):9–14. doi: 10.1016/S1507-1367(10)60076-4.
  91. Cormack RA, Tempny CM, D'Amico AV. Optimizing target coverage by dosimetric feedback during prostate brachytherapy. Int J Radiat Oncol Biol Phys. 2000;48(4):1245–1249. doi: 10.1016/S0360-3016(00)00742-2.
  92. Taschereau R, Pouliot J, Roy J, Tremblay D. Seed misplacement and stabilizing needles in transperineal permanent prostate implants. Radiotherapy and Oncology. 2000;55(1):59–63. doi: 10.1016/S0167-8140(00)00162-6.
  93. David A, Brennan V, Cohen G, Damato A. Is there a clinically meaningful change in anatomy during planning of US HDR prostate brachytherapy? Radiother Oncol. 2019;133:S586. doi: 10.1016/S0167-8140(19)31472-0.
  94. Wu CHD, Thind K, Husain S, Watt E. Prostate and catheter motion in prostate hdr brachytherapy: from operating room to shielded delivery vault. Radiother Oncol. 2019;139:S29. doi:10.1016/S0167-8140(19)33352-3.
  95. Peddada AV, Blasi OC, White GA, Monroe AT, Jennings SB, Gibbs GL. Prevention of needle displacement in multifraction high-dose-rate prostate brachytherapy: A prospective volumetric analysis and technical considerations. Pract Radiat Oncol. 2015;5:228–237. doi: 10.1016/j.prro.2014.11.004.
  96. Dinkla AM, Pieters BR, Koedooder K, Wieringen N, Laarse R, Bel A. Prostate volume and implant configuration during 48 hours of temporary prostate brachytherapy: Limited effect of oedema. Radiat Oncol. 2014;9. doi: 10.1186/s13014-014-0272-9.
  97. Kawakami S, Ishiyama H, Terazaki T et al. Catheter displacement prior to the delivery of high-dose-rate brachytherapy in the treatment of prostate cancer patients. J Contemp Brachytherapy. 2014;6:161–166. doi: 10.5114/jcb.2014.43619.
  98. Foster W, Cunha JAM, Hsu IC, Weinberg V, Krishnamurthy D, Pouliot J. Dosimetric impact of interfraction catheter movement in high-dose rate prostate brachytherapy. Int J Radiat Oncol Biol Phys. 2011;80:85–90. doi: 10.1016/j.ijrobp.2010.01.016.
  99. Milickovic N, Mavroidis P, Tselis N et al. 4D analysis of influence of patient movement and anatomy alteration on the quality of 3D U/S-based prostate HDR brachytherapy treatment delivery. Med Phys. 2011;38(9):4982–4993. doi: 10.1118/1.3618735.

100. Yoshida K, Yamazaki H, Nose T et al. Needle applicator displacement during high-dose-rate interstitial brachytherapy for prostate cancer. *Brachytherapy*. 2010;9(1):36–41. doi: 10.1016/j.brachy.2009.04.006.
101. Mate TP, Gottesman JE, Hatton J, Gribble M, Van Hollebeke L. High dose-rate afterloading <sup>192</sup>Iridium prostate brachytherapy: Feasibility report. *Int J Radiat Oncol Biol Phys*. 1998;41(3):525–533. doi: 10.1016/S0360-3016(98)00097-2.
102. Whiting P, Rutjes AW, Reitsma JB, Bossuyt PM, Kleijnen J. The development of QUADAS: a tool for the quality assessment of studies of diagnostic accuracy included in systematic reviews. *BMC medical research methodology*. 2003;3(1):1–13. doi: 10.1186/1471-2288-3-25.
103. D’Souza D, Baldassarre F, Morton G, Falkson C, Batchelar D. Imaging technologies for high dose rate brachytherapy for cervical cancer: a systematic review. *Clinical Oncology*. 2011;23(7):460–475. doi:10.1016/j.clon.2011.02.014.

# 3

## **A Literature Review of Bioinspired Needles**

Published as:

Fung-A-Jou Z., Bloembergen J., Breedveld P. (2023). Bioinspired medical needles: a review of the scientific literature. *Bioinspiration & Biomimetics*, 18(4):041002. doi: 10.1088/1748-3190/acd905.



## Abstract

Needles are commonly used in medical procedures. However, current needle designs have some disadvantages. Therefore, a new generation of hypodermic needles and MicroNeedle (MN) patches drawing inspiration from mechanisms found in nature (i.e., bioinspiration) is being developed. In this systematic review, 80 articles were retrieved from Scopus, Web of Science, and PubMed and classified based on the strategies for needle-tissue interaction and propulsion of the needle. The needle-tissue interaction was modified to reduce grip for smooth needle insertion or enlarge grip to resist needle retraction. The reduction of grip can be achieved passively through form modification and actively through translation and rotation of the needle. To enlarge grip, interlocking with the tissue, sucking the tissue, and adhering to the tissue were identified as strategies. Needle propelling was modified to ensure stable needle insertion, either through external (i.e., applied to the prepuncturing movement of the needle) or internal (i.e., applied to the postpuncturing movement of the needle) strategies. External strategies include free-hand and guided needle insertion, while friction manipulation of the tissue was found to be an internal strategy. Most needles appear to be using friction reduction strategies and are inserted using a free-hand technique. Furthermore, most needle designs were inspired by insects, specifically parasitoid wasps, honeybees, and mosquitoes. The presented overview and description of the different bioinspired interaction and propulsion strategies provide insight into the current state of bioinspired needles and offer opportunities for medical instrument designers to create a new generation of bioinspired needles.

### 3.1 Introduction

#### 3.1.1 Background

##### *Bioinspired medical needles*

Although needles are considered minimal invasive surgical instruments, current needle designs have numerous disadvantages [1]. Two types of needles can be distinguished: hypodermic needles and MicroNeedle (MN) patches. Hypodermic needles are hollow, single needle systems that puncture the skin to inject or subtract matter [2]. The definition of MN patches varies in the literature, but here, they are defined as patches with an array of short (length < 3 mm) microneedles that penetrate the skin no further than the dermis or epidermis. Hypodermic needles are subject to needle displacement due to needle deformation, organ movement, and human error tissue displacement [3]. This can be problematic for the physician in terms of accurately reaching a target, but it can also cause tissue damage resulting in pain and fear for the patient [4]. In the brain, it can lead to serious consequences such as swelling and bleeding [5]. MN patches are less invasive than hypodermic needles due to their shallow penetration depth and small diameter. However, they still have their disadvantages, such as poor adhesion ability and antimicrobial activity [6], inconsistent drug distribution, durability issues [7], and strength issues. Microneedles are prone to bending or breaking during manual insertion or having high deviations in insertion height when inserted into soft and inhomogeneous skin tissue [8].

The proposed solutions for improving needles by, for instance, making them sharper and thinner are limited [4]. Therefore, a new generation of needles that draws inspiration from mechanisms found in nature, such as stingers, thorns, teeth, tongues, or quills, is being developed. This approach is called bioinspiration, which is the art of studying nature and its principles and exploring ways to implement those principles and mechanisms into novel solutions. While there is still much to discover about their design and manufacturability, bioinspired needles have the potential to revolutionize medical healthcare. They can be used for a variety of percutaneous procedures (i.e., medical procedures through the skin), including drug delivery, blood extraction, focal therapy, and biopsies. Throughout this chapter, the term 'needle' refers to the bioinspired medical needle, while the term 'stinger' refers to the biological stinger.

##### *Needle mechanics*

Different forces come into play when a needle punctures the skin and moves through the tissue. The forces acting on a needle include the cutting force ( $\mathbf{F}_c$ ) and the friction force ( $\mathbf{F}_f$ ) (Figure 3.1a). The cutting force acts normal to the bevel surface as a result of cutting the tissue, this includes the plastic deformation acting from the soft tissue and the force resulting from the tissue stiffness at the tip. The friction force ( $\mathbf{F}_f$ ) acts along the needle shaft due to friction between the needle and tissue and is also a function of the internal stiffness of the soft tissue. Due to bending of the needle, there exist x- and y-components of the forces, with the

x-components being counteracted by the insertion force ( $\mathbf{F}_i$ ), which is the force required to insert the needle into the tissue. The insertion force is defined as Eq. 3.1 [9]:

$$\mathbf{F}_i = \mathbf{F}_{f,x} + \mathbf{F}_{c,x} \quad (3.1)$$

The insertion force can be decreased by decreasing the friction force and/or the cutting force. The friction force might be changed using the relative velocity or the contact area [9]. Decreasing the cutting force causes a decrease in tissue damage, which results in less pain and a faster recovery.

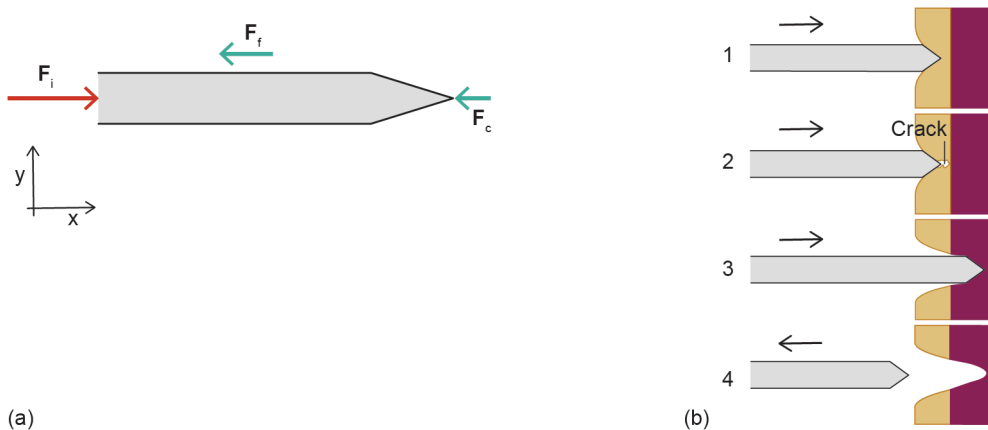
Figure 3.1b shows the needle insertion process divided into the following four stages where different forces play a role [10]:

1. Loading deformation: the needle advances outside the tissue and pushes against the skin, while the needle insertion force is increasing;
2. Rupture: a crack propagates into the tissue at the maximum insertion force and the insertion force drops;
3. Cutting: cutting event after rupture, where the crack gets larger in line with the needle displacement;
4. Unloading deformation: needle insertion stops, and the needle is removed.

During Stages 1 and 2 (i.e., puncturing), the cutting force plays a more significant role, whereas during Stages 3 and 4 (i.e., internal insertion), the friction force is more important. In the case of MN patches, the puncturing of the skin (Stages 1 and 2) is more important than the internal movement through the tissue, since the microneedles do not go deeper than the skin layers, whereas for hypodermic needles, the movement through the tissue (Stages 3 and 4) and bending of the needle are more important than the puncturing of the skin, since the needles travel a longer distance through the tissue.

### 3.1.2 Problem definition

In the relatively new field of using bioinspiration in medical instrument design, designers may



**Figure 3.1. Needle insertion.** (a) Forces acting on the needle during insertion, with  $\mathbf{F}_i$  = insertion force [N],  $\mathbf{F}_c$  = cutting force [N],  $\mathbf{F}_f$  = friction force [N]. (b) Stage 1 of needle insertion: loading deformation. Stage 2 of needle insertion: rupture due to crack propagation. Stage 3 of needle insertion: cutting. Stage 4 of needle insertion: unloading.

feel overwhelmed in the vast amount of bioinspiration sources and potential strategies. This study focuses on the scientific literature to provide guidance on the bioinspiration sources, medical applications, and manufacturing methods of the proposed needle designs. Although some reviews on bioinspired MN patches [11] and mosquito-inspired needles [12] exist, to our knowledge, no comprehensive overview of all bioinspired needles in the scientific literature is available.

### 3.1.3 Goal and structure

This study presents an overview of the scientific literature on bioinspired medical needles. An overview of the scientific literature on bioinspired medical needles provides insights into the future development and direction in the field of bioinspired needles and identifies opportunities for innovation. In Chapter 3.2, the method used to collect all included articles is described. Chapters 3.3 and 3.4 outline the classification of the collected articles. Finally, the findings and future perspectives are discussed in Chapter 3.5.

## 3.2 Methods

### 3.2.1 Literature search

To create a comprehensive overview of the current developments of bioinspired needles, a search in Scopus, Web of Science (WoS), and PubMed was performed (last update: 31 January 2023). This search was executed systematically by dividing the research goal into two related concepts: 'Device' and 'Approach,' and search terms were generated for each concept (Table 3.1). The field (e.g., medical) and function (e.g., surgery) were excluded as search concepts, as including them would have led to a limited selection of articles. For Concept 1, the search term '\*Needle\*' was the only term used because other equivalents such as 'probe' or 'medical instrument' were found to be too general and did not generate more relevant articles.

For Concept 2, commonly used synonyms of bioinspiration found in the literature were included. The term 'biomechanical' was excluded, since the results showed mechanical models of biological principles instead of bioinspired designs. The search query was limited to articles written in English, and conference reviews were excluded because the articles they cover were already covered in the regular search. The search was executed in the title, abstract, and keywords of Scopus, the topic operator (TS) of Web of Science, and the title and abstract of PubMed. The resulting Scopus query, adjusted for WoS and PubMed (see Supplementary material), was as follows: *TITLE-ABS-KEY ((bio-inspir\* OR bioinspir\* OR "Biolog\* inspire\*" OR biomim\* OR "Nature inspir\*" OR Nature-inspir\* OR bionic\*) AND (\*needle\*)) AND (LIMIT-TO (LANGUAGE, "English")) AND (EXCLUDE (DOCTYPE, "cr"))*.

### 3.2.2 Eligibility criteria

The following criteria were used to select articles from the search results. An article was included if it featured a bioinspired needle design that was either tested in the physical world



Table 3.1. Concepts and corresponding search terms.

Concepts: combine with AND		
	Concept 1: Device	Concept 2: Approach
Search terms: combine with OR	*Needle*	Bioinspir*
		Bio-inspir*
		“Biolog* inspi*”
		Biomim*
		“Nature inspir*”
		Nature-inspir*
		Bionic*

or through computational modeling, where 'bioinspired' was defined as incorporating aspects of a mechanism found in nature. The term 'needle' was defined as a slender hollow instrument used for introducing matter or removing matter from the body (as by insertion into the skin), or an extremely thin solid instrument used for acupuncture and inserted through the skin [13].

Because we focused specifically on needle designs, we excluded scaffolds with a nanoneedle-shaped bioinspired structure, as well as needle-like hydrophobic surfaces, bioinspired phantoms or materials (e.g., tea extract or hair), robot-needle systems, and control systems, where a description of the needle was not provided. Additionally, we excluded instances of misuse of the term 'bioinspired,' where the source of bioinspiration was not named, and it was unclear which aspects were used in the design. Finally, we excluded general bioinspired coatings or multifunctional hydrogels that were not specifically designed for a needle.

3.2.3 Literature search results

The search resulted in 555 articles in Scopus, 485 articles in WoS, and 143 articles in PubMed. After removing duplicates, a total of 633 unique articles remained. The references of the reviews found in these 633 articles were scanned (snowballing), resulting in the inclusion of an additional 10 articles, bringing the total to 643 articles. The titles of these articles were screened, leaving 274 articles. In addition, 13 reviews were excluded since these would contain articles that were already included in this review. The remaining articles were evaluated based on their abstract and figures using the criteria outlined in Chapter 3.2.2, resulting in the exclusion of 157 articles. Upon full-text reading, 24 articles were excluded for not meeting the eligibility criteria, resulting in the inclusion of 80 articles in this review (Supplementary material). Figure 3.2 shows an overview of the search results.

3.2.4 Classification of bioinspired needles

The collected articles were classified into two categories, namely 'Interacting' and 'Propelling,' as presented in Figure 3.3. 'Interacting' refers to the interaction between the needle and tissue, which can be altered to reduce or enlarge grip, as explained in Chapters 3.3.1 and

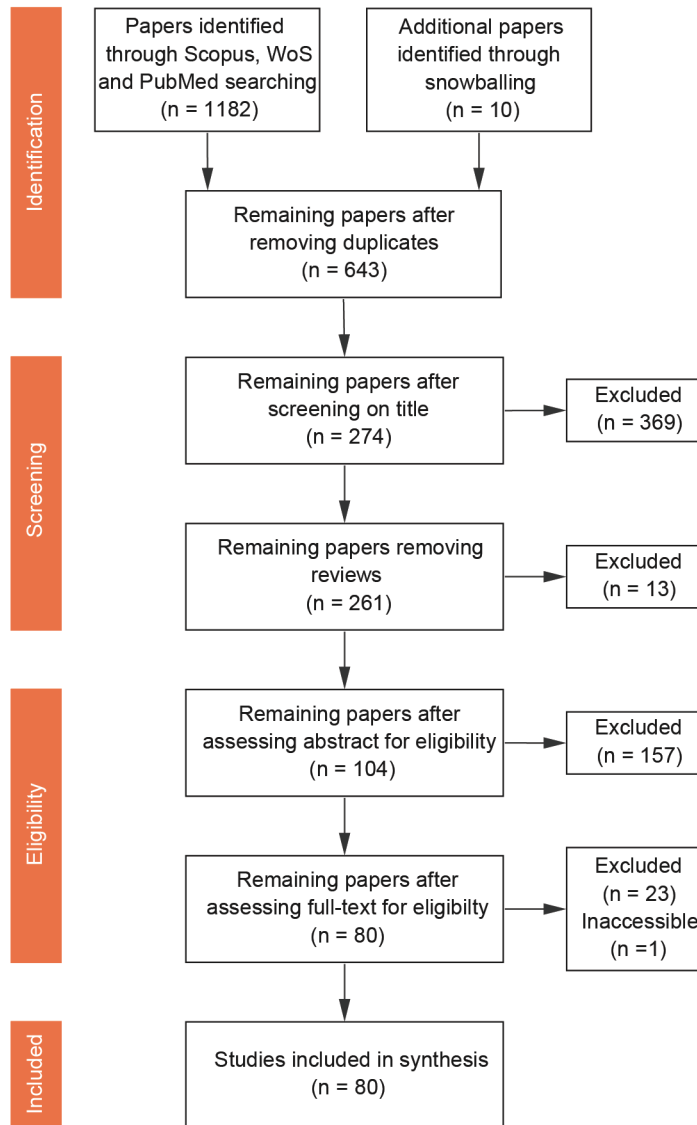
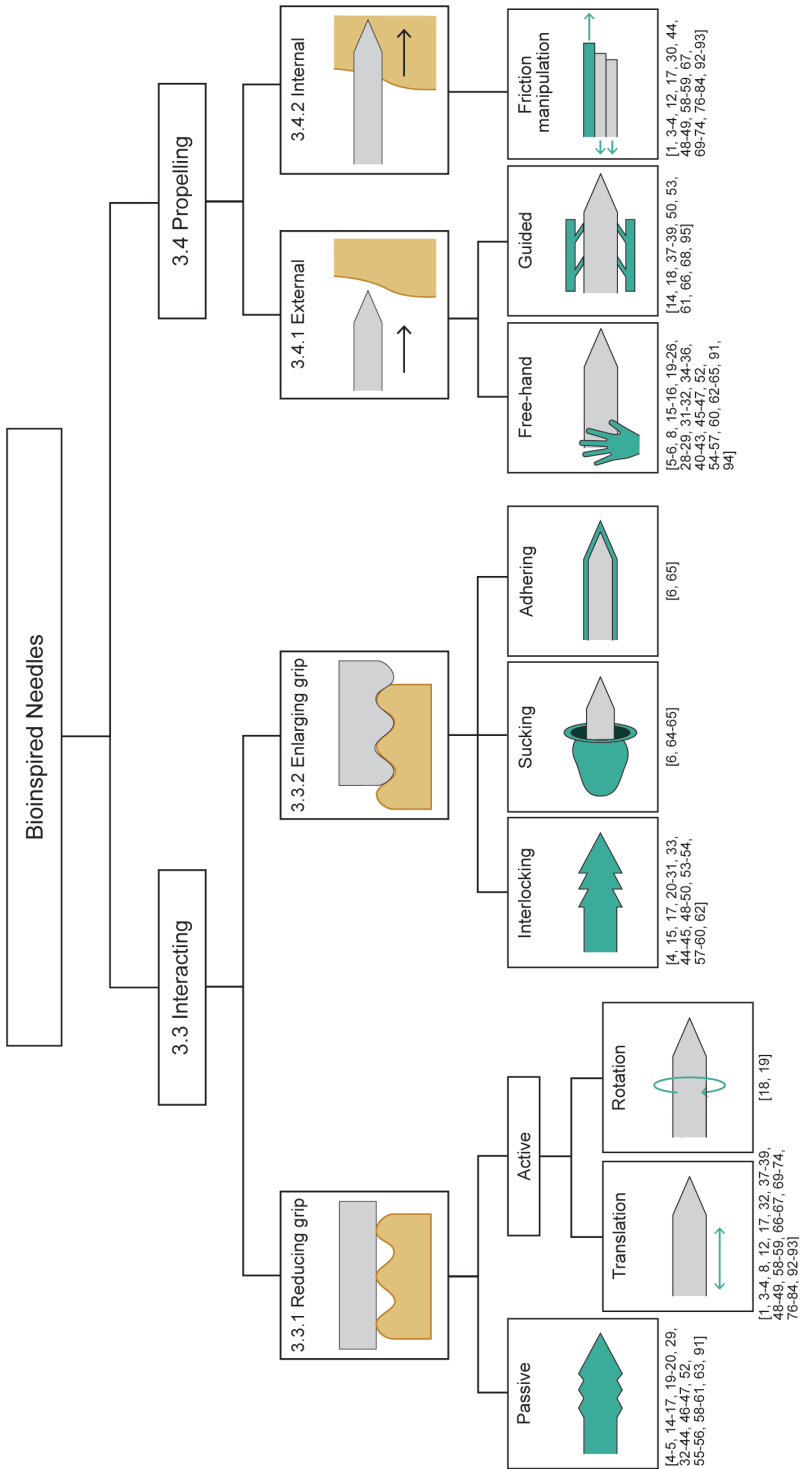


Figure 3.2. PRISMA diagram of the search strategy and article selection method.

3.3.2. 'Reducing grip' was further subdivided into two types of needles: needles that passively reduce grip (e.g., by adjusting the form of the needle using barbs) and needles that actively reduce grip (e.g., by applying a rotating or translating motion during needle insertion). 'Enlarging grip' was divided into three types of needles that use interlocking (e.g., using thorns), sucking (e.g., using suction cups), and adhering (e.g., using an adhesive layer) strategies. As for 'Propelling,' it was classified into the needle's prepuncturing movement outside the body (i.e., external) and postpuncturing movement through the body (i.e., internal), of which the



**Figure 3.3. Classification of bioinspired needles based on the needle-tissue interaction and the propulsion strategies of the needle.** This classification also serves as a schematic illustration of the layout of Chapters 3.3 and 3.4. The green color indicates the modified part of the needle. References of the collected articles that use this strategy are listed below each strategy. Note: some articles describe needles that use multiple strategies.

different strategies are discussed in Chapter 3.4. 'External' was classified into free-hand needle insertion and guided needle insertion.

### 3.3 Interacting

#### 3.3.1 Reducing grip

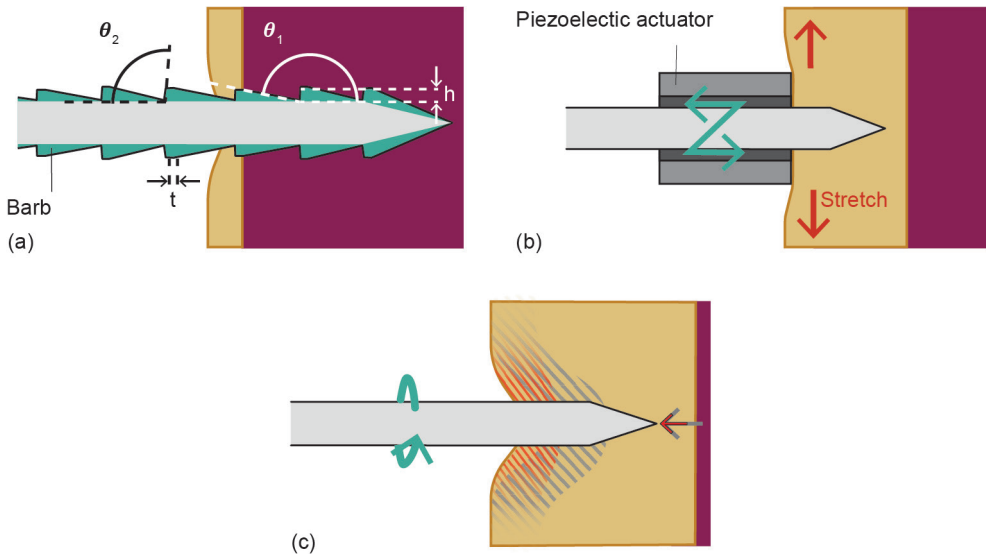
Two-thirds of the collected articles present needle designs that aim to reduce the grip between the needle and tissue. Figure 3.3 shows passive and active strategies for grip reduction, such as adjusting the form of the needle, translating (i.e., vibrating), or rotating it. Often, multiple strategies are combined to optimize grip reduction.

##### *Passive*

Thirty-three articles were collected presenting needles that use passive grip reduction through form modification. This strategy was the most commonly used strategy for grip reduction. It is also found in nature where it occurs in a large variety of organisms, such as insect stingers, thorns of plants, and even natural phenomena like ice formation. The mosquito and honeybee are most commonly used as sources of bioinspiration, as both have barbs on their stinger to distribute the insertion forces between the stinger and tissue. This strategy can be applied to both hypodermic needles and MN patches. Most designs did not specify a medical application and were designed for percutaneous procedures.

Sahlabadi *et al.* [14] developed a needle for percutaneous procedures such as brachytherapy, brain surgery, and biopsy, mimicking the barbs of a honeybee stinger (Figure 3.4a). The design was optimized to decrease the insertion force resulting in a decrease in tissue damage and pain and a higher targeting accuracy. The three-dimensional (3D)-printed polymer needle has a diameter of 1-3 mm and a length of 180 mm, with barbs revolved around the needle axis. The barbs form gaps on the needle surface, resulting in a smaller frictional area and thus reducing the insertion force. The gap space between two consecutive barbs is a function of the front angle, back angle, height, and thickness of the barbs, which were optimized to decrease the insertion force while maintaining the bending stiffness. The design led to a total reduction in insertion force of 35% in PolyVinyl Chloride (PVC) gel and 46% in liver tissue compared to conventional needles with a point or bevel tip. Experiments showed a decrease of 21-26% in the insertion force regardless of the needle scale.

Notably, all long hypodermic needles (i.e., needle length > 60 mm) were inspired by various insect stingers, such as those of the honeybee, parasitoid wasp, and mosquito. Needles developed for blood extraction were all inspired by the mosquito. The inspiration for smaller hypodermic needles and MN patches is much more diverse, with plants [15], mammals, birds, reptiles, and even a natural phenomenon based on the formation of ice [16] used as sources of inspiration for minimizing the insertion forces through form modification (i.e., passive grip reduction).



**Figure 3.4. Needle designs that reduce grip using different strategies.** The drawings show the needle (gray), the grip-reducing element (green), the outline of skin the needle encounters (yellow), and the internal tissue (purple). (a) Barbed honeybee-inspired needle using passive grip reduction, based on [14]. The gap space between two consecutive barbs is a function of the front angle ( $\theta_1$ ), back angle ( $\theta_2$ ), height ( $h$ ), and thickness ( $t$ ) of the barbs. These parameters were optimized to decrease the insertion force while maintaining the bending stiffness. (b) Mosquito-inspired MicroNeedle (MN) using active grip reduction through translation (i.e., mechanical vibration) actuated by a piezoelectric actuator and skin stretching (red arrows), based on [8]. (c) Honeybee-inspired MN using active grip reduction through rotation. The drawing shows the skin deformation (gray hatched) without rotating the needle and the decreased skin deformation (red hatched) when rotating the needle, and the axial friction force (gray arrow) without rotating the needle and the decreased axial friction force (red arrow) when rotating the needle, based on [18].

### Active

#### Translation

Thirty-three articles were collected presenting needles that use translation as a strategy for grip reduction. In nature, this strategy is found in bees, wasps, and mosquitoes that can alter the vibration frequency of their stingers. The parasitoid wasp was the most commonly used source of inspiration for friction manipulation, which enables self-propelling properties, Chapter 3.4 elaborates on this topic. The remaining 11 articles were all inspired by the mosquito and contained designs for hypodermic needles and MN patches. The most frequently described medical application was blood extraction, which matches the blood-sucking function of the female mosquito proboscis (i.e., mouthpart for feeding and sucking).

Kim *et al.* [8] investigated the effect of mechanophysical stimuli on insertion forces as background information for a drug-delivery MN patch inspired by the mosquito proboscis (Figure 3.4b). The mosquito proboscis consists of a labrum, a hollow needle in the center with capillary capacities for blood-sucking, and two maxillae placed to the left and right of the labrum with a jagged shape for anchoring the tissue, surrounded by a labium. Mosquitoes use two distinct motions while piercing the skin: (1) pressing down their labium to stretch the

skin and (2) vibrating their fascicle bundle; both motions change the skin resistance.

These static and dynamic mechanophysical stimuli were tested *ex vivo* with standard cylindrical stainless steel acupuncture needles with a diameter of 60-140  $\mu\text{m}$  and an insertion velocity of 0.1-2 mm/s on porcine skin. To test the static stimulus, the skin was stretched 0-20%, and it was found that this mainly affected the insertion precision. To test the dynamic stimulus, the needle was vibrated with a frequency of 1-1000Hz and amplitude of 1-10  $\mu\text{m}$ , and the authors concluded that it controlled the degree and deviation of skin resistance. The result was a deep, easy, and controlled insertion with low insertion forces.

Suzuki *et al.* [17] designed a hypodermic microneedle for painless blood extraction, using the same properties as the female mosquito proboscis. The needle was composed of two half-needles with a semicircular channel and jagged edges combined into a hollow needle, with capillary force for blood extraction. The jagged edges have interlocking features that are discussed in Chapter 3.3.2 Interlocking. The total needle has a length of 2 mm and a diameter of 0.1 mm, and it moves forward by advancing the labrum and maxillae alternately. The needle was fabricated with an ultra-precision 3D laser lithography system, based on the two-photon absorption phenomenon. Photocurable polymer materials IP-Dip and IP-S were cross-linked with a laser beam, positioned by a Computer-Aided Design (CAD) model. The needle was tested in artificial skin and it was found that vibration motion is effective for reducing the insertion force. The insertion force was also reduced for an alternately advanced motion. However, the difference between no vibration, alternating vibration, and in-phase vibration was not clearly distinctive.

### Rotation

Two articles were collected presenting needles that use rotation as a grip reduction strategy. In nature, this strategy is employed by honeybees with a rotating stinger shaft and flies (*Stomoxys*) with rotating teeth for tearing open tissue [18]. Rotation was demonstrated in both hypodermic needles and MN patches for percutaneous procedures, drug delivery, or biomarker monitoring. It was used as an alternative to 'passive grip reduction' to maintain the mechanical robustness of the needle and save manufacturing costs.

Cai *et al.* [18] employed this strategy to design a biomonitoring MN patch based on the honeybee's rotating stinger (Figure 3.4c). The objective was to achieve higher needle strength and lower deviation in insertion depth than conventional MN patches. A commercial stainless steel acupuncture needle was used as a substitute for a microneedle with a conical tip, a diameter of 0.21 mm, and a length of 1.2 mm. The design aimed to reduce the internal insertion force, i.e., the insertion force after puncturing the skin, by decreasing the friction force, which has the highest contribution to the insertion force. Finite Element Method (FEM) tests and *ex vivo* porcine skin tests showed a 45.7% reduction in the maximum insertion force. The authors also showed that the insertion force decreased by increasing the rotational velocity, up to a certain point. Furthermore, there was a decrease in skin deformation and a faster skin recovery while holding the needle inside the skin.

Wang and Cong [19] developed a needle that was not designed for rotation, but rotation occurred as a favorable side effect. The hole pattern of the mole cricket's tergum and the Chinese sturgeon's skin was mimicked to create an injection needle that could reduce pain without limiting the insertion depth. A syringe needle with a diameter of 1.6 mm and a length of 25.4 mm was modified using machining to create a pattern of holes along the needle shaft. The holes reduced the contact area between the needle and skin tissue, resulting in a reduction of friction as the needle moved through the skin tissue. Furthermore, due to the holes, the needle wall, air, and skin tissue formed a rolling bearing model that contributed to the drag reduction. Simultaneously, micro-vibrations arose in the skin tissue, which increased both the flow speed of the biological fluids and the lubrication effects. The needle surface design with a hole diameter of 0.09 mm and a hole interval of 0.9 mm resulted in a 44.05% drag reduction in silicon compared to smooth syringe needles.

In the collected articles, the needle designs that employed active strategies are less diverse than those utilizing passive strategies. The bioinspiration was mainly drawn from the mosquito, parasitoid wasp, honeybee, and mole cricket, and only a small number of articles described needles that apply these strategies.

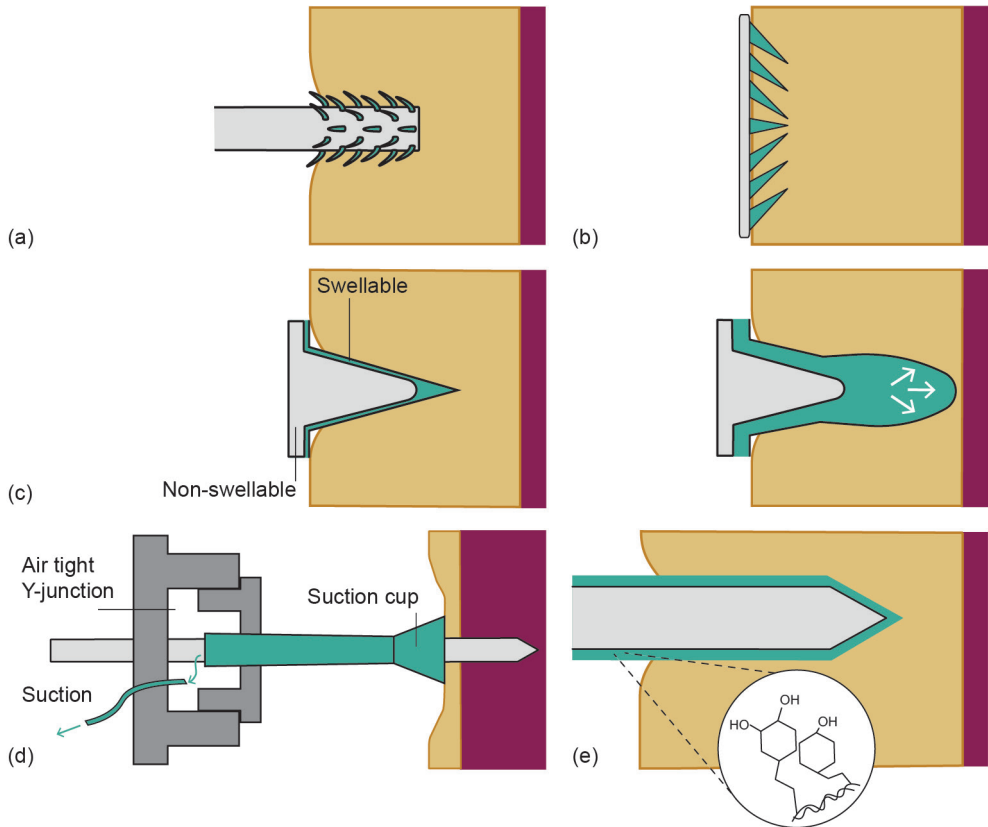
### 3.3.2 Enlarging grip

Enlarging grip might be necessary for stable drug delivery in MN patches and stable needle insertion of hypodermic needles. Three strategies can be employed for: (1) mechanical interlocking, (2) sucking, and (3) adhering.

#### *Interlocking*

Twenty-eight articles were collected presenting needles that use interlocking as a strategy to enlarge grip, where three different methods can be distinguished. The first method is using the same passive strategy to reduce grip, but now modifying the form in order to enlarge grip. This is seen in nature in the porcupine and wasp that have barbs on their quills and stinger, respectively, to anchor to their predator's skin as a form of self-defense [20, 21]. Moreover, it is seen in the thorns of plants and many parasites to anchor to their host. The second method is clamping, which is seen in the claws of eagles and mantises, as well as the mouths of lampreys and sharks [22-25]. The third method is swelling, used by endoparasites to anchor themselves to their host's intestinal walls [26, 27]. Mechanical interlocking was only applied in MN patches and short hypodermic needles that do not go deeper than the epidermis. It is most commonly used for medical applications like drug delivery and blood extraction.

Some needles that were designed for interlocking strategies had the positive side effect of also lowering the puncture force as described in Chapter 3.3.1 Passive, resulting in a low insertion force and high tissue adhesion [20]. To illustrate, Liu *et al.* [28] designed a microneedle for prolonged monitoring and drug release in the intestines based on the proboscis of the parasitic spiny-headed worm (Figure 3.5a), which has barbs along its proboscis to move through the gut with minimal locomotion. Scanning Electron Microscopic (SEM) images



**Figure 3.5. Needle designs that enlarge grip using different strategies.** The drawings show the needle (gray), the grip enlarging element (green), the outline of skin the needle encounters (yellow), and the internal tissue (purple). (a) Needle applying interlocking by form modification using a barbed MicroNeedle (MN) design inspired by the parasitic spiny-headed worm, based on [28]. (b) MN patch applying interlocking by clamping using serrations inspired by the mantises' forelegs, based on [23]. (c) Swellable MN patch applying interlocking using a swellable layer for mechanical interlocking inspired by the swelling properties of the spint-headed worm, based on [27]. (d) Needle applying suction using an air-tight Y-junction and a suction cup inspired by the suction cups on octopus tentacles, based on [65]. (e) MN applying adhering with a mussel byssus-inspired adhesive PolyDopAmine (PDA) hydrogel layer, based on [6].

of the proboscis were converted to a hollow needle design with a diameter of  $108\text{--}74\text{ }\mu\text{m}$  from base to tip and a length of 1 mm. This length is necessary for puncturing the gut wall and reaching the mucus blanket and epithelial barrier. The barbs, with a diameter, length, and curve of respectively  $8\text{ }\mu\text{m}$ ,  $40\text{--}30\text{ }\mu\text{m}$ , and  $50^\circ$ , are equally distributed over a length of  $0.5\text{ mm}$  from the needle tip, which is the most effective barb region. The microneedles were 3D-printed with Direct Laser Writing (DLW), which uses two-photon photopolymerization to cure photoresist, and were then attached to a PolyDiMethylSiloxane (PDMS) backing. This technique has high precision and is suitable for manufacturing the overhanging barbs.

The barbed needle design showed a significant increase of the retraction force compared to barbless needles while maintaining a low insertion force, when tested in *ex vivo* porcine



small-intestine tissue. Compared to other state-of-art barbed microneedles (e.g., the honey-bee-inspired needle [29]), the retraction force remained the same while the insertion force was two times smaller, resulting in a ten times higher retraction/insertion force ratio.

Zhang *et al.* [23] used inspiration from the serrated microstructure of the mantis' forelegs to design a minimally invasive drug delivery MN patch (Figure 3.5b). Using SEM imaging, the forelegs of the mantis were observed and converted to a ferrofluid-configured mold. This mold was filled with a biocompatible polymer for Transdermal Drug Delivery (TDD) (i.e., 50 mL of silk fibroin solution 30% w/v) and cured under UltraViolet (UV) light. The resulting MN patch consists of microneedles with different diameters and lengths around 0.25  $\mu\text{m}$  and 0.6  $\mu\text{m}$ , respectively, and with an inclination angle ranging from 30° to 90°. Because of this inclination angle, the MN patch has the same grasping and holding properties as the mantis and clamps itself to the tissue. A rotation-and-load-bearing test was performed on *ex vivo* porcine skin and showed a decrease in the inclination angle of the microneedles, enhancing the ability of the MN patch to withstand external forces. An angle of 30° showed the best holding capabilities, while the patch with 90°-microneedle inclination angles (i.e., perpendicular to the surface) would immediately fall off. This result was confirmed by a second test where the MN patches were attached to living mice. These second tests also showed successful insertion of the microneedles and rapid recovery of the tissue. Lastly, the *in vivo* mice tests and *in vitro* tests showed sustained drug delivery.

Another way of interlocking was applied by Jeon *et al.* [26] and Yang *et al.* [27] who designed swellable MN patches based on the swelling properties of endoparasites (Figure 3.5c). Yang *et al.* [27] used inspiration from the spiny-headed worm, specifically the *Pomphorhynchus Laevis*, for a drug-delivery MN patch. The spiny-headed worm uses its proboscis to puncture the intestinal wall of its host, where it expands a bulb using its retractor muscles at the base of its proboscis to interlock the proboscis and the intestinal wall tissue. The MN patch was designed to apply a similar method to interlock the MN patch and the tissue. The cone-shaped microneedles with a base diameter of 280  $\mu\text{m}$  and a length of 700  $\mu\text{m}$  have a hydrophobic non-swellable core and a hydrophilic swellable outer layer. The hydrophilic outer layer absorbs the tissue fluids and swells to 20% of the tip height into a mushroom shape, while the core remains stiff.

The MN patch was fabricated in a PDMS mold, filled with a PolyStyrene-block-PolyAcrylic Acid (PS-b-PAA) casting (i.e., outer layer) and PS homopolymer filling (i.e., core). Tests in hydrogel showed that it takes 10 minutes for the microneedles to get into the maximum swollen state and 15 minutes to recover back to their conical shape after removal. It also showed that the MN patch could be removed without breaking it and that the adhesion strength significantly increased when the microneedles were in their swollen state. Multiple movement cycles with pig joints were executed to show that a strong fixation was achieved. Tests in intestine mucosal tissue showed a 3.5 times increase in adhesion strength compared to staples and a removal force of 4.5 N/cm<sup>2</sup>. The results were minimal tissue damage, reduced

infection risk, and sustained delivery of bioactive therapeutics.

Twelve articles were collected presenting needles that use both 'passive grip reduction' and 'interlocking for grip enlargement' strategies. In these needle designs, the form of the needle was modified for smooth insertion, and interlocking mechanisms were applied to resist retraction. Table 3.2 displays various needle tips that use form modification for grip enlargement and/or grip reduction, demonstrating the numerous possibilities of bioinspiration for the same strategy while applying different implementation methods. Again, all blood-extraction needles are based on the mosquito's proboscis, and the designs adopted different properties of proboscis, such as vibration or form modification [4, 30]. Interestingly, the swellable needle developed by Yang *et al.* [27] swells to form a mushroom shape, while Li *et al.* [31] use a stiff mushroom shape as the favorable geometry for interlocking tissue.

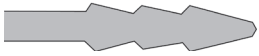

















### *Sucking*

Three articles were collected presenting needles that use sucking as a strategy to enhance grip, with two of the three designs using it in combination with adhering. All needles use bioinspiration from the octopus and the suction cups on its tentacles. This suction strategy was found solely in MN patches with drug delivery as the medical application.

The single article presenting a needle that used only suction as a strategy to enhance grip was published by Fu *et al.* [64], who designed an MN patch for pancreatic cancer treatment inspired by the suction cups on the tentacle of the octopus. The MN patch consists of an array of microneedles with suction cups in between, which can adhere to the irregular surface of tumors. The microneedles have a conical shape with an estimated diameter of 450  $\mu\text{m}$  and a length of 600  $\mu\text{m}$ . The suction cups have a conical cavity and mimic the octopus tentacle. The whole MN patch was made of a Gelatin MethAcryloyl (GelMA) hydrogel that was poured into a mold and cured with UV light. A peeling-strength test on *ex vivo* porcine pancreas demonstrated that the suction cup MN patch adhered better than a conventional MN patch. The capacity for drug delivery was measured, and it was confirmed that the drug release kinetics could be mediated by adjusting the concentration of GelMA hydrogel. The MN patch was tested *in vivo* on mice with tumors alongside a conventional treatment method and a control group. The results showed no difference between the intraperitoneal injection and the suction cup MN patch, indicating good tolerability, biocompatibility, and biosafety. It demonstrates that the suction MN patch could induce pancreatic cancer cell apoptosis by releasing the carried gemcitabine.

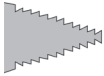

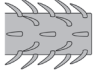

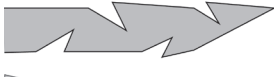
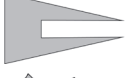

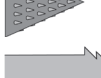
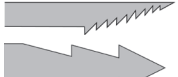







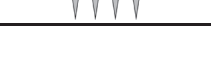

Joymungul *et al.* [65] proposed a gripe-needle design based on both the sucking and adhering capabilities of the octopus' suction cup to perform an incision task in the optic nerve area (Figure 3.5d). The gripe-needle was based on the octopus' technique for grasping and boring sea snail shells. The stickiness of the octopus' suction cup increases sealing and surface contact with the shell, while the suction chamber creates a pressure gradient to maximize force grip. Once the shell is in a stable position, the octopus drills a hole into it with its radula (i.e., mouthpart). The gripe-needle consists of a cone-shaped suction cup made using

**Table 3.2. Needle tip designs that use form modification to reduce grip during tissue insertion and/or mechanical interlocking to enlarge grip during retraction.** Illustration of the source(s) of bioinspiration, source(s) of bioinspiration, medical application(s), ability to reduce grip for smooth needle insertion (yes or no), ability to increase grip to resist needle retraction (yes or no), and reference(s).

Illustration	Bioinspiration	Medical application	Reduce grip for smooth insertion	Increase grip to resist retraction	Reference
	Mosquito	Percutaneous procedure	Yes	No	[32]
	Honeybee	Percutaneous procedure	Yes	Yes	[29, 33]
	Porcupine	Percutaneous procedure	Yes	Yes	[20]
	Lamprey	Wound healing	Yes	Yes	[22]
	Parasitoid wasp	Percutaneous procedure	Yes	No	[34-36]
	Mosquito	Percutaneous procedure	Yes	No	[37, 38]
	Mosquito, Honeybee	Biopsy, Percutaneous procedure	Yes	No	[5, 14, 39-41]
	Mosquito	Biopsy	Yes	No	[42]
	Snake	Drug delivery	Yes	No	[43]
	Mosquito	Drug delivery	Yes	Yes	[44]
	Shark	Wound healing	No	Yes	[25]
	Mosquito, Honeybee, Porcupine	Drug delivery	No	Yes	[45]
	Mosquito	Blood extraction	Yes	No	[46]
	Mosquito	Blood extraction	Yes	No	[47]
	Mosquito	Blood extraction	No	Yes	[30, 48, 49]
	Mosquito	Biopsy	No	Yes	[50]
	Mosquito	Deep brain stimulation	Yes	No	[51]
	Mushroom	Drug delivery, Information storage	No	Yes	[31]

continued on next page

Table 3.2. Continued.

Illustration	Bioinspiration	Medical application	Reduce grip for smooth insertion	Increase grip to resist retraction	Reference
	Limpet	Drug delivery	Yes	No	[52]
	Golden margined century plant	Performance monitoring	Yes	Yes	[15]
	Spiny-headed worm	Drug delivery, Biomarker monitoring	No	Yes	[53]
	Spiny-headed worm	Drug delivery, Biomarker monitoring	No	Yes	[53]
	Honeybee	Myocardial infarction treatment	No	Yes	[54]
	Bird bill	Drug delivery	Yes	No	[55]
	Mosquito	Blood extraction	Yes	No	[56]
	European true bug	Drug delivery	No	Yes	[57]
	Mosquito	Blood extraction	Yes	Yes	[4, 17, 58, 59]
	Honeybee	Percutaneous procedure	Yes	Yes	[60]
No image	Mosquito	Blood extraction	Yes	No	[61]
	Kingfisher, Porcupine	Wound healing	No	Yes	[62]
	Mole cricket, Chinese sturgeon	Percutaneous procedure	Yes	No	[19]
	Mosquito	Percutaneous procedure	Yes	No	[63]
	Spiny-headed worm	Drug delivery	No	Yes	[27]
	Ladybug, wasp	Wound healing	No	Yes	[21]
	Eagle	Wound healing	No	Yes	[24]
	Mantis	Drug delivery	No	Yes	[23]
	Ice	Drug delivery	Yes	No	[16]

photopolymer resin 3D printing with double-sided adhesive acrylic gel tape with cut grooves attached to its base. A nitinol outer tube connects the top of the cup to a Y-junction (i.e., the suction chamber), which is made of two rubber caps of 7 mm and 12 mm in diameter, respectively. A suction syringe is connected to the air-tight Y-junction to create an under pressure. A drug-delivery syringe is attached to another nitinol tube that can move coaxially inside the outer tube. Four variations of the prototype were made to test the feasibility of the design in four experiments, respectively: (1) a proof-of-concept prototype showed sufficient gripping and shear force on different materials in wet and dry conditions, (2) a test on bubble wrap showed successful incision, (3) an eye-sample test showed successful access to the optic nerve, and (4) tests on a porcine eye sample showed a force grip above the required 1 N, however, this force was not maintained effectively during insertion. Overall, the gripping force significantly increases on semi-rough surfaces when increasing the suction cup pressure. During the incision task, the grooves maintained vacuum grip and increased cup adhesion, but decreased the cup's lifetime. Pulling and shear loading tests showed that the surface wetness enhanced vacuum grip.

### Adhering

Zhang *et al.* [6] used a combination of suction and adhesion strategies inspired by the octopus and mussel in the design of a multifunctional MN patch for drug delivery (Figure 3.5e). In addition, the authors incorporated antibacterial properties based on the *Paenibacillus polymyxa* bacteria that restrain the growth of other bacteria. The MN patch consists of a flexible PolyDopAmine (PDA) hydrogel base, which is equipped with an array of Poly(Ethylene Glycol) DiAcrylate (PEGDA)-sodium alginate MNs that have a diameter of 300  $\mu\text{m}$  and length of 600  $\mu\text{m}$ . Each MN is encircled by six concave chambers with a diameter of 375  $\mu\text{m}$  and a dome-like protuberance inside, integrated into the base. The MN patch was produced using a mold in which the material was cured. To replicate the molecular structure of the mussel's protein, a part of the dopamine in a mixture with gelatin was oxidized and cross-linked to the gelatin through chemical reactions. The oxidized and unoxidized dopamines formed a stable PDA hydrogel through various interactions, of which the various inner chemical groups enabled adhesion. The PDA hydrogel also possessed supramolecular interactions, giving the MN patch self-repairing properties. The PDA-hydrogel base mimics the microstructure of the octopus tentacle, giving it sucking abilities in dry, wet, and moist environments. The antimicrobial peptin polymyxin of the *P. polymyxa* bacteria was loaded at both the MN tips and PDA base. The self-repairing properties were tested by putting two MN patch segments together, the segments would immediately weld together without external stimuli. *Ex vivo* porcine skin tests demonstrated that the MN patch strongly adhered to the skin when lifted, bent, and moisturized or immersed in water. A knuckle test was performed, which showed excellent adhesion when bent along the knuckle up to 90°. A weight test showed adhesion up to 60 kg, which is 240 times its own mass. A peeling-off test was conducted to compare the multifunctional MN patch to (1) an MN patch without PDA hydrogel and without suction

cups (i.e., a normal MN patch), (2) an MN patch with only a PDA hydrogel base, and (3) an MN patch with only suction cups. The multifunctional MN patch performed best under overall circumstances, while the normal MN patch performed worst. A rat model showed sustained drug release and less inflammation compared to the MN patch without polymyxin. Lastly, the study demonstrated that the polymyxin killed 80% of the *E. coli* bacteria.

### 3.4 Propelling

#### 3.4.1 External

##### *Free-hand*

The majority of the collected articles, 40 out of 80, present a needle design that utilized the strategy of free-hand insertion, encompassing all needles that were not designed for propelling. Almost all MN patches, 21 out of 22, were inserted free-hand, as they were only meant to puncture the skin layers and allow the drug to distribute itself without the need to reach a specific target, unlike hypodermic needles, which require a physician to ensure accuracy to reach the desired target. This strategy did not employ any bioinspiration, and due to the large number of articles in this category, a wide range of medical applications were described.

##### *Guided*

Eleven articles were collected presenting needles that used guidance as a strategy for safe needle insertion. This strategy is mostly used for hypodermic needles, although Cai *et al.* [18] employed guidance for an MN patch. The mosquito was the primary source of inspiration for these designs, although the honeybee and fly were also used.

Suzuki *et al.* [66] were inspired by the mosquito and developed a needle-guidance system for stable insertion of needles with a diameter of 100  $\mu\text{m}$  or less for blood extraction, or drug delivery. The needle-guidance system is based on the needle-like proboscis of the mosquito, which has a diameter of 50  $\mu\text{m}$  that is wrapped in its labium and punctures the skin while grasping the proboscis with the tip of its labium. This technique shortens the effective length of the proboscis, preventing buckling. The needle-guidance system consists of a solid stainless steel acupuncture needle, with a diameter of 100  $\mu\text{m}$  and a length of 4 mm. This needle was placed into a compliant mechanism, of which the components were cut out of a PolyOxyMethylene (POM) 0.5-mm thick plate using femtosecond laser cutting. The components were fixed together with epoxy adhesive and had a PolyCarbonate (PC) cover. The buckling load in soft tissue depends on the needle length, needle end state, needle material, and tissue stiffness and is expressed as Eq. 3.2 [67]:

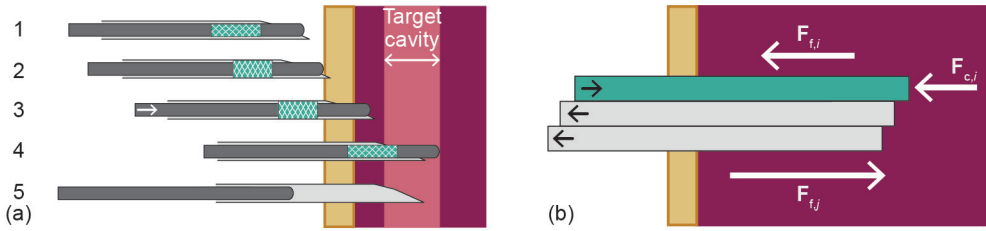
$$P = n\pi^2 \frac{EI}{l_b^2} + \frac{\mu L^2}{\pi^2} \quad (3.2)$$

where  $n$  is the coefficient corresponding to the end states of the needle [-],  $E$  is the Young's Modulus of the needle material [ $\text{N mm}^{-2}$ ],  $I$  is the moment of inertia of area of the needle

[mm<sup>4</sup>],  $l_b$  is the effective buckling length of the needle [mm], and  $\mu$  is the spring stiffness of the tissue where the needle is pushed through [N/m]. The needle will not buckle if the insertion force as described in Eq. 3.1 is lower than the buckling load ( $\mathbf{P} > \mathbf{F}_b$ ). A smaller effective buckling length results in an increase in the buckling load, which means the needle can resist a higher insertion load. A smaller effective length was achieved by adding two support points to the guiding system, providing the needle two with fixed ends that double the buckling load. The needle is advanced cycle by cycle, similar to the lead-delivery system of a mechanical pencil. The authors proposed bellow tubes for a future needle design that can extend and retract to allow drug delivery or blood extraction without hindering the needle motion [66]. A preliminary test without load was performed by ejecting the needle into the air, which showed successful advancement of the needle with an extrusion length of 0.1 mm/cycle. A puncturing test in hydrogel agarose, as artificial skin, was performed successfully but showed an unintentional curvature in the needle path. The performed puncturing test in a PDMS elastomer sheet was unsuccessful, due to slipping at the grasping component. A load-force test showed slipping at  $\pm 0.011$  N, while a load of  $\pm 0.078$  N is required for puncturing PDMS, which has characteristics resembling human skin.

Inspired by the chameleon's tongue, O'Cearbhaill *et al.* [68] designed a needle with a radial mechanical clutch to prevent overshoot injuries in intravenous access, laparoscopic, and endo- and transluminal interventions. The radial clutch is formed by 16 biaxial stainless steel flat wires braided over a 1.1-mm diameter mandrel and crimped to a blunt rounded-tip stylet with 80-mm proximal and 50-mm distal length segments. This stylet-mounted clutch system is a universal design that is compatible with hypodermic or endoscopic needles. Here, it is assembled with a standard double-bevel, 100-mm length, 14- or 15-Gauge needle to compose the mechanical clutch needle. The chameleon's tongue has helical-wound collagen fibers in which the muscle extends axially to push the tongue forward. When compressed, the tongue is in tension, and when triggered, it extends to its relaxed conformation. The chameleon's tongue has a bony interior similar to the internal body of a needle and the helical wound fibers behave like biaxial braids that extend radially when compressed. Figure 3.6a shows the five actuation phases of the needle clutch. The design was tested in human cadavers and showed successful deployment through the peritoneum (i.e., the membrane that surrounds the abdominal organs) and successful needle disengagement from the stylet. In an *ex vivo* porcine test, the needle demonstrated successful emergency airway access when entering the trachea (i.e., the throat) and stopped before hitting the back wall, preventing tracheal or vocal chord damage. A test in a porcine ear vein illustrated safe vascular access without the risk of damage due to puncturing through the target.

While the above examples use 'guidance' as the primary strategy for safe needle insertion, it is often combined with other strategies for grip reduction or enlargement. Liu *et al.* [28] designed an insertion system added to the needle discussed in Chapter 3.3.2 Interlocking to have both stable needle insertion and tissue adherence.



**Figure 3.6. Needle designs using different propelling strategies.** The drawings show the needle (gray), the propelling element (green), the outline of the skin the needle encounters (yellow), and the internal tissue (purple). (a) Chameleon-tongue-inspired needle-clutch design for guided external needle propelling, based on [68], including the needle (gray), the stylet (dark gray), the clutch (green hatched), and the target cavity (pink). The figure shows five actuation stages of the needle design: (1) unloaded, no friction between stylet and needle, (2) the needle tip hits the tissue surface, the blunt stylet cannot puncture so the axial compression leads to radial expansion of the braided clutch, (3) the stylet and needle couple through friction and advance through the tissue as one, (4) the target cavity is hit, which causes a drop in resistance and only the stylet advances, in this way overshoot is prevented with automatically stopping when the target is reached, (5) the stylet can now safely be retracted. (b) Wasp-inspired needle design principle for internal needle propelling using friction manipulation, based on [69]. Ovipositor-inspired needle insertion into tissue with one advancing needle segment that experiences a friction force ( $F_{f,i}$ ) and a cutting force ( $F_{c,i}$ ) and two retracting needle segments that experience a friction force ( $F_{f,j}$ ) in the opposite direction.

### 3.4.2 Internal

#### Friction manipulation

Twenty-nine articles were collected presenting needles that use friction manipulation. Almost two-thirds of the needles were inspired by the parasitoid wasp, while the remainder were inspired by the mosquito. The parasitoid wasp has an ovipositor (i.e., an egg-laying organ) that consists of two or more valves connected with a dovetail interlocking mechanism that allows them to slide with respect to each other. The wasp advances one valve while retracting the other(s) to move through wood to reach a host to lay eggs while reducing the risk of buckling. The mosquito uses a similar mechanism as the wasp in combination with vibration, which served as a source of inspiration for Izumi *et al.* [48] and Suzuki *et al.* [66] as described in Chapter 3.3.1 Active. The internal friction-manipulation strategy was mainly used for hypodermic needles, with medical applications such as blood extraction, biopsy, and focal therapy. However, most prototypes do not have a specific application yet and are designed for general percutaneous procedures.

One of the articles that describes a needle inspired by the ovipositor of the parasitoid wasp was written by Bloembergen *et al.* [69] who developed a self-propelling needle for biopsy and focal laser ablation to treat prostate cancer (Figure 3.6b). The needle system consists of a needle and a manual actuation unit that drives the needle. The needle consists of six parallel 0.25-mm nitinol rods with a length of 200 mm and a total diameter of 0.8 mm connected at the tip by a shrinking tube glued to one of the rods. The self-propelling motion is achieved



by using the friction forces acting on the needle as described in Chapter 3.1.1. By advancing one rod a certain distance while retracting the others a fifth of that distance, the friction force on the retracting rods counterbalances the sum of the friction and cutting forces on the advancing rod. As a result, the needle moves forward step by step. *Ex vivo* tests in human prostate tissue inside a Magnetic Resonance Imaging (MRI) system showed that the needle tip position was visible in the MR image and demonstrated successful propelling with zero external push of the needle, preventing large tissue motion and deformation. However, the measured slip ratio of 0.82-0.96 mm implies a large difference between the expected and true traveled distances of the needle.

Another needle that uses the principle of friction manipulation and used the parasitoid wasp as a source of inspiration was developed by Frasson *et al.* [70], they designed a steerable, multi-part, flexible needle for soft tissue interventions such as brain surgery. The needle consists of two interlocking segments that can move independently from each other, enabling the needle to be steered in a planar trajectory. Four prototypes were developed each with a length of 200 mm, a diameter of 12 mm or 9 mm, and a bevel-tip angle of 45° or 20°. Each needle segment contains two holes for securing the needle to mechanical transmission cables and two functional channels. One channel is for delivery or draining and the other contains an electro-magnetic tracking sensor that tracks the needle's position and orientation. To prevent buckling outside the tissue, the part of the needle that is not entering the tissue is supported by a trocar. The needle segments were 3D printed using the flexible rubber Digital Material™ DM 70shoreA, the tips were 3D printed using a more rigid material DM 95shoreA to ensure a fixed bevel-tip without tip buckling. VeroWhite rigid plastic was added to the distal end of the needle to improve material toughness at the stress points where the mechanical transmission cables are connected. The interlocking segments of the needle allow it to be steered in a plane. The advanced segment becomes the leading segment and the offset between the segments creates an unsupported length that determines the deflection magnitude. Modifying this offset reorients the approach angle of the tip and thus controls the needle trajectory. The prototypes were evaluated in a gelatin phantom that replicates the canine brain, and different steering offsets were actuated via software. The evaluation showed an approximately linear relation between the curvature and steering offset. Furthermore, a smaller needle diameter resulted in a larger curvature but with greater planar motion uncertainty. Lastly, a larger tip angle resulted in a larger curvature but also led to greater instability due to the forces acting on a smaller bevel-tip area.

The friction manipulation strategy is well-suited for steering due to the independent movement of the parallel needle segments. This is the only strategy that explores steering of the needle and the corresponding challenges due to the high compliancy and deformability of soft tissue. The needle designs are still prototypes with diameters varying between 12 mm [70, 71] and 0.03 mm [30] and the number of needle segments varying between two [70, 72], three [30, 44, 48, 49, 67], four [1, 71, 73-84], six [67, 69], and seven [3, 12].

## 3.5 Discussion

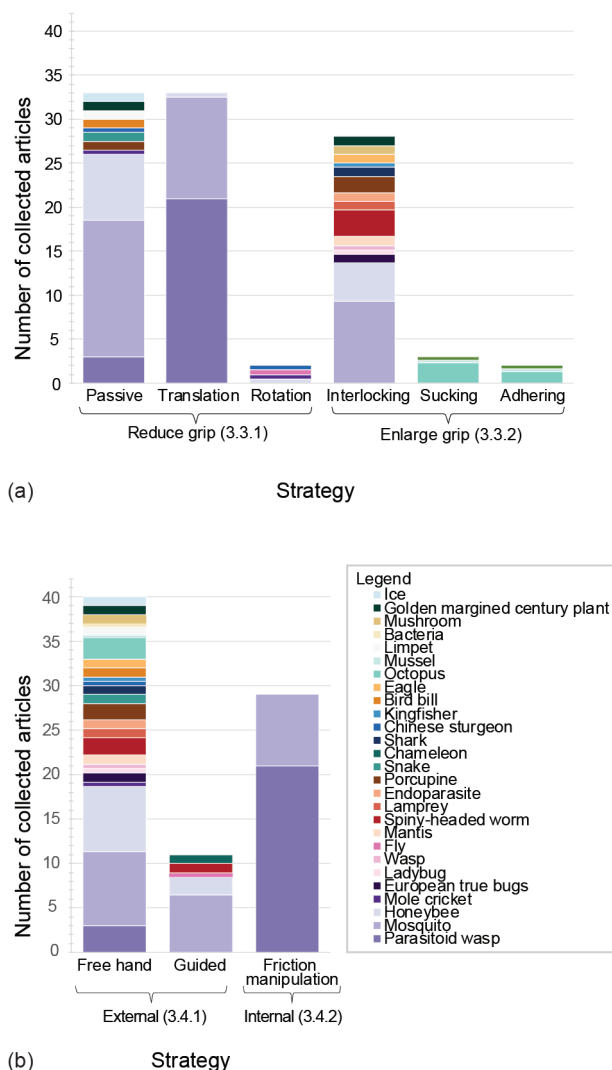
### 3.5.1 Comparative analysis

This review provides an overview of the working principles of bioinspired medical needles. The bioinspired needle designs can be classified based on how they modify the needle-tissue interaction and the propelling of the needle through the tissue. The needle design can modify the interaction with the tissue to serve two goals: (1) reducing the grip for smooth needle insertion and (2) enlarging the grip to resist needle retraction.

Figure 3.7a shows that the majority of the collected articles present bioinspired medical needles that use either translation as an active strategy or form modification as a passive strategy to reduce grip. Translation, as one of the most frequently described strategies, might be related to it not only being used as the main strategy in the form of vibration but also for friction manipulation. Form modification as one of the most frequently described strategies may be correlated to the upward trend of additive manufacturing in medical devices [85], since the needle form is often modified using 3D printing. Only a few articles (i.e., two articles) were found describing needles that use rotation as a strategy. This may be because rotating the needle focuses more on the actuation instead of the design of the needle itself. There may be opportunities in exploring the use of rotation techniques in needle design, by taking inspiration from the boring techniques of shipworms or the ovipositors of locusts.

The enlarging grip strategy was mainly used in MN patches that need to attach to the skin for a longer period of time. Figure 3.7a shows that the majority of collected articles use interlocking as a strategy to enlarge grip. This result may be explained by the abundance of interlocking features in nature. In addition, since interlocking is mainly realized through form modification, the same explanation of the upward trend in additive manufacturing as for passive form modification applies. An interesting finding is that the most common method of form modification is adding barbs, which is both used to reduce grip in a passive way and enlarge grip through interlocking. In nature, this method is seen in animals and plants. The smallest number of collected articles (i.e., three articles) describe needles using sucking and adhering as a strategy to enlarge grip. One could speculate that this is due to the fact that only the octopus was used as a source of inspiration and the complexity of its suction cup. Other organisms could be explored, such as the mouth of tadpoles or the water management system of tree roots. The lamprey's mouth, for instance, is used for interlocking and also has sucking capabilities.

The results of the classification based on propelling show that the majority of collected articles describe needles that implement free-hand insertion (Figure 3.7b). This may be explained by the fact that most needles have not (yet) implemented a needle-propelling strategy. Friction manipulation is the second largest propelling group, which correlates with translation being the largest interacting group since friction-manipulation and translation strategies are often applied together. It is possible that there are alternative ways to manipulate friction without using translation. As for now, only friction manipulation is used as a



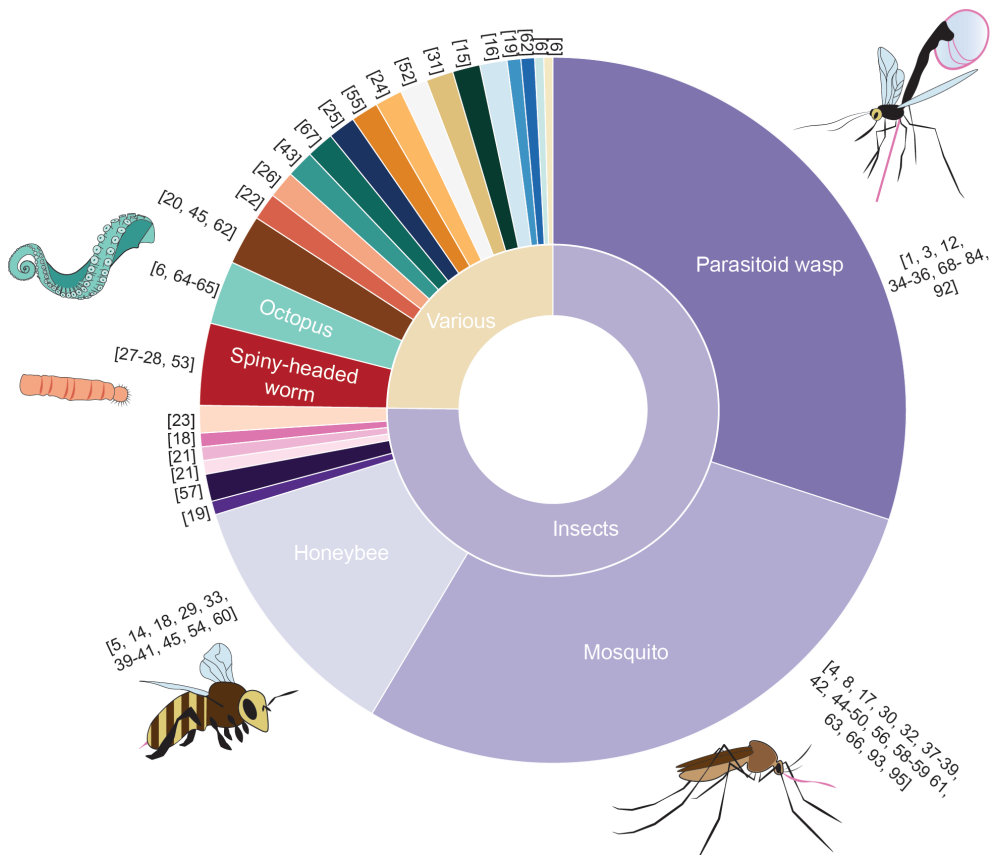
**Figure 3.7.** Number of collected articles, classified based on the needle's source of bioinspiration and strategy for (a) needle-tissue interaction (reduce grip or enlarge grip) and (b) propelling (free hand, guided, or friction manipulation). Note: articles describing needles that use multiple bioinspiration sources for one strategy are counted as one entity divided over the number of different bioinspiration sources (e.g., 1/2 parasitoid wasp and 1/2 mosquito).

strategy to implement steering, but it may be possible that alternative bioinspired strategies for steering exist. Surprisingly, guided needles are the smallest group, this could have the same explanation as above that most articles did not consider the needle propelling design yet. Another possible explanation could be that a guidance system is designed separately (i.e., excluding the needle).

In almost all collected articles, a combination of strategies was used to improve the needle

design. In nature, multiple strategies are often combined as well; for example, the mosquito first anchors into the skin and then advances by using friction manipulation and vibration. In general, further research is needed to determine the optimal combination(s) of needle-tissue interaction and propelling strategies for different medical applications.

Figure 3.8 shows that the main sources of bioinspiration are insects (indicated by the purple-tinted colors), which may be due to the presence of needle-like stingers in many insects. Another common source of inspiration is parasites, which may be related to their infiltrating characteristics. An interesting finding is that for the translation strategy, only insects were used as a source of inspiration, while for interlocking, a wider variety of bioinspiration sources was used. These results may partially be explained by the many varieties in nature that can be found using interlocking strategies. Overall, animals were more commonly used as a source of inspiration than other organisms such as plants or fungi. However, these other organisms also offer a variety of interesting strategies and shapes worth exploring.



**Figure 3.8. Distribution of bioinspiration sources in the collected articles.** Note: articles that use multiple bioinspiration sources are counted as one entity divided over the number of different bioinspiration sources (e.g., 1/2 parasitoid wasp and 1/2 mosquito).

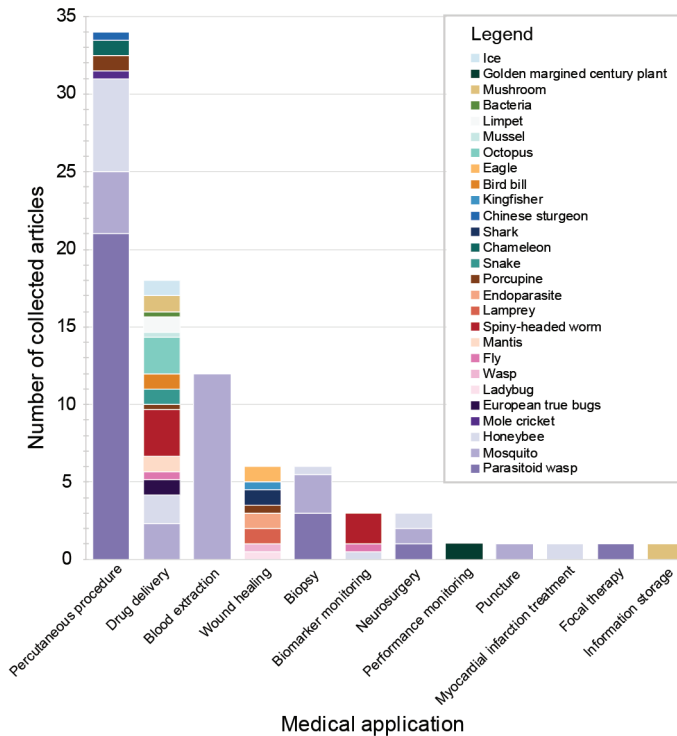
Among the developed needles in the collected articles, additive manufacturing is the most commonly used manufacturing method, with 33 out of 80 articles utilizing some form of 3D printing. Within the 3D printing techniques used, UV lithography with photoresin is particularly prevalent due to its high precision. Other 3D printing techniques include material extrusion and magneto-rheological drawing lithography, with material choices depending on the specific 3D printing method, this results in plastics being the most commonly used material. Molding is the second most common manufacturing method and is used in 15 out of 80 articles. The molds were commonly made out of PDMS, although metal molds made from aluminum were also used. Silk fibroin, silicon, or hydrogel were used to fill the mold and were cured with a UV light. Another technique that is utilized in 12 out of 80 articles is removing material via laser cutting or etching. Lastly, 12 out of 80 articles used off-the-shelf parts assembled into the final prototype, with some parts modified by laser cutting. The material choices depended on the desired properties of the needle design and the employed manufacturing method. For flexible designs, rubber was often chosen while for designs that needed more strength, ceramics and metals were used. Some articles specifically focused on material and manufacturing method selection, such as Schneider *et al.* [36], who explored different manufacturing methods and corresponding materials. A few articles only included a computer-simulated model of the needle, rather than a manufactured design.

Most of the collected articles did not define a specific medical application and were designed for general percutaneous procedures (Figure 3.9). This is likely because most of the designs are still in the prototype phase and are not yet commercially available. While designing for a general purpose may be beneficial to create widely applicable needles, designing for a specific medical application can be beneficial when optimizing for a task. Drug delivery is the largest specific medical application of MN patches, as they are primarily designed for this purpose. Since it is important to stay attached to the skin during drug delivery, the main strategy is grip enlargement for which a variety of bioinspiration sources was used. Interesting to note is that mosquitoes are the only organisms used as inspiration for blood extraction applications, likely due to their blood-sucking abilities. Further research should be undertaken to investigate the potential of other bloodsucking organisms and their usability for this medical application.

### 3.5.2 Limitations and recommendations

A systematic approach was employed to increase the likelihood of identifying relevant bioinspired needle designs. Nevertheless, it is possible that relevant articles on bioinspired medical needles were missed due to, for instance, missing relevant keywords. The literature search was conducted using general terms such as bioinspiration rather than specific organisms. Snowballing resulted in additional articles with titles including 'mosquito-inspired needle'. Therefore, it is likely that there are other specific bioinspired terms used in article titles that were not found when using the more general keyword 'bioinspiration.'

As already stated by Rahamim and Azagury [86] there should be a general use of bioinspi-



**Figure 3.9. Number of collected articles, classified based on the needle's medical application and source bioinspiration.** Note: articles describing needles that use multiple bioinspiration sources are counted as one entity divided over the number of different bioinspiration sources (e.g., 1/2 parasitoid wasp and 1/2 mosquito).

ration terms to prevent misuse or disuse of the term. Moreover, it can increase the audience and progress of the field. It is possible that the collected articles do not represent the entire field, as a large number of the articles were published by the same research groups and contain developments on previous publications of the same prototype. Additionally, only a limited number of databases (i.e., Scopus, Web of Science, and PubMed) were used for the reproducibility of this study. Furthermore, the articles were manually selected following the eligibility criteria, however, manual selection is always biased due to the interpretation of the criteria.

It might be difficult to draw conclusions about which strategy is most effective based on the results published in different articles. The test setups varied among articles; for instance, in some articles, needles were tested *ex vivo* on porcine skin or organ tissue, while others were tested *in vivo* on mice or *in vitro* on tissue phantoms made of PVC or silicon. The measured variables of the tests varied as well; some articles reported the reduced insertion forces, while others reported the durability or drug distribution.

An interesting direction for future research is the use of biomaterials for the needle design, such as Yoshida and Takei [87], who designed a needle from a human hair or Olatunji *et al.* [88], who created a needle from fish scales. A second interesting direction is the use of bio-

logical processes, such as Gao *et al.* [89], who used bioinspired crystallization for the needle design. In addition to investigating needles themselves, it may be useful to consider robotic needle systems. Zhang *et al.* [90] showed a robotic needle system design based on a leech, this system, rather than steering the needle to the target, moves the tissue, and thus the target, to the sucking arm. For grip-enlarging strategies, it may be useful to examine gripper designs instead of needle designs. There were only three articles collected describing needle designs using suction and adhesion strategies. These needle designs have significant overlap with medical gripper designs. Therefore, medical gripper designs could potentially be integrated with needles as demonstrated by Joymungul *et al.* [65].

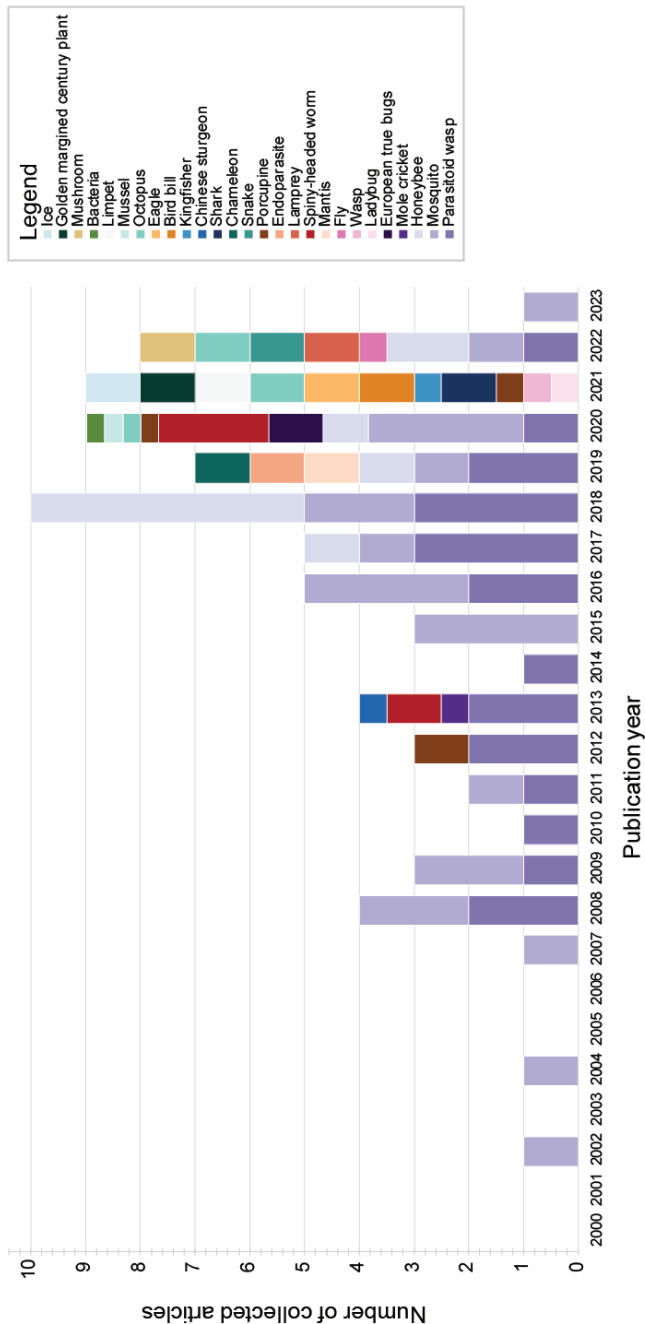
### 3.5.3 Temporal distribution and future perspective

The design of medical needles using bioinspiration is a relatively new field, with the first article on the topic being published in 2002 [56]. Figure 3.10 shows an increasing number of publications concerning bioinspired needles over the last 20 years. Not only has the quantity increased, but also the variety of the used bioinspiration sources has increased. During the first 15 years, bioinspiration for needle design was largely limited to the parasitoid wasp and mosquito. However, in the past four years, a variety of over 25 species has been investigated, and this trend is likely to continue in the future. The adhering and sucking strategies appeared in 2020 and 2021. Thus, we can expect that especially those strategies will develop in the future. However, it is important to note that the included articles consider prototypes that are not yet suitable for clinical practice. This is particularly evident in the fabrication methods, where, as stated before, 3D printing is most commonly used. While 3D printing is useful for prototyping, it is not suitable for high-volume production due to its high costs. More suitable production methods include the use of molds such as ferrofluid molding, as used by Zhang *et al.* [23]. The development of production techniques will enable the development of bioinspired needles and the fabrication of needles in their required shape.

The implementation of bioinspired needles in clinical practice is expected to take time due to the need for thorough testing and compliance with healthcare regulations. However, it is likely that bioinspired needles will become a less painful and more accurate alternative to current hypodermic needles and MN patches. Additionally, MN patches might be used as wearable drug delivery systems for conditions such as diabetes.

## 3.6 Conclusion

This review provides a comprehensive overview of the current developments in bioinspired needles for medical applications. A scientific literature search of bioinspired needles was conducted using Scopus, Web of Science, and PubMed. In total, 80 articles were included and classified according to their needle-tissue interaction and needle propulsion. The needle-tissue interaction can be modified to reduce or enlarge grip strategies. Passive and active strategies were identified to reduce grip, including form modification, translation, and



**Figure 3.10. Temporal distribution of the collected articles, classified based on the source of bioinspiration.** Note: articles describing needles that use multiple bioinspiration sources are counted as one entity divided over the number of different bioinspiration sources (e.g., 1/2 parasitoid wasp and 1/2 mosquito). strategies.



rotation. Among them, form modification was the most commonly used. To increase grip, interlocking, sucking, and adhering strategies were identified, with interlocking being the most common. External needle propulsion strategies include free hand and guided, with free hand being the most common, but lacking a bioinspired aspect. Internal propelling could be achieved through friction manipulation of the tissue. Multiple strategies can be combined to design an optimal needle for accurate targeting, minimal tissue damage, and pain reduction, surpassing conventional hypodermic needles and MN patches. While these designs are still in developmental stages, they provide ample opportunity for designers to improve existing prototypes or draw inspiration from these strategies to create a new generation of bioinspired needles that could have a significant impact on the medical world.

## Supplementary material

The appendices underlying this study are available at doi: 10.1088/1748-3190/acd905.

## References

- Matheson E, Watts T, Secoli R, y Baena FR. Cyclic motion control for programmable bevel-tip needle 3D steering: A simulation study. 2018 IEEE International Conference on Robotics and Biomimetics (ROBIO); 2018: IEEE. doi: 10.1109/ROBIO.2018.8665117.
- Hypodermic needle. 2023. In Cambridge Dictionary [Available from: <https://dictionary.cambridge.org/dictionary/english/needle?q=hypodermic+needle>].
- Scali M, Pusch T, Breedveld P, Dodou D. Ovipositor-inspired steerable needle: design and preliminary experimental evaluation. *Bioinspiration & Biomimetics*. 2017;13(1):016006. doi: 10.1088/1748-3190/aa92b9.
- Suzuki M, Sawa T, Takahashi T, Aoyagi S. Fabrication of microneedle mimicking mosquito proboscis using nanoscale 3D laser lithography system. *International Journal of Automation Technology*. 2015;9(6):655-61. doi: 10.20965/ijat.2015.p0655.
- Sahlabadi M, Khodaei S, Jezler K, Hutapea P. Study of bioinspired surgery needle advancing in soft tissues. *Smart Materials, Adaptive Structures and Intelligent Systems*; 2017: American Society of Mechanical Engineers. doi: 10.1115/SMASIS2017-3915.
- Zhang X, Chen G, Yu Y, Sun L, Zhao Y. Bioinspired adhesive and antibacterial microneedles for versatile transdermal drug delivery. *Research*. 2020. doi: 10.34133/2020/3672120.
- Chen Z, He J, Qi J, Zhu Q, Wu W, Lu Y. Long-acting microneedles: a progress report of the state-of-the-art techniques. *Drug Discovery Today*. 2020;25(8):1462-8. doi: 10.1016/j.drudis.2020.05.006.
- Kim J, Park S, Nam G, Choi Y, Woo S, Yoon S-H. Bioinspired microneedle insertion for deep and precise skin penetration with low force: Why the application of mechanophysical stimuli should be considered. *Journal of the Mechanical Behavior of Biomedical Materials*. 2018;78:480-90. doi: 10.1016/j.jmbbm.2017.12.006.
- Roesthuis RJ, Van Veen YR, Jahya A, Misra S. Mechanics of needle-tissue interaction. 2011 IEEE/RSJ international conference on intelligent robots and systems; 2011: IEEE. doi: 10.1109/IROS.2011.6094969.
- Mahvash M, Dupont PE. Mechanics of dynamic needle insertion into a biological material. *IEEE transactions on biomedical engineering*. 2009;57(4):934-43. doi: 10.1109/TBME.2009.2036856.
- Makvandi P, Maleki A, Shabani M, Hutton AR, Kirkby M, Jamaledin R, et al. Bioinspired microneedle patches: Biomimetic designs, fabrication, and biomedical applications. *Matter*. 2022;5(2):390-429. doi: 10.1007/s40820-021-00611-9.

12. Scali M, Kreeft D, Breedveld P, Dodou D. Design and evaluation of a wasp-inspired steerable needle. *Proceedings of SPIE; Portland, Oregon, United States: International Society for Optics and Photonics*; 2017. p. 1016207.
13. Needle. 2022. In *Merriam Webster Dictionary* [Available from: <https://www.merriam-webster.com/dictionary/needle>].
14. Sahlabadi M, Hutapea P. Novel design of honeybee-inspired needles for percutaneous procedure. *Bioinspiration & biomimetics*. 2018;13(3):036013. doi: 10.1088/1748-3190/aaa348.
15. Li Y, Zhou W, Liu C, Geng D, Dai J, Xie Y, et al. Fabrication and characteristic of flexible dry bioelectrodes with microstructures inspired by golden margined century plant leaf. *Sensors and Actuators A: Physical*. 2021;321:112397. doi: 10.1016/j.sna.2020.112397.
16. Zhang X, Fu X, Chen G, Wang Y, Zhao Y. Versatile ice microneedles for transdermal delivery of diverse actives. *Advanced Science*. 2021;8(17):2101210. doi: 10.1002/adv.202101210.
17. Suzuki M, Sawa T, Takahashi T, Aoyagi S. Ultrafine three-dimensional (3D) laser lithographic fabrication of microneedle and its application to painless insertion and blood sampling inspired by mosquito. 2015 IEEE/RSJ International Conference on Intelligent Robots and Systems (IROS); 2015: IEEE. doi: 10.1109/IROS.2015.7353754.
18. Cai Y, Huang S, Zhang Z, Zhang J, Zhu X, Chen X, et al. Bioinspired rotation microneedles for accurate transdermal positioning and ultramiminal-invasive biomarker detection with mechanical robustness. *Research*. 2022. doi: 10.34133/2022/9869734.
19. Wang JY, Cong Q. Experimental study of the concave bionic drag reduction needles. *Applied Mechanics and Materials*. 2014;461:702-6. doi: 10.4028/www.scientific.net/AMM.461.702.
20. Cho WK, Ankrum JA, Guo D, Chester SA, Yang SY, Kashyap A, et al. Microstructured barbs on the North American porcupine quill enable easy tissue penetration and difficult removal. *Proceedings of the National Academy of Sciences*. 2012;109(52):21289-94. doi: 10.1073/pnas.1216441109.
21. Zhang X, Chen G, Cai L, Wang Y, Sun L, Zhao Y. Bioinspired pagoda-like microneedle patches with strong fixation and hemostasis capabilities. *Chemical Engineering Journal*. 2021;414:128905. doi: 10.1016/j.cej.2021.128905.
22. Deng Y, Yang C, Zhu Y, Liu W, Li H, Wang L, et al. Lamprey-teeth-inspired oriented antibacterial sericin microneedles for infected wound healing improvement. *Nano letters*. 2022;22(7):2702-11. doi: 10.1021/acs.nanolett.1c04573.
23. Zhang X, Wang F, Yu Y, Chen G, Shang L, Sun L, et al. Bio-inspired clamping microneedle arrays from flexible ferrofluid-configured moldings. *Science bulletin*. 2019;64(15):1110-7. doi: 10.1016/j.scib.2019.06.016.
24. Zhang X, Chen G, Sun L, Ye F, Shen X, Zhao Y. Claw-inspired microneedle patches with liquid metal encapsulation for accelerating incisional wound healing. *Chemical Engineering Journal*. 2021;406:126741. doi: 10.1016/j.cej.2020.126741.
25. Guo M, Wang Y, Gao B, He B. Shark tooth-inspired microneedle dressing for intelligent wound management. *Acs Nano*. 2021;15(9):15316-27. doi: 10.1021/acsnano.1c06279.
26. Jeon EY, Lee J, Kim BJ, Joo KI, Kim KH, Lim G, et al. Bio-inspired swellable hydrogel-forming double-layered adhesive microneedle protein patch for regenerative internal/external surgical closure. *Biomaterials*. 2019;222:119439. doi: 10.1016/j.biomaterials.2019.119439.
27. Yang SY, O'Cearbhaill ED, Sisk GC, Park KM, Cho WK, Villiger M, et al. A bio-inspired swellable microneedle adhesive for mechanical interlocking with tissue. *Nature communications*. 2013;4(1):1702. doi: 10.1038/ncomms2715.
28. Liu S, Chu S, Banis GE, Beardslee LA, Ghodssi R. Biomimetic barbed microneedles for highly robust tissue anchoring. 2020 IEEE 33rd International Conference on Micro Electro Mechanical Systems (MEMS); 2020: IEEE. doi: 10.1109/JMEMS.2020.2999448.
29. Chen Z, Lin Y, Lee W, Ren L, Liu B, Liang L, et al. Additive manufacturing of honeybee-inspired microneedle for easy skin insertion and difficult removal. *ACS applied materials & interfaces*. 2018;10(35):29338-46. doi: 10.1021/acsami.8b09563.

30. Izumi H, Suzuki M, Kanzaki T, Aoyagi S. Realistic imitation of mosquito's proboscis-sharp and jagged needle and their cooperative inserting motion. *Transducers 2009 International Solid-State Sensors, Actuators and Microsystems Conference*; 2009: IEEE.
31. Li Q, Xu R, Fan H, Xu J, Xu Y, Cao P, et al. Smart mushroom-inspired printable and lightly detachable (MILD) microneedle patterns for effective COVID-19 vaccination and decentralized information storage. *ACS nano*. 2022;16(5):7512-24. doi: 10.1021/acsnano.1c10718.
32. Aoyagi S, Izumi H, Fukuda M. Biodegradable polymer needle with various tip angles and consideration on insertion mechanism of mosquito's proboscis. *Sensors and Actuators A: Physical*. 2008;143(1):20-8. doi: 10.1016/j.sna.2007.06.007.
33. Chen Z, Ren L, Li J, Yao L, Chen Y, Liu B, et al. Rapid fabrication of microneedles using magnetorheological drawing lithography. *Acta Biomaterialia*. 2018;65:283-91. doi: 10.1016/j.actbio.2017.10.030.
34. Frasson L, Parittotokkaporn T, Davies BL, Baena FRy. Early developments of a novel smart actuator inspired by nature. *International journal of intelligent systems technologies and applications*. 2010;8(1-4):409-22. doi: 10.1109/MMVIP.2008.4749526.
35. Frasson L, Parittotokkaporn T, Schneider A, Davies B, Vincent J, Huq S, et al. Biologically inspired microtexturing: Investigation into the surface topography of next-generation neurosurgical probes. *30th Annual International Conference of the IEEE Engineering in Medicine and Biology Society: IEEE*; 2008. p. 5611-4.
36. Schneider A, Frasson L, Parittotokkaporn T, y Baena FMR, Davies BL, Huq SE. Biomimetic microtexturing for neurosurgical probe surfaces to influence tribological characteristics during tissue penetration. *Microelectronic Engineering*. 2009;86(4-6):1515-7. doi: 10.1016/j.mee.2009.02.027.
37. Gidde STR, Acharya SR, Kandel S, Pleshko N, Hutapea P. Assessment of tissue damage from mosquito-inspired surgical needle. *Minimally Invasive Therapy & Allied Technologies*. 2022;31(7):1112-21. doi: 10.1080/13645706.2022.2051718.
38. Gidde STR, Islam S, Kim A, Hutapea P. Experimental study of mosquito-inspired needle to minimize insertion force and tissue deformation. *Proceedings of the Institution of Mechanical Engineers, Part H: Journal of Engineering in Medicine*. 2023;237(1):113-23. doi: 10.1177/09544119221137133.
39. Gidde STR, Ciuciu A, Devaravar N, Doracio R, Kianzad K, Hutapea P. Effect of vibration on insertion force and deflection of bioinspired needle in tissues. *Bioinspiration & biomimetics*. 2020;15(5):054001. doi: 10.1088/1748-3190/ab9341.
40. Sahlabadi M, Hutapea P. Tissue deformation and insertion force of bee-stinger inspired surgical needles. *Journal of Medical Devices*. 2018;12(3):034501. doi: 10.1115/1.4040637.
41. Sahlabadi M, Khodaei S, Jezler K, Hutapea P. Insertion mechanics of bioinspired needles into soft tissues. *Minimally Invasive Therapy & Allied Technologies*. 2018;27(5):284-91. doi: 10.1080/13645706.2017.1418753.
42. Giovannini M, Ren H, Wang X, Ehmann K. Tissue cutting with microerrated biopsy punches. *Journal of Micro-and Nano-Manufacturing*. 2017;5(4):041004. doi: 10.1115/1.4037726.
43. Sravani KG, Desala RK, Chand P, Sathvik K, Rao KS, Lay-Ekuakille A. Design and analysis of bio-inspired micro-needle for drug delivery applications. *IEEE Transactions on NanoBioscience*. 2022;22(2):237-44. doi: 10.1109/TNB.2022.3185633.
44. Gittard SD, Narayan RJ, Ovsianikov A, Chichkov BN. Rapid prototyping of biomimetic structures: fabrication of mosquito-like microneedles by two-photon polymerization. *MRS Online Proceedings Library (OPL)*. 2009;1239:1239-VV01-11. doi: 10.1557/PROC-1239-VV01-11.
45. Han D, Morde RS, Mariani S, La Mattina AA, Vignali E, Yang C, et al. 4D printing of a bioinspired microneedle array with backward-facing barbs for enhanced tissue adhesion. *Advanced Functional Materials*. 2020;30(11):1909197. doi: 10.1002/adfm.201909197.
46. Hara Y, Yamada M, Tatsukawa C, Takahashi T, Suzuki M, Aoyagi S. Fabrication of stainless steel microneedle with laser-cut sharp tip and its penetration and blood sampling performance. *International Journal of Automation Technology*. 2016;10(6):950-7. doi: 10.20965/ijat.2016.p0950.

47. Hara Y, Yamada M, Tatsukawa C, Takahashi T, Suzuki M, Aoyagi S. Laser Fabrication of Jagged-Shaped Stainless Steel Microneedle Imitating Mosquito's Maxilla. *International Journal of Automation Technology*. 2016;10(6):958-64.
48. Izumi H, Yajima T, Aoyagi S, Tagawa N, Arai Y, Hirata M, et al. Combined harpoonlike jagged microneedles imitating mosquito's proboscis and its insertion experiment with vibration. *IEEE Transactions on Electrical and Electronic Engineering*. 2008;3(4):425-31.
49. Izumi H, Suzuki M, Aoyagi S, Kanzaki T. Realistic imitation of mosquito's proboscis: Electrochemically etched sharp and jagged needles and their cooperative inserting motion. *Sensors and Actuators A: Physical*. 2011;165(1):115-23.
50. Li AD, Putra KB, Chen L, Montgomery JS, Shih A. Mosquito proboscis-inspired needle insertion to reduce tissue deformation and organ displacement. *Scientific Reports*. 2020;10(1):12248. doi: 10.1038/s41598-020-68596-w.
51. Li F, Huang Z, Xu L. Path planning of 6-DOF venipuncture robot arm based on improved a-star and collision detection algorithms. 2019 IEEE international conference on robotics and biomimetics (ROBIO); 2019: IEEE. doi: 10.1109/ROBIO49542.2019.8961668.
52. Li X, Shan W, Yang Y, Joralmón D, Zhu Y, Chen Y, et al. Limpet tooth-inspired painless microneedles fabricated by magnetic field-assisted 3D printing. *Advanced functional materials*. 2021;31(5):2003725. doi: 10.1002/adfm.202003725.
53. Liu S, Chu S, Beardslee LA, Ghodssi R. Hybrid and passive tissue-anchoring mechanism for ingestible resident devices. *Journal of Microelectromechanical Systems*. 2020;29(5):706-12. doi: 10.1109/JMEMS.2020.2999448.
54. Lu Y, Ren T, Zhang H, Jin Q, Shen L, Shan M, et al. A honeybee stinger-inspired self-interlocking microneedle patch and its application in myocardial infarction treatment. *Acta biomaterialia*. 2022;153:386-98. doi: 10.1016/j.actbio.2022.09.015.
55. Mizuno Y, Takasawa K, Hanada T, Nakamura K, Yamada K, Tsubaki H, et al. Fabrication of novel-shaped microneedles to overcome the disadvantages of solid microneedles for the transdermal delivery of insulin. *Biomedical Microdevices*. 2021;23:1-8. doi: 10.1007/s10544-021-00576-x.
56. Oka K, Aoyagi S, Arai Y, Isono Y, Hashiguchi G, Fujita H. Fabrication of a micro needle for a trace blood test. *Sensors and Actuators A: Physical*. 2002;97:478-85. doi: 10.1016/S0924-4247(01)00872-X.
57. Plamadeala C, Gosain SR, Hischen F, Buchroithner B, Puthukodan S, Jacak J, et al. Bio-inspired microneedle design for efficient drug/vaccine coating. *Biomedical microdevices*. 2020;22:1-9. doi: 10.1007/s10544-019-0456-z.
58. Suzuki M, Takahashi T, Aoyagi S. 3D laser lithographic fabrication of hollow microneedle mimicking mosquitos and its characterisation. *International Journal of Nanotechnology*. 2018;15(1-3):157-73. doi: 10.1504/IJNT.2018.089545.
59. Suzuki M, Sawa T, Terada Y, Takahashi T, Aoyagi S. Fabrication of microneedles precisely imitating mosquito's proboscis by nanoscale tree dimensional laser lithography and its characterization. 2015 Transducers-2015 18th International Conference on Solid-State Sensors, Actuators and Microsystems (TRANSDUCERS); 2015: IEEE.
60. Tran L-G, Nguyen T-Q, Park W-T. Bio-inspired barbed microneedle for skin adhesion with interlocking mechanics. 2019 IEEE 32nd International Conference on Micro Electro Mechanical Systems (MEMS); 2019: IEEE. doi: 10.1109/MEMSYS.2019.8870874.
61. Tsuchiya K, Isobata K, Sato M, Uetsuji Y, Nakamachi E, Kajiwaru K, et al. Design of painless microneedle for blood extraction system. *BioMEMS and Nanotechnology III*; 2007: SPIE. doi: 10.1117/12.759058.
62. Velivela PT, Letov N, Liu Y, Zhao YF. Application of domain integrated design methodology for bio-inspired design-a case study of suture pin design. *Proceedings of the Design Society*. 2021;1:487-96. doi: 10.1017/pds.2021.49.
63. Wang J, Chen Y, Ren L, Li Y, Zhou C. Bionic technology research study based on the non-

- smooth surface morphology of the mosquito mouthparts. 2016 6th International Conference on Mechatronics, Computer and Education Informationization (MCEI 2016); 2016: Atlantis Press. doi: 10.2991/mcei-16.2016.72.
64. Fu X, Zhang X, Huang D, Mao L, Qiu Y, Zhao Y. Bioinspired adhesive microneedle patch with gemcitabine encapsulation for pancreatic cancer treatment. *Chemical Engineering Journal*. 2022;431:133362. doi: 10.1016/j.cej.2021.133362.
  65. Joymungul K, Mitros Z, Da Cruz L, Bergeles C, Sadati SH. Gripe-needle: a sticky suction cup gripper equipped needle for targeted therapeutics delivery. *Frontiers in Robotics and AI*. 2021;8:752290. doi: 10.3389/frobt.2021.752290.
  66. Suzuki M, Motooka F, Takahashi T, Aoyagi S. Development of microneedle puncture device that prevents buckling of needle by delivery operation. *Journal of Robotics and Mechatronics*. 2020;32(2):382-9. doi: 10.20965/jrm.2020.p0382.
  67. Scali M, Breedveld P, Dodou D. Experimental evaluation of a self-propelling bio-inspired needle in single-and multi-layered phantoms. *Scientific reports*. 2019;9(1):1-13. doi: 10.1038/s41598-019-56403-0.
  68. O'Carbhaill ED, Laulicht B, Mitchell N, Yu L, Valic M, Masiakos P, et al. A radial clutch needle for facile and safe tissue compartment access. *Medical devices & sensors*. 2019;2(5-6):e10049. doi: 10.1002/mds3.10049.
  69. Bloembergen J, Trauzettel F, Coolen B, Dodou D, Breedveld P. Design and evaluation of an MRI-ready, self-propelled needle for prostate interventions. *PLoS ONE*. 2022;17(9):e0274063. doi: 10.1371/journal.pone.0274063.
  70. Frasson L, Ferroni F, Ko SY, Dogangil G, y Baena FR. Experimental evaluation of a novel steerable probe with a programmable bevel tip inspired by nature. *Journal of robotic surgery*. 2012;6(3):189-97. doi: 10.1007/s11701-011-0277-4.
  71. Ko SY, Frasson L, y Baena FR. Closed-loop planar motion control of a steerable probe with a "programmable bevel" inspired by nature. *IEEE Transactions on Robotics*. 2011;27(5):970-83. doi: 10.1109/TRO.2011.2159411.
  72. Ko SY, y Baena FR. Toward a miniaturized needle steering system with path planning for obstacle avoidance. *IEEE Transactions on Biomedical Engineering*. 2012;60(4):910-7. doi: 10.1109/TBME.2012.2227741.
  73. Sprang T, Breedveld P, Dodou D. Wasp-inspired needle insertion with low net push force. *Conference on Biomimetic and Biohybrid Systems*; 2016: Springer. doi: 10.1007/978-3-319-42417-0\_28.
  74. Burrows C, Secoli R, y Baena FR. Experimental characterisation of a biologically inspired 3D steering needle. 2013 13th International Conference on Control, Automation and Systems (ICCAS 2013); 2013: IEEE. doi: 10.1109/ICCAS.2013.6704141.
  75. Burrows C, Liu F, y Baena FR. Smooth on-line path planning for needle steering with non-linear constraints. 2015 IEEE/RSJ International Conference on Intelligent Robots and Systems (IROS); 2015: IEEE. doi: 10.1109/IROS.2015.7353739.
  76. Ko SY, y Baena FR. Trajectory following for a flexible probe with state/input constraints: An approach based on model predictive control. *Robotics and Autonomous systems*. 2012;60(4):509-21. doi: 10.1016/j.robot.2011.11.011.
  77. Leibinger A, Oldfield MJ, Rodriguez y Baena F. Minimally disruptive needle insertion: a biologically inspired solution. *Interface focus*. 2016;6(3):20150107. doi: 10.1098/rsfs.2015.0107.
  78. Matheson E, Rodriguez y Baena F. Biologically inspired surgical needle steering: technology and application of the programmable bevel-tip needle. *Biomimetics*. 2020;5(4):68. doi: 10.3390/biomimetics5040068.
  79. Matheson E, Secoli R, Burrows C, Leibinger A, Rodriguez y Baena F. Cyclic motion control for programmable bevel-tip needles to reduce tissue deformation. *Journal of Medical Robotics Research*. 2019;4(01):1842001. doi: 10.1142/S2424905X18420011.
  80. Oldfield M, Burrows C, Kerl J, Frasson L, Parittotokkaporn T, Beyrau F, et al. Highly resolved

- strain imaging during needle insertion: results with a novel biologically inspired device. *Journal of the mechanical behavior of biomedical materials*. 2014;30:50-60. doi: 10.1016/j.jmbbm.2013.10.016.
81. Oldfield MJ, Leibinger A, Seah TET, y Baena FR. Method to reduce target motion through needle-tissue interactions. *Annals of biomedical engineering*. 2015;43(11):2794-803. doi: 10.1007/s10439-015-1329-0.
82. Secoli R, Rodriguez F. Experimental validation of curvature tracking with a programmable bevel-tip steerable needle. 2018 International Symposium on Medical Robotics (ISMR); 2018: IEEE. doi: 10.1109/ISMR.2018.8333302.
83. Viridyawan V, Oldfield M, y Baena FR. Laser Doppler sensing for blood vessel detection with a biologically inspired steerable needle. *Bioinspiration & biomimetics*. 2018;13(2):026009. doi: 10.1088/1748-3190/aaa6f4.
84. Viridyawan V, Baena FRY. Vessel pose estimation for obstacle avoidance in needle steering surgery using multiple forward looking sensors. 2018 IEEE/RSJ International Conference on Intelligent Robots and Systems (IROS); 2018: IEEE. doi: 10.1109/IROS.2018.8594198.
85. Culmone C, Smit G, Breedveld P. Additive manufacturing of medical instruments: A state-of-the-art review. *Additive Manufacturing*. 2019;27:461-73. doi: 10.1016/j.addma.2019.03.015.
86. Rahamim V, Azagury A. Bioengineered biomimetic and bioinspired noninvasive drug delivery systems. *Advanced Functional Materials*. 2021;31(44):2102033. doi: 10.1002/adfm.202102033.
87. Yoshida Y, Takei T. Fabrication of a microneedle using human hair. *Japanese Journal of Applied Physics*. 2009;48(9R):098007. doi: 10.1143/JJAP.48.098007.
88. Olatunji O, Igwe CC, Ahmed AS, Alhassan DO, Asieba GO, Diganta BD. Microneedles from fish scale biopolymer. *Journal of Applied Polymer Science*. 2014;131(12). doi: 10.1002/app.40377.
89. Gao Y, Zhang W, Cheng YF, Cao Y, Xu Z, Xu LQ, et al. Intradermal administration of green synthesized nanosilver (NS) through film-coated PEGDA microneedles for potential antibacterial applications. *Biomaterials Science*. 2021;9(6):2244-54. doi: 10.1039/D0BM02136A.
90. Zhang W, Zhang Y, Liu Y. Design and control of a bionic needle puncture robot. *The International Journal of Medical Robotics and Computer Assisted Surgery*. 2021;17(2):e2200. doi: 10.1002/rcs.2200.



# 4

## **A Patent Review of Focal Therapy Instruments**

Published as:

Bloemberg J., van Riel L., Dodou D., Breedveld P. (2021). Focal therapy for localized cancer: a patent review. Expert Review of Medical Devices, 18(8):751-769. doi: 10.1080/17434440.2021.1943360.





## **Abstract**

Conventional cancer treatments such as radical surgery and systemic therapy targeting the organ or organ system might have side effects because of damage to the surrounding tissue. For this reason, there is a need for new instruments that focally treat cancer. This review provides a comprehensive overview of the patent literature on minimally and noninvasive focal therapy instruments to treat localized cancer. The medical section of the Google Patents database was scanned, and 128 patents on focal therapy instruments published in the last two decades (2000-2021) were retrieved and classified. The classification is based on the treatment target (cancer cell or network of cancer cells), treatment purpose (destroy the cancerous structure or disable its function), and treatment means (energy, matter, or a combination of both). We found patents describing instruments for all groups, except for the instruments that destroy a cancer cell network structure by applying matter (e.g., particles) to the network. The description of the different treatment types may serve as a source of inspiration for new focal therapy instruments to treat localized cancer.

## 4.1 Introduction

### 4.1.1 Background

Patients diagnosed with cancer encounter a dilemma: the choice of the type of treatment. There is a wide range of possible cancer treatment modalities, including radical surgery, radiotherapy, and systemic treatment, such as chemotherapy, hormonal therapy, or immunotherapy [1]. Treatments targeted at the organ or the organ system might have side effects because of damage to the surrounding tissue [1-3]. A strategy to overcome this problem is to focus the treatment on the cancer cells (i.e., the lesion), thereby preserving noncancerous tissue, a method called focal therapy [4-6].

There is no consensus in the literature on the exact definition of focal therapy. In this review, we defined focal therapy as a minimally or noninvasive therapy that focuses on the localized killing of cancer cells without resecting them. The remaining dead cancer cells are subsequently resorbed via normal body mechanisms [7]. Focal therapy is possible when the cancer is detected at an early stage because then the cancer cells are still positioned locally in an organ-confined space [8-10].

The localized killing by focal therapy aims at different organizational levels of the body as compared to conventional treatment such as systemic therapy. The structural hierarchy of the human anatomy consists of distinct levels of organization that increase in complexity: the cellular, tissue, organ, organ system, and organismal level [11]. The cancer tissue/network comprises the cancer cells and their vascular network for the supply of oxygen and nutrients and the removal of waste products, essential for the cancer progression [12]. Every level of organization is characterized by its anatomy (the structure) and physiology (the function), both being essential for its existence [11]. Focal therapy targets either the tissue or the cell level, whereas radical surgery targets the cancer cell network and a margin of normal tissue surrounding it (e.g., the whole organ in radical prostatectomy), and systemic therapy targets the organ system [13-15].

### 4.1.2 Problem definition

Cancer treatments such as radical surgery and systemic therapy damage not only the cancer cells but also the surrounding tissue, leading to undesirable side effects [1-3]. The damage might lead to functional problems. For example, prostate cancer patients who receive a standard radical treatment, including radical prostatectomy or radiotherapy, are at risk of side effects that impair urinary, sexual, or bowel function [16-18].

Focal cancer treatment reduces the risk of side effects. Focal treatment is possible when the cancer is unifocal. Recently, there has been an increasing interest in focally treating unifocal prostate cancer [3]. The anatomy and physiology of both the cancer cell and the network of cancer cells facilitate a wide range of focal therapy instruments. Focal therapy instruments comprise a collection of instruments using different means (e.g., energy such as ultrasound waves) to target various properties of the lesion to cause local cell death [6, 19].

A clear classification of focal therapy instruments, described in the patent literature, would serve as an overview of the treatment types applied by focal therapy instruments. This study focuses on patent literature because it provides insights into the future directions of the technologies applied by the instruments described in patents. To our knowledge, a comprehensive overview of the patent literature on focal therapy instruments to treat localized cancer is not yet available.

### 4.1.3 Goal and structure

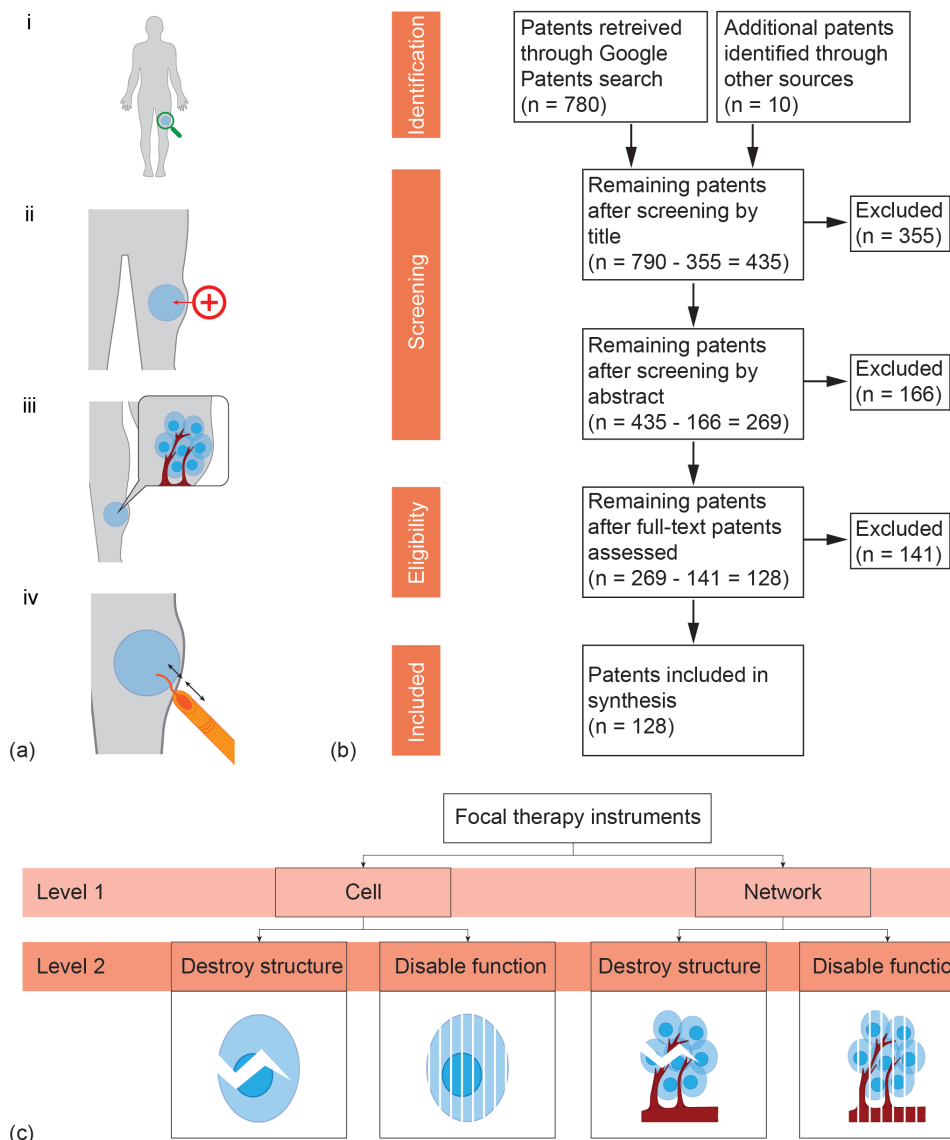
This study presents a comprehensive overview of the patent literature on focal therapy instruments to treat localized cancer. We decided to focus on focal treatment instruments for unifocal cancer in general, because the working principle of instruments to treat, for example, prostate cancer, could also be of interest for the treatment of unifocal cancers in other organs such as the breast, kidney, or liver. An overview of the patent literature on focal therapy instruments provides insights into the future directions of the technologies applied by these instruments. The relevant patents were classified based on their treatment target, purpose, and means. First, the method of the patent search on focal therapy instruments is described in Chapter 4.2. Next, the instruments found in the patents are categorized and described. The classification of the focal therapy instruments targeting the individual cancer cells is described in Chapter 4.3. The classification of the focal therapy instruments targeting the network of cancer cells is described in Chapter 4.4. Then, the commercially available instruments are discussed in Chapter 4.5. The types of treatment and the instruments are discussed in relation to the temporal distribution of the classified patents in Chapter 4.6. Chapter 4.7 presents the conclusion.

## 4.2 Methods

### 4.2.1 Patent search

A search within the patent literature for medical instruments used for focal therapy to treat localized cancer was conducted using the Google Patents database (accessed June 2021). Our search query was a Boolean search term consisting of a combination of keywords related to (1) the focal character of the treatment, (2) the type of treatment, (3) the pathology to be treated, and (4) the treatment tool and its design (Figure 4.1a).

We looked for the above-mentioned combination of search terms at the claims, title, and abstract of the patents. We restricted our search to patents linked to the Patent Cooperation Treaty (PCT), by using the prefix “WO” in the search term. Furthermore, we restricted our patent literature search to patents published after 1 January 2000. Lastly, we restricted our search within the medical field with the World Intellectual Property Organization (WIPO) code “A61”, which corresponds to the medical or veterinary science and hygiene class of human necessities. This class contains several subclasses and lower-level groups. Taking all of this into account, we focused our search on the following subclass and groups: “A61N”



**Figure 4.1. (a) Visual representation of (a) the search query, (b) the patent selection method, and (c) the classification.** (a) The search query consists of four groups of keywords that (i) limit the search to focal activities (rather than global/systemic), (ii) limit the search to treatments to cure the target area, (iii) limit the search to localized cancer, and (iv) limit the search to the tool design. (b) Schematic representation of the patent selection method. (c) Focal therapy instruments are classified as either targeting the individual cancer cells or the network of cancer cells. In either case, two types of treatment purposes can be distinguished: to destroy the structure or to disable the function.

representing “Electrotherapy, magnetotherapy, radiation therapy, ultrasound therapy”; “A61B6” representing “Apparatus for radiation diagnosis, e.g., combined with radiation therapy equipment”; “A61B18” representing “Surgical instruments, devices or methods for

transferring non-mechanical forms of energy to or from the body”; “A61B34” representing “Computer-aided surgery; Manipulators or robots specially adapted for use in surgery”. The entire search query was:

(CL = ((focal OR ablati\* OR thermal OR cryo\* OR "focused ultrasound" OR photodynamic OR brachy\*) AND (therapy OR treatment OR surgery) AND (cancer OR tumour OR neoplasm) AND (instrument OR instrumentation OR "equipment design" OR "machine design" OR apparatus OR needle OR probe)) OR TI = ((focal OR ablati\* OR thermal OR cryo\* OR "focused ultrasound" OR photodynamic OR brachy\*) AND (therapy OR treatment OR surgery) AND (cancer OR tumour OR neoplasm) AND (instrument OR instrumentation OR "equipment design" OR "machine design" OR apparatus OR needle OR probe)) OR AB = ((focal OR ablati\* OR thermal OR cryo\* OR "focused ultrasound" OR photodynamic OR brachy\*) AND (therapy OR treatment OR surgery) AND (cancer OR tumour OR neoplasm) AND (instrument OR instrumentation OR "equipment design" OR "machine design" OR apparatus OR needle OR probe))) (A61B6 OR A61B18 OR A61B34 OR A61N) country:WO before:publication:20210601 after:publication:20000101 language:ENGLISH.

#### 4.2.2 Eligibility criteria

The scope of this study was to make an overview of medical instruments that use focal therapy to treat localized cancer. Solely patents explaining the mechanical design of an *in vivo* focal therapy instrument to treat internal localized cancer were included. Patents for general focal therapy devices (i.e., not specifying the type of focal therapy, such as a single instrument that houses a catheter for cryotherapy, thermal treatment or delivery of a chemical agent or a single instrument designed to achieve ablation by microwave, radiofrequency, ultraviolet, ultrasound, or laser energy) and patents only focusing on the method of focal therapy but not on a device were excluded. Instruments only intended for veterinary medicine and instruments only for imaging, positioning, navigating, or monitoring were also excluded. Patents that only added a feature that does not relate to the focal working mechanism of an instrument presented in a different patent were excluded as well.

#### 4.2.3 Patent search results

The search yielded 780 patents (last update June 1, 2021). Based on the eligibility criteria, the titles, and when in doubt, the abstracts, figures, and full-texts were checked subsequently. After full-text inspection, 128 patents were identified, fulfilling all eligibility criteria (Figure 4.1b).

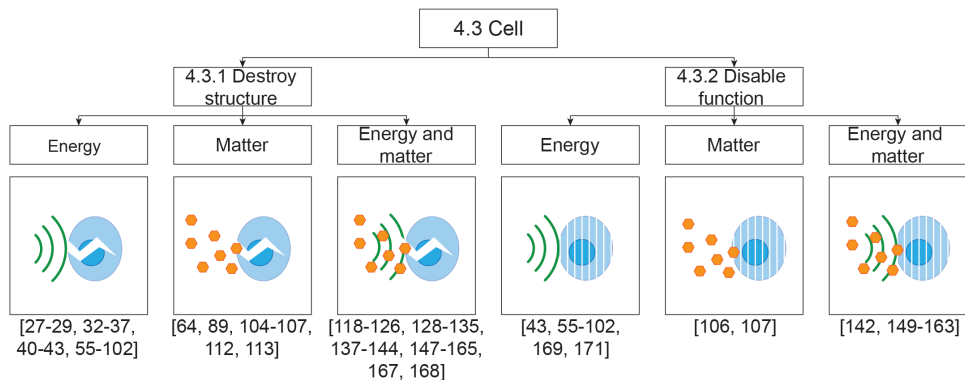
#### 4.2.4 Classification of focal therapy instruments

The results of our patent search revealed two types of targets for the focal therapy treatment: the individual cancer cells and the network of the cancer cells. In both cases, two types of treatment purposes were identified: to destroy the structure or to disable the function (Figure 4.1c). For each of these purposes, we made a distinction between instruments that use energy (e.g., heat caused by electromagnetic waves, ultrasound waves, or thermally con-

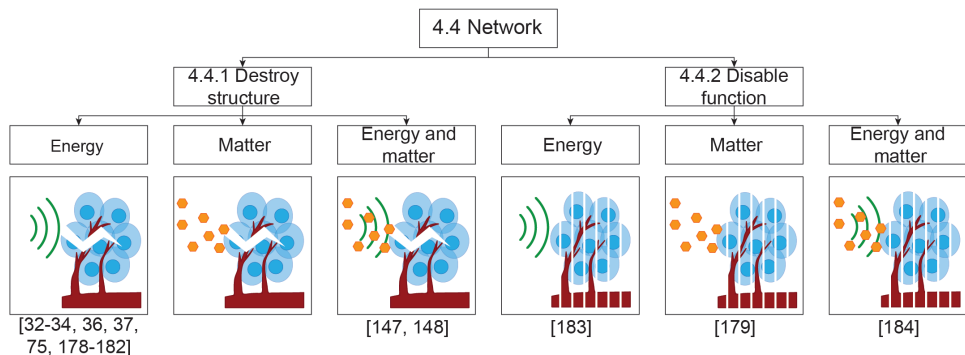
ductive elements) to interact with the individual cells or the network, instruments that use matter (e.g., chemical substances such as ethanol and antiandrogen), and instruments that use a combination of energy and matter (e.g., magnetic particles in combination with a magnetic field or photosensitive particles activated by light).

### 4.3 Destroy cancer cells on a cell level

Focal therapy instruments that target the individual cancer cells apply their treatment on each cell, thereby destroying the structure (Chapter 4.3.1) or disabling the function (Chapter 4.3.2) of each cell. The classification of the patents on focal therapy instruments to treat cancer on the individual cancer cell level resulted in six groups of focal therapy instruments. Figure 4.2a presents a graphical summary of the instrument classification, listing all the retrieved patents for each group of focal therapy instruments. Each subsubsubchapter describes the mechanical design variations of the focal therapy instruments classified into one group and the specific cancer types for which the instruments are designed.



(a)



(b)

**Figure 4.2. (a) Classification of focal therapy instruments to destroy cancer cells on cell level. (b) Classification of focal therapy instruments to destroy cancer cells on network level. These classifications also serve as schematic illustrations of the layout of Chapters 4.3 and 4.4.**

### 4.3.1 Destroy cell structure

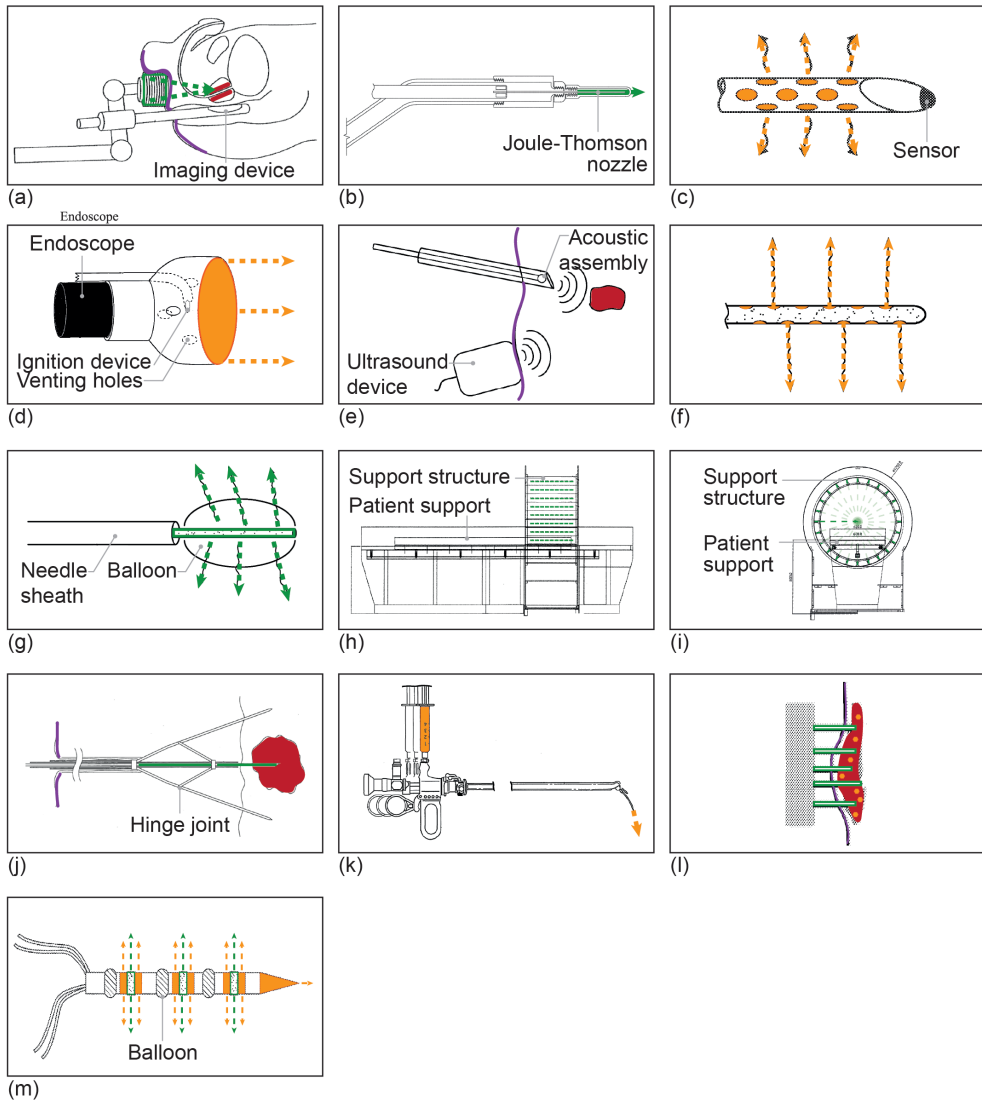
#### *Destroy cell structure by applying energy*

Sixty-seven patents were retrieved presenting instruments that destroy the structure of cancer cells by applying energy to the cells. A number of mechanical design variations, applying various types of energy, have been developed, targeting different parts of the cell structure. To date, most focal therapies using energy as a destruction mechanism are achieved by either High-Intensity Focused Ultrasound (HIFU) or cryotherapy [20-22]. Other focal therapies using energy to destroy the cell structure comprise IrReversible Electroporation (IRE), brachytherapy using ionizing radiation, and various treatment methods inducing thermal ablation or photodisruption [23].

Ultrasound is a form of mechanical wave transmission [24]. HIFU can be used for both thermal and mechanical destruction mechanisms [25]. Non-thermal ultrasound induces dense, energetic bubble clouds or boiling bubbles combined with shock fronts causing cell death by mechanical disintegration, called histotripsy [26]. Histotripsy is achieved using acoustic pulses with an intensity that is at least five times higher than the intensity of ultrasound used in thermal ablation [25]. As an example of non-thermal ultrasound, the instrument described by Roberts *et al.* [27] contains an external ultrasound transducer placed on a robotic arm to treat prostate tumors (Figure 4.3a). The ultrasound system is in acoustic contact with the patient's perineum. It controllably applies ultrasound energy into the prostate by maintaining a bubble cloud within the image generated by a transrectal ultrasound probe. A similar external ultrasound transducer design was developed for brain cancer treatment [28]. A design for an internal probe that delivers pulsed electric energy for non-thermal cell destruction was described by Gleiman *et al.* [29].

Cryoablation relies on removing thermal energy from tissue to cause local freezing and consequently physical disruption due to mechanisms such as intracellular ice, ice crystals that cause shear stress, or extracellular ice crystals that remove water from cells [30]. The low temperature is achieved by the Joule-Thomson effect that describes the decrease in temperature of a fluid caused by the decrease in pressure on the fluid [31]. To illustrate, in the cryoprobe described by Surtees *et al.* [32] (Figure 4.3b), the tip of the cryoprobe is positioned adjacent to the target cells and is cooled by a cryogen gas to less than -50 °C and subsequently heated to 5 °C using both active and passive thawing in free-thaw-freeze cycles [5], causing cell destruction. The cryogen gas is throttled through a Joule-Thomson nozzle and subsequently circulated within the probe. Heat is drawn from the target cells, and a growing ice mass is formed around the tip, eventually encompassing the target cells. The instrument further includes an ultrasound component for intra-procedural monitoring. Similar cryoprobes have been proposed by a number of inventors [33-35]. Other design variations include an instrument consisting of multiple rigid probes in a grid [36] or a flexible endoscopic catheter [37].

An electric field in contact with cells causes IRE by changing the electrochemical potential across the cell membrane, which opens the cell membrane causing the cells to die [38]. The



**Figure 4.3. Patents of focal therapy instruments to destroy the cancer cell structure or disable the cancer cell function.** The drawings show the outline of skin the instrument encounters (purple), the energy transducing element (green), the energy sent to the target (green dashed), the matter source (orange), the matter sent (orange dashed), and the target region (red). (a) Instrument for nonthermal ultrasound treatment, from [27]. (b) Instrument for cryoablation, from [32]. (c) Distal tip of instrument for chemical ablation, from [104]. (d) Cap for cold plasma ablation, from [112]. (e) PhotoDynamic Therapy (PDT) instrument inserted in the patient showing the ultrasound monitoring system, from [118]. (f) Photosensitizer released from the perforations in the distal needle shaft, from [118]. (g) Needle sheath withdrawn exposes the fiber optic tip for light delivery, from [118]. (h) Instrument for magnetic treatment (front view), from [169]. (i) Instrument for magnetic treatment (side view), from [169]. (j) Instrument for thermal treatment using radio waves, from [58]. (k) Instrument for antiandrogen administration, from [107]. (l) Instrument using injectable Magneto-Electric NanoParticles (MENPs) and a magnetic field system, from [142]. (m) Instrument for thermal treatment using electrodes and dissolvable salts, from [152].



irreversibility depends on the voltage, waveform, and frequency of the current [39]. IRE instruments designed to be introduced inside the body can consist of an implant [40] or a percutaneous handheld probe [41-43].

Electromagnetic radiation can be described as a wave or a collection of particles, known as photons [44]. We classified focal therapy instruments using electromagnetic radiation as instruments using energy instead of matter because photons possess no rest mass. The electromagnetic spectrum can be divided into non-ionizing and ionizing radiation. The boundary between non-ionizing and ionizing radiation occurs in the ultraviolet field but is not strictly defined [45]. Ionizing radiation causes chemical bonds to break by removing electrons, whereas non-ionizing radiation only causes heating of the substance [45]. Ionizing radiation causes cell death by depositing energy in cancer cells, thereby damaging their genetic material [46]. Instruments have been developed using different types of ionizing radiation, including X-ray radiation [47-49], gamma-radiation [50], and light radiation [51, 52].

Ablative technologies relying on high temperatures ( $> 60\text{ }^{\circ}\text{C}$ ) affect both the cell structure and the cell function causing coagulative necrosis [39]. Coagulative necrosis is a form of necrosis where both the structural proteins and the enzymes of the cell are damaged, which partly explains the late onset of dead tissue removal in this type of necrosis [39, 53]. Instruments can use different heat-generating or transmitting mechanisms to achieve cell death, including non-ionizing electromagnetic waves (i.e., radio waves, microwaves, and light), thermally conductive elements, and ultrasound waves. For electromagnetic waves, there is a trade-off between penetration depth and focusing [54]. Therefore, most instruments relying on electromagnetism are instruments in direct contact with the target tissue (e.g., internal probes or implants). This applies to radio wave probes [55-74], radio wave implants [75], microwave probes [76-84], and laser light probes [85, 86]. Direct contact is also necessary for heat-conducting and electrification probes [43, 87-89]. An exception is an external microwave system that uses two or more microwave transducers with reinforcing wave patterns to achieve the required penetration depth without direct contact with the target tissue [90]. Besides non-ionizing electromagnetic waves, ultrasound (e.g., HIFU) can also destroy and disable cancer cells [25]. Thermal HIFU does not cause mechanical disintegration of the cells like non-thermal HIFU, but it causes coagulative necrosis. HIFU can achieve adequate tissue penetration without affecting the focusing because it is a mechanical wave [54], which enables the design of external ultrasound transducers [91-96], as well as internal ultrasound probes [97-101] and implants [102] for thermal ultrasound.

Most patents focusing on destroying cancer cells based on energy principles describe instruments used for cancer treatment in general. However, some patents describe body-part-specific cancer treatments, including brain cancer [28, 102], lung cancer [61, 66, 74, 90], breast cancer [93, 96], endometrial cancer [67], adrenal cancer [64], prostate, thyroidal, bladder, or kidney cancer [27, 47, 50, 51, 94], and cancer in body tracts such as the gastrointestinal or urinary tract [47, 52].

*Destroy cell structure by applying matter*

Eight patents were retrieved presenting instruments that destroy the structure of the cancer cell by applying matter to the cells. Focal therapy modalities using matter to destroy the cell structure are chemical ablation and Cold Atmospheric Plasma (CAP).

Chemical ablation is the non-thermal, percutaneous ablation of target cells using ablative substances (e.g., ethanol) [103]. The ablative substance generally achieves cell destruction by dehydration of the cytoplasm, protein denaturation, and coagulation necrosis [103]. Toth *et al.* [104] describe a suitable probe for the internal delivery of a chemical agent (Figure 4.3c). The distal end of the probe is able to penetrate the target tissue and has delivery ports arranged along it. A balloon at the tip ensures contact between the target tissue and the delivery ports. Sensors at the tip allow for intra-procedural monitoring by measuring temperature, physiological changes, and/or electrophysiological changes associated with the delivery process. Similar chemical delivery probes are presented in a number of other patents [64, 89, 105-107].

CAP is a treatment modality based on quasi-neutral ionized gas [108]. CAP creates reactive oxygen and nitrogen species (e.g., hydroxyl, hydrogen peroxide, and nitrogen dioxide), which selectively kill cancer cells, by amongst others DNA damage [109-111]. Barthel [112] describes plasma-producing caps that fit at the end of an endoscope (Figure 4.3d). The cap contains multiple plasma delivery ports and an ignition device to produce the ionized plasma. The endoscope camera can be used for intra-procedural monitoring. A similar design was presented by Krasik *et al.* [113].

Some patents for destroying cancer cell structures using matter have been developed for body-part-specific cancers, including esophageal cancer [112], adrenal cancer [64], and prostate cancer [105, 107].

*Destroy cell structure by applying energy and matter*

Forty-six patents have been found presenting instruments that destroy the structure of the cancer cells by applying both energy and matter to them. PhotoDynamic Therapy (PDT) is one of the best-studied focal therapy modalities for cancer treatment [114]. Other focal therapy modalities using combined energy and matter to destroy the cell structure are particle brachytherapy, reversible electroporation, and cryotherapy.

PDT involves administering a photosensitizer followed by activating the photosensitizer by the irradiation of a specific wavelength [115-117]. The activated photosensitizer generates radical oxygen species (superoxide and hydroxyl) that cause irreparable damage to the cell structure, thereby killing the cells [115]. Chen *et al.* [118] developed a needlelike probe comprising an internal passageway to introduce an acoustic assembly (Figure 4.3e), a photosensitizer assembly (Figure 4.3f), and a photoactivation assembly (Figure 4.3g). The probe can be positioned percutaneously or endoscopically and comprises a balloon to lock the device in place. An external steering mechanism is used to orient the distal end of the probe within the target region. The acoustic assembly in combination with the ultrasound device is used as an intra-procedural monitoring system. The photosensitizer is delivered from the perforations

in the distal needle shaft of the photosensitizer assembly to the target cells adjacent to the outer surface of the target region. The photosensitizer is activated by an optical fiber delivered through the photoactivation assembly. Similar probe designs [119-122], or design variations with separate internal delivery instruments [123, 124], or an internal and external delivery instrument [125, 126] have also been reported.

Ionizing radiation with charged particles is able to cause DNA damage in cancer cells [127]. In contrast to the ionizing radiation using photons described in Chapter 4.3.1 Destroy cell structure by applying energy, we classified ionizing radiation with charged particles as instruments that use matter because the charged particles do possess a mass. Patents were found using alpha-particles [128-131], beta-particles [131, 132], neutrons [133], or positrons [134]. Most instruments have been developed to be placed internally (i.e., internal probes, needles, or implants) [128-132] because of the low penetration depth of particles, except for neutrons. High energy atoms, called plasma, do not target the cell DNA but aim at destroying the cell structure as a whole by thermal tissue evaporation, using an internal probe [135].

Reversible electroporation is able to cause cell death by increasing the membrane permeability to enable access to a cytotoxic agent (electrochemotherapy) [136]. The electrodes and the cytotoxic agent can be co-positioned [137, 138] or introduced separately [139]. IRE can be enhanced by systemically administered nanoparticles that increase the treatment area or the cancer cell selectivity [140, 141], magneto-electric nanoparticles responsive to magnetic fields [142], or a conductive fluid [143, 144].

Cryotherapy instruments, as described in Chapter 4.3.1 Destroy cell structure by applying energy, are hindered by the risk of sticking to and tearing tissue, as well as their requirement for precise contact [145, 146]. We found two patents describing a flexible catheter that delivers low-temperature matter (spray cryotherapy), to overcome these problems [147, 148].

Some hyperthermia mechanisms to destroy cancer cells require a combination of energy and matter. A distinction can be made between a single medium that contains both the energy and the matter (e.g., a heated fluid or vapor delivered with an internal probe) [149, 150] and different mediums for the energy and the matter. For the latter, a distinction can be made between a single instrument that administers both the energy and the matter (e.g., an internal probe with distinct channels) [151-156], separate instruments for the energy and the matter [157, 158], and a single instrument that delivers either one of them (externally for ultrasound and magnetic systems and internally for electromagnetic wave systems) and a general instrument used in surgery to deliver the other (e.g., nanoparticles administered by injection, orally, or nasally) [159-165]. Another mechanism for focal treatment is local drug delivery using thermosensitive liposomes [166]. The internally administered liposomes can be activated by an internal probe [167] or an external system [168].

Most patents developed to destroy cancer cells based on combined energy and matter principles describe an instrument used for cancer treatment in general. However, some instruments for body-part-specific cancer treatment have also been reported, including brain

cancer [143], lung cancer [148], cancer in the female reproductive system [147], and prostate cancer [150].

#### 4.3.2 Disable cell function

##### *Disable cell function by applying energy*

Fifty-one patents were retrieved presenting instruments that disable the function of the cancer cells by applying energy to the cells. Both magnetism and hyperthermia can be used to disable the cell function.

In Vishwanath [169], an external magnetic system for cell degeneration was described. Cell degeneration is achieved by normalizing the cell membrane potential, causing an increased influx of calcium and potassium ions and oxygen, an increased efflux of sodium and water, and a reduction of the intracellular acidity. Only cancer cells are affected because of their low membrane potential as compared to healthy cells [170]. The system described by Vishwanath [169] consists of multiple magnetic field generators circumferentially fixed on a support structure (Figures 4.3h,i). The system is placed externally from the patient in such a way that the target cells are at the focal region of magnetic field generators. Monitoring of the treatment can be done using pre- and post-treatment imaging modalities, such as ultrasound, Computed Tomography (CT), or Magnetic Resonance Imaging (MRI). Another design variation of an instrument that changes the cell membrane potential is a probe with contact electrodes [171].

Other instruments use hyperthermia mechanisms, which damage the cell directly (see Chapter 4.3.1 Destroy cell structure by applying energy), but also disable the cell function [39]. Habib [58] developed a set of radio-wave emitting needles that can be deployed by a hinge joint at the central needle (Figure 4.3j). The radiofrequency power can be applied across different combinations of needles. The instrument can be used in conjunction with an imaging system, such as ultrasound, for intra-procedural monitoring. Some examples of cell functions that are disabled are the process of facilitated diffusion across the cell membrane with the assistance of membrane proteins and the mitochondrial function [172, 173]. Other instruments that apply hyperthermia mechanisms using energy to disable the cell function have been found in a number of patents [43, 55-102].

Most patents developed to disable cancer cells based on energy principles describe an instrument used for cancer treatment in general. However, some instruments for body-part-specific cancer treatment are reported as well, including brain cancer [28, 102], lung cancer [61, 66, 74, 90], breast cancer [93, 96], endometrial cancer [67], adrenal cancer [64], and prostate, thyroidal, bladder, or kidney cancer [94].

##### *Disable cell function by applying matter*

Using matter to disable the function of cancer cells targets (the production of) essential elements for the proliferation of the cancer cells with hormones or other agents. Only two patents have been found presenting instruments that target these essential elements using

matter.

Neisz *et al.* [107] describe a probe for administering an antiandrogen that suppresses the androgen production by the testes (Figure 4.3k), for example, bicalutamide [174]. For androgen-dependent prostate cancer, androgen (typically testosterone) is required for the development of the tumor [175]. The transurethral probe contains a needle designed to be deployed against the prostate urethra. The probe includes a scope sheath with an eye-port for intra-procedural visual guidance. A similar design was presented by Barnett *et al.* [106] that can deliver various types of agents to block the production of essential elements for the cancer cells. Some possible agents are bicalutamide for prostate cancer cells and tamoxifen for breast cancer cells [176]. Tamoxifen inhibits estrogen binding to estrogen receptors, a binding required for tumor growth of the breast cancer cells [176].

#### *Disable cell function by applying energy and matter*

Sixteen patents were retrieved presenting instruments that disable the function of the cancer cells by applying both energy and matter to the cells. Both magneto-electric nanoparticles and particles enhancing hyperthermia mechanisms disable the cancer cell function in combination with applied energy.

Liang [142] developed injectable Magneto-Electric NanoParticles (MENPs) (Figure 4.3l). The MENPs are attracted to cancer cells because of the different electrical potentials of cancer cells and healthy cells. An external magnetic system induces three magnetic fields: the first magnetic field produces a higher concentration of MENPs at the tumor site, the second achieves nano-electroporation to penetrate targeted cells, and the third both disables the function of the target cells and physically damages the cells by mechanical motion of the MENPs inside the cell. Adding an MRI device may enable intra-procedural monitoring.

Other patents in this group use hyperthermia mechanisms to both destroy the cells and disable the cell function. Ruse *et al.* [152] presented an instrument consisting of multiple rigid electrode shafts with dissolvable salts (Figure 4.3m). The dissolvable salts mix with bodily fluids, resulting in an electrically conductive ionic solution. Inflatable components along the shafts provide mechanical stability. Each electrode shaft has a thermal sensor for intra-procedural temperature monitoring. Furthermore, the electrode bands and the non-conductive shaft portions can be distinguished using ultrasound imaging. Other instruments using hyperthermia mechanisms to disable the cell function using both energy and matter have been found in a number of patents [149-163].

Most patents that propose to disable cancer cells based on combined energy and matter principles describe an instrument used for cancer treatment in general, except for one patent developed for prostate cancer treatment [150]. Almost all instruments classified as disabling the individual cell function (Groups 4, 5, and 6) were also classified as destroying the individual cell structure (Groups 1, 2, and 3). These instruments apply a hybrid method that affects both the cell structure and the cell function to achieve cell death. The most frequently applied hybrid methods in instruments that target individual cancer cells are high-temperature abla-

tive technologies using solely energy or combined energy and matter. All patents classified as disabling the cancer cell function apply a hybrid method that combines destruction and disabling mechanisms, except for a patent by Vishwanath [169] and a patent by Sano *et al.* [171] describing focal therapy instruments that focus solely on disabling the cancer cell function.

#### 4.4 Destroy cancer cells on a network level

Focal therapy instruments targeting the network of cancer cells apply their treatment not on each cell but treat a network of cells as a whole. The cell network is able to live because of the supply of nutrients and the discharge of waste, enabled by the vascular system of the network. This function is disabled when the blood vessels and lymphatic vessels leading toward and from the cancer cells are either destructed (Chapter 4.4.1) or obstructed (i.e., disabled, Chapter 4.4.2) [177]. Both the destruction and obstruction of the pathways leading toward and from the cancer cells can be achieved by energy, matter, or a combination of energy and matter. The classification of the patents on focal therapy instruments to treat cancer on the network level resulted in six groups of focal therapy instruments (Figure 4.2b). Each sub-subsubchapter describes the mechanical design variations of the focal therapy instruments classified into one group and the specific cancer type for which the instruments are designed.

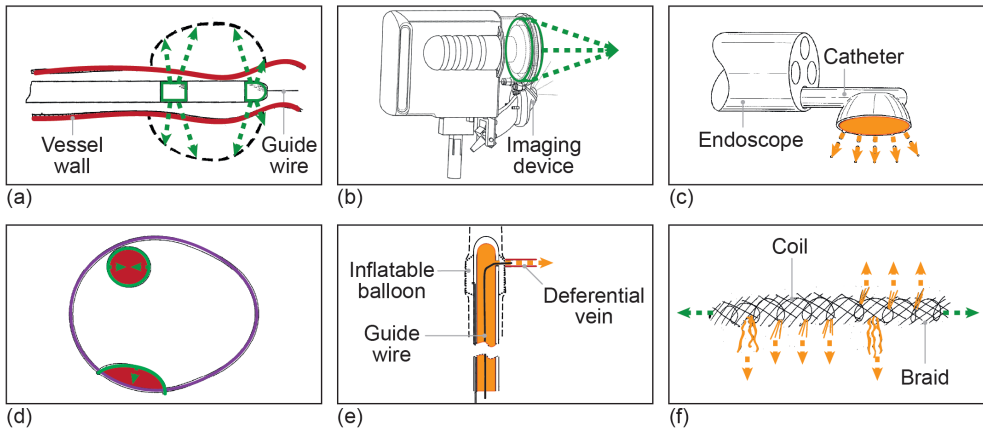
##### 4.4.1 Destroy network structure

###### *Destroy network structure by applying energy*

Eleven patents have been found presenting instruments that destroy the structure of a cancer cell network by applying energy to the network as a whole (Figure 4.2b). The vascular system of the cancer cells can be destroyed with energy by either targeting the individual blood vessels or targeting the overall blood supply.

Habib [178] describes a flexible catheter containing multiple electrodes for thermal ablation of a blood vessel supplying a tumor using radiofrequency current (Figure 4.4a). The catheter is mounted on a guidewire, and the distal tip comprises extendable elements that can be deployed outwards from the shaft to contact the hollow vessel wall. Temperature sensors at the catheter tip allow for intra-procedural monitoring. Similar patents on instruments applying a heated lumen around the vessel [179] or inserting a catheter with a thermal probe inside a vessel [180] have been found. Another design variation comprises an ablating implant inserted in the blood vessel [75, 181]. Besides thermal ablation, cryoablation is also able to cause vascular injury (as well as direct cell destruction, making cryoablation a hybrid method, see Chapter 4.3.1 Destroy cell structure by applying energy), leading to cell death [5]. A number of instruments have been proposed that induce cryoablation of blood vessels by removing thermal energy [32-34, 36, 37].

Instead of targeting the individual blood vessels, another design variation targets the overall blood supply of cancer cells by embolizing a shell of tissue surrounding a group of cancer cells, thereby enclosing the cancer cells. Parsons *et al.* [182] describe an instrument that



**Figure 4.4. Patents of focal therapy instruments to destroy the cancer cell network structure or disable the cancer cell network function.** The drawings show the outline of skin the instrument encounters (purple), the energy transducing element (green), the energy sent to the target (green dashed), the matter source (orange), the matter sent (orange dashed), and the target region (red). (a) Instrument using electrodes to embolize a vessel leading to cancer cells, from [178]. (b) Instrument using flexible electrodes to embolize a shell of tissue surrounding a network of cancer cells, from [182]. (c) Instrument using cryoablation to cause vascular damage, from [147]. (d) Instrument to constrict cancer cells and their blood flow, from [183]. (e) Instrument to deliver a sclerosing agent to the deferential vein to prevent testosterone from reaching the prostate, from [179]. (f) Instrument using pressure and an anti-cancer factor to block a vessel leading to cancer cells, from [184].

applies HIFU to the perimeter of the tumor, thereby both interrupting the blood supply of the cells in the interior region and treating the interior region by indirect heating (Figure 4.4b). The focal zone of the HIFU instrument is moved along the perimeter of the target volume. The time required to treat the target tissue is reduced as compared to the treatment of the target tissue by direct ablation. The instrument includes an ultrasound imaging transducer for intra-procedural monitoring.

Most patents focusing on disabling cancer networks based on energy principles describe an instrument used for cancer treatment in general, except for a patent developed for lung cancer [180] and a patent developed for endometrial cancer treatment [182].

#### *Destroy network structure by applying energy and matter*

Two patents were retrieved describing instruments that destroy the cell network by applying energy and matter to the network. Cryoablation using low-temperature matter causes vascular injury (as well as direct cell destruction, see Chapter 4.3.1 Destroy cell structure by applying energy and matter), leading to cell death [5]. Krinsky [147] describes a catheter coupled to a cryogen source that is inserted through a lumen of an endoscope into the patient's vagina or cervix to treat cancer in the female reproductive system. The catheter contains one or more openings for the cryogen that is sprayed directly on the target tissue (Figure 4.4c). The endoscope can additionally house an imaging camera lens for intra-procedural monitoring. Johnston [148] described a similar cryoablation instrument for lung cancer treatment.



#### 4.4.2 Disable network function

##### *Disable network function by applying energy*

Only one patent has been found describing an instrument that disables the cell network by applying energy. Specifically, Connors *et al.* [183] describe an inflatable implant to be placed around a network of cancer cells (Figure 4.4d). This implant consists of a flexible housing filled with a high vapor pressure medium that forms a shell around the cancer cells. The inner surface of the implant inflates over time, thereby constricting the cells and the blood flow to the cells by the applied pressure. The instrument has been developed to treat problems with pressure in the body, such as urinary incontinence, and to treat cancer cell networks. The implant can optionally include an electronic device to monitor and control the expansion and contraction intra-procedurally.

##### *Disable network function by applying matter*

Gat *et al.* [179] describe an instrument that disables the network function by applying matter. The instrument was developed to treat testosterone-dependent prostate cancer using an intravascular catheter. The catheter is capable of sclerosing an internal spermatic vein (i.e., the deferential vein), thereby preventing blood rich in testosterone from reaching the prostate (Figure 4.4e). A guidewire within the catheter enables the positioning of the catheter's orifice in front of the target junction and an inflatable balloon to hold the catheter in place and prevent the agent from reaching other regions than the target region. Intra-procedural imaging using optical fibers, ultrasound, or CT allows for the positioning of the catheter. The catheter then injects a sclerosing agent into the opening of the target vein, which causes swelling that cuts off the blood flow, after which the vein shrinks. Optionally, an anti-androgen is injected after occluding.

##### *Disable network function by applying energy and matter*

Only one patent [184] has been retrieved that describes an instrument that disables the cancer network function by applying energy and matter. The patent describes an implant that obstructs blood vessels while emitting a bioactive agent, such as an anti-cancer factor (Figure 4.4f). The instrument comprises a helical coil designed to be deployed inside the patient's blood vessel. A braid positioned over the helical coil like a sleeve contains fibrous elements comprising the bioactive material. Plugs attached to the braid obstruct the target vessel. External imaging modalities can be used to monitor the positioning of the implant. The instrument was designed to obstruct abnormal blood flow sites, such as blood vessels that carry blood to cancer cell networks.

### 4.5 Commercially available instruments

This subchapter provides a glimpse of the current commercially available focal therapy instruments to treat localized cancer. Most commercially available instruments destroy the cancer cell structure by applying energy (Group 1), such as cryotherapy and hyperthermia



treatments, which are hybrid treatments that also affect the cell function (Group 4), or by applying combined energy and matter (Group 3) such as PDT and electrochemotherapy (Table 4.1). The patents related to the commercially available instruments were collected by analyzing to which company the patent was assigned and evaluating the resemblances between the patented instrument and the commercially available instrument.

Common cryotherapy probes are the IceSeed<sup>TM</sup> MRI or IceRod<sup>TM</sup> MRI (Boston Scientific, Natick, MA) [185] used with the Visual-ICE Cryoablation system [203]. A patent for these probes was presented by Zvuloni *et al.* [36]. Another commercially available cryoprobe is distributed by Endocare (Healthtronics/Endocare Inc., Irvine, CA), which is used under ultrasound guidance [186]. All three cryoprobes create an ice ball formation at the tip by compressed argon gas that passes through a central channel [204].

IRE has been approved in Europe (CE certificate), as well as by the FDA in the US [205]. The NanoKnife (AngioDynamics, Queensbury, NY) [187, 188] is the first instrument based on IRE [206]. Two patents on instruments discussed in this study are assigned to AngioDynamics and are related to the NanoKnife as they show similar treatment mechanisms [42, 43]. The NanoKnife consists of a set of monopolar probes and one bipolar probe that are positioned with ultrasound or CT guidance [207].

Common thermal mechanisms that disable cell function and destroy cell structure are RadioFrequency Ablation (RFA), microwave ablation, HIFU, and focal laser ablation. Multiple companies manufacture RFA instruments, which are used under ultrasound or CT guidance. Boston Scientific (Natick, MA) distributes the LeVeen Needle Electrode [189], consisting of twelve curved electrodes that open in an umbrella shape. Three found patents on RFA probes are assigned to Boston Scientific and show a similar umbrella shape and treatment mechanism as the LeVeen Needle Electrode [60, 70, 71]. Covidien (Mansfield, MA) distributes the Cool-tip RFA System [190], in which the probe contains either a single electrode or a set of up to three electrodes. AngioDynamics (Queensbury, NY) developed a number of RFA devices, including the StarBurst XL and the StarBurst Semi-Flex [191], the latter being able to bend up to 90 degrees in all directions. The probe contains nine deployable electrodes and an active trocar tip. AngioDynamics also distributes the Solero Microwave Tissue Ablation System, which contains an internal thermocouple for intra-procedural monitoring [192]. These commercially available RFA and microwave ablation instruments are instruments for cancer treatment in general based on coagulative necrosis. A transurethral HIFU system for prostate cancer treatment under MRI guidance is distributed by Profound Medical Inc. (Toronto, Canada) and called the TULSA-PRO [193]. They also distributed the Sonalleve MR-HIFU system (in cooperation with Philips Healthcare (Best, The Netherlands)) [194, 195] for breast cancer treatment under MRI guidance. Two patents on external HIFU systems discussed in this study are assigned to Philips Healthcare and show a similar treatment mechanism as the Sonalleve MR-HIFU system [91, 96]. Commercially available HIFU instruments for transrectal prostate cancer treatment under ultrasound guidance are the Focal One HIFU

Table 4.1. Overview of commercially available focal therapy instruments to treat localized cancer.

Instrument	Company	Reference	Related Patent(s)	Classification Group(s)	Focal Therapy Method
IceSeed™ MRI	Boston Scientific, Natick, MA	[185]	[36]	1. Destroy cell structure by applying energy	Cryotherapy
IceRod™ MRI	Boston Scientific, Natick, MA	[185]	[36]		
Endocare™ precision cryoprobe	Healthtronics/Endocare Inc., Irvine, CA	[186]			
NanoKnife	AngioDynamics, Queensbury, NY	[187, 188]	[42, 43]		IRE
LeVeen Needle Electrode	Boston Scientific, Natick, MA	[189]	[60, 70, 71]		
Cool-tip RFA System	Covidien, Mansfield, MA	[190]			
Starburst XL	AngioDynamics, Queensbury, NY	[191]			RFA
Starburst Semi-Flex	AngioDynamics, Queensbury, NY	[191]		1. Destroy cell structure by applying energy and 4. Disable cell function by applying energy	Microwave ablation
Solero Microwave Tissue Ablation System	AngioDynamics, Queensbury, NY	[192]			
TULSA-PRO	Profound Medical Inc., Toronto, Canada	[193]			
Sonalleve MR-HIFU	Profound Medical Inc., Toronto, Canada and Philips Healthcare, Best, The Netherlands	[194, 195]	[91, 96]		
Focal One HIFU device	EDAP TMS, Vaulx-en-Velin, France	[196]			HIFU
Ablatherm Robotic HIFU device	EDAP TMS, Vaulx-en-Velin, France	[197]			
Sonablate	SonaCare Medical, Charlotte, NC	[198]			
Foscan or padeliporfin (TOOKAD) and a laser diode	Applied Optronics Corp., South Plainfield, NJ	[199-201]		3. Destroy cell structure by applying energy and matter	PDT
Cliniporator 2	IGEA, Carpi, Italy	[202]			Electrochemo-therapy

IRE = IrReversible Electroporation, RFA = RadioFrequency Ablation, HIFU = High-Intensity Focused Ultrasound, PDT = PhotoDynamic Therapy.

device, the Ablatherm Robotic HIFU device (EDAP TMS, Vaulx-en-Velin, France), and the Sonablate (SonaCare Medical, Charlotte, NC) [196-198].

PDT in common clinical practice consists of an injection of a photosensitizer, such as Foscan or padeliporfin (TOOKAD) [199, 200], and the internal or external application of

red light. A diode laser (Applied Optonics Corp., South Plainfield, NJ) [201] can be used to deliver light fibers to the internal cancer site [199]. For reversible electroporation used in electrochemotherapy to eventually cause irreversible damage, the Cliniporator 2 (IGEA, Carpi, Italy) [202] is in clinical practice in more than 100 clinical centers in the European Union [208]. Measurements of the voltage and current supplied allow for intra-procedural monitoring. For more information about commercially available tumor ablation instruments, we refer the reader to [3, 19, 209].

## 4.6 Discussion

### 4

#### 4.6.1 Main findings

This study aimed to provide a comprehensive overview of the patent literature on focal therapy instruments to treat localized cancer. Twelve groups of treatment types performed by the focal therapy instruments were identified based on the treatment target, purpose, and means. A total of 18.0% of the relevant patents have been published and filed by independent inventors, 69.5% by companies, and 12.5% by academic institutions, indicating that, although both companies and academic institutions show interest in focal therapy instruments to treat cancer, the field is mostly industry-driven.

Once looking at the temporal distribution of the classification of the patents in Figure 4.5, it becomes apparent that certain focal treatment types are more frequently applied for than others. These treatment types target the individual cancer cells with solely energy or combined with matter (Groups 1, 3, and 4). This trend is consistent with the instrument types that are commercially available (see Chapter 4.5).

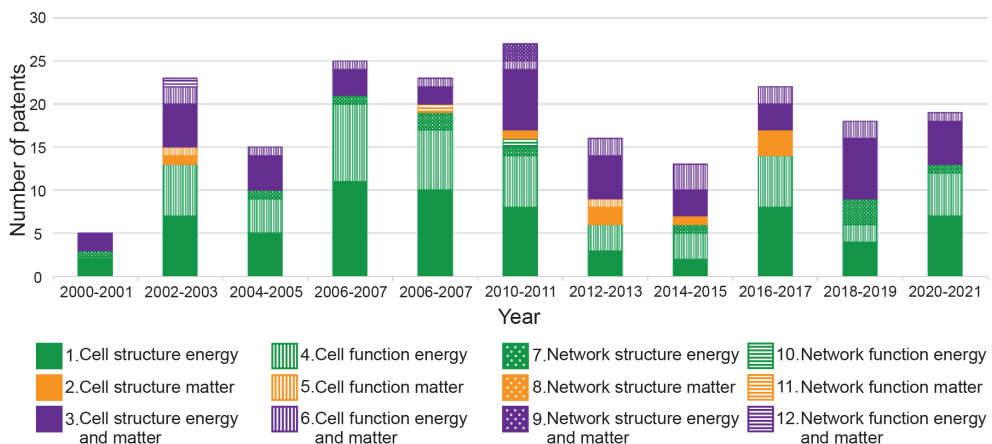
Regarding the treatment target, most patents describe an instrument targeted at the individual cancer cell rather than at the cancer cell network. Cancer cells can be seen as the direct target of cancer treatment, whereas blood vessels are an indirect target to treat those cancer cells. The blood vessels of cancer networks are poorly organized, which impairs particle delivery as cancer treatment [210, 211]. Therapies targeting the blood vessels of cancer networks are relatively new and have only moved from the laboratory to the clinic since 1992 [212].

Considering the treatment purpose, a high number of patents describe an instrument that destroys a structure as compared to an instrument that disables a function. One could speculate that the preference for focal cancer treatment types that destroy a structure is due to their general destruction mechanism. A structure is concrete and can be examined, in other words: a structure provides a static image, whereas a function is intangible and explainable only in terms of its underlying structures. This explains why there is less information about the functional changes due to cancer, in contrast to the structural/anatomic changes [213]. To disrupt the cancer cell or network function, information is required about the vital function and how to disrupt it, which requires imaging of the cell's dynamic workings. For the dynamic workings, often only indirect monitoring methods exist, making the area of physiological

modeling less intuitive than anatomical modeling [214]. A general destruction mechanism might, therefore, be easy to design as compared to a function-disabling mechanism. MRI, often used for monitoring, has only recently evolved from being purely anatomy-based to a discipline that is able to incorporate both anatomic and physiologic information with the addition of functional MRI [215-217].

With regard to the treatment means, most patents describe an instrument using energy. The low preference in using matter to treat cancer might be explained by the long-term toxicity concerns of remaining matter, especially non-biodegradable matter [218, 219]. Energy does not possess this risk of long-term toxicity, as the energy is removed from the body together with the removal of the energy source. Another barrier of matter is the body's labeling of foreign particles by opsonization to stimulate the removal of those foreign particles [218]. In opsonization, the foreign particles are covered with nonspecific proteins to make them more visible to phagocytic cells, so phagocytosis can occur [218, 220].

Figure 4.5 shows that there is no specific trend toward the design of an instrument that accomplishes a certain type of treatment. The temporal distribution of the patents in the field of focal therapy instruments shows a persisting number of patents being published with an increase from 2016 on. Focal therapy rapidly advanced in the 1990s, as cross-sectional imaging became commercially available and widespread [39, 103]. Focal therapy first gained clinical acceptance as a method for treating cancer in the liver, kidney, lung, and bone [103]. In 2016, a randomized controlled trial was conducted to evaluate the outcomes of the three contemporary treatment modalities of localized prostate cancer (i.e., active monitoring, surgical resection, and radiotherapy) called the ProtecT trial. After a median follow-up of 10 years of 1643 randomized participants, Hamdy *et al.* [18] demonstrated no significant difference in prostate-cancer-specific mortality. Nevertheless, the rates of disease progression



**Figure 4.5.** Temporal distribution of relevant patents published, classified based on the instrument's treatment target (cell or network of cells), purpose (destroy the structure or disable the function), and means (energy, matter, and combined energy and matter). The patents retrieved were published between January 2000 and June 2021.

and rates of metastasis development were higher for active monitoring than for surgery and radiotherapy [18]. This outcome increased the interest in less radical treatments, such as focal therapy, for localized prostate cancer [221]. An explanation of the increasing number of published patents from 2016 onwards could be the outcomes of studies such as the ProtecT trial and the increased rate of early diagnosis of prostate cancer [222], the latter increases the chances for positive outcomes of focal therapy, as the cancer is still locally confined [5]. Patients with organ-confined cancer were considered suitable candidates for focal therapy in multiple consensus projects on focal therapy as prostate cancer treatment [223].

Furthermore, Figure 4.5 shows that patents published on focal therapy instruments that destroy or disable the individual cancer cell using energy (Groups 1 and 4) and destroy the individual cell using combined energy and matter (Group 3) remain dominant throughout the years. Nevertheless, there is a trend toward an equal distribution of the different groups applied for in patented focal therapy instruments, leading to a more varied spectrum of focal therapy instruments in the patent literature. Instruments destroying cell structure using matter (Group 2), disabling cell function using energy and matter (Group 6), and destroying network structure using energy (Group 7) gain their share in the focal therapy field besides the dominant focal treatment types (Groups 1, 3, and 4). Patents on instruments that disable a network function (Groups 10, 11, and 12) filed until 2011 can be seen in Figure 4.5, indicating that inventors touched upon these treatment types. However, these treatment types were no longer applied for in the patent literature of the last eight years. This smothering effect might indicate that disabling the network function is medically not feasible. Disabling of a cancer network by obstructing the blood vessels results in metabolic stress, which might turn on the “angiogenic switch” [224], increasing the tumor angiogenesis to compensate for the obstructed blood vessels. Patents on instruments that disable cell function using matter (Group 5) and instruments that destroy network structure using energy and matter (Group 9) are also not applied for anymore.

The observation that instruments for destroying or disabling the individual cancer cell using energy (Groups 1 and 4) show similar changes in the number of patents throughout the years can be explained by instruments that apply hybrid methods. Almost all patents classified as disabling the individual cell function (Group 4, 5, and 6) are also classified as destroying the individual cell structure (Groups 1, 2, and 3), performing hybrid methods. This means that there are barely any patents describing focal therapy instruments that focus solely on disabling the cancer cell function. The group of patents that perform a hybrid method mainly consists of instruments that rely on high-temperature ablative technologies that affect both the cell structure and the cell function causing coagulative necrosis [39].

#### 4.6.2 Design suitability for medical purposes

In this review, the mechanical design principles were analyzed by looking at patented working principles without considering the technical and medical feasibility of these principles, which usually cannot be found in patent literature. The main risks of choosing focal therapy are the

multifocality of cancer and the risk of undetectable micro-metastases [3, 225]. Adequate patient selection is, therefore, of utmost importance. Multifocality implies the presence of two or more tumor foci (microscopically visible groups of cells) separated by healthy tissue, whereas unifocal means that only one tumor focus is observed [226, 227]. Multifocal cancer treated with focal therapy might result in incomplete treatment because of missed foci, leading to cancer recurrence [228, 229].

Another hurdle lies in the efficacy of the indirect cancer cell treatment by targeting its vascular network. Tumor growth and metastatic spread of cancer tissue require the formation of a new vascular network called angiogenesis, consisting of blood vessels and lymphatic vessels [12, 211]. Therapies targeting the formation of the cancer network using systemic antiangiogenic drugs only yielded modest responses and no long-term survival benefits [230]. These results were explained by resistance mechanisms of the cancer cells (evasive resistance) that cause revascularization [231]. Therefore, the efficacy of the instruments described in the patents targeting the network of cancer cells is questionable considering these resistance mechanisms. Vascular targeted therapies might result in such an elaborate vaporization of vessels that the tumor is unable to neovascularize. However, when the vaporization is not elaborate enough, instruments that destroy or disable the vascular system of the cancer cells might encounter similar resistance strategies of the cancer cells.

Considering implants that require placement around the network of cancer cells, such as the inflatable implant presented in a patent by Connors *et al.* [183] (see Chapter 4.4.2 Disable network function by applying energy), we question the medical feasibility concerning the dissemination of tissue at the trajectory of implant placement. The implant is designed to be positioned around a network of cancer cells. However, the separation of the network of cancer cells from the surrounding cells to enable the implant placement might lead to the dissemination of malignant tissue in the body.

#### 4.6.3 Further research

This review focuses on the mechanical design of focal therapy instruments applying different treatment types. The search was restricted to focal therapy instruments to treat cancer, thereby leaving out focal therapy instruments originally designed for the treatment of other medical causes. As focal therapy is not only of interest for cancer treatment but also for the treatment of for example, abnormal blood flow in the heart, the results from other medical technology fields could lead to other creative solutions for cancer treatment. The definition used for focal therapy in this review excludes instruments developed for resecting cancer cells. An example of such an instrument is an instrument that focally ablates cancer cells prior to the resection to prevent bleeding during the resection. The field of instrumentations that use focal therapy prior to resection might illustrate new treatment types that could be applied to focal therapy instruments that do not apply this subsequent resection.

This review considers patents to provide a comprehensive overview of the patent literature on focal therapy instruments to treat localized cancer. For further research, it is of interest to

explore the corresponding scientific literature as well as to analyze the performance of the instruments described in the patents. For focal therapy to be viable, accurate imaging is required for proper diagnosis of cancer localization and to accurately reach the location of the cancer cells with the instrument [232]. Conventional imaging modalities comprise CT, ultrasound, and MRI, from which MRI enables the highest accuracy [232]. For MRI-guided focal therapy, the focal therapy instrument must be developed with special precautions regarding MRI compatibility [233]. For further research, it is important to integrate instrument development with the used imaging modality and its imposed requirements for the instrument, e.g., no metallic, ferromagnetic, or conductive materials for MRI-compatible instruments [234].

The IDEAL framework for surgical innovation (idea, development, exploration, assessment, and long-term study) allows for an estimation of the clinical development phase of the medical instruments [235]. For future research, a contemplation of the selected patents against the IDEAL framework could be an interesting addition to this study.

#### 4.6.4 Five-year view

The trend toward an equal distribution of the different groups of patented focal therapy instruments results in a wider range of possible focal therapy instruments to treat cancer. The commercial availability and the clinical use are the results of different steps in the design process. We expect that the trend of a wider range of patents on focal therapy instruments will extend to the instruments tested on their medical feasibility. These upcoming focal therapy instruments might broaden the existing spectrum of commercially available instruments that use energy to destroy and disable the cancer cell structure and function, respectively (Groups 1 and 4), and instruments that destroy the cancer cell structure using combined energy and matter (Group 3). Focal therapy instruments focused on destroying the cancer cell structure using matter (Group 2), disabling the cancer cell function using both energy and matter (Group 6), and destroying the network structure using energy (Group 7) can be seen as a new generation of focal therapy instruments to treat cancer.

As far as new focal cancer cell treatment mechanisms are concerned, we identified one unexplored, yet theoretically feasible treatment mechanism: to destroy the network structure using matter (Group 8). Instruments in this group would locally apply particles that destroy the vascular system of the cancer cells. The particles would function without the application of energy, and they would target the vascular system without directly affecting the individual cancer cells. The medical and mechanical feasibility of this treatment mechanism for cancer remains to be investigated.

## 4.7 Conclusion

This review chapter provides a comprehensive overview and classification of the patent literature on focal therapy instruments to treat localized cancer. We analyzed the different mechanical designs present in the instrument patents. The medical section of the Google Patents



database was reviewed, and 128 patents published in the last two decades (2000-2021) were discussed. We proposed a classification of the possible treatment types applied by instruments for focal therapy based on the target, purpose, and means of treatment. At the fundamental level, the individual cancer cells and the network of cancer cells were distinguished as targets. The working mechanism can be based on destroying the structure or disabling the function. Based on the means of establishing this treatment mechanism, the means can be distinguished as energy, matter, or combined energy and matter. The most preferred treatments applied by the instruments were identified as to destroy the cell structure using solely energy or combined energy and matter, or to disable the cell function using energy. The description of the different instrument functions may serve as a source of inspiration for new focal therapy instruments to treat localized cancer.

## References

1. Miller KD, Nogueira L, Mariotto AB, Rowland JH, Yabroff KR, Alfano CM, et al. Cancer treatment and survivorship statistics, 2019. *CA: a cancer journal for clinicians*. 2019;69(5):363-85. doi: 10.3322/caac.21565.
2. Beets GL, Figueiredo NF, Beets-Tan RG. Management of rectal cancer without radical resection. *Annual review of medicine*. 2017;68:169-82. doi: 10.1146/annurev-med-062915-021419.
3. Eggener SE, Scardino PT, Carroll PR, Zelefsky MJ, Sartor O, Hricak H, et al. Focal therapy for localized prostate cancer: a critical appraisal of rationale and modalities. *The Journal of urology*. 2007;178(6):2260-7. doi: 10.1016/j.juro.2007.08.072.
4. Ahmed HU, Pendse D, Illing R, Allen C, van der Meulen JH, Emberton M. Will focal therapy become a standard of care for men with localized prostate cancer? *Nature clinical practice Oncology*. 2007;4(11):632-42. doi: 10.1038/ncponc0959.
5. Lodeizen O, de Bruin M, Eggener S, Crouzet S, Ghai S, Varkarakis I, et al. Ablation energies for focal treatment of prostate cancer. *World journal of urology*. 2019;37(3):409-18. doi: 10.1007/s00345-018-2364-x.
6. Donaldson IA, Alonzi R, Barratt D, Barret E, Berge V, Bott S, et al. Focal therapy: patients, interventions, and outcomes—a report from a consensus meeting. *European urology*. 2015;67(4):771-7. doi: 10.1016/j.eururo.2014.09.018.
7. Wu F, Zhou L, Chen WR. Host antitumour immune responses to HIFU ablation. *International Journal of Hyperthermia*. 2007;23(2):165-71. doi: 10.1080/02656730701206638.
8. Heidenreich A, Bellmunt J, Bolla M, Joniau S, Mason M, Matveev V, et al. EAU guidelines on prostate cancer. Part 1: screening, diagnosis, and treatment of clinically localised disease. *European urology*. 2011;59(1):61-71. doi: 10.1016/j.eururo.2010.10.039.
9. Kutikov A, Kunkle DA, Uzzo RG. Focal therapy for kidney cancer: a systematic review. *Current opinion in urology*. 2009;19(2):148-53. doi: 10.1097/MOU.0b013e328323f7d7.
10. Wu F, Wang ZB, Cao YD, Zhu XQ, Zhu H, Chen WZ, et al. “Wide local ablation” of localized breast cancer using high intensity focused ultrasound. *Journal of surgical oncology*. 2007;96(2):130-6. doi: 10.1002/jso.20769.
11. Marieb EN, Hoehn K. *Human anatomy & physiology*. Tenth edition ed: Pearson education; 2016.
12. Nishida N, Yano H, Nishida T, Kamura T, Kojiro M. Angiogenesis in cancer. *Vascular health and risk management*. 2006;2(3):213. doi: 10.2147/vhrm.s23213.
13. Hsieh W-S, Simons JW. Systemic therapy of prostate cancer. *New concepts from prostate cancer tumor biology*. *Cancer treatment reviews*. 1993;19(3):229-60. doi: 10.1016/0305-7372(93)90037-R.



14. Fischer JJ, Papac RJ. Theoretical considerations in combinations of localized and systemic therapy for neoplastic disease. *Journal of theoretical biology*. 1972;37(1):105-14. doi: 10.1016/0022-5193(72)90117-8.
15. Walsh PC. Radical prostatectomy for localized prostate cancer provides durable cancer control with excellent quality of life: a structured debate. *The Journal of urology*. 2000;163(6):1802-7. doi: 10.1016/S0022-5347(05)67547-7.
16. Sanda MG, Dunn RL, Michalski J, Sandler HM, Northouse L, Hembroff L, et al. Quality of life and satisfaction with outcome among prostate-cancer survivors. *New England Journal of Medicine*. 2008;358(12):1250-61. doi: 10.1056/NEJMoa074311.
17. Potosky AL, Davis WW, Hoffman RM, Stanford JL, Stephenson RA, Penson DE, et al. Five-year outcomes after prostatectomy or radiotherapy for prostate cancer: the prostate cancer outcomes study. *Journal of the National Cancer Institute*. 2004;96(18):1358-67. doi: 10.1093/jnci/djh259.
18. Hamdy FC, Donovan JL, Lane J, Mason M, Metcalfe C, Holding P, et al. 10-year outcomes after monitoring, surgery, or radiotherapy for localized prostate cancer. *N Engl J Med*. 2016;375:1415-24. doi: 10.1056/NEJMoa1606220.
19. Saldanha DF, Khiatani VL, Carrillo TC, Yap FY, Bui JT, Knuttinen MG, et al. Current tumor ablation technologies: basic science and device review. *Seminars in interventional radiology*; 2010 Sep.: © Thieme Medical Publishers. doi: 10.1055/s-0030-1261782.
20. van der Poel HG, van den Bergh RC, Briers E, Cornford P, Govorov A, Henry AM, et al. Focal therapy in primary localised prostate cancer: the European Association of Urology position in 2018. *European urology*. 2018;74(1):84-91. doi: 10.1016/j.eururo.2018.01.001.
21. Jácome-Pita F, Sánchez-Salas R, Barret E, Amaruch N, Gonzalez-Enguita C, Cathelineau X. Focal therapy in prostate cancer: the current situation. *Ecancermedicalscience*. 2014;8. doi: 10.3332/ecancer.2014.435.
22. De la Rosette J, Ahmed H, Barentsz J, Johansen TB, Brausi M, Emberton M, et al. Focal therapy in prostate cancer—report from a consensus panel. *Journal of Endourology*. 2010;24(5):775-80. doi: 10.1089/end.2009.0596.
23. Niemz MH. *Laser-tissue interactions*. Berlin, Heidelberg: Springer; 2007.
24. Huber P, Mann M, Melo L, Ehsan A, Kong D, Zhang L, et al. Focused ultrasound (HIFU) induces localized enhancement of reporter gene expression in rabbit carotid artery. *Gene Therapy*. 2003;10(18):1600-7. doi: 10.1038/sj.gt.3302045.
25. van den Bijgaart RJ, Eikelenboom DC, Hoogenboom M, Fütterer JJ, den Brok MH, Adema GJ. Thermal and mechanical high-intensity focused ultrasound: perspectives on tumor ablation, immune effects and combination strategies. *Cancer Immunology, Immunotherapy*. 2017;66(2):247-58. doi: 10.1007/s00262-016-1891-9.
26. Khokhlova VA, Fowlkes JB, Roberts WW, Schade GR, Xu Z, Khokhlova TD, et al. Histotripsy methods in mechanical disintegration of tissue: Towards clinical applications. *International journal of hyperthermia*. 2015;31(2):145-62. doi: 10.3109/02656736.2015.1007538.
27. Roberts WW, Hall TL, Cain CA, Fowlkes JB, Xu Z, Kusner MT, et al., inventors; The Regents Of The University Of Michigan, assignee. Micromanipulator control arm for therapeutic and imaging ultrasound transducers. W.O. patent 2011028603A2. 2011 March 10.
28. Xu Z, Sukovich J, Pandey AS, Cain CA, Gurm HS, inventors; The Regents Of The University Of Michigan, assignee. Histotripsy therapy systems and methods for the treatment of brain tissue. W.O. patent 2016210133A1. 2016 June 23.
29. Gleiman SS, Mercer NS, O'Brien TJ, Waldstreicher JR, Taylor KJ, Mangual Arbelo LL, et al., inventors; Galary, Inc., assignee. Devices, systems and methods for the treatment of abnormal tissue. W.O. patent 2020215007A1. 2020 October 22.
30. Baust J, Gage A, Johansen TB, Baust J. Mechanisms of cryoablation: clinical consequences on malignant tumors. *Cryobiology*. 2014;68(1):1-11. doi: 10.1016/j.cryobiol.2013.11.001.
31. Roy BN. *Fundamentals of classical and statistical thermodynamics*: Wiley Online Library;

2002.

32. Surtees B, Mcchesney E, Young S, Hu Y, Durr NJ, Blair T, et al., inventors; The Johns Hopkins University, assignee. Carbon dioxide-based percutaneous cryosurgical system W.O. patent 2019213205A1. 2019 November 17.

33. Zhou L, inventor; Thomas Jefferson University, assignee. Cryoneedle and cryotherapy system. W.O. patent 2008054487A2. 2008 May 8.

34. Korpan N, Zharkov J, inventors; Nikolai Korpan, Jaroslav Zharkov, assignee. Device for carrying out cryosurgical interventions, especially for treating tumors. W.O. patent 2000047121A2. 2000 December 21.

35. Yang C, Xu B, Wu Y, Chang Z, inventors; Accu Target Medipharma (Shanghai) Co., Ltd., assignee. Adjustable cryoablation needle. W.O. patent 2021027397A1. 2021 February 18.

36. Zvuloni R, Amir U, inventors; Galil Medical Ltd., assignee. Apparatus and method for accurately delimited cryoablation W.O. patent 2004086936A2. 2004 October 14.

37. Clarke B, inventor; Nitro Medical Limited, assignee. Cryoablation. W.O. patent WO2018087563A1. 2017 November 10.

38. Davalos RV, Mir L, Rubinsky B. Tissue ablation with irreversible electroporation. *Annals of biomedical engineering*. 2005;33(2):223. doi: 10.1007/S10439-005-8981-8.

39. Chu KF, Dupuy DE. Thermal ablation of tumours: biological mechanisms and advances in therapy. *Nature Reviews Cancer*. 2014;14(3):199-208. doi: 10.1038/nrc3672.

40. Davalos RV, Arena CB, Caldwell J, inventors; Virginia Tech Intellectual Properties, Inc., assignee. Integration of very short electric pulses for minimally to noninvasive electroporation. W.O. patent 2010118387A1. 2010 October 14.

41. Hobbs EP, Lovewell JG, Pearson RM, inventors; AngioDynamics, Inc., assignee. Irreversible electroporation and tissue regeneration. W.O. patent 2010093692A2. 2010 August 19.

42. Applying WM, William C. Hamilton J, Mikus PW, inventors; AngioDynamics, Inc., assignee. Electroporation device and method W.O. patent 2009137800A2. 2009 November 12.

43. Long GL, Ghabrial RM, Plescia DN, Vakharia OJ, inventors; Ethicon Endo-Surgery Inc., assignee. Electrical ablation devices. W.O. patent 2010080974A1. 2010 July 15.

44. Dimitrova T, Weis A. The wave-particle duality of light: A demonstration experiment. *American Journal of Physics*. 2008;76(2):137-42. doi: 10.1119/1.2815364.

45. Zamanian A, Hardiman C. Electromagnetic radiation and human health: A review of sources and effects. *High Frequency Electronics*. 2005;4(3):16-26.

46. Baskar R, Lee KA, Yeo R, Yeoh K-W. Cancer and radiation therapy: current advances and future directions. *International journal of medical sciences*. 2012;9(3):193. doi: 10.7150/ijms.3635.

47. Francescatti D, Lovoi PA, inventors; Xoft, Inc., assignee. Endoscopic/percutaneous electronic radiation applicator and method of use. W.O. patent 2008005435A2. 2008 January 10.

48. Fehre J, Granz B, Lanski M, Nanke R, inventors; Siemens Aktiengesellschaft, assignee. Device for x-ray brachytherapy, and method for positioning a probe introduced into a body for x-ray brachytherapy. W.O. patent 2007060049A1. 2007 May 31.

49. Gutman G, Strumban E, inventors; Advanced X-Ray Technology, Inc., assignee. X-ray needle apparatus and method for radiation treatment W.O. patent 2006068671A2. 2005 August 16.

50. Flynn R, Dadkhah H, Patwardhan K, Cho M, inventors; University Of Iowa Research Foundation, assignee. A rotating shield brachytherapy system W.O. patent 2017184728A1. 2017 October 26.

51. Murray SC, Davenport SA, Coleman T, inventors; Laserscope, assignee. Methods for laser treatment of soft tissue W.O. patent 2002091935A1. 2002 November 21.

52. Ganz RA, inventor; Robert A. Ganz, assignee. Apparatus and method for debilitating or killing microorganisms within the body. W.O. patent 2000078393A1. 2000 December 28.

53. Alvarez A, Lacalle J, Cañavate M, Alonso-Alconada D, Lara-Celador I, Alvarez F, et al. Cell death. A comprehensive approximation. *Necrosis. Microsc Science, Technology, Appl Educ* 2. 2010.

54. Zhu L, Altman MB, Laszlo A, Straube W, Zoberi I, Hallahan DE, et al. Ultrasound hyper-

thermia technology for radiosensitization. *Ultrasound in medicine & biology*. 2019. doi: 10.1016/j.ultrasmedbio.2018.12.007.

55. Mo S-K, Kim N-T, inventors; Seung-Kee Mo, Nam-Tae Kim, assignee. Device for treating tumor and fat using microwave. W.O. patent 2003103768A1. 2003 December 18.

56. Wang Z, inventor; The University Of Dundee, assignee. Radio frequency surgical probe. W.O. patent 2013076440A1. 2013 May 30.

57. Mulier SMM, Verhaegen G, Mulier MWJ, Bossche JLVd, Mulier KPM, inventors; Vesalius Medical Technologies Bvba, assignee. Device and method for radio frequency ablation (RFA). W.O. patent 2011113943A1. 2011 September 22.

58. Habib N, inventor; Emcision Limited, assignee. Device and method for the treatment of diseased tissue such as tumours. W.O. patent 2008084244A2. 2008 July 17.

59. Thistle RC, inventor; Boston Scientific Scimed, Inc., assignee. Low-profile, expanding single needle ablation probe. W.O. patent 2007094887A2. 2007 August 23.

60. McCullagh O, Spiridigliozzi JC, Sauvageau DJ, inventors; Boston Scientific Scimed Inc, Spiridigliozzi John C, assignee. Co-access bipolar ablation probe. W.O. patent 2006073879A2. 2006 July 13.

61. Venturelli L, inventor; Fogazzi Di Venturelli, Andrea & C. S.N.C., assignee. Rf hyperthermia with needle electrodes enclosing a volume. W.O. patent 2003090636A1. 2003 November 6.

62. Cockburn JF, Cockburn DJA, Wemyss-Holden S, inventors; The Norfolk And Norwich University Hospital Nhs Trust, assignee. Electro-surgical needle apparatus. W.O. patent 2006082413A1. 2006 August 10.

63. Faure A, inventor; Université de Franche-Comté, assignee. Medical device using a coiled electrode. W.O. patent 2004100812A1. 2004 November 25.

64. Mori K, inventor; Kenji Mori, assignee. Cautery needle device, high frequency cautery therapy system, and chemical cautery therapy system. W.O. patent 2017126265A1. 2017 July 27.

65. O'dea J, Mchugh A, Griffin P, inventors; Flip Technologies Limited, assignee. An ablation system and a device and a method for ablating matter in a lumen or a cavity. W.O. patent 2009001326A1. 2008 December 31.

66. Panescu D, Gelfand M, Leung M, inventors; Zidan Medical, Inc., assignee. Devices for treating lung tumors W.O. patent 2019051274A2. 2019 March 14.

67. Utley DS, Gerberding BC, Taimisto MH, Chung W, Marler JD, Filimon V, inventors; Barrx Medical, Inc., assignee. System and method for ablational treatment of uterine cervical neoplasia. W.O. patent 2009154654A1. 2009 December 23.

68. Pacey A, Habib N, inventors; Emcision Limited, assignee. Apparatus and method for treating tissue such as tumours W.O. patent 2007135437A1. 2007 November 29.

69. Behl RS, Grosser M, Huang AL, inventors; Radiotherapeutics Corporation, assignee. Methods and systems for focused bipolar tissue ablation W.O. patent 2002022032A1. 2002 March 21.

70. Young K, Zervas JW, inventors; Boston Scientific Scimed, Inc., assignee. Ablation probe with flared electrodes. W.O. patent 2006049810A1. 2006 May 11.

71. Young K, Bukowski SP, inventors; Boston Scientific Scimed, Inc., assignee. Electrosurgical probe having current enhancing protrusions W.O. patent 2009086409A1. 2009 July 9.

72. Miller BJ, Sherar M, McCann C, Jewett M, Kachura JR, Furse A, et al., inventors; University Health Network, assignee. Coil electrode for thermal therapy W.O. patent 2012100355A1. 2012 January 30.

73. Bo Xiao, Jie Qin, Tang W, inventors; Medsphere International, assignee. Radio-frequency ablation electrode device with double-layer umbrella-shaped probes. W.O. patent 2015051594A1. April 16.

74. Morris D, Altoukhi K, Valle S, Morris C, inventors; Ablation Gen 2 Pty Ltd, assignee. Devices and methods for ablating tissue. W.O. patent 2020150782A1. 2020 July 20.

75. Clerck LD, inventor; Medical Development Technologies S.A., assignee. Heatable implant device for tumor treatment. W.O. patent 2019120489A1. 2019 June 27.

76. Hancock CP, Chaudry MS, Goodman AM, inventors; Christopher Paul Hancock, Mohammed Sabih Chaudry, Andrew Marc Goodman, assignee. Tissue ablation apparatus and method of ablating tissue W.O. patent 2004047659A2. 2004 June 10.
77. Hancock CP, White M, Burn P, Shah P, Hales P, inventors; Creo Medical Limited, assignee. Electrosurgical probe for delivering microwave energy. W.O. patent 2017103209A1. 2017 June 22.
78. Chornenky V, Swanson V, Hodge RG, Davis PG, inventors; Medtronic Ave Inc, assignee. Hyperthermia radiation apparatus and method for treatment of malignant tumors. W.O. patent 2002045790A2. 2002 June 13.
79. Hancock CP, White M, Burn P, inventors; Creo Medical Limited, assignee. Electrosurgical instrument with impedance transformer for delivering microwave energy. W.O. patent 2016203257A1. 2016 December 22.
80. Tosoratti N, inventor; H.S. - Hospital Service - S.P.A., assignee. Microwave device for the ablation of tissues W.O. patent 2006084676A1. 2006 August 17.
81. Buttar NS, Song L-MWK, Asirvatham SJ, inventors; Mayo Foundation For Medical Education And Research, assignee. Thermal therapy systems and methods. W.O. patent 2016126461A1. 2016 August 11.
82. Hancock P, inventor; Creo Medical, assignee. Electrosurgical apparatus for treating biological tissue with microwave energy. W.O. patent 2021052913A1. 2021 March 25.
83. Pfannenstiel A, Fallahi H, Prakash P, inventors; Kansas State University Research Foundation, Precision Microwave Inc., assignee. Minimally invasive microwave ablation device. W.O. patent 2020242973A1. 2020 December 3.
84. Hancock CP, Taplin W, Ullrich G, Preston S, inventors; Creo Medical Limited, assignee. Electrosurgical instrument. W.O. patent 2020114878A1. 2020 June 11.
85. Masotti L, inventor; EL.En. S.P.A., Esaote S.P.A., assignee. Device for treating tumors by laser thermotherapy. W.O. patent 2005055848A2. 2005 June 23.
86. Dzerins O, Pfafrods D, inventors; Sia Light Guide Optics International, assignee. Device for treatment of body tissue. W.O. patent 2020058447A1. 2020 March 26.
87. Shafirstein G, Ferguson SL, Waner M, inventors; Board Of Trustees Of The University Of Arkansas, assignee. Conductive interstitial thermal therapy device W.O. patent 2004019809A2. 2004 March 11.
88. Huang S-C, Wen H-S, Yang T-F, Liao C-C, inventors; Taiwan Earning Co. Ltd., assignee. Tumor ablation system. W.O. patent 2017193938A1. 2017 November 16.
89. Wago T, Shuto B, Iwabuchi A, inventors; Incorporated National University Iwate University, assignee. A drug delivery system using an acupuncture needle. W.O. patent 2013183791A1. 2013 December 12.
90. Fallik J, inventor; Joel Fallik, assignee. 3d microwave system and methods. W.O. patent 2010019840A1. 2010 February 18.
91. Virta TJV, inventor; Koninklijke Philips Electronics N.V., assignee. Ultrasonic treatment apparatus with a protective cover. W.O. patent 2010032186A1. 2010 March 25.
92. Jiang J, Dong J, Ma H, Chen Y, Zhou Y, inventors; Shanghai A & S Science Technology Development Co., Ltd., assignee. Hifu tumor ablating system. W.O. patent 2007056905A1. 2007 May 24.
93. Chauhan S, Ng WS, inventors; Nanyang Technological University, assignee. Ultrasonic treatment of breast cancer. W.O. patent 2003059434A2. 2003 July 24.
94. Lacoste F, inventor; Theraclion, assignee. Head for imaging and treating organs of living beings and method for making same. W.O. patent 2006129045A2. 2006 December 7.
95. Quigley DP, Gal A, Phillips MH, inventors; Sono Esthetx, Inc., assignee. Method, system, and apparatus for line-focused ultrasound therapy W.O. patent 2008144274A2. 2008 November 27.
96. Bruggers JW, inventor; Koninklijke Philips Electronics N.V., assignee. Apparatus for thermal treatment of tissue. W.O. patent 2008026134A1. 2008 March 6.
97. Carpentier A, Itzcovitz J, inventors; Alexandre Carpentier, Julian Itzcovitz, assignee. A medi-

- cal system comprising a percutaneous probe. W.O. patent 2009125002A1. 2009 October 15.
98. Nguyen-Dinh A, Dufait R, Notard C, Canney M, Chapelon J-Y, Chavrier F, et al., inventors; Vernon S.A., Carthera S.A.S., Institut National De La Sante Et De La Recherche Medicale (Inserm), Universite Pierre Et Marie Curie (Paris 6), assignee. Interstitial ultrasonic disposable applicator for tissue thermal conformal volume ablation and monitoring the same. W.O. patent 2014141052A1. 2014 September 18.
99. Rem-Bronneberg D, inventor; Koninklijke Philips N.V., assignee. Ultrasound ablation device. W.O. patent 2017144288A1. 2017 August 31.
100. Lau MPH, Teng N, Vaezy S, Lebedev A, Lau MW, Connolly MJ, inventors; Mirabilis Medica Inc., assignee. Methods and apparatus for the treatment of menometrorrhagia, endometrial pathology, and cervical neoplasia using high intensity focused ultrasound energy. W.O. patent 2007143281A2. 2007 December 13.
101. Bronskill MJ, Chopra R, inventors; Sunnybrook Health Sciences Centre and Women's College Health Sciences Centre, assignee. Technique and apparatus for ultrasound therapy W.O. patent 2002032506A1. 2002 April 25.
102. Carpentier A, Lafon C, Chapelon J-Y, Canney MS, Beccaria K, inventors; Universite Pierre Et Marie Curie (Paris 6), Assistance Publique - Hopitaux De Paris, Carthera, assignee. Apparatus for the treatment of brain affections and method implementing thereof. W.O. patent 2011101492A2. 2011 August 25.
103. Ahmed M, Brace CL, Lee Jr FT, Goldberg SN. Principles of and advances in percutaneous ablation. *Radiology*. 2011;258(2):351-69. doi: 10.1148/radiol.10081634.
104. Toth L, Schwartz R, inventors; Landy Toth, Robert Schwartz, assignee. Precision chemical ablation and treatment of tissues. W.O. patent 2016014750A1. 2016 January 28.
105. Fischell DR, Fischell TA, Ragland RR, Kent DJ, Denison AE, Johnson ET, et al., inventors; Ablative Solutions, Inc., assignee. Peri-vascular tissue ablation catheter with support structures W.O. patent 2014070558A1. 2014 May 8.
106. Barnett BP, Gailloud P, Yung RC, inventors; The Johns Hopkins University, assignee. Drug eluting hydrogels for catheter delivery. W.O. patent 2012012772A2. 2012 January 26.
107. Neisz JJ, Escandon MAS, inventors; Ams Research Corporation, assignee. Surgical kit for treating prostate tissue. W.O. patent 2003005889A2. 2003 January 23.
108. Volotskova O, Hawley TS, Stepp MA, Keidar M. Targeting the cancer cell cycle by cold atmospheric plasma. *Scientific reports*. 2012;2:636. doi: 10.1038/srep00636.
109. Graves DB. Reactive species from cold atmospheric plasma: implications for cancer therapy. *Plasma Processes and Polymers*. 2014;11(12):1120-7. doi: 10.1002/ppap.201400068.
110. Keidar M, Walk R, Shashurin A, Srinivasan P, Sandler A, Dasgupta S, et al. Cold plasma selectivity and the possibility of a paradigm shift in cancer therapy. *British journal of cancer*. 2011;105(9):1295-301. doi: 10.1038/bjc.2011.386.
111. Bartsch H, Nair J. Chronic inflammation and oxidative stress in the genesis and perpetuation of cancer: role of lipid peroxidation, DNA damage, and repair. *Langenbeck's Archives of Surgery*. 2006;391(5):499-510. doi: 10.1007/s00423-006-0073-1.
112. Barthel JS, inventor; H. Lee Moffitt Cancer Center & Research Institute, assignee. Endoscopic caps for ionized plasma confinement, shaping and control for therapeutic purposes. W.O. patent 2011022069A2. 2011 February 24.
113. Krasik Y, Felsteiner J, Slutsker Y, Gil Z, Cohen J, Binenbaum Y, inventors; Technion Research & Development Foundation Limited, Rambam Med Tech Ltd., assignee. Cold plasma generating system W.O. patent 2016079742A1. 2016 May 26.
114. Ahdoot M, Lebastchi AH, Turkbey B, Wood B, Pinto PA. Contemporary treatments in prostate cancer focal therapy. *Current opinion in oncology*. 2019;31(3):200. doi: 10.1097/CCO.0000000000000515.
115. Agostinis P, Berg K, Cengel KA, Foster TH, Girotti AW, Gollnick SO, et al. Photodynamic



- therapy of cancer: an update. *CA: a cancer journal for clinicians*. 2011;61(4):250-81. doi: 10.3322/caac.20114.
116. Dolmans DE, Fukumura D, Jain RK. Photodynamic therapy for cancer. *Nature reviews cancer*. 2003;3(5):380-7. doi: 10.1038/nrc1071.
  117. Dougherty TJ, Gomer CJ, Henderson BW, Jori G, Kessel D, Korbek M, et al. Photodynamic therapy. *JNCI: Journal of the national cancer institute*. 1998;90(12):889-905.
  118. Chen JC, Keltner L, Naimushin AN, inventors; James C. Chen, Llew Keltner, Alexei N. Naimushin, assignee. Systems, devices, and methods for tissue therapy. W.O. patent 2016040383A1. 2016 March 17.
  119. Rylander CG, Kosoglu MA, Hood RL, Robertson JL, Rossmeisl JH, Grant DC, et al., inventors; Virginia Tech Intellectual Properties, Inc., assignee. Fiber array for optical imaging and therapeutics W.O. patent 2012154284A2. 2012 November 15.
  120. Patrice T, Neuberger W, Bode H-P, Bourre L, inventors; Ceramoptec Industries, Inc., assignee. Treatment for epithelial diseases W.O. patent 2002007630A1. 2002 January 31.
  121. Shang H, inventor; Beijing Yestarpent Agency co., Ltd, assignee. Photodynamic therapy and diagnosis device capable of optical fiber puncturing. W.O. patent 2020019305A1. 2020 January 30.
  122. Schultheis B, Keiper O, Meinel J, Russert H, Grimm J, Willmes L, et al., inventors; Ag. Schott, assignee. Illumination system having an optical waveguide with substantially radially emitting diffuser element, and method for production thereof. W.O. patent 2020127762A2. 2020 June 25.
  123. Maeda H, inventor; Hiroshi Maeda, assignee. Light radiating probe for photodynamic therapy employing endoscope. W.O. patent 2018092814A1. 2018 May 24.
  124. Chen JC, Barnard WL, Shine DB, Miazga J, inventors; Light Sciences Oncology, Inc., assignee. Low-profile intraluminal light delivery system and methods of using the same. W.O. patent 2011020064A2. 2011 February 17.
  125. Chen J, Christophersen J, Yeo N, Heacock G, inventors; Light Sciences Corporation, assignee. Systems and methods for photodynamic therapy. W.O. patent 2003061696A2. 2003 July 31.
  126. Rogers GS, inventor; Gary S. Rogers, assignee. Continuous low irradiance photodynamic therapy system and method. W.O. patent 2007146101A2. 2007 December 21.
  127. El Ghissassi F, Baan R, Straif K, Grosse Y, Secretan B, Bouvard V, et al. A review of human carcinogens—part D: radiation. *The lancet oncology*. 2009;10(8):751-2.
  128. Kelson I, Keisari Y, Schmidt M, Gat A, Magen O, Keret G, et al., inventors; Alpha Tau Medical Ltd., assignee. Controlled release of radionuclides. W.O. patent 2019193464A1. 2019 October 10.
  129. Kelson I, Keisari Y, Schmidt M, Magen O, Sosnovitch A, Keret G, et al., inventors; Alpha Tau Medical Ltd., assignee. Radiotherapy seeds and applicators. W.O. patent 2019171308A1. 2019 September 12.
  130. Kelson I, Arazi L, inventors; Ramot At Tel Aviv University Ltd., assignee. Method and device for radiotherapy. W.O. patent 2004096293A2. 2004 November 11.
  131. Nakaji P, Brachman D, McBride H, Youssef EY, inventors; Theresa, Thomas, assignee. Dosemetrically customizable brachytherapy carriers and methods thereof in the treatment of tumors W.O. patent 2012149580A1. 2012 November 1.
  132. Desantis M, Cipriani C, inventors; Maria Desantis, Cesidio Cipriani, assignee. Composition, device and method for conformational intra-tissue beta brachytherapy. W.O. patent 2018138744A1. 2018 August 2.
  133. Halpern DS, inventor; Isotron, Inc., assignee. Neutron brachytherapy device and method. W.O. patent 2001019450A2. 2001 March 22.
  134. Chen S-W, inventor; Empire Technology Development Llc, assignee. Method and system for radioisotope ion beam gamma therapy. W.O. patent 2012030297A1. 2012 March 8.
  135. Tanrisever NE, inventor; Naim Erturk Tanrisever, assignee. Plasma arc surgical device and method. W.O. patent 2002030308A1. 2002 April 18.
  136. Sersa G, Miklavcic D, Cemazar M, Rudolf Z, Pucihar G, Snoj M. Electrochemotherapy in

treatment of tumours. *European Journal of Surgical Oncology (EJSO)*. 2008;34(2):232-40. doi: 10.1016/j.ejso.2007.05.016.

137. Rodriguez JF, Phung BD, Twitty CG, Jin J, inventors; Oncosec Medical Incorporated, assignee. Electroporation systems, methods, and apparatus W.O. patent 2019213421A1. 2019 November 7.

138. Chen Y, inventor; Hangzhouready Biological Technology Co., Ltd, assignee. Electric pulse ablation device capable of synergistic administration W.O. patent 2020232849A1. 2020 November 26.

139. Schroepel EA, Kroll MW, Kroll K, inventors; Edward A. Schroepel, Mark W. Kroll, Kai Kroll, assignee. Method and device for treating cancer with electrical therapy in conjunction with chemotherapeutic agents and radiation therapy. W.O. patent 2004037341A2. 2004 May 6.

140. Davalos RV, Rylander MN, Arena CB, inventors; Virginia Tech Intellectual Properties, Inc., assignee. Irreversible electroporation using nanoparticles. W.O. patent 2010151277A1. 2010 December 29.

141. Soikum S, Thomsen L, Dodgson JR, inventors; Giantcode Corporation Pte Ltd, assignee. Method, device and system for targeted cell lysis. W.O. patent 2011135294A1. 2011 April 26.

142. Liang P, inventor; Ping Liang, assignee. Methods for killing cancer cells and cellular imaging using magneto-electric nano-particles and external magnetic field. W.O. patent 2016025768A1. 2016 February 18.

143. Eggers PE, Thapliyal HV, inventors; Arthrocare Corporation, assignee. Systems and methods for electrosurgical treatment of tissue in the brain and spinal cord W.O. patent 2000007507A1. 2000 February 17.

144. Long GL, Plecia DN, Shires PK, inventors; Ethicon Endo-Surgery, Inc., assignee. Electrical ablation devices. W.O. patent 2011081996A2. 2011 July 7.

145. Schumann C, Hetzel M, Babiak AJ, Hetzel J, Merk T, Wibmer T, et al. Endobronchial tumor debulking with a flexible cryoprobe for immediate treatment of malignant stenosis. *The Journal of thoracic and cardiovascular surgery*. 2010;139(4):997-1000. doi: 10.1016/j.jtcvs.2009.06.023.

146. Au JT, Carson J, Monette S, Finley DJ. Spray cryotherapy is effective for bronchoscopic, endoscopic and open ablation of thoracic tissues. *Interactive cardiovascular and thoracic surgery*. 2012;15(4):580-4. doi: 10.1093/icvts/ivs192.

147. Krinsky WS, inventor; Reset Medical, Inc., assignee. Method for cryospray ablation in reproductive tissues. W.O. patent 2010118325A2. 2010 October 14.

148. Johnston MH, inventor; Mark H. Johnston, assignee. Tracheobronchial pulmonary cryogenic therapeutic method and apparatus. W.O. patent 2010117777A2. 2010 October 14.

149. Field LA, Gerlach D, inventors; Empire Technology Development Llc, assignee. Devices and techniques for ablative treatment W.O. patent 2015099786A1. 2015 July 2.

150. Hoey M, Mauch G, Schrom M, inventors; Nxthera, Inc., assignee. Systems and methods for treating prostate cancer. W.O. patent 2014153082A2. 2014 September 25.

151. Carmel Y, Wyk RV, Shkavarunets A, inventors; Electromedical Associates Llc, assignee. Devices and methods for ablating and removing a tissue mass. W.O. patent 2009131928A1. 2009 October 29.

152. Ruse RB, Bohanan SJ, Crawford ED, Nabors WL, inventors; Richard B. Ruse, Scott J. Bohanan, E. David Crawford, William L. Nabors, assignee. Method and apparatus for treating cancer W.O. patent 2013022939A1. 2013 February 14.

153. Kubota S, inventor; Shigehiro Kubota, assignee. Laser therapy method, highly laser beam-absorbing media to be used in the therapy and laser therapy apparatus with the use of the same. W.O. patent 2002036201A1. 2002 May 10.

154. Myhr G, inventor; Cancerure As, assignee. Therapeutic probe, method and system. W.O. patent 2005002671A1. 2005 January 13.

155. Theuer AE, inventor; Gerhard Franz Walter, assignee. Medical device for treating tumor tissue. W.O. patent 2010049176A1. 2010 May 6.

156. Hobbs EHO, Gary M; Miessau, James A; Condra, Jon H, inventor; Hobbs, Eamonn; Onik,

- Gary M; Miessau, James A; Condra, Jon H, assignee. In situ therapeutic cancer vaccine creation system and method. W.O. patent 2020131885A1. 2020 June 25.
157. Fomitchev-Zamilov MI, Hymer W, Kosik A, inventors; Quantum Cure, Inc., Quantum Vortex, Inc., assignee. Method and apparatus for cancer treatment. W.O. patent 2014204978A1. 2014 December 24.
158. Lamb KJ, inventor; Karl J. Lamb, assignee. System and method for hyperthermic tumor treatment. W.O. patent 2012006290A2. 2012 January 12.
159. Handy ES, Ivkov R, Ellis-Busby D, Foreman A, Brauhut SJ, Gwost DU, et al., inventors; Triton Biosystems Inc., assignee. Thermotherapy via targeted delivery of nanoscale magnetic particles. W.O. patent 2003022360A2. 2003 March 20.
160. Goodrich GP, Schwartz JA, Murphy AM, inventors; Nanospectra Biosciences, Inc., assignee. Devices and the use thereof in methods for ablation therapy W.O. patent 2018112261A1. 2018 June 21.
161. Kislev H, inventor; Kpe Ltd., assignee. Nanoparticle mediated ultrasound therapy and diagnostic imaging. W.O. patent 2006051542A1. 2006 May 18.
162. Peyman GA, inventor; Gholam A. Peyman, assignee. Cancer treatment methods using thermotherapy and/or enhanced immunotherapy. W.O. patent 2019071261A1. 2019 April 11.
163. Srimathveeravalli G, Reiner T, Solomon S, inventors; Memorial Sloan Kettering Cancer Center, assignee. Systems and methods for enhancing delivery of diagnostic and/or therapeutic compositions in vivo using electric pulses. W.O. patent 2017173089A1. 2017 October 5.
164. Baron E, inventor; I-Check, Inc, assignee. Integrated system for noninvasive focused energy treatment using energy activated drugs. W.O. patent 2006030534A1. 2006 March 23.
165. Coptly A, inventor; Synergymed Devices Inc., assignee. Precise ablation treatment of cancer using synergetic effects of electromagnetic radiation with nanoparticles. W.O. patent 2020141527A1. 2020 July 9.
166. Koning GA, Eggermont AM, Lindner LH, ten Hagen TL. Hyperthermia and thermosensitive liposomes for improved delivery of chemotherapeutic drugs to solid tumors. *Pharmaceutical research*. 2010;27(8):1750-4. doi: 10.1007/s11095-010-0154-2.
167. Mon J, inventor; Boston Scientific Corporation, assignee. Method of treating cancer comprising introduction of heat and delivery of liposome containing an active agent or thermo-activated drug, gene or virus to tissue. W.O. patent 2008039188A1. 2008 April 3.
168. Fenn AJ, Mon J, Smith D, inventors; Celsion Corporation, assignee. Monopole phased array thermotherapy applicator for deep tumors W.O. patent 2004022159A1. 2004 March 18.
169. Vishwanath GV, inventor; Sbf Healthcare Private Limited, assignee. Sequentially programmed magnetic field therapeutic system (spm). W.O. patent 2010095147A2. 2010 August 26.
170. Blackiston DJ, McLaughlin KA, Levin M. Bioelectric controls of cell proliferation: ion channels, membrane voltage and the cell cycle. *Cell cycle*. 2009;8(21):3527-36. doi: 10.4161/cc.8.21.9888.
171. Sano MB, Arena CBA, Verbridge; SS, Davalos RV, inventors; Virginia Tech Intellectual Properties, Inc., assignee. Selective modulation of intracellular effects of cells using pulsed electric fields. W.O. patent 2015175570A1. 2015 November 19.
172. Fajardo LF, Egbert B, Marmor J, Hahn GM. Effects of hyperthermia in a malignant tumor. *Cancer*. 1980;45(3):613-23. doi: 10.1002/1097-0142(19800201)45:3<613::AID-CNCR2820450331>3.0.CO;2-E.
173. Willis W, Jackman M, Bizeau M, Pagliassotti M, Hazel J. Hyperthermia impairs liver mitochondrial function in vitro. *American Journal of Physiology-Regulatory, Integrative and Comparative Physiology*. 2000;278(5):R1240-R6. doi: 10.1152/ajpregu.2000.278.5.r1240.
174. Kolvenbag GJ, Blackledge GR, Gotting-Smith K. Bicalutamide (Casodex®) in the treatment of prostate cancer: history of clinical development. *The Prostate*. 1998;34(1):61-72. doi: 10.1002/(SICI)1097-0045(19980101)34:1<61::AID-PROS8>3.0.CO;2-N.
175. Sharifi N, Gulley JL, Dahut WL. Androgen deprivation therapy for prostate cancer. *Jama*. 2005;294(2):238-44. doi: 10.1001/jama.294.2.238.
176. Osborne CK. Tamoxifen in the treatment of breast cancer. *New England Journal of Medicine*.



- 1998;339(22):1609-18. doi: 10.1056/NEJM19981126339220.
177. Denekamp J. Vascular attack as a therapeutic strategy for cancer. *Cancer and Metastasis Reviews*. 1990;9(3):267-82. doi: 10.1007/BF00046365.
178. Habib N, inventor; Emcision Ltd, Nagy Habib, assignee. Vessel sealing device and methods. W.O. patent 2007135431A2. 2007 November 29.
179. Gat Y, Goren M, inventors; Yigal Gat, Menachem Goren, assignee. Methods and apparatus for treating the prostate. W.O. patent 2009010964A2. 2009 January 22.
180. Barry RLB, Henne EM, inventors; Intuitive Surgical Operations, Inc., assignee. Systems and methods for localized endoluminal thermal liquid treatment. W.O. patent 2021007255A1. 2021 January 14.
181. Gray J, Zamarripa N, inventors; Boston Scientific Scimed, Inc., assignee. Occlusion device detachable by inflation of a balloon. W.O. patent 2015120155A1. 2015 August 13.
182. Parsons JE, Connolly MJ, Darlington GP, Horth R, Murkowski J, Reed JA, inventors; Mirabilis Medica, Inc., assignee. Method and apparatus for treating tissues with HIFU. W.O. patent 2010040140A2. 2010 April 8.
183. Connors KG, Schutt EG, Gillespie J, Dayton P, inventors; Attenuex Technologies, Inc., assignee. Implant with high vapor pressure medium W.O. patent 2010068467A1. 2010 June 17.
184. Ken CGM, Patel TJ, inventors; Concentric Medical, assignee. Device for vaso-occlusion. W.O. patent 2003037191A1. 2003 May 8.
185. BostonScientific.com. VISUAL ICE™ Cryoablation Needles [Available from: <https://www.bostonscientific.com/en-US/products/cryoablation/visual-ice/visual-ice-cryoablation-needles.html>].
186. HealthTronics.com. Endocare™ precision cryoprobes [Available from: [https://www.healthtronics.com/wp-content/uploads/2017/02/Cryoprobe-Brochure-Rev-E\\_opt.pdf](https://www.healthtronics.com/wp-content/uploads/2017/02/Cryoprobe-Brochure-Rev-E_opt.pdf)].
187. AngioDynamics.com. NanoKnife 3.0 System [Available from: <https://www.angiodynamics.com/products/2/The-NanoKnife-System/>].
188. AngioDynamics.com. NanoKnife 3.0 Irreversible Electroporation (IRE) [Available from: [https://www.angiodynamics.com/img/resources/ANGB\\_1070\\_US\\_REV\\_01\\_NanoKnife\\_3.0-Web-586599.pdf](https://www.angiodynamics.com/img/resources/ANGB_1070_US_REV_01_NanoKnife_3.0-Web-586599.pdf)].
189. BostonScientific.com. LEVEEN™ Needle Electrodes [Available from: [https://www.boston-scientific.com/content/dam/bostonscientific/pi/portfolio-group/rfa/RF\\_3000\\_LeVeen%20Needle%20Sell%20Sheet%20\(PI-323104-AA\).pdf](https://www.boston-scientific.com/content/dam/bostonscientific/pi/portfolio-group/rfa/RF_3000_LeVeen%20Needle%20Sell%20Sheet%20(PI-323104-AA).pdf)].
190. Medtronic.com. Cool-tip™ RF Ablation System E Series [Available from: <https://www.medtronic.com/covidien/en-us/products/ablation-systems/cool-tip-rf-ablation-system-e-series.html>].
191. AngioDynamics.com. StarBurst® XL & Semi-Flex RFA Devices [Available from: <https://www.angiodynamics.com/products/6/StarBurst-XL-Semi-Flex-RFA-Devices/>].
192. AngioDynamics.com. Solero microwave tissue ablation system [Available from: [https://www.angiodynamics.com/img/resources/Solero\\_Product\\_Brochure-092167.pdf](https://www.angiodynamics.com/img/resources/Solero_Product_Brochure-092167.pdf)].
193. ProfoundMedical.com. TULSA-PRO [Available from: <https://profoundmedical.com/new-tulsa/>].
194. ProfoundMedical.com. The Sonalleve system [Available from: <https://profoundmedical.com/sonalleve/>].
195. Philips.nl. Sonalleve MR-HIFU Therapy platform [Available from: <https://www.philips.nl/healthcare/product/HC781360/sonalleve-mr-hifu>].
196. edap-tms.com. Focal One Focal HIFU for Prostate Cancer [Available from: <https://www.edap-tms.com/en/products-services/prostate-cancer/focal-one>].
197. edap-tms.com. Ablatherm HIFU Non-invasive treatment for prostate cancer [Available from: <https://www.edap-tms.com/en/products-services/prostate-cancer/ablatherm-hifu>].
198. Sonacaremedical.com. Sonablate HIFU targeted prostate ablation [Available from: <https://sonacaremedical.com/surgeons/our-products/sonablate>].
199. Cramers P, Ruevekamp M, Oppelaar H, Dalesio O, Baas P, Stewart F. Foscan® uptake and

- tissue distribution in relation to photodynamic efficacy. *British journal of cancer*. 2003;88(2):283-90. doi: 10.1038/sj.bjc.6600682.
200. Azzouzi A-R, Vincendeau S, Barret E, Cicco A, Kleinclauss F, van der Poel HG, et al. Padeliporfin vascular-targeted photodynamic therapy versus active surveillance in men with low-risk prostate cancer (CLIN1001 PCM301): an open-label, phase 3, randomised controlled trial. *The Lancet Oncology*. 2017;18(2):181-91.
201. Applied-Optronics.com. High power laser diodes fiber coupled package [Available from: <http://www.applied-optronics.com/pdf/4.pdf>].
202. IGEA.it. Cliniporator [Available from: [https://www.igea.it/sites/default/files/CLINIPORATOR/CLINIPORATOR\\_SIMPLE%20SOLUTION\\_ENG\\_IGEA0130418.pdf](https://www.igea.it/sites/default/files/CLINIPORATOR/CLINIPORATOR_SIMPLE%20SOLUTION_ENG_IGEA0130418.pdf)].
203. BostonScientific.com. VISUAL ICE™ Cryoablation System [Available from: <https://www.bostonscientific.com/en-US/products/cryoablation/visual-ice.html>].
204. Lau B, Shah TT, Valerio M, Hamid S, Ahmed HU, Arya M. Technological aspects of delivering cryotherapy for prostate cancer. *Expert review of medical devices*. 2015;12(2):183-90. doi: 10.1586/17434440.2015.990377.
205. Wendler JJ, Porsch M, Fischbach F, Pech M, Schostak M, Liehr U-B. Letter to the Editor Concerning "Irreversible Electroporation (IRE) Fails to Demonstrate Efficacy in a Prospective Multi-center Phase II Trial on Lung Malignancies: The ALICE Trial" by Ricke et al. 2015. *Cardiovascular and interventional radiology*. 2015;38(4):1064. doi: 10.1007/s00270-015-1096-1.
206. Silk M, Tahour D, Srimathveeravalli G, Solomon SB, Thornton RH. The state of irreversible electroporation in interventional oncology. *Seminars in interventional radiology*; 2014 Jun.: Thieme Medical Publishers. doi: 10.1055/s-0034-1373785.
207. Jourabchi N, Beroukhim K, Tafti BA, Kee ST, Lee EW. Irreversible electroporation (NanoKnife) in cancer treatment. *Gastrointestinal Intervention*. 2014;3(1):8-18. doi: 10.1016/j.gii.2014.02.002.
208. Rebersek M, Miklavcic D, Bertacchini C, Sack M. Cell membrane electroporation-Part 3: the equipment. *IEEE Electrical Insulation Magazine*. 2014;30(3):8-18. doi: 10.1109/MEI.2014.6804737.
209. Mulier S, Miao Y, Mulier P, Dupas B, Pereira P, de Baere T, et al. Electrodes and multiple electrode systems for radiofrequency ablation: a proposal for updated terminology. *European radiology*. 2005;15(4):798-808. doi: 10.1007/s00330-004-2584-x.
210. Chauhan VP, Stylianopoulos T, Martin JD, Popović Z, Chen O, Kamoun WS, et al. Normalization of tumour blood vessels improves the delivery of nanomedicines in a size-dependent manner. *Nature nanotechnology*. 2012;7(6):383.
211. Folkman J. Tumor angiogenesis: therapeutic implications. *New england journal of medicine*. 1971;285(21):1182-6. doi: 10.1201/b23252-48.
212. Folkman J. Fighting cancer by attacking its blood supply. *Scientific American*. 1996;275(3):150-4.
213. Witte MH, Jones K, Wilting J, Dictor M, Selg M, McHale N, et al. Structure function relationships in the lymphatic system and implications for cancer biology. *Cancer and Metastasis Reviews*. 2006;25(2):159-84. doi: 10.1007/s10555-006-8496-2.
214. Westwood J. Anatomical and physiological models for surgical simulation. *Medicine Meets Virtual Reality: The Convergence of Physical & Informational Technologies: Options for a New Era in Healthcare*. 1999;62(999):23.
215. Cha S. Update on brain tumor imaging: from anatomy to physiology. *American Journal of Neuroradiology*. 2006;27(3):475-87.
216. Giedd JN. The teen brain: insights from neuroimaging. *Journal of adolescent health*. 2008;42(4):335-43. doi: 10.1016/j.jadohealth.2008.01.007.
217. Sankineni S, Osman M, Choyke PL. Functional MRI in prostate cancer detection. *BioMed research international*. 2014;2014. doi: 10.1155/2014/590638.
218. Nie S. Understanding and overcoming major barriers in cancer nanomedicine. *Nanomedicine*. 2010;5(4):523-8. doi: 10.2217/nnm.10.23.

219. Stern ST, McNeil SE. Nanotechnology safety concerns revisited. *Toxicological sciences*. 2008;101(1):4-21. doi: 10.1093/toxsci/kfm169.
220. Barry SE. Challenges in the development of magnetic particles for therapeutic applications. *International journal of hyperthermia*. 2008;24(6):451-66. doi: 10.1080/02656730802093679.
221. Chiang HA, Haleblan GE. Current Role of Focal Therapy. *Prostate Cancer Imaging: An Engineering and Clinical Perspective*. 2018.
222. DeSantis CE, Ma J, Jemal A. Trends in stage at diagnosis for young breast cancer patients in the United States. *Breast cancer research and treatment*. 2019;173(3):743-7. doi: 10.1007/s10549-018-5042-1.
223. Van Den Bos W, Muller BG, Ahmed H, Bangma CH, Barret E, Crouzet S, et al. Focal therapy in prostate cancer: international multidisciplinary consensus on trial design. *European urology*. 2014;65(6):1078-83. doi: 10.1016/j.eururo.2014.01.001.
224. Carmeliet P, Jain RK. Angiogenesis in cancer and other diseases. *nature*. 2000;407(6801):249-57. doi: 10.1038/35025220.
225. Wehbi E, Musquera M, Alcaraz A, Hanna S, Fleshner NE, Zlotta AR. Focal Therapy Will Be the Future Treatment Modality: The Motion “Con”. *European urology supplements*. 2009;8(5):433-8. doi: 10.1016/j.eursup.2009.01.006.
226. Cserni G, Bori R, Sejbien I, Vörös A, Kaiser L, Hamar S, et al. Unifocal, multifocal and diffuse carcinomas: A reproducibility study of breast cancer distribution. *The Breast*. 2013;22(1):34-8. doi: 10.1016/j.breast.2012.05.004.
227. Coombs NJ, Boyages J. Multifocal and multicentric breast cancer: does each focus matter? *Journal of Clinical Oncology*. 2005;23(30):7497-502. doi: 10.1200/jco.2005.02.1147.
228. Karavitakis M, Ahmed HU, Abel PD, Hazell S, Winkler MH. Tumor focality in prostate cancer: implications for focal therapy. *Nature reviews Clinical oncology*. 2011;8(1):48. doi: 10.1038/nrclinonc.2010.190.
229. Meiers I, Waters DJ, Bostwick DG. Preoperative prediction of multifocal prostate cancer and application of focal therapy: review 2007. *Urology*. 2007;70(6):S3-S8. doi: 10.1016/j.urology.2007.06.1129.
230. Jain RK. Normalization of tumor vasculature: an emerging concept in antiangiogenic therapy. *Science*. 2005;307(5706):58-62. doi: 10.1126/science.1104819.
231. Bergers G, Hanahan D. Modes of resistance to anti-angiogenic therapy. *Nature Reviews Cancer*. 2008;8(8):592-603. doi: 10.1038/nrc2442.
232. Turkbey B, Pinto PA, Choyke PL. Imaging techniques for prostate cancer: implications for focal therapy. *Nature Reviews Urology*. 2009;6(4):191. doi: 10.1038/nrurol.2009.27.
233. ASTM F2503-13, Standard practice for marking medical devices and other items for safety in the magnetic resonance environment. ASTM International, West Conshohocken, PA 2013.
234. Kanal E, Barkovich AJ, Bell C, Borgstede JP, Bradley Jr WG, Froelich JW, et al. ACR guidance document on MR safe practices: 2013. *Journal of Magnetic Resonance Imaging*. 2013;37(3):501-30. doi: 10.1002/jmri.24011.
235. McCulloch P, Cook JA, Altman DG, Heneghan C, Diener MK. IDEAL framework for surgical innovation 1: the idea and development stages. *Bmj*. 2013;346. doi: 10.1136/bmj.f3012.

---

## PART 2.

### NEEDLE DESIGN

Propulsion, Transport & Steering





# 5

## **From Ovipositor to Self-Propelled Transport Needle**

Published as:

Bloemberg J.\*, van Wees S.\*, Kortman V.G., Sakes A. (2025). Design of a wasp-inspired biopsy needle capable of self-propulsion and friction-based tissue transport. *Frontiers in Bioengineering and Biotechnology*, 12:1497221. doi: 10.3389/fbioe.2024.1497221 (\*these authors have contributed equally to this work).





## 5.1 Introduction

### 5.1.1 Pancreatic tissue sampling

Pancreatic cancer is increasingly common and highly fatal, necessitating effective detection methods [1-3]. Diagnosis relies heavily on histological and cytological analysis of masses or lesions [4-6], often through percutaneous biopsy procedures [7-9].

Ideally, a biopsy needle should be thin to minimize complications like bleeding and patient discomfort while providing continuous sampling of intact tissue. Fine Needle Aspiration Biopsy (FNAB) and Core Biopsy (CB) are the primary percutaneous methods, with FNAB using thin needles (22-25 G) to retrieve cytological and fluid samples using aspiration and CB employing thicker needles (19-13.5 G) to obtain an intact cylindrical tissue sample, called a core, via a discrete cutting action [10].

Despite their slenderness and ability for continuous sampling, FNAB needles for pancreatic biopsies have been associated with a higher incidence of false negatives compared to CB needles [11, 12]. Tikkakoski *et al.* [13] reported a 13% false negative rate in ultrasound-guided fine-needle pancreatic biopsy. This high rate may stem from needle deflection due to buckling, which can cause the needle to miss the target area, a known issue in breast biopsies [14]. Additionally, aspiration-based methods can result in device clogging, making them unreliable for obtaining intact tissue samples needed for histological evaluation [15]. The push toward smaller, less invasive tools highlights the need for improved biopsy methods that balance needle size with tissue sampling efficacy.

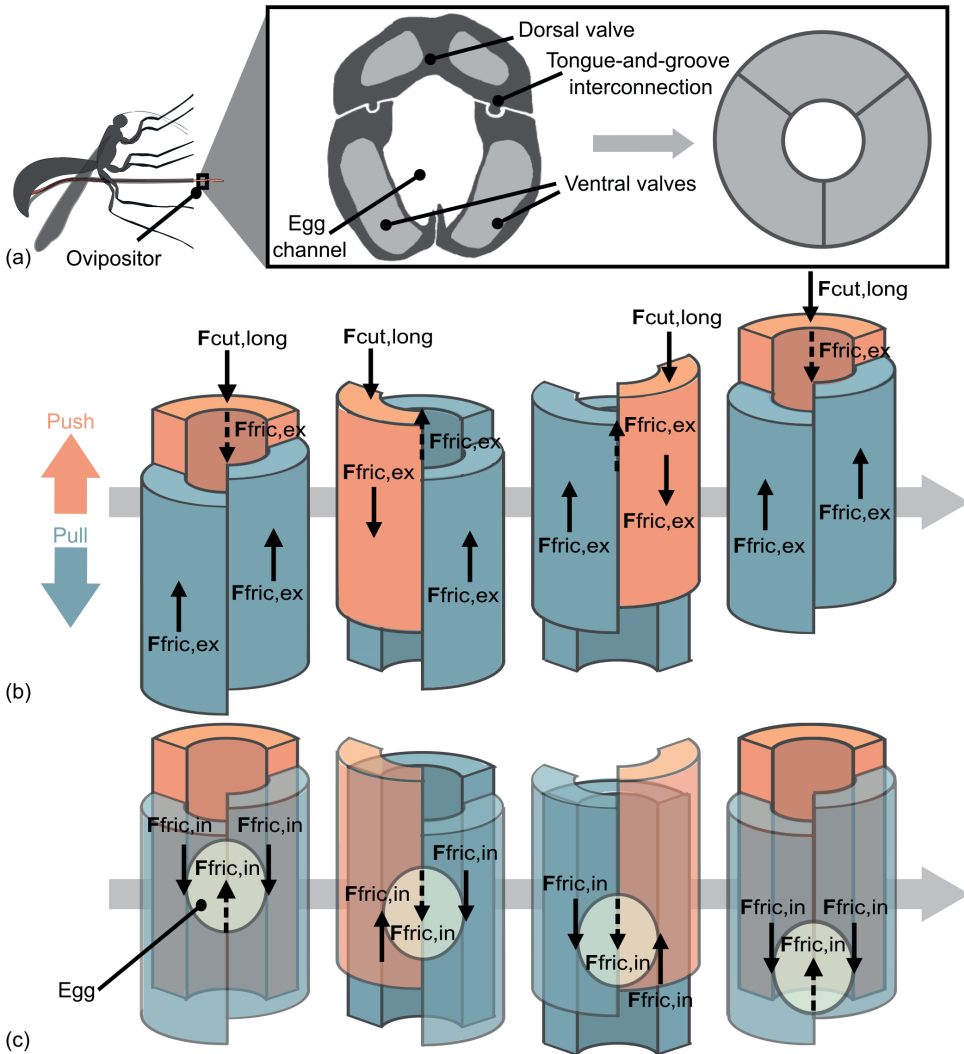
### 5.1.2 Bio-inspiration: Ovipositor-based tools for minimally invasive surgery

In an attempt to overcome clogging problems in aspiration-based devices, devices that employ alternative mechanisms for tissue transport have been developed. For instance, Kortman *et al.* [16] developed a cable-actuated conveying mechanism for tissue transport that uses the friction between continuously rotating conveying cables and tissue. To overcome buckling problems in thin needles, extensive research is ongoing into lowering the needle's penetration load by optimizing the needle tip design, introducing needle vibrations, increasing the insertion speed, and increasing skin tension factors [17-19]. However, needle designs that can overcome both clogging and buckling problems have yet to be shown.

In nature, the ovipositor of parasitic wasps, used for depositing eggs deep into substrates [20, 21], is a remarkable biological structure resembling biopsy needles, as both are long, thin structures designed to penetrate a substrate while simultaneously transporting something (either an egg or tissue) through the lumen. Despite usually having a diameter of only 0.2 - 0.3 mm, some ovipositors can penetrate up to 20 mm into trees to lay their eggs [22, 23]. The structure of the ovipositor is different from traditional biopsy needles as it consists of three longitudinally connected valves, one dorsal and two ventral valves. These valves surround the channel that the egg passes through, as can be seen in Figure 5.1a. The valves feature a tongue-and-groove mechanism called the olistheter mechanism, facilitating a longitudinal







**Figure 5.1. Schematic representation of the wasp ovipositor structure and movement.** (a) Cross-section of the ovipositor of the parasitic wasp, showing three valves, the egg channel, and the tongue-and-groove interconnection, with a simplified schematic of the valves. (b) Ovipositor's reciprocating push-pull cycle for self-propulsion. In this cycle, one valve (orange) advances, encountering longitudinal cutting ( $F_{cut, long}$ ) and external friction force ( $F_{fric, ex}$ ), whilst the other two valves (blue) retract but remain stationary with respect to the surrounding substrate due to external friction force ( $F_{fric, ex}$ ) applied on them by the surrounding substrate. (c) Ovipositor's push-pull cycle for egg transport. In this cycle, one valve (orange) advances, creating internal friction ( $F_{fric, in}$ ) with the egg, while the other two (blue) retract, generating greater internal friction force ( $F_{fric, in}$ ), moving the egg downward. The dashed lines indicate forces applied by the back valve.

sliding motion of the individual valves [24]. During insertion into substrates, the olistheter mechanism enables the valves to translate in a continuous reciprocating manner, with one valve advancing (i.e., push) whilst the other two valves retract (i.e., pull) in a continuous cycle [22, 25]. It has been hypothesized that this reciprocating movement gives rise to two

functionalities: (1) self-propulsion and (2) friction-based egg transport. These functionalities have inspired the designs of two distinct types of medical devices: self-propelling needles and friction-based tissue transporters.

#### *Self-propelling needles*

Self-propelling needles are inspired by the ovipositor's ability to propel through substrates without buckling. The self-propelling motion is achieved because the longitudinal forces on the advancing valve are counterbalanced by the longitudinal forces on the retracting valves [21, 26, 27]. The advancing valve is pushed into the substrate and experiences a cutting force from substrate deformation in front of the valve and an external friction force caused by contact with the surrounding substrate [28-30]. Similarly, the retracting valves experience a friction force in the opposite direction as they are retracted. Although a pulling force on the retracting valves would cause them to retract in free air, we assume that within a substrate, external friction forces prevent relative sliding between the retracting valves and the surrounding substrate, causing the ovipositor to propagate into the substrate over one cycle. Figure 5.1b shows a schematic representation of the ovipositor and relevant forces during self-propulsion. The self-propelling motion and the lateral compressive forces applied by the tissue on the needle segments can result in the needle moving forward with a zero net push force on the needle, making it less prone to buckling as it propagates through a substrate. To achieve a net zero external push force, the forces on the valves or needle segments should be in balance, as indicated in Eq. 5.1.

$$-\sum (\mathbf{F}_{\text{fric,ex,ad}} + \mathbf{F}_{\text{cut,long}}) = \sum \mathbf{F}_{\text{fric,ex,re}} \quad (5.1)$$

where  $\mathbf{F}_{\text{fric,ex,ad}}$  and  $\mathbf{F}_{\text{fric,ex,re}}$  denote the friction forces on the external surfaces of the advancing and retracting valves interacting with the substrate in Newtons, respectively.  $\mathbf{F}_{\text{cut,long}}$  represents the cutting force on the advancing valve in the longitudinal direction in Newtons. Inertial forces on the valves are considered negligible due to their minimal mass, and inter-valve friction forces are neglected.

Within the medical field, multiple self-propelling needles inspired by the ovipositor have been developed. Studies by Oldfield *et al.* [31], Fransson *et al.* [32], and Leibinger *et al.* [27] demonstrated that multi-segment needles with reciprocating motion can self-propel, which reduces tissue displacement and tissue damage around the needle compared to traditional needles, which are pushed into the body. Due to challenges in scaling down the tongue-and-groove interconnection method of the ovipositor while integrating flexibility, Scali *et al.* [33] and Bloembergen *et al.* [34] used parallel-oriented nitinol rods of equal, circular cross-section to mimic the valves. A heat shrink tube was used to bundle the rods, resulting in sub-millimeter diameter needles in both designs. Self-propulsion of a wasp-inspired needle is accomplished by a set of parallel needle segments that can both advance and retract with respect to one another. The advancing needle segments experience both a cutting force due to the tissue's plastic deformation and stiffness and a friction force along the length of the needle in contact



with the surrounding tissue [35]. The retracting needle segments, however, only experience a friction force. The needle self-propels through the tissue if the friction generated by the retracting needle segments counterbalances the friction and cutting forces of the advancing needle segments. This can be achieved by keeping the number of advancing needle segments lower than the number of retracting needle segments (as in Eq. 5.1). Therefore, at least three needle segments are required for the self-propulsion principle.

#### *Tissue-transportation devices*

Besides facilitating self-propulsion, the reciprocating translation of the ovipositor valves has also been hypothesized to facilitate egg transport from the body of the wasps to the ovipositor tip [36]. Friction forces between the egg and the internal surface of the ovipositor valves ( $\mathbf{F}_{\text{fric,in}}$ ) are thought to govern this transport as the ovipositor valves move in their reciprocating manner. The net longitudinal force on the egg ( $\mathbf{F}_{\text{egg,long}}$ ), measured in Newtons, to move the egg through the ovipositor equals the sum of internal friction forces ( $\mathbf{F}_{\text{fric,in}}$ ) in Newtons (Eq. 5.2).

$$\mathbf{F}_{\text{egg,long}} = \sum \mathbf{F}_{\text{fric,in}} \quad (5.2)$$

For successful egg deposition, the frictional force between the advancing valves and the egg must exceed that of the retracting valve and the egg (Eq. 5.3). In this case, the egg will move with the advancing valves, toward the tip. Conversely, for movement in the opposite direction, in which the egg moves from the tip of the ovipositor toward the base, like a tissue sample being retrieved, this condition should be inverted (Eq. 5.4). In Figure 5.1c, a schematic representation of the ovipositor and the relevant forces during egg transport from the tip toward the base of the ovipositor are provided.

$$\sum \mathbf{F}_{\text{fric,in,ad}} > \sum \mathbf{F}_{\text{fric,in,re}} \quad (5.3)$$

$$\sum \mathbf{F}_{\text{fric,in,ad}} < \sum \mathbf{F}_{\text{fric,in,re}} \quad (5.4)$$

here,  $\mathbf{F}_{\text{fric,in,ad}}$  and  $\mathbf{F}_{\text{fric,in,re}}$  are the friction forces inside the ovipositor, between the egg and the advancing and retracting valves, respectively. All forces are measured in Newtons. Gravity's influence on egg transport is considered negligible due to the egg's small mass.

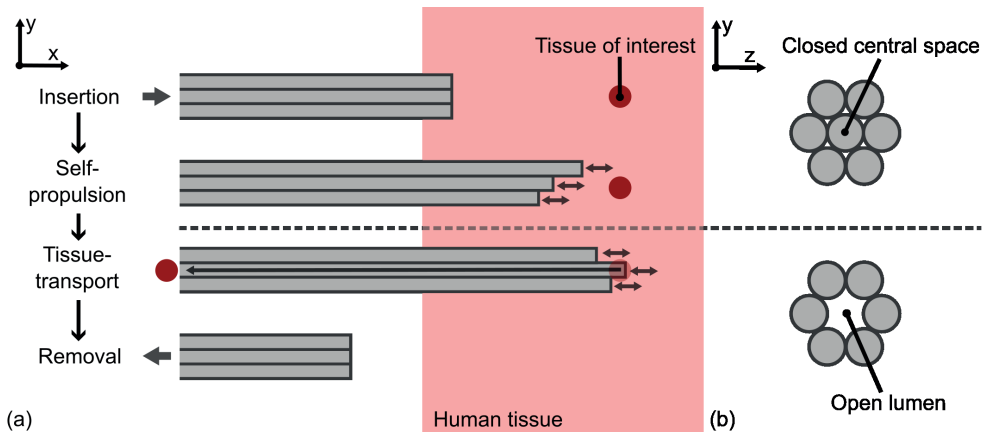
Multiple friction-based tissue-transport designs have been inspired by the egg movement through the ovipositor. These designs are used to transport tissue samples from the distal end inside the body to the local base outside the body for extraction purposes. Sakes *et al.* [37] created a morcellator design ( $\varnothing_{\text{outer}}$ : 7 mm,  $\varnothing_{\text{inner}}$ : 4.5 mm) resembling the ovipositor by mimicking its segments as blades. Instead of a tongue-and-groove mechanism, the interconnection was facilitated using the stiffness of the blades and an external brass tube to prevent outward motion. De Kater *et al.* [38] replaced the blades with magnetic galvanized steel cables to integrate flexibility into the system ( $\varnothing_{\text{outer}}$ : 10 mm,  $\varnothing_{\text{inner}}$ : 5 mm). To maintain an open central lumen for tissue transport, ring magnets were placed around the cables, forming a tubular structure with a lumen, without internal protrusions.

In order to initiate friction-based tissue transport, the tissue to be transported needs to experience a resultant friction force with the surrounding parallel cables in the desired transport direction. The resultant friction force comprises advancing frictional components and retracting frictional components corresponding to the motion of the cables. If we assume that the gravity of the tissue that needs to be transported can be neglected, tissue transportation from the distal end to the local base can be achieved if the sum of the friction between the retracting cables and the tissue exceeds the sum of the friction between the advancing cables and the tissue. This can be achieved by keeping the number of advancing cables lower than the number of retracting cables (as in Eq. 5.4). Therefore, at least three surrounding cables are required for the friction-based tissue transport.

### 5.1.3 Combining self-propulsion and tissue transport

Integrating both self-propulsion and friction-based tissue transport into a single slender design, inspired by the ovipositor, could offer a novel alternative to current biopsy needles. This design could self-propel to a tissue of interest and use friction-based transport to move the tissue sample through the biopsy needle in two distinct phases: (1) the self-propulsion phase and (2) the tissue-transport phase. The phases and required needle cross-sections during the phases are illustrated in Figure 5.2a and 5.2b, respectively.

By combining both the self-propulsion and transport principles of the ovipositor of parasitic wasps, deflection and clogging issues of current thin biopsy needles are negated by relying on friction for both needle insertion and tissue transport. However, combining these functionalities is challenging. A biopsy needle with multiple parallel segments forming a lumen, similar to the ovipositor structure, depends on external friction between the exter-



**Figure 5.2. Biopsy phases.** (a) Schematic illustration of functioning of a wasp-inspired biopsy needle in distinct phases: Insertion into tissue, Self-propulsion to the tissue of interest, Tissue-transport through the lumen (and removal of the tissue sample for examination), and Removal of the biopsy needle from the tissue. (b) Desired cross-sections of the wasp-inspired biopsy needle during the different phases: During the Insertion and the Self-propulsion phases, the central space remains closed to prevent the needle from inadvertently resecting the tissue. In the Tissue-transport phase, a lumen is required to enable tissue transport through the needle.

nal surface of the needle segments and surrounding tissue for self-propulsion, as well as on internal friction between the tissue sample and the internal surface of the segments for tissue transport. Any interconnecting structure must not interfere with both internal and external contact surfaces. As shown in previous designs, moving away from the ovipositor-inspired tongue-and-groove mechanism is necessary to miniaturize the needle dimensions [33, 34] and to introduce flexibility [38]. Former tissue-transport designs have maintained a lumen using external structures that interfere with external surface contact, whereas former self-propelling needles have no lumen to facilitate internal surface contact, highlighting the difficulty of integrating both wasp-inspired functionalities into a slender, flexible biopsy needle.

#### 5.1.4 Goal of this study

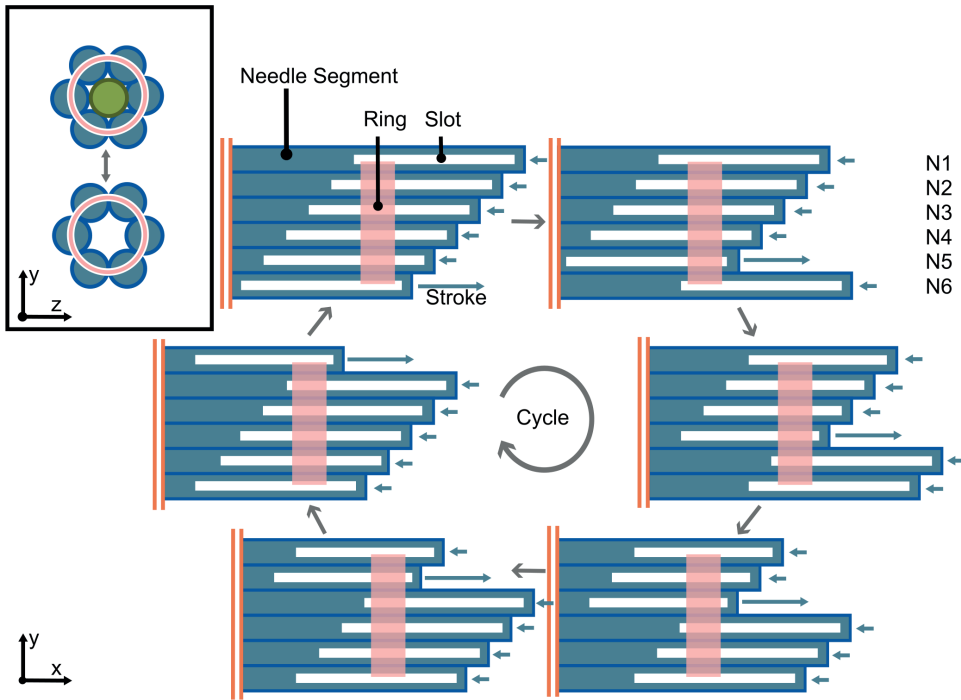
This study aims to combine the two ovipositor-inspired functionalities, self-propulsion and friction-based tissue transport, into a single, slender biopsy needle design. This approach could offer a viable friction-based alternative to current biopsy needles, particularly for deep biopsies like pancreatic percutaneous biopsies that are currently limited by issues such as buckling and clogging in smaller, aspiration-based needles. Building on previous flexible needle and tissue-transport designs using parallel rods to mimic the valves of the ovipositor, this study will adapt the interconnection method of these needle segments and evaluate the potential of the integrated design as a biopsy needle.

## 5.2 Design

### 5.2.1 Needle

The proposed wasp-inspired biopsy needle design consists of six parallel needle segments that mimic the ovipositor valves. A total number of three outer needle segments would have been sufficient to ensure that the number of retracting needle segments exceeds the number of advancing needle segments. However, to enable a central lumen for tissue transport, we opted for six outer needle segments and a seventh central needle segment that can be removed before the tissue-transport phase. Each needle segment has an equal circular cross-section and a beveled tip. The six needle segments are held in a hexagonal arrangement by a ring passing through slots along the length of the segments, as shown in the cross-sectional view in Figure 5.3a. This ring-through-slot interconnection restricts the radial translation while allowing longitudinal translation of each needle segment for self-propulsion and tissue transport. The interconnection also prevents the rotation of the needle segments around their longitudinal axis, maintaining the orientation of the beveled tips toward the center.

The individual longitudinal translation of the needle segments allows the biopsy needle to mimic the reciprocating movement of the ovipositor valves. Instead of using the 1:2 reciprocating movement sequence of the ovipositor, where one valve is advanced as two are retracted, a 1:5 motion sequence, as used in previous self-propelling designs [34] and tissue-transport designs [37, 38] is used. The six needle segments are longitudinally translated using this



**Figure 5.3. Working principle of the ring-through-slots interconnection of the biopsy needle.** (a) the ring (pink) constrains radial translation and rotation of six needle segments (N1-N6, blue), maintaining a hexagonal configuration. This can be with or without a central needle segment to fill the lumen (green) depending on the corresponding phase of the procedure. (b) 2D flattened representation of the longitudinal translation of the individual needle segments over one cycle using a 1:5 motion sequence. In this motion sequence, the needle segments are advanced one-by-one over one stroke length ( $S$ ) while retracting the other five segments by one-fifth of this stroke length. The vertical parallel lines (orange) indicate that this is a visualization of the tip of the needle and the segments extend further on this side.

motion sequence over a cycle of six steps. During each step, one needle segment moves forward by a specified distance, called the stroke length ( $S$ ), while the other five segments move backward by one-fifth of this stroke length ( $1/5 S$ ). After one cycle, the needle segments return to their starting positions, as illustrated in Figure 5.3b.

The needle segments were designed to be 1 mm in diameter, allowing for the transport of a cylindrical tissue sample, or core, of 1 mm in diameter, which is a common diameter for biopsy samples [39]. The total diameter of the biopsy needle was 3 mm. A trade-off existed in the number of slots introduced into the needle segments: introducing more slots along the length of the needle could potentially comprise the ability of each needle segment to resist the cutting forces, whilst this simultaneously is advantageous for maintaining the hexagonal arrangement of the entire needle. To balance this, we introduced two slots with a spacing of 100 mm. The first slot was placed near the base of the needle and the second slot was positioned 4 mm from the needle tip to prevent the needle segments from diverging at the tip during self-propulsion. To facilitate the assembly of the needle segments and rings, the



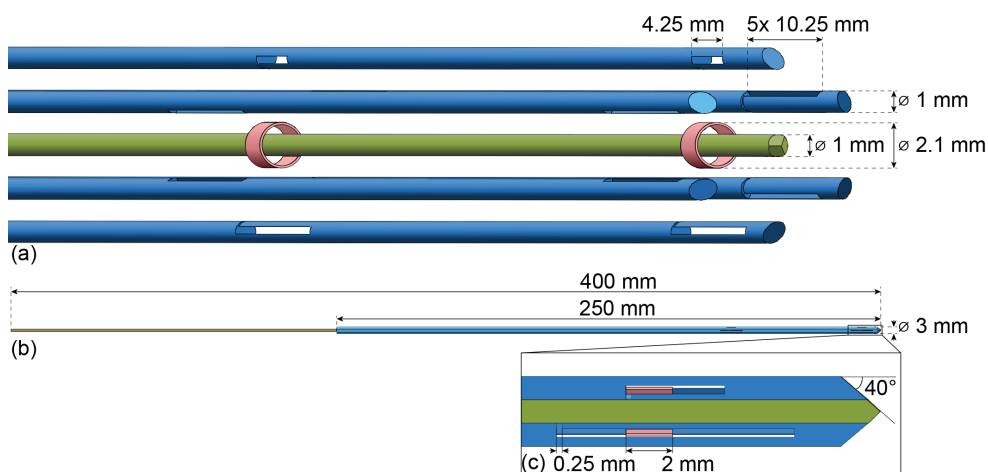
slots were not designed to be rectangular but L-shaped to provide an entry point for the rings. Figure 5.4 shows the concept design and assembly of the needle.

The six needle segments enclose the tissue transportation lumen, which must be either filled or unfilled depending on the biopsy procedure phase (Figure 5.2b). During the self-propelling phase, the biopsy needle travels to the tissue of interest. The lumen should be filled to prevent a cylindrical piece of tissue from being cut out as the biopsy needle travels into the tissue. To achieve this, a seventh needle segment (indicated in green in Figure 5.4a) was introduced in the design to fill the lumen when needed. This central needle segment ideally participates in the reciprocating movement during the self-propelling phase and should be able to be removed during the tissue-transport phase, when a lumen is needed.

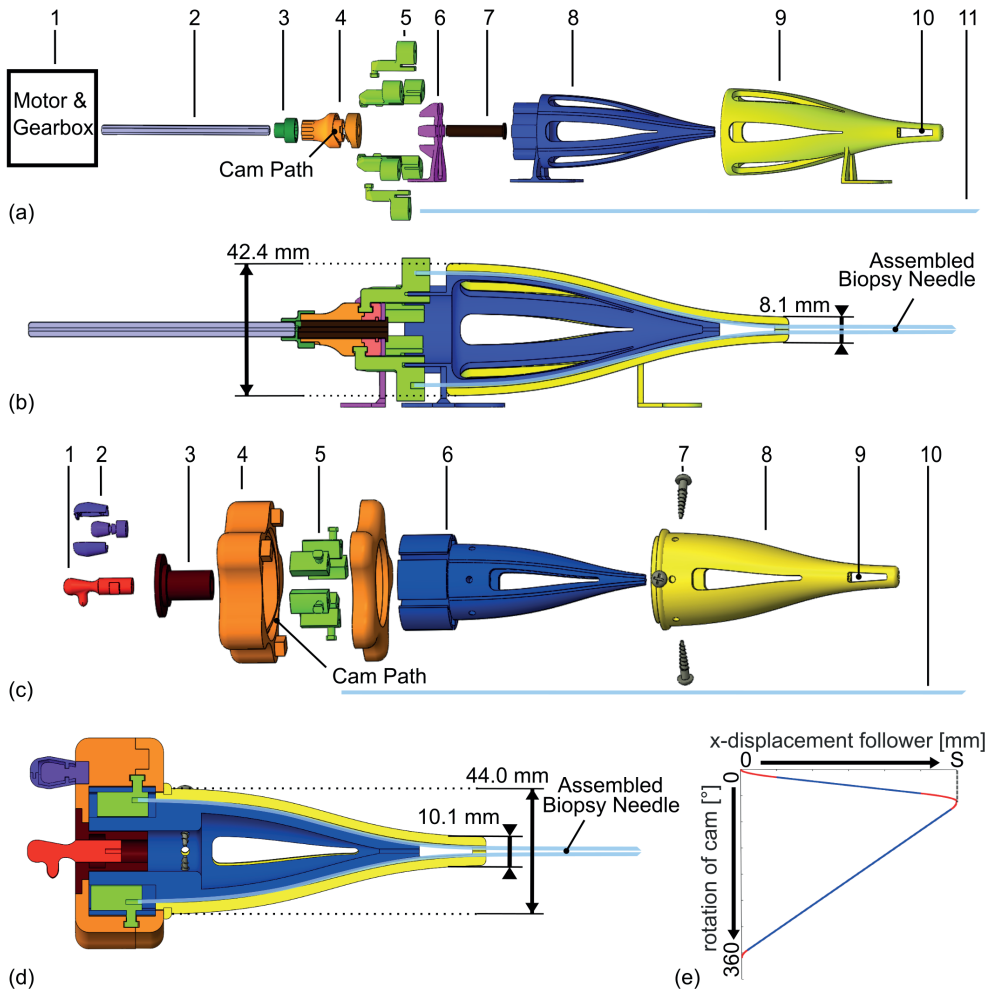
### 5.2.2 Actuation

To achieve the 1:5 motion sequence, the needle segments had to be actuated simultaneously and continuously. Two actuation systems were designed: (1) one motorized system for testing purposes (Figure 5.5a,b) and (2) one manual system for the final prototype to minimize components and create a compact assembly (Figure 5.5c,d). A rotary cam-and-follower system was used for both actuators (Figure 5.5a,c, Part 4 in orange). The cams contained a groove, the cam path, guiding the followers (Figure 5.5a,c, Part 5 in green) to produce continuous linear translation (x-displacement) in the 1:5 motion sequence as the cam rotates. By attaching needle segments to the followers, the linear displacement was transferred to the needle segments, resulting in the 1:5 motion sequence of the biopsy needle overall.

To allow for sufficient space to clamp the needle segments into the followers, the needle



**Figure 5.4. Conceptual design of the wasp-inspired biopsy needle.** (a) Exploded view of the needle design, consisting of six needle segments with slots (blue), two interconnecting rings (pink), and one central needle segment (green), indicating their respective diameters and slot sizes. (b) Assembly of the needle, indicating its total diameter and length of the needle segments with slots and the central needle segment. (c) Cross-section of the needle tip, indicating the bevel angle of the needle segments, the width of the L-shaped slot, and ring length.



**Figure 5.5. Exploded views and cross-sections of the motorized actuation system (a, b) and manual actuation system (c, d) for the wasp-inspired biopsy needle.** The motorized actuation system consists of a motor and gearbox (a.1), axle (a.2), cam connector piece (a.3), cam (bottom and top) (a.4), needle segment holders (followers) (a.5), supporting structures (a.6, a.7), inner and outer converging cone (a.8, a.9), outer cone opening (a.10) and needle segments (a.11). The manual actuation system consists of a central needle segment connector (c.1), a spinner knob (c.2), supporting structure (c.3), cam (bottom and top) (c.4), needle segment holders (followers) (c.5), inner and outer converging cones (c.6, c.8), screws (c.7), outer cone opening (c.9) and needle segments (c.10). (e) The x-displacement of the followers over a 360° rotation of the cam, translating one stroke length ( $S$ ) in the positive x-direction over 60° and one  $S$  in the negative x-direction over the following 300°. The graph shows linear (blue) and parabolic (red) displacement segments, ensuring a smooth cam path.

segments transition from a larger diameter at the actuation system to a smaller diameter at the needle tip. Similar to the design presented by Bloemberg *et al.* [34], a double cone at the distal end of the actuation system (Figure 5.5a, Part 8/Part 9 in blue/yellow, Figure 5.5c, Part 6/Part 8 in blue, yellow) guides the segments through S-shaped channels, to ensure smooth



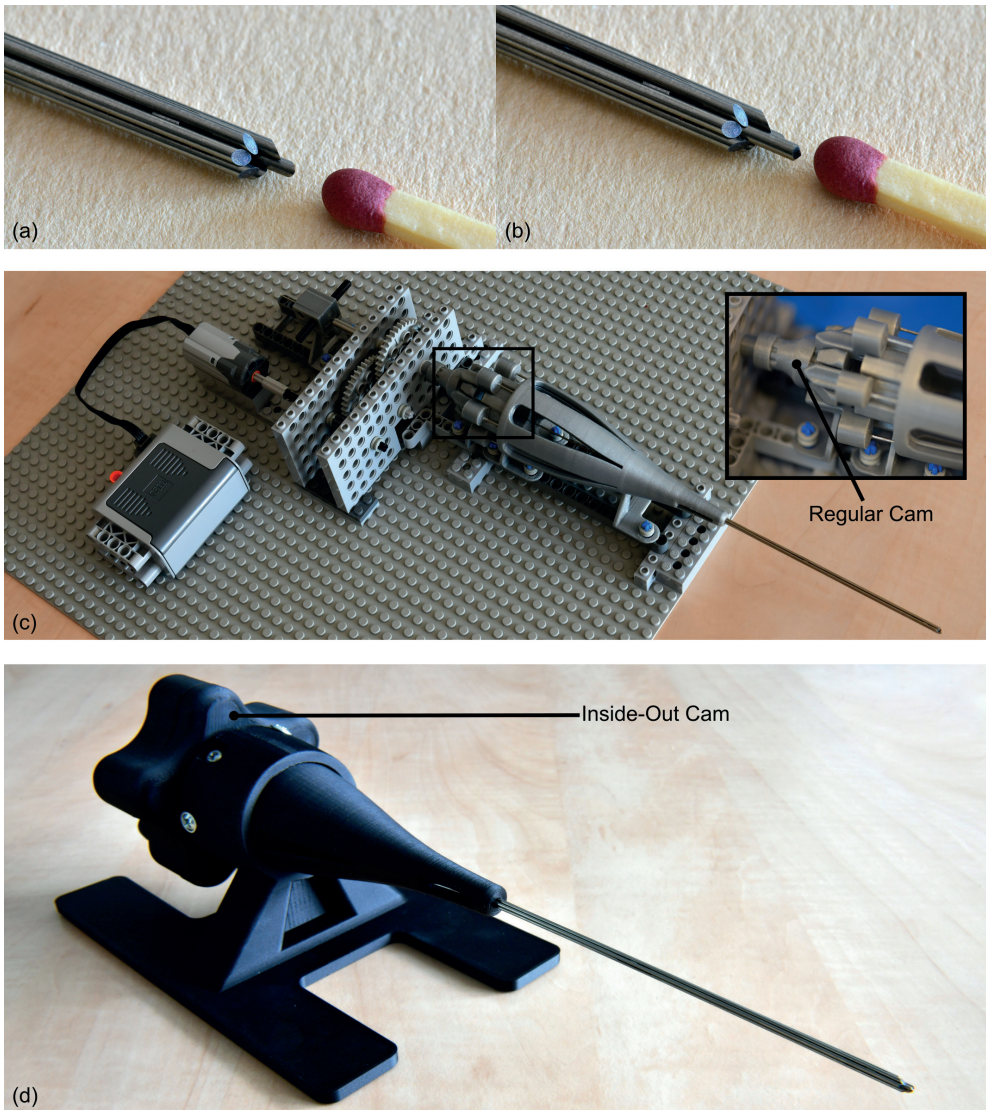
movement and prevent buckling. At the place where the needle segments diverge there is an opening in the outer cone (Figure 5.5a, Part 10, Figure 5.5c, Part 9) to allow the tissue core to exit the biopsy needle after transport.

For the motorized actuation system, a regular barrel cam was used, where the followers surround the cam path. However, for the manual actuation system, an inside-out cam design was chosen, with the cam path surrounding the followers. Furthermore, the cam used for manual actuation was star-shaped and approximately the size of a human palm (about 80 mm [40]) to allow for sufficient grip and, thus, easy manual actuation. Both cams shared the same cam path and thus the same stroke length, resulting in the identical motion sequence of the followers in the longitudinal direction (Figure 5.5e), and were designed following guidelines from the Machinery's Handbook (30th Edition, [41]).

### 5.2.3 Prototype

The needle prototype consists of seven superelastic straightened nitinol rods, each 1 mm in diameter and 250 mm in length (Titaniumshop, Overijssel, the Netherlands). For the slot extrusion, Wire Electrical Discharge Machining (WEDM), known for its non-contact material removal process, was employed. This method allows for precise slot creation without imposing cutting forces on the segments [42, 43]. WEDM was used to create two L-shaped slots (10.25 mm x 0.40 mm) in the distal end of five needle segments. Additionally, a sixth needle segment, i.e., the carrier needle segment, featured smaller L-shaped slots (4.25 mm x 0.40 mm) to carry the rings forward. The length of these slots determines the maximum possible stroke length, which is equal to 4 mm. The seventh central needle segment can simply be inserted and removed easily when necessary. An additional 150 mm of length was added to the central needle segment for this purpose. Furthermore, WEDM was utilized to create the beveled tips of the needle segments (40°). The two interconnecting rings (outer diameter 2.1 mm, inner diameter 1.9 mm, length 2.0 mm) were made of stainless steel. Figure 5.6a shows the assembled needle excluding the central needle segment and Figure 5.6b shows the assembled needle including the central needle segment.

The motorized actuation system integrated off-the-shelf LEGO Technic parts and 3D-printed parts using Silver Metallic PLA on the Fused Deposition Modeling (FDM) printer Ultimaker S5 (Ultimaker, Utrecht, the Netherlands). A LEGO Technic Power Functions Medium motor with a rotational speed of 405 RPM (9V) in a no-load situation was used. A gearbox, created with LEGO gears, was used to adjust the rotational speed of the motor to the desired rotational speeds of the cam for the experiments. The manual actuation system was entirely 3D printed out of Onyx (Markforged, Waltham, MA, USA), using the FDM printer Markforged Mark Two (Markforged, Waltham, MA, USA). For both actuators, the needle segments were glued into the followers using *Loctite 401 Instant Adhesive* (Loctite, Westlake OH, USA). Figure 5.6c and Figure 5.6d show the assemblies of the motorized and manual actuation systems, respectively. Figure 5.7 illustrates the 1:5 motion sequence of the needle segments during actuation over one cycle.



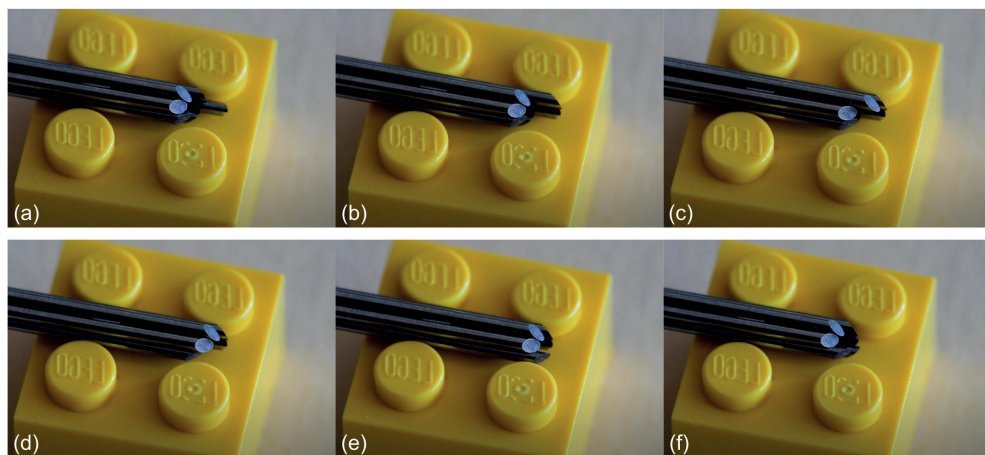
**Figure 5.6. Prototype of the wasp-inspired biopsy needle.** (a) Close-up of the needle tip, made of six nitinol rods interconnected using rings guided through slots in the needle segments. The stainless-steel rings keep the segments in a hexagonal arrangement, resulting in a central lumen of 1 mm in diameter. (b) The lumen can be filled by a seventh needle segment. (c) Motorized actuation system, which utilizes a regular (barrel) cam, created using 3D printing and off-the-shelf LEGO parts, to create the 1:5 motion sequence of the biopsy needle. (d) Manual actuation system, which utilizes an inside-out cam, fully produced using 3D printing, to create the 1:5 motion sequence of the biopsy needle.

## 5.3 Evaluation

### 5.3.1 Experimental goal

The goal of the evaluation of the wasp-inspired biopsy needle was twofold: (1) assessing





**Figure 5.7. One cycle of needle segment translations without the central needle segment.** Each 60-degree rotation of the cam results in the advancement of one needle segment over the stroke length, while retracting the other five segments over one-fifth of this stroke length. (a–f) correspond to the rotation of the cam over 60°, 120°, 180°, 240°, 300° and 360°, respectively.

the core-transport capability and (2) assessing the self-propulsion ability. These objectives were addressed in two separate experiments. Experiment 1 focused on core transport while Experiment 2 focused on self-propulsion. Figure 5.8 gives a schematic overview of both experiments. During testing, the setup involved moving tissue phantoms toward the prototype to enable keeping the prototype stationary. This contrasts a realistic scenario where the needle would advance through tissue, but since the relative movement between the needle and the tissue phantom is the same, it was assumed that this would not influence the test results. Data analysis and visualization were conducted using Python in PyCharm Community Edition 2024.1.1 (JetBrains, Prague, Czech Republic).

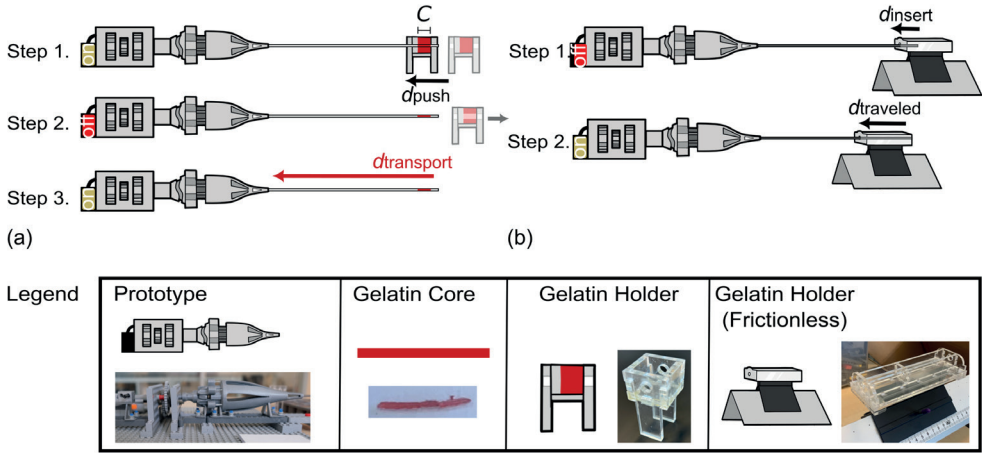
### 5.3.2 Experiment 1: Core-transport capability

#### *Experimental variables*

##### **Independent variables**

**Core length:** Core sample lengths typically range from 8 mm to 20 mm for pancreatic biopsies, with specific size requirements varying based on testing types, methods, and platforms [44–46]. The capability of the prototype to transport tissue cores of different lengths (5 mm, 10 mm, 15 mm) was tested to validate its use for different core sizes.

**Stroke length:** Larger stroke lengths theoretically lead to quicker core transport, as the core transport per cycle is dependent on the stroke length. To evaluate the effects of different stroke lengths on the efficiency and rate of transport, experiments were conducted using varying stroke lengths, up until the maximum allowable stroke length possible for the slot lengths of the prototype (2 mm, 3 mm, 4 mm).



**Figure 5.8. Schematic representation of Experiments 1 and 2 to test core-transport and self-propulsion principles.** (a) Graphical overview of the experimental protocol of Experiment 1 “Core-transport capability”. Step 1: A gelatin block with width  $C$  in a gelatin holder is translated over the needle by a distance  $d_{push}$ . Step 2: This leaves a gelatin core of length  $C$  in the needle. Step 3: The motor is turned on, causing the needle to transport the gelatin core over a distance  $d_{transport}$  within  $t_{measured}$ . (b) Graphical overview of the experimental protocol of Experiment 2 “Self-propulsion capability”. Step 1: A piece of gelatin in a frictionless gelatin holder is slid over the needle by a distance  $d_{insert}$  with the motor off. Step 2: The motor is turned on, allowing self-propulsion to occur.

**Rotational velocity:** The rotational velocity of the cam determines the frequency of needle segment cycles per unit time. Higher rotational speeds could potentially accelerate tissue transport, optimizing biopsy procedure efficiency. Theoretical rotational speeds of 10.1 RPM, 24.3 RPM, and 50.6 RPM would be achieved using gearbox ratios of 0.025, 0.06, and 0.125, respectively.

**Tissue phantom elasticity:** Gelatin was chosen as a tissue phantom due to its ability to mimic the mechanical properties of human tissue [47, 48]. Gelatin samples were prepared at different concentrations (5 wt%, 10 wt%, 15 wt%) by mixing porcine gelatin powder with boiled tap water, after which they were allowed to set for about 15 hours in slab molds measuring 25 mm x 25 mm x 18 mm. The chosen concentrations correspond to moduli of elasticity of approximately 5.3 kPa, 17 kPa, and 31 kPa, respectively [33]. This range was selected to approximate the mechanical properties of healthy pancreatic tissue, perilesional regions, and solid pancreatic tumors, with moduli of elasticity of 4 kPa, 23.9 kPa, and 42.9 kPa, respectively [49].

### Dependent variables

**Transport efficiency:** The transport efficiency ( $TE$ ), measured in percentages, is crucial as it impacts procedural time and potentially the tissue sample quality.  $TE$  was quantified by comparing the measured core-transport duration ( $t_{measured}$ ) to the theoretical duration ( $t_{theoretical}$ ) over the transport distance ( $d_{transport}$ ) (Eq. 5.5). The transport distance ( $d_{transport}$ ), in mm, was calculated as the total needle length (120 mm), measured from the distal tip of the



needle to the opening in the outer cone of the actuator, minus the core length. The measured transport time ( $t_{\text{measured}}$ ) in seconds, was visually assessed from video footage, where the starting time ( $t_{\text{start}}$ ) was the point at which the core was completely enclosed in the distal tip of the biopsy needle and the motor was turned on. The end time ( $t_{\text{end}}$ ) was the first moment the core could be seen entering the opening in the outer cone of the actuator. The theoretical transport time ( $t_{\text{theoretical}}$ ), in seconds, was calculated by dividing the transport distance by the rotational speed of the cam ( $\omega$ ), in RPM, which was assessed from the video footage, multiplied by the stroke length ( $S$ ), in mm (Eq. 5.6). The numerator was multiplied by a factor of 60 for conversion to seconds. Because we assume for our continuous mode of actuation that the tissue phantom core remains stationary with respect to the retracting needle segments, a factor of 6/5 was used in the denominator.

$$TE = \frac{t_{\text{theoretical}}}{t_{\text{measured}}} \cdot 100\% \quad (5.5)$$

$$t_{\text{theoretical}} = \frac{d_{\text{transport}} \cdot 60}{\omega \cdot \frac{6}{5} S} \quad (5.6)$$

**Transport rate:** To evaluate overall system performance, the transport rate ( $TR$ ), measured in mm/s, was included as a dependent variable. It quantifies the biopsy core-transport distance within one second (Eq. 5.7).

$$TR = \frac{d_{\text{transport}}}{t_{\text{measured}}} \quad (5.7)$$

### Experimental facility

The experimental setup included the motorized actuator assembly, held stationary, and a PolyMethyl MethAcrylate (PMMA) gelatin holder (with inner dimensions of 17 mm x 17 mm x 17 mm), which could translate linearly toward the prototype. To create the desired core length ( $C$ ), the gelatin samples were cut to the appropriate size before use (17 mm x 17 mm x  $C$  mm). Unless indicated otherwise, a 0.06 gear ratio and 10 wt% gelatin were used.

### Experimental procedure

The core-transport assessment was split into two sub-experiments. Table 5.1 provides the experimental conditions for the different sub-experiments. Experiment 1A evaluated the effect of the gelatin core length and stroke length on the transportation efficiency and rate in a 3x3 factorial design, exploring potential interaction effects between the parameters. In Experiment 1B, the impact of the rotational velocity and gelatin elasticity on the transport efficiency and transport rate was assessed, using the core and stroke length combination that achieved the highest transport efficiency in Experiment 1A.

For both sub-experiments, the same procedure was followed. To create a transportable core, the needle self-propelled through the gelatin until the holder had translated 30 mm. During this translation, the biopsy needle cut out a core with a diameter of 1 mm ( $\phi_{\text{inner}}$ ). After this translation, the motor was turned off and the gelatin holder was removed. The motor was

Table 5.1. Experimental conditions for Experiments 1A and 1B.

Condition	Stroke length [mm]	Core length [mm]	Gear ratio	Gelatin concentration [wt%]
Experiment 1A				
A1	2	5	0.06	10
A2	2	10	0.06	10
A3	2	15	0.06	10
A4	3	5	0.06	10
A5	3	10	0.06	10
A6	3	15	0.06	10
A7	4	5	0.06	10
A8	4	10	0.06	10
A9	4	15	0.06	10
Experiment 1B				
B1	From 1A*	From 1A*	0.025	10
B2	From 1A*	From 1A*	0.125	10
B3	From 1A*	From 1A*	0.06	5
B4	From 1A*	From 1A*	0.06	15

\*The stroke length and core length that yielded the highest transport efficiency in Experiment 1A were used in Experiment 1B.

then turned on again, leading to the transportation of the gelatin core from the distal tip of the biopsy needle to the opening in the outer cone of the actuator. Each experiment was recorded using a video camera focused on the outer cone opening. The experiment concluded when the core became visible in the opening. The core was then removed using tweezers, and the needle was cleaned with lukewarm water and tweezers to ensure the removal of gelatin debris from the inside. Each condition was repeated five times. Figure 5.8a shows a schematic overview of this protocol.

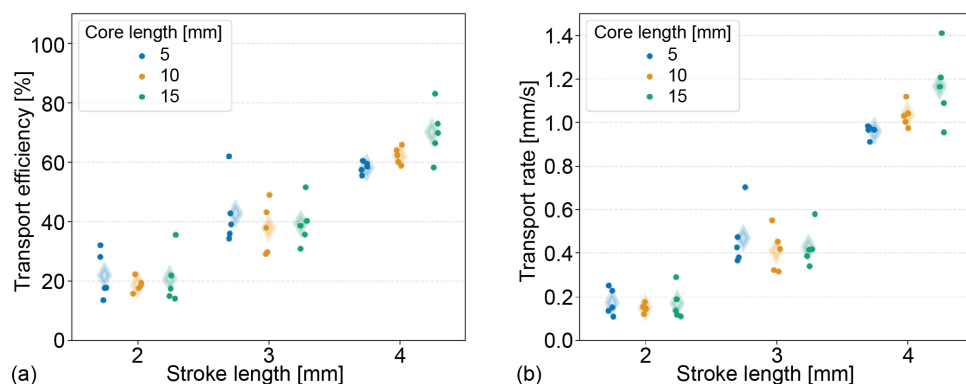
### Results

Table 5.2 shows the mean and Standard Deviation (SD) of the *TE* and *TR* per condition of Experiment 1A. The combination of a stroke length of 4 mm and a core length of 15 mm yielded the highest mean transport efficiency ( $69.9\% \pm 9.1\%$ ) and transport rate ( $1.16 \text{ mm/s} \pm 0.17 \text{ mm/s}$ ). These parameters were, therefore, used in Experiment 1B. The lowest mean transport efficiency ( $18.6\% \pm 2.4\%$ ) and mean transport rate ( $0.15 \text{ mm/s} \pm 0.02 \text{ mm/s}$ ) was achieved by the combination of a 2-mm stroke length and 10-mm core length. The results of Experiment 1A are visualized in separate grouped strip plots (Figure 5.9).

Table 5.3 shows the mean and SD of the *TE* and *TR* per condition of Experiment 1B. Additionally, the measured angular velocity ( $\omega$ ) of the cam is noted, as this differs from the theoretical value. The 0.06 gear ratio with 10 wt% gelatin concentration group presented the highest mean transport efficiency ( $69.9\% \pm 9.1\%$ ) and transport rate ( $1.16 \text{ mm/s} \pm 0.17 \text{ mm/s}$ ).

**Table 5.2. Test results of Experiment 1A**, showing the conditions ( $S$  = stroke length [mm],  $C$  = core length [mm]), and the resulting mean and Standard Deviation (SD) of the Transport Efficiency ( $TE$ ) and the Transport Rate ( $TR$ ). Each condition was tested five-fold. The maximum and minimum  $TE$  and  $TR$  are indicated in bold.

Condition	$TE$ [%]	$TR$ [mm/s]
A1 (S2-C05)	$21.6 \pm 7.9$	$0.17 \pm 0.06$
A2 (S2-C10)	<b><math>18.6 \pm 2.4</math></b>	<b><math>0.15 \pm 0.02</math></b>
A3 (S2-C15)	$20.6 \pm 8.8$	$0.17 \pm 0.07$
A4 (S3-C05)	$42.7 \pm 11.2$	$0.47 \pm 0.14$
A5 (S3-C10)	$37.6 \pm 8.6$	$0.41 \pm 0.10$
A6 (S3-C15)	$38.2 \pm 7.7$	$0.43 \pm 0.09$
A7 (S4-C05)	$58.1 \pm 1.9$	$0.96 \pm 0.03$
A8 (S4-C10)	$62.1 \pm 2.9$	$1.03 \pm 0.05$
A9 (S4-C15)	<b><math>69.9 \pm 9.1</math></b>	<b><math>1.16 \pm 0.17</math></b>



**Figure 5.9. Grouped strip plots displaying (a) the transport efficiency [%] and (b) the transport rate [mm/s] for different test conditions; using stroke lengths of 2 mm, 3 mm, and 4 mm and core lengths of 5 mm, 10 mm, and 15 mm, respectively. The mean is indicated by a translucent diamond.**

The lowest mean transport efficiency ( $44.6\% \pm 1.4\%$ ) was achieved by the combination of a gear ratio of 0.06 and a gelatin concentration of 5 wt%. The lowest mean transport rate ( $0.40 \text{ mm/s} \pm 0.02 \text{ mm/s}$ ) was achieved by the combination of a gear ratio of 0.025 and a gelatin concentration of 10 wt%. The results of Experiment 1B are visualized in separate strip plots (Figure 5.10).

### 5.3.3 Experiment 2: Self-propulsion capability

#### *Experimental variables*

The experiment did not have any independent variables.

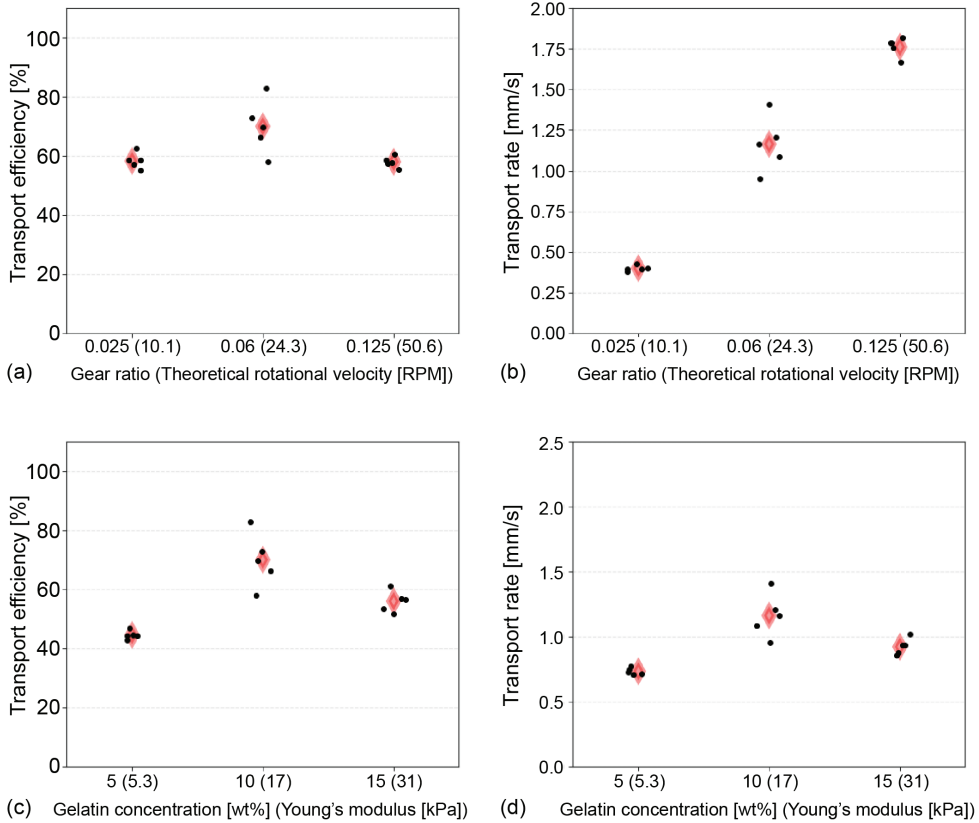
#### **Dependent variables**

**Self-propelling rate:** The self-Propelling Rate ( $PR$ ), measured in mm/s, directly affects the procedural duration. It is defined as the distance ( $d_{\text{travel}}$ ), in mm, the needle self-propels within

**Table 5.3. Test results of Experiment 1B**, showing the conditions ( $S$  = stroke length [mm],  $C$  = core length [mm],  $GR$  = gear ratio,  $GC$  = gelatin concentration [wt%]), as well as the mean and standard deviation (SD) of the angular velocity of the cam ( $\omega$ ), the Transport Efficiency ( $TE$ ), and the Transport Rate ( $TR$ ).

Condition	$\omega$ [RPM]	$TE$ [%]	$TR$ [mm/s]
A9 (S4 - C15)*	$20.8 \pm 0.3$	<b><math>69.9 \pm 9.1</math></b>	<b><math>1.16 \pm 0.17</math></b>
B1 (GR025 - GC10)	$8.5 \pm 0.07$	$58.4 \pm 2.8$	<b><math>0.40 \pm 0.02</math></b>
B2 (GR125 - GC10)	$38.0 \pm 0.9$	$58.0 \pm 1.8$	$1.76 \pm 0.06$
B3 (GR060 - GC05)	$20.6 \pm 0.3$	$44.6 \pm 1.4$	$0.73 \pm 0.03$
B4 (GR060 - GC15)	$20.7 \pm 0.1$	<b><math>55.9 \pm 3.6</math></b>	$0.92 \pm 0.06$

\*These results are taken from Experiment 1A.



**Figure 5.10. Strip plots showing the Transport efficiency ( $TE$ ) and Transport rate ( $TR$ ) for different gear ratios (a, b) and gelatin concentrations (c, d).** The mean per conditional group is indicated by a red diamond. The results from the 0.06 (24.3 RPM) gear ratio and 10 wt% (17 kPa) gelatin concentration condition are taken from Experiment 1A.

a set time ( $t_{\text{travel}}$ ), in seconds (Eq. 5.8). Variable  $t_{\text{travel}}$  was fixed at 120 seconds, and millimeter paper was used to measure  $d_{\text{travel}}$ .

$$PR = \frac{d_{\text{travel}}}{t_{\text{travel}}} \quad (5.8)$$



**Self-propelling efficiency:** The efficiency of self-propulsion was assessed by the Slip Ratio ( $SR$ ). The  $SR$  quantifies the relative slip of the needle as it propels. We assumed that slip was the sole reason that the measured self-Propelling Rate ( $PR_{\text{measured}}$ ) was lower than the theoretical self-Propelling Rate ( $PR_{\text{theoretical}}$ ). The  $SR$  is calculated using the  $PR_{\text{measured}}$  and  $PR_{\text{theoretical}}$  in mm/s (Eq. 5.9). The measured self-propelling rate was determined experimentally by assessing how far the needle could self-propel within a given time. The theoretical self-propelling rate was derived from the rotational velocity of the cam ( $\omega_{\text{actual}}$ ) in RPM, measured from video footage and divided by 60 to get the rotations per second, and the stroke length in mm, multiplied by a factor of 6/5 to account for the continuous actuation of the needle segments where we assume for the self-propelling motion that the retracting needle segments remain stationary with respect to the tissue phantom, while the advanced needle segment moves forward (Eq. 5.10).

$$SR = 1 - \frac{PR_{\text{measured}}}{PR_{\text{theoretical}}} \quad (5.9)$$

$$PR_{\text{theoretical}} = \frac{\omega_{\text{actual}}}{60} \cdot \frac{6}{5} S \quad (5.10)$$

#### *Experimental facility*

The motorized actuator prototype was aligned with a PMMA gelatin holder (with inner dimensions of 80 mm x 20 mm x 20 mm). Gelatin of 10 wt% was used after it had been allowed to set for about 15 hours. The gelatin holder fit on an air track (Eurofysica), which facilitated near-frictionless linear translation of the gelatin holder toward the actuation system. The central needle segment filled the lumen during testing. The gelatin holder was translated manually over a distance of 20 mm ( $d_{\text{insert}}$ ). This manual insertion was done to ensure there was sufficient initial contact between the needle surface and the gelatin to facilitate friction-based self-propulsion. The stroke length used was 4 mm and the gear ratio was 0.06, yielding a theoretical rotational speed of 24.3 RPM.

#### *Experimental procedure*

Figure 5.8b illustrates the experimental procedure, which was repeated five times. After manual insertion, the motor was turned on, allowing the gelatin to translate toward the prototype. After 120 seconds, the motor was turned off and the exact traveled distance was determined from the video footage. Finally, the needle was cleaned with lukewarm water to remove potential gelatin debris.

#### *Results*

Within the experimental group, the mean  $PR$  and  $SR$ , including SD, were, respectively,  $PR = 0.247 \text{ mm/s} \pm 0.061 \text{ mm/s}$  and  $SR = 0.842 \pm 0.042$ .

### **5.3.4 Proof-of-principle sequential functioning**

As a proof of principle, it was assessed whether the self-propulsion and core transport could be performed sequentially. Using the setup of Experiment 2, the wasp-inspired biopsy needle was inserted 20 mm into a gelatin block (10 wt%), measuring 80 mm in total length. The

motor was turned on, allowing the needle to self-propel over a distance of 45 mm, after which the central needle segment was removed by pulling it out to allow for core extraction over the remaining 15 mm, yielding a core of 15 mm. The near-frictionless air track was then deactivated, immobilizing the gelatin block as the gelatin core was transported from the distal tip to the opening in the outer cone of the actuator. A video showing the proof-of-principle of sequential functioning can be found in the Supplementary material.

## 5.4 Discussion

### 5.4.1 Main findings

The proof-of-principle evaluation implied two main findings. It showed that the wasp-inspired biopsy needle was: (1) able to transport a gelatin core, mimicking tissue, using friction-based transport and (2) was able to self-propel. Additionally, it showed that self-propulsion and core transport could be performed sequentially.

The optimal conditions for core transport in our needle design included a 4-mm stroke length, 15-mm core length, theoretical rotational velocity of 24.3 RPM (actual 20.8 RPM), and 10-wt% gelatin composition, achieving a transport efficiency of  $69.9\% \pm 9.1\%$  and a transport rate of  $1.16 \text{ mm/s} \pm 0.17 \text{ mm/s}$ . Increasing the stroke length not only enhanced the transport rate as expected but also improved efficiency, resulting in a positive impact on the overall transport rate. This phenomenon might be attributed to the advancing needle segment having a higher velocity as the stroke length is increased. A higher velocity could lead to relatively lower friction forces between the advancing needle segment and the gelatin core, leading to more efficient core transport. The flexible wasp-inspired tissue transport design of de Kater *et al.* [37] was able to transport tissue with a similar transport rate of  $0.83 \text{ mm/s} \pm 0.08 \text{ mm/s}$  under similar circumstances (horizontal orientation, 10-wt% gelatin, 25 RPM, stroke length of 5.2 mm), despite the larger lumen (3.8 mm). During current CB procedures, tissue cores measuring 1-2 cm in length are typically obtained [14], which is similar to the core lengths retrieved during our core-transport assessment. Moreover, our needle design can theoretically transport tissue cores up to the entire length of the needle, which is challenging for aspiration-based devices due to clogging issues.

The self-propulsion capability evaluation showed the needle achieving a slip ratio of  $0.842 \pm 0.042$  and a self-propelling rate of  $0.257 \text{ mm/s} \pm 0.0611 \text{ mm/s}$ . In comparison, the self-propelling needle by Scali *et al.* [33] (diameter 0.8 mm), also using 10-wt% gelatin, exhibited a lower mean slip ratio of 0.3. The larger diameter of our prototype ( $\varnothing_{\text{outer}}$ : 3 mm) may contribute to increased gelatin displacement and rupturing around the needle, leading to the formation of a cavity around the needle, thereby reducing the contact area between the needle and surrounding gelatin. A reduction in the contact area between the needle segments and the gelatin will reduce the overall friction force, making it less likely that the friction force of the retracting needle segments can counterbalance the cutting and friction force on the

advancing needle segment, causing slip. Miniaturizing the outer dimensions of the needle could potentially mitigate this phenomenon.

The wasp-inspired biopsy needle offers significant advantages over conventional biopsy needles for percutaneous biopsy procedures. It avoids buckling and clogging due to its friction-based propulsion and core-transport methods, allowing for downsizing while maintaining the capability to transport intact tissue samples for histological examination.

### 5.4.2 Limitations and future research

During the evaluation, gelatin was chosen as a suitable tissue phantom due to its elasticity that can resemble human tissue, cost-effectiveness, and accessibility. However, gelatin phantoms do not fully capture the complexity of real tissues, particularly concerning the heterogeneity of human tissue, in specific tumor tissue [50]. Due to its homogeneity, gelatin exhibits brittle fracture behavior, leading to sudden rupturing when subjected to mechanical stress [51]. This could lead to increased fragmentation during core transport and could lead to cavity formation around the needle during self-propulsion. Furthermore, for needle propulsion experiments, other mechanical properties than the elasticity, for example, the friction coefficient between needle and tissue and the tissue's shear modulus and ultimate strength, could also be of interest. Transitioning to human tissue poses challenges such as variable stiffness between tissue types [28], complicating self-propulsion. For instance, Bloemberg *et al.* [34] reported slip ratios ranging from 0.82 to 0.96 in *ex vivo* prostate tissue. An interesting next step would, therefore, be to validate the wasp-inspired biopsy needle in complex tissue models like multi-layered phantoms and *ex vivo* tissue. When moving toward *ex vivo* tissue studies and clinical trials, developing protocols in compliance with the ISO 13485 standard and the Medical Device Regulation 2017/745 will enable us to compare our needle with commercially available alternatives.

The self-propulsion principle of the wasp ovipositor that was implemented in our needle design allowed the needle to self-propel through different gelatin substrates. In order for the self-propulsion principle of the needle to hold, continuous contact between the outer needle surface and the substrate is required. Therefore, during our self-propulsion evaluation, the needle was manually inserted by 20 mm in the gelatin phantom before being actuated. In clinical practice, the needle first has to puncture the skin of the patient, before being able to self-propel through the tissue. The skin introduces a surface stiffness force due to the needle puncturing the skin until the moment of puncture [28]. To overcome this, manual insertion of the needle through the skin could be an option using an initial puncture needle, ensuring sufficient contact between the outer needle surface and the surrounding tissue.

The current 3-mm outer diameter of the wasp-inspired biopsy needle prototype represents an improvement over larger former tissue-transport designs ( $\varnothing_{\text{outer}}$ : 7 mm,  $\varnothing_{\text{outer}}$ : 10 mm) [37, 38]) for use in biopsy procedures, but falls short of standard biopsy needles (18 G, outer diameter of 1.27 mm). Future efforts should, therefore, focus on the miniaturization of the needle. The current slot manufacturing method could allow for prototype production on a

smaller scale using nitinol rods and stainless-steel capillary tubes with smaller diameters. However, further miniaturization may be limited by WEDM, typically using wires of 0.15 - 0.3 mm [43]. High precision WEDM, capable of handling wires as fine as 0.025 - 0.1 mm [52] could, in theory, produce smaller slots and, therefore, aid in further miniaturizing the needle dimensions.

Additionally, given the hexagonal arrangement, reducing the outer diameter will also decrease the lumen diameter, thereby decreasing the amount of tissue that can be retrieved. Since the required amount of tissue differs per diagnostic test [45], to enhance functionality, a relatively large lumen is preferred. To increase the lumen diameter, we propose employing multiple central needle segments or a single central needle segment with a larger diameter.

Navigating around vital structures during percutaneous biopsy procedures, especially near the pancreas where structures like the bowel, liver, kidney, or major vessels can block direct access [53], is challenging. Incorporating steerability into biopsy needles can aid in overcoming this challenge. Bevel tips, commonly used in intravascular injections [54], prove effective for maneuvering within the body. Research by Scali *et al.* [33] shows successful needle steering using six nitinol rods by simulating an approximated bevel-shaped tip. Alternatively, a prebend central needle segment could be employed to facilitate needle steering. Incorporating either approach into our biopsy needle design could further enhance its functionality.

Our current needle design showcases two use scenarios: (1) needle propulsion, and (2) substrate transportation from the needle tip to the needle base. On top of that, the functionality of our biopsy needle could inspire designs beyond its scope as the motion sequence could also be reversed to facilitate the delivery of substances from the needle base to the needle tip, such as the delivery of medicine, radioactive particles, or high-viscosity hydrogels for cartilage repair, to enhance the delivery of low-viscosity samples compared to current expulsion-based delivery methods [55].

## 5.5 Conclusion

In conclusion, our study introduces a wasp-inspired biopsy needle capable of both self-propulsion and friction-based core transport. Drawing from previous wasp-inspired designs, we integrated these functionalities by transitioning from external interconnecting structures to a ring passing through slots along the needle segments. The prototype demonstrated the ability to perform these functionalities separately and sequentially, offering a viable alternative to current biopsy needles that are prone to buckling and clogging during downsizing. This innovation is particularly promising for procedures requiring long, thin, and precise biopsy needles, such as in percutaneous pancreatic biopsies. Further advancements, including miniaturization and the integration of steering, could expand the biopsy needle's application scope, potentially improving tissue sampling accuracy and reducing patient complications.

## Supplementary material

The appendices and data underlying this study are available at: [frontiersin.org/articles/10.3389/fbioe.2024.1497221/full#supplementary-material](https://frontiersin.org/articles/10.3389/fbioe.2024.1497221/full#supplementary-material).

## Acknowledgements

We would like to acknowledge the involvement of DEMO (Dienst Elektronische en Mechanische Ontwikkeling) at the TU Delft in the manufacturing of the needle prototype.

## References

1. Partyka O, Pajewska M, Kwaśniewska D, Czerw A, Deptała A, Budzik M, et al. Overview of pancreatic cancer epidemiology in Europe and recommendations for screening in high-risk populations. *Cancers*. 2023;15(14):3634. doi: 10.3390/cancers15143634.
2. Rahib L, Smith BD, Aizenberg R, Rosenzweig AB, Fleshman JM, Matrisian LM. Projecting cancer incidence and deaths to 2030: the unexpected burden of thyroid, liver, and pancreas cancers in the United States. *Cancer research*. 2014;74(11):2913-21. doi: 10.1158/0008-5472.CAN-14-0155.
3. Sarantis P, Koustas E, Papadimitropoulou A, Papavassiliou AG, Karamouzis MV. Pancreatic ductal adenocarcinoma: Treatment hurdles, tumor microenvironment and immunotherapy. *World journal of gastrointestinal oncology*. 2020;12(2):173. doi: 10.4251/wjgo.v12.i2.173.
4. Tyng CJ, Almeida MFA, Barbosa PN, Bitencourt AG, Berg JAA, Maciel MS, et al. Computed tomography-guided percutaneous core needle biopsy in pancreatic tumor diagnosis. *World journal of gastroenterology: WJG*. 2015;21(12):3579. doi: 10.3748/wjg.v21.i12.3579.
5. Mittal A, Le A, Kahlam A, Haider SF, Prasath V, Khrais A, et al. Pancreatic Cancer Biopsy Modalities: Comparing Insurance Status, Length of Stay, and Hospital Complications Based on Percutaneous, Endoscopic, and Surgical Biopsy Methods. *Cureus*. 2023;15(5). doi: 10.7759/cureus.39660.
6. Balen FG, Little A, Smith AC, Theis BA, Abrams KR, Houghton J, et al. Biopsy of inoperable pancreatic tumors does not adversely influence patient survival time. *Radiology*. 1994;193(3):753-5. doi: 10.1148/radiology.193.3.7526415.
7. Yamao K, Sawaki A, Mizuno N, Shimizu Y, Yatabe Y, Koshikawa T. Endoscopic ultrasound-guided fine-needle aspiration biopsy (EUS-FNAB): past, present, and future. *Journal of gastroenterology*. 2005;40:1013-23. doi: 10.1007/s00535-005-1717-6.
8. Crowe DR, Eloubeidi MA, Chhieng DC, Jhala NC, Jhala D, Eltoun IA. Fine-needle aspiration biopsy of hepatic lesions: computerized tomographic-guided versus endoscopic ultrasound-guided FNA. *Cancer Cytopathology: Interdisciplinary International Journal of the American Cancer Society*. 2006;108(3):180-5. doi: 10.1002/cncr.21912.
9. Voss M, Hammel P, Molas G, Palazzo L, Dancour A, O'toole D, et al. Value of endoscopic ultrasound guided fine needle aspiration biopsy in the diagnosis of solid pancreatic masses. *Gut*. 2000;46(2):244-9. doi: 10.1136/gut.46.2.244.
10. May B, Rossiter A, Heyworth P. Core biopsy and FNA: A comparison of diagnostic yield in lymph nodes of different ultrasound determined malignant potential. *American Society of Clinical Oncology*; 2018.
11. Liu J, Huang W, Wang S, Wu Z, Wang Z, Ding X, et al. Comparison of core needle biopsy and fine-needle aspiration methods in CT-guided percutaneous sampling of pancreatic tumors. *Journal of Cancer Research and Therapeutics*. 2023;19(4):904-9. doi: 10.4103/jcrt.jcrt\_1290\_22.
12. Caymaz I, Afandiyeva N. Diagnostic Evaluation of Solid Pancreatic Lesions: Endoscopic Ultrasound-Guided Fine Needle Aspiration Versus Percutaneous Ultrasound-Guided Core Needle Biopsy. *CardioVascular and Interventional Radiology*. 2023;46(11):1596-602. doi: 10.1007/s00270-023-03494-y.
13. Tikkakoski T, Siniluoto T, Päivänsalo M, Typpö T, Turunen J, Apaja-Sarkkinen M. Diagnostic

- accuracy of ultrasound-guided fine-needle pancreatic biopsy. *Rofo: Fortschritte auf dem Gebiete der Röntgenstrahlen und der Nuklearmedizin*. 1992;156(2):178-81. doi: 10.1055/s-2008-1032860.
14. Sabel M. Chapter 3-the breast mass, breast biopsies, and benign lesions of the breast. *Essentials of Breast Surgery Philadelphia*: Mosby. 2009:41-65. doi: 10.1016/B978-0-323-03758-7.00003-X.
  15. Madjidyar J, Vidal LP, Larsen N, Jansen O. Influence of thrombus composition on thrombectomy: ADAPT vs. balloon guide catheter and stent retriever in a flow model. *RöFo-Fortschritte auf dem Gebiet der Röntgenstrahlen und der bildgebenden Verfahren*; 2020. © Georg Thieme Verlag KG. doi: 10.1055/a-0998-4246.
  16. Kortman VG, Verberne Y, Jovanova J, Sakes A. Advancing minimally invasive surgery: A cutting-edge cable-actuated conveying mechanism for reliable tissue transportation. *PLoS ONE*. 2023;18(12):e0295585. doi: 10.1371/journal.pone.0295585.
  17. Hirsch L, Gibney M, Berube J, Manocchio J. Impact of a modified needle tip geometry on penetration force as well as acceptability, preference, and perceived pain in subjects with diabetes. *Journal of diabetes science and technology*. 2012;6(2):328-35. doi: 10.1177/193229681200600216.
  18. Lenau TA, Hesselberg T, Drakidis A, Silva P, Gomes S. Mosquito inspired medical needles. *Bioinspiration, Biomimetics, and Bioreplication 2017*; 2017: SPIE. doi: 10.1117/12.2261399.
  19. Irwin T, Speirs A, Merrett C. The effect of skin tension, needle diameter and insertion velocity on the fracture properties of porcine tissue. *Journal of the Mechanical Behavior of Biomedical Materials*. 2021;123:104660. doi: 10.1016/j.jmbbm.2021.104660.
  20. Vincent J, King M. The mechanism of drilling by wood wasp ovipositors. *Biomimetics (USA)*. 1995.
  21. Sakes A, Dodou D, Breedveld P. Buckling prevention strategies in nature as inspiration for improving percutaneous instruments: a review. *Bioinspiration & biomimetics*. 2016;11(2):021001. doi: 10.1088/1748-3190/11/2/021001.
  22. Cerkvenik U, Van de Straat B, Gussekloo SW, Van Leeuwen JL. Mechanisms of ovipositor insertion and steering of a parasitic wasp. *Proceedings of the National Academy of Sciences*. 2017;114(37):E7822-E31. doi: 10.1073/pnas.1706162114.
  23. Quicke DL, Fitton MG. Ovipositor steering mechanisms in parasitic wasps of the families Gasteruptionidae and Aulacidae (Hymenoptera). *Proceedings of the Royal Society of London Series B: Biological Sciences*. 1995;261(1360):99-103. doi: 10.1098/rspb.1995.0122.
  24. Quicke D, Fitton M, Tunstead J, Ingram S, Gaitens P. Ovipositor structure and relationships within the Hymenoptera, with special reference to the Ichneumonidae. *Journal of Natural History*. 1994;28(3):635-82. doi: 10.1080/00222939400770301.
  25. van Meer NM, Cerkvenik U, Schlepütz CM, van Leeuwen JL, Gussekloo SW. The ovipositor actuation mechanism of a parasitic wasp and its functional implications. *Journal of anatomy*. 2020;237(4):689-703. doi: 10.1111/joa.13216.
  26. Scali M. Self-propelling needles: From biological inspiration to percutaneous interventions: Delft University of Technology; 2020.
  27. Leibinger A, Oldfield MJ, Rodriguez y Baena F. Minimally disruptive needle insertion: a biologically inspired solution. *Interface focus*. 2016;6(3):20150107. doi: 10.1098/rsfs.2015.0107.
  28. Okamura AM, Simone C, O'leary MD. Force modeling for needle insertion into soft tissue. *IEEE transactions on biomedical engineering*. 2004;51(10):1707-16. doi: 10.1109/TBME.2004.831542.
  29. Fung-A-Jou Z, Bloembergen J, Breedveld P. Bioinspired medical needles: a review of the scientific literature. *Bioinspiration & Biomimetics*. 2023. doi: 10.1088/1748-3190/acd905.
  30. Yang C, Xie Y, Liu S, Sun D. Force modeling, identification, and feedback control of robot-assisted needle insertion: a survey of the literature. *Sensors*. 2018;18(2):561. doi: 10.3390/s18020561.
  31. Oldfield MJ, Leibinger A, Seah TET, y Baena FR. Method to reduce target motion through needle-tissue interactions. *Annals of biomedical engineering*. 2015;43(11):2794-803. doi: 10.1007/s10439-015-1329-0.
  32. Frasson L, Ko S, Turner A, Parittotokkaporn T, Vincent JF, Rodriguez y Baena F. STING: a

- soft-tissue intervention and neurosurgical guide to access deep brain lesions through curved trajectories. *Proceedings of the Institution of Mechanical Engineers, Part H: Journal of Engineering in Medicine*. 2010;224(6):775-88. doi: 10.1243/09544119JEM663.
33. Scali M, Breedveld P, Dodou D. Experimental evaluation of a self-propelling bio-inspired needle in single-and multi-layered phantoms. *Scientific reports*. 2019;9(1):1-13. doi: 10.1038/s41598-019-56403-0.
34. Bloemberg J, Trauzettel F, Coolen B, Dodou D, Breedveld P. Design and evaluation of an MRI-ready, self-propelled needle for prostate interventions. *PLoS ONE*. 2022;17(9):e0274063. doi: 10.1371/journal.pone.0274063.
35. Ng KW, Goh JQ, Foo SL, Ting PH, Lee TK, Esuvaranathan K, et al. Needle deflection studies for optimal insertion modeling. *International Journal of Bioscience, Biochemistry and Bioinformatics*. 2013;3(6):570. doi: 10.7763/IJBBB.2013.V3.278.
36. Austin A, Browning T. A mechanism for movement of eggs along insect ovipositors. *International Journal of Insect Morphology and Embryology*. 1981;10(2):93-108. doi: 10.1016/S0020-7322(81)80015-3.
37. Sakes A, Van de Steeg IA, De Kater EP, Posthoorn P, Scali M, Breedveld P. Development of a novel wasp-inspired friction-based tissue transportation device. *Frontiers in Bioengineering and Biotechnology*. 2020;8:575007. doi: 10.3389/fbioe.2020.575007
38. de Kater EP, Sakes A, Bloemberg J, Jager DJ, Breedveld P. Design of a flexible wasp-inspired tissue transport mechanism. *Frontiers in Bioengineering and Biotechnology*. 2021;9:782037. doi: 10.3389/fbioe.2021.782037/full.
39. Rogowska AZ. Ultrasound-guided percutaneous core-needle biopsy of focal pancreatic lesions—practical aspects. *Journal of Ultrasonography*. 2022;22(89):117-20. doi: 10.15557/JoU.2022.0019.
40. Fallahi AA, Jadidian AA. The effect of hand dimensions, hand shape and some anthropometric characteristics on handgrip strength in male grip athletes and non-athletes. *Journal of human kinetics*. 2011;29:151. doi: 10.2478/v10078-011-0049-2.
41. Oberg E, Jones FD, Horton HL, Ryffel HH. *Machinery's handbook*. 30th edition ed: Industrial Press; 2016.
42. Prasad K, Chakraborty S. A decision guidance framework for non-traditional machining processes selection. *Ain Shams Engineering Journal*. 2018;9(2):203-14. doi: 10.1016/j.asej.2015.10.013.
43. Sarala Rubi C, Prakash JU, Juliyana SJ, Čep R, Salunkhe S, Kouril K, et al. Comprehensive review on wire electrical discharge machining: a non-traditional material removal process. *Frontiers in Mechanical Engineering*. 2024;10:1322605. doi: 10.3389/fmech.2024.1322605.
44. Gwoździejewicz K, Studniarek M, Czarnowska-Cubała M, Pieńkowska J, Markiet K. Usefulness of core biopsy in diagnosis of pancreatic tumours. *Polish Journal of Radiology*. 2023;88:e529. doi: 10.5114/pjr.2023.132890.
45. Bhamidipati D, Verma A, Sui D, Maru D, Mathew G, Lang W, et al. An analysis of research biopsy core variability from over 5000 prospectively collected core samples. *NPJ Precision Oncology*. 2021;5(1):94. doi: 10.1038/s41698-021-00234-8.
46. Yap TA, Banerji U, De Bono JS, Workman P. Biopsy-derived biomarkers in phase I trials: building confidence in drug development. *Journal of Clinical Oncology*. 2016;34(20):2431-2. doi: 10.1200/JCO.2016.67.0075.
47. Farrer AI, Odéen H, de Bever J, Coats B, Parker DL, Payne A, et al. Characterization and evaluation of tissue-mimicking gelatin phantoms for use with MRgFUS. *Journal of therapeutic ultrasound*. 2015;3(1):1-11. doi: 10.1186/s40349-015-0030-y.
48. Amiri SA, Berckel PV, Lai M, Dankelman J, Hendriks BH. Tissue-mimicking phantom materials with tunable optical properties suitable for assessment of diffuse reflectance spectroscopy during electrosurgery. *Biomedical Optics Express*. 2022;13(5):2616-43. doi: 10.1364/BOE.449637.
49. Nabavizadeh A, Payen T, Iuga AC, Sagalovskiy IR, Desrouilleres D, Saharkhiz N, et al. Noninvasive Young's modulus visualization of fibrosis progression and delineation of pancreatic ductal



- adenocarcinoma (PDAC) tumors using Harmonic Motion Elastography (HME) in vivo. *Theranostics*. 2020;10(10):4614. doi: 10.7150/thno.37965.
50. Polyak K. Heterogeneity in breast cancer. *The Journal of clinical investigation*. 2011;121(10):3786-8. doi: 10.1172/JCI60534.
51. Czerner M, Martucci JF, Fasce LA, Ruseckaite RA, Frontini PM. Mechanical and fracture behavior of gelatin gels. *13th Int Conf Fract*; 2013.
52. Slătineanu L, Dodun O, Coteață M, Nagiț G, Băncescu IB, Hrițuc A. Wire electrical discharge machining—A review. *Machines*. 2020;8(4):69. doi: 10.3390/machines8040069.
53. Lin C-Y, Ou M-C, Liu Y-S, Chuang M-T, Shan Y-S, Tsai H-M, et al. A CT-guided fat trans-  
versing coaxial biopsy technique for pancreatic lesion biopsy that avoids major organs and vessels. *Saudi Journal of Gastroenterology*. 2017;23(6):341-7. doi: 10.4103/sjg.SJG\_199\_17.
54. Smuck M, Andrew JY, Tang C-T, Zemper E. Influence of needle type on the incidence of  
intravascular injection during transforaminal epidural injections: a comparison of short-bevel and  
long-bevel needles. *The Spine Journal*. 2010;10(5):367-71. doi: 10.1016/j.spinee.2009.12.018.
55. Øvrebø Ø, Perale G, Wojciechowski JP, Echaliier C, Jeffers JR, Stevens MM, et al. Design and  
clinical application of injectable hydrogels for musculoskeletal therapy. *Bioengineering & Translational  
Medicine*. 2022;7(2):e10295. doi: 10.1002/btm2.10295.







# 6

## **From Ovipositor to Self-Propelled Steerable Needle**

Published as:

Bloemberg J., Jager D.J., Breedveld P., Sakes A. (2025). Steering strategies for wasp inspired self propelled needles. Scientific Reports, 15:31018. doi: 10.1038/s41598-025-15031-7.





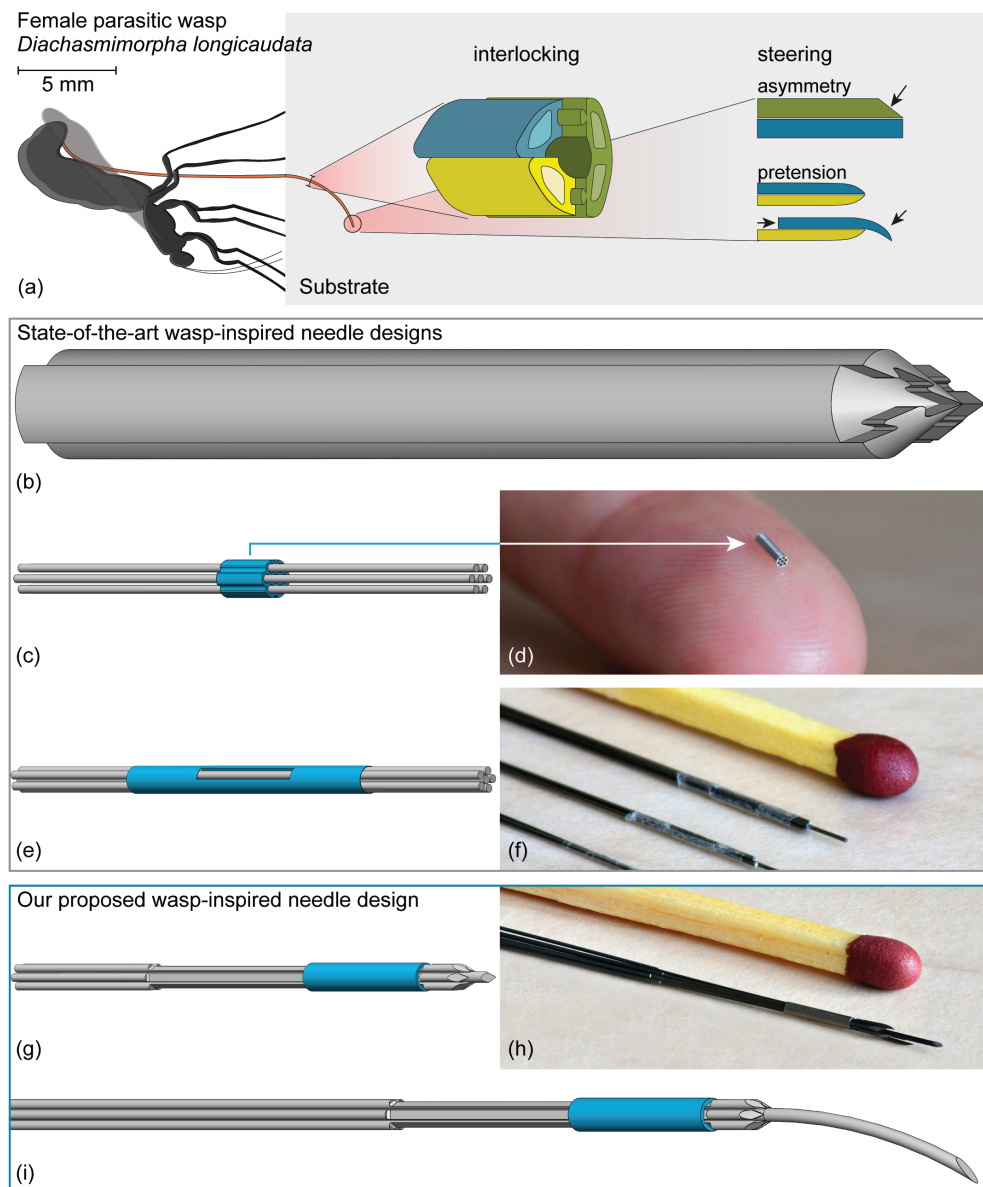
## 6.1 Introduction

From a mechanical standpoint, positioning a thin needle into a solid substrate is difficult because the needle can easily bend and buckle. However, female parasitic wasps do this regularly when they use their long and thin needle-like organ, called the ovipositor, to deposit eggs in a host hidden in wood (e.g., *Megarhyssa atrata* Fabricus (Hymenoptera: Ichneumonidae) [1]) or fruit (e.g., *Diachasmimorpha longicaudata* Ashmead (Hymenoptera: Braconidae) [2]). The wasp ovipositor consists of three parallel segments, called “valves”, which are longitudinally connected by the olistheter mechanism, a jigsaw puzzle-like structure, which allows for sliding of the valves while preventing their separation [3]. The egg channel runs through the center of the three valves [4]. Using its abdominal musculature, the wasp can move the valves longitudinally relative to each other [3].

The exact mechanisms the parasitic wasp uses for ovipositor insertion and buckling prevention are still being studied. However, Cerkvenik *et al.* [5] identified two main mechanisms of ovipositor insertion: (1) pushing the ovipositor into the substrate as a whole, which was observed only in soft substrates, and (2) inserting with alternating valve movements, which was observed in both soft and solid substrates. In the second mechanism, the wasp moves the valves alternately to achieve a so-called “self-propelled motion” [5, 6]. First, one of the valves advances deeper into the tissue, whereas the other valves are held stationary [6, 7]. The friction forces of the stationary valves in contact with the surrounding substrate counteract the friction and cutting forces of the advancing valve in contact with the surrounding substrate because of the difference in surface area between the stationary and advancing valves [7]. The wasp alternates the advancing movements between the valves to propel the ovipositor through the substrate incrementally. This alternating valve mechanism enables ovipositor insertion while avoiding net push forces and axial loads that would otherwise result in the wasp being pushed away from the substrate, given the wasp’s small mass, and bending, buckling, or breaking of the ovipositor [5, 6].

In addition to ovipositor insertion along a straight path without buckling, the female parasitic wasp can also curve and steer its ovipositor to reach the desired target (Figure 6.1a) [5]. In the scientific literature, several hypotheses attempt to explain the steering mechanism of the wasp ovipositor. According to one prevalent hypothesis, a parasitic wasp can steer its ovipositor because of its asymmetric beveled tip [5]. When moving such an asymmetric beveled tip through a substrate, the off-axis reaction forces applied by the substrate on the tip cause the ovipositor to bend [8], resulting in a curved path [9]. Moreover, the bevel shape can presumably be enhanced by changing the relative position of the valves, creating an offset at the tip in the required direction. On the other hand, it is hypothesized that the valves of the ovipositor exhibit pretension and tend to curve to one side when not opposed by the other valves [5]. When the valves are aligned with their tips, the pretensions in the valves counteract each other, resulting in a straight structure. In contrast, when a valve protrudes, its tip curves inward toward the other valves. For both ovipositor steering hypotheses, the ability to steer





**Figure 6.1. Interlocking and steering in (a) female parasitic wasp ovipositors, (b-f) state-of-the-art wasp-inspired needles, and (g-i) our proposed wasp-inspired needle.** (a) The ovipositor of female parasitic wasps consists of “valves” (green, yellow, and blue) that are interlocked by the olitheter mechanism, a jigsaw puzzle-like structure. The wasps are hypothesized to steer their ovipositor by asymmetry and pretension of their ovipositor valves (based on Cerkvenik *et al.* [5]). (b) Four wedge-shaped sections with a puzzle-like interlocking mechanism that mimics the wasp’s olitheter mechanism (based on Burrows *et al.* [27]). (c) Flower-shaped interlocking ring (blue) around seven needle segments (gray) (based on Scali *et al.* [14]), (d) photo of the interlocking ring (from [14]). (e) Ultrathin-walled heat shrink tube (blue) that bundles six needle segments (gray) (based on Scali *et al.* [13]), (f) photo of several needle segment tips with the heat shrink tube (from [13]). (g) Our proposed needle consists of six needle segments with indentations (gray), a hexagonal interlocking ring (blue), and a central needle segment (gray), (h) photo of our proposed needle, (i) our proposed needle in the steering configuration with a prebent bevel-shaped central needle segment.

offers a means to control the ovipositor trajectory during insertion.

Inspired by the ovipositor of the parasitic wasps, a variety of self-propelled and steerable needles consisting of multiple parallel needle segments have been proposed in the scientific literature [10-20]. The self-propelled motion in these needles is achieved by advancing a smaller number of needle segments than the number of stationary needle segments, thereby counterbalancing the cutting and friction force of the advancing needle segments by the friction force generated by the remaining stationary segments [19]. Research has shown that tissue motion and damage in the needle vicinity are reduced when a multisegmented needle actuated with a reciprocal advancing motion is used as compared to merely pushing the needle through the tissue [10, 11, 21].

Inspired by the bevel shape of the wasp ovipositor, omnidirectional steering of wasp-inspired needles was reported in the scientific literature by inducing an offset between the needle segments, creating a discrete bevel-shaped tip [10, 12, 14, 20]. However, the steering curvature achieved with bevel-shaped needles is limited and dependent on the needle-tissue interaction forces [22]. We hypothesize that implementing prebending in the needle, similar to the pretension in the ovipositor of the parasitic wasp, could sharpen the steering curvature. A comparable steering strategy has been successfully applied in concentric tube needles using precurved outer tubes and inner wires [23]. However, these tubes are not capable of a self-propelled motion to prevent needle buckling.

For the wasp-inspired self-propelling and steering mechanisms to work, the needle segments must be interlocked at the tip to avoid separation. A common interlocking mechanism described in the scientific literature mimics the ovipositor's olistheter mechanism (Figure 6.1b) [10, 20, 24-28]. For example, Burrows *et al.* [27] and Aktas *et al.* [28] developed 3D-printed 4-mm and thermally-drawn 1.3-mm diameter needles, respectively, consisting of wedge-shaped parallel needle segments, which slide alongside one another, using jigsaw puzzle-like structures that interlock the needle segments along their entire length. A disadvantage of this interlocking mechanism is that it is difficult to miniaturize. In order to miniaturize the needle diameter to submillimeter dimensions, Scali *et al.* [12, 14] stepped away from the wasp-inspired interlocking mechanism and used a flower-shaped ring as the interlocking mechanism (Figures 6.1c,d). However, the increased cross-sectional area caused by the flower-shaped ring allows for potential tissue accumulation between the needle segments and increases the cutting forces, thereby hindering the self-propelled motion of the needle. Furthermore, the flower-shaped ring does not constrain the axial rotation of individual needle segments. Needle segment rotation is not a problem when we use blunt needle segments. However, when we use bevel-shaped needle segments to sharpen the needle or to allow for steering, rotation of the needle segments can cause these segments to misalign and not point toward the center. This misalignment may lead to divergence of the bevel-shaped segments and potentially allow tissue accumulation between them.

In follow-up designs, Scali *et al.* [13] and Bloembergen *et al.* [15, 16, 29] replaced the flow-



er-shaped ring with an ultrathin-walled heat shrink tube as the interlocking mechanism (Figures 6.1e,f). The heat shrink tube is glued to one of the needle segments to bundle the needle segments at the tip. This solution only minimally increases the needle diameter. However, the heat shrink tube does not constrain the axial rotation of the needle segments.

Previous research has demonstrated the efficacy of using wasp-inspired mechanisms in the development of self-propelled and steerable needles [10, 12-16, 20, 24-29]. To date, their steering capabilities have been attained by mimicking the asymmetric bevel shape of the wasp ovipositor. Furthermore, the parallel needle segments were interlocked via a hard-to-miniaturize jigsaw puzzle-like structure, a flower-shaped ring that hinders the self-propelled motion of the needle, or a heat shrink tube that does not constrain axial rotation.

This study explores an alternative steering system inspired by the parasitic wasp complemented by a novel interlocking mechanism. The steering system incorporates prebending and asymmetry within the centrally positioned needle segment (Figures 6.1g-i). Our novel interlocking mechanism constrains axial rotation of the needle segments without locally increasing the overall needle diameter. Accordingly, we present a submillimeter needle suitable for insertion via a self-propelled motion and omnidirectional steering.

## 6

## 6.2 Design

### 6.2.1 Needle

#### *Interlocking*

In this study, we present a new design of a submillimeter-diameter self-propelled steerable needle, the Prebent Ovipositor Needle, with an improved interlocking mechanism. The Prebent Ovipositor Needle has an outer diameter of 0.89 mm, making it suitable for percutaneous interventions. To prevent separation of the needle segments at the tip, our interlocking mechanism consists of a hexagonal interlocking ring (in blue) and six outer needle segments (in gray) arranged in a circle around a central needle segment (in gray) (Figures 6.1g,h). The outer needle segments contain lancet-shaped tips that face inward toward the central needle segment, whereas the central needle segment has a triangular sharp tip, resulting in an assembled needle with a symmetric sharp tip (Figure 6.1g). Additionally, the outer needle segments contain indentations that leave a semicircular cross-section over a distance of 12 mm. The interlocking ring fits around the needle segments at the position of the indentations. As a result, the wall thickness of the interlocking ring is equal to the radius of the outer needle segments, ensuring that the interlocking ring neither enlarges the overall needle diameter nor allows for potential tissue accumulation between the needle segments.

Our interlocking ring design ensures that the lancet-shaped tips of the outer needle segments always point toward the central needle segment. The length of the interlocking ring is shorter than the length of the indentations, allowing relative translation of the six outer needle segments along the axial direction to initiate wasp-inspired self-propelled motion. The

indentations allow needle assembly through two sequential steps: (1) individually threading the outer needle segments through the interlocking ring and (2) guiding the central needle segment through the center to align the indentations of the outer needle segments with the internal surfaces of the interlocking ring.

### *Self-propelling*

The resulting Prebent Ovipositor Needle design enables a self-propelled motion through the relative movement of the outer needle segments. This self-propelled motion is achieved by counterbalancing the cutting and friction forces perceived by the advancing segments with the friction force generated by the stationary segments [19]. For effective self-propulsion, the friction forces between the substrate and the stationary needle segments must be equal to the combined friction and cutting forces perceived by the advancing needle segments. Consequently, we decided on a motion sequence where one outer needle segment advances while five outer needle segments remain stationary with respect to the substrate. This motion sequence can be actuated by a control and actuation system.

The needle's self-propelled motion relies on sequentially translating the six outer needle segments in seven steps per actuation cycle. During Steps 1-6 (Figure 6.2a), one outer needle segment is advanced by a defined distance of "6/5 stroke length" with respect to the substrate, whereas the other five outer needle segments remain stationary relative to the substrate. Step 7 of the actuation cycle is a reset step, in which the interlocking ring is moved forward to the tip of the needle segments by consecutively advancing and retracting one of the outer needle segments. When there is no slippage of the stationary needle segments with respect to the substrate, the needle self-propels step by step into the substrate.

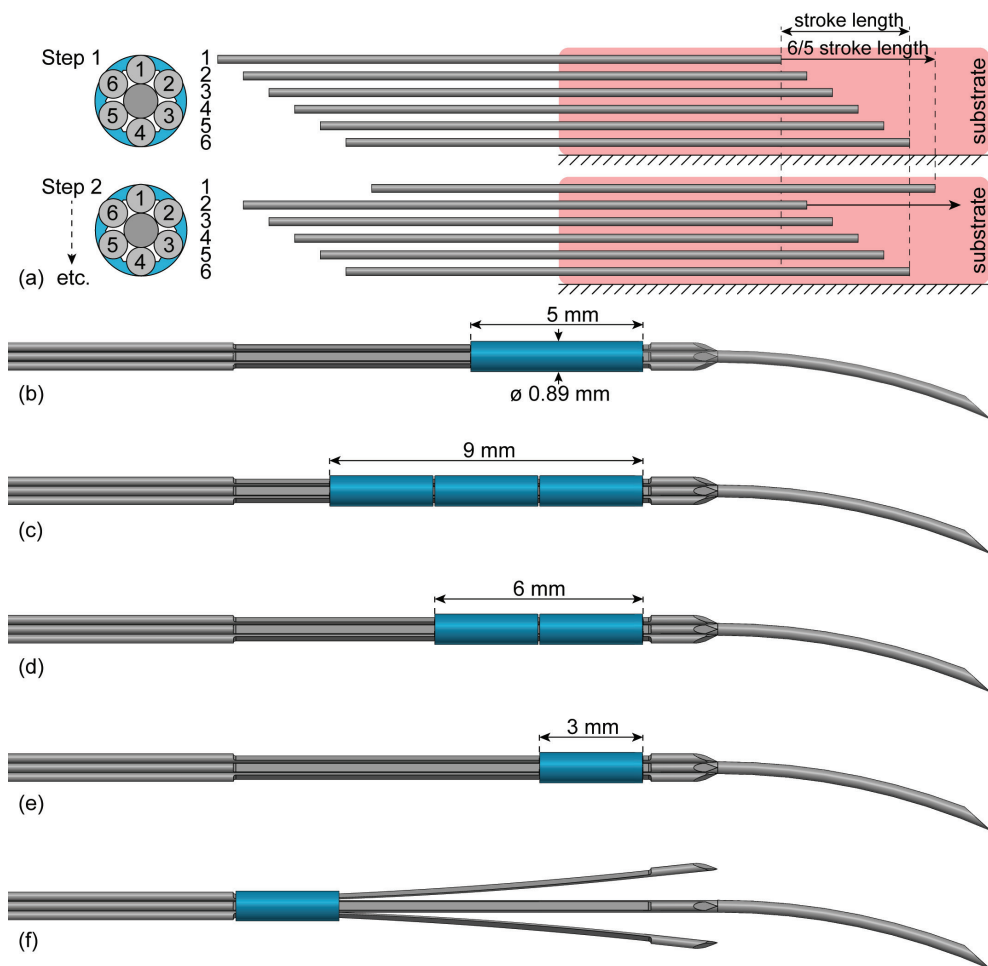
### *Steering*

The parasitic wasp is hypothesized to steer its ovipositor through the pretension and asymmetry in its valves [5]. We decided to implement these mechanisms in our Prebent Ovipositor Needle. The central needle segment can be either a straight triangular needle segment (Figure 6.1g) or a prebent bevel-shaped needle segment (Figure 6.1i). When a central needle segment with a triangular sharp tip is used, the needle follows a straight trajectory during insertion into a substrate. In contrast, using the prebent bevel-shaped needle segment enables the needle to steer. The curvature of the prebent influences the extent of needle bending and the sharpness of the generated curve. By axially rotating the central needle segment, the steering direction can be changed to achieve omnidirectional steering.

Multiple versions of the interlocking ring were developed throughout the design process to optimize the interlocking mechanism for both the self-propelled motion and the steering motion. The initial design featured an interlocking ring with a length of 5 mm (Figure 6.2b, referred to as "1R5" from hereon). In the other designs, we split the 12-mm indentation length of the outer needle segments into four parts of equal length. Consequently, we opted to develop a range of configurations, including three interlocking rings of 3 mm each (Figure 6.2c, referred to as "3R3" from hereon), resulting in a minimal stroke length of 3 mm, two







**Figure 6.2. Self-propelled steerable needle tip designs.** (a) Self-propelled motion sequence: during Steps 1-6 of the actuation cycle, one outer needle segment moves forward over 6/5 stroke length with respect to the surrounding substrate (pink). (b) A single interlocking ring measuring 5 mm in length. (c-e) Three, two, and one interlocking ring(s) measuring 3 mm in length each. (f) Divergence of the outer needle segments with a single 3-mm interlocking ring.

3-mm interlocking rings (Figure 6.2d, referred to as “2R3” from hereon), and a single 3-mm interlocking ring (Figures 6.2e,f, referred to as “1R3” from hereon). This variety allowed us to evaluate the balance between stability and flexibility within the needle design during both the self-propelled and steering motion.

### 6.2.2 Prototype

Our needle prototype comprises seven parallel-positioned nitinol segments, which are superelastic and straight-annealed, and an interlocking ring that constrains needle segment rotation. The interlocking ring was produced out of a stainless-steel capillary tube (outer

diameter of 0.89 mm). To create the hexagonal-shaped hole (inradius of 0.32 mm), we used wire Electrical Discharge Machining (EDM). The hexagon has rounded corners with a radius of 0.075 mm, corresponding to the wire radius used in the wire EDM process. The needle segments consist of a single central needle segment with a diameter of 0.35 mm and six outer needle segments with a diameter of 0.25 mm, each with a length of 200 mm.

The needle segments were sharpened by wire EDM to increase the tip's cutting efficiency and minimize the required insertion force. The straight central needle segment was sharpened to a triangular angle of 20°, whereas the prebent central needle segment was sharpened to an asymmetric bevel angle of 20°. The outer needle segments were sharpened to form lancet-shaped tips with an angle of 20°, similar to previously described wasp-inspired needles [20, 29]. In the assembled needle, the sharpened tips of the outer needle segments point toward the center, with their bevels facing outward. Additionally, to accommodate the interlocking ring, 12-mm indentations were created in the outer needle segments by wire EDM, starting 2 mm from the tip of the needle segment. At the location of the indentation, the cross-section of the outer needle segment resembles half a cylinder, with the flat surface facing outward. This results in a radial clearance between the outer needle segments and the inner surface of the hexagonal-shaped hole of the interlocking ring of 20 μm.

In order to create a prebent shape at the tip of the central needle segment, we used a heat treatment method that defines the shape of the superelastic nitinol needle segment while retaining its superelastic properties [30]. The nitinol needle segment was constrained in an aluminum fixture, secured with bolts to achieve a shape featuring a 30° bending angle and an 8-mm curvature length at the needle tip. The thermal treatment involved placing the mold with the nitinol needle segment in a small chamber furnace, where it was heated to a temperature of 550 °C for 20 minutes. During this process, the needle segment was kept in its deformed shape. Following the heating period, the mold with the needle segment, was rapidly cooled by quenching it in room-temperature water. As a result, the nitinol acquired a prebent austenitic shape at room temperature while retaining its superelastic characteristics.

## 6.3 Evaluation

### 6.3.1 Experimental goal

For the performance evaluation, we assessed the performance of the Prebent Ovipositor Needle in soft tissue-mimicking phantoms made of gelatin with a gelatin weight ratio (wt) of 5 wt%. The use of 5-wt% gelatin results in a modulus of elasticity of 5.3 kPa as determined by Scali *et al.* [13], this modulus of elasticity approximates healthy liver tissue (< 6 kPa) [31]. The performance of the Prebent Ovipositor Needle was evaluated based on its propulsion and steering performance. The propulsion performance was quantified in terms of the propulsion efficiency ( $\eta$  [%]), slip ratio ( $s_r$  [-]), and insertion speed ( $v$  [mm/s]):

$$\eta = \frac{d_m}{d_e} \cdot 100\% \quad (6.1)$$



$$s_r = 1 - \frac{d_m}{d_e} \quad (6.2)$$

$$v = \frac{d_m}{t} \quad (6.3)$$

where  $d_m$  [mm] is the measured insertion distance of the needle with respect to the tissue-mimicking phantom,  $d_e$  [mm] is the expected insertion distance, and  $t$  [s] is the measured insertion time. For  $\eta = 100\%$  and  $s_r = 1$ , the advancing needle segment moves forward into the tissue-mimicking phantom while the remaining needle segments remain stationary relative to the tissue-mimicking phantom, meaning that there is no slip between stationary needle segments and the tissue-mimicking phantom, creating a forward needle motion at maximum speed. Variable  $d_e$  was calculated via Eq. 6.4:

$$d_e = \frac{6}{5} \cdot S \cdot C \quad (6.4)$$

where  $S$  [mm] is the stroke length, which was set to 2 mm, and  $C$  [-] is the number of actuation cycles, which was set to 25, resulting in  $d_e = 60$  mm; for more details on the expected insertion distance, see Appendix 6.A. The 2-mm stroke length, approximately twice the needle's 0.89-mm diameter, facilitates incremental movement of the outer needle segments through the substrate while following the central needle segment trajectory and minimizing the risk of needle segment buckling. The number of actuation cycles is constrained by the total needle length and the experimental setup.

To quantify the steerability of the needle, we evaluated the measured straight insertion distance,  $d_s$ , and the deflection of the needle from a straight path,  $d_d$ . The ratio of distance  $d_d$  to distance  $d_s$  is called the deflection-to-insertion ratio ( $d_r$  [-]) and was calculated via Eq. 6.5:

$$d_r = \frac{d_d}{d_s} \quad (6.5)$$

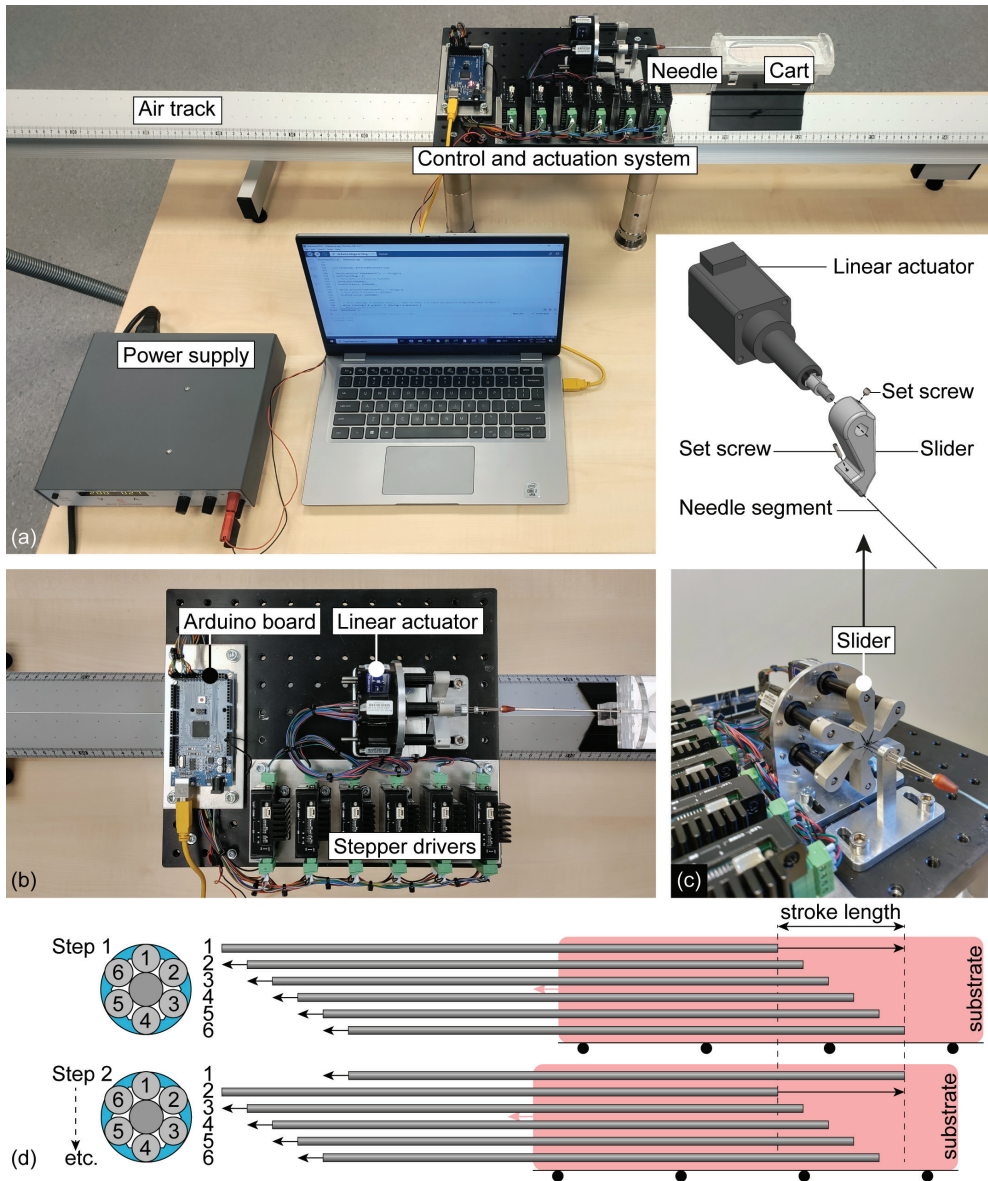
where  $d_d$  [mm] represents the difference between the needle's initial and final distances relative to its centerline. These distances were measured as the deviation of the needle tip perpendicular to the imaginary straight line that the needle would have followed if it had not been steered. Besides  $d_r$ , the needle's steerability was quantified by its achieved curvature ( $\kappa$  [mm<sup>-1</sup>]), which is the amount by which a curve deviates from a straight line. In the case of a circle, the curvature is the reciprocal of its radius. To calculate  $\kappa$ , we approximated the needle's final trajectory as a segment of a circle with a radius  $R$  [mm] that was fitted to the needle's final trajectory via Eq. 6.6:

$$\kappa = \frac{1}{R} = \frac{2d_d}{d_s^2 + d_d^2} \quad (6.6)$$

where variables  $\kappa$  and  $d_r$  are large when the radius of curvature is small, indicating that the needle makes a sharp curve. Both  $d_r = 0$  and  $\kappa = 0$  mm<sup>-1</sup> indicate a straight needle insertion trajectory.

### 6.3.2 Experimental facility

In order to achieve the required self-propelled motion sequence, the needle was connected to a control and actuation system (Figures 6.3a,b). The control system comprises an Arduino board (*MEGA 2560*) in conjunction with six stepper drivers (*Moons' SR3-MINI*). The control



**Figure 6.3. Experimental setup for the evaluation of the Prebent Ovipositor Needle performance.** (a) The control and actuation system was mounted on an aluminum base plate. The needle, connected to the control and actuation system, is propelled and steered into a tissue-mimicking phantom carried by a cart on an air track. (b) Top view of the control and actuation system comprising an Arduino board, six stepper drivers, and six linear actuators. (c) Each linear actuator and outer needle segment was clamped to a slider using set screws. (d) Self-propelled motion sequence: during Steps 1-6 of the actuation cycle, one outer needle segment moves forward over the stroke length while the other outer needle segments move slowly backward over one-fifth of the stroke length thereby self-propelling the needle step by step into the substrate by pulling the substrate (pink) on the cart on the air track (illustrated by black wheels) toward the control and actuation system.

system controls the actuation system, which actuates the six outer needle segments to achieve the required self-propelled motion sequence. This actuation system contains six linear actuators (*Thomson MLAX8A05-0157S0039-E4-S01*, displacement resolution 1.57  $\mu\text{m}$ ) that enable the back-and-forth movement of the six outer needle segments. The linear actuators were arranged in a circular configuration to correspond with the positions of the six outer needle segments.

As the linear actuators run at a larger diameter than the six needle segments do, sliders and capillary tubes are used to guide the needle segments toward the central needle segment and ensure that they reach their final insertion diameter. Each linear actuator is connected to a slider that points toward the center (Figure 6.3c). The outer portion of the slider is securely clamped to an actuator rod via a set screw. Each outer needle segment is fastened to the central portion of a slider with another set screw, ensuring parallel alignment of the needle segments during actuation. Finally, the capillary tubes further guide the outer needle segments toward the central needle segment and their final insertion diameter. In order to prevent buckling of the needle between the actuation system and the tissue-mimicking phantom, the needle is fed through four capillary tubes ( $T_1$ ,  $T_2$ ,  $T_3$ , and  $T_4$ ) arranged in a telescopic manner. The tube diameters are  $T_1 = 2.5$  mm,  $T_2 = 2.0$  mm,  $T_3 = 1.6$  mm, and  $T_4 = 1.2$  mm. The lengths of  $T_1$ - $T_3$  are 30 mm and that of  $T_4$  is 40 mm. Within the substrate, the substrate exerts an inward force toward the needle's centerline on the needle segments, thereby preventing the buckling of the individual needle segments.

The experimental setup consisted of the Prebent Ovipositor Needle connected to the control and actuation system, mounted to a solid aluminum breadboard (*MB2530/M*, Thorlabs, Inc., Newton, NJ), and a tissue-mimicking phantom placed on a customized Perspex cart on an air track (Eurofysica, 's-Hertogenbosch, The Netherlands) (Figure 6.3a). Rather than moving the needle toward the tissue-mimicking phantom, we chose to move the tissue-mimicking phantom toward the stationary needle. This setup involved keeping the needle stationary and connected to the control and actuation system that facilitates the relative motion of the needle segments for the self-propelled motion. The tissue-mimicking phantom was placed on the cart on the air track to allow a near-frictionless horizontal translation of the tissue-mimicking phantom. The Prebent Ovipositor Needle self-propels if it pulls the tissue-mimicking phantom toward the control and actuation system by pulling itself deeper into the tissue-mimicking phantom (Figure 6.3d).

The needle's self-propelled motion relies on the control and actuation system that sequentially translates the six outer needle segments in seven steps per actuation cycle. During Steps 1-6, each outer needle segment is advanced once by the stroke length in a single step and slowly retracted with respect to the actuation system during five steps, with each retraction step covering one-fifth of the stroke length. When there is no slip, the retracting needle segments remain stationary with respect to the substrate and during each actuation cycle, the outer needle segments are advanced by  $6/5$  stroke length with respect to the substrate. This

continuous motion of the outer needle segments applies a constant strain to the surrounding substrate.

For the tissue-mimicking phantoms, gelatin powder of type *Dr. Oetker 1-50-230004* (Dr. Oetker Professional, Amersfoort, The Netherlands) was mixed with water with a gelatin weight ratio of 5 wt%. The gelatin/water mixture was poured into molds and stored overnight at 5 °C for solidification. Afterward, the solidified gelatin/water mixture was cut to its final dimensions with a stamping die (width 40 mm, length 110 mm, height 20 mm) and placed on the cart. Millimeter graph paper attached at the bottom of the cart and the ruler of the air track were used as a reference to measure variables  $d_m$ ,  $d_s$ , and  $d_d$  during needle propulsion with an approximative accuracy of 0.5 mm. To ensure the repeatability of the measurement method, the experimental setup was not moved in between the measurements.

### 6.3.3 Experimental procedure

For each measurement, a new gelatin phantom was placed on the cart. Before each measurement, the Prebent Ovipositor Needle was inserted over an initial distance of 30 mm inside the tissue-mimicking phantom to ensure initial contact between the needle segments and the phantom. During every measurement, a camera, vertically positioned on a tripod, captured the position of the needle inside the tissue-mimicking phantom to measure variables  $d_m$ ,  $d_s$ , and  $d_d$ . Every measurement was performed with an actuated speed of 10 mm/s for the advancing needle segments, the stroke length,  $S$ , set to 2 mm, and the number of actuation cycles,  $C$ , set to 25. Each condition was repeated six times.

### 6.3.4 Data analysis

To statistically compare our evaluated conditions (i.e., 1R5 forward versus 1R5 down, 1R5 down versus 1R5 up, and 1R5 up versus 2R3 up) for  $\eta$  and  $d_r$ , Mann-Whitney U tests with exact two-tailed  $p$ -values were performed. Due to the small sample sizes ( $n = 6$  per condition) and the presence of non-normal distributions in one of the dependent variables for one condition (i.e.,  $\eta$  for 1R5 up), Mann-Whitney U tests were chosen for all pairwise condition comparisons. This type of nonparametric test does not assume normality and is more appropriate and robust for small samples with potential parametric assumption violations. This led to a total of six statistical comparisons. To control the risk of Type I error from multiple comparisons, a Bonferroni correction was applied, resulting in an adjusted significance threshold of  $\alpha = 0.0083$  (0.05 divided by six tests). Only  $p$ -values below this threshold were considered statistically significant. The analysis was done in IBM SPSS Statistics 29.0.0.







### 6.3.5 Results

We conducted three consecutive experiments to evaluate the effects of (1) the central needle design, (2) the steering direction, and (3) the interlocking ring configuration on the performance of the Prebent Ovipositor Needle. The results for  $\eta$ ,  $s_r$ ,  $v$ ,  $d_r$ , and  $\kappa$  are summarized in Table 6.1 and Figure 6.4 and example measurements of variables  $d_m$ ,  $d_s$ ,  $d_d$ , and  $\kappa$  are visualized





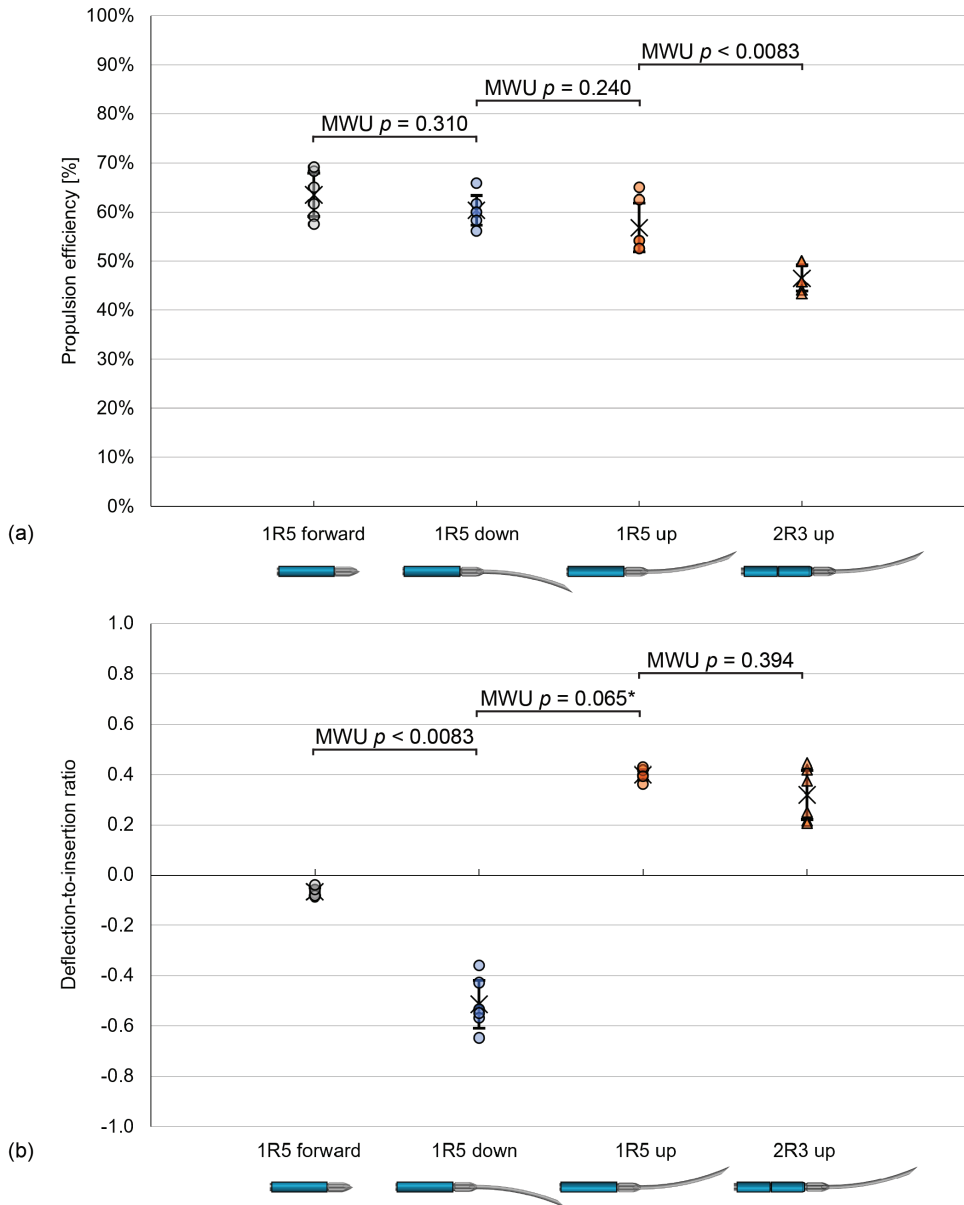
**Table 6.1.** Experimental results of self-propelling and steering performance evaluations of the Prebent Ovipositor Needle in a 5-wt% gelatin phantom mimicking healthy liver tissue, showing the condition, number of repetitions (i.e., how often the condition was evaluated in a new gelatin phantom), propulsion efficiency, slip ratio, insertion speed, deflection-to-insertion ratio, and curvature, with mean values and standard deviations. A positive deflection-to-insertion ratio and curvature correspond to upward steering, and a negative deflection-to-insertion ratio and curvature correspond to downward steering. Meaning of abbreviations of the different conditions: 1R5 forward = straight triangular central segment and a single 5-mm interlocking ring, 1R5 down = prebent bevel-shaped central segment steering downward and a single 5-mm interlocking ring, 1R5 up = prebent bevel-shaped central segment steering upward and a single 5-mm interlocking ring, 3R3 up = prebent bevel-shaped central needle segment steering upward and three 3-mm interlocking rings, 2R3 up = prebent bevel-shaped central segment steering upward and two 3-mm interlocking rings, and 1R3 up = prebent bevel-shaped central needle segment steering upward and a single 3-mm interlocking ring.

Condition	Number of repetitions, $n$	Propulsion performance			Steering performance	
		Propulsion efficiency [%], $\eta$ (mean $\pm$ SD)	Slip ratio, $s_r$ (mean $\pm$ SD)	Insertion speed [mm/s], $v$ (mean $\pm$ SD)	Deflection-to-insertion ratio, $d_r$ (mean $\pm$ SD)	Curvature [mm <sup>-1</sup> ], $\kappa$ (mean $\pm$ SD)
1R5 forward 	6	63 $\pm$ 4	0.37 $\pm$ 0.04	0.85 $\pm$ 0.06	-0.07 $\pm$ 0.02	-0.003 $\pm$ 0.001
1R5 down 	6	60 $\pm$ 3	0.40 $\pm$ 0.03	0.79 $\pm$ 0.06	-0.51 $\pm$ 0.09	-0.026 $\pm$ 0.005
1R5 up 	6	57 $\pm$ 5	0.43 $\pm$ 0.05	0.76 $\pm$ 0.07	0.40 $\pm$ 0.02	0.023 $\pm$ 0.002
3R3 up* 	2	3 0	0.97 1.00	0.04 0.00	0 n/a	0 n/a
2R3 up 	6	47 $\pm$ 3	0.53 $\pm$ 0.03	0.62 $\pm$ 0.03	0.32 $\pm$ 0.10	0.022 $\pm$ 0.006
1R3 up* 	2	30 57	0.70 0.43	0.40 0.76	0.35 0.25	0.037 0.015

\*For the 3R3 and 1R3 conditions, the values of individual repetitions are provided instead of mean  $\pm$  standard deviation, as the conditions were only evaluated twice.

in Figures 6.5a-d. First, we compared the downward-steering prebent bevel-shaped central needle design (1R5 down) to the straight triangular central needle design (1R5 forward). No statistically significant difference was found for  $\eta$  between the 1R5 forward (median = 63%) and 1R5 down (median = 60%) conditions ( $U = 11.5$ ,  $p = 0.310$ ), indicating no statistically significant difference in propulsion efficiency between straight and steering trajectories. However, the 1R5 down condition (median = -0.54) showed a significantly difference in  $d_r$  as compared to the 1R5 forward condition (median = -0.07,  $U = 0$ ,  $p = 0.002$ ), indicating effective downward steering.

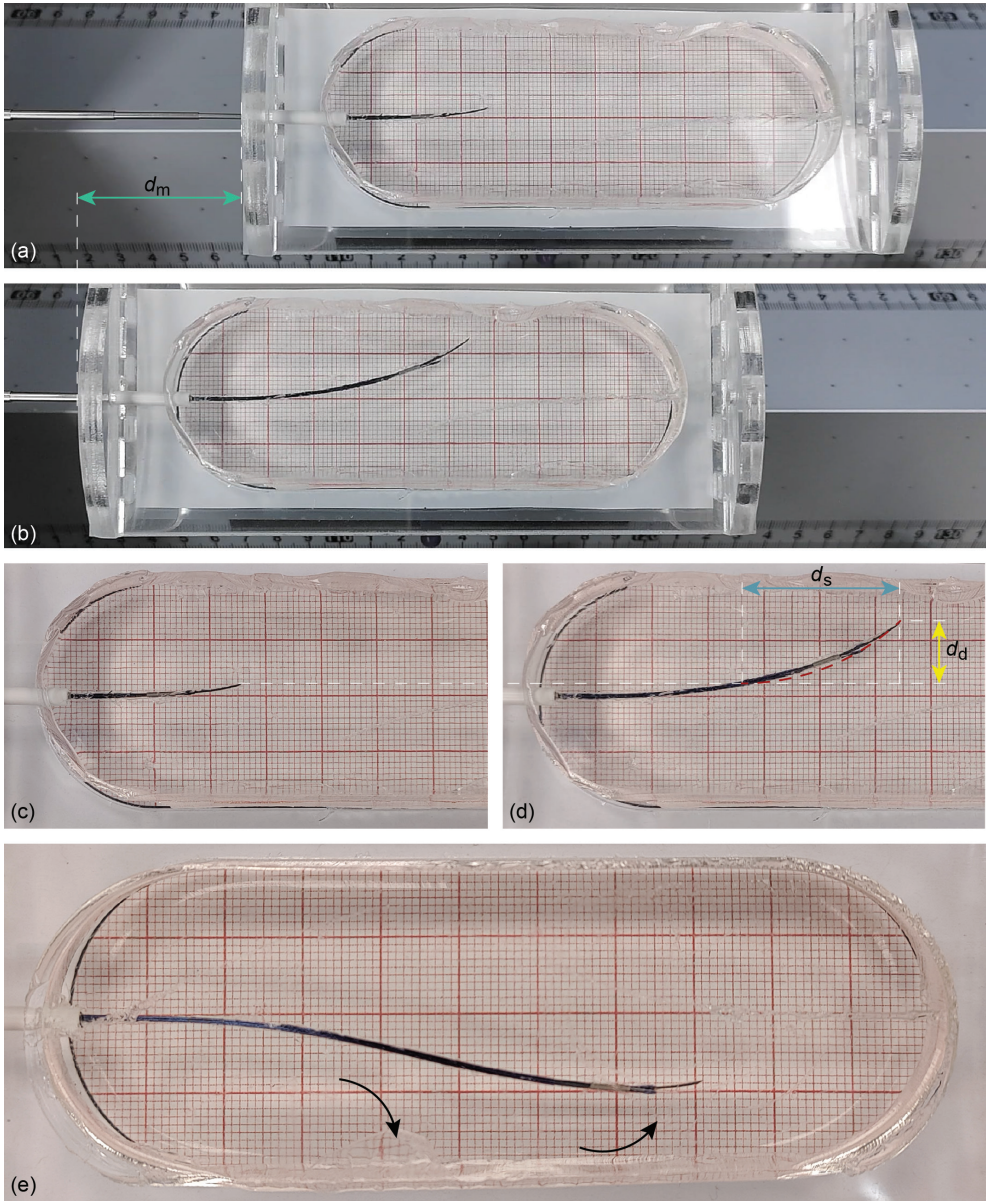
Second, we evaluated whether the steering performance was consistent across different steering directions by comparing the propulsion and steering performance when the prebent



**Figure 6.4. Experimental results of (a) propulsion and (b) steering performance evaluations of the Prebent Ovipositor Needle in a 5-wt% gelatin phantom mimicking healthy liver tissue.** The circles represent single trials, the crosses represent mean values, and the error bars represent the standard deviation. A positive deflection-to-insertion ratio corresponds to steering upward, and a negative deflection-to-insertion ratio corresponds to steering downward. Meaning of abbreviations of the different conditions shown at the x-axes: 1R5 forward = straight triangular central segment and a single 5-mm interlocking ring, 1R5 down = prebent bevel-shaped central segment steering downward and a single 5-mm interlocking ring, 1R5 up = prebent bevel-shaped central segment steering upward and a single 5-mm interlocking ring, and 2R3 up = prebent bevel-shaped central segment steering upward and two 3-mm interlocking rings. Annotations in the figure denote the  $p$ -values of the Mann-Whitney U (MWU) test. A  $p$ -value less than 0.0083 indicates a significant difference.

\*The Mann-Whitney U test was performed on the absolute values of  $d_f$  between the 1R5 up and 1R5 down conditions.





**Figure 6.5. Images of the needle inside the gelatin-based tissue-mimicking phantom.** Images of a needle with a single 5-mm interlocking ring steering upward: (a) the initial frame and (b) the final frame showing variable  $d_m$  [mm] (green), the measured insertion distance of the needle with respect to the tissue-mimicking phantom. Close-ups of (c) the initial frame and (d) the final frame showing variables  $d_s$  [mm] (blue), the measured straight insertion distance, and  $d_d$  [mm] (yellow), the deflection of the needle from a straight path, and an overlay of the computed curvature (red dashed). (e) Final position of the needle after changing the steering direction. The arrows show the direction of steering. The steering direction changed from downward to upward.

bevel-shaped central segment was directed upward (1R5 up) and downward (1R5 down). No statistically significant difference was found for  $\eta$  between the 1R5 up (median = 54%) and 1R5 down (median = 60%) conditions ( $U = 10$ ,  $p = 0.240$ ). Furthermore, no statistically significant difference was found for the absolute  $d_r$  between the 1R5 up (median = 0.40) and 1R5 down (median = 0.54) conditions ( $U = 6.5$ ,  $p = 0.065$ ). These results indicate no statistically significant differences in either propulsion or steering performance for equal prebents in different steering directions.

Finally, we investigated the impact of different interlocking ring configurations by comparing the 1R5, 3R3, 2R3, and 1R3 designs. Since the second experiment demonstrated that the steering direction did not affect the propulsion and steering performance, we focused solely on the effects of the interlocking ring design in a single steering direction: upward steering. The 3R3 configuration (Figure 6.2c) hindered needle advancement within the tissue-mimicking phantom due to its 9-mm interlocking ring length. During the reset step (Step 7), the overall friction force perceived by the three interlocking rings moving forward as a single, 9-mm long unit exceeded the friction between the five stationary outer needle segments and the substrate, causing the stationary needle segments to be pushed backward and start slipping relative to the substrate. The 1R3 configuration (Figure 6.2e) led to divergence of the needle segments within the tissue-mimicking phantom (Figure 6.2f) because the 3-mm ring allows the needle segments to protrude by 11 mm beyond the ring. This divergence strongly increases the force required to advance the ring over the needle segments, ultimately blocking the needle's advancement within the substrate. Therefore, the 3R3 and 1R3 designs are not feasible for a self-propelled steerable motion. A statistical analysis of the remaining interlocking ring configurations, 1R5 (Figure 6.2b) and 2R3 (Figure 6.2d), resulted in the 1R5 up condition (median = 0.40) showing a statistically significant difference in  $\eta$  as compared to the 2R3 up condition (median = 0.31,  $U = 0$ ,  $p = 0.002$ ). However, no statistically significant difference was found for  $d_r$  between the 1R5 up (median = 0.40) and 2R3 up (median = 0.31) conditions ( $U = 12$ ,  $p = 0.394$ ). These results suggest an advantage of the single 5-mm ring design in terms of the propulsion performance over the double 3-mm ring design, while no statistically significant difference in steering performance was found.

### 6.3.6 Explorative experiments

We conducted a set of additional tests to explore the behavior of the Prebent Ovipositor Needle in different settings. First, we performed a qualitative test to evaluate the ability of the needle to change its steering direction during insertion in a 5-wt% gelatin phantom mimicking healthy liver tissue. In this test, the needle segments were actuated over twenty actuation cycles while steering downward, followed by another twenty actuation cycles steering upward. The steering direction was changed by slightly retracting the central needle segment, axially rotating it over  $180^\circ$ , and slightly advancing it again. The measurement revealed that the needle was able to change direction during the self-propelled insertion (Figure 6.5e).

Second, we investigated the behavior of the Prebent Ovipositor Needle in its 1R5 down

and 1R5 up configurations in terms of its propulsion and steering performance using a shorter stroke length,  $S$ , of 1 mm instead of 2 mm. For each configuration, we conducted two tests over 50 actuation cycles. The results revealed propulsion efficiency,  $\eta$ , percentages of 38% and 44% to 45% for the 1R5 down and 1R5 up conditions, respectively. Although these efficiencies are comparable to each other, they are smaller than those achieved for  $S = 2$  mm, with mean  $\eta$  percentages of  $60\% \pm 3\%$  and  $57\% \pm 5\%$ , respectively. These preliminary results suggest that the needle may propel more efficiently when actuated at a longer stroke length,  $S$ , as compared to a shorter stroke length. However, further research with additional stroke lengths is required to confirm this trend. The deflection-to-insertion ratio,  $d_r$ , values for  $S = 1$  mm were -0.58 to -0.54 for the 1R5 down condition and 0.41 to 0.7 for the 1R5 up condition, both of which are comparable to those achieved for  $S = 2$  mm, with mean  $d_r$  values of  $-0.51 \pm 0.09$  and  $0.40 \pm 0.02$  (Table 6.1), respectively. This suggests that the needle steers with equal efficiency regardless of whether it is actuated at longer or shorter stroke lengths.

Finally, we investigated the behavior of the Prebent Ovipositor Needle in its 1R5 forward configuration in stiffer substrates. For this purpose, we used 10-wt% gelatin for the tissue-mimicking phantoms, which resulted in a modulus of elasticity of 17 kPa as determined by Scali *et al.* [13], approximating healthy prostate or cirrhotic liver tissue [31, 32]. We conducted two tests with the 1R5 forward configuration actuated with stroke length,  $S$ , of 2 mm and number of actuation cycles,  $C$ , of 25. The results revealed that the Prebent Ovipositor Needle self-propelled through the stiff substrate with a propulsion efficiency,  $\eta$ , of 52% to 58% and deflection-to-insertion ratio,  $d_r$ , of -0.05 to 0.00. Both the measured propulsion efficiency,  $\eta$ , and deflection-to-insertion ratio,  $d_r$ , in the 10-wt% tissue-mimicking phantoms are slightly smaller than those reported for the 5-wt% tissue-mimicking phantoms, which are  $63\% \pm 4\%$  and  $-0.07 \pm 0.02$  (Table 6.1), respectively. This indicates that the needle propels slightly faster and steers with slightly sharper curves in soft substrates as compared to stiff substrates. The reduced propulsion efficiency in stiff substrates can be attributed to the increased cutting force, which arises from the plastic deformation of the substrate and the resistance due to the substrate stiffness at the needle tip [33].

## 6.4 Discussion and conclusion

In contrast to previously developed wasp-inspired self-propelled and steerable needles that rely on inducing an offset between the needle segments to create a discrete bevel-shaped tip for steering [10, 12, 14, 20], we presented a steerable needle that incorporates an alternative steering mechanism inspired by the parasitic wasp, specifically, the use of prebending combined with a bevel-shaped tip within the needle segments. Additionally, our needle features a new needle interlocking mechanism that constrains needle segment rotation. Our needle comprises seven parallel needle segments, with the central needle segment tip being either straight and triangular for a forward trajectory, or prebent and bevel-shaped for steering purposes. By rotating the prebent needle segment, our needle is capable of omnidirectional steering, allow-

ing for trajectory changes without the need for axial rotation of the entire needle. Changing the steering direction without axial rotation prevents the generation of torsional stress by the surrounding tissue on the needle, thereby preventing angular lag between the orientation of the needle base and tip [34]. Consequently, our prebending steering method can enhance the controllability of the needle trajectory while potentially reducing the risk of tissue damage as compared to steerable needles that require axial rotation of the entire needle [35].

In our data analysis, we performed statistical comparisons with nonparametric tests and corrections for multiple comparisons. However, the low number of repetitions per condition (i.e.,  $n = 6$ ) is a limitation of this study. This may have impacted the ability to detect small but potentially meaningful differences in propulsion or steering performance between interlocking ring design and steering conditions. Consequently, non-statistically significant findings should be interpreted with caution.

For the forward self-propelled motion, the mean slip ratio,  $s_r$ , measured in 5-wt% tissue-mimicking phantoms was 0.37 (number of repetitions,  $n$ , of 6, for the 1R5 up condition) for our needle consisting of six 0.25-mm diameter outer needle segments and a 0.35-mm central needle segment. This value is considerably larger than the slip ratio reported by Scali *et al.* [14] for a needle consisting of seven 0.25-mm diameter needle segments connected with a flower-shaped ring evaluated in 4-wt% tissue-mimicking phantoms, which has a mean  $s_r$  of 0.21 ( $n = 5$ ). The different slip ratios can be attributed to the use of a softer tissue-mimicking phantom (4 wt% compared with 5 wt%) by Scali *et al.* [14], which contributes to reduced cutting forces at the tip of the needle, leading to a smaller  $s_r$ . Our slip ratio is also larger than the slip ratio reported by Scali *et al.* [13] for a discrete bevel-tip needle consisting of six 0.25-mm segments connected with a heat shrink tube evaluated in 5-wt% tissue-mimicking phantoms, which has a mean  $s_r$  of 0.28 ( $n = 10$ ). This difference may be explained by the fact that Scali *et al.* [13] used fewer needle segments (six compared with seven) than we did, resulting in a smaller overall needle diameter than our needle (0.8 mm compared with 0.89 mm). In our needle, the central needle segment does not contribute to the friction forces that help the self-propelled motion but does increase the cutting forces at the tip of the needle. Previous work confirmed that the peak axial needle insertion force increases with increasing needle size [36].

For the steering motion, the mean deflection-to-insertion ratio,  $d_r$ , for our 1R5 up configuration in 5-wt% tissue-mimicking phantoms was 0.40 ( $n = 6$ ). This value is considerably larger than the deflection-to-insertion ratios reported by Scali *et al.* [12, 14] for discrete bevel-tip needles with mean  $d_r$  values of 0.0686 ( $n = 5$ ) and 0.097 ( $n = 8$ ). The different deflection-to-insertion ratios indicate more effective steering with a prebent bevel-shaped needle tip than with a discrete bevel tip.

Returning to the source of inspiration for our needle, the parasitic wasp, Cerkvenik *et al.* [5] reported a median insertion speed,  $v$ , of 0.73 mm/s for the fruit-fly parasitic wasp (*Diachasmimorpha longicaudata* Ashmead (Hymenoptera: Braconidae)) probing in a





gel with an elastic modulus of 36 kPa. This reported speed is comparable to the mean  $v$  of the Prebent Ovipositor Needle, which is 0.75 mm/s ( $n = 24$ ). Additionally, the wasp demonstrated complex insertion trajectories characterized by multiple bends in different directions, similar to the capabilities of our needle (Figure 6.5). However, differences arise when comparing the curvature,  $\kappa$ , of the wasp ovipositor and the Prebent Ovipositor Needle. Cerkvenik *et al.* [5] reported a median  $\kappa$  of 0.2 mm<sup>-1</sup> for the parasitic wasp, whereas the Prebent Ovipositor Needle in the 1R5 configuration demonstrated absolute mean  $\kappa$  of 0.023 mm<sup>-1</sup> ( $n = 6$ ) and 0.026 mm<sup>-1</sup> ( $n = 6$ ), for steering upward and downward, respectively, indicating the wasp ovipositor achieved much sharper curves than our needle. Nevertheless, when we correct for the diameter of the ovipositor and needle by calculating the dimensionless curvature (i.e.,  $|\kappa|$  multiplied by the ovipositor width or needle diameter), our Prebent Ovipositor Needle in the 1R5 configuration showed larger mean dimensionless curvatures, ranging from 0.010 ( $n = 6$ ) to 0.012 ( $n = 6$ ), than the reported median dimensionless curvature of the parasitic wasp, which is only 0.0060 [5]. This indicates that, after correcting for the needle diameter, our needle achieved curvatures that go beyond those attained by the parasitic wasp.

In the current prototype, we developed and evaluated a steerable needle with a prebent tip of a single length. Adebar *et al.* [37] demonstrated that an increase in the length of the prebent tip in an articulated-tip needle results in a larger curvature,  $\kappa$ . In future work, the achievable  $\kappa$  of the Prebent Ovipositor Needle can be enhanced by increasing the length of the prebent tip. We hypothesize that an increase in the prebent angle and length of the prebent tip results in more pronounced needle bending, leading to a sharper curve, which can be used to control needle steering.

During the experiments, we observed that the needle segments occasionally diverged at the tip. This divergence may be attributed to our interlocking mechanism, which interlocks the needle segments at the indentation rather than at the tip of the needle. The absence of interlocking support at the needle tip can lead to the diverging of the needle segments because of the needle-tissue interaction forces encountered during insertion, compromising the propulsion efficiency,  $\eta$ , and the effectiveness of the steering mechanism. Moreover, the divergence may cause potential tissue damage, making it an important research topic for future wasp-inspired needles. This divergence of the needle segments was not observed during the evaluations of the Prebent Ovipositor Needle with a single 5-mm interlocking ring and with two 3-mm interlocking ring. However, needle segment divergence was observed in the preliminary evaluation of the Prebent Ovipositor Needle with a single 3-mm interlocking ring. To address this limitation in future designs, we recommend repositioning the indentations and, thereby, the interlocking ring closer to the needle tip or exploring alternative interlocking designs that provide interlocking support along the entire needle length, from the base to the tip, inspired by the olistheter mechanism of the wasp's ovipositor.

One of the consequences of needle insertion into soft tissue is tissue displacement [38]. Leibinger *et al.* [11] demonstrated that wasp-inspired self-propelled motion can reduce tissue

motion and deformation. The outer needle segments continuously push and pull the tissue around them, applying a constant strain to the tissue. As a result, viscoelastic materials such as tissue show stress relaxation, meaning that the internal stress within the material does not remain constant but rather decreases [39]. This stress relaxation may help mitigate the extent of tissue trauma during needle insertion. In future *ex vivo* experiments with our Prebent Ovipositor Needle, tissue damage can be assessed through histological evaluation [40], allowing for detailed analysis of cellular integrity, tissue morphology, and any potential structural changes induced by the needle insertion.

Our experiments demonstrated the ability of the Prebent Ovipositor Needle to self-propel and steer in tissue-mimicking phantoms. We assessed the steering performance based on the deflection-to-insertion ratio,  $d_r$ , and the curvature,  $\kappa$ . However, for a critical evaluation of the needle's steering performance in a clinical setting, future studies should assess the endpoint error [41]. Furthermore, image guidance techniques can be used to visualize the trajectory of the needle inside the tissue, and implementing a feedback control mechanism within the actuation system can enable real-time correction of this trajectory. Moreover, we evaluated our needle in a controlled environment using tissue-mimicking phantoms. To develop a complete picture of the propulsion and steering performance of the needle in a clinical setting, *ex vivo* and *in vivo* tissue experiments are required. Previous studies have already successfully demonstrated the ability of similar wasp-inspired needles to self-propel through *ex vivo* tissue [15, 16]. These previous studies suggest that our needle can perform similarly.

The needle presented in this study represents just one of many potential designs that can be derived from our steerable needle concept. The number, diameter, and length of the needle segments can be changed to accommodate specific medical applications. Additionally, the central needle segment can be replaced with a hollow tube, enabling tissue sample extraction or the insertion of functional elements, such as an optical fiber for optical biopsy or for focal laser ablation to treat prostate cancer [42].

## Supplementary material

The data underlying this study are available at doi: 10.4121/da8b9a7b-c274-4c85-b527-00794811bad1.

## Acknowledgements

We thank Jacques Brinkman from metrology support at the Faculty of Mechanical Engineering, Delft University of Technology, for his help on the hardware of the control and actuation system. We thank Danny de Gans from the Department of Electronic and Mechanical Support Division, Faculty of Electrical Engineering, Mathematics and Computer Science, Delft University of Technology for his help on the software of the control and actuation system.



## References

1. Le Lannic J, N  on J-P. Functional morphology of the ovipositor in *Megarhyssa atrata* (Hymenoptera, Ichneumonidae) and its penetration into wood. *Zoomorphology*. 1999;119(2):73-9. doi: 10.1007/s004350050082.
2. Leyva JL, Browning HW, Gilstrap FE. Effect of host fruit species, size, and color on parasitization of *Anastrepha ludens* (Diptera: Tephritidae) by *Diachasmimorpha longicaudata* (Hymenoptera: Braconidae). *Environmental Entomology*. 1991;20(5):1469-74. doi: 10.1093/ee/20.5.1469.
3. Quicke D, Fitton M, Tunstead J, Ingram S, Gaitens P. Ovipositor structure and relationships within the Hymenoptera, with special reference to the Ichneumonoidea. *Journal of Natural History*. 1994;28(3):635-82. doi: 10.1080/00222939400770301.
4. van Meer NM, Cerkvenik U, Schlep  tz CM, van Leeuwen JL, Gussekloo SW. The ovipositor actuation mechanism of a parasitic wasp and its functional implications. *Journal of anatomy*. 2020;237(4):689-703. doi: 10.1111/joa.13216.
5. Cerkvenik U, Van de Straat B, Gussekloo SW, Van Leeuwen JL. Mechanisms of ovipositor insertion and steering of a parasitic wasp. *Proceedings of the National Academy of Sciences*. 2017;114(37):E7822-E31. doi: 10.1073/pnas.1706162114.
6. Vincent J, King M. The mechanism of drilling by wood wasp ovipositors. *Biomimetics (USA)*. 1995.
7. Cerkvenik U, Dodou D, van Leeuwen JL, Gussekloo SW. Functional principles of steerable multi-element probes in insects. *Biological Reviews*. 2019;94(2):555-74. doi: 10.1111/brv.12467.
8. Ko SY, Davies BL, y Baena FR. Two-dimensional needle steering with a "programmable bevel" inspired by nature: Modeling preliminaries. 2010 IEEE/RSJ International Conference on Intelligent Robots and Systems; 2010: IEEE. doi: 10.1109/IROS.2010.5650859.
9. Misra S, Reed KB, Douglas AS, Ramesh K, Okamura AM. Needle-tissue interaction forces for bevel-tip steerable needles. 2008 2nd IEEE RAS & EMBS International Conference on Biomedical Robotics and Biomechatronics; 2008: IEEE. doi: 10.1109/BIOROB.2008.4762872.
10. Frasson L, Ko S, Turner A, Parittotokkaporn T, Vincent JF, Rodriguez y Baena F. STING: a soft-tissue intervention and neurosurgical guide to access deep brain lesions through curved trajectories. *Proceedings of the Institution of Mechanical Engineers, Part H: Journal of Engineering in Medicine*. 2010;224(6):775-88. doi: 10.1243/09544119JEM663.
11. Leibinger A, Oldfield MJ, Rodriguez y Baena F. Minimally disruptive needle insertion: a biologically inspired solution. *Interface focus*. 2016;6(3):20150107. doi: 10.1098/rsfs.2015.0107.
12. Scali M, Kreeft D, Breedveld P, Dodou D. Design and evaluation of a wasp-inspired steerable needle. *Proceedings of SPIE; Portland, Oregon, United States: International Society for Optics and Photonics*; 2017. p. 1016207.
13. Scali M, Breedveld P, Dodou D. Experimental evaluation of a self-propelling bio-inspired needle in single- and multi-layered phantoms. *Scientific reports*. 2019;9(1):1-13. doi: 10.1038/s41598-019-56403-0.
14. Scali M, Pusch T, Breedveld P, Dodou D. Ovipositor-inspired steerable needle: design and preliminary experimental evaluation. *Bioinspiration & Biomimetics*. 2017;13(1):016006. doi: 10.1088/1748-3190/aa92b9.
15. Bloemberg J, Hoppener B, Coolen B, Sakes A, Breedveld P. Design and evaluation of a pneumatic actuation unit for a wasp-inspired self-propelled needle. *PLoS ONE*. 2024;19(7):e0306411. doi: 10.1371/journal.pone.0306411.
16. Bloemberg J, Trauzettel F, Coolen B, Dodou D, Breedveld P. Design and evaluation of an MRI-ready, self-propelled needle for prostate interventions. *PLoS ONE*. 2022;17(9):e0274063. doi: 10.1371/journal.pone.0274063.
17. Bloemberg J, van Wees S, Kortman VG, Sakes A. Design of a wasp-inspired biopsy needle capable of self-propulsion and friction-based tissue transport. *Frontiers in Bioengineering and Biotechnology*. 2025;12:1497221. doi: 10.3389/fbioe.2024.1497221.

18. Parittotokkaporn T, Frasson L, Schneider A, Huq SE, Davies BL, Degenaar P, et al. Soft tissue traversal with zero net force: Feasibility study of a biologically inspired design based on reciprocal motion. 2008 IEEE International Conference on Robotics and Biomimetics; 2009: IEEE. doi: 10.1109/ROBIO.2009.4912983.
19. Scali M. Self-propelling needles: From biological inspiration to percutaneous interventions: Delft University of Technology; 2020. doi: 10.4233/uuid:523e3e5f-08f0-4acb-ab45-abaa7ace3967.
20. Frasson L, Ferroni F, Ko SY, Dogangil G, y Baena FR. Experimental evaluation of a novel steerable probe with a programmable bevel tip inspired by nature. *J Robot Surg.* 2012;6(3):189-97. doi: 10.1007/s11701-011-0277-4.
21. Oldfield MJ, Leibinger A, Seah TET, y Baena FR. Method to reduce target motion through needle-tissue interactions. *Annals of biomedical engineering.* 2015;43(11):2794-803. doi: 10.1007/s10439-015-1329-0.
22. Scali M, Pusch TP, Breedveld P, Dodou D. Needle-like instruments for steering through solid organs: A review of the scientific and patent literature. *Proceedings of the Institution of Mechanical Engineers, Part H: Journal of Engineering in Medicine.* 2017;231(3):250-65. doi: 10.1177/0954411916672149.
23. Gilbert HB, Neimat J, Webster RJ. Concentric tube robots as steerable needles: Achieving follow-the-leader deployment. *IEEE Transactions on Robotics.* 2015;31(2):246-58. doi: 10.1109/TRO.2015.2394331.
24. Parittotokkaporn T, Frasson L, Schneider A, Davies B, Degenaar P, y Baena FR. Insertion experiments of a biologically inspired microtextured and multi-part probe based on reciprocal motion. 2010 Annual International Conference of the IEEE Engineering in Medicine and Biology; 2010: IEEE. doi: 10.1109/IEMBS.2010.5627410.
25. Ko SY, y Baena FR. Toward a miniaturized needle steering system with path planning for obstacle avoidance. *IEEE Transactions on Biomedical Engineering.* 2012;60(4):910-7. doi: 10.1109/TBME.2012.2227741.
26. Burrows C, Secoli R, y Baena FR. Experimental characterisation of a biologically inspired 3D steering needle. 2013 13th International Conference on Control, Automation and Systems (ICCAS 2013); 2013: IEEE. doi: 10.1109/ICCAS.2013.6704141.
27. Burrows C, Liu F, Leibinger A, Secoli R, Rodriguez y Baena F. Multi-target planar needle steering with a bio-inspired needle design. *Advances in Italian Mechanism Science: Springer;* 2017. p. 51-60.
28. Aktas A, Demircali AA, Secoli R, Temelkuran B, Rodriguez y Baena F. Towards a procedure-optimised steerable catheter for deep-seated neurosurgery. *Biomedicines.* 2023;11(7):2008. doi: 10.3390/biomedicines11072008.
29. Bloemberg J, Fung-A-Jou Z, Breedveld P, Sakes A. Design and evaluation of a ball spline wasp-inspired needle. *Frontiers in Bioengineering and Biotechnology.* 2024;12:1468605. doi: 10.3389/fbioe.2024.1468605
30. Smith S, Hodgson E. Shape setting nitinol. *Proceedings of the Materials and Processes for Medical Devices Conference;* 2004. doi: 10.1361/cp2003mpmd266.
31. Mueller S, Sandrin L. Liver stiffness: a novel parameter for the diagnosis of liver disease. *Hepatic medicine: evidence and research.* 2010;49-67. doi: 10.2147/HMER.S7394.
32. Zhang M, Nigwekar P, Castaneda B, Hoyt K, Joseph JV, di Sant'Agnese A, et al. Quantitative characterization of viscoelastic properties of human prostate correlated with histology. *Ultrasound in medicine & biology.* 2008;34(7):1033-42. doi: 10.1016/j.ultrasmedbio.2007.11.024.
33. Ng KW, Goh JQ, Foo SL, Ting PH, Lee TK, Esuvaranathan K, et al. Needle deflection studies for optimal insertion modeling. *International Journal of Bioscience, Biochemistry and Bioinformatics.* 2013;3(6):570. doi: 10.7763/IJBBB.2013.V3.278.
34. Swensen JP, Cowan NJ. Torsional dynamics compensation enhances robotic control of tip-steerable needles. 2012 IEEE International Conference on Robotics and Automation: IEEE; 2012. p. 1601-6.



35. Bui VK, Park S, Park J-O, Ko SY. A novel curvature-controllable steerable needle for percutaneous intervention. *Proceedings of the Institution of Mechanical Engineers, Part H: Journal of Engineering in Medicine*. 2016;230(8):727-38. doi: 10.1177/0954411916648988.
36. van Gerwen DJ, Dankelman J, van den Dobbelsteen JJ. Needle-tissue interaction forces—A survey of experimental data. *Medical engineering & physics*. 2012;34(6):665-80. doi: 10.1016/j.medengphy.2012.04.007.
37. Adebar TK, Greer JD, Laeseke PF, Hwang GL, Okamura AM. Methods for improving the curvature of steerable needles in biological tissue. *IEEE Transactions on Biomedical Engineering*. 2015;63(6):1167-77. doi: 10.1109/TBME.2015.2484262.
38. Deurloo EE, Gilhuijs KG, Kool LJS, Muller SH. Displacement of breast tissue and needle deviations during stereotactic procedures. *Investigative radiology*. 2001;36(6):347-53.
39. Misra S, Ramesh K, Okamura AM. Modeling of tool-tissue interactions for computer-based surgical simulation: A literature review. *Presence*. 2008;17(5):463-91. doi: 10.1162/pres.17.5.463.
40. Gidde STR, Acharya SR, Kandel S, Pleshko N, Hutapea P. Assessment of tissue damage from mosquito-inspired surgical needle. *Minimally Invasive Therapy & Allied Technologies*. 2022;31(7):1112-21. doi: 10.1080/13645706.2022.2051718.
41. de Vries M, Sikorski J, Misra S, van den Dobbelsteen JJ. Axially rigid steerable needle with compliant active tip control. *PLoS ONE*. 2021;16(12):e0261089. doi: 10.1371/journal.pone.0261089.
42. van Riel LA, van Kollenburg RA, Vis AN, van Leeuwen PJ, de Reijke TM, de Bruin DM, Oddens JR. Safety and feasibility of Soractelite transperineal focal laser ablation for prostate cancer and short-term quality of life analysis from a multicenter pilot study. *European urology open science*. 2022;39:48-54. doi: 10.1016/j.euros.2022.02.012.

## Appendix 6.A Needle propulsion efficiency

In the scientific literature, wasp-inspired needle designs that can be advanced through the tissue without applying an external push force have been proposed. The needles consist of multiple parallel segments that can slide with respect to each other. A bundling mechanism holds the needle segments together at the tip to limit the diverging of the needle segments. The self-propelled motion is achieved by counterbalancing the cutting and friction force of the advancing segments with the friction force generated by the stationary or retracting segments [1]. To achieve the self-propelled motion of the needle, Eq. 6.A1 must hold.

$$\sum_{i=1}^a (\mathbf{F}_{\text{fric},i} + \mathbf{F}_{\text{cut},i}) \leq \sum_{j=1}^r (\mathbf{F}_{\text{fric},j}) \quad (6.A1)$$

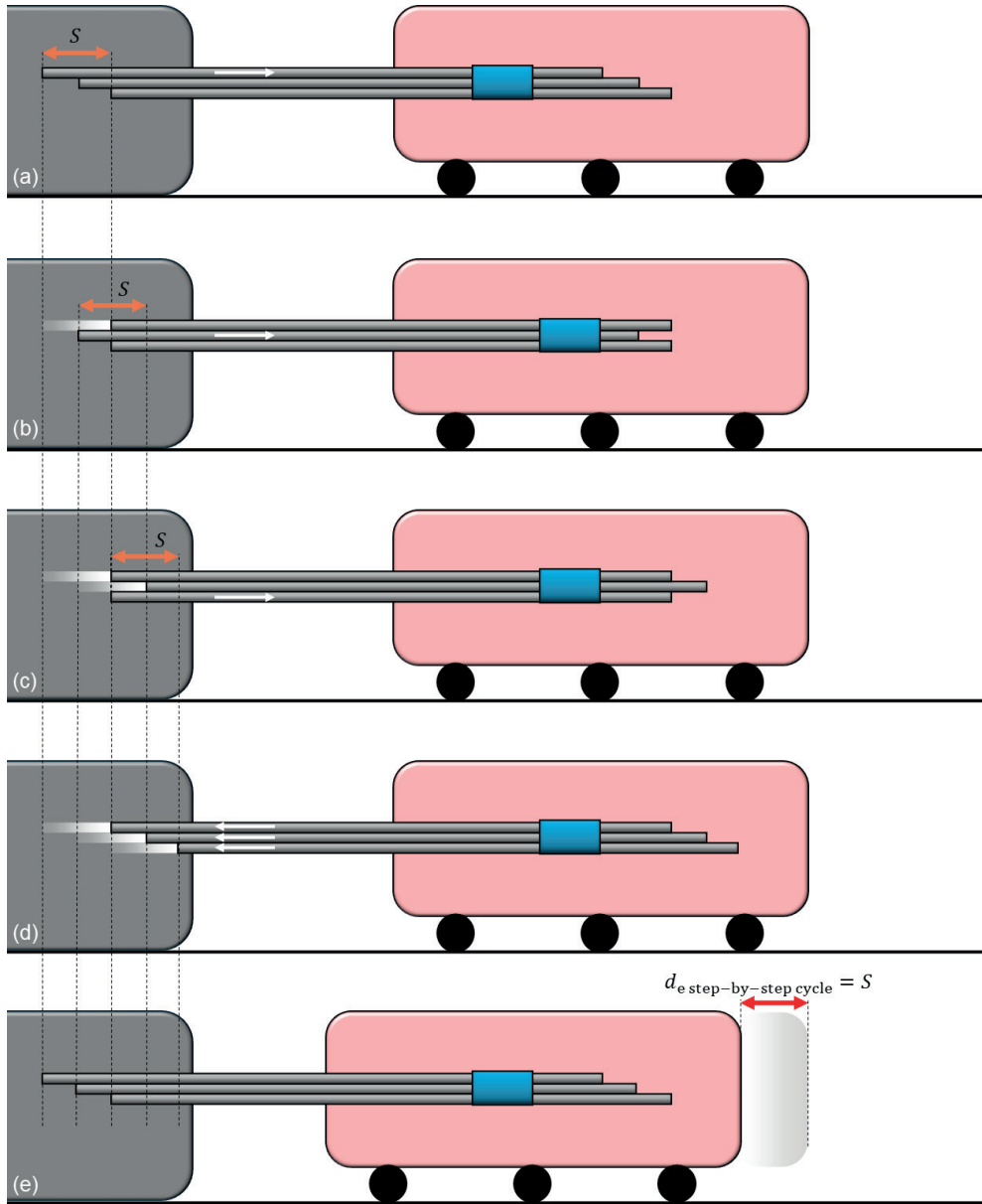
where  $a$  is the number of advancing needle segments,  $r$  is the number of stationary or retracting needle segments, and  $\mathbf{F}_{\text{fric}}$  and  $\mathbf{F}_{\text{cut}}$  are the friction and cutting force, respectively. For the self-propelled motion to occur, the friction force of the stationary or retracting needle segments with the surrounding tissue should be equal to the sum of the friction and cutting forces of the advancing needle segments with the surrounding tissue, which can be achieved by keeping the number of advancing needle segments smaller than the number of stationary or retracting needle segments ( $a < r$ ) amongst others. This way, the stationary or retracting needle segments remain stationary with respect to the tissue, whilst the advancing segment moves forward into the tissue. Assuming equal friction between all needle segments and the surrounding tissue, the wasp-inspired self-propelled needle requires at least three parallel needle segments, of which two segments either remain stationary or retract, while one segment advances to achieve self-propulsion.

### 6.A.2 Actuation mode

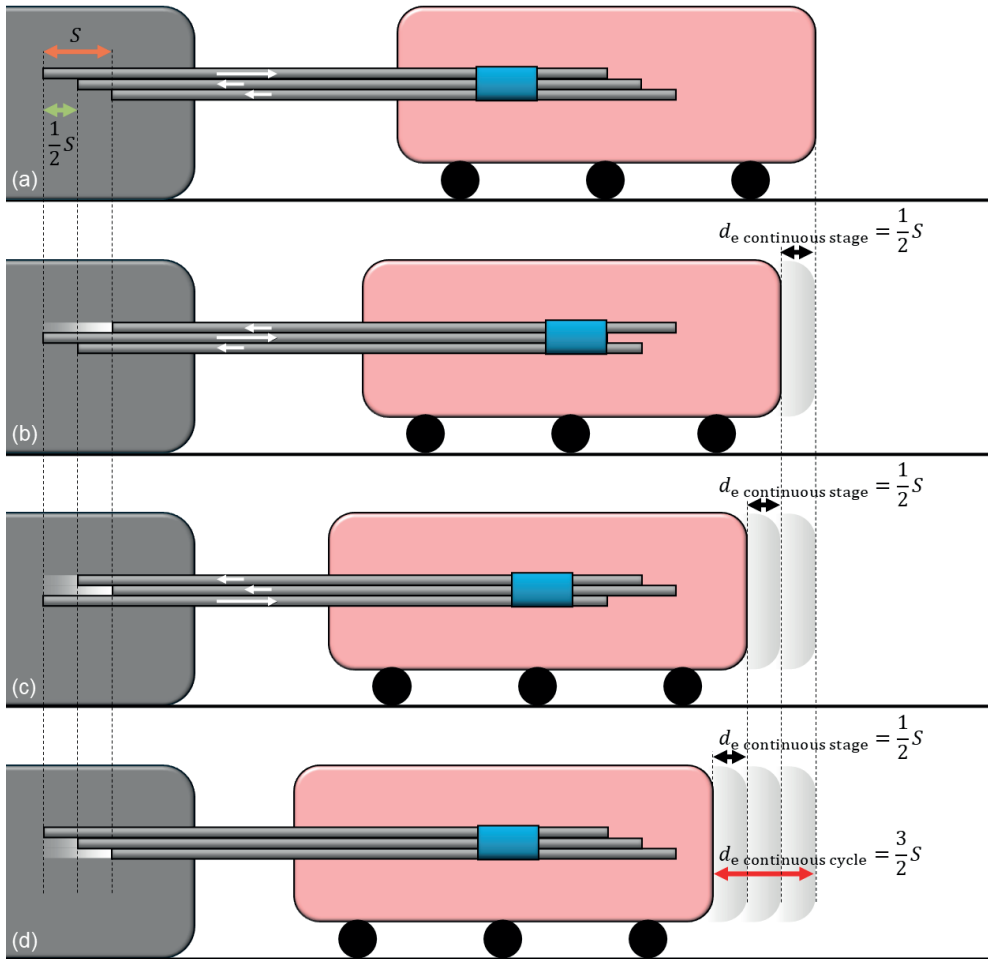
The needle segments of wasp-inspired needles in the scientific literature are actuated using one of the following two actuation modes: (1) step-by-step motion and (2) continuous motion. In the first actuation mode, called the “step-by-step motion” (Figure 6.A1), the needle segments advance one by one over a pre-defined distance, called the “stroke”. Once all needle segments have reached that distance, they simultaneously retract over the same stroke distance. The two-phase motion sequence, which involves advancing the needle segments one by one followed by retracting all needle segments simultaneously, is referred to as a “cycle”. In the scientific literature, several needle designs were actuated following the step-by-step motion sequence [2-4].

In the second actuation mode, called the continuous motion (Figure 6.A2), the needle segments move simultaneously and are always in motion. In this motion sequence, one needle segment advances over the stroke distance, while the other needle segments retract. For a needle consisting of three needle segments, this means that during every stage of the motion, one needle segment advances over the stroke distance while the remaining two segments retract over half the stroke distance. During one cycle, all needle segments have advanced over the stroke distance in one stage and retracted over the stroke distance in multiple stages.





**Figure 6.A1. Visualization of the step-by-step motion sequence for a self-propelled needle**, consisting of three parallel needle segments (light gray) bundled by a bundling mechanism (blue) actuated by the actuation system (dark gray) to propel through tissue (pink) on a low-friction cart (black).  $S$  is the stroke distance, over which the needle segments are advanced and  $d_{\text{e step-by-step cycle}}$  is the expected propulsion distance of the needle after one cycle by following the step-by-step motion sequence, which is equal to the stroke distance. The rows show the subsequent steps in the step-by-step motion cycle. (a) Segment 1 moves forward over  $S$ . (b) Segment 2 moves forward over  $S$ . (c) Segment 3 moves forward over  $S$ . (d) All segments are retracted over  $S$ . (e) Final position after one cycle.



**Figure 6.A.2. Visualization of the continuous motion sequence for a self-propelled needle**, consisting of three parallel needle segments (light gray) bundled by a bundling mechanism (blue) actuated by the actuation system (dark gray) to propel through tissue (pink) on a low-friction cart (black).  $S$  is the stroke distance, over which the needle segments are advanced per cycle,  $d_{e \text{ continuous stage}}$  is the expected propulsion distance of the needle after one stage of the cycle by following the continuous motion sequence, and  $d_{e \text{ continuous cycle}}$  is the expected propulsion distance of the needle after one cycle by following the continuous motion sequence, which is equal to  $3/2 S$ . The rows show the subsequent stages in the continuous motion cycle. (a) Segment 1 moves forward over  $S$ , whilst Segments 2 and 3 move backward over  $1/2 S$ . (b) Segment 2 moves forward over  $S$ , whilst Segments 1 and 3 move backward over  $1/2 S$ . (c) Segment 3 moves forward over  $S$ , whilst Segments 1 and 2 move backward over  $1/2 S$ . (d) Final position after one cycle.

In the scientific literature, several needle and tissue transport designs were actuated following the continuous motion sequence [5-8] (and the first additional experiment in [2]).

### 6.A.3 Propulsion efficiency

In order to determine the slip ratio or the efficiency of the needle propulsion, the amount of slip between the needle segments and the tissue (phantom) can be measured. The propulsion



efficiency can be computed by dividing the measured propulsion distance of the needle,  $d_m$ , by the expected propulsion distance of the needle,  $d_e$ , as in Eq. 6.A2.

$$\eta = \frac{d_m}{d_e} \cdot 100\% \quad (6.A2)$$

The slip ratio of the needle can be calculated as in Eq. 6.A3.

$$s_{\text{ratio}} = 1 - \left(\frac{d_m}{d_e}\right) \quad (6.A3)$$

The expected propulsion distance of the needle per cycle depends on the actuation mode and the stroke length. For the step-by-step motion, the expected propulsion distance of the needle per cycle is equal to the stroke length ( $d_{\text{e step-by-step cycle}} = S$ ). However, for the continuous motion, the expected propulsion distance of the needle per cycle depends on the stroke length and on the number of simultaneously advancing and retracting needle segments during one stage of the cycle, as in Eq. 6.A4. Here, we assume that the retracting needle segments remain stationary with respect to the tissue and the advanced segment moves forward. Therefore, for continuous motion, the expected propulsion distance of the needle per cycle exceeds the stroke length, as in Eq. 6.A5.

$$d_{\text{e continuous stage}} = \left(\frac{a}{r}\right) \cdot S \quad (6.A4)$$

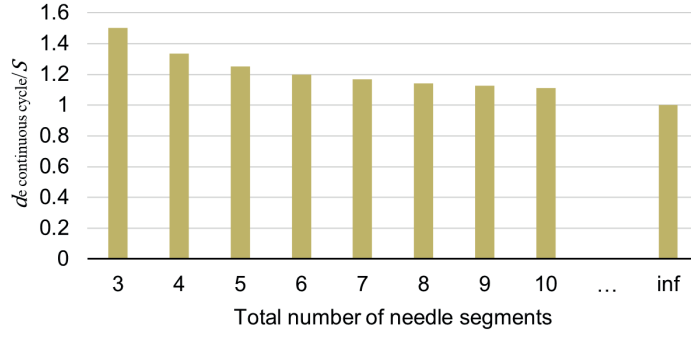
$$d_{\text{e continuous cycle}} = \left(\frac{n}{r}\right) \cdot S \quad (6.A5)$$

where  $n$  is the total number of needle segments,  $a$  is the number of advancing needle segments,  $r$  is the number of retracting needle segments, and  $S$  is the stroke length.

Consequently, for continuous motion, increasing the number of needle segments decreases the ratio of the total number of needle segments (i.e.,  $a + r = n$ ) to the number of retracting needle segments (i.e.,  $r$ ) and, therefore, decreases the expected propulsion distance. More specifically, the expected propulsion distance divided by the stroke over the total number of needle segments will approach a horizontal asymptote at  $(d_{\text{e continuous cycle}})/S = 1$  (Figure 6.A3). The expected propulsion distance per cycle for continuous motion approaches the expected propulsion distance per cycle for step-by-step motion, which is equal to the stroke distance if the number of needle segments increases whilst keeping the advancing needle segments at one.

#### 6.A.4 Expected velocity

During the insertion of a needle in tissue, the velocity of the needle impacts tissue deformation and damage. Mahvash *et al.* [9] showed that maximizing the needle velocity minimizes tissue deformation and damage and, consequently, results in less needle insertion position error. For wasp-inspired self-propelled needles, the expected needle velocity ( $v_{Ne}$ ) and therefore also the actual insertion velocity of the needle depends on the actuation mode, the number of parallel needle segments, and the actuation velocity of the individual needle segments ( $v_s$ ). Given the same actuation velocity of the individual needle segments and the same number of needle segments, the expected needle velocity for the step-by-step motion (Eq. 6.A6) is lower than that for the continuous motion (Eq. 6.A7), which is caused by the lower expected actuation



**Figure 6.A3. The expected propulsion distance divided by the stroke distance for the continuous motion.**  $d_{e \text{ continuous cycle}}$  is the expected propulsion distance per cycle for continuous motion,  $S$  is the stroke distance over which the needle segments are advanced per cycle, and “inf” means an infinite number of needle segments. When the total number of needle segments increases while keeping the number of advancing needle segments at one, the expected propulsion distance per cycle over the stroke approaches a horizontal asymptote at  $d_{e \text{ continuous cycle}} / S = 1$ .

efficiency for the step-by-step motion (Eq. 6.A8) compared to that of the continuous motion (Eq. 6.A9).

$$v_{N \text{ e step-by-step}} = \frac{\Delta x}{\Delta t} = \frac{d_{e \text{ step-by-step cycle}}}{t_{n+1} - t_0} = \frac{S}{(n+1) \cdot \frac{S}{v_s}} = \frac{v_s}{n+1} \quad (6.A6)$$

$$v_{N \text{ e continuous}} = \frac{\Delta x}{\Delta t} = \frac{d_{e \text{ continuous cycle}}}{t_n - t_0} = \frac{\frac{n}{r} S}{n \cdot \frac{S}{v_s}} = \frac{v_s}{r} \quad (6.A7)$$

$$\eta_{A \text{ e step-by-step}} = \frac{1}{n+1} \cdot 100\% \quad (6.A8)$$

$$\eta_{A \text{ e continuous}} = \frac{1}{r} \cdot 100\% \quad (6.A9)$$

where  $d_{e \text{ step-by-step cycle}}$  is the expected propulsion distance of the needle per cycle for the step-by-step motion,  $d_{e \text{ continuous cycle}}$  is the expected propulsion distance of the needle per cycle for the continuous motion,  $t$  is the time at a certain step or stage in the motion cycle,  $S$  is the stroke distance,  $n$  is the total number of needle segments, and  $r$  is the number of retracting needle segments.

## References

1. Scali M. Self-propelling needles: From biological inspiration to percutaneous interventions: Delft University of Technology; 2020. doi: 10.4233/uuid:523e3e5f-08f0-4acb-ab45-abaa7ace3967.
2. Scali M, Breedveld P, Dodou D. Experimental evaluation of a self-propelling bio-inspired needle in single-and multi-layered phantoms. Scientific reports. 2019;9(1):1-13. doi: 10.1038/s41598-019-56403-0.
3. Scali M, Kreeft D, Breedveld P, Dodou D. Design and evaluation of a wasp-inspired steerable needle. Proceedings of SPIE; Portland, Oregon, United States: International Society for Optics and Photonics; 2017. p. 1016207.
4. Bloemberg J, Hoppener B, Coolen B, Sakes A, Breedveld P. Design and evaluation of a pneumatic actuation unit for a wasp-inspired self-propelled needle. PLoS ONE. 2024;19(7):e0306411. doi:

10.1371/journal.pone.0306411.

5. Bloemberg J, Trauzettel F, Coolen B, Dodou D, Breedveld P. Design and evaluation of an MRI-ready, self-propelled needle for prostate interventions. *PLoS ONE*. 2022;17(9):e0274063. doi: 10.1371/journal.pone.0274063.

6. de Kater EP, Sakes A, Bloemberg J, Jager DJ, Breedveld P. Design of a flexible wasp-inspired tissue transport mechanism. *Frontiers in Bioengineering and Biotechnology*. 2021;9:782037. doi: 10.3389/fbioe.2021.782037/full.

7. Sakes A, Van de Steeg IA, De Kater EP, Posthoorn P, Scali M, Breedveld P. Development of a novel wasp-inspired friction-based tissue transportation device. *Frontiers in Bioengineering and Biotechnology*. 2020;8:575007. doi: 10.3389/fbioe.2020.575007.

8. Bloemberg J, van Wees S, Kortman VG, Sakes A. Design of a wasp-inspired biopsy needle capable of self-propulsion and friction-based tissue transport. *Frontiers in Bioengineering and Biotechnology*. 2025;12:1497221. doi: 10.3389/fbioe.2024.1497221.

9. Mahvash M, Dupont PE. Fast needle insertion to minimize tissue deformation and damage. 2009 IEEE International Conference on Robotics and Automation; 2009; Kobe, Japan: IEEE. doi: 10.1109/ROBOT.2009.5152617.

---

## PART 3.

### ACTUATION DESIGN

From Experimental Facility to MRI Compatibility







# 7

## Exploring Wasp-Inspired Manual Actuation

Published as:

Bloemberg J., Trauzettel F., Coolen B., Dodou D., Breedveld P. (2022). Design and evaluation of an MRI-ready, self-propelled needle for prostate interventions. PLoS ONE, 17(9):e0274063. doi: 10.1371/journal.pone.0274063.





## 7.1 Introduction

### 7.1.1 Focal laser ablation

Prostate cancer is the second most common cancer diagnosed in men and the fifth leading cause of cancer-related deaths for men worldwide in 2020 [1]. When prostate cancer is diagnosed at an early stage, it can be treated locally using focal therapy that reduces the risk of side effects by preserving noncancerous tissue [2]. Focal laser ablation of the prostate is an appealing focal therapy option as it leads to homogeneous tissue necrosis caused by a laser fiber and does not appear to alter the sexual and urinary function of the patient [3].

Prostate cancer diagnosis and focal laser ablation require needle insertion to obtain core biopsies [4, 5] and position optical fibers near the target zone [6]. To this end, the clinician inserts the needle by pushing it through the tissue, which might lead to tissue strain in the needle vicinity [7], which in turn might cause functional damage to the surrounding tissues and organs [8], including the urethra, the rectum's anterior wall, and the pelvic sidewall [9]. Moreover, tissue motion and deformation might lead to needle positioning errors and poor control of the needle path [10]. As a result, clinicians typically need multiple attempts to reach the target location, leading to an increased risk of tissue damage [7]. Moreover, pushing the needle through the tissue requires an axial force on the needle. When this axial force exceeds the needle's critical load, the needle will deflect laterally—a phenomenon called buckling [11]. The lateral deflection might damage tissue in the needle vicinity and lead to poor control of the needle path [12, 13].

### 7.1.2 State-of-the-art in self-propelled needles

In an attempt to reduce tissue damage during needle insertion, needle designs have been developed that can be advanced without being pushed through the tissue. For instance, Ilami *et al.* [14] developed a needle with a magnetic tip that utilizes electromagnetic force and torque actuation to advance the needle through the tissue. Schwehr *et al.* [15] proposed a needle design that likewise utilizes electromagnetic torque to steer combined with a screw tip to allow the needle to pull itself through the tissue. A disadvantage of needle designs that utilize an electromagnetic field is that they are not compatible with Magnetic Resonance Imaging (MRI). Besides electromagnetically actuated needles, wasp-inspired self-propelled needles have been developed [7, 16–18]. Female parasitic wasps pass their eggs through an ovipositor into their hosts, which sometimes hide in a solid substrate such as wood [19]. The tube-like ovipositor consists of three slender, parallel-positioned segments, called valves [20], which advance and retract with respect to each other in a reciprocating manner [20] (Figure 7.1a). A groove-and-tongue mechanism interlocks the valves along their length [21, 22]. The advancing-retracting motion of the valves has two functions. First, it keeps the unsupported length of the individual valves low [11]. Second, moving the individual valves forward one by one while retracting the others provides stability to the wasp's ovipositor and prevents buckling [11, 23]. The advancement and retraction forces produce a net force near zero, enabling a



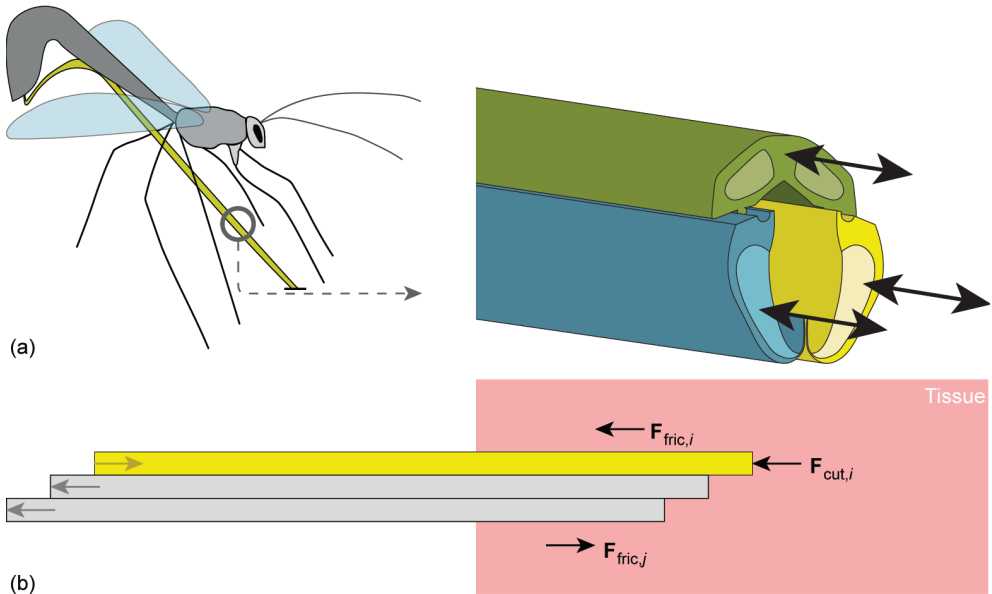
self-propelled motion.

Self-propelled needles do not require an external push force to advance through the tissue. They consist of multiple parallel segments that can slide along each other. The self-propelled motion is achieved by counterbalancing the cutting and friction force of the advancing segments by the friction force generated by other stationary or retracting segments [18]. For a self-propelled motion of the needle, Eq. 7.1 holds:

$$\sum_{i=1}^p (\mathbf{F}_{\text{fric},i} + \mathbf{F}_{\text{cut},i}) \leq \sum_{j=1}^r (\mathbf{F}_{\text{fric},j}) \quad (7.1)$$

where  $p$  is the number of advancing needle segments,  $r$  is the number of retracting needle segments, and  $\mathbf{F}_{\text{fric}}$  and  $\mathbf{F}_{\text{cut}}$  are the friction and cutting force, respectively (Figure 7.1b). For the self-propelled motion to occur, the friction force of the retracting needle segments should counterbalance the sum of the friction and cutting forces of the advancing needle segments. In this way, the needle as a whole self-propels through the tissue by gradually moving the needle segments forward.

Worldwide, a number of ovipositor-inspired needles have been developed so far. Oldfield *et al.* [24], Frasson *et al.* [25], and Leibinger *et al.* [7] showed that tissue motion and damage around a needle are reduced when using a multi-segmented needle actuated with a reciprocal advancing-retracting motion compared to pushing the needle as a whole through the tissue.



**Figure 7.1. Visualization of the motion sequence of the ovipositor of a parasitic wasp.** (a) The ovipositor consists of three parallel valves that can move reciprocally (based on Cerkenik *et al.* [20]). (b) Schematic illustration of ovipositor-inspired needle insertion into tissue with one advancing needle segment (yellow) and two retracting needle segments (gray).  $\mathbf{F}_{\text{fric},i}$  is the friction force along the advancing needle segment,  $\mathbf{F}_{\text{cut},i}$  is the cutting force on the tip of the advancing needle segment, and  $\mathbf{F}_{\text{fric},j}$  is the friction of the retracting needle segments, which works in the opposite direction as the friction force of the advancing needle segments.

Parittotokkaporn *et al.* [23] showed that probes with a directional friction pattern inspired by the wasp ovipositor, actuated with an advancing-retracting motion, could move tissue along the needle surface without applying an external push force to the tissue. Scali *et al.* [26, 27] replaced the complex-shaped interlocking groove-and-tongue mechanism of the wasp valves with nitinol rods devoid of serrations and bundled by a shrinking tube, resulting in an ultrathin 0.4-mm diameter needle with six longitudinal segments [27]. Actuated by electric motors, the needle self-propels without buckling by advancing one needle segment at a time and slowly retracting the other five segments [26]. Furthermore, it is possible to steer the needle by inducing an offset between the needle segments, creating a discrete bevel-shaped tip [26].

### 7.1.3 Goal of this study

Wasp-inspired self-propelled needles could enable the clinician to reach the target tissue while avoiding unwanted tissue damage in and around the prostate. To guide needle positioning for focal laser ablation, MRI is an attractive imaging option because it provides visualization of the target zone and real-time temperature monitoring [28, 29]. Current prototypes of wasp-inspired self-propelled needles use electric motors to actuate the individual needle segments [18, 25]. These needles cannot be used in MRI-guided procedures, as the electric motors interfere with the magnetic field. The aim of this research was, therefore, to design an MR-safe actuation system for a self-propelled needle and to evaluate its performance in human prostate tissue.

## 7.2 Design

### 7.2.1 Design requirements

The complete design, called Ovipositor MRI-Needle, consists of a needle and an actuation unit. Following the design of Scali *et al.* [27], we decided to focus our research on a self-propelled wasp-inspired needle consisting of six parallel needle segments with a central lumen. To reach the prostate transperineally [30], we opted for a needle length of 200 mm. To comply with conventional needles used for optical biopsy and optical treatment fiber positioning [6], we used a maximum needle diameter of 1 mm. To enable evaluation in a closed-bore preclinical 7-T MRI system (MR Solutions, Guildford, United Kingdom) with an inner diameter of the RadioFrequency (RF) coil of 65 mm, we developed an actuation unit fitting within this coil, the actuation unit's diameter not exceeding 65 mm, and the actuation unit containing a 2-mm diameter central hollow core to allow insertion of a functional element, such as an optical fiber. Finally, the materials used in the needle and the actuation unit are MRI-compatible to allow placing them inside the MRI system.

### 7.2.2 Overall system design

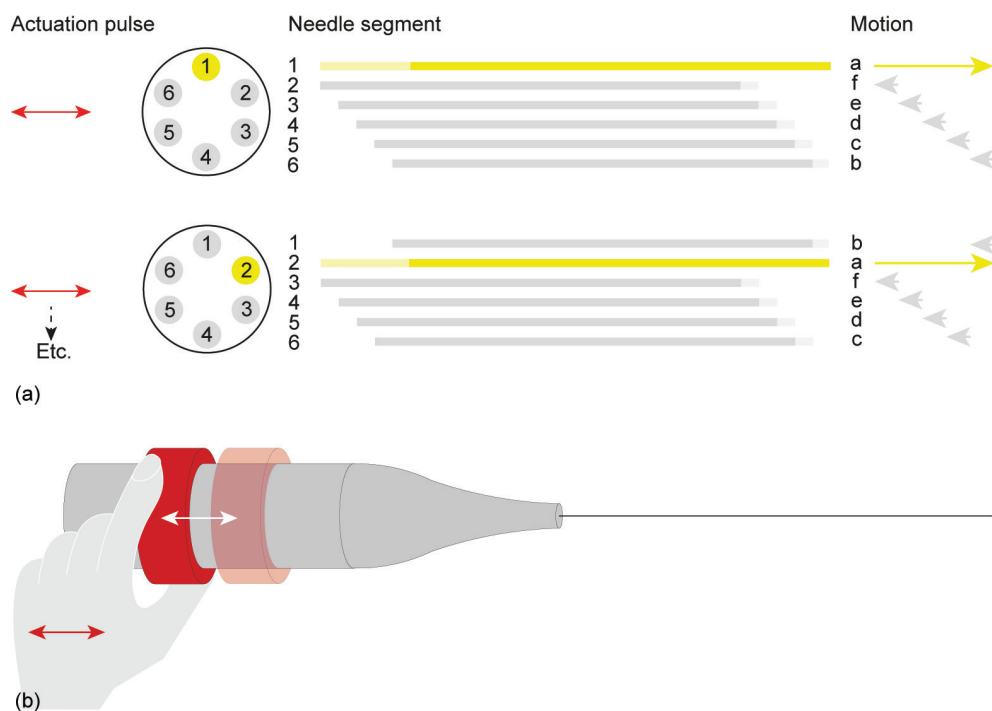
The needle's self-propelled motion requires a sequential translation of the six needle segments



in six steps per cycle. During every step of the motion, one needle segment moves forward over a specified distance called the “stroke,” while the other five needle segments move slowly backward over one-fifth of the stroke distance (Figure 7.2a). The needle segments are continuously in motion in order to apply a constant strain to the surrounding tissue. We opted for a manually controlled actuation unit that allows the operator to drive the needle in simple discrete actuation steps, avoiding the need to set the exact advancing or retracting distance for each needle segment during each actuation step. Figure 7.2b shows how the operator drives the actuation unit by a stepwise manual translation of a translation ring (in red). The actuation unit converts the reciprocating motion of the translation ring into a global rotating motion of an internal selector, after which the selector selects and actuates the needle segments in the required order and over the required distance.

### Selector

The design of the selector is based on the so-called click-pen mechanism of a ballpoint pen, Figure 7.3 [31]. The click-pen mechanism converts the discrete motion of pressing the button at the end of the pen into a rotation and a subsequent translation of the ballpoint tip. Fig-



**Figure 7.2. Visualization of the motion sequence of the needle segments.** (a) During the motion, one needle segment moves forward over the stroke distance while the other needle segments move slowly backward over one-fifth of the stroke distance in a consecutive manner. (b) Manual translation of a translation ring (red) drives the actuation system. The actuation system converts the reciprocating motion of the translation ring into a sequential translation of the six needle segments.

ure 7.4 shows the working principle of our selector (in green). The cylindrical mechanism is simplified and visualized in a two-dimensional (2D) schematic illustration to explain the working principle. The columns in Figure 7.4 show the subsequent steps in the motion cycle. The rows in Figure 7.4 show the different layers of the selector. The selector (Figures 7.4a-d) contains two sets of aligned teeth. A fixed housing (in gray) also contains two sets of teeth. For the housing, the teeth at the right are shifted over half a tooth width. The selector is actuated by the input motion: a reciprocating translating motion in the horizontal x-direction. When the operator moves the selector in the positive x-direction (Figure 7.4a), the teeth on the right side of the selector come in contact with the teeth on the right side of the housing (Figure 7.4b, the interacting teeth of the housing are indicated in dark gray). The interaction between the teeth causes the selector to move in the negative y-direction over half the pitch distance of the teeth until the selector motion is blocked by the teeth so that it cannot move any further. In the following step, the selector is moved in the negative x-direction (Figure 7.4c) until the selector's left teeth come in contact with the housing's left teeth (Figure 7.4d), causing the selector to move again in the negative y-direction over half the teeth' pitch distance until the motion is again blocked. The interaction between the teeth of the selector and the housing converts the reciprocating horizontal motion that actuates the selector into a stepwise vertical translation.

#### Cam

Figures 7.4e-h show how the selector contains small protruding cylinders (in dark green) that can slide in straight horizontal slots in a cam (in orange). The housing prevents the cam

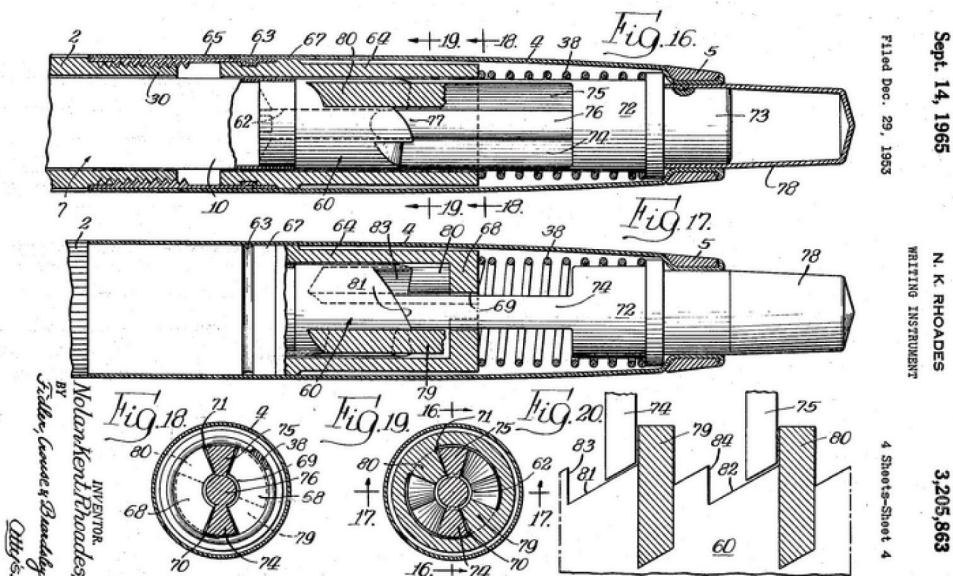
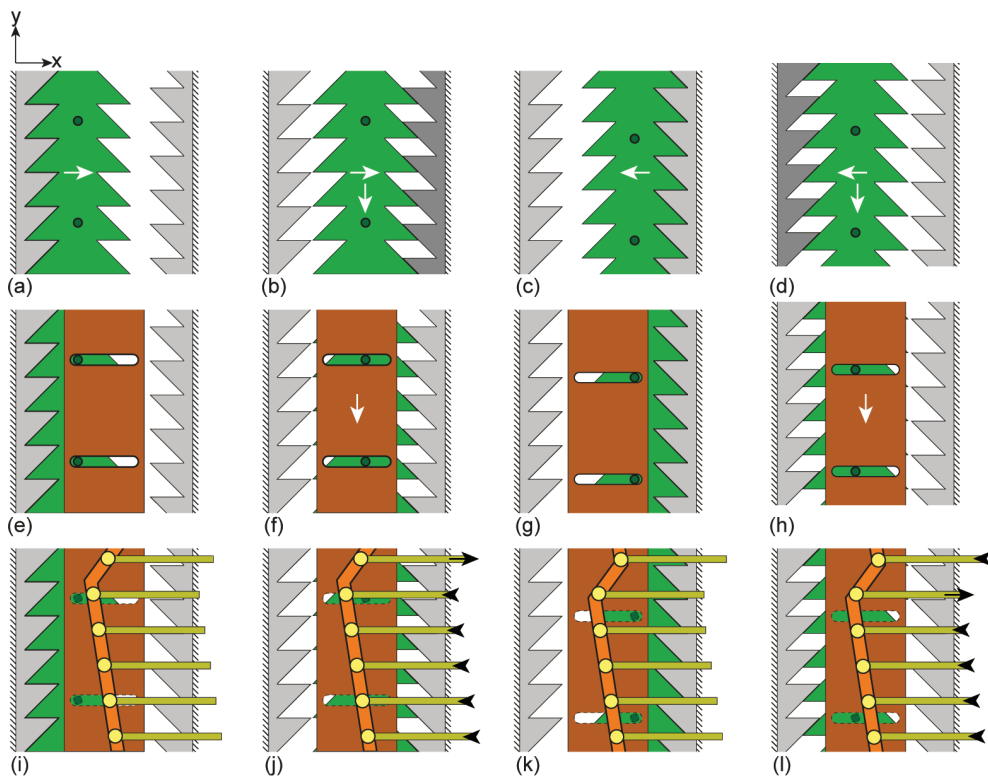


Figure 7.3. Click-pen mechanism of a ballpoint pen. Illustration of one of the first patented click-pen mechanisms (Parker Pen Co Ltd) [31].





**Figure 7.4.** Schematic representation of the selector motion mechanism in 2D, including the selector (green), housing (gray), cam (orange), and needle segment holders (yellow). The columns show the subsequent steps in the motion cycle. The rows show the different layers of the selector.

from translating in the horizontal  $x$ -direction. When the selector is translated in the positive or negative  $x$ -direction, the protruding cylinders transmit the selector's stepwise translation in the  $y$ -direction to the cam. Figures 7.4i-l show that the cam contains a V-shaped slot (in light orange). Six needle segment holders (Figures 7.4i-l, in yellow) contain small protruding cylinders (in light yellow) that can slide in the cam's V-shaped slot. The housing restricts the motion of the needle segment holders to a translation in the  $x$ -direction driven by the motion of the V-shaped slot. The asymmetric shape of the V causes one needle segment holder to move in the positive  $x$ -direction, with the other needle segment holders moving slowly in the negative  $x$ -direction.

#### *Working principle in 3D*

The stepwise translation of the selector in the  $y$ -direction in the simplified 2D illustration in Figure 7.4 is, in reality, a stepwise rotation around the  $x$ -axis in 3D. Figure 7.5 shows the 3D working principle of the selector (in green), surrounded by a concentric housing (in gray) and driving the six needle segment holders (in yellow) via the cam (in orange). The inside of the mechanism contains a hollow core to introduce additional instrumentation. The housing

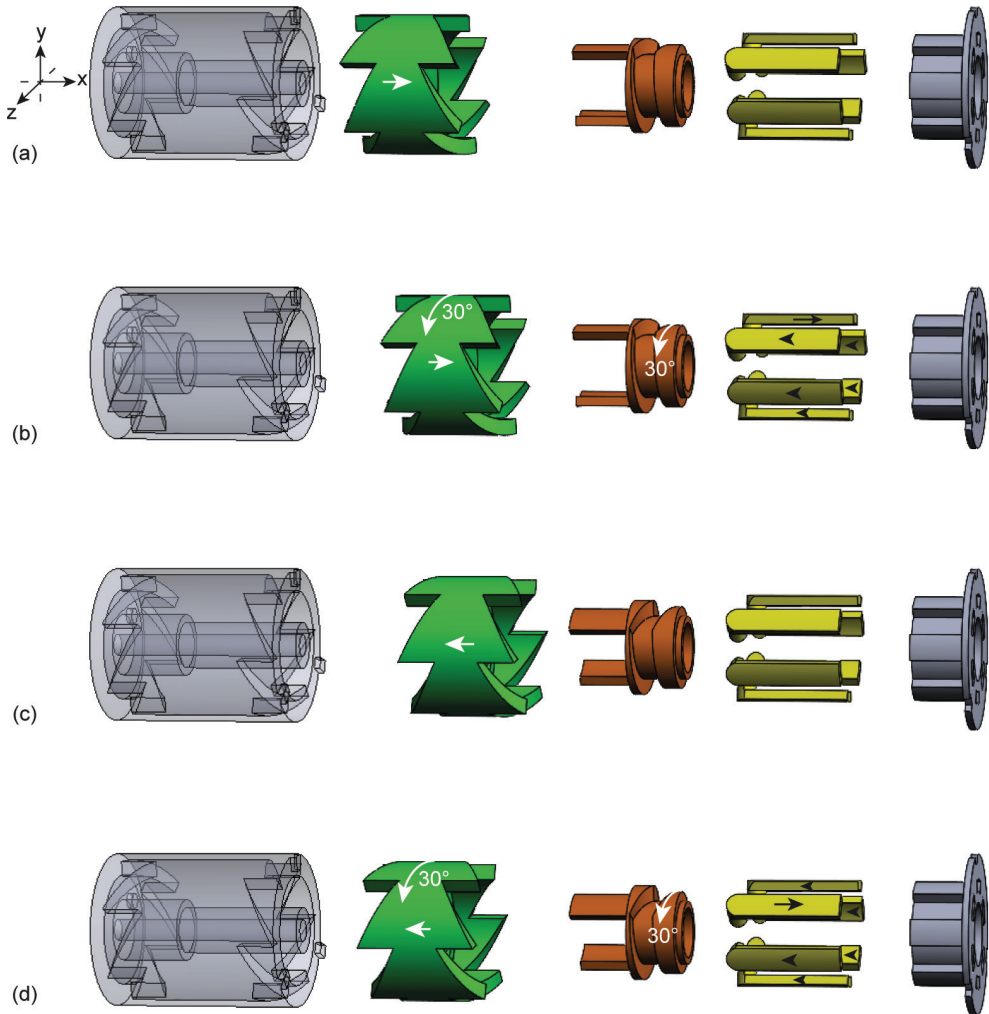


Figure 7.5. Schematic motion sequence of the selector in 3D, including the selector (green), housing (gray), cam (orange), and needle segment holders (yellow).

and the selector both contain six teeth on the left and right sides. Therefore, the selector's translation in the positive or negative x-direction results in a  $30^\circ$  rotation around its x-axis as the selector slides over half the pitch distance of the teeth.

We designed the actuation unit using Solidworks (Dassault Systems Solidworks Corporation; Waltham, MA, USA). To facilitate the manual actuation of the selector, we added a translation ring to the actuation unit (Figure 7.6, Part 4 in red). The operator drives the translation ring with a reciprocating translating motion. Cylindrical pins on the translation ring interact with a circumferential slot in the selector, transmitting the translating motion in the x-direction while allowing the selector to rotate without the need for the operator's hand

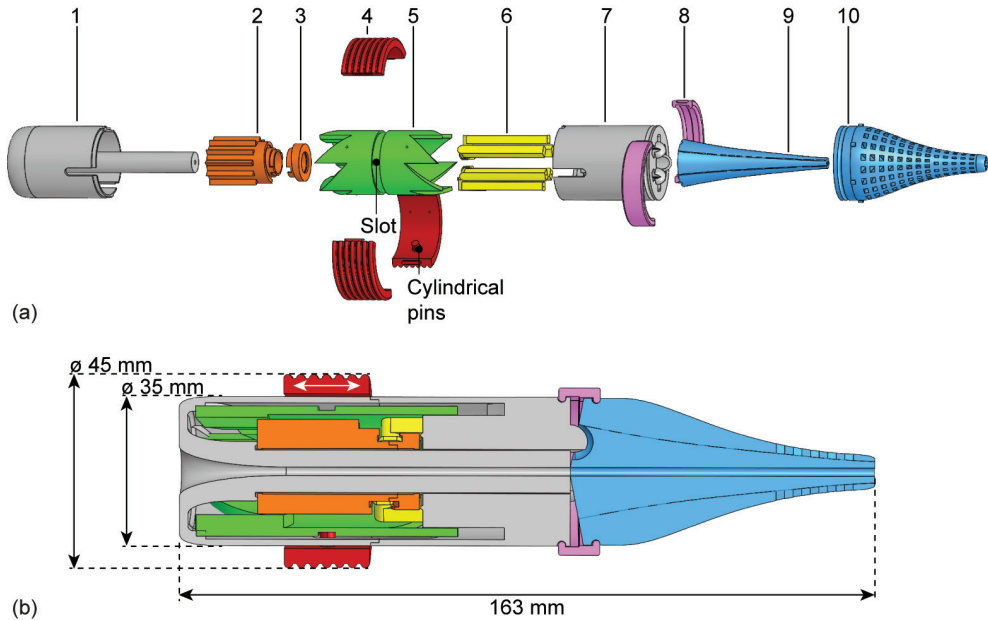


Figure 7.6. Exploded view (a) and cross-section (b) of the actuation unit of the Ovipositor MRI-Needle, consisting of a housing bottom (1), cam bottom (2), cam top (3), translation ring (4), selector (5), needle segment holder (6), housing top (7), lock ring (8), inner double cone (9), and outer double cone (10).

to rotate.

The needle segments run through the actuation unit at a larger diameter than at the needle tip. In order to guide the needle segments smoothly from the actuation unit to the needle tip, a double cone (blue) was designed at the distal side of the actuation unit. The double cone gently decreases the distance between the needle segments by guiding them smoothly through S-shaped channels from the actuation unit to the needle tip. These channels allow the needle segments to move back and forth freely while avoiding buckling.

### 7.2.3 Prototype

#### Material selection

The American Society for Testing and Materials (ASTM) F2503 standard distinguishes three classifications for medical devices in the MR environment: MR-safe, MR-conditional, and MR-unsafe [32]. MR-safe devices are composed of electrically non-conductive, non-metallic, and non-magnetic materials; these devices are inherently safe to use in an MR environment [32]. Additionally, MR compatibility indicates the usability of the device in an MR environment, including potential image quality issues introduced by the device, according to ASTM F2119 [33].

#### Needle

For use inside an MRI system, the Ovipositor MRI-Needle must be at least MR conditional

and MR compatible. Nitinol is metallic and, therefore, MR conditional at best. Nitinol is paramagnetic, meaning an external magnetic field weakly magnetizes it while it loses its magnetism when the external magnetic field is removed [34]. Nitinol has a lower magnetic susceptibility than stainless steel; hence it produces fewer image artifacts than stainless steel [35, 36]. Therefore, medical devices made from nitinol are frequently used in MRI-guided clinical procedures [37, 38]. The susceptibility difference between a nitinol needle and the surrounding tissue may give rise to signal voids (due to strong  $T2^*$  related signal decay) in the vicinity of the needle, which can be exploited as visualization of the nitinol needle [38, 39].

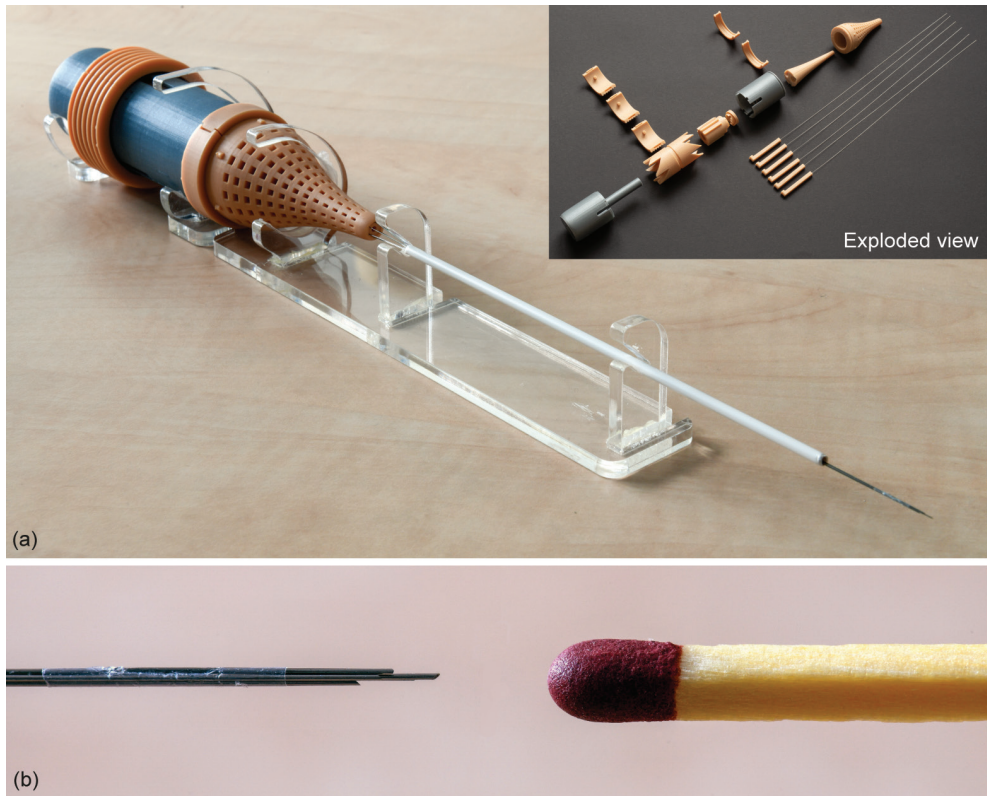
To comply with the diameter of conventional optical biopsy needles and optical treatment fiber positioning, the needle in this study consists of six 0.25-mm diameter rods, i.e., the needle segments. The needle segments are superelastic straight annealed nitinol rods with a diameter of 0.25 mm and a length of 276 mm, of which we placed 76 mm inside the actuation unit and 200 mm outside. The needle length is 200 mm to reach the prostate transperineally [30]. We glued the nitinol rods (*Pattex Gold Gel 1432562*, Henkel AG and Co., Düsseldorf, Germany) inside the needle segment holders (Figure 7.7). The cyanoacrylate-based glue is inherently biocompatible [40]. Figure 7.7a shows the tips of the needle segments, sharpened to an angle of  $40^\circ$  with wire electrical discharge machining. A 10-mm long shrinking tube (Vention Medical, expanded inner diameter 0.814 mm, wall thickness 0.013 mm) holds the six nitinol rods together at the tip to limit the diverging of the needle segments while only minimally increasing the needle diameter. The shrinking tube is glued (*Pattex Gold Gel 1432562*, Henkel AG and Co., Düsseldorf, Germany) to one of the needle segments to maintain its position at the needle tip. The remaining needle segments can move freely back and forth through the shrinking tube while the needle segments are bundled at the tip. The resulting diameter of the needle, including the shrinking tube, is 0.84 mm.

#### *Actuation unit*

We used three-dimensional (3D) printing for the production of the actuation unit. The double cone of the actuation unit consists of two parts, an inner and an outer part, containing external and internal semi-circular grooves, respectively. We composed the double cone out of two parts with semi-circular grooves rather than one part with circular channels to prevent closing off those channels while using the StereoLithography (SLA) 3D-printing process. Figure 7.6a shows that the double cone's outer part contains a hive structure. The hive structure leads to short grooves and short horizontal bridges across the grooves. A bridge is a material that links two raised points. Long bridges are likely to fail during the 3D-printing process or break during the post-processing of the 3D-printed component, thus closing off the needle grooves. The hive structure facilitates the 3D-printing process by creating short bridges that will not fail [41].

Figure 7.7b shows the 3D-printed components of the actuation unit as well as the assembled prototype. The components of the actuation unit were 3D printed on two different 3D printers, an SLA printer and a Fused Deposition Modeling (FDM) printer. Two printers with





**Figure 7.7. Ovipositor MRI-Needle.** (a) Assembled prototype. The gray parts, i.e., the housing components, were produced using Fused Deposition Modeling technology (FDM) in PolyLactic Acid (PLA) on an Ultimaker 3 printer. The orange parts, i.e., the actuation unit's internal components and the inner and outer double cones, were produced using StereoLithography (SLA) technology in *Dental Model resin V2* (Formlabs) on a Formlabs Form 3B printer. A transparent PolyMethyl MethAcrylate (PMMA) support structure supports the prototype, and a white PLA guide tube supports the needle in the support structure. (b) Close-up of the needle tip consisting of six sharpened nitinol rods held together by a shrinking tube (Vention Medical) glued to one of the six rods.

different print settings with respect to the layer height were used to allow for a smooth gliding motion of the selector inside the housing. If the selector and housing were printed with the same layer height, they would fit together like puzzle pieces, leading to jamming of the selector inside the housing. The components of the actuation unit were printed with Formlabs and Ultimaker 3D printers, using *Dental Model V2 resin* (Formlabs) and PolyLactic Acid (PLA), respectively, both materials being MR safe. We printed the SLA parts using a Formlabs Form 3B printer with a layer height of 0.050 mm, and the FDM parts using an Ultimaker 3 printer with a layer height of 0.1 mm. During assembly, we glued the housing bottom and housing top together (*Pattex Gold Gel 1432562*, Pattex, Henkel AG and Co., Düsseldorf, Germany). The height of the cam track dictates a 4-mm stroke in the positive x-direction for the needle segment holders over a 60° rotation of the cam. During the following 300° rotation, the cam track dictates in steps a total of 4-mm stroke in the negative x-direction. The actuation unit's

length is 163 mm (Figure 7.6b), the outer diameter is 35 mm, and the outer diameter of the translation ring is 45 mm. The hollow core has a diameter of 2 mm.

## 7.3 Evaluation

### 7.3.1 Experimental goal

In a proof-of-principle experiment, the functioning of the developed Ovipositor MRI-Needle was evaluated in *ex vivo* human prostate tissue inside a preclinical 7-T MRI system (MR Solutions, Guildford, United Kingdom) at the Amsterdam University Medical Center (AUMC, Department of Biomedical Engineering and Physics). The discarded human prostate sample was collected anonymously at the Amsterdam University Medical Center ([www.amsterdamumc.org](http://www.amsterdamumc.org)). The human prostate sample came from a deceased patient who had approved to donate his body to science, and his prostate was collected after autopsy. Therefore, this experiment was not subject to the Medical Research Involving Human Subjects Act (WMO), and it did not have to undergo review by an accredited Medical Research Ethics Committee or the Central Committee on Research Involving Humans.

We evaluated the performance of the Ovipositor MRI-Needle in terms of the slip of the needle with respect to the prostate tissue. More specifically, we calculated the slip ratio over an entire measurement as in Eq. 7.2:

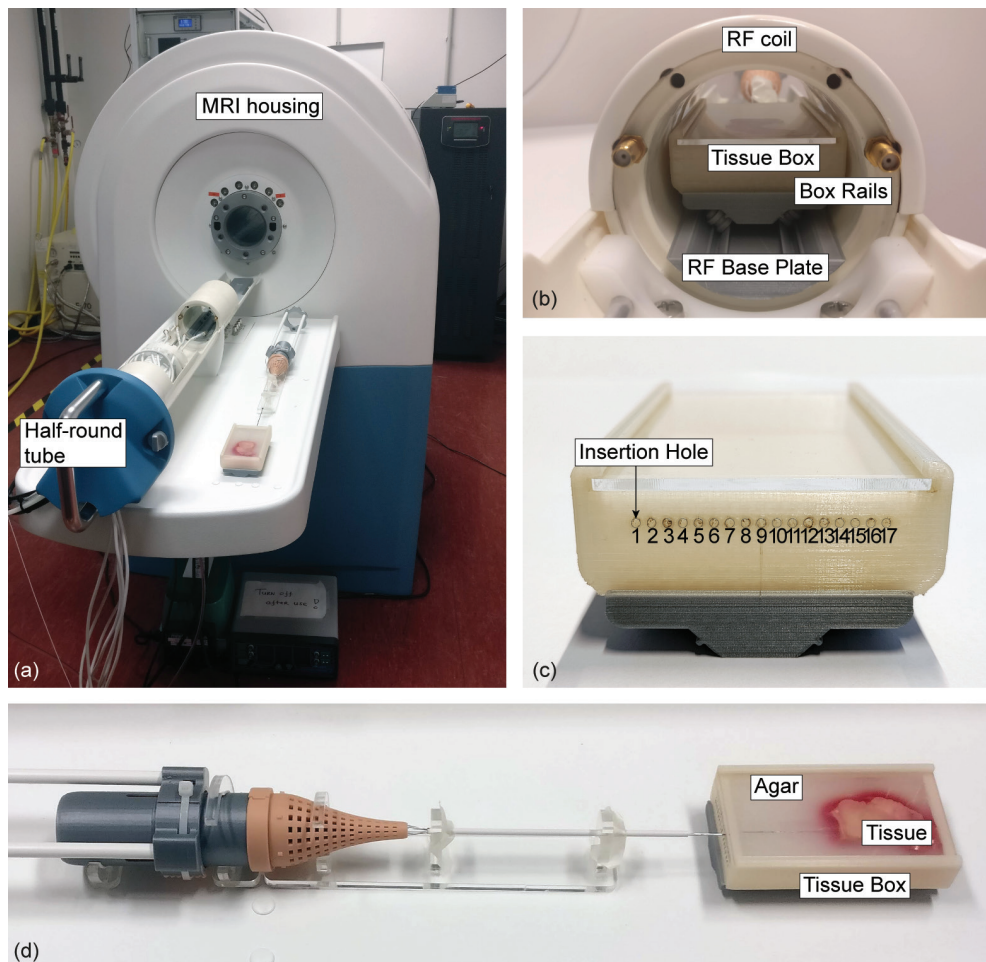
$$s_{\text{ratio}} = 1 - \left( \frac{d_m}{d_e} \right) \quad (7.2)$$

where  $d_m$  and  $d_e$  are the measured and expected traveled distance, respectively. The expected traveled distance is 4.8 mm in one cycle due to the 4-mm stroke dictated by the cam track and the six actuation steps per actuation cycle. In one cycle, all six needle segments are advanced in one step and retracted in five steps, meaning that one cycle equals a full rotation of the cam. For one cycle, we had to translate the translation ring for 12 repetitions. During one measurement, the needle was actuated for ten cycles, i.e., 120 translations of the translation ring, which means that the total expected traveled distance during one cycle was equal to 48 mm. The measured traveled distance is the difference in the position of the needle tip we measured in the MR images before and after the needle actuation for ten cycles.

### 7.3.2 Experimental facility

Figure 7.8 shows the experimental setup, consisting of the Ovipositor MRI-Needle, an *ex vivo* human prostate tissue sample embedded in agar in a tissue box, and a preclinical 7-T MRI system (MR Solutions, Guildford, United Kingdom). Instead of moving the needle toward the tissue, we decided to move the tissue in the tissue box toward the needle. Specifically, we kept the actuation unit stationary, fixed to the MRI system, to use the manual actuation force solely for the translation of the needle segments with zero external push force. The principle of needle insertion with zero external push force holds if the self-propelled needle pulls the tissue toward itself by pulling itself deeper into the tissue, thereby pulling the tissue





**Figure 7.8. Experimental setup of the *ex vivo* prostate tissue experiment.** (a) The instrument was placed in a half-round tube with a support structure in between. The half-round tube was slid into the MRI bore. (b) Close-up of the RadioFrequency (RF) coil with the tissue box on the RF base plate, guided on rails. (c) Close-up of the proximal side of the tissue box containing seventeen insertion holes. (d) Close-up of the *ex vivo* prostate tissue embedded in solidified 2.5 wt% agar, with the needle inserted through the agar in front of the tissue.

box toward the needle. The MRI system contained a half-round tube that could be slid into and out of the housing of the MRI system. On top of the half-round tube, a RadioFrequency (RF) coil was positioned. Inside the RF coil, the tissue sample can be positioned to allow for visualization using MRI acquisitions. During the performance evaluation of the Ovipositor MRI-Needle, we were interested in the position of the needle tip; therefore, the tissue box was placed inside the RF coil. The RF coil has an inner radius of 65 mm. In order to test the Ovipositor MRI-Needle inside the MRI system, we needed a movable support structure for the tissue box to allow low-friction horizontal translation of the tissue box inside the RF

coil while constraining the rolling motion in the lateral direction. The low-friction structure consisted of box rails attached to the tissue box, an RF base plate attached to the RF coil, and wheels between the box rails and RF base plate; for more details, see the Supplementary material.

We prepared the biological sample by placing a piece of *ex vivo* human prostate tissue (width 25 mm, length 50 mm, height 10 mm) in a preparation box with liquid agar (2.5 wt%). Storing the box in the refrigerator overnight fixated the tissue in the agar. We cut the sample to the correct dimensions (width 50 mm, length 90 mm, height 10 mm, weight 52 g) to fit inside the tissue box used in the experiment, with the prostate tissue at the tissue's box distal end aligned with a central hole in the wall of the box for insertion of the needle. The remaining part of the tissue box filled with agar allowed an initial insertion depth of 40 mm of the needle into the agar before entering the prostate tissue. To enable multiple slip ratio measurements in a single prostate tissue sample, the box contained multiple holes for insertion of the needle, allowing testing in different parts of the prostate sample with a new needle trajectory for each measurement. The insertion holes were placed at a distance of 2.5 mm from each other to avoid overlapping needle trajectories, resulting in a total of seventeen holes numbered from one to seventeen from left to right (Figure 7.8c). We positioned the needle in front of the tissue so it could move through the tissue. Unfortunately, because of tissue inhomogeneities or the absence of tissue behind the holes, experiments could only be carried out in a few specific holes (no. 6, 7, and 9). The tissue behind these specific holes appears homogenous in the MR images. Hence, we assumed the behaviour of the needle to be the same for the experiments using these holes.

### 7.3.3 Experimental procedure

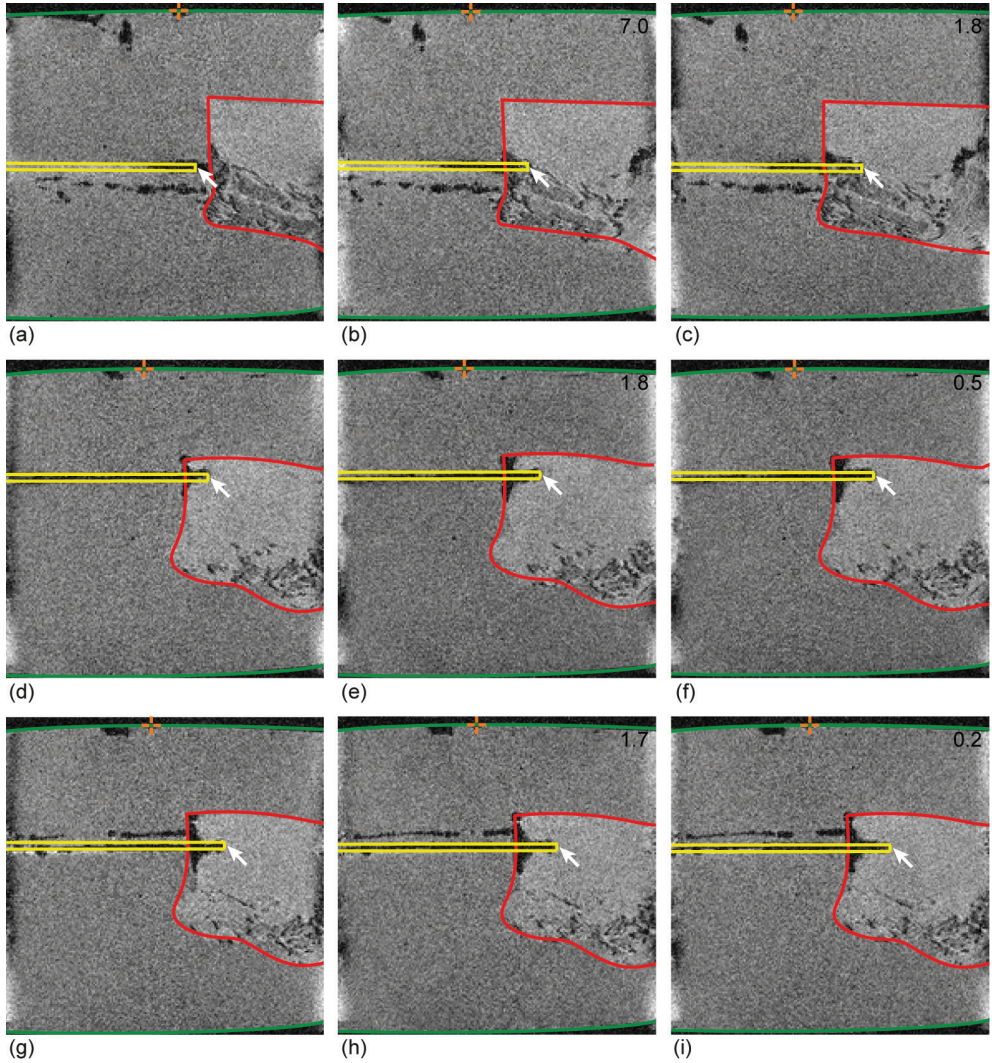
In our experiment, we used 3D gradient-echo acquisitions to capture the needle position with respect to the prostate tissue and the tissue box (see the Supplementary material for imaging parameters). We conducted three measurements using three different insertion holes in a randomized order. During a single measurement, the Ovipositor MRI-Needle was actuated for ten actuation cycles, i.e., 120 translations of the translation ring. For every measurement, a 3D gradient echo acquisition captured the static needle position at the start and after the ten actuation cycles. The Supplementary material contains a detailed explanation of the steps in the experimental protocol. After each measurement, we cleaned the needle with water and alcohol. All measurements were conducted in one day.

### 7.3.4 Results

3D gradient-echo acquisitions visualized the start and end position of the needle tip. Figure 7.9 shows the MR images of the needle tip positions (Original MR images can be found in the Supplementary material). Table 7.1 shows the insertion depth and traveled distance measurements. The initial insertion depth was that of the needle tip when it was positioned in front of the prostate tissue. The traveled distance was the distance the needle traveled inside







**Figure 7.9.** MR images of the needle inside the agar and *ex vivo* prostate tissue. Each row represents one measurement. The first column shows the initial frame where the tip is positioned inside the agar in front of the prostate tissue. The second column shows the frame after actuation over five cycles. The third column shows the frame after the second actuation over five cycles. The yellow, red, and green contours show the needle, the prostate tissue, and the tissue box sides, respectively. The arrow marks the needle tip. The orange crosshair shows the reference point on the side of the box that indicates a 40-mm insertion depth. The number in the upper right corner in black shows the measured traveled distance of the tissue box,  $d_m$ , in mm, with respect to the previous MR image.

the prostate tissue. The needle was able to propel itself through the prostate tissue. However, the needle did experience slip. We measured a slip ratio in the range of 0.82-0.96. This slip indicates that the needle segments unintentionally slide with respect to the tissue, resulting in a shorter measured traveled distance than the expected traveled distance.

**Table 7.1. Results of the *ex vivo* evaluation.** For each measurement, the following information is reported: the insertion hole used on the tissue box, measured traveled distance [mm] of the box, number of cycles needed to travel that distance, expected traveled distance [mm] that the box would have traveled if no slip occurred, and the slip ratio.

Measurement	Insertion hole	Initial insertion depth [mm]	Measured traveled distance, $d_m$ [mm]	Cycles	Expected traveled distance, $d_e$ [mm]*	Slip ratio, $s_{ratio}^*$
1	9	44.1	8.8	10	48	0.82
2	6	50.9	2.3	10	48	0.95
3	7	51.9	1.9	10	48	0.96

\*Results for  $d_e$  and  $s_{ratio}$  differ from Table 1 presented in the article [42], we informed the editor to publish a corrigendum to that article.

## 7.4 Discussion

### 7.4.1 Needle performance

This study reported on the design and experimental validation of a self-propelled needle with an MRI-ready actuation system. The evaluation of the needle in *ex vivo* prostate tissue showed the needle was able to advance through the tissue. However, the needle did experience a high slip ratio. We measured a slip ratio in the range of 0.82-0.96. The slip ratio of our needle in *ex vivo* prostate tissue is comparable to that of the self-propelled needle developed by Scali [18], who reported a slip ratio in the range of 0.87-0.90 for the continuously moving needle in *ex vivo* porcine liver tissue. The high slip ratio in our measurements indicates that the cutting and friction forces acting on the advancing needle segment and the friction forces on the wheels of the support structure altogether were near the friction forces on the retracting needle segments (Eq. 7.1). Furthermore, despite the shrinking tube, the needle segments diverged a little at their tips like an opening umbrella during the experiment, hindering the needle segments' advancing motions, thereby increasing the needle's slip ratio. The degree to which the segments diverged at the needle tip could not be quantified because of the low resolution of the MRI system used.

### 7.4.2 Limitations

The needle segments were designed and sharpened so that the needle segments point toward the middle of the needle. However, the needle segments did not always point toward the middle of the assembled prototype. This could be explained by the way the needle segments are bundled. Along the length of the 200-mm needle, the needle segments were only connected at the tip by a 10-mm long shrinking tube. Hence, the needle segments could change position during the experiment, causing the needle segments to rotate and entangle. Because the needle segments did not point toward the middle, their bevel-shaped tips might have caused them to diverge and allow tissue accumulation between them. In future designs, we aim to point all bevel-shaped tips toward the middle of the needle tip by restricting their rotation to prevent the needle segments from diverging.

At the needle tip, the six needle segments are surrounded by the shrinking tube, which might hinder the needle's self-propelling motion through the tissue. However, as the needle is advanced further into the tissue, the surface area of the needle segments in direct contact with the tissue increases, whereas the surface area of the shrinking tube in contact with the tissue remains unchanged. Consequently, the influence of the shrinking tube on the self-propelling motion declines as the needle advances further into the tissue. In a future version of the Ovipositor MRI-Needle, we will investigate methods to replace the shrinking tube with another connection mechanism to improve the needle's self-propelling motion.

### 7.4.3 Future work

In this study, we placed the tissue in a box that moved toward the needle. For application in transperineal laser ablation, the needle will have to self-propel through the perineal skin and into the prostate while the patient stays still inside the MRI bore. The actuation unit can be placed on a robotic arm suited to move the needle toward the cancerous tissue. The current Ovipositor MRI-Needle uses a discrete manual translating motion of the translation ring as its input. In future work, the translation ring could be replaced with a motorized actuation unit that is safe for use in an MRI environment. Electric motors are not an option due to the interference of these motors with the magnetic field. Alternative actuation methods are piezo motors, ultrasonic motors, Bowden cables, pneumatics, hydraulics, magnetic spheres, and shape memory alloy actuators. In a hospital setup, pneumatics are advantageous as pressurized air is commonly available in an MRI room. An important drawback of pneumatics is that air is compressible, so the only well-defined pneumatic actuator positions are the beginning and end positions [43]. This makes pneumatic actuators more suited for a discrete stepwise motion instead of continuous motion. Our selector mechanism is currently actuated by a stepwise manual translation, which can relatively easily be replaced by a stepwise pneumatic actuation mechanism.

In our experiment, the performance evaluation of the Ovipositor MRI-Needle was limited to an evaluation in a single *ex vivo* frozen-thawed prostate sample embedded in agar. Larger sample sizes are needed for future evaluations, considering that the mechanical properties of the prostate tissue of different men are not the same but comprise ranges of values.

Another limitation was that the sample was frozen quickly at  $-80^{\circ}\text{C}$  in liquid nitrogen and thawed prior to the experiment. While rapid freezing reduces ice crystal formation in the tissue and minimizes morphological changes [44], Venkatasubramanian *et al.* [45] demonstrated that freezing tissue in liquid nitrogen could affect tissue stiffness compared to fresh tissue, with the exact effects of this freeze-thaw cycle on the mechanical properties of the tissue being still unknown. However, this effect might not influence the needle's self-propelling motion as in our experiment, the Ovipositor MRI-Needle could self-propel through tissue that had been frozen. In comparison, Scali [18] evaluated the performance of a wasp-inspired self-propelled needle in *ex vivo* four hours post mortem porcine tissue that did not undergo a freeze-thaw cycle and showed that the needle could self-propel through relatively fresh *ex vivo* tissue with

a comparable slip ratio as the Ovipositor MRI-Needle in *ex vivo* prostate tissue.

Another limitation related to our experiment conditions is that the agar (2.5 wt%) in which the prostate tissue was embedded was stiffer than the prostate tissue itself, which could have affected the self-propelling motion of our Ovipositor MRI-Needle. Scali *et al.* [27] showed that the slip ratio of a self-propelled needle was higher in tissue stiffer compared to less stiff phantoms. This indicates that the stiff agar in our experiment could have increased the slip ratio of the Ovipositor MRI-Needle compared to when the needle would advance through prostate tissue.

In future studies, *in vivo* experiments are needed to test the performance of the needle in a more realistic clinical scenario. When moving toward an *in vivo* study, we foresee some challenges, such as the imaging system, the presence of blood flow through the prostate gland, and the presence of multi-layered tissue. For *in vivo* tests inside porcine animal models, we need an MRI system with a bore and RF coil that fits the animal model, as the currently used preclinical MRI system has an RF coil diameter of only 65 mm. Alternatively, other imaging options like ultrasound could be used, which will have their own advantages and disadvantages, such as low contrast for soft tissues [46]. The presence of blood flow could decrease the needle-tissue friction required for the self-propelling motion. However, the parasitic wasp is able to advance through more liquid substrates such as fruits (e.g., figs) [47, 48] thanks to harpoon-like serrations on the valves, which increase friction [48]. Similarly, a micro-textured directional surface topography could be added to the needle surface, as shown by Parittotokkaporn *et al.* [49]. Another challenge is that in an *in vivo* model, there is more and multi-layered tissue between the insertion point (i.e., the perineum) and the target position inside the prostate gland. However, other self-propelled needles have been shown to be able to advance in multi-layered tissue-mimicking phantoms consisting of gelatin with different stiffnesses [27]. Moreover, when the needle is inserted through multiple layers of tissue and thus deeper into the tissue, the self-propelling motion is expected to work better, as the role of the cutting force of the single advanced segment becomes less pertinent compared to the friction forces of the retracted segments.

In this study, we kept the actuation unit stationary while the box was placed on a low-friction support structure that moved toward the needle. In clinical practice, the needle will have to self-propel inside the patient while the tissue remains in place. The actuation unit could be placed on a dedicated robotic arm to manipulate the needle toward the patient, following the pace of the self-propelling motion of the needle. Moreover, for the future production of the needle segments, industrial needle manufacturing processes could be used to produce a needle with a sharper tip (e.g., a lancet point) to facilitate the propulsion through the tissue.

Currently, clinicians typically need multiple attempts to reach the target location, leading to an increased risk of tissue damage [7]. Moreover, a narrow pubic arch or a large prostate can obstruct the needle trajectory, making it difficult to reach certain prostate locations [50]. Steerable needles can help the clinician compensate for positioning errors and follow a curved



path to reach all positions inside the prostate while avoiding anatomical obstacles. In a future version of the Ovipositor MRI-Needle, a steering mechanism can be incorporated. Steering can be achieved by creating an offset between the needle segment tips to approximate a bevel-shaped tip. The surrounding tissue exerts forces on the bevel-shaped tip in an asymmetric fashion, resulting in the bending of the needle in the direction of the bevel [51]. Research by Scali *et al.* [26] on wasp-inspired steerable needles showed that approximated bevel-shaped tips could be used to steer the needle successfully. Research into steering will be incorporated in future prototypes of our needle.

Considering the needle's primary goal, its use in MRI-guided transperineal optical biopsy and focal laser ablation, the MR safety and compatibility of the components of the Ovipositor MRI-Needle should in the future be addressed using the ASTM test methods [32]. Radiofrequency heating caused by the nitinol needle should be evaluated experimentally, as the nitinol needle is a long and electrically conductive structure that couples with the electric field of the RF coil in an MRI system [52]. The coupling induces high voltages at the end of the needle, which might cause heating of the surrounding tissue that poses a potential safety hazard to the patient [52, 53]. Alternatively, the nitinol needle segments could be replaced by needle segments made of electrically non-conductive, non-metallic, and non-magnetic materials such as polymer needle segments or glass fibers. An MRI-ready, self-propelled, steerable needle can serve as a platform technology for the precise positioning of a functional element in a target region in the body.

## 7.5 Conclusion

This work presents the design and experimental validation of a self-propelled needle with an MRI-ready actuation system. We have shown that a discrete manual translating motion can actuate the reciprocating motion of the six parallel needle segments using a selector. A continuous hollow core through the actuation unit allows for needle functionalization with an optical fiber for optical biopsy and focal laser ablation. The prototype's components, excluding the needle, are easily manufactured solely by 3D printing using MR-safe materials. The needle consists of six sharpened nitinol rods. It was possible to determine the needle tip's position in the MR image, as the nitinol needle did not cause severe image artifacts. The evaluation of the prototype in *ex vivo* human prostate tissue in an MRI system showed that the needle was able to self-propel through the tissue. However, it experiences a high slip ratio. The Ovipositor MRI-Needle is a step forward in developing a self-propelled needle for MRI-guided transperineal focal laser ablation to treat prostate cancer.

## Supplementary material

The appendices and data underlying this study are available at doi: 10.4121/c3b6bba1-9c3d-44c4-b59a-cbdb33198792.



## Acknowledgements

We would like to thank David Jager from DEMO (Dienst Elektronische en Mechanische Ontwikkeling) at the TU Delft for sharpening the needle segments and Daniel Martijn de Bruin, Luigi van Riel, Gustav Strijkers, and Theo de Reijke from the AUMC (Amsterdam University Medical Centers) for the discussions about the application of the project in focal laser ablation for prostate cancer treatment and their help in designing the setup and performing the experiment.

## References

1. Sung H, Ferlay J, Siegel RL, Laversanne M, Soerjomataram I, Jemal A, et al. Global cancer statistics 2020: GLOBOCAN estimates of incidence and mortality worldwide for 36 cancers in 185 countries. *CA: a cancer journal for clinicians*. 2021;71(3):209-49. doi: 10.3322/caac.21660.
2. Lodeizen O, de Bruin M, Eggener S, Crouzet S, Ghai S, Varkarakis I, et al. Ablation energies for focal treatment of prostate cancer. *World journal of urology*. 2019;37(3):409-18. doi: 10.1007/s00345-018-2364-x.
3. Oto A, Sethi I, Karczmar G, McNichols R, Ivancevic MK, Stadler WM, et al. MR imaging-guided focal laser ablation for prostate cancer: phase I trial. *Radiology*. 2013;267(3):932-40. doi: 10.1148/radiol.13121652.
4. Hodge KK, McNeal JE, Stamey TA. Ultrasound guided transrectal core biopsies of the palpably abnormal prostate. *The Journal of urology*. 1989;142(1):66-70. doi: 10.1016/S0022-5347(17)38663-9.
5. de la Taille A, Antiphon P, Salomon L, Cherfan M, Porcher R, Hoznek A, et al. Prospective evaluation of a 21-sample needle biopsy procedure designed to improve the prostate cancer detection rate. *Urology*. 2003;61(6):1181-6. doi: 10.1016/S0090-4295(03)00108-0.
6. Patelli G, Ranieri A, Paganelli A, Mauri G, Pacella CM. Transperineal laser ablation for percutaneous treatment of benign prostatic hyperplasia: a feasibility study. *Cardiovascular and interventional radiology*. 2017;40(9):1440-6. doi: 10.1007/s00270-017-1662-9.
7. Leibinger A, Oldfield MJ, Rodriguez y Baena F. Minimally disruptive needle insertion: a biologically inspired solution. *Interface focus*. 2016;6(3):20150107. doi: 10.1098/rsfs.2015.0107.
8. Wright RM, Ramesh K. An axonal strain injury criterion for traumatic brain injury. *Biomechanics and modeling in mechanobiology*. 2012;11(1-2):245-60. doi: 10.1007/s10237-011-0307-1.
9. Moreira P, van de Steeg G, Krabben T, Zandman J, Hekman EE, van der Heijden F, et al. The MIRIAM robot: A novel robotic system for mr-guided needle insertion in the prostate. *Journal of medical robotics research*. 2017;2(04):1750006. doi: 10.1142/S2424905X17500064.
10. DiMaio SP, Salcudean SE. Needle insertion modeling and simulation. *IEEE Transactions on robotics and automation*. 2003;19(5):864-75. doi: 10.1109/TRA.2003.817044.
11. Sakes A, Dodou D, Breedveld P. Buckling prevention strategies in nature as inspiration for improving percutaneous instruments: a review. *Bioinspiration & biomimetics*. 2016;11(2):021001. doi: 10.1088/1748-3190/11/2/021001.
12. Abolhassani N, Patel R, Moallem M. Needle insertion into soft tissue: A survey. *Medical engineering & physics*. 2007;29(4):413-31. doi: 10.1016/j.medengphy.2006.07.003.
13. Abolhassani N, Patel RV, Ayazi F. Minimization of needle deflection in robot-assisted percutaneous therapy. *The international journal of medical Robotics and computer assisted surgery*. 2007;3(2):140-8. doi: 10.1002/rcs.136.
14. Ilami M, Ahmed RJ, Petras A, Beigzadeh B, Marvi H. Magnetic needle steering in soft phantom tissue. *Scientific reports*. 2020;10(1):1-11. doi: 10.1038/s41598-020-59275-x.
15. Schwehr TJ, Sperry AJ, Rolston JD, Alexander MD, Abbott JJ, Kuntz A. Toward targeted therapy in the brain by leveraging screw-tip soft magnetically steerable needles. *Proceedings of the Hamlyn*

Symposium on Medical Robotics; 2022. doi: 10.31256/HSMR2022.40.

16. Frasson L, Ferroni F, Ko SY, Dogangil G, y Baena FR. Experimental evaluation of a novel steerable probe with a programmable bevel tip inspired by nature. *J Robot Surg*. 2012;6(3):189-97. doi: 10.1007/s11701-011-0277-4.

17. Viridyawan V, Oldfield M, y Baena FR. Laser Doppler sensing for blood vessel detection with a biologically inspired steerable needle. *Bioinspiration & biomimetics*. 2018;13(2):026009. doi: 10.1088/1748-3190/aaa6f4.

18. Scali M. Self-propelling needles: From biological inspiration to percutaneous interventions. 2020. doi: 10.4233/uuid:523e3e5f-08f0-4acb-ab45-abaa7ace3967.

19. Quicke DL, Fitton MG. Ovipositor steering mechanisms in parasitic wasps of the families Gasteruptionidae and Aulacidae (Hymenoptera). *Proceedings of the Royal Society of London Series B: Biological Sciences*. 1995;261(1360):99-103. doi: 10.1098/rspb.1995.0122.

20. Cerkvenik U, Van de Straat B, Gussekloo SW, Van Leeuwen JL. Mechanisms of ovipositor insertion and steering of a parasitic wasp. *Proceedings of the National Academy of Sciences*. 2017;114(37):E7822-E31. doi: 10.1073/pnas.1706162114.

21. Vilhelmsen L, Isidoro N, Romani R, Basibuyuk HH, Quicke DL. Host location and oviposition in a basal group of parasitic wasps: the subgenual organ, ovipositor apparatus and associated structures in the Orussidae (Hymenoptera, Insecta). *Zoomorphology*. 2001;121(2):63-84. doi: 10.1007/s004350100046.

22. Quicke D, Fitton M, Tunstead J, Ingram S, Gaitens P. Ovipositor structure and relationships within the Hymenoptera, with special reference to the Ichneumonidae. *Journal of Natural History*. 1994;28(3):635-82. doi: 10.1080/00222939400770301.

23. Parittotokkaporn T, Frasson L, Schneider A, Huq SE, Davies BL, Degenaar P, et al. Soft tissue traversal with zero net force: Feasibility study of a biologically inspired design based on reciprocal motion. 2008 IEEE International Conference on Robotics and Biomimetics; 2009: IEEE. doi: 10.1109/ROBIO.2009.4912983.

24. Oldfield MJ, Leibinger A, Seah TET, y Baena FR. Method to reduce target motion through needle-tissue interactions. *Annals of biomedical engineering*. 2015;43(11):2794-803. doi: 10.1007/s10439-015-1329-0.

25. Frasson L, Ko S, Turner A, Parittotokkaporn T, Vincent JF, Rodriguez y Baena F. STING: a soft-tissue intervention and neurosurgical guide to access deep brain lesions through curved trajectories. *Proceedings of the Institution of Mechanical Engineers, Part H: Journal of Engineering in Medicine*. 2010;224(6):775-88. doi: 10.1243/09544119JEM663.

26. Scali M, Pusch T, Breedveld P, Dodou D. Ovipositor-inspired steerable needle: design and preliminary experimental evaluation. *Bioinspiration & Biomimetics*. 2017;13(1):016006. doi: 10.1088/1748-3190/aa92b9.

27. Scali M, Breedveld P, Dodou D. Experimental evaluation of a self-propelling bio-inspired needle in single- and multi-layered phantoms. *Scientific reports*. 2019;9(1):1-13. doi: 10.1038/s41598-019-56403-0.

28. Lindner U, Lawrentschuk N, Weersink RA, Davidson SR, Raz O, Hlasny E, et al. Focal laser ablation for prostate cancer followed by radical prostatectomy: validation of focal therapy and imaging accuracy. *European urology*. 2010;57(6):1111-4. doi: 10.1016/j.eururo.2010.03.008.

29. Stafford RJ, Shetty A, Elliott AM, Klumpp SA, McNichols RJ, Gowda A, et al. Magnetic resonance guided, focal laser induced interstitial thermal therapy in a canine prostate model. *The Journal of urology*. 2010;184(4):1514-20. doi: 10.1016/j.juro.2010.05.091.

30. Phee L, Xiao D, Yuen J, Chan CF, Ho H, Thng CH, et al. Ultrasound guided robotic system for transperineal biopsy of the prostate. *Proceedings of the 2005 IEEE international conference on robotics and automation*; 2005: IEEE. doi: 10.1109/ROBOT.2005.1570297.

31. Kent RN, inventor; Parker Pen Co Ltd, assignee. Writing instrument patent US3205863A. 1953 Sept. 14.

32. ASTM F2503-13, Standard practice for marking medical devices and other items for safety in the magnetic resonance environment. ASTM International, West Conshohocken, PA2013.
33. ASTM F2119-07(2013), Standard test method for evaluation of MR Image artifacts from passive implants. ASTM International, West Conshohocken, PA2013.
34. Kim Y-H, Choi M, Kim J-W. Are titanium implants actually safe for magnetic resonance imaging examinations? *Archives of plastic surgery*. 2019;46(1):96. doi: 10.5999/aps.2018.01466.
35. Stöckel D. Nitinol - A material with unusual properties. *Endovascular Update*. 1998;1(1):1-8.
36. Al-Maatoq M, Boese A, Henke H-W, Friebe M. Primary design concept for non-metallic needle for MRI guided spinal applications. 2019 41st Annual International Conference of the IEEE Engineering in Medicine and Biology Society (EMBC); 2019: IEEE.
37. Barras C, Myers K. Nitinol – its use in vascular surgery and other applications. *European Journal of Vascular and Endovascular Surgery*. 2000;19(6):564-9. doi: 10.1053/ejvs.2000.1111.
38. Melzer A, Michitsch S, Konak S, Schaefer G, Bertsch T. Nitinol in magnetic resonance imaging. *Minimally Invasive Therapy & Allied Technologies*. 2004;13(4):261-71. doi: 10.1080/13645700410020269.
39. Kahn T, Busse H. *Interventional magnetic resonance imaging*: Springer; 2012.
40. Korde JM, Kandasubramanian B. Biocompatible alkyl cyanoacrylates and their derivatives as bio-adhesives. *Biomaterials science*. 2018;6(7):1691-711. doi: 10.1039/C8BM00312B.
41. Culmone C, Henselmans PW, van Starckenburg RI, Breedveld P. Exploring non-assembly 3D printing for novel compliant surgical devices. *PLoS ONE*. 2020;15(5):e0232952. doi: 10.1371/journal.pone.0232952.
42. Bloemberg J, Trauzettel F, Coolen B, Dodou D, Breedveld P. Design and evaluation of an MRI-ready, self-propelled needle for prostate interventions. *PLoS ONE*. 2022;17(9):e0274063. doi: 10.1371/journal.pone.0274063.
43. Groenhuis V, Stramigioli S. Laser-cutting pneumatics. *IEEE/ASME transactions on mechatronics*. 2015;21(3):1604-11. doi: 10.1109/TMECH.2015.2508100.
44. Fischer AH, Jacobson KA, Rose J, Zeller R. Cryosectioning tissues. *CSH Protoc*. 2008;3(8). doi: 10.1101/pdb.prot4991.
45. Venkatasubramanian RT, Grassl ED, Barocas VH, Lafontaine D, Bischof JC. Effects of freezing and cryopreservation on the mechanical properties of arteries. *Annals of Biomedical engineering*. 2006;34(5):823-32. doi: 10.1007/s10439-005-9044-x.
46. Jolesz FA. *Intraoperative imaging and image-guided therapy*: Springer Science & Business Media; 2014.
47. Ovruski S, Aluja M, Sivinski J, Wharton R. Hymenopteran parasitoids on fruit-infesting Tephritidae (Diptera) in Latin America and the southern United States: diversity, distribution, taxonomic status and their use in fruit fly biological control. *Integrated Pest Management Reviews*. 2000;5(2):81-107. doi: 10.1023/A:1009652431251.
48. Ghara M, Kundanati L, Borges RM. Nature's swiss army knives: ovipositor structure mirrors ecology in a multitrophic fig wasp community. *PLoS ONE*. 2011;6(8):e23642. doi: 10.1371/journal.pone.0023642.
49. Parittotokkaporn T, Frasson L, Schneider A, Davies B, Degenaar P, y Baena FR. Insertion experiments of a biologically inspired microtextured and multi-part probe based on reciprocal motion. 2010 Annual International Conference of the IEEE Engineering in Medicine and Biology; 2010: IEEE. doi: 10.1109/IEMBS.2010.5627410.
50. Wallner K, Chiu-Tsao ST, Roy J, Arterbery VE, Whitmore W, Jain S, et al. An improved method for computerized tomography-planned transperineal 125iodine prostate implants. *The Journal of Urology*. 1991;146:90-5. doi: 10.1016/S0022-5347(17)37721-2.
51. Scali M, Pusch TP, Breedveld P, Dodou D. Needle-like instruments for steering through solid organs: A review of the scientific and patent literature. *Proceedings of the Institution of Mechanical Engineers, Part H: Journal of Engineering in Medicine*. 2017;231(3):250-65. doi: 10.1177/0954411916672149.



52. Nitz WR, Oppelt A, Renz W, Manke C, Lenhart M, Link J. On the heating of linear conductive structures as guide wires and catheters in interventional MRI. *Journal of Magnetic Resonance Imaging*. 2001;13(1):105-14. doi: 10.1002/1522-2586(200101)13:1<105::AID-JMRI1016>3.0.CO;2-0.
53. Konings MK, Bartels LW, Smits HF, Bakker CJ. Heating around intravascular guide-wires by resonating RF waves. *Journal of Magnetic Resonance Imaging*. 2000;12(1):79-85. doi: 10.1002/1522-2586(200007)12:1<79::AID-JMRI9>3.0.CO;2-T.

# 8

## Enabling Wasp-Inspired Actuation for Steering

Extended version of the conference abstract published as:

Bloemberg J., Sakes A., Breedveld P. (2024). Wasp-inspired steerable needle for transperineal focal laser ablation. Proceedings of the 16<sup>th</sup> Hamlyn Symposium on Medical Robotics. London, United Kingdom, 25-28 June 2024.





## 8.1 Introduction

In Transperineal Laser Ablation (TPLA), needles are used to position an optical fiber near the tumor site to treat prostate cancer. Commonly used needles are rigid and bound to straight trajectories, which might lead to access restriction due to pubic arch interference or targeting errors resulting from needle deflection caused by needle-tissue interaction [1]. To minimize both access restriction to the target site and needle targeting errors, steerable needles can be used. Steerable needles can modify needle-tissue interactions during insertion and, therefore, control the needle trajectory to reach the target site accurately.

In the scientific literature, several steerable needle designs have been proposed, including bevel-tip needles [2], concentric tube needles [3], tendon-driven needles [4, 5], and wasp-inspired bevel-tip needles, i.e., programmable bevel-tip needles [6-10] and discrete bevel-tip needles [11, 12]. Bevel-tip needles with predefined shapes are limited to 2D steering along a fixed radius. 3D steering requires axial rotation of the bevel-tip needle, which can induce torsional stress on the needle body. This stress may cause an angular lag between the orientation of the needle base and tip, complicating control over the needle's trajectory [13]. Secondly, concentric tube needles consist of telescopically assembled elastic pre-curved tubes, which do not require a rotation of the outside tube in contact with the surrounding tissue. However, the pre-curved tubes offer limited flexibility for path adjustment. Thirdly, tendon-driven needles enable a change of the tip orientation through the manipulation of the internal tendons, which induces tissue displacement and might result in tissue trauma. On the other hand, programmable and discrete bevel-tip needles that are inspired by the ovipositor of the female parasitic wasp possess the following advantages over other steerable needle designs: (1) the steering direction can be set to any direction in 3D without axial rotation of the needle, (2) the steering ability can be changed during insertion, and (3) the self-propelled motion decreases tissue deformation at the needle-tissue interface [14]. Therefore, wasp-inspired discrete bevel-tip needles are the focus of this study.

Female parasitic wasps possess a thin and steerable needle-like structure called the ovipositor to deposit eggs in a host while avoiding buckling and presumably while being able to steer in 3D without axial rotation. The wasp can move its ovipositor through solid substrates such as wood by reciprocally moving the parallel valves that constitute it [15]. The protrusion-retraction motion of the valves produces a near-zero external push force due to the valves' friction with the surrounding substrate, enabling a self-propelling steerable movement. Steering of the ovipositor is hypothesized to be achieved by its asymmetric beveled tip [15]. When moving such an asymmetric beveled tip through a substrate, the off-axis reaction forces applied by the substrate on the tip cause the ovipositor to bend, resulting in a curved path [16]. The mechanisms by which the ovipositor advances and steers through solid substrates have inspired the design of needles and probes capable of actively propelling and adjusting their trajectories within tissue phantoms and human tissues [6-9, 11, 12, 17-19].

Wasp-inspired bevel-tip needles are particularly interesting for TPLA application thanks

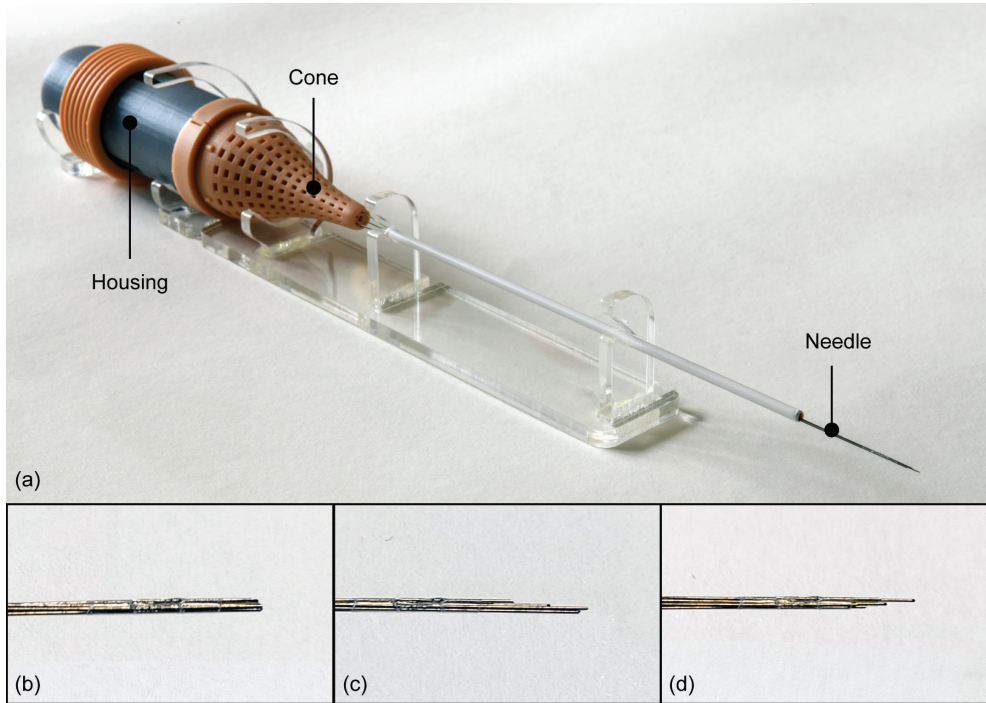
to their self-propulsion and trajectory adjustment capabilities without the need for axial rotation, allowing for more accurate placement of the optical fiber. In previous wasp-inspired bevel-tip needles, optical fibers were inserted through hollow lumens inside the needle segments [9]. However, the implementation of an optical fiber for TPLA that functions as one of the needle segments in a wasp-inspired steerable needle at a submillimeter scale has yet to be validated. Moreover, we do not know the effect of needle steering on the optical fiber for TPLA applications, as currently during TPLA procedures, the fiber is positioned through a rigid needle bound to straight trajectories. This study shows an ovipositor-inspired needle that can steer and propel through a tissue phantom to position an optical fiber during TPLA with zero external push force and without buckling.

## 8.2 Materials and methods

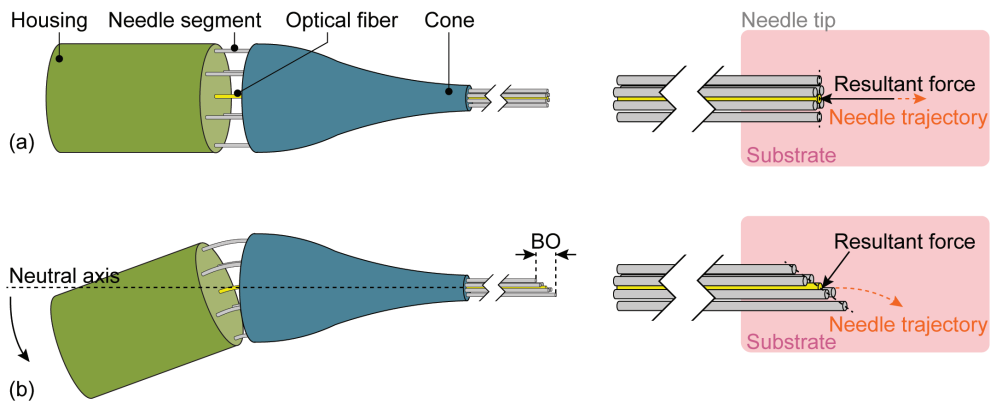
### 8.2.1 Wasp-inspired needle design

Our manually actuated wasp-inspired needle design (Figure 8.1) consists of six parallel 0.25-mm diameter nitinol rods bundled at the tip using a heat shrink tube (Vention Medical, expanded inner diameter 0.814 mm, wall thickness 0.013 mm) and is driven by a 3D-printed manual actuation system in the handle. The tips of the needle segments were sharpened to an angle of 40° using wire Electrical Discharge Machining (EDM) to enhance the tip's cutting efficiency and to minimize the insertion force required. This needle design has previously demonstrated self-propulsion through *ex vivo* prostate tissue [19] (Chapter 7). The needle achieves self-propelled motion by advancing one needle segment while retracting the other five, where the combined friction force of the five retracting segments with the surrounding substrate counterbalances the sum of the friction and cutting forces experienced by the advancing needle segment. A cam located in the handle actuates the advancing and retracting motions of the needle segments.

The main innovation of the needle described in this study is its ability to steer and guide an optical fiber for TPLA toward the needle tip. We added steerability to the needle design by creating an offset between the needle segments to approximate a bevel-shaped tip. The surrounding tissue exerts forces on the bevel-shaped tip in an asymmetric fashion, resulting in the bending of the needle. To achieve the discrete bevel-shaped tip, we developed a global steering unit integrated into the handle, rather than individually advancing the selected needle segments using separate motors as done in the approach by Scali *et al.* [11, 12]—a more complex and time-consuming approach. To allow for global steering, the housing of the handle could be rotated relative to the cone that converges the needle segments, similar to a 2-degrees-of-freedom joystick, see Figure 8.2. Rotating the housing pushes and pulls the needle segments into and out of the cone, thereby shifting the needle segments over the required offset in a controlled manner, resulting in a discrete bevel-shaped tip.



**Figure 8.1. Manually-actuated wasp-inspired needle.** (a) Complete prototype with close-ups of the needle tip in three configurations: (b) blunt tip, (c) bevel up, and (d) bevel down.



**Figure 8.2. Schematic of the global steering unit of the wasp-inspired needle.** (a) Neutral position, the needle segments and optical fiber align at the tip (blunt tip), leading to a forward trajectory due to the resultant force from the substrate. (b) Rotating the housing away from the neutral axis shifts the needle segments, creating a bevel offset (BO, bevel up). The asymmetric force distribution on the bevel-shaped tip causes the needle to bend downward. Rotating the housing downward steers the needle downward inside the substrate. Increasing the bending angle from the neutral axis enhances the bevel offset (BO), resulting in a greater curvature of the needle trajectory.

### 8.2.2 Experimental goal and variables

The experiment of this explorative study aimed to investigate the needle's self-propelling and steering performance in gelatin phantoms whilst guiding a 300- $\mu\text{m}$  optical fiber for TPLA through the needle's central lumen, resulting in a total needle outer diameter of 0.8 mm. For the self-propelling performance, we calculated the propulsion efficiency as in Eq. 8.1:

$$\eta_p = \left( \frac{d_m}{d_e} \right) 100\% \quad (8.1)$$

where  $d_m$  [mm] and  $d_e$  [mm] are the measured and expected traveled distance, respectively. During one actuation cycle, the cam of the actuation system is rotated once, resulting in all needle segments advancing and retracting over the stroke distance once. Because we assume that for the self-propelled motion the gelatin phantom remains stationary with respect to the retracting needle segments, the expected traveled distance is equal to the stroke distance of the needle segments dictated by the cam track in the housing, i.e.,  $S$  [mm], multiplied by the number of actuation cycles, i.e.,  $C$ , multiplied by a factor of 6/5, as in Eq. 8.2:

$$d_e = \frac{6}{5} SC \quad (8.2)$$

During one measurement, the needle was actuated for 20 cycles, resulting in a total expected traveled distance ( $d_e$ ) of 96 mm. The measured traveled distance ( $d_m$ ) is the difference in the position of the needle tip we measured in the images before and after needle actuation.

For the steering performance, we used the deflection-to-insertion ratio as a measure as in Eq. 8.3:

$$d_{\text{ratio}} = \frac{d_d}{d_m} \quad (8.3)$$

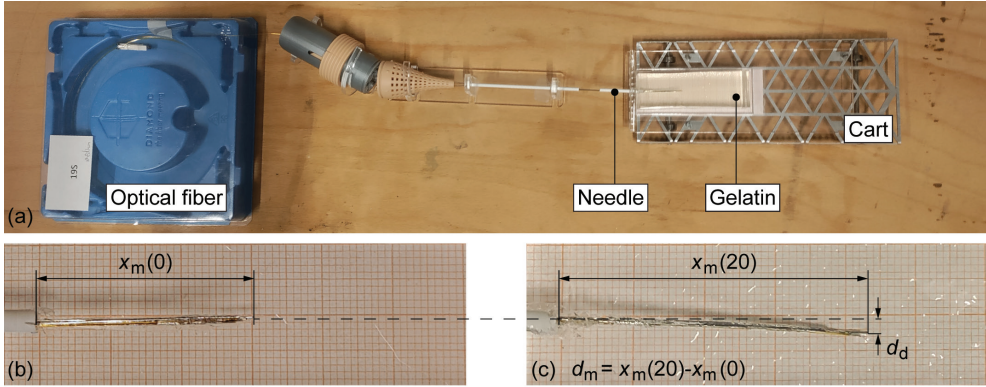
where  $d_d$  [mm] and  $d_m$  [mm] are the measured deflection and measured traveled distance, respectively. The deflection distance is the needle's deflection from the straight path. The independent variable was the steering direction, which was set to forward, up, or down. When the steering direction was up or down, the bevel offset (i.e., the offset between the needle segments) was set to 4 mm. The gelatin concentration (i.e., 10 wt%) and the number of actuation cycles (i.e., 20) were kept constant for all measurements.

### 8.2.3 Experimental facility and procedure

The experimental setup consisted of the needle with integrated fiber in its lumen, a gelatin phantom on a lightweight low-friction aluminum cart, and a camera to capture the position of the needle in the gelatin (Figure 8.3). For the gelatin phantom, gelatin powder of type *Dr. Oetker 1-50-230004* (Dr. Oetker Professional, Amersfoort, The Netherlands) was mixed with water with a gelatin weight ratio (wt) of 10%, resulting in a modulus of elasticity of 17 kPa [18], which is similar to that of prostate tissue [20].

To prevent disturbances from manual actuation and ensure zero external push force, the actuation unit remained stationary, and the gelatin tissue phantom was positioned on a low-friction cart. The principle of self-propelled needle insertion with zero external push force holds if the needle pulls the gelatin phantom toward itself by pulling itself deeper into





**Figure 8.3. Experimental setup for evaluating the self-propelling and steering performance of the needle.** (a) The setup includes an optical fiber, the needle (steering upward), and a gelatin phantom on a cart. Examples of (b) the start position and (c) the end position of the needle within the gelatin phantom.  $x_m(0)$  represents the initial measured distance of the needle in the substrate,  $x_m(20)$  is the distance after the 20 actuation cycles,  $d_m$  is the difference between the start and end position, and  $d_d$  is the deflection distance.

the gelatin. For every measurement, we captured the needle position with respect to the gelatin phantom at the start of, during, and after 20 actuation cycles. The needle tip's position was recorded using a camera mounted on a tripod, positioned directly above the needle to capture a top-down view of the needle tip within the gelatin phantom. Millimeter graph paper was placed at the bottom surface of the low-friction cart to serve as a reference for the traveled distance of the needle tip relative to the gelatin phantom during the experiments. After each measurement, the needle was removed from the phantom and cleaned with water. Each condition was repeated four times, resulting in a total of 12 measurements.

### 8.3 Results

Table 8.1 and Figures 8.4,5 present the results of the self-propelling and steering measurements. The evaluation showed that the needle with integrated optical fiber could advance through 10-wt% gelatin, although it did experience a low mean propulsion efficiency of in between 9-19%.

Upward steering was only successful in one of four trials (25%), in the other trials, unexpectedly, the needle either steered in the opposite direction or continued a forward trajectory. Downward steering was successful in three out of four trials (75%). In one trial, the needle continued a forward trajectory. The mean deflection-to-insertion ratio was higher for downward steering than for upward steering. The greatest deflection-to-insertion ratio measured was -0.088 for downward steering.

During the steering motion, the optical fiber must follow a curved trajectory in tandem with the needle's curvature. An additional power output test (Appendix 8.A) showed that bending the optical fiber over trajectories with a bending radius of 500 mm and an angle of  $8.9^\circ$  (i.e.,  $d_{\text{ratio}} = 0.078$ ) to 16.5 mm and an angle of  $270^\circ$  (i.e.,  $d_{\text{ratio}} > 1$ , the minimum

Table 8.1. Experimental conditions, propulsion efficiencies ( $\eta_p$ ), and deflection-to-insertion ratios ( $d_{ratio}$ ).  $BO$  = bevel offset. A positive  $d_{ratio}$  means an upward steering curvature and a negative  $d_{ratio}$  a downward curvature.

Steering direction	$BO$ [mm]	$\eta_p$ [%] (mean $\pm$ SD)	$d_{ratio}$ [-] (mean $\pm$ SD)
Forward	0	$9 \pm 5$	$-0.0078 \pm 0.014$
Up	4	$12 \pm 3$	$0.0036 \pm 0.031$
Down	4	$19 \pm 12$	$-0.060 \pm 0.035$

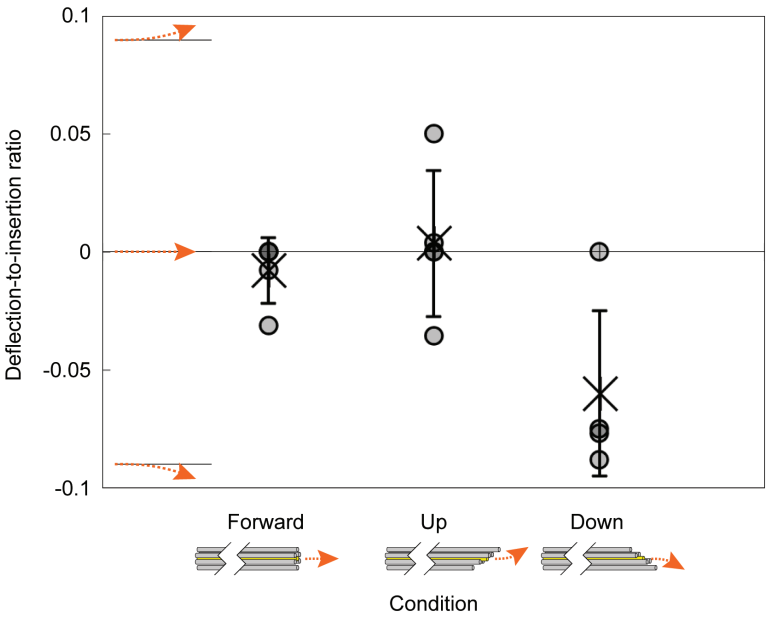


Figure 8.4. Deflection-to-insertion ratio for different steering conditions (forward, up, or down). A negative ratio indicates a downward steering curvature, while a positive ratio indicates an upward curvature. Gray circles represent single trials, crosses the mean values, and error bars the standard deviation ( $\pm 1$  SD).

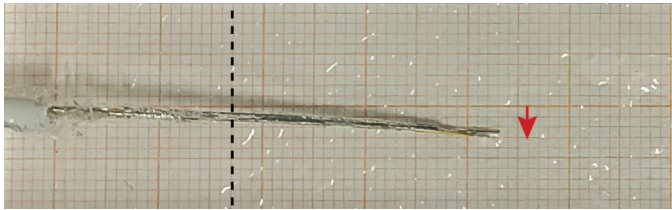


Figure 8.5. Final position of the needle within the gelatin during a steering trial (downward steering). The dashed line indicates the start of steering. The arrow shows the steering direction.

bending radius of the fiber) only caused a power loss of up to 8% at a power of 3 W (i.e., the required power for TPLA). The successful bending of the optical fiber with low power losses implies that optical fibers can safely be used in steerable needles with a bending radius of up to 16.5 mm.

## 8.4 Discussion and conclusion

In this study, we presented the design of a self-propelled, steerable needle inspired by the wasp's ovipositor that allows for positioning an optical fiber near a target site without buckling. The simultaneous steering and self-propelling motions allow for the needle to be inserted over a curved trajectory without buckling, thereby improving the controllability of the needle. Moreover, the adjustable bevel-shaped tip using the global steering mechanism allows for changing the direction of steering without the need for individual actuation of the needle segments or for axial rotation, which prevents the generation of torsional stress on the needle body. Therefore, this steering method can improve the needle trajectory controllability while potentially decreasing the risk of tissue damage compared to flexible, steerable needles that require axial rotation [21].

The experimental results showed that our needle could successfully self-propel through 10-wt% gelatin phantoms, although it did experience a low mean propulsion efficiency of 9-19%. This is comparable to the efficiencies reported for similar needles in tissues and tissue phantoms with a comparable stiffness (i.e., 4-9% in 10-wt% gelatin [22], 12% in *ex vivo* porcine liver tissue [22], and 4-18% in *ex vivo* human prostate tissue [19]). The low propulsion efficiency of our needle may be attributed to the friction between the cart and the surface on which it rolled and the friction within the cart's ball-bearing wheels. In clinical practice, the needle will have to self-propel through the perineal skin and into the prostate while the patient stays still. To accommodate this, the needle could be advanced within the actuation system to move the needle toward the patient, following the pace of the self-propelled motion, similar to the ball-spline actuation system presented by Bloembergen *et al.* [23].

During the self-propelled motion, the needle successfully steered the optical fiber downward with a mean deflection-to-insertion ratio of -0.060. This is comparable to those reported for needles with a similar diameter by Scali *et al.* [11] (i.e., 0.097 for rightward steering with a 1.6-mm diameter needle), and Scali *et al.* [12] (i.e., 0.078 for rightward steering with a 1.2-mm diameter needle) on discrete bevel-tip needles. Yet, Ko *et al.* [24], reported a ratio of 0.67 for a 12-mm diameter bevel-steering probe. The low deflection-to-insertion ratio for upward steering poses a limitation to our needle's targeting accuracy. Both the low deflection-to-insertion ratio for upward steering and the negative ratio during forward steering can partially be explained by unintended needle rotation along its length due to low torsion stiffness, as well as buckling of the needle segments within the global steering unit, which currently lacks support to prevent such buckling. Future prototypes could address needle rotation by implementing a different needle bundling mechanism designed to restrict it. Additionally, buckling of the needle segments within the global steering unit could be prevented by locally increasing the needle segment diameter, thereby increasing the second moment of area. Furthermore, we plan to further develop the needle's steerability capabilities to achieve higher deflection-to-insertion ratios by, for example, using pre-bending in the tips of the needle segments [25]. Such a needle design could potentially improve needle trajectory controllability and positioning

accuracy for prostate cancer treatment using TPLA in the future.

The current prototype is manually driven, which limits the precision and repeatability of its self-propulsion capabilities in a clinical setting. Implementing a pneumatic actuation system could enhance accuracy and user control across various image guidance systems, including Magnetic Resonance Imaging (MRI) [22]. Furthermore, future versions of the needle could benefit from using industrial needle manufacturing processes to create a sharper tip (e.g., a lancet point) to facilitate the propulsion through the tissue and improve the self-propelling efficiency. Additionally, adherence to regulations like the Medical Device Regulation 2017/745 (MDR) is crucial to ensure the safety, quality, and performance of the needle in patients.

This explorative study demonstrates the needle's self-propulsion and steering capabilities in gelatin phantoms. We assessed the steering capability based on the deflection-to-insertion ratio. However, to be able to evaluate the needle's steering performance in clinical settings, future studies should evaluate the end point error similar to the design evaluation conducted by de Vries *et al.* [5]. This approach will provide a better understanding of the needle's targeting accuracy and positioning errors, which are critical for clinical translation. Lastly, to develop a full picture of a future version of the needle prototype in a clinical setting, *ex vivo* and *in vivo* human-tissue experiments are required. In *ex vivo* experiments, tissue damage could be assessed through histological evaluation [26]. As we transition to *in vivo* studies, we anticipate challenges such as the presence of fluids and multi-layered tissues, which may diminish the needle-tissue friction necessary for the self-propelled motion. In contrast, parasitic wasps effectively navigate fluid-like substances, such as fruit, thanks to directional friction patterns on their ovipositor valves. Frasson *et al.* [27] successfully incorporated a microtexture on the needle surface, providing an interesting avenue to explore for our needle in the future. Additionally, challenges arise from multiple tissue layers, and stiffer and heterogeneous tissue. Nevertheless, previous studies have already successfully demonstrated the ability of the self-propelled needle to advance through multi-layered tissue phantoms [18], stiff tissue phantoms [23], as well as heterogeneous (*ex vivo*) tissue [19].

## Supplementary material

The data underlying this study are available at doi: 10.4121/35f36ae3-00b0-4775-96df-b6b-3b292aa4c.

## References

1. Bloemberg J, de Vries M, van Riel LA, de Reijke TM, Sakes A, Breedveld P, et al. Therapeutic prostate cancer interventions: a systematic review on pubic arch interference and needle positioning errors. *Expert Review of Medical Devices*. 2024;21(7):625-41. doi: 10.1080/17434440.2024.2374761.
2. Misra S, Reed KB, Douglas AS, Ramesh K, Okamura AM. Needle-tissue interaction forces for bevel-tip steerable needles. 2008 2nd IEEE RAS & EMBS International Conference on Biomedical Robotics and Biomechatronics; 2008: IEEE. doi: 10.1109/BIOROB.2008.4762872.
3. Gilbert HB, Neimat J, Webster RJ. Concentric tube robots as steerable needles: Achieving

- follow-the-leader deployment. *IEEE Transactions on Robotics*. 2015;31(2):246-58. doi: 10.1109/TRO.2015.2394331.
4. van de Berg NJ, Dankelman J, van den Dobbelsteen JJ. Design of an actively controlled steerable needle with tendon actuation and FBG-based shape sensing. *Medical engineering & physics*. 2015;37(6):617-22. doi: 10.1016/j.medengphy.2015.03.016.
5. de Vries M, Sikorski J, Misra S, van den Dobbelsteen JJ. Axially rigid steerable needle with compliant active tip control. *PLoS ONE*. 2021;16(12):e0261089. doi: 10.1371/journal.pone.0261089.
6. Watts T, Secoli R, y Baena FR. A mechanics-based model for 3-d steering of programmable bevel-tip needles. *IEEE Transactions on Robotics*. 2019;35(2):371-86. doi: 10.1109/TRO.2018.2879584.
7. Secoli R, Matheson E, Pinzi M, Galvan S, Donder A, Watts T, et al. Modular robotic platform for precision neurosurgery with a bio-inspired needle: System overview and first in-vivo deployment. *PLoS ONE*. 2022;17(10):e0275686. doi: 10.1371/journal.pone.0275686.
8. Favaro A, Secoli R, y Baena FR, De Momi E. Optimal pose estimation method for a multi-segment, programmable bevel-tip steerable needle. *IEEE/RSJ International Conference on Intelligent Robots and Systems (IROS)*: IEEE; 2020. p. 3232-8.
9. Donder A, y Baena FR. 3-d path-following control for steerable needles with fiber bragg gratings in multi-core fibers. *IEEE Transactions on Biomedical Engineering*. 2022;70(3):1072-85. doi: 10.1109/TBME.2022.320914.
10. Burrows C, Secoli R, y Baena FR. Experimental characterisation of a biologically inspired 3d steering needle. *13th international conference on control, automation and systems (ICCAS)*: IEEE; 2013. p. 1252-7.
11. Scali M, Kreeft D, Breedveld P, Dodou D. Design and evaluation of a wasp-inspired steerable needle. *Proceedings of SPIE; Portland, Oregon, United States: International Society for Optics and Photonics*; 2017. p. 1016207.
12. Scali M, Pusch T, Breedveld P, Dodou D. Ovipositor-inspired steerable needle: design and preliminary experimental evaluation. *Bioinspiration & Biomimetics*. 2017;13(1):016006. doi: 10.1088/1748-3190/aa92b9.
13. Reed KB, Okamura AM, Cowan NJ. Modeling and control of needles with torsional friction. *IEEE transactions on biomedical engineering*. 2009;56(12):2905-16. doi: 10.1109/TBME.2009.2029240.
14. Matheson E, Watts T, Secoli R, y Baena FR. Cyclic motion control for programmable bevel-tip needle 3D steering: A simulation study. *2018 IEEE International Conference on Robotics and Biomimetics (ROBIO)*; 2018: IEEE. doi: 10.1109/ROBIO.2018.8665117.
15. Cerkvenik U, Van de Straat B, Gussekloo SW, Van Leeuwen JL. Mechanisms of ovipositor insertion and steering of a parasitic wasp. *Proceedings of the National Academy of Sciences*. 2017;114(37):E7822-E31. doi: 10.1073/pnas.1706162114.
16. Ko SY, Davies BL, y Baena FR. Two-dimensional needle steering with a “programmable bevel” inspired by nature: Modeling preliminaries. *2010 IEEE/RSJ International Conference on Intelligent Robots and Systems*; 2010: IEEE. doi: 10.1109/IROS.2010.5650859.
17. Frasson L, Ko S, Turner A, Parittotokkaporn T, Vincent JF, Rodriguez y Baena F. STING: a soft-tissue intervention and neurosurgical guide to access deep brain lesions through curved trajectories. *Proceedings of the Institution of Mechanical Engineers, Part H: Journal of Engineering in Medicine*. 2010;224(6):775-88. doi: 10.1243/09544119JEIM663.
18. Scali M, Breedveld P, Dodou D. Experimental evaluation of a self-propelling bio-inspired needle in single- and multi-layered phantoms. *Scientific reports*. 2019;9(1):1-13. doi: 10.1038/s41598-019-56403-0.
19. Bloemberg J, Trauzettel F, Coolen B, Dodou D, Breedveld P. Design and evaluation of an MRI-ready, self-propelled needle for prostate interventions. *PLoS ONE*. 2022;17(9):e0274063. doi: 10.1371/journal.pone.0274063.
20. Zhang M, Nigwekar P, Castaneda B, Hoyt K, Joseph JV, di Sant'Agnese A, et al. Quantitative characterization of viscoelastic properties of human prostate correlated with histology. *Ultrasound in*

- medicine & biology. 2008;34(7):1033-42. doi: 10.1016/j.ultrasmedbio.2007.11.024.
21. Bui VK, Park S, Park J-O, Ko SY. A novel curvature-controllable steerable needle for percutaneous intervention. *Proceedings of the Institution of Mechanical Engineers, Part H: Journal of Engineering in Medicine*. 2016;230(8):727-38. doi: 10.1177/0954411916648988.
  22. Bloemberg J, Hoppener B, Coolen B, Sakes A, Breedveld P. Design and evaluation of a pneumatic actuation unit for a wasp-inspired self-propelled needle. *PLoS ONE*. 2024;19(7):e0306411. doi: 10.1371/journal.pone.0306411.
  23. Bloemberg J, Fung-A-Jou Z, Breedveld P, Sakes A. Design and evaluation of a ball spline wasp-inspired needle. *Frontiers in Bioengineering and Biotechnology*. 2024;12:1468605. doi: 10.3389/fbioe.2024.1468605.
  24. Ko SY, Frasson L, y Baena FR. Closed-loop planar motion control of a steerable probe with a “programmable bevel” inspired by nature. *IEEE Transactions on Robotics*. 2011;27(5):970-83. doi: 10.1109/TRO.2011.2159411.
  25. Adebar TK, Greer JD, Laeseke PF, Hwang GL, Okamura AM. Methods for improving the curvature of steerable needles in biological tissue. *IEEE Transactions on Biomedical Engineering*. 2015;63(6):1167-77. doi: 10.1109/TBME.2015.2484262.
  26. Gidde STR, Acharya SR, Kandel S, Pleshko N, Hutapea P. Assessment of tissue damage from mosquito-inspired surgical needle. *Minimally Invasive Therapy & Allied Technologies*. 2022;31(7):1112-21. doi: 10.1080/13645706.2022.2051718.
  27. Frasson L, Parittotokkaporn T, Schneider A, Davies B, Vincent J, Huq S, et al. Biologically inspired microtexturing: Investigation into the surface topography of next-generation neurosurgical probes. *30th Annual International Conference of the IEEE Engineering in Medicine and Biology Society: IEEE*; 2008. p. 5611-4.

## Appendix 8.A Optical fiber evaluation

### 8.A.1 Introduction

Inside a needle for TransPerineal Laser Ablation (TPLA), an optical fiber is inserted to transfer the laser energy to the target site (i.e., the tumor inside the prostate gland). Therefore, in a steerable TPLA needle, the optical fiber needs to follow a curved trajectory in tandem with the needle's curvature. Severe deflection of the optical fiber could potentially lead to power loss at the tip due to bending losses within the fiber. Laser light exiting the fiber core and entering the fiber cladding will be absorbed, resulting in a loss of power at the fiber tip [1]. Information on the power output during curved trajectories is crucial for the integration of optical fibers in steerable needles, as well as for determining the correct power setting on the laser. The study in this appendix experimentally investigates the impact of guiding an optical fiber along a curved trajectory on its power output.

### 8.A.2 Materials and methods

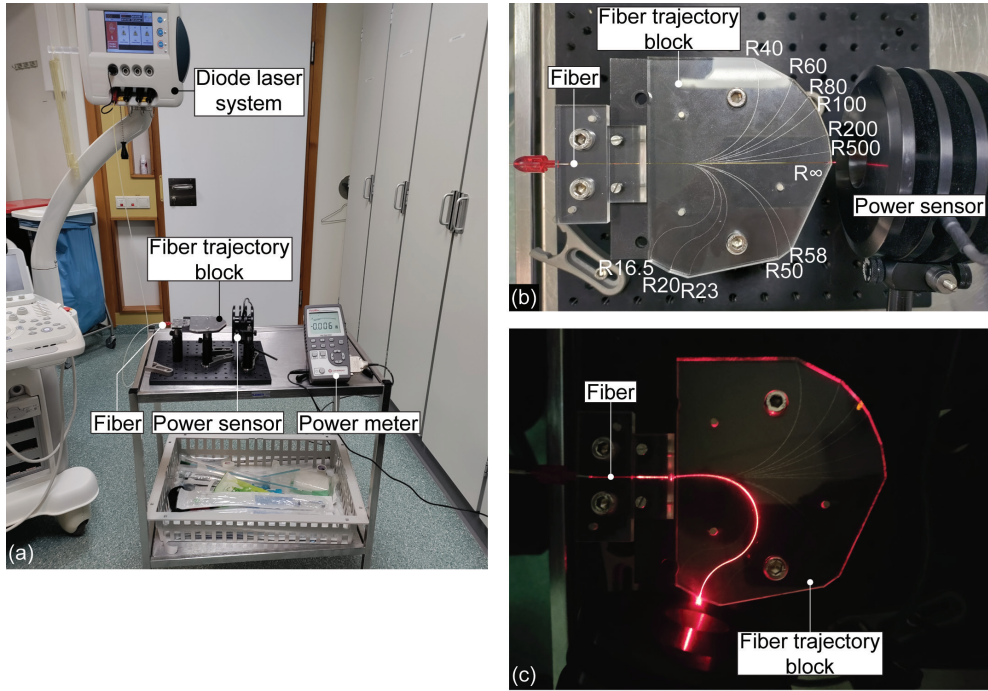
The experiment aimed to investigate the impact of fiber bending with distinct curvature on the power output. The experimental setup consisted of a single-use bare optical TPLA fiber (Asclepion Laser Technologies, GmbH, Jena, Germany) operating at 1064 nm, a diode laser system (SoracteLite, EchoLaser X4 system, Elesta S.p.A., Florence, Italy), a fiber trajectory block, a power sensor (PowerMax PM30, Coherent, Saxonburg, Pennsylvania, USA), and a laser power meter (FieldMaxII-TO, Coherent, Saxonburg, Pennsylvania, USA) (Figure 8.A1a). The fiber had a length of 2 m, a core diameter of 300  $\mu\text{m}$ , a clad diameter of 330  $\mu\text{m}$ , and a Numerical Aperture (NA) of 0.22. Measurements were performed at a fixed power of 3 W. A laser power meter behind the fiber trajectory block measured the output laser power of the fiber after it was bent along a curved trajectory in the fiber trajectory block (Figure 8.A1b).

The fiber trajectory block consisted of an aluminum plate containing 0.5-mm diameter, 0.5-mm deep semi-cylindrical tracks, and a transparent Perspex top attached to the aluminum plate using magnets. The curvature length of the tracks was kept constant at 77.8 mm for all trajectories, corresponding to a 270° bending angle for a bending radius of 16.5 mm. The bending radius varied between 500 mm and 16.5 mm (i.e., the minimum bending radius of the fiber equivalent to the clad diameter multiplied by 50). Accordingly, the bending angle varied between 8.9° and 270°. Furthermore, the fiber trajectory block also contained a straight trajectory with an infinite bending radius and a 0° bending angle as a control measure.

During a single measurement, the fiber was inserted into a track of the fiber trajectory block. Subsequently, the diode laser system was turned on at a power of 3 W (Figure 8.A1c). To determine the output power of the fiber passing through the track of the fiber trajectory block, a power sensor and laser power meter were placed at the distal tip of the fiber. Each fiber trajectory of the fiber trajectory block was measured twice, resulting in 24 measurements in total. The same optical fiber was used for each measurement.







**Figure 8.A1.** (a) Experimental setup for evaluating the impact of fiber bending on the power output. (b) Top view of the laser fiber in the straight trajectory of the fiber trajectory block, indicating the different bending radii of the corresponding trajectories. (c) Top view of the laser fiber in a curved trajectory of the fiber trajectory block when the diode laser system was turned on at a power of 3 W.

### 8.A.3 Results

The power output experiments showed that bending the optical fiber over trajectories with a bending radius of 500 to 16.5 mm only minimally impacted the power output, as shown in Table 8.A1. The measured output signal ranged between 2.75 W and 3.21 W, with a mean power output of 2.98 W and a standard deviation of 0.14 W. The greatest difference between input and output power of 0.25 W was measured for the smallest bending radius (i.e., 16.5 mm), the greatest bending radius (i.e., 500 mm), and the straight trajectory (i.e., bending radius =  $\infty$  mm). The successful bending of the optical fiber with low power losses implies that optical fibers can safely be used in steerable needles with a bending radius of up to 16.5 mm.



Table 8.A1. Measured power outputs per bending configuration.  $d_{\text{ratio}}$  = deflection-to-insertion ratio.

Bending radius [mm]	Bending angle [°]	$d_{\text{ratio}}$ [-]	Power output 1 [W]	Power output 2 [W]
$\infty^*$	0*	0	3.08	2.75
500	8.9	0.078	3.10	2.75
200	22.3	0.19	3.10	2.85
100	44.6	0.41	3.18	2.81
80	55.7	0.52	3.19	2.85
60	74.3	0.75	3.21	2.81
58	76.8	0.79	3.01	2.99
50	90.0	1	3.03	2.99
40	111.4	>1	3.19	3.01
23	193.7	>1	2.95	2.98
20	222.8	>1	2.87	3.02
16.5	270	>1	2.75	3.01

\* $\infty$  mm bending radius and 0° bending angle is equal to a forward trajectory (i.e., no steering).

## References

1. Mues AC, Teichman JM, Knudsen BE. Evaluation of 24 holmium: YAG laser optical fibers for flexible ureteroscopy. The Journal of urology. 2009;182(1):348-54. doi: 10.1016/j.juro.2009.02.112.



# 9

## **Fusing Wasp-Inspired Actuation with Pneumatics**

Published as:

Bloemberg J., Hoppener B., Coolen B., Sakes A., Breedveld P. (2024). Design and evaluation of a pneumatic actuation unit for a wasp-inspired self-propelled needle. PLoS ONE, 19(7):e0306411. doi: 10.1371/journal.pone.0306411.





## 9.1 Introduction

### 9.1.1 Transperineal laser ablation

For patients diagnosed with prostate cancer, there are multiple treatment options, including radical surgery, radiotherapy, and systemic treatment, such as chemotherapy, hormonal therapy, or immunotherapy [1]. Treatments targeting the entire gland can result in unwanted side effects due to damage to the surrounding healthy tissue [1-3]. To address this issue, one potential approach is to apply focal therapy [4-6], a method that targets only the cancerous cells (i.e., the lesion) while safeguarding the adjacent healthy tissue. TransPerineal Laser Ablation (TPLA) is one such focal therapy with fewer side effects than whole gland options [7]. TPLA is a novel minimally invasive thermo-ablative technique that induces cell death using optical fibers that are inserted into the prostate through transperineally positioned needles [8]. Clinical trials have demonstrated promising results in inducing tissue ablation with minimal treatment-related side effects [7-9].

For TPLA, Magnetic Resonance Imaging (MRI) guidance offers several advantages over guidance from other imaging modalities such as ultrasound, including superior soft tissue contrast for visualizing tumors and real-time temperature monitoring [9-12]. These advantages motivate the development of new Magnetic Resonance (MR) safe or MR conditional needles. According to the American Society for Testing and Materials (ASTM) standard F2503-13 [13], MR safe devices pose no known hazards resulting from exposure to an MR environment, whereas MR conditional devices pose no known hazards resulting from exposure to a specified MR environment with specified conditions of use.

### 9.1.2 MRI-compatible needles

Due to its constricted workplace and strong magnetic field with oscillating gradients, an MRI system poses unique challenges to medical instrument engineers designing MR safe or MR conditional needles and physicians performing the prostate interventions when the prostate is near the MRI system's isocenter. A number of researchers, such as Cepek *et al.* [14, 15] and Bloemberg *et al.* [16], have developed manually actuated systems, which allow the needle(s) to be positioned while the patient is inside the MRI bore. However, in these systems, the physician is required to work within the confined space of the MRI bore. Another solution is keeping the physician at a distance using an automated needle system that is actuated by a technology that does not use metallic, magnetic, or conductive materials [13].

A number of MR safe/conditional actuation methods have been proposed and demonstrated, such as piezomotors [17], Bowden cables [18, 19], hydraulics [20], and pneumatics [21-25]. In a hospital setup, pneumatics is advantageous as pressurized air is commonly available in an MRI room and can be controlled with a standard pneumatic valve manifold. An important drawback of pneumatics, however, is the compressibility of air, which means that the only well-defined pneumatic actuator positions are the start and end positions [26]. Nevertheless, this inherent characteristic of pneumatics makes it suitable for step-wise posi-



tion control [27].

Over the years, various research groups have developed pneumatic actuation systems for needles with the potential for use in MRI-guided interventional procedures. For example, Stoianovici *et al.* [21] developed an actuation system for transperineal prostate biopsy, the MrBot, which is driven by six rotational stepper actuation systems [28]. In addition, Groenhuis *et al.* [27] developed both linear and rotational teeth geometry stepper actuation systems using three-dimensional (3D)-printed parts and seals for a breast biopsy application.

In these pneumatically actuated needles, the actuation systems are designed for conventional needles that are pushed through the tissue, which requires an axial force on the needle. When this axial force exceeds the needle's critical load, the needle will deflect laterally—a mechanical failure mode known as buckling [29]. The lateral deflection poses a risk of damaging tissue in the vicinity of the needle and can result in poor control of the needle's path [30, 31]. To reduce tissue damage during needle insertion and allow for accurate needle positioning, wasp-inspired needles have been developed that can be advanced without being pushed through the tissue [32–35]. In the scientific literature, other sources of bio-inspiration, such as the mosquito [36, 37], were used for needles employing different working principles [38]. Furthermore, wasp-inspired propulsion has also been shown to be useful in a drilling device for medical applications [39].

### 9.1.3 Wasp-inspired needles

Female parasitic wasps use their ovipositor to deposit their eggs into hosts, which may hide in a dense material such as wood [40]. The ovipositor of the parasitic wasp species *Diachasmimorpha longicaudata* Ashmead (Hymenoptera: Braconidae) is very long ( $5.7 \pm 0.6$  mm) [41] and thin (30–50  $\mu$ m) [42] and comprises three slender, parallel segments referred to as valves [43], which reciprocate by advancing and retracting them with respect to each other (Figure 9.1). The advancing and retracting forces generate a net push force near zero, allowing for self-propulsion within a substrate.

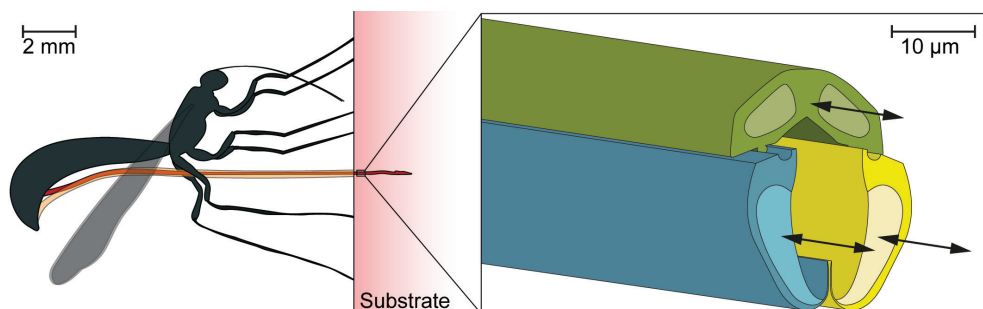


Figure 9.1. Visualization of the ovipositor of a female parasitic wasp *Diachasmimorpha longicaudata* Ashmead (Hymenoptera: Braconidae). Sheaths (orange) support the ovipositor (red) outside the substrate (pink) that she is probing in. The ovipositor consists of three parallel valves (green, yellow, blue) that can move reciprocally (based on Cerkvenik *et al.* [43]).

Wasp-inspired self-propelled needles apply this self-propulsion principle to advance through tissue. They are composed of parallel segments that can slide along each other (Figure 9.2a). Inserting a needle into tissue results in forces acting on the needle by the surrounding tissue. Okamura *et al.* [44] demonstrated that these forces are the sum of the surface stiffness force ( $\mathbf{F}_{\text{stiff}}$ ), cutting force ( $\mathbf{F}_{\text{cut}}$ ), and friction force ( $\mathbf{F}_{\text{fric}}$ ). To insert a needle into tissue, the operator should apply an insertion force ( $\mathbf{F}_{\text{in}}$ ) that overcomes the sum of these forces acting on the needle.

The surface stiffness force ( $\mathbf{F}_{\text{stiff}}$ ) arises at the needle tip and can be described as the pre-puncture force and is due to the elasticity of the tissue layer and occurs when puncturing the skin or a stiffer tissue layer than the current surrounding tissue, e.g., when puncturing the membrane around an organ [45]. In this pre-puncture phase, the needle is not cutting the tissue, but instead compressing it until it punctures the skin or surface membrane [46]. In the post-puncture phase, after the needle has punctured the tissue layer, the surface stiffness force returns to zero.

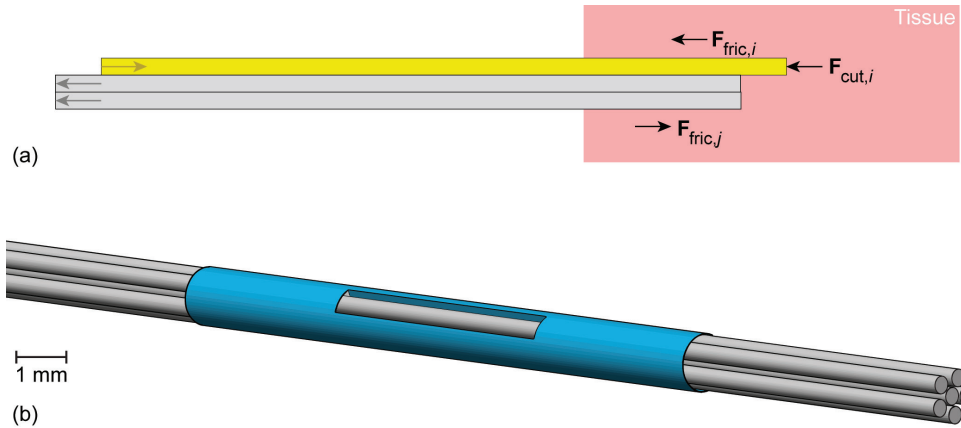
Both the cutting and friction forces are post-puncture forces. The cutting force arises at the needle tip when slicing through the tissue due to the plastic deformation of the tissue and the tissue stiffness experienced at the tip of the needle because the needle still encounters stiffness as it cuts through the tissue [47]. When assuming the tissue structure is homogeneous, the cutting force remains roughly constant throughout the insertion [48]. The friction force occurs along the length of the needle inside the tissue and arises due to Coulomb friction, adhesive friction, and viscous friction [49]. The Coulomb friction force (i.e., static friction force) depends linearly on the normal force acting on the needle body as a reaction to the compression applied by the needle that compresses the tissue out from the needle path, which is affected by the needle diameter and the coefficient of friction between the needle and the tissue [49]. The adhesive friction force is caused by the surface roughness of the needle, which is caused by the tendency of the tissue to stick to the needle surface. The viscous friction force (i.e., dynamic friction force or damping) depends on the damping force during needle translation through the tissue and is proportional to the relative velocity between the needle and surrounding tissue [50].

The self-propelled motion of the needle is accomplished by balancing the cutting and friction forces of the advancing segments with the friction force generated by the remaining stationary or retracting segments [35]. Equation 9.1 represents the conditions required for the self-propulsion of the needle [51].

$$\sum_{i=1}^a (\mathbf{F}_{\text{stiff},i} + \mathbf{F}_{\text{fric},i} + \mathbf{F}_{\text{cut},i}) \leq \sum_{j=1}^r (\mathbf{F}_{\text{fric},j}) \quad (9.1)$$

where  $a$  refers to the number of advancing needle segments,  $r$  refers to the number of retracting or stationary needle segments,  $a+r$  is the total number of needle segments, and  $\mathbf{F}_{\text{stiff}}$ ,  $\mathbf{F}_{\text{fric}}$ , and  $\mathbf{F}_{\text{cut}}$  represent the surface stiffness, friction, and cutting forces, respectively.  $\mathbf{F}_{\text{stiff}}$  is only present when puncturing tissue layers and is not present whilst self-propelling through homogeneous tissue [51]. The self-propelled motion of the needle requires the friction force generated by the retracting or stationary needle segments to counterbalance the combined





**Figure 9.2. Visualizations of ovipositor-inspired needles.** (a) Schematic two-dimensional (2D) illustration of ovipositor-inspired needle insertion into tissue with one advancing needle segment (yellow) and two retracting needle segments (gray) in the post-puncture phase after the needle has penetrated the outer tissue layer, therefore,  $\mathbf{F}_{\text{stiff}}$  is not present.  $\mathbf{F}_{\text{fric},i}$  is the friction force along the advancing needle segment,  $\mathbf{F}_{\text{cut},i}$  is the cutting force on the tip of the advancing needle segment, and  $\mathbf{F}_{\text{fric},j}$  is the friction force along the retracting needle segments, which works in the opposite direction as the friction force of the advancing needle segments. (b) Schematic three-dimensional (3D) illustration of the ovipositor-inspired needle consisting of six parallel segments (gray) that can slide along each other and are bundled by a shrink tube (blue).

friction and cutting forces of the advancing needle segments. By doing so, the needle is able to gradually move forward through the tissue as a whole with a self-propelled motion. As the needle propels deeper into the tissue, the surface area of the needle segments in direct contact with the tissue increases, increasing the friction forces on the needle segment linearly with insertion depth while the cutting force remains roughly constant throughout the insertion [48]. Scali *et al.* [51, 52] and Bloemberg *et al.* [16] developed various wasp-inspired self-propelled needles with a submillimeter external diameter consisting of three to seven parallel segments that can slide along each other and are bundled by a ring or a heat shrink tube. The needles self-propel with zero external push force without buckling, by advancing one needle segment at a time over a short distance and slowly retracting the other segments, thereby the friction force of the stationary needle segments counterbalances the sum of the friction and cutting forces of the advancing needle segment [16, 51].

#### 9.1.4 Goal of this study

Wasp-inspired self-propelled needles could allow for accurate needle positioning for targeted medical MRI-guided procedures to treat prostate cancer, while avoiding unwanted tissue damage. Current prototypes of wasp-inspired self-propelled needles employ either electric motors [35, 51, 53, 54] or manual activation [16] to actuate the individual needle segments. Electric motors are not suitable for MRI-guided procedures as they employ metallic, magnetic, and conductive materials, which makes the needles MR unsafe [13]. Manual activation is less suitable for MRI-guided procedures as it requires the physician to work manually within the confined space of the MRI bore. In this research, we propose a pneumatic actuation unit

for a wasp-inspired needle that enables physicians to operate the needle under MRI guidance without having to manually actuate the needle within the confined space of the MRI bore.

## 9.2 Design

### 9.2.1 Needle

The complete design, called the Pneumatic Ovipositor Needle, consists of a needle, an actuation unit, and a control unit. Following our previous design [16] (Chapters 7,8), we decided to focus our research on a self-propelled wasp-inspired needle consisting of six 200-mm long parallel needle segments to reach the prostate transperineally (Figure 9.2b) [55]. The needle self-propels through the substrate by first moving the six needle segments forward one by one (i.e., the advancing phase), followed by moving all six needle segments backward simultaneously (i.e., the retracting phase). In this study, the two-phase motion sequence, which involves advancing the six needle segments one by one followed by retracting all six needle segments simultaneously, will be referred to as a “cycle.” The distance that each needle segment travels per cycle is called the “stroke length.”

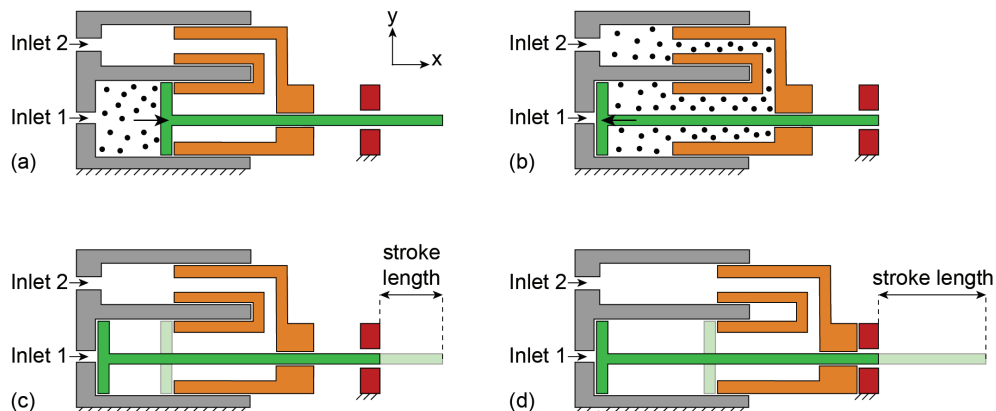
### 9.2.2 Actuation unit

The actuation unit consists of six pneumatic cylinders, six needle clamps, and a cone. The six pneumatic cylinders are positioned in a circle, so each piston has the cross-sectional shape of 1/6th of a circle. Figure 9.3 shows the working principle of one pneumatic cylinder. The mechanism is simplified and visualized in a two-dimensional (2D) schematic cross-sectional illustration to explain the working principle. The pneumatic cylinder consists of a piston (in green), a piston housing (in gray), a piston stop (in orange), and a piston guide (in red). Each piston can translate in the positive and negative x-direction driven by two pneumatic tubes connected to two separate inlets. By pressurizing Inlet 1, the piston moves in the positive x-direction (Figure 9.3a) and by pressuring Inlet 2, the air will flow through the piston stop, moving the piston in the negative x-direction (Figure 9.3b).

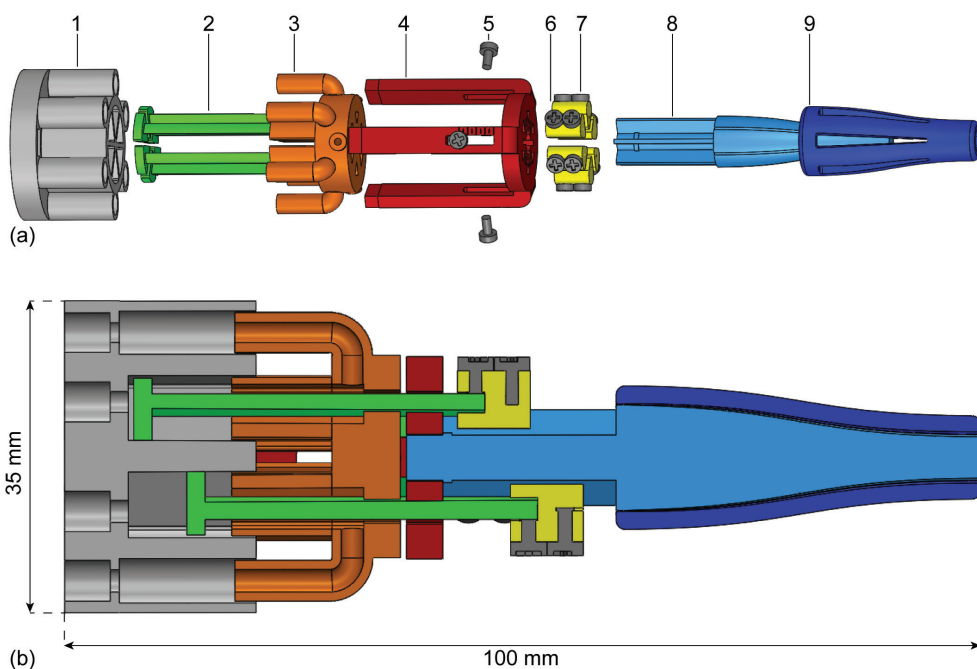
The piston stop, which fits into the piston housing and is constrained from sliding out of the housing by the piston guide, allows adjustment of the piston stroke length. The piston stop can be moved and locked in place by screw fasteners in the piston guide and piston stop. For a short stroke length, the piston stop is moved and locked at a position close to the piston housing (i.e., in the negative x-direction) (Figure 9.3c), whereas for a long stroke length, the piston stop is moved and locked at a position far from the piston housing (i.e., in the positive x-direction) (Figure 9.3d). The stroke length can be varied in the range of 2-10 mm.

To facilitate easy attachment and detachment of the needle segments to the pistons, piston tips (Figure 9.4a in yellow) were created. Each piston tip has two openings on the distal and proximal sides for securing the piston and needle segment using screw fasteners, respectively.

The needle segments run through the actuation unit at a larger diameter than at the needle tip. A cone (in blue) at the distal side of the actuation unit smoothly guides the needle seg-



**Figure 9.3.** Schematic illustration of the pneumatic cylinder design composed of the piston housing (gray), piston (green), piston stop (orange), and piston guide (red). (a) When Inlet 1 is pressurized, the piston translates in the positive x-direction. (b) When Inlet 2 is pressurized, the piston translates in the negative x-direction. The piston stop can translate along the x-axis to allow for an adjustable stroke length between 2 mm (c) and 10 mm (d). The piston stop can be locked in place by tightening screw fasteners (not shown) in the piston guide and piston stop.



**Figure 9.4.** Exploded view (a) and cross-section (b) of the entire pneumatic actuation unit, consisting of a piston housing (1), piston (2), piston stop (3), piston guide (4), screws to secure the piston stop (5), piston tip (6), screws to secure the piston tip to the piston and the needle segment (7), inner part of the cone (8), and outer part of the cone (9).

ments from the actuation unit to the needle tip through S-shaped channels, which allow the needle segments to slide back and forth freely while avoiding buckling. To prevent blockage of the channels during the stereolithography 3D-printing process, we composed the cone out of two parts (Figure 9.4b), each containing semi-cylindrical grooves rather than a single part containing cylindrical channels.

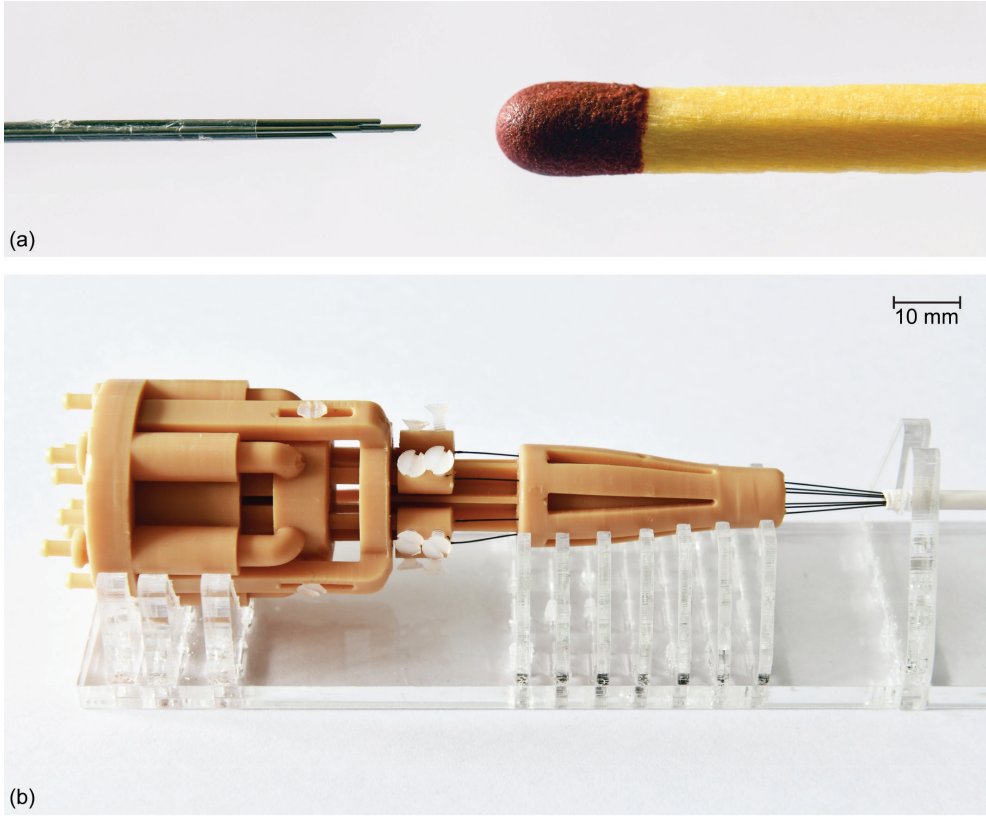
### 9.2.3 Control unit

Pressurized air is required to actively translate the pistons of the actuation unit. The pressure in each cylinder chamber is controlled by a system of electromagnetic valves of type *Festo MHP2-MS1H-5/2-M5* (Festo AG & Co. KG, Esslingen am Neckar, Germany), supplied with a system (gauge) pressure ( $P$ ). The 5/2-way valves have two outputs, when no signal is sent to the valve, the first output, which we connected to Inlet 2, is pressurized, moving the piston in the negative x-direction, thereby retracting the needle segment. When applying an electrical signal, the second output, which we connected to Inlet 1, is pressurized, moving the piston in the positive x-direction, thereby advancing the needle segment. The six valves are controlled by an *Arduino Uno board SMD R3 A000073* (Arduino SRL, Strambino, Italy) powered by a 24V power supply via transistor amplifiers. The actuation unit and needle are placed inside the MRI bore, while the MR-unsafe components (i.e., the valves, the Arduino Uno board, transistor amplifiers, and power supply) must be placed outside the Faraday cage of the MRI system. Therefore, tubes were used to connect the actuation unit to the valves.

### 9.2.4 Prototype

Following our previous design [16] (Chapters 7,8), the needle in this study consists of six MR-conditional superelastic straight annealed nitinol rods with a diameter of 0.25 mm and a length of 200 mm (Figure 9.5a). These needle segments were held together at the tip using 10-mm long *Heat Shrink Tubing 103-0139* (Nordson Medical Corp., Westlake, OH, USA, expanded inner diameter 0.814 mm, wall thickness 0.013 mm). This tube was employed to limit the needle segments from diverging while only minimally increasing the needle diameter. To maintain its position at the needle tip, the heat shrink tube was glued to one of the needle segments using *Pattex Gold Gel 1432562* (Pattex, Henkel AG & Co, Düsseldorf, Germany). The remaining needle segments can move freely back and forth through the heat shrink tube. The resulting total diameter of the needle, including the heat shrink tube, is 0.84 mm.

A stereolithography 3D-printing process was used for the production of the actuation unit prototype due to its ability to produce high-resolution features in the range of 25  $\mu\text{m}$  [56]. All components of the actuation unit were printed using a Formlabs Form 3B printer with a layer height of 0.025 mm using MR-safe *Dental Model V2 resin RS-F2-DMBE-02* (Formlabs, Somerville, MA, USA) with the exception of the screws. MR-safe polyamide plastic screws of type *Toolcraft 839944 DIN 963 M2 x 10 mm* (Toolcraft Machining, Inc., Germantown, WI, USA) were selected. The assembled actuation unit has a length of 100 mm and an outer diameter of 35 mm (Figures 9.4b and 9.5b).



**Figure 9.5. Pneumatic Ovipositor Needle.** (a) Close-up of the needle tip consisting of six nitinol needle segments held together by a heat shrink tube that is glued to one of the six needle segments. (b) Assembled prototype manufactured using the stereolithography technology in *Dental Model V2 resin RS-F2-DMBE-02* (Formlabs, Somerville, MA, USA). A transparent PolyMethyl MethAcrylate (PMMA) structure supports the prototype.

9

## 9.3 Evaluation

### 9.3.1 Experimental goal

To evaluate the performance of the Pneumatic Ovipositor Needle under controlled conditions, an experiment in gelatin phantoms was performed. The experiment's goal was twofold: investigate the performance behavior of the needle actuated by the pneumatic actuation unit for (1) different stroke lengths and (2) different piston interval times. The performance of the developed Pneumatic Ovipositor Needle was evaluated in gelatin phantoms in terms of the slip of the needle with respect to the gelatin phantom tissue. More specifically, we calculated the slip ratio of the needle while it advanced through the phantom tissue, using Eq. 9.2.

$$s_{\text{ratio}} = 1 - \left( \frac{d_m}{d_t} \right) \quad (9.2)$$

where  $d_m$  and  $d_t$  are the measured and theoretical maximum traveled distance, respectively. Per cycle, the theoretical maximum traveled distance ( $d_t$ ) equals the stroke length ( $S$ ). To eval-

uate the slip ratio of the needle throughout all actuation cycles, we used a laser displacement sensor instead of MRI to continuously measure the traveled distance ( $d_m$ ).

### 9.3.2 Experimental variables

The dependent variable was the slip ratio ( $s_{ratio}$ ) between the needle and gelatin for each cycle.

The independent variables were the stroke length ( $S$ ) of the needle segments and the piston interval time ( $I$ ). To investigate the effect of the stroke length ( $S$ ),  $S$  was set at 2 or 4 mm, while keeping  $I$  at 0.5 s. For investigating the effect of the interval time ( $I$ ),  $I$  was set at 0.5, 0.3, or 0.1 s, while keeping  $S$  at 4 mm. A shorter interval time means a shorter cycle time, so in theory this results in the needle moving faster through the substrate.

The control variables were the system (gauge) pressure ( $P$ ) of 0.5 bar and the number of actuation cycles ( $C$ ) set to 30. To evaluate the slip ratio ( $s_{ratio}$ ) of the needle throughout all actuation cycles, the traveled distance ( $d_m$ ) was measured continuously. Table 9.1 shows the four experiment conditions evaluated in gelatin phantoms.

### 9.3.3 Experimental facility

Figure 9.6 shows the experimental setup consisting of the needle connected to the actuation and control units, cart, gelatin phantom, air supply, and data acquisition unit. Instead of moving the needle toward the gelatin, the gelatin was placed on a low-friction aluminum cart and moved toward the actuation unit over PolyMethyl MethAcrylate (PMMA) rails. The principle of needle insertion with zero external push force holds if the self-propelled needle pulls the tissue toward itself by pulling itself deeper into the tissue, thereby pulling the cart toward the needle. The cart (220 x 90 mm<sup>2</sup>) allowed for low-friction movement using four ball bearings, following the experiment design by Scali *et al.* [51]. Millimeter paper was attached to the cart and used as a reference during needle insertion. A linear laser displacement sensor of type *optoNCDT* (Micro-Epsilon Messtechnik GmbH & Co. KG, Ortenburg, Germany) was used to record the position of the cart during the experiments. A data acquisition unit *NI*

**Table 9.1. Experimental conditions and mean slip ratio mean for the phantom experiment.** The following information is reported: the condition name, stroke length,  $S$  [mm], interval time,  $I$  [s], between pressurization of the subsequent pneumatic cylinders of the actuation unit, number of actuation cycles the needle was actuated for,  $C$ , total theoretical maximum traveled distance,  $d_t$  [mm], that the gelatin phantom cart would have traveled if no slip at all occurred, total mean measured traveled distance,  $d_m$  [mm], and slip ratio,  $s_{ratio}$ .

Condition	Stroke length, $S$ [mm]	Interval time, $I$ [s]	Number of actuation cycles, $C$	Total theoretical maximum traveled distance, $d_t$ [mm]	Total mean measured traveled distance, $d_m$ [mm] (mean $\pm$ SD)	Slip ratio, $s_{ratio}$ (mean $\pm$ SD)
S2-I05	2	0.5	30	60	4.3 $\pm$ 3.6	0.926 $\pm$ 0.123
S4-I05	4	0.5	30	120	7.7 $\pm$ 4.6	0.935 $\pm$ 0.089
S4-I03	4	0.3	30	120	10.4 $\pm$ 6.2	0.912 $\pm$ 0.081
S4-I01	4	0.1	30	120	5.0 $\pm$ 2.4	0.955 $\pm$ 0.049



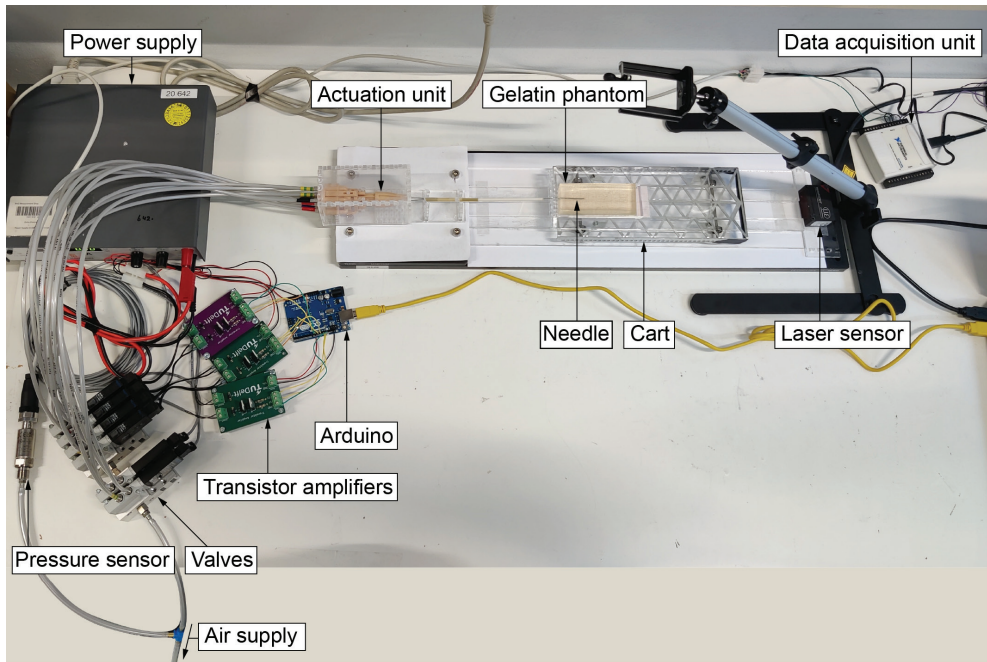


Figure 9.6. Photo of the experimental setup used during the phantom experiment, with the needle inserted into the gelatin phantom.

USB-6211 16-bit (National Instruments Corporation, Austin, TX, USA) in conjunction with LabVIEW 2014 (National Instruments Corporation, Austin, TX, USA) was used to collect the laser sensor data. The air pressure entering the valves was monitored using a pressure sensor of type Autosen AP202 (Autosen GmbH, Essen, Germany) and regulated using a pressure regulator of type Norgren B72G-2GK-ST3-RMN (Norgren Ltd, Lichfield, United Kingdom), which was connected to the air supply. To connect the control unit to the actuation unit, we used 30-cm long, 4-mm outer diameter air hoses of type Festo 152584 PUN-4X0,75-SI (Festo AG & Co. KG, Esslingen am Neckar, Germany). The air supply and pressure regulator were connected to the control unit using 200-cm long, 6-mm outer diameter air hoses of type Festo 152586 PUN-6X1-SI (Festo AG & Co. KG, Esslingen am Neckar, Germany).

For the experiments, gelatin powder of type Dr. Oetker 1-50-230004 (Dr. Oetker Professional, Amersfoort, The Netherlands) was mixed with water with a gelatin weight ratio (wt) of 10%, resulting in a modulus of elasticity of 17 kPa [51], which is similar to that of prostate tissue [57, 58]. We chose to create gelatin phantoms with a modulus of elasticity similar to that of prostate tissue because there is limited knowledge in the scientific literature about mimicking other mechanical properties of prostate tissue in gelatin phantoms relevant for needle insertion. The gelatin/water mixture was poured into silicone molds and stored overnight at 5 °C to solidify. Afterward, the gelatin phantoms were cut to their final dimensions (width 38 mm, length 100 mm, height 20 mm).

### 9.3.4 Experimental procedure

For each measurement, a new gelatin phantom (mean  $\pm$  standard deviation =  $62.5 \pm 4.2$  g) was placed on the cart. The needle was inserted over an initial distance of 35 mm inside the gelatin, to ensure initial contact between the needle segments and the gelatin and to ensure the prototype was inserted in a straight direction. The laser sensor was turned on and the needle actuation started. Each test condition was repeated ten times. During every measurement, a linear laser displacement sensor captured the position of the cart (the Supplementary material shows a detailed explanation of the steps in the experiment protocol).

### 9.3.5 Data analysis

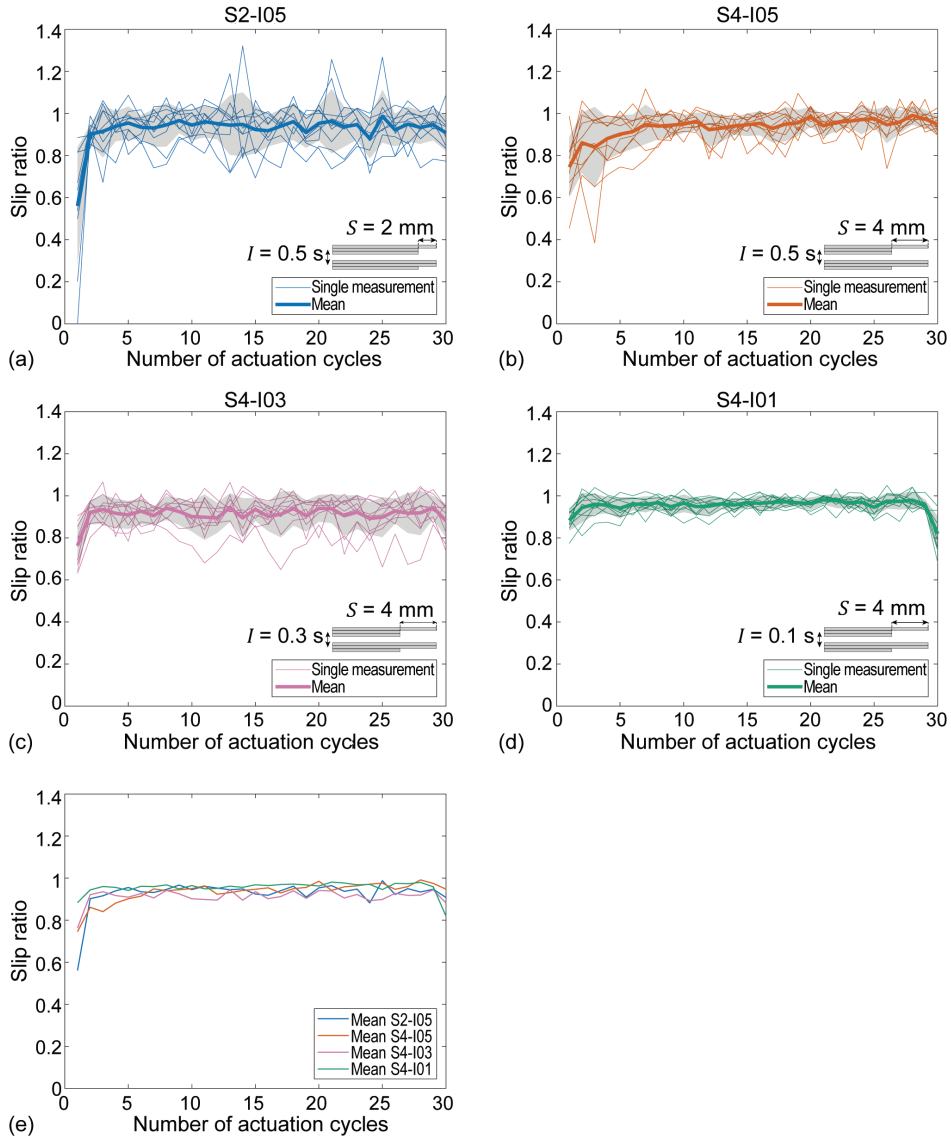
The raw data recorded by the laser sensor during the measurements was imported in MATLAB R2020B. The data included the position data of the cart against the time. A Savitzky-Golay filter was used for filtering noise. To evaluate the performance, we calculated the slip ratio ( $s_{\text{ratio}}$ ) for each cycle (Eq. 9.2). For the stroke length evaluation, we performed the Wilcoxon signed-rank test for two related groups of nonparametric data (i.e., S2-I05 and S4-I05). For the interval time evaluation, we performed Friedman's ANOVA for three related groups of nonparametric data (i.e., S4-I05, S4-I03, and S4-I01). To further examine the statistical differences between the data, three Wilcoxon signed-rank tests were conducted. The significance level was set at  $p < 0.05$ .

### 9.3.6 Results

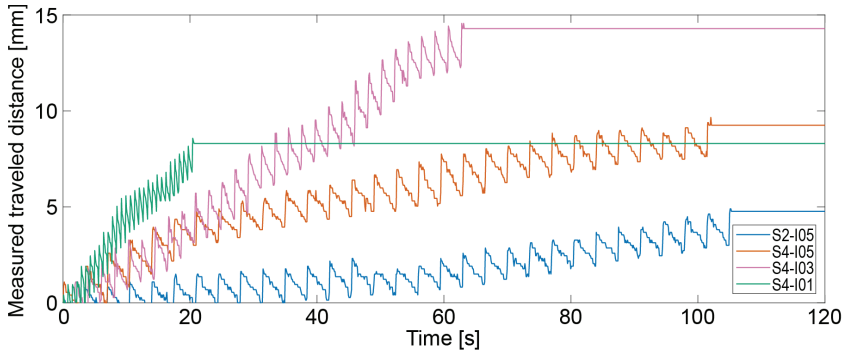
Figure 9.7 shows the slip ratio over the number of actuation cycles for each experiment condition. Table 9.1 shows the mean and standard deviation of the slip ratio for each experiment condition. The mean slip ratios for Conditions S2-I05 and S4-I05 are  $0.926 \pm 0.123$  and  $0.935 \pm 0.089$ , respectively. However, the Wilcoxon signed-rank test showed there was no significant difference between both conditions ( $z = -0.662$ ,  $p = 0.508$ ) when comparing the slip ratios for the different stroke lengths. The mean slip ratios for Conditions S4-I05, S4-I03, and S4-I01 are  $0.935 \pm 0.089$ ,  $0.912 \pm 0.081$ , and  $0.955 \pm 0.049$ , respectively. A Friedman test ( $p = 1.588\text{e-}10$ ) showed that there are at least two conditions with significant differences from each other when comparing the slip ratios for the different interval times. The Wilcoxon signed-rank tests showed that the slip ratio of Condition S4-I01 is significantly different from the slip ratios of Conditions S4-I05 ( $z = -2.905$ ,  $p = 0.37\text{e-}3$ ) and S4-I03 ( $z = -8.230$ ,  $p = 1.881\text{e-}16$ ). The slip ratio of Condition S4-I05 also proved to be significantly different from the slip ratio of Condition S4-I03 ( $z = 3.59$ ,  $p = 3.294\text{e-}4$ ). Furthermore, the slip ratio variability was lower for a shorter stroke length (i.e., 2 mm) compared to a longer stroke length (i.e., 4 mm). Additionally, the slip ratio variability was reduced with lower interval times (i.e., 0.3 and 0.1 s) in contrast to a higher interval time (i.e., 0.5 s). Figure 9.8 shows typical graphs retrieved by the sensor data for the different experiment conditions. Despite the lowest interval time condition showing the highest slip ratio, the needle moved faster through the substrate because of its shorter cycle time. In the Supplementary material of this



chapter, a video shows the tip of the Pneumatic Ovipositor Needle in gelatin during actuation.



**Figure 9.7. Results of the Pneumatic Ovipositor Needle phantom experiment.** The subfigures show the slip ratio over the number of actuation cycles of the needle in gelatin phantoms for actuation with (a) 2-mm stroke length and a 0.5-s interval time, (b) 4-mm stroke length and a 0.5-s interval time, (c) 4-mm stroke length and a 0.3-s interval time, and (d) 4-mm stroke length and a 0.1-s interval time. The thin lines represent the single measurements, the thick line is the mean value, the gray area around the mean value represents the standard deviation. (e) Mean slip ratios for the different experiment conditions over the number of actuation cycles.



**Figure 9.8.** Plot of measured distance traveled by the cart [mm] vs. time [s] of the phantom experiment, showing typical graphs retrieved by the sensor data for each condition evaluated. The local minima show the position of the cart when all needle segments are advanced, and the local maxima represent the position of the cart when all needle segments are retracted during the step-by-step actuation. The distance between two peaks defines a cycle. For all conditions, the needle was actuated for 30 actuation cycles, so for 0.5-s, 0.3-s, and 0.1-s interval times, the measurement took 105 s, 63 s, and 21 s, respectively. A shorter interval time means a shorter cycle time, so this resulted in the needle moving faster through the substrate.

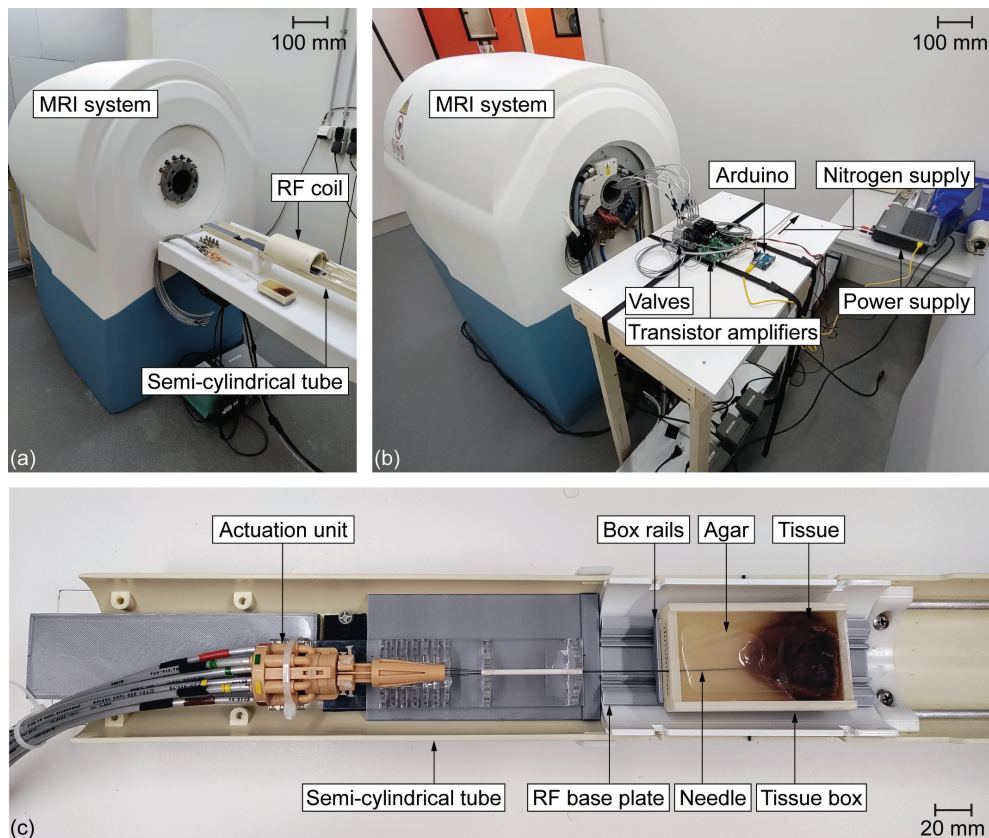
### 9.3.7 Additional MRI experiment

To demonstrate the potential of the needle inside an MRI environment, an additional proof-of-principle experiment using *ex vivo* porcine liver tissue in a preclinical 7-Tesla MRI system (MR Solutions, Guildford, United Kingdom) at the Amsterdam University Medical Center (AUMC, department of Biomedical Engineering and Physics) was performed. Due to the limited accessibility of *ex vivo* human prostate tissue, we employed *ex vivo* porcine liver tissue as an alternative, given its comparable modulus of elasticity of 15-20 kPa [59] to prostate tissue [57, 58]. Ethical approval was not required for the study involving animals in accordance with the local legislation and institutional requirements because the tissue sample used was commercially available porcine liver tissue obtained from a local butcher.

Figure 9.9 shows the experimental setup consisting of the needle connected to the actuation and control units, the MRI system, the tissue sample in a tissue box on a low-friction cart design located inside a RadioFrequency (RF) coil, and nitrogen supply. For a more comprehensive explanation of the low-friction cart design inside the RF coil, please refer to the description provided in our previous work [16].

We prepared the biological sample (width 50 mm, length 90 mm, height 10 mm, weight 46 g) by placing a piece of *ex vivo* porcine liver tissue (width 50 mm, length 45 mm, height 10 mm) in the tissue box with liquid agar (1.0 wt%). The liver tissue was positioned at the distal end of the tissue box and the remaining part of the tissue box was filled with agar, which facilitated the insertion of the needle for approximately 45 mm into the agar before reaching the liver tissue. Storing the box in the refrigerator overnight ensured fixation of the tissue in the agar.

A 3D gradient-echo acquisition was performed continuously for 3 minutes to image the needle position during needle actuation with respect to the liver tissue and the tissue



**Figure 9.9. Experimental setup used during the Magnetic Resonance Imaging (MRI) experiment.** (a) Front of the MRI system where the Pneumatic Ovipositor Needle was placed in a semi-cylindrical tube that slides into the MRI bore. The semi-cylindrical tube supports a RadioFrequency (RF) coil for signal reception, in which the tissue box was placed. (b) Back of the MRI system where the hoses connecting the valves to the Pneumatic Ovipositor Needle and the actuation unit enter the MRI bore. (c) Close-up of the semi-cylindrical tube from above with the actuation unit and the tissue box on the RF base plate, guided on box rails. In the tissue box, the *ex vivo* porcine liver tissue was embedded in solidified 1-wt% agar.

box. Because we used a continuous pseudo-radial k-space sampling pattern, this allowed for retrospective 3D image reconstruction at different temporal resolutions. Therefore, we obtained high-quality 3D images of both the initial and final static position of the needle, as well as reconstructions with higher temporal resolution (7.5 s) during movement of the tissue along the needle (see the Supplementary material for the imaging parameters and a detailed explanation of the steps in the experiment protocol). Figure 9.10 shows the MR images of the needle tip positions and the Supplementary material shows the dynamic MRI video. The measurement showed that the needle was able to propel itself forward inside the liver tissue with a slip ratio of 0.88.

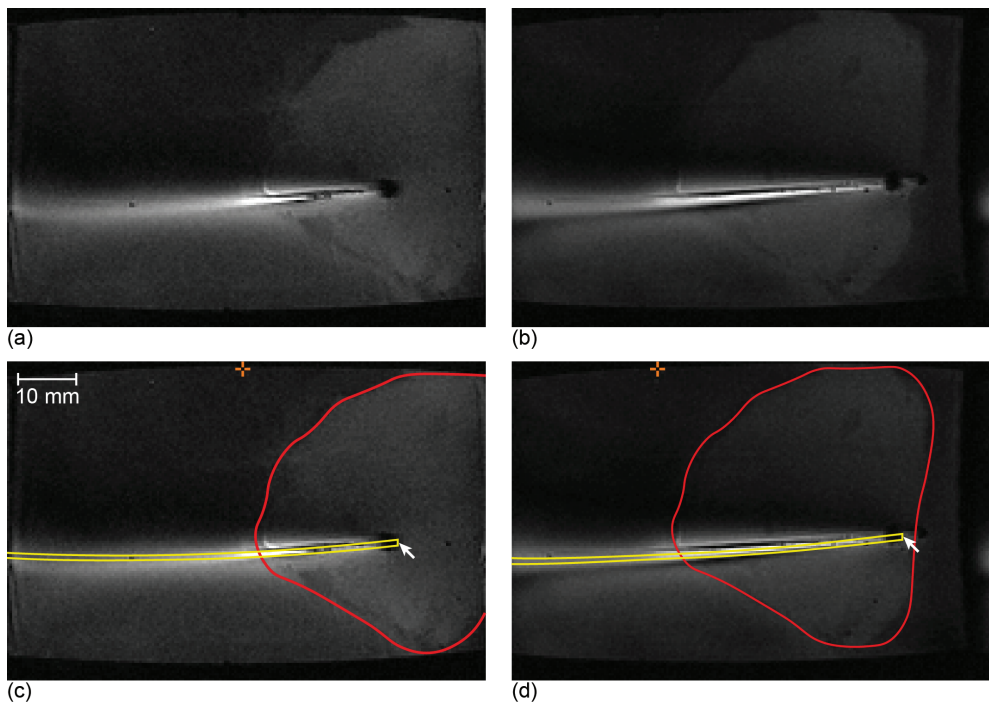
## 9.4 Discussion

### 9.4.1 Main findings

Compared to previous work done by Scali *et al.* [51], our measured mean slip ratio is high. A possible explanation for our high slip ratio results could be that the insertion force required to move the needle segments forward was high because of the high insertion speed caused by the pneumatic actuation. DiMaio and Salcudean [60] and Meltsner *et al.* [61] showed that both cutting and friction forces of needles in tissue phantoms increase with increasing insertion velocities. Furthermore, the compressibility of air may have resulted in a lower actual stroke length compared to the stroke length the needle was actuated for.

### 9.4.2 Limitations

In both phantom and MRI experiments, the inertia of the cart, as well as the experienced friction might have influenced the slip results. The mass of the cart and the gelatin phantom or tissue tends to increase the slip in the retracting phase of the needle segments, whereas



**Figure 9.10. Magnetic Resonance (MR) images of the needle inside the agar and *ex vivo* porcine liver tissue.** Original MR images (a) where the needle tip is inserted through the agar and partially through the liver tissue and (b) after actuation over thirty actuation cycles. Annotated MR images (c) where the needle tip is inserted through the agar and partially through the liver tissue and (d) after actuation over thirty actuation cycles. The yellow and red contours show the needle and liver tissue, respectively. The arrow marks the needle tip. The orange crosshair shows the reference point on the side of the box that indicates a 40-mm insertion depth.

the contrary holds for the advancing phase. In the retracting phase, the resultant force on the needle inside the tissue (phantom) is likely to be lower than the force required to overcome the bearing friction and cart inertia. Therefore, an effect of inertia and bearing friction cannot be ruled out.

In the experimental setup, air hoses were used to interconnect the air supply with the control and actuation units. However, in the MRI experiment, the length of the air hoses connecting the control and actuation unit was required to be longer than during the phantom experiment (70 cm vs. 30 cm, respectively) to maintain a certain distance between the MR-unsafe control unit and the center of the MRI system. Assuming a constant nominal standard airflow for the pneumatic valves, an increase in the air hose length results in an increase in the pressure drop and delay and friction effects in the air hose [27]. These effects cause a variation in the pressure inside the actuation unit between the phantom experiment with shorter air hoses and the MRI experiment with longer air hoses, potentially affecting the actual stroke length of the needle segments and slip ratio of the needle. Furthermore, to prevent air leakage in future versions of the Pneumatic Ovipositor Needle, replacing the pistons with bellows could be investigated [62, 63].

In the experiments, gelatin phantoms and *ex vivo* porcine liver tissue with a modulus of elasticity similar to that of prostate tissue were used. However, for needle insertion experiments, other mechanical properties, such as the needle-tissue friction coefficient, shear modulus, and ultimate strength of the tissue are of higher interest than the modulus of elasticity of the tissue. Furthermore, material properties may vary from human to porcine tissue [64]. Therefore, we recommend investigating the mechanical properties of human prostate tissue, *ex vivo* tissue specimens, and tissue-mimicking materials that are important for needle insertion and propulsion, thereby also considering the tissue's nonlinearity and heterogeneity.

### 9.4.3 Recommendations and future research

The Pneumatic Ovipositor Needle was designed as a delivery needle for TPLA to treat prostate cancer. The integration of the optical fiber in the Pneumatic Ovipositor Needle requires a hollow core in the actuation unit positioned between the pneumatic cylinders, allowing six needle segments, concentrically arranged around a 300- $\mu\text{m}$  diameter optical fiber for TPLA [65], resulting in a total needle outer diameter of 0.8 mm. In the two-phase motion sequence of the needle, retracting all six needle segments simultaneously could advance the centrally positioned optical fiber into the substrate. The surface area of the needle segments in direct contact with the optical fiber is the same as the surface area of the needle segments in direct contact with each other in the current prototype. Consequently, we do not expect the optical fiber to influence the friction forces of the needle. However, in theory, the optical fiber does increase the cutting force during the retraction phase. In future work, it will be interesting to perform experiments to determine the cutting and friction forces acting on the needle.

To develop a full picture of the Pneumatic Ovipositor Needle in a clinical setting, *in vivo*

experiments are needed. When moving toward an *in vivo* study, we foresee some challenges, including the presence of fluids (i.e., blood) and multi-layered tissue. The presence of fluids like blood may reduce the needle-tissue friction required for the self-propelled motion. On the other hand, the parasitic wasp is able to move effectively through fluid-like substances like fruits thanks to directional friction patterns that increase friction [66]. Inspired by these friction patterns, Parittotokkaporn *et al.* [67] added a directional friction pattern to the needle surface. This could be an interesting avenue to explore for our needle in the future.

Another challenge that arises from an *in vivo* model is the presence of multiple tissue layers between the insertion point, which is the perineum, and the target position within the prostate gland. Each tissue layer adds its own cutting, stiffness, and friction forces [68, 69]. The ability of the self-propelled needle to advance in multi-layered tissue-mimicking phantoms with varying stiffness has been exemplified successfully in a previous study [51]. In addition, real tissue is inhomogeneous and differences in tissue characteristics are present within and between human beings, which makes the forces that act on the needle inside the body difficult to predict.

Lastly, during the performance evaluation in this study, we kept the actuation unit stationary while the tissue was placed on a low-friction cart that moved toward the needle. In clinical practice, the patient will have to remain stationary while the needle self-propels inside the tissue. To accommodate this, the needle could be moved inside the actuation unit to manipulate the needle toward the patient, following the pace of the self-propelled motion of the needle. To further increase the effectiveness of the procedure and decrease the chance of unwanted tissue damage [32] and pubic arch interference [70], the ability to actively and intuitively steer the tip of the needle during the procedure should be researched.

## 9.5 Conclusion

In this study, a pneumatic actuation unit for a self-propelled ovipositor-inspired needle consisting of six needle segments for MRI-guided procedures is presented. The pneumatic actuation unit design allows an adjustable output stroke length of 2 to 10 mm, where the stroke length is the distance that each needle segment travels per needle actuation cycle. Furthermore, the actuation unit and needle consist solely of MR-safe and -conditional materials and the control unit allows for control of the system with an adjustable interval time and a single air input. The evaluation of the prototype in 10-wt% gelatin phantoms showed that the needle was able to self-propel through the phantoms. Additionally, we measured the lowest slip ratio of  $0.912 \pm 0.081$  for a stroke length of 4 mm and an interval time of 0.3 s. The experiment of the prototype inside a preclinical MRI system showed the needle could also self-propel through *ex vivo* porcine liver tissue with a slip ratio of approximately 0.88. The pneumatic actuation unit is a step forward in developing a self-propelled needle for MRI-guided percutaneous procedures.





## Supplementary material

The appendices and data underlying this study are available at doi: 10.4121/460d12fa-b29f-40e0-a095-c5109bbaec10.v1.

## Acknowledgements

We would like to thank Gertjan Mulder and Jacques Brenkman for discussions about pneumatics and their help in designing the setup, and we would like to thank Judith de Vos for preparing the tissue sample.

## References

1. Miller KD, Nogueira L, Mariotto AB, Rowland JH, Yabroff KR, Alfano CM, et al. Cancer treatment and survivorship statistics, 2019. *CA: a cancer journal for clinicians*. 2019;69(5):363-85. doi: 10.3322/caac.21565.
2. Beets GL, Figueiredo NF, Beets-Tan RG. Management of rectal cancer without radical resection. *Annual review of medicine*. 2017;68:169-82. doi: 10.1146/annurev-med-062915-021419.
3. Eggener SE, Scardino PT, Carroll PR, Zelefsky MJ, Sartor O, Hricak H, et al. Focal therapy for localized prostate cancer: a critical appraisal of rationale and modalities. *The Journal of urology*. 2007;178(6):2260-7. doi: 10.1016/j.juro.2007.08.072.
4. Ahmed HU, Pendse D, Illing R, Allen C, van der Meulen JH, Emberton M. Will focal therapy become a standard of care for men with localized prostate cancer? *Nature clinical practice Oncology*. 2007;4(11):632-42. doi: 10.1038/ncponc0959.
5. Donaldson IA, Alonzi R, Barratt D, Barret E, Berge V, Bott S, et al. Focal therapy: patients, interventions, and outcomes—a report from a consensus meeting. *European urology*. 2015;67(4):771-7. doi: 10.1016/j.eururo.2014.09.018.
6. Lodeizen O, de Bruin M, Eggener S, Crouzet S, Ghai S, Varkarakis I, et al. Ablation energies for focal treatment of prostate cancer. *World journal of urology*. 2019;37(3):409-18. doi: 10.1007/s00345-018-2364-x.
7. van Riel LA, van Kollenburg RA, Vis AN, van Leeuwen PJ, de Reijke TM, de Bruin DM, et al. Safety and Feasibility of Soractelite Transperineal Focal Laser Ablation for Prostate Cancer and Short-term Quality of Life Analysis from a Multicenter Pilot Study. *European urology open science*. 2022;39:48-54. doi: 10.1016/j.euros.2022.02.012.
8. Natarajan S, Raman S, Priester AM, Garritano J, Margolis DJ, Lieu P, et al. Focal laser ablation of prostate cancer: phase I clinical trial. *The Journal of urology*. 2016;196(1):68-75. doi: 10.1016/j.juro.2015.12.083.
9. Lindner U, Lawrentschuk N, Weersink RA, Davidson SR, Raz O, Hlasny E, et al. Focal laser ablation for prostate cancer followed by radical prostatectomy: validation of focal therapy and imaging accuracy. *European urology*. 2010;57(6):1111-4. doi: 10.1016/j.eururo.2010.03.008.
10. Stafford RJ, Shetty A, Elliott AM, Klumpp SA, McNichols RJ, Gowda A, et al. Magnetic resonance guided, focal laser induced interstitial thermal therapy in a canine prostate model. *The Journal of urology*. 2010;184(4):1514-20. doi: 10.1016/j.juro.2010.05.091.
11. Hoeks CM, Barentsz JO, Hambroek T, Yakar D, Somford DM, Heijmink SW, et al. Prostate cancer: multiparametric MR imaging for detection, localization, and staging. *Radiology*. 2011;261(1):46-66. doi: 10.1148/radiol.11091822.
12. Gouel P, Decazes P, Vera P, Gardin I, Thureau S, Bohn P. Advances in PET and MRI imaging of tumor hypoxia. *Frontiers in Medicine*. 2023;10. doi: 10.3389/fmed.2023.1055062.
13. ASTM F2503-13, Standard practice for marking medical devices and other items for safety in

- the magnetic resonance environment. ASTM International, West Conshohocken, PA2013.
14. Cepek J, Chronik BA, Lindner U, Trachtenberg J, Davidson SR, Bax J, et al. A system for MRI-guided transperineal delivery of needles to the prostate for focal therapy. *Medical physics*. 2013;40(1):012304. doi: 10.1118/1.4773043.
  15. Cepek J, Lindner U, Ghai S, Louis AS, Davidson SR, Gertner M, et al. Mechatronic system for in-bore MRI-guided insertion of needles to the prostate: An in vivo needle guidance accuracy study. *Journal of Magnetic Resonance Imaging*. 2015;42(1):48-55. doi: 10.1002/jmri.24742.
  16. Bloembergen J, Trauzettel F, Coolen B, Dodou D, Breedveld P. Design and evaluation of an MRI-ready, self-propelled needle for prostate interventions. *Plos one*. 2022;17(9):e0274063. doi: 10.1371/journal.pone.0274063.
  17. Su H, Camilo A, Cole GA, Hata N, Tempany CM, Fischer GS. High-field MRI-compatible needle placement robot for prostate interventions. *Studies in health technology and informatics*. 2011;163:623. doi: 10.3233/978-1-60750-706-2-623.
  18. Hungr N, Bricault I, Cinquin P, Fouard C. Design and validation of a CT-and MRI-guided robot for percutaneous needle procedures. *IEEE transactions on robotics*. 2016;32(4):973-87. doi: 10.1109/TRO.2016.2588884.
  19. Runciman M, Avery J, Zhao M, Darzi A, Mylonas GP. Deployable, variable stiffness, cable driven robot for minimally invasive surgery. *Frontiers in Robotics and AI*. 2020;6:141. doi: 10.3389/frobt.2019.00141.
  20. Mahcicek DI, Yildirim KD, Kasaci G, Kocaturk O. Preliminary Evaluation of Hydraulic Needle Delivery System for Magnetic Resonance Imaging-Guided Prostate Biopsy Procedures. *Journal of Medical Devices*. 2021;15(4). doi: 10.1115/1.4051610.
  21. Stoianovici D, Kim C, Petrisor D, Jun C, Lim S, Ball MW, et al. MR safe robot, FDA clearance, safety and feasibility of prostate biopsy clinical trial. *IEEE/ASME Transactions on Mechatronics*. 2016;22(1):115-26. doi: 10.1109/TMECH.2016.2618362.
  22. Bomers J, Bosboom D, Tigelaar G, Sabisch J, Fütterer J, Yakar D. Feasibility of a 2nd generation MR-compatible manipulator for transrectal prostate biopsy guidance. *European radiology*. 2017;27(4):1776-82. doi: 10.1007/s00330-016-4504-2.
  23. Sajima H, Kamiuchi H, Kuwana K, Dohi T, Masamune K. MR-safe pneumatic rotation stepping actuator. *Journal of Robotics and Mechatronics*. 2012;24(5):820-7. doi: 10.20965/jrm.2012.p0820.
  24. Groenhuis V, Siepel FJ, Stramigioli S, inventors; Twente Universiteit, assignee. Pneumatic stepper motor and device comprising at least one such pneumatic stepper motor patent US20200182267A1. 2017.
  25. Groenhuis V, Siepel FJ, Stramigioli S. Sunram 5: A Magnetic Resonance-Safe Robotic System for Breast Biopsy, Driven by Pneumatic Stepper Motors. *Handbook of Robotic and Image-Guided Surgery*; Elsevier; 2020. p. 375-96.
  26. Groenhuis V, Stramigioli S. Laser-cutting pneumatics. *IEEE/ASME transactions on mechatronics*. 2015;21(3):1604-11. doi: 10.1109/TMECH.2015.2508100.
  27. Groenhuis V, Stramigioli S. Rapid prototyping high-performance MR safe pneumatic stepper motors. *IEEE/ASME transactions on mechatronics*. 2018;23(4):1843-53. doi: 10.1109/TMECH.2018.2840682.
  28. Stoianovici D, Patriciu A, Petrisor D, Mazilu D, Kavoussi L. A new type of motor: pneumatic step motor. *IEEE/ASME Transactions On Mechatronics*. 2007;12(1):98-106. doi: 10.1109/TMECH.2006.886258.
  29. Sakes A, Dodou D, Breedveld P. Buckling prevention strategies in nature as inspiration for improving percutaneous instruments: a review. *Bioinspiration & biomimetics*. 2016;11(2):021001. doi: 10.1088/1748-3190/11/2/021001.
  30. Abolhassani N, Patel R, Moallem M. Needle insertion into soft tissue: A survey. *Medical engineering & physics*. 2007;29(4):413-31. doi: 10.1016/j.medengphy.2006.07.003.
  31. Abolhassani N, Patel RV, Ayazi F. Minimization of needle deflection in robot-assisted



- percutaneous therapy. *The international journal of medical Robotics and computer assisted surgery*. 2007;3(2):140-8. doi: 10.1002/rcs.136.
32. Leibinger A, Oldfield MJ, Rodriguez y Baena F. Minimally disruptive needle insertion: a biologically inspired solution. *Interface focus*. 2016;6(3):20150107. doi: 10.1098/rsfs.2015.0107.
  33. Frasson L, Ferroni F, Ko SY, Dogangil G, y Baena FR. Experimental evaluation of a novel steerable probe with a programmable bevel tip inspired by nature. *Journal of robotic surgery*. 2012;6(3):189-97. doi: 10.1007/s11701-011-0277-4.
  34. Viridyawan V, Oldfield M, y Baena FR. Laser Doppler sensing for blood vessel detection with a biologically inspired steerable needle. *Bioinspiration & biomimetics*. 2018;13(2):026009. doi: 10.1088/1748-3190/aaa6f4.
  35. Scali M. Self-propelling needles: From biological inspiration to percutaneous interventions. 2020. doi: 10.4233/uuid:523e3e5f-08f0-4acb-ab45-abaa7ace3967.
  36. Acharya SR, Hutapea P. An experimental study on the mechanics and control of SMA-actuated bioinspired needle. *Bioinspiration & Biomimetics*. 2023;18(6):066008. doi: 10.1088/1748-3190/acfb65.
  37. Gidde STR, Islam S, Kim A, Hutapea P. Experimental study of mosquito-inspired needle to minimize insertion force and tissue deformation. *Proceedings of the Institution of Mechanical Engineers, Part H: Journal of Engineering in Medicine*. 2023;237(1):113-23. doi: 10.1177/09544119221137133.
  38. Fung-A-Jou Z, Bloemberg J, Breedveld P. Bioinspired medical needles: a review of the scientific literature. *Bioinspiration & Biomimetics*. 2023. doi: 10.1088/1748-3190/acd905.
  39. Nakajima K, Schwarz O. How to use the ovipositor drilling mechanism of hymenoptera for developing a surgical instrument in biomimetic design. *International Journal of Design & Nature and Ecodynamics*. 2014;9(3):177-89. doi: 10.2495/DNE-V9-N3-177-189.
  40. Quicke DL, Fitton MG. Ovipositor steering mechanisms in parasitic wasps of the families Gasteruptionidae and Aulacidae (Hymenoptera). *Proceedings of the Royal Society of London Series B: Biological Sciences*. 1995;261(1360):99-103. doi: 10.1098/rspb.1995.0122.
  41. Leyva JL, Browning HW, Gilstrap FE. Effect of host fruit species, size, and color on parasitization of *Anastrepha ludens* (Diptera: Tephritidae) by *Diachasmimorpha longicauda* (Hymenoptera: Braconidae). *Environmental Entomology*. 1991;20(5):1469-74. doi: 10.1093/ee/20.5.1469.
  42. Cerkvenik U, Van Leeuwen JL, Kovalev A, Gorb SN, Matsumura Y, Gussekloo SW. Stiffness gradients facilitate ovipositor bending and spatial probing control in a parasitic wasp. *Journal of Experimental Biology*. 2019;222(9):jeb195628. doi: 10.1242/jeb.195628.
  43. Cerkvenik U, Van de Straat B, Gussekloo SW, Van Leeuwen JL. Mechanisms of ovipositor insertion and steering of a parasitic wasp. *Proceedings of the National Academy of Sciences*. 2017;114(37):E7822-E31. doi: 10.1073/pnas.1706162114.
  44. Okamura AM, Simone C, O'leary MD. Force modeling for needle insertion into soft tissue. *IEEE transactions on biomedical engineering*. 2004;51(10):1707-16. doi: 10.1109/TBME.2004.831542.
  45. Simone C, Okamura AM. Modeling of needle insertion forces for robot-assisted percutaneous therapy. *Proceedings 2002 IEEE International Conference on Robotics and Automation (Cat No 02CH37292)*; 2002: IEEE. doi: 10.1109/ROBOT.2002.1014848.
  46. Heverly M, Dupont P, Friedman J. Trajectory optimization for dynamic needle insertion. *Proceedings of the 2005 IEEE international conference on robotics and automation*; 2005: IEEE. doi: 10.1109/ROBOT.2005.1570349.
  47. Ng KW, Goh JQ, Foo SL, Ting PH, Lee TK, Esuvaranathan K, et al. Needle deflection studies for optimal insertion modeling. *International Journal of Bioscience, Biochemistry and Bioinformatics*. 2013;3(6):570. doi: 10.7763/IJBBB.2013.V3.278.
  48. Hing JT, Brooks AD, Desai JP. Reality-based needle insertion simulation for haptic feedback in prostate brachytherapy. *Proceedings 2006 IEEE International Conference on Robotics and Automation, 2006 ICRA 2006*; 2006: IEEE. doi: 10.1109/ROBOT.2006.1641779.
  49. Kataoka H, Washio T, Chinzei K, Mizuhara K, Simone C, Okamura AM. Measurement of

- the tip and friction force acting on a needle during penetration. *Medical Image Computing and Computer-Assisted Intervention—MICCAI 2002: 5th International Conference Tokyo, Japan, September 25–28, 2002 Proceedings, Part I* 5; 2002: Springer. doi: 10.1007/3-540-45786-0\_27.
50. Roesthuis RJ, Van Veen YR, Jahya A, Misra S. Mechanics of needle-tissue interaction. 2011 IEEE/RSJ international conference on intelligent robots and systems; 2011: IEEE. doi: 10.1109/IROS.2011.6094969.
51. Scali M, Breedveld P, Dodou D. Experimental evaluation of a self-propelling bio-inspired needle in single-and multi-layered phantoms. *Scientific reports*. 2019;9(1):1-13. doi: 10.1038/s41598-019-56403-0.
52. Scali M, Pusch T, Breedveld P, Dodou D. Ovipositor-inspired steerable needle: design and preliminary experimental evaluation. *Bioinspiration & Biomimetics*. 2017;13(1):016006. doi: 10.1088/1748-3190/aa92b9.
53. Frasson L, Ko S, Turner A, Parittotokkaporn T, Vincent JF, Rodriguez y Baena F. STING: a soft-tissue intervention and neurosurgical guide to access deep brain lesions through curved trajectories. *Proceedings of the Institution of Mechanical Engineers, Part H: Journal of Engineering in Medicine*. 2010;224(6):775-88. doi: 10.1243/09544119JEM663.
54. Scali M, Kreeft D, Breedveld P, Dodou D. Design and evaluation of a wasp-inspired steerable needle. *Bioinspiration, Biomimetics, and Bioreplication 2017; 2017: International Society for Optics and Photonics*. doi: 10.1117/12.2259978.
55. Phee L, Xiao D, Yuen J, Chan CF, Ho H, Thng CH, et al. Ultrasound guided robotic system for transperineal biopsy of the prostate. *Proceedings of the 2005 IEEE international conference on robotics and automation; 2005: IEEE*. doi: 10.1109/ROBOT.2005.1570297.
56. Melchels FP, Feijen J, Grijpma DW. A review on stereolithography and its applications in biomedical engineering. *Biomaterials*. 2010;31(24):6121-30. doi: 10.1016/j.biomaterials.2010.04.050.
57. Zhang M, Nigwekar P, Castaneda B, Hoyt K, Joseph JV, di Sant'Agnese A, et al. Quantitative characterization of viscoelastic properties of human prostate correlated with histology. *Ultrasound in medicine & biology*. 2008;34(7):1033-42. doi: 10.1016/j.ultrasmedbio.2007.11.024.
58. Barr RG, Memo R, Schaub CR. Shear wave ultrasound elastography of the prostate: initial results. *Ultrasound quarterly*. 2012;28(1):13-20. doi: 10.1097/RUQ.0b013e318249f594.
59. Öpik R, Hunt A, Ristolainen A, Aubin PM, Kruusmaa M. Development of high fidelity liver and kidney phantom organs for use with robotic surgical systems. 2012 4th IEEE RAS & EMBS international conference on biomedical robotics and biomechatronics (BioRob); 2012: IEEE. doi: 10.1109/BioRob.2012.6290831.
60. DiMaio SP, Salcudean SE. Needle insertion modeling and simulation. *IEEE Transactions on robotics and automation*. 2003;19(5):864-75. doi: 10.1109/TRA.2003.817044.
61. Meltsner M, Ferrier N, Thomadsen B. Observations on rotating needle insertions using a brachytherapy robot. *Physics in Medicine & Biology*. 2007;52(19):6027. doi: 10.1088/0031-9155/52/19/021.
62. Suzumori K, Matsumaru T, Iikura S, inventors; Google Patents, assignee. Elastically deformable fluid actuator patent US4976191A. 1990.
63. Comber DB, Slightam JE, Gervasi VR, Neimat JS, Barth EJ. Design, additive manufacture, and control of a pneumatic MR-compatible needle driver. *IEEE Transactions on Robotics*. 2016;32(1):138-49. doi: 10.1109/TRO.2015.2504981.
64. Johnson B, Campbell S, Campbell-Kyureghyan N. Characterizing the material properties of the kidney and liver in unconfined compression and probing protocols with special reference to varying strain rate. *Biomechanics*. 2021;1(2):264-80. doi: 10.3390/biomechanics1020022.
65. Pacella CM, Breschi L, Bottacci D, Masotti L. Physical principles of laser ablation. *Image-guided Laser Ablation: Springer*; 2020. p. 7-18.
66. Ghara M, Kundanati L, Borges RM. Nature's Swiss Army knives: ovipositor structure mirrors ecology in a multitrophic fig wasp community. *PLoS ONE*. 2011;6(8):e23642. doi: 10.1371/journal.

pone.0023642.

67. Parittotokkaporn T, Frasson L, Schneider A, Davies B, Degenaar P, y Baena FR. Insertion experiments of a biologically inspired microtextured and multi-part probe based on reciprocal motion. 2010 Annual International Conference of the IEEE Engineering in Medicine and Biology; 2010: IEEE. doi: 10.1109/IEMBS.2010.5627410.

68. Gerovichev O, Marayong P, Okamura AM. The effect of visual and haptic feedback on manual and teleoperated needle insertion. International Conference on Medical Image Computing and Computer-Assisted Intervention; 2002: Springer. doi: 10.1007/3-540-45786-0\_19.

69. Carra A, Avila-Vilchis JC. Needle insertion modeling through several tissue layers. 2010 2nd International Asia Conference on Informatics in Control, Automation and Robotics (CAR 2010); 2010: IEEE. doi: 10.1109/CAR.2010.5456857.

70. Wallner K, Chiu-Tsao S-T, Roy J, Arterbery VE, Whitmore W, Jain S, et al. An improved method for computerized tomography-planned transperineal 125iodine prostate implants. The Journal of urology. 1991;146(1):90-5. doi: 10.1016/S0022-5347(17)37721-2.

---

## PART 4.

### ACTUATION DESIGN

From Needle Holder to Universal Actuator





# 10

## **A Telescopic Actuator for a Self-Propelled Needle**

Published as:

Bloemberg J.\*, Fung-A-Jou Z.\*, Breedveld P., Sakes A. (2024) Design and evaluation of a ball spline wasp-inspired needle. *Frontiers in Bioengineering and Biotechnology*, 12:1468605. doi: 10.3389/fbioe.2024.1468605 (\*these authors have contributed equally to this work).



## Abstract

In percutaneous interventions, needles are used to reach target locations inside the body. However, when the needle is pushed through the tissue, forces arise at the needle tip and along the needle body, making the needle prone to buckling. Recently, needles that prevent buckling inspired by the ovipositor of female parasitic wasps have been developed. Building on these needle designs, this study proposes a manual actuation system that allows the operator to drive the wasp-inspired needle through stationary tissue. The needle consists of six 0.3-mm spring steel wires, of which one is advanced while the others are retracted. The advancing needle segment has to overcome a cutting and friction force while the retracting ones experience a friction force in the opposite direction. The actuation system moves the needle segments in the required sequence using a low-friction ball spline mechanism. The moving components of the needle have low inertia, and its connection to the actuation system using a ball spline introduces a small friction force, generating a small push force on the needle that facilitates the needle's propulsion into tissue while preventing needle buckling. Experimental testing evaluated the needle's ability to move through stationary 15-wt% gelatin tissue phantoms for different actuation velocities. It was found that the needle moved through the tissue phantoms with mean slip ratios of 0.35, 0.31, and 0.29 for actuation velocities of  $\pi$ ,  $2\pi$ , and  $3\pi$  rad/s, respectively. Furthermore, evaluation in 15-wt%, 10-wt%, and 5-wt% gelatin tissue phantoms showed that decreasing the gelatin concentration decreased the mean slip ratios from 0.35 to 0.19 and 0.18, respectively. The needle actuation system design is a step forward in developing a wasp-inspired needle for percutaneous procedures that prevents buckling.



## 10.1 Introduction

### 10.1.1 Wasp-inspired needles

Percutaneous interventions are used to create a passageway to a target location inside the body, inject or extract fluids, extract tissue samples, and position instruments such as radioactive seeds and optical fibers at precise locations in deep-seated tissue structures, such as the prostate gland. Biopsies, regional anesthesia, brachytherapy, and focal laser ablation rely on needles to perform the procedure. When a clinician inserts the needle by pushing it through the tissue, forces arise at the needle tip and along the needle body [1]. When the axial force on the needle exceeds the needle's critical load, the needle will deflect laterally due to buckling [2]. The lateral deflection might cause tissue damage and lead to poor control of the needle trajectory, potentially decreasing precision [3, 4]. Buckling phenomena are typically not a part of the needle trajectory plan, yet they are reported in deep-tissue needle insertion experiments [5, 6].

Buckling is a failure mode where an equilibrium configuration becomes unstable under excessive compression, leading to a sudden lateral deflection and potential obstruction of the lumen of the needle. Slender ideal columns under compression are subject to Euler buckling. The critical Euler buckling load can be calculated as Eq. 10.1.

$$F_{cr} = \frac{\pi^2 EI}{(KL)^2} \quad (10.1)$$

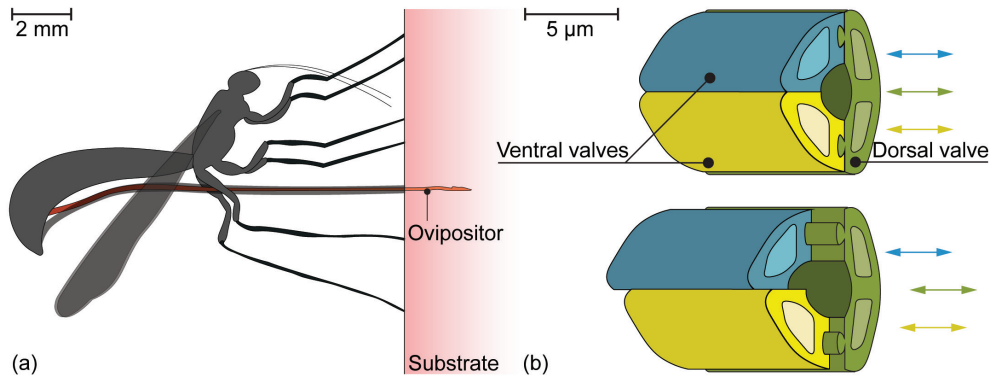
where  $E$  is the Young's Modulus of the needle [ $\text{N mm}^{-2}$ ],  $I$  the second moment of area of the cross-section of the needle [ $\text{mm}^4$ ],  $K$  a coefficient that takes into account the end conditions of the needle [-], and  $L$  the unsupported length of the needle [ $\text{mm}$ ] [7]. The extended critical Euler buckling load equation (Eq. 10.2) defines the critical load for a needle inserted into a substrate.

$$F_{cr \text{ ext}} = \frac{\pi^2 EI}{(KL)^2} + \frac{\mu L^2}{\pi^2} \quad (10.2)$$

where  $\mu$  is the spring stiffness of the substrate [ $\text{N mm}^{-2}$ ] [8, 9]. To prevent buckling during needle insertion, the insertion force ( $F_{in}$ ) applied to the needle inside the substrate should remain below the critical load of the needle ( $F_{cr \text{ ext}}$ ) [2].

To prevent needle buckling and reduce tissue damage during needle insertion, needles inspired by the ovipositor of the female parasitic wasp have been developed that can be advanced through the tissue without an external push force [10-13]. Female parasitic wasps use their ovipositor to lay eggs within hosts, which may hide in compact substrates such as wood [14]. The ovipositor of the parasitic wasp *Diachasmimorpha longicaudata* Ashmead (Hymenoptera: Braconidae) is characterized by its considerable length ( $5.7 \pm 0.6 \text{ mm}$ ) [15] and small diameter ( $30\text{-}50 \text{ }\mu\text{m}$ ) [16]. It consists of three slender, parallel segments, called valves [17], which reciprocate through advancing and retracting movements with respect to each other (Figure 10.1). The reciprocal advancing and retracting forces create a net insertion





**Figure 10.1. Visualization of the motion sequence of the ovipositor of a parasitic wasp.** (a) The parasitic wasp uses its ovipositor to lay eggs in a substrate. (b) The ovipositor consists of three parallel valves (green, yellow, and blue) that can move reciprocally (based on Cerkvenik *et al.* [17]).

force near zero, facilitating self-propulsion within a substrate without buckling.

The wasp-inspired needles use multiple mechanisms to prevent buckling. Firstly, the needle consists of multiple parallel needle segments that employ an advancing-retraction mechanism, where one needle segment is advanced while the other needle segments are retracted. The advantage of this advancing-retraction mechanism compared to pushing the entire needle through the tissue is the decreased axial load applied to the needle. The friction and cutting forces of the advancing needle segment inside the substrate are (partially) counterbalanced by the friction force in the opposite direction of the retracted needle segments, thereby decreasing the insertion force required to insert the needle into the substrate, thus decreasing  $F_{in}$ . Secondly, the needle segments move incrementally forward, traversing over a short distance per needle movement, the unsupported length  $L$  inside the substrate is therefore kept low and independent of insertion depth, thereby increasing  $F_{cr ext}$ .

### 10.1.2 Problem definition

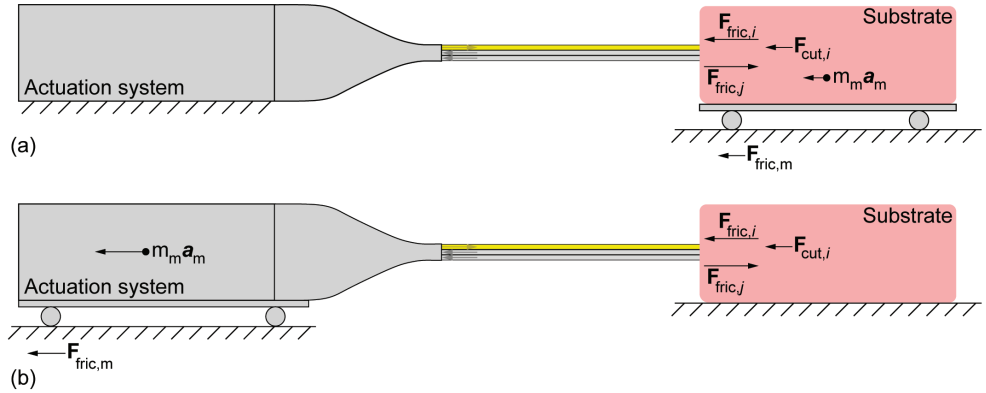
Inserting a needle into tissue results in forces acting on the needle by the surrounding tissue. Okamura *et al.* [1] demonstrated that these forces are the sum of the surface stiffness force ( $F_{stiff}$ ) due to the needle puncturing the skin or surface membrane until the moment of puncture [18], cutting force ( $F_{cut}$ ) due to the plastic deformation and tissue stiffness experienced at the tip of the needle [19], and friction force ( $F_{fric}$ ) along the needle length inside the tissue due to Coulomb friction, adhesive friction, and viscous friction [20]. The motion of the wasp-inspired needle is initiated after puncturing the skin or membrane and is accomplished by parallel needle segments, more specifically by  $a$  advancing segments that move forward and  $r$  retracting segments that move backward. The advancing segments experience a cutting and friction force, whereas the stiffness force is zero when assuming homogeneous tissue after puncturing. The retracting segments experience a friction force in the opposite direction compared to the advancing segments [21]. Using the conditions for the self-propulsion of the

wasp-inspired needle and Newton's second law, we get:

$$\sum_{i=1}^a (\mathbf{F}_{\text{stiff},i} + \mathbf{F}_{\text{fric},i} + \mathbf{F}_{\text{cut},i}) + \mathbf{F}_{\text{fric},m} + m_m \mathbf{a}_m \leq \sum_{j=1}^r \mathbf{F}_{\text{fric},j} \quad (10.3)$$

where  $\mathbf{F}_{\text{stiff},i}$  is the stiffness force on the tip of the advancing needle segment, which is assumed to be zero,  $\mathbf{F}_{\text{fric},i}$  is the friction force along the advancing needle segment,  $\mathbf{F}_{\text{cut},i}$  is the cutting force on the tip of the advancing needle segment, and  $\mathbf{F}_{\text{fric},j}$  is the friction force along the retracting needle segments, which works in the opposite direction as the friction force of the advancing needle segments. Furthermore,  $\mathbf{F}_{\text{fric},m}$  is the friction force of the moving components, and  $m_m$  and  $\mathbf{a}_m$  their mass and acceleration, respectively. The needle self-propels through the tissue if the friction force generated by the retracting needle segments counterbalances the friction and cutting force of the advancing needle segments and the friction force and inertia of the moving components. This way, the retracting needle segments remain stationary with respect to the tissue, whilst the advancing segments move forward into the tissue.

For the self-propelled motion to be effective, the friction force and inertia of the moving components should be negligibly small. Current wasp-inspired self-propelled needles were constructed in either of the following configurations. In the first configuration, the actuation system remained stationary while the substrate was placed on a low-weight, low-friction support structure that could move towards the needle following the pace of the self-propelled motion of the needle [12, 13, 22-24] (Figure 10.2a). However, in clinical practice, the needle must self-propel inside the patient while the substrate, and thus the patient, remains in place. In the second configuration, the substrate remained stationary while the actuation system and the needle were placed on a low friction cart that could move towards the substrate following



**Figure 10.2. Visualization of the motion sequence of the wasp-inspired needles.** During the motion, one needle segment (in yellow) moves forward over the stroke distance while the others (in gray) move slowly backward.  $\mathbf{F}_{\text{fric},i}$  is the friction force along the advancing needle segment,  $\mathbf{F}_{\text{cut},i}$  is the cutting force on the tip of the advancing needle segment, and  $\mathbf{F}_{\text{fric},j}$  is the friction force along the retracting needle segments, which works in the opposite direction as the friction force of the advancing needle segments.  $\mathbf{F}_{\text{fric},m}$  is the friction force of the moving components, and  $m_m$  and  $\mathbf{a}_m$  their mass and acceleration, respectively. (a) Configuration where the actuation system remains stationary while the substrate moves toward the needle. (b) Configuration where the substrate remains stationary while the actuation system and the needle move toward the substrate.

the pace of the self-propelled motion of the needle [25] (Figure 10.2b). A disadvantage of the second configuration is that the inertia and friction of the needle, including its actuation system, oppose the self-propulsion of the needle.

### 10.1.3 Goal of this study

Current prototypes of wasp-inspired self-propelled needles are designed as experimental setups in which either the needle and actuation system remained stationary while the tissue (phantom) was moved toward them [12, 13, 22-24], or the tissue remained stationary while the needle and actuation system could move [25]. Both options are not optimal for integration in clinical practice and the performance of the needle due to the inertia that negatively affects the needle's self-propelled motion. In clinical practice, the needle will have to self-propel inside the patient while both the actuation system and the tissue remain in place. Therefore, this study aims to design a stationary manual actuation system for a needle that uses the self-propelling principle of the parasitic wasp and can travel through stationary tissue (phantoms). Specifically, the moving components that connect the needle segments to the actuation system should have negligible influence on the self-propelled motion of the needle. Therefore, the moving components that connect the needle segments to the actuation system should have low inertia and the connection itself should introduce friction forces near zero.

## 10.2 Design

### 10.2.1 Needle

The complete design, called the Splinositor, consists of a needle and an actuation system. The needle consists of six parallel needle segments following the designs by Scali *et al.* [13] and Bloemberg *et al.* [22] (Chapter 7). The needle self-propels through the substrate by a sequential translation of the six needle segments in six steps per cycle (Figure 10.3). During every step of the cycle, one needle segment moves forward over a specified distance called the “stroke”, while the other five needle segments move slowly backward over one-fifth of the stroke distance, similar to the needle design by Bloemberg *et al.* [22] (Chapter 7). Every needle segment is moved forward over the stroke distance once during one cycle.

When the distal ends of the needle segments are positioned inside tissue, they experience friction forces with the surrounding tissue. When the self-propelling principle, as in Eq. 10.3 holds, the retracting needle segments remain stationary with respect to the tissue, whilst the advancing segment moves forward into the tissue. By repeating the actuation cycle, the needle as a whole advances in the tissue.

### 10.2.2 Actuation system

We opted for a manually controlled actuation system that allows the operator to drive the needle directly and intuitively using a continuous manual rotation around the axis of needle insertion, i.e., the horizontal y-direction. By using the manual actuation force solely for an

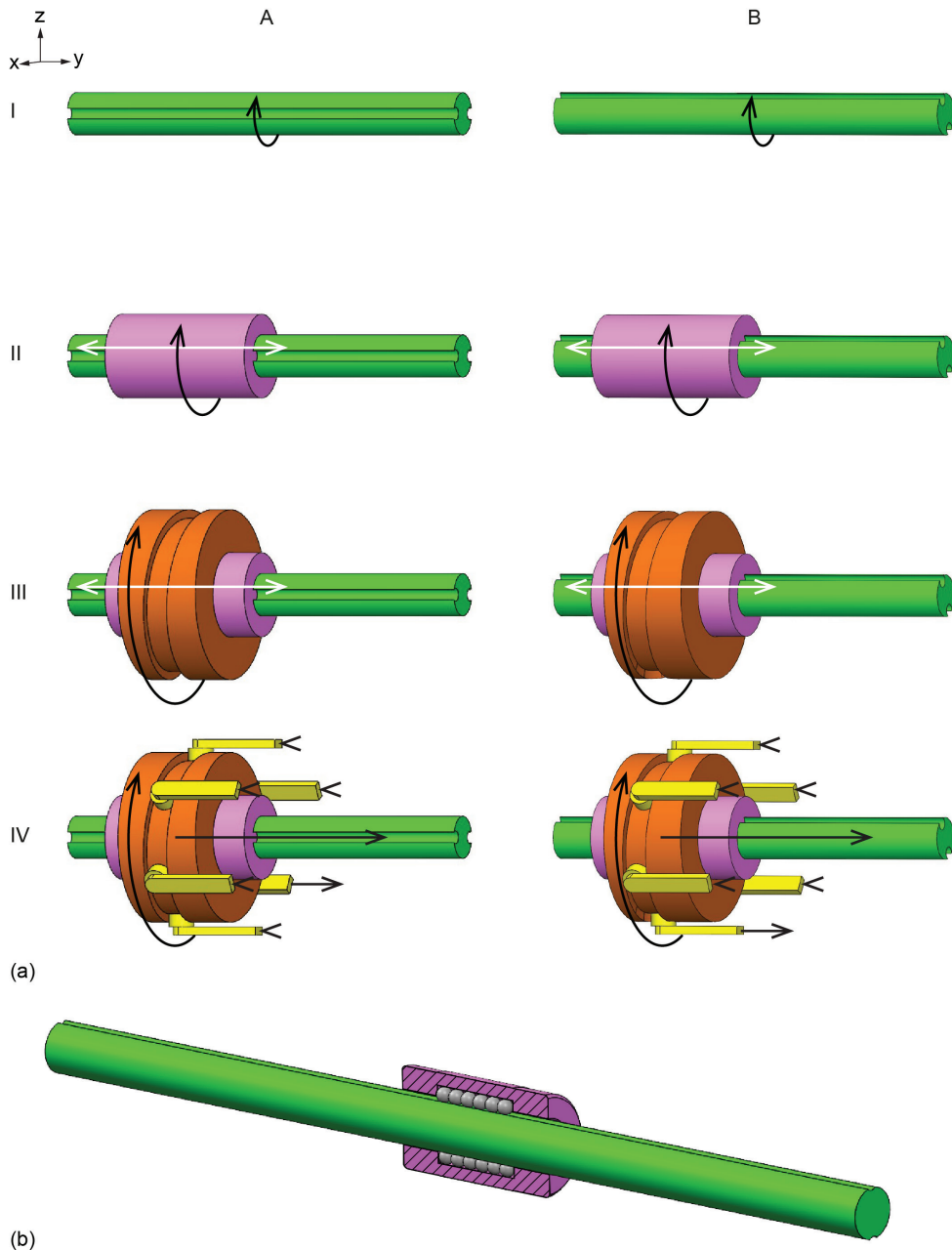


**Figure 10.3.** Visualization of the motion sequence of the needle segments of the wasp-inspired needle. During the motion, one needle segment (in yellow) moves forward over the stroke distance while the other needle segments (in gray) move slowly backward over one-fifth of the stroke distance in a consecutive manner.

input rotation, the operator cannot apply an external insertion force to the needle to push the needle into the tissue. Consequently, the operator cannot interfere with the self-propelled motion of the needle segments. The actuation system converts the input rotation into a sequential translation of the six needle segments in the required order and over the required stroke distance while minimizing the number of components that travel with the needle segments.

To explain the working principle of our actuation system, the mechanism is simplified and visualized in a schematic illustration in Figure 10.4a, where Columns A and B show two phases in the motion cycle (i.e., 60° difference) and Rows I-IV show the different layers of the actuation system. The input motion is a rotation of the drive cylinder (in green) around the y-axis. The drive cylinder contains horizontal grooves. A follower cylinder (in pink) contains rims that fit in the drive cylinder's grooves. Hence, the grooves and rims transmit the rotation around the y-axis to the follower cylinder while enabling a translation in the y-direction of the follower cylinder relative to the drive cylinder. Around the follower cylinder, a cam is positioned containing a V-shaped slot, in which six cam followers (in yellow) can slide. The motion of the cam followers was restricted to solely a translation in the y-direction, driven by the motion of the V-shaped slot. The asymmetric shape of the V-shape in the slot causes one cam follower to move in the positive y-direction while the other cam followers move in the negative y-direction.

To minimize the friction force introduced by the connection of the needle to the actuation system, we implemented a ball spline mechanism (Figure 10.4b). The ball spline incorporates balls within the grooves in both the drive and follower cylinder, facilitating linear rolling translation of the follower cylinder relative to the drive cylinder while simultaneously transmitting rotation. The components of the actuation system that move with the needle segments include the follower cylinder, ball bearings of the ball spline mechanism, cam, and cam followers that house the needle segments. Because of the low-friction ball spline mechanism, the moving components of the actuation system introduce a friction force near zero.



**Figure 10.4. Schematic representation of the actuation system motion mechanism.** (a) The actuation system includes the drive cylinder (green), follower cylinder (pink), cam (orange), and cam followers (yellow) that contain the needle segments. Columns A and B show two phases in the motion cycle (i.e., 60° difference) and Rows I-IV show the different layers of the actuation system. (b) The ball spline mechanism, including the drive cylinder (green) with grooves, cross-section of the ball spline follower cylinder (pink) with grooves, and ball bearings (gray) rolling within the grooves.

### 10.2.3 Final design

We used Solidworks (Dassault Systems Solidworks Corporation; Waltham, MA, USA) as Computer-Aided Design (CAD) software to design the Splinositor (Figure 10.5). To facilitate the manual actuation of the drive cylinder, we added a crank to the actuation mechanism that transmits the input rotation to the drive cylinder and the cam. The height of the cam track dictates a 4-mm stroke in the positive y-direction for the cam followers over a 60° rotation of the cam. During the following 300° rotation, the cam track dictates a 4-mm stroke in the negative y-direction. We chose off-the-shelf ball bearings as followers of the cam. Each cam follower contains a bearing axis, to attach it to a key, which was attached to a cam follower cylinder of a linear guide axis. A needle segment holder was also attached to the key. The six linear guides restrict the motion of the needle segment holders to a translation along the y-axis.

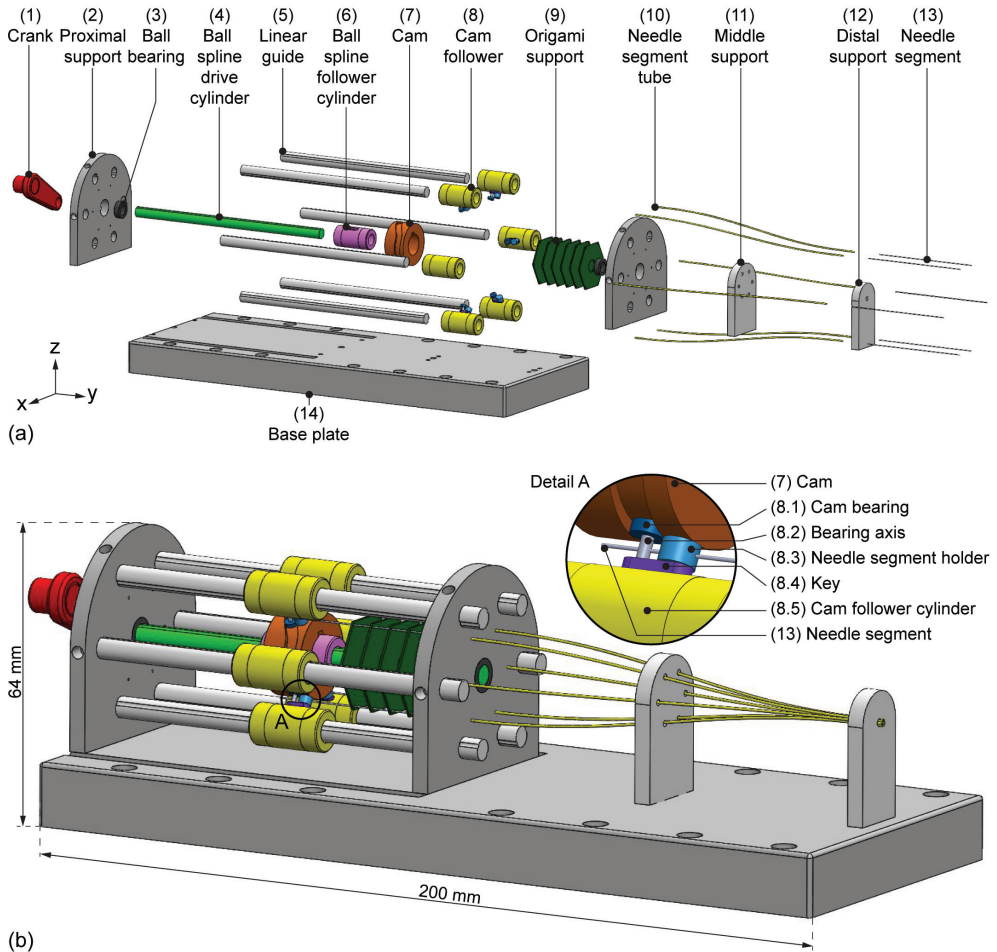
To prevent buckling of the needle segments before they enter the needle segment tubes, the needle segments require a support structure. We needed a movable support structure capable of translating along with the cam, as the unsupported needle length decreases when the needle segments propel in the tissue. We chose to implement an origami structure, i.e., a tube derived from the Miura-origami (Miura-ori) pattern [26], which is stiff in the z-direction but flexible in the y-direction. When the cam moves in the positive y-direction, the Miura-ori tube contracts. The Miura-ori tube contains small holes through which the needle segments pass, guiding and supporting the needle segments' movement along the y-axis while avoiding buckling.

Through the actuation system, the needle segments run at a larger diameter than at the needle tip. To guide the needle segments smoothly from the actuation system to the needle tip, needle segment tubes with an S-curve were used. The S-curved needle segment tubes gently decrease the distance between the needle segments by guiding them smoothly through the S-shaped needle segment tubes from the actuation system to the needle tip. These tubes provide continuous support to the needle segments to avoid buckling, while allowing them to move along the y-axis freely.

### 10.2.4 Prototype

The needle in this study consists of six spring steel rods, i.e., the needle segments, with a diameter of 0.3 mm and a length of 230 mm (Figure 10.6a). The tips of the needle segments were sharpened to an angle of 20° with wire Electrical Discharge Machining (EDM). The needle segments were held together at the tip using a 10-mm long heat shrink tube (103-0352, Nordson Medical Corp., Westlake, OH, USA). This tube was employed to limit the needle segments from diverging while only minimally increasing the needle diameter. To maintain its position at the needle tip, the heat shrink tube was glued to one of the needle segments using *Pattex Gold Gel 1432562* (Pattex, Henkel AG & Co, Düsseldorf, Germany). The remaining needle segments can move freely back and forth through the heat shrink tube. The resulting total diameter of the needle, including the heat shrink tube, is 1.0 mm.

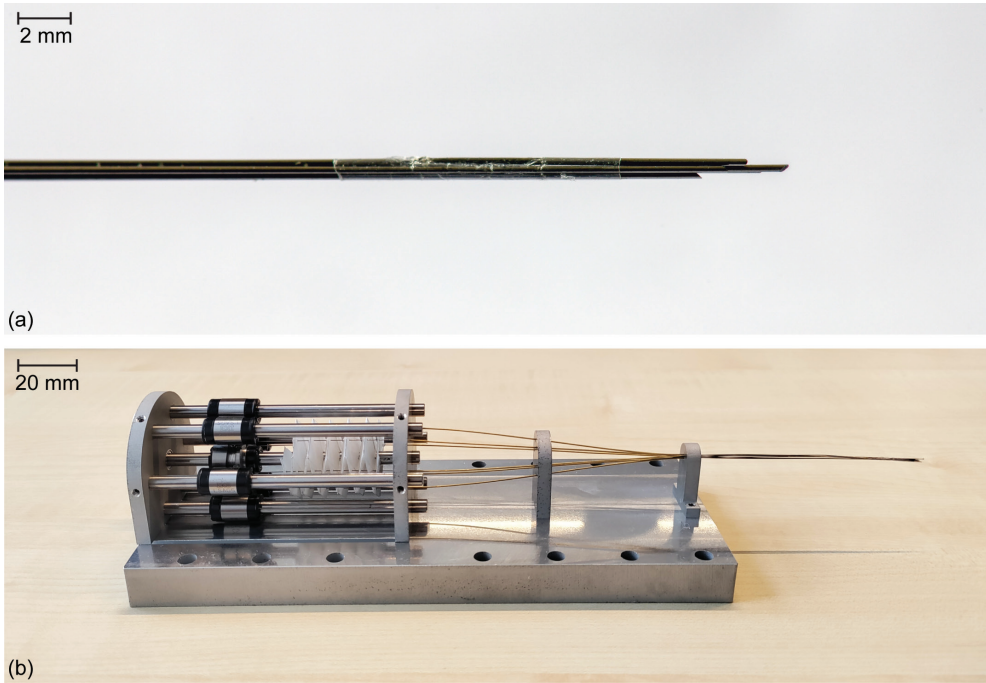




**Figure 10.5. Schematic representation of the complete design of the Splinositor.** (a) Exploded view. Crank (1), proximal support (2), ball bearing (3), drive cylinder of the ball spline (4), linear guide axis (5), follower cylinder of the ball spline (6), cam (7), cam follower (8), origami support structure (9), needle segment tube (10), middle support (11), distal support (12), needle segment (13), base plate (14). (b) Complete design assembly. The cam follower (8) that rolls within the cam (7) consists of the cam bearing (8.1), bearing axis (8.2), needle segment holder (8.3), key (8.4), and cam follower cylinder (8.5).

Figure 10.6b shows the assembled prototype. The crank was produced using three-dimensional (3D) printing, specifically the fused deposition technology in PolyLactic Acid (PLA) on an Ultimaker 3 printer. The ball splines used in the core mechanism of the actuation system (i.e., the drive cylinder) and the linear guides are stainless steel *Ball Splines LSAG10C1R200* (IKO Nippon Thompson Co. Ltd., Tokyo, Japan). The drive cylinder, with a length of 100 mm, facilitates a 100-mm travel distance of the needle inside the tissue. The central ball spline was positioned between two stainless steel *Deep Groove Ball Bearings DDL-850ZZMTHA1P-13LY121* (MinebeaMitsumi Inc., Tokyo, Japan). The cam was milled out of 7075-T6 alumi-





**Figure 10.6. Final Splinositor prototype.** (a) Close-up of the needle tip consisting of six sharpened spring steel rods held together by a heat shrink tube (Nordson Medical Corp.) glued to one of the six rods. (b) Assembled Splinositor prototype.

num. The six cam bearings are stainless steel *Deep Groove Ball Bearings DDL-310HA1P25LO1* (MinebeaMitsumi Inc., Tokyo, Japan). The bearing axes are 125-245 HV30 steel *Cylindrical Pins 2338H8100010005* (Bossard, Zug, Switzerland). The aluminum needle segment holders and keys were produced using wire EDM. The proximal, middle, and distal supports form the actuation system's support blocks, and were made from 7075-T6 aluminum using wire EDM. The support blocks were attached to the aluminum base plate that was also produced using wire EDM. The Miura-ori tube was cut and folded out of lightweight drawing paper. The needle segment tubes (inner diameter 0.4 mm, outer diameter 0.6 mm) were constructed from brass due to the advantageous low coefficient of friction between brass and the steel needle segments.

## 10.3 Evaluation

### 10.3.1 Experimental goal and variables

To evaluate the performance of the Splinositor under controlled conditions, we performed two experiments in gelatin phantoms. The experiments aimed to investigate the performance behavior of the needle actuated (1) for different actuation velocities and (2) inside different

gelatin phantoms, both in terms of the slip of the needle with respect to the gelatin phantom. More specifically, we calculated the slip ratio of the needle while it advanced through the phantom, using Eq. 10.4.

$$s_{\text{ratio}} = 1 - \left( \frac{d_m}{d_t} \right) \quad (10.4)$$

where  $d_m$  and  $d_t$  are the measured and theoretical maximum traveled distance, respectively. The measured traveled distance is the difference in the position of the needle tip we measured in the video footage before and after needle actuation. The theoretical maximum traveled distance depends on the motion sequence (5:1), the stroke distance ( $S$ ), which was 4 mm by design, and the number of actuation cycles ( $C$ ) and was calculated using Eq. 10.5.

$$d_t = \frac{6}{5} SC \quad (10.5)$$

The first experiment aimed to find the most efficient technical configuration of the Splinositor inside gelatin phantoms with a concentration of 15% weight (wt) powder in water. The independent variables were the mobility of the ball spline and the actuation speed ( $\omega$ ) of the needle. To investigate the effect of the central ball spline, we evaluated the prototype in two conditions in which: (1) the central ball spline was fixed to constrain its translation in the y-direction while allowing rotation around the y-axis, while the gelatin sample was placed on a low-friction cart, and (2) the central ball spline was able to move like intended (i.e., mobile) and the gelatin sample remained stationary. To investigate the effect of the actuation angular velocity ( $\omega$ ),  $\omega$  was set at  $\pi$ ,  $2\pi$ , or  $3\pi$  rad/s using a metronome.

The second experiment aimed to investigate the effect of the stiffness of the gelatin phantom on the Splinositor performance for the configuration with a mobile ball spline and an actuation velocity of  $\pi$  rad/s. The independent variable was the concentration of gelatin powder in the phantoms, which was set at 5 wt%, 10 wt%, and 15 wt%. These concentrations lead to gelatin samples with moduli of elasticity of approximately 5.3 kPa, 17 kPa, and 31 kPa [13], respectively. The 5-wt% gelatin phantom approximates soft tissue such as healthy liver tissue (<6 kPa) [27]. The 10-wt% gelatin phantom approximates tissue with an intermediate stiffness such as muscle tissue (12–32 kPa) [28] and healthy prostate tissue (16 kPa) [29]. The 15-wt% gelatin phantom approximates stiff tissue such as cancerous prostate tissue (40 kPa) [29, 30].

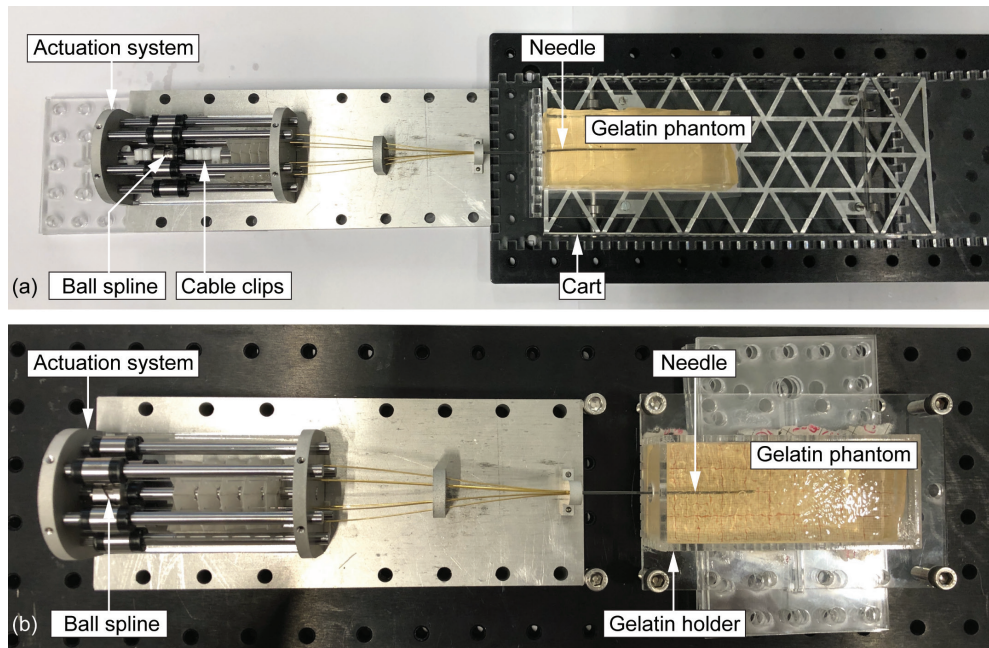
In both experiments, the dependent variable was the slip ratio ( $s_{\text{ratio}}$ ) between the needle and gelatin tissue phantom over one entire measurement. The control variable was the number of actuation cycles ( $C$ ) set to 15. Table 10.1 shows the eight experimental conditions evaluated in gelatin phantoms.

### 10.3.2 Experimental facility and procedure

The experimental setup with the fixed ball spline differed slightly from the setup with the moving ball spline. The experimental setup with the fixed ball spline consisted of the Splinositor prototype with cable clips to fix the ball spline in place and a gelatin tissue phantom on a low-friction cart (Figure 10.7a). The experimental setup with the moving ball spline consisted

**Table 10.1. Experimental conditions and mean slip ratios for the performance evaluation of the prototype in gelatin phantoms.** Experimental condition, central ball spline position fixed (BF) or mobile (BM), actuation velocity [rad/s], gelatin weight concentration [wt%], total measured traveled distance [mm] (mean  $\pm$  standard deviation,  $n = 3$ ), slip ratio (mean  $\pm$  standard deviation,  $n = 3$ ).

Condition	Central ball spline	Actuation velocity, $\omega$ [rad/s]	Gelatin weight concentration [wt%]	Total measured traveled distance, $d_m$ [mm] (mean $\pm$ SD)	Slip ratio, $s_{ratio}$ (mean $\pm$ SD)
BF-V1-15%	Fixed	$\pi$	15	$33 \pm 4$	$0.54 \pm 0.052$
BF-V2-15%	Fixed	$2\pi$	15	$26 \pm 5$	$0.64 \pm 0.063$
BF-V3-15%	Fixed	$3\pi$	15	$25 \pm 1$	$0.66 \pm 0.017$
BM-V1-15%	Mobile	$\pi$	15	$47 \pm 3$	$0.35 \pm 0.047$
BM-V2-15%	Mobile	$2\pi$	15	$50 \pm 4$	$0.31 \pm 0.060$
BM-V3-15%	Mobile	$3\pi$	15	$51 \pm 4$	$0.29 \pm 0.052$
BM-V1-10%	Mobile	$\pi$	10	$58 \pm 0$	$0.19 \pm 0.007$
BM-V1-5%	Mobile	$\pi$	5	$59 \pm 1$	$0.18 \pm 0.011$



**Figure 10.7. Experimental setup.** (a) Setup with a fixed ball spline and a mobile gelatin phantom on a low-friction cart. (b) Setup with a fixed gelatin phantom and a mobile ball spline mechanism.

of the prototype and a gelatin tissue phantom contained within a gelatin holder mounted on PMMA plates, which aligned the gelatin holder with the needle, mounted on the breadboard (Figure 10.7b). The position of the needle tip was recorded using a video camera (iPhone 8)

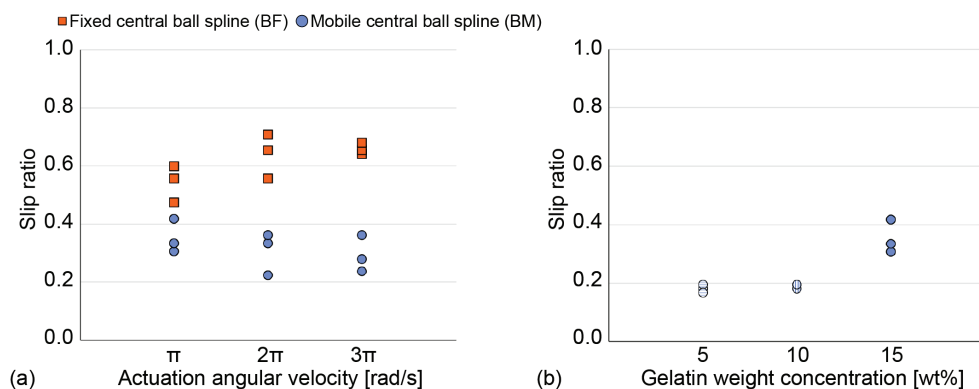


mounted on a tripod, positioned directly above the needle to capture a top-down view of the needle tip within the gelatin phantom. Millimeter graph paper was placed at the bottom surface of the gelatin cart and gelatin holder to give reference to the traveled distance of the needle tip with respect to the gelatin phantom during the experiments with an approximative accuracy of 0.5 mm. To ensure the repeatability of the measurement method, the experimental setup was not moved in between the measurements.

For the gelatin phantoms, gelatin powder of type *Dr. Oetker 1-50-230004* (Dr. Oetker Professional, Amersfoort, The Netherlands) was mixed with water. The gelatin/water mixtures were poured into molds and stored overnight at 5 °C to solidify. Subsequently, the gelatin phantoms were cut to their final dimensions, measuring 40 mm in width, 100 mm in length, and 20 mm in height.

### 10.3.3 Results

Table 10.1 shows the mean and standard deviation of the slip ratio for each experimental condition. Figure 10.8 shows the slip ratio for each trial. In 15 wt% gelatin, the mean slip ratio was 0.32 for the experimental conditions where the central ball spline was able to move like intended ( $n = 9$ ) and 0.61 for the experimental conditions where the central ball spline was fixed in position and the tissue was placed on a low friction cart ( $n = 9$ ). Also, the mean slip ratio for each velocity evaluated was lower for the conditions where the central ball spline was able to move as intended than for the conditions where the central ball spline was fixed. Increasing the actuation velocity from  $\pi$  to  $2\pi$  to  $3\pi$  rad/s resulted in a decrease in the mean slip ratio for conditions where the ball spline was able to move while resulting in an increase in the mean slip ratio for conditions where the ball spline remained fixed. Lastly, decreasing the gelatin weight concentration from 15 wt% to 10 wt% to 5 wt% resulted in a decrease in the mean slip ratio.



**Figure 10.8.** Slip ratio of the needle in gelatin phantoms (a) for different actuation angular velocities and (b) for different gelatin weight concentrations. The orange squares indicate the single trials for the condition with a fixed base plate, a fixed ball spline, and a mobile gelatin sample on a low-friction cart. The blue circles indicate the single trials for the condition with a fixed base plate, a fixed gelatin sample, and a mobile ball spline.

## 10.4 Discussion

### 10.4.1 Main findings

We have presented the design of a manual actuation system for a needle that uses the self-propelling principle of the female parasitic wasp and can travel through stationary tissue phantoms. The manually controlled actuation system allows the operator to drive the needle directly and intuitively using a continuous manual input rotation. Based on the ball spline mechanism, the actuation system allows the needle to propel through tissue phantoms, while avoiding buckling.

For each actuation velocity evaluated, the slip ratio was higher for the fixed ball spline configuration than that for the movable ball spline. The high slip ratio for the fixed ball spline configuration indicates that the cutting and friction forces acting on the advancing needle segment and the inertia of the tissue cart and friction force acting on the bearings of the tissue cart altogether were near the friction forces on the retracting needle segments (Eq. 10.3). Furthermore, it indicates that the inertia of the tissue cart and friction force acting on the bearings of the tissue cart hinder the self-propelled motion of the wasp-inspired needle more than the inertia and friction force introduced by the components of the actuation system that travel with the needle segments in the positive  $y$ -direction for the movable ball spline configuration.

The performance evaluation of the Splinositor prototype in the movable ball spline configuration inside 15-wt% gelatin phantoms showed mean slip ratios of 0.35, 0.31, and 0.29 for actuation velocities of  $\pi$  rad/s,  $2\pi$  rad/s, and  $3\pi$  rad/s, respectively. This slip ratio is lower than found in previous research by Scali *et al.* [13] in 15 wt% gelatin phantoms (i.e., slip ratio 0.45-0.8), and by Bloembergen *et al.* [22] in *ex vivo* human prostate tissue (0.82-0.96). The mean slip ratios of 0.18 and 0.19 of the Splinositor prototype in the 5-wt% and 10-wt% gelatin phantoms, respectively, are slightly lower than the slip ratios found in previous research by Scali *et al.* [13] in 5-wt% and 10-wt% gelatin phantoms (i.e., slip ratios 0.2 and 0.3, respectively). This indicates that the low net insertion force exerted on the needle segments by the actuation system of the Splinositor reduces the slip ratio, thereby enhancing the efficiency of needle advancement through gelatin phantoms, compared to wasp-inspired needles that can self-propel through gelatin phantoms with a zero net insertion force.

### 10.4.2 Buckling prevention

Previous work regarding wasp-inspired needles shows that a wasp-inspired needle can self-propel through a substrate with a zero net insertion force or even a net pulling force [12, 13, 22-24]. However, to prevent buckling, the insertion force does not need to be zero or negative, rather, it should remain below the critical load of the needle. Therefore, the insertion force exerted on the needle segments by the actuation system should remain below the critical load of the needle segments. When taking the following needle design and tissue parameters:  $E_{\text{steel}} = 200$  GPa,  $\varnothing_{\text{needle segment}} = 0.3$  mm,  $K = 0.78$  for a needle inserted into tissue [31],

$L = 20$  mm and 4 mm, which are the maximum unsupported lengths of a needle segment in the actuation system and the substrate, respectively, and  $\mu \approx 8$  kPa for soft tissue [9], the theoretical critical load for each needle segment is approximately 3.2 N. Force measurements of manual insertion of our needle bundle, consisting of six needle segments, into 5-wt% and 10-wt% gelatin phantoms using a force gauge showed peak insertion forces of  $0.15 \pm 0.082$  N (mean  $\pm$  standard deviation,  $n = 3$ ) and  $0.80 \pm 0.15$  N (mean  $\pm$  standard deviation,  $n = 3$ ), respectively. This indicates that the insertion force on each needle segment during insertion of the needle bundle in 5-wt% and 10-wt% gelatin samples remains below the critical load of the needle segments. However, in 15-wt% gelatin phantoms, the needle bundle buckled, making it incapable of successful insertion. This indicates that the insertion force on each needle segment required to push the needle bundle into 15-wt% gelatin phantoms was higher than the critical load of the needle segments.

On the other hand, performance evaluation of Splinositor inside 15-wt% gelatin phantoms showed needle insertion without buckling. Therefore, we can conclude that the insertion force exerted on the needle segments by the actuation system remained below the critical load of the needle. We performed force measurements using a force gauge to show the insertion force exerted on the needle segments by the actuation system. The peak force was in the range of 0.05-0.40 N ( $0.18 \pm 0.12$  N; mean  $\pm$  standard deviation,  $n = 5$ ), which indicates the low net insertion force of 0.05-0.40 N remains below the critical load of the needle and therefore prevents needle buckling.

### 10.4.3 Limitations

The actuation system design in this study allows the needle to travel over 100 mm. This travel distance is limited by the length of the drive cylinder of the ball spline. The follower cylinder of the ball spline and, thus, the cam and the needle segments can travel 100 mm in the y-direction. This travel distance can be extended by extending the drive cylinder length, however, this would linearly increase the length of the actuation system design.

The current design consists of a tabletop actuation system and a needle. However, for the design to replace the conventional needles used in percutaneous procedures in a clinical setting, the design should be adapted to a hand-held device. In future prototypes, the actuation system could be miniaturized and included in a handle that moves forward following the wasp-inspired motion of the needle.

The components of the actuation system that travel with the needle segments in the positive y-direction have a mass, and therefore, their effect of inertia cannot be ruled out. These components include the follower cylinder of the ball spline, cam, cam followers, and origami structure. To decrease the inertia, the mass of the moving components could be minimized, and the actuation sequence could be adapted to a continuous motion, so the components move with a constant velocity.

Throughout the experiments, we ensured the horizontal alignment of the experimental setup by using a spirit level. This was crucial to prevent gravitational effects on the move-



ment of the follower cylinder of the ball spline and, consequently, the needle segments. In the horizontal position, gravity works solely in the z-direction, which is perpendicular to the direction of motion of the needle segments and the corresponding moving components. When the operator tilts the prototype at an angle, creating an inclined plane, the wasp-inspired motion of the needle segments becomes subject to the gravitational forces within the actuation system. In the tilted position, the force of gravity resolves into two components, one parallel to the inclined surface and the other perpendicular to the inclined surface. The force component parallel to the inclined surface would influence the friction forces involved in the wasp-inspired motion.

At the needle tip, the six needle segments are bundled by a heat shrink tube, which might hinder the needle's propagation into a substrate (e.g., a gelatin phantom or tissue sample). The needle's wasp-inspired propulsion with a low net insertion force depends on the surface area of the needle segments in direct contact with the substrate. As the needle is advanced further into the substrate, the surface area of the needle segments in direct contact with the tissue increases, whereas the surface area of the heat shrink tube in contact with the substrate remains unchanged. Consequently, the influence of the heat shrink tube on the needle propulsion declines as the needle advances further into the tissue. Future versions of the Splinositor could incorporate a different bundling mechanism to improve the needle's wasp-inspired propulsion mechanism.

#### 10.4.4 Recommendations and future research

To assess the prototype's functioning in a clinical setting, *ex vivo* or *in vivo* experiments should be conducted. These experiments will shed light on the effects of inhomogeneous tissue properties and the presence of different tissue layers (e.g., skin, fat, and muscle) with different mechanical properties (e.g., modulus of elasticity), as well as blood, on the self-propelling performance of the needle. The ability of the self-propelled needle to advance in *ex vivo* human prostate tissue has been exemplified successfully in a previous study [22]. Furthermore, Scali *et al.* [13] showed that the self-propelled needle could advance in multilayered tissue phantoms.

To clinically use the Splinositor as a passageway to a target location inside the body, to inject or extract fluids, extract tissue samples, and position instruments such as radioactive seeds and optical fibers in the body, a functional element should be added as a central element of the needle or should replace one of the needle segments. In future work, it will be interesting to investigate the implementation of a functional element, such as an optical fiber or a tube connected to a syringe, into the Splinositor and investigate the effect on its self-propelled motion. Furthermore, the Splinositor employs a manual actuation system. Further studies could explore alternative actuation methods that allow for downscaling of the actuation system, such as piezoelectric actuation.

In this study, we developed a stationary manual actuation system for a needle that uses the self-propelling principle of the parasitic wasp and can travel through stationary tissue. The

moving components of the needle have low inertia. Its connection to the actuation system using a ball spline introduces a small friction force, generating a small insertion force on the needle that facilitates the needle's propulsion into tissue while preventing needle buckling. In future work, it will be interesting to develop an actuation system capable of exerting an insertion force equivalent in magnitude to the pulling force induced by the wasp-inspired self-propelled motion within the tissue.

## 10.5 Conclusion

This study presents the design of a manually actuated needle that uses the self-propelling principle of the female parasitic wasp and can travel through stationary tissue phantoms. We have shown that a continuous input rotation can actuate the reciprocating motion of six parallel needle segments using a ball spline-based actuation system. The prototype allows the tissue to remain in place while the needle propels inside the tissue using a low net insertion force of 0.05–0.40 N ( $0.18 \pm 0.12$  N; mean  $\pm$  standard deviation) exerted by the actuation system. The mean slip ratio for each velocity evaluated in 15-wt% gelatin was lower for the conditions where the central ball spline was able to move like intended (i.e., 0.35, 0.31, and 0.29 for  $\pi$  rad/s,  $2\pi$  rad/s, and  $3\pi$  rad/s, respectively) than for the conditions where the central ball spline was fixed (i.e., 0.54, 0.64, and 0.66 for  $\pi$  rad/s,  $2\pi$  rad/s, and  $3\pi$  rad/s, respectively). This indicates that the actuation system's low net insertion force helps propel the needle through the tissue with a low slip ratio and without buckling. Furthermore, evaluation in 15-wt%, 10-wt%, and 5-wt% gelatin tissue phantoms showed that decreasing the gelatin concentration decreased the mean slip ratios from 0.35 to 0.18 and 0.19, respectively. In conclusion, the ball spline-based actuation system is a step forward in developing a wasp-inspired needle for percutaneous procedures that prevents buckling.

## Supplementary material

The appendices and data underlying this study are available at doi: 10.4121/90412947-edbb-452e-ace9-f757f6860ea7.

## Acknowledgements

The authors would like to thank David Jager, Remi van Starkenburg, and Mario van der Wel of the DEMO workshop of Delft University of Technology for their help in manufacturing the prototype.

## References

1. Okamura AM, Simone C, O'leary MD. Force modeling for needle insertion into soft tissue. *IEEE transactions on biomedical engineering*. 2004;51(10):1707–16. doi: 10.1109/TBME.2004.831542.
2. Sakes A, Dodou D, Breedveld P. Buckling prevention strategies in nature as inspiration for improving percutaneous instruments: a review. *Bioinspiration & biomimetics*. 2016;11(2):021001. doi:



10.1088/1748-3190/11/2/021001.

3. Abolhassani N, Patel RV, Ayazi F. Minimization of needle deflection in robot-assisted percutaneous therapy. *The international journal of medical Robotics and computer assisted surgery*. 2007;3(2):140-8. doi: 10.1002/rcs.136.
4. Abolhassani N, Patel R, Moallem M. Needle insertion into soft tissue: A survey. *Medical engineering & physics*. 2007;29(4):413-31. doi: 10.1016/j.medengphy.2006.07.003.
5. Reed KB, Majewicz A, Kallem V, Alterovitz R, Goldberg K, Cowan NJ, et al. Robot-assisted needle steering. *IEEE robotics & automation magazine*. 2011;18(4):35-46. doi: 10.1109/MRA.2011.942997.
6. Rucker DC, Das J, Gilbert HB, Swaney PJ, Miga MI, Sarkar N, et al. Sliding mode control of steerable needles. *IEEE Transactions on Robotics*. 2013;29(5):1289-99. doi: 10.1109/TRO.2013.2271098.
7. L. E. Principes généraux du mouvement des fluides. 1757.
8. Chen W-F, Atsuta T. *Theory of beam-columns, volume 2: space behavior and design*: J. Ross Publishing; 2007.
9. He X, Chen Y, Tang L. Modeling of flexible needle for haptic insertion simulation. 2008 IEEE Conference on Virtual Environments, Human-Computer Interfaces and Measurement Systems; 2008: IEEE. doi: 10.1109/VECIMS.2008.4592777.
10. Frasson L, Ko S, Turner A, Parittotokkaporn T, Vincent JF, Rodriguez y Baena F. STING: a soft-tissue intervention and neurosurgical guide to access deep brain lesions through curved trajectories. *Proceedings of the Institution of Mechanical Engineers, Part H: Journal of Engineering in Medicine*. 2010;224(6):775-88. doi: 10.1243/09544119JEIM663.
11. Leibinger A, Oldfield MJ, Rodriguez y Baena F. Minimally disruptive needle insertion: a biologically inspired solution. *Interface focus*. 2016;6(3):20150107. doi: 10.1098/rsfs.2015.0107.
12. Scali M, Pusch T, Breedveld P, Dodou D. Ovipositor-inspired steerable needle: design and preliminary experimental evaluation. *Bioinspiration & Biomimetics*. 2017;13(1):016006. doi: 10.1088/1748-3190/aa92b9.
13. Scali M, Breedveld P, Dodou D. Experimental evaluation of a self-propelling bio-inspired needle in single-and multi-layered phantoms. *Scientific reports*. 2019;9(1):1-13. doi: 10.1038/s41598-019-56403-0.
14. Quicke DL, Fitton MG. Ovipositor steering mechanisms in parasitic wasps of the families Gasteruptiidae and Aulacidae (Hymenoptera). *Proceedings of the Royal Society of London Series B: Biological Sciences*. 1995;261(1360):99-103. doi: 10.1098/rspb.1995.0122.
15. Leyva JL, Browning HW, Gilstrap FE. Effect of host fruit species, size, and color on parasitization of *Anastrepha ludens* (Diptera: Tephritidae) by *Diachasmimorpha longicauda* (Hymenoptera: Braconidae). *Environmental Entomology*. 1991;20(5):1469-74. doi: 10.1093/ee/20.5.1469.
16. Cerkvenik U, Van Leeuwen JL, Kovalev A, Gorb SN, Matsumura Y, Gussekloo SW. Stiffness gradients facilitate ovipositor bending and spatial probing control in a parasitic wasp. *Journal of Experimental Biology*. 2019;222(9):jeb195628. doi: 10.1242/jeb.195628.
17. Cerkvenik U, Van de Straat B, Gussekloo SW, Van Leeuwen JL. Mechanisms of ovipositor insertion and steering of a parasitic wasp. *Proceedings of the National Academy of Sciences*. 2017;114(37):E7822-E31. doi: 10.1073/pnas.1706162114.
18. Heverly M, Dupont P, Triedman J. Trajectory optimization for dynamic needle insertion. *Proceedings of the 2005 IEEE international conference on robotics and automation*; 2005: IEEE. doi: 10.1109/ROBOT.2005.1570349.
19. Ng KW, Goh JQ, Foo SL, Lee TK, Esuvaranathan K, et al. Needle deflection studies for optimal insertion modeling. *International Journal of Bioscience, Biochemistry and Bioinformatics*. 2013;3(6):570. doi: 10.7763/IJBBS.2013.V3.278.
20. Kataoka H, Washio T, Chinzei K, Mizuhara K, Simone C, Okamura AM. Measurement of the tip and friction force acting on a needle during penetration. *Medical Image Computing and Computer-Assisted Intervention—MICCAI 2002: 5th International Conference Tokyo, Japan, September 25–28, 2002 Proceedings, Part I 5*; 2002: Springer. doi: 10.1007/3-540-45786-0\_27.

21. Scali M. Self-propelling needles: From biological inspiration to percutaneous interventions: Delft University of Technology; 2020. doi: 10.4233/uuid:523e3e5f-08f0-4acb-ab45-abaa7ace3967.
22. Bloembergen J, Trauzettel F, Coolen B, Dodou D, Breedveld P. Design and evaluation of an MRI-ready, self-propelled needle for prostate interventions. *PLoS ONE*. 2022;17(9):e0274063. doi: 10.1371/journal.pone.0274063.
23. Scali M, Kreeft D, Breedveld P, Dodou D. Design and evaluation of a wasp-inspired steerable needle. *Proceedings of SPIE*; Portland, Oregon, United States: International Society for Optics and Photonics; 2017. p. 1016207.
24. Parittotokkaporn T, Frasson L, Schneider A, Huq SE, Davies BL, Degenaar P, et al. Soft tissue traversal with zero net force: Feasibility study of a biologically inspired design based on reciprocal motion. 2008 IEEE International Conference on Robotics and Biomimetics; 2009: IEEE. doi: 10.1109/ROBIO.2009.4912983.
25. Sprang T, Breedveld P, Dodou D. Wasp-inspired needle insertion with low net push force. *Conference on Biomimetic and Biohybrid Systems*; 2016: Springer. doi: 10.1007/978-3-319-42417-0\_28.
26. Wu H, Fang H, Chen L, Xu J. Transient dynamics of a miura-origami tube during free deployment. *Physical Review Applied*. 2020;14(3):034068. doi: 10.1103/PhysRevApplied.14.034068.
27. Mueller S, Sandrin L. Liver stiffness: a novel parameter for the diagnosis of liver disease. *Hepatic medicine: evidence and research*. 2010;49-67. doi: 10.2147/HMER.S7394.
28. Kot BCW, Zhang ZJ, Lee AWC, Leung VYF, Fu SN. Elastic modulus of muscle and tendon with shear wave ultrasound elastography: variations with different technical settings. *PLoS ONE*. 2012. doi: 10.1371/journal.pone.0044348.
29. Zhang M, Nigwekar P, Castaneda B, Hoyt K, Joseph JV, di Sant'Agnese A, et al. Quantitative characterization of viscoelastic properties of human prostate correlated with histology. *Ultrasound in medicine & biology*. 2008;34(7):1033-42. doi: 10.1016/j.ultrasmedbio.2007.11.024.
30. Barr RG, Memo R, Schaub CR. Shear wave ultrasound elastography of the prostate: initial results. *Ultrasound quarterly*. 2012;28(1):13-20. doi: 10.1097/RUQ.0b013e318249f594.
31. Hulburt T, Booth J, Pan P, Brown P. Characterization of spinal needle buckling behavior. *Journal of Medical Devices*. 2019;13(4):041003. doi: 10.1115/1.4043920.



## **A Universal Actuator for a Self-Propelled Needle**

Published as:

Bloemberg J., van der Wel M., Sakes A., Breedveld P. (2025). Design and evaluation of a mechanical pencil-based actuator for a wasp-inspired needle. PLoS ONE, 20(7): e0326584. doi: 10.1371/journal.pone.0326584.



## Abstract

In percutaneous interventions, long and thin needles are used to reach deep target locations within the body. However, inserting a long and thin needle into the tissue can cause needle buckling, resulting in poor control of the needle's trajectory and reduced targeting accuracy. In nature, the female parasitic wasp prevents the buckling of her long and slender ovipositor through a self-propelled motion. This study presents a stationary actuation system that can advance a wasp-inspired self-propelled needle consisting of seven 0.3-mm stainless steel rods with a theoretically unlimited insertion length. Based on the pencil lead advance mechanism in mechanical pencils that advances the pencil lead at a fixed increment when the pencil button is pushed, our actuation system advances the seven needle segments that comprise our needle by locking, advancing, releasing, and retracting the advance mechanisms. Experimental evaluation demonstrated that the actuation system successfully executes these actions, enabling step-by-step propulsion of the needle segments in gelatin-based tissue-mimicking phantoms. Moreover, the needle achieved mean motion efficiencies of  $98 \pm 2\%$ ,  $68 \pm 5\%$ , and  $57 \pm 7\%$  in air, 5-wt% gelatin, and 10-wt% gelatin, respectively, over 15 actuation cycles. This actuation system prototype, which is based on a mechanical pencil, is a step forward in developing self-propelled needles for targeting deep tissue structures.

## 11.1 Introduction

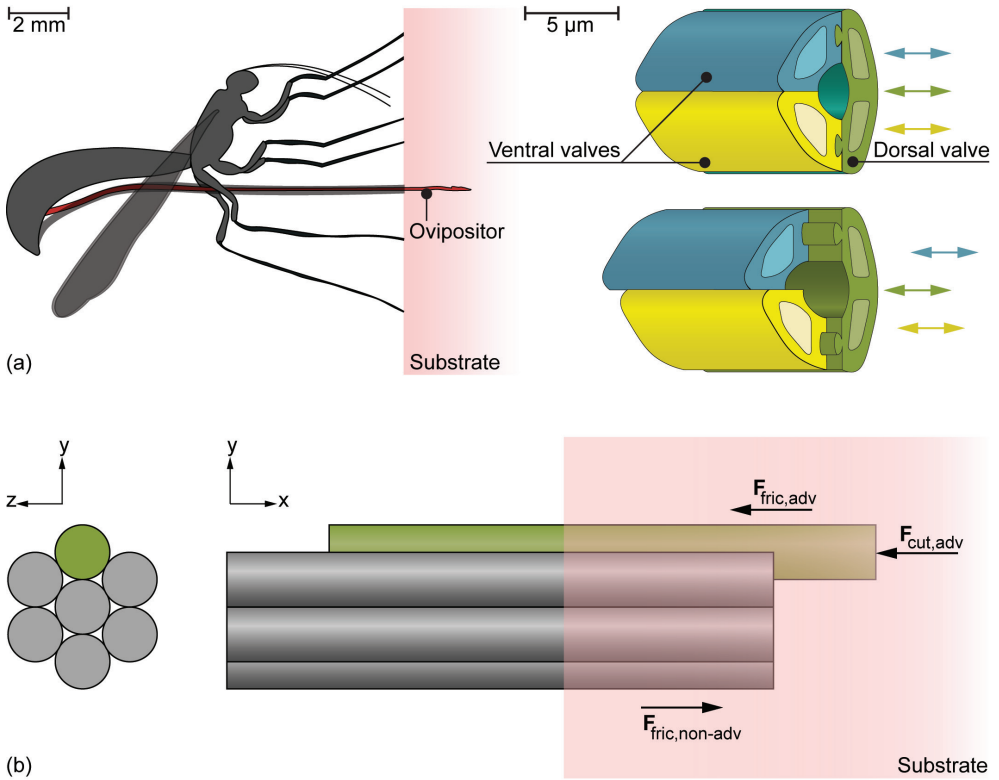
Needles serve as passageways to target specific locations within the body, facilitating a wide range of applications, such as extracting tissue samples for biopsies and positioning instruments for needle-based therapies in deep tissue structures such as the prostate gland. When a needle is pushed through the tissue, forces arise at the needle tip and along the needle shaft [1]. Okamura *et al.* [1] demonstrated that inside homogeneous tissue, these forces comprise cutting and friction forces. To move a needle through tissue, the operator should apply a force that overcomes the sum of these forces acting on the needle. If the axial force on the needle tip exceeds the critical load of the needle, the needle buckles [2]. Needle buckling might lead to poor control of the needle path, thereby decreasing needle targeting accuracy, which affects the effectiveness of biopsies and needle-based therapies [3].

To prevent needle buckling, self-propelled needles inspired by the ovipositor of the female parasitic wasp have been developed [4-11] (Figure 11.1a, Table 11.1). Wasp-inspired self-propulsion inside a substrate is accomplished by a set of parallel needle segments that can advance with respect to one another (Figure 11.1b). The advancing needle segments experience both a cutting force at their tips and a friction force along the length of their shafts in contact with the surrounding substrate [12]. The non-advancing needle segments, however, only experience a friction force in the opposite direction. If the sum of the friction and cutting forces on the advancing needle segments is equal to the sum of the friction forces on the non-advancing needle segments, the wasp-inspired needle can propel forward through a substrate with a zero net insertion force (Eq. 11.1), as shown in previous works [4-11]. This can be achieved by keeping the number of advancing needle segments smaller than the number of non-advancing needle segments so that the difference between the forces acting on the two groups of needle segments increases with the insertion distance.

$$\sum_{i=1}^a (\mathbf{F}_{\text{fric,adv},i} + \mathbf{F}_{\text{cut,adv},i}) \leq \sum_{j=1}^n (\mathbf{F}_{\text{fric,non-adv},j}) \quad (11.1)$$

where  $a$  is the number of advancing needle segments,  $n$  is the number of non-advancing needle segments,  $\mathbf{F}_{\text{fric,adv}}$  is the friction force along the shafts of the advancing needle segments,  $\mathbf{F}_{\text{cut,adv}}$  is the cutting force on the tips of the advancing needle segments, and  $\mathbf{F}_{\text{fric,non-adv}}$  is the total amount of friction along the shafts of the non-advancing needle segments, which works in the opposite direction to the friction force of the advancing needle segments.

In existing prototypes of ovipositor-inspired needles, the needle and actuation system are integrated [4-11]. As a result, when the needle advances into the tissue, the actuation system must move in conjunction with it. The inertia of the moving components adversely affects the needle's self-propelled motion. To address this issue, Bloemberg *et al.* [14] developed an actuation system that keeps the external parts of the actuation system stationary, allowing only the needle and internal parts to move (Chapter 10). However, a limitation of this mechanism is that the length of the actuation system restricts the achievable needle insertion distance. Therefore, this study aims to design a stationary actuation system capable of advancing a wasp-inspired self-propelled needle over very long insertion distances.



**Figure 11.1. Schematic representation of ovipositor-inspired needle motion.** (a) Schematic illustration of a female parasitic wasp using its ovipositor to lay eggs inside a substrate. The ovipositor consists of three parallel “valves” (green, yellow, and blue) that can move reciprocally (based on Cerkenik *et al.* [15]). (b) Schematic illustration of ovipositor-inspired needle insertion into tissue with one advancing needle segment (green) and six non-advancing needle segments (gray).  $F_{\text{fric,adv}}$  is the friction force along the advancing needle segment,  $F_{\text{cut,adv}}$  is the cutting force on the tip of the advancing needle segment, and  $F_{\text{fric,non-adv}}$  is the total amount of friction of the non-advancing needle segments, which works in the opposite direction to the friction force of the advancing needle segment.

## 11.2 Design

### 11.2.1 Needle

Our design comprises a needle and a motorized actuation system. The needle consists of seven parallel needle segments inspired by the parallel valves of the parasitic wasp ovipositor (Figure 11.1b). To accommodate a central functional needle segment, such as an optical fiber, we opted for six outer needle segments surrounding a seventh segment, which can be substituted with the functional segment. In the two-dimensional cross-section, arranging six cylindrical needle segments concentrically around the seventh needle segment forms an optimal configuration when all needle segments have the same diameter. Each outer needle segment contacts the central needle segment as well as two adjacent needle segments. This minimizes

**Table 11.1. State-of-the-art in wasp-inspired needles, showing the reference, the number of needle segments the needle comprises, the outer diameter of the needle in [mm], the material of the needle segments, and a description of the needle design.**

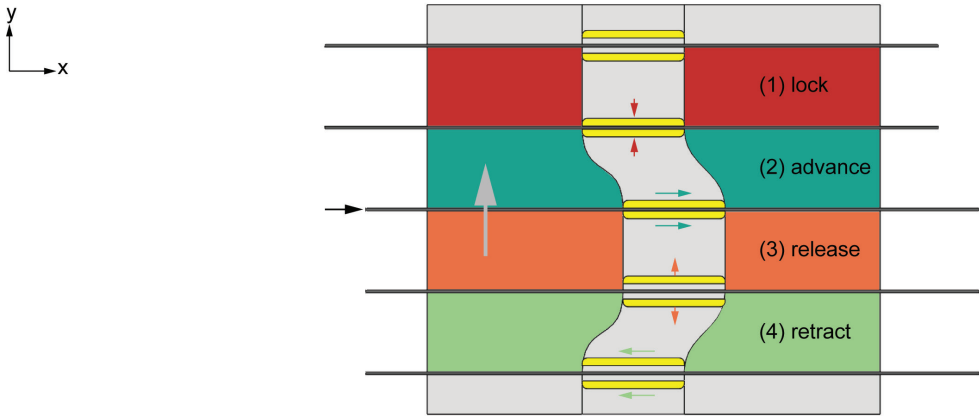
Reference	Number of needle segments	Outer diameter [mm]	Material	Needle design
Frasson <i>et al.</i> [4]	2	4.4	Tango Black™	Axially interlocked halves
Leibinger <i>et al.</i> [5]	4	4	VeroGrey	Axially interlocked quadrants
Scali <i>et al.</i> [6]	7	1.55	Nitinol	Converging/diverging ring with 7 holes interlocks the needle segments
Scali <i>et al.</i> [8]	7	1.2	Nitinol	Flower-shaped ring with 7 holes interlocks the needle segments
Scali <i>et al.</i> [7]	6	0.84	Nitinol	Heat shrink tube interlocks the needle segments
	3	0.59		
	6	0.42		
Bloemberg <i>et al.</i> [9, 10] (Chapters 9, 7)	6	0.84	Nitinol	Heat shrink tube interlocks the needle segments
Bloemberg <i>et al.</i> [14] (Chapter 10)	6	1.0	Steel	Heat shrink tube interlocks the needle segments
Bloemberg <i>et al.</i> [11] (Chapter 5)	7	3	Nitinol	Internal ring through needle segment slots interlocks the needle segments

the total cross-sectional area and results in the least empty space between the needle segments where tissue could potentially accumulate. Using the wasp's self-propelling principle, the needle self-propels through the substrate by incrementally advancing the seven needle segments forward one by one. In this study, the motion sequence that involves advancing all seven needle segments one time is referred to as one "actuation cycle." The distance each needle segment travels per actuation cycle is called the "needle stroke distance."

### 11.2.2 Actuation system

To achieve long needle insertion distances through incremental steps, the actuation system must sequentially advance the individual needle segments. For each needle segment, this can be accomplished via a clamp that operates in a four-step cycle: (1) locking, (2) advancing, (3) releasing, and (4) retracting (Figure 11.2). First, the clamp (in yellow) locks around the needle segment, thereby clamping the needle segment at a defined position (in red). Second, the locked clamp advances, thus advancing the needle segment forward (in dark green). Third, the clamp releases the needle segment at the new position (in orange). Finally, the clamp moves backward to its original position (in light green), whereas the needle segment remains in its propelled position. Once the clamp arrives at its original position, it can clamp the needle segment at its new propelled position (in red). This cycle repeats until the needle segment arrives at its destination.

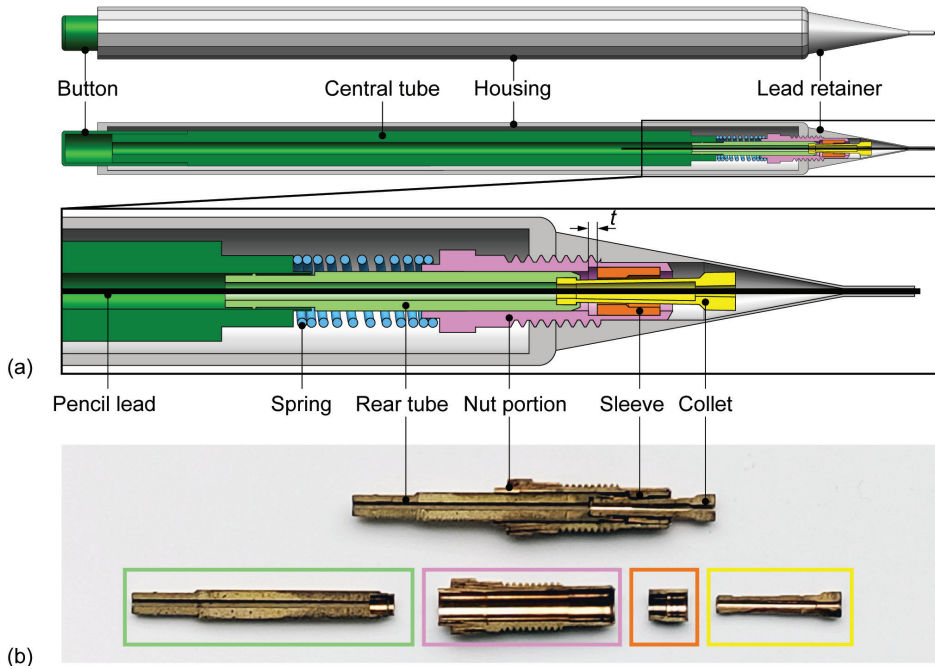




**Figure 11.2.** 2D schematic representation of the clamp mechanism to achieve needle actuation in incremental steps. The figure shows the simplified motion sequence of clamps actuated by a cam track (gray). During the red phase of the cam, the clamp (yellow) is locked around the needle segment (black). During the dark green phase of the cam, the clamp follows the cam track in the positive x-direction, thereby moving the needle segment in the positive x-direction. During the orange phase of the cam, the needle segment is released. During the light green phase of the cam, the clamp follows the track in the negative x-direction while the needle segment remains in its propelled position.

The incremental needle segment advance mechanism mirrors the functionality of a mechanical pencil, where pressing the button advances the pencil lead by a fixed amount (Figure 11.3). The mechanical pencil comprises five complex-shaped components that can move with respect to each other: (1) a housing, lead retainer, and nut portion (in gray and pink), (2) a button, central tube, and rear tube (in dark and light green) formed around a three-finger collet (in yellow), (3) a sleeve (in orange), (4) a compression spring (in blue), and (5) a pencil lead (in black). Among these components, the advance mechanism (in lighter colors) consists of the nut portion, the rear tube, the collet, the sleeve, and the spring. The nut portion contains two ridges that limit the horizontal translation of the sleeve over a distance  $t$  (Figure 11.3a). The sleeve is positioned around the collet. The collet is similar to that found in milling machines and closes around the pencil lead (in black). When the sleeve is positioned at the tip of the collet, the collet's fingers are closed, and the pencil lead is held firmly in place for writing. Conversely, when the sleeve is retracted from the tip of the collet, as shown in Figure 11.3a, the fingers of the collet are opened, and their grip on the pencil lead is released, allowing it to move.

To explain the mechanism of the mechanical pencil, we assume that the first component (i.e., the housing, lead retainer, and nut portion) remains stationary while the button is pressed. Pressing the button on the mechanical pencil causes the advance mechanism to move from its locked to its released state by translating the second component (i.e., the button, central tube, rear tube, and collet), causing the spring to compress. The sleeve also moves with the collet over distance  $t$  until the sleeve encounters the right ridge of the nut portion. Until this moment, the sleeve was positioned at the tip of the collet because of the friction between



**Figure 11.3. The pencil lead advance mechanism of a mechanical pencil.** (a) Schematic illustration of the assembly and cross-section view of the pencil lead advance mechanism in its released state showing the button and central tube (dark green), housing and lead retainer (gray), pencil lead (black), spring (blue), rear tube (light green), nut portion (pink), sleeve (orange), and collet (yellow). Distance  $t$  indicates the distance over which the sleeve can move within the nut portion, constrained by the ridges of the nut portion. (b) Picture of the cross-section of a pencil lead advance mechanism highlighting the rear tube (green), nut portion (pink), sleeve (in orange), and collet (yellow).

the sleeve and the collet, thereby closing the collet's fingers and advancing the pencil lead firmly held by the collet. The right ridge of the nut portion limits the sleeve's forward motion, determining the pencil lead's advancement distance. When the sleeve is halted, the rear tube and the collet move further forward, overcoming the friction between the sleeve and the collet and pushing the collet's fingers out of the sleeve, causing the collet's fingers to open and release the pencil lead. The lead retainer at the tip of the pencil prevents the pencil lead from falling out of the pencil or retracting due to the frictional force between the lead retainer and the pencil lead.

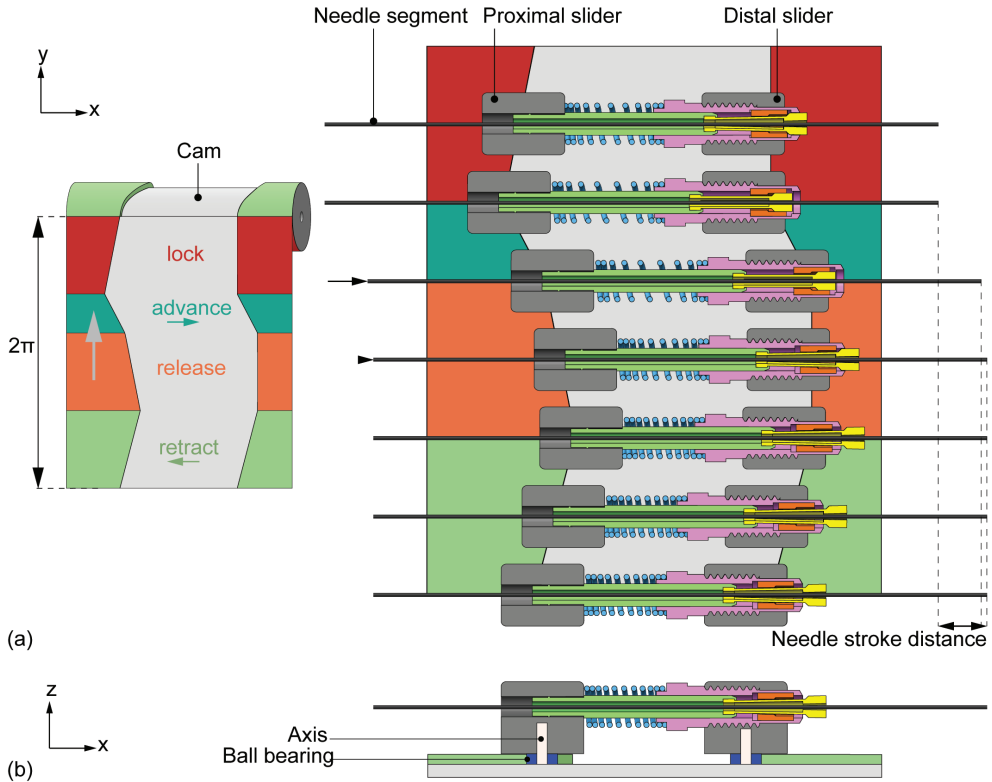
Once the button is released, the spring extends, and the advance mechanism moves from its released state to its locked state by retracting the central tube, rear tube, and collet. The collet's retraction pulls the sleeve back over distance  $t$  into its original position within the nut portion. The collet's fingers remain open until the sleeve encounters the left ridge of the nut portion, closing the collet's fingers again around the pencil lead. The pencil lead remains extended despite the collet's movement due to greater friction between the pencil lead and the lead retainer than between the pencil lead and the open collet. Without the lead retainer,

the frictional force between the pencil lead and the collet would cause the pencil lead to retract with the collet during its backward motion. Finally, the spring force causes the collet to retract even further to its original position, and the sleeve closes the collet's fingers around the pencil lead at its propelled position, securing the pencil lead and preventing it from retracting during writing.

We adapted an existing pencil lead advance mechanism of a mechanical pencil as the base for our needle segment advance mechanism. Rather than advancing a pencil lead, our needle segment advance mechanism enables the movement of a needle segment with the same diameter as the pencil lead. The advance mechanism is in its locked state when the spring is extended, thereby clamping the needle segment. Conversely, when the spring is compressed, the advance mechanism is in its released state, allowing it to translate in the longitudinal direction to clamp the needle segment at its new position.

In our actuation system design, seven advance mechanisms, arranged in a circle, drive the seven needle segments. To actuate the advance mechanisms, we use a cam containing two tracks that are followed by sliders attached to the distal and proximal ends of the advance mechanisms. The spring within each advance mechanism ensures continuous contact between the sliders and the cam tracks. A frame encasing the cam constrains the movement of the sliders to solely a translation in the horizontal  $x$ -direction. Consequently, the motion of the advance mechanisms is restricted to solely a translation in the  $x$ -direction, guided by the cam tracks.

To explain the motion cycle of our actuation system, the mechanism is simplified and visualized in a schematic illustration in Figure 11.4. The input motion is a rotation of the cam (in light gray) around its longitudinal  $x$ -axis. The cam controls the position of the proximal and distal sliders (in dark gray) that operate the advance mechanisms. The cam tracks govern the motion of each advance mechanism through four distinct phases of rotation: the red, dark green, orange, and light green phases, similar to Figure 11.2. First, the proximal slider of the advance mechanism moves in the negative  $x$ -direction, causing the spring to extend and the advance mechanism to lock the needle segment (red phase). We added the second and fourth cam phases because the pencil lead's advancement distance  $t$  is too short for our needle stroke distance. In the second cam phase, both the proximal and distal sliders move in the positive  $x$ -direction, moving the advance mechanism in its locked state forward and thus advancing the locked needle segment (dark green phase). Third, the distal slider remains stationary as the proximal slider continues to move in the positive  $x$ -direction, compressing the spring and releasing the needle segment (orange phase). In the fourth and final phase, both the proximal and distal sliders move in the negative  $x$ -direction, retracting the advance mechanism in its released state while the released needle segment remains in its propelled position (light green phase). Once the advance mechanism returns to its original position, it locks the needle segment at its new propelled position (red phase). This cycle repeats until the needle segment reaches its target location.

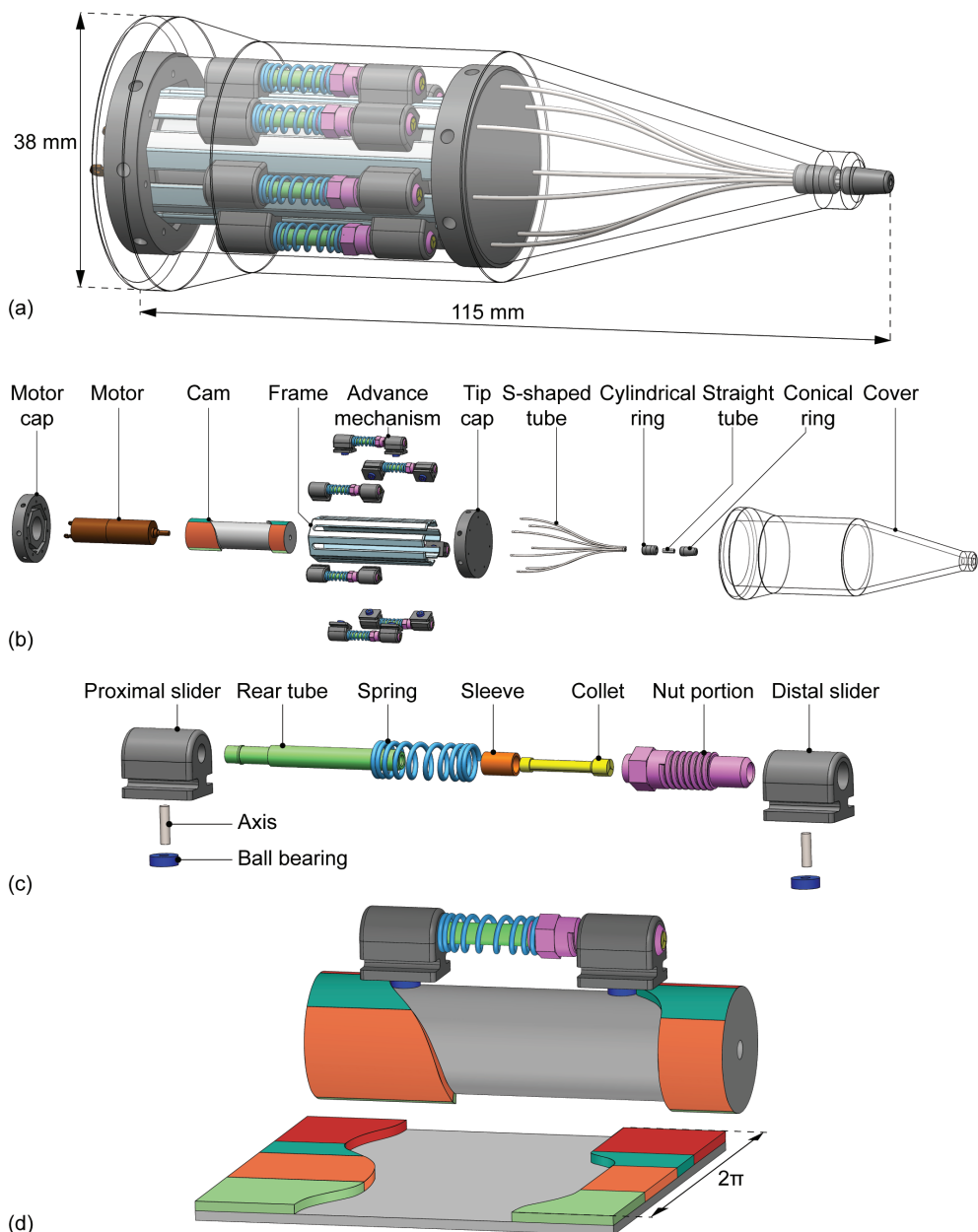


**Figure 11.4. Schematic representation of the needle segment advance mechanism actuated by a cam.** (a) The rolled-out cam shows the needle segment advance mechanism that comprises seven adapted pencil lead advance mechanisms (shown in the cross-section top view) that function as the clamp mechanisms actuated by the cam. (b) Cross-section side view of one needle segment advance mechanism with the proximal and distal sliders (dark gray) running in the cam tracks using ball bearings (dark blue) on axes (white).

### 11.2.3 Final design

The final design contains seven advance mechanisms, one for each needle segment, and each is operated by two sliders that follow the cam tracks (Figure 11.5). To facilitate the self-propelled motion, only one of the seven needle segments is in the dark green phase during each step of the actuation cycle, ensuring that the number of advancing needle segments remains less than the number of non-advancing segments. The cam's dark and light green phases each provide a 4-mm stroke. The orange and red phases result in a 3-mm stroke for releasing and locking the advance mechanisms. The corners of the cam tracks between the phases were rounded to facilitate smooth transitions between the cam phases. One actuation cycle is defined as a single full rotation of the cam, during which all seven needle segments are advanced once over the needle stroke distance.

In the actuation system, the needle segments run at a larger diameter than at the needle



**Figure 11.5. Design drawing of the final design.** (a) Assembly. (b) Exploded view. (c) Exploded view of the advance mechanism adapted from the Pentel P203 pencil lead advance mechanism. (d) Cam showing one of the seven advance mechanisms in the cam tracks and rolled-out cam.

tip. The seven needle segments are arranged in a circular formation within the actuation system, whereas at the needle tip, one segment is centrally positioned with six segments arranged

in a circle around it. To guide the seven needle segments smoothly from the actuation system to the needle tip, seven S-shaped tubes followed by seven straight tubes were used. The needle segments run through the S-shaped tubes that gradually decrease the distance between the needle segments from the actuation system to the needle tip. These tubes provide continuous support to the needle segments to avoid buckling while allowing free movement along the x-axis. The seven straight tubes further guide the needle segments into their insertion formation, where one segment is centrally located and six segments surround it. The friction between the tubes and the needle segments exceeds the friction between the open collets and the needle segments during the light green phase as the advance mechanisms retract. Consequently, the needle segments stay at their propelled positions while the collets are retracted.

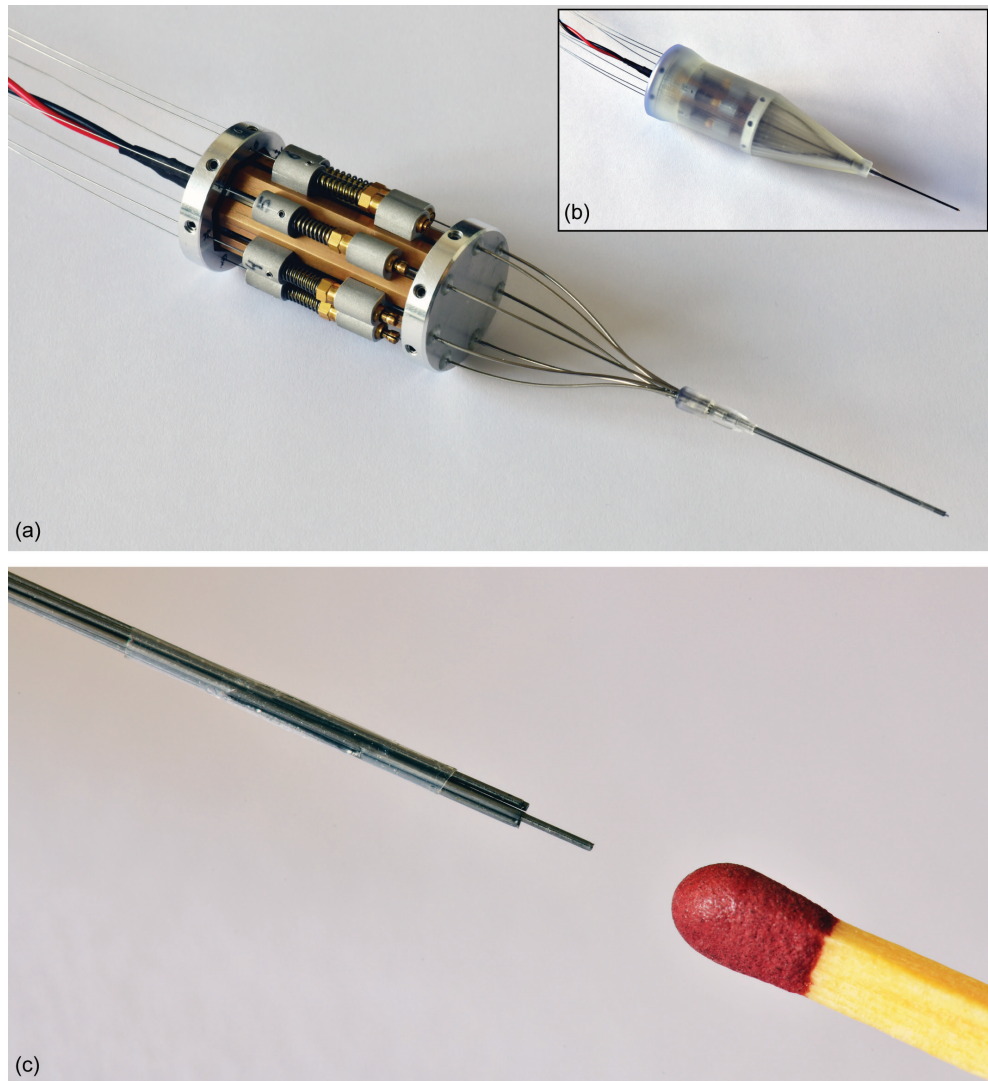
#### 11.2.4 Prototype

The actuation system design limits the needle segment diameter to 0.3 mm but does not impose any restrictions on the needle segment length. The needle used in this study consists of seven blunt spring steel rods with a diameter of 0.3 mm and a length of 1 m. Following the designs of Scali *et al.* [7] and Bloemberg *et al.* [9, 10, 14], the needle segments were held together at the tip using a 10-mm long heat shrink tube (103-0352, Nordson Medical Corp., Westlake, OH, United States). This bundling mechanism prevents the needle segments from diverging while only slightly increasing the overall diameter of the needle. To maintain its position at the needle tip, the heat shrink tube was secured to one of the needle segments using *Pattex Gold Gel* (1432562, Pattex, Henkel AG and Co., Düsseldorf, Germany). The remaining needle segments can move freely through the heat shrink tube. The total diameter of the needle, including the heat shrink tube, is 1.0 mm.

The assembled prototype, called the Ovipositor Needle Clamp Actuator (ONCA), is shown in Figure 11.6. Components of the needle segment advance mechanisms were adapted from off-the-shelf *Pentel P203 mechanical pencils* (Pentel Co. Ltd., Penteru Kabushiki Gaisha, Japan), specifically the rear tube, nut portion, sleeve, and collet. The rather stiff pencil springs were replaced with softer *DR970 springs* (Alcomex springs, Opmeer, Netherlands;  $\varnothing_{\text{outer}} = 3.6$  mm,  $\varnothing_{\text{wire}} = 0.4$  mm,  $L_0 = 12.80$  mm,  $K = 0.78$  N/mm,  $L_c = 5.50$  mm) because the tactile feedback from the stiffer springs is unnecessary for our prototype. The proximal and distal sliders were produced out of Aluminum 7075-T6 by wire Electrical Discharge Machining (EDM), after which the holes for the needle segments and axes were drilled, and screw threads were added for fixation of the nut portions. The bearing axes were machined at length out of high-speed steel by wire EDM. The bearings are stainless steel *Deep Groove Ball Bearings DDL-310HA1P25LO1* (MinebeaMitsumi Inc., Tokyo, Japan).

The cam, motor cap, and tip cap were produced by CNC milling and turning of Aluminum 7075-T6. The frame was constructed from brass, providing low friction with the aluminum sliders. The outer heptagon shape of the frame and its slots for the sliders were CNC milled. Subsequently, the inner heptagon shape was machined by wire EDM. Finally, the frame was machined to its final length by wire EDM. The S-shaped tubes (inner diameter of 0.4 mm and





**Figure 11.6. Ovipositor Needle Clamp Actuator (ONCA).** (a) Without cover. (b) With cover. (c) Close-up of the needle tip consisting of seven rods held together by a shrinking tube (Nordson Medical) glued to one of the seven rods.

outer diameter of 0.6 mm) were manually bent from stainless steel. The cover, cylindrical ring, and conical ring were produced by stereolithography 3D printing on a Formlabs Form 3B printer using Clear resin (Formlabs, Somerville, MA, USA). The motor used is a *1016M012G* DC-micromotor with a 10/1 256:1 gearbox (Faulhaber, Schönaich, Germany).



## 11.3 Evaluation

### 11.3.1 Experimental goal

To evaluate the performance of the ONCA, we conducted experiments in air and in tissue-mimicking phantoms. The goal was to investigate the ONCA's insertion performance in terms of its motion efficiency,  $\eta_m(C)$ , over the number of actuation cycles,  $C$ . More specifically, we investigated how  $\eta_m(C)$  was influenced by two factors: (1) the slip between the needle segments and the advance mechanisms, which reflects the actuation system's clamp efficiency,  $\eta_c(C)$ , and (2) the slip between the stationary needle segments and the substrate (i.e., air or tissue-mimicking phantoms), which reflects the needle's propulsion efficiency,  $\eta_p(C)$ .

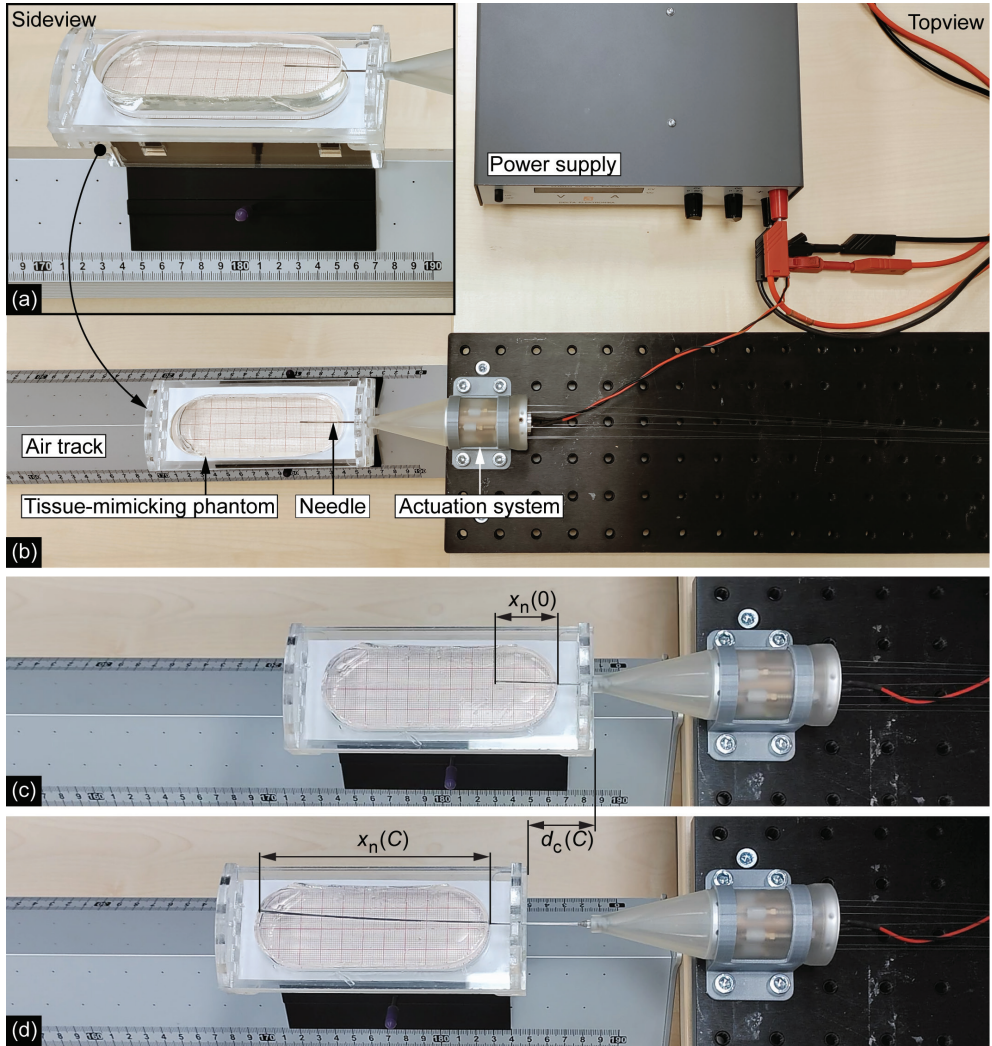
- $C$  [-]: number of actuation cycles
- $\eta_m(C)$  [%]: motion efficiency of the ONCA
- $\eta_c(C)$  [%]: clamp efficiency of the advance mechanisms inside the actuation system of the ONCA
- $\eta_p(C)$  [%]: propulsion efficiency of the needle of the ONCA

For  $\eta_c(C)=100\%$ , the advance mechanism clamps function perfectly, and the needle segments do not slip with respect to the advance mechanisms. We assumed that when the needle travels in the air, the advance mechanisms operate at  $\eta_c(C) = 100\%$  and advance the needle segments over the needle stroke distance during every actuation cycle. When the needle travels in a tissue-mimicking phantom, the cutting and friction forces acting on the needle segments can decrease  $\eta_c(C)$ , thereby advancing the needle segments over less than the needle stroke distance during every actuation cycle.

For  $\eta_p(C) = 100\%$ , the needle advances into the substrate over the same distance that the advance mechanisms move the needle segments during each actuation cycle. This means that the advancing needle segments advance in the substrate while the non-advancing needle segments remain stationary with respect to the substrate, meaning there is no slippage between the stationary needle segments and the substrate.

### 11.3.2 Experimental facility

The experimental setup consists of the ONCA kept stationary in a holder and the substrate (i.e., a tissue-mimicking phantom) on a Perspex cart (Figures 11.7a,b). The cart fits on an air track (Eurofysica), facilitating near-frictionless linear translation of the cart. Millimeter paper was attached at the bottom of the cart and used as a reference for the traveled distance,  $d_n(C)$ , of the needle tip in the substrate on the cart. The variable  $d_n(C)$  was measured by calculating the difference between the initial needle insertion distance,  $x_n(0)$ , and the insertion distance,  $x_n(C)$ , in the substrate after a number of actuation cycles  $C$  from the video footage (Figures 11.7c,d). Moreover, we measured the distance  $d_c(C)$  over which the cart was pushed forward with respect to the air track during needle insertion. The variable  $d_c(C)$  was determined by calculating the difference between the initial cart position and the cart position after the number of actuation cycles,  $C$ , with respect to the air track from the video footage using



**Figure 11.7. Experimental setup.** (a) Side view of the cart in the experimental setup. (b) Top view of the experimental setup. (c) Example of the initial position of the needle inside the tissue-mimicking phantom. Variable  $x_n(0)$  is the measured initial insertion distance of the needle in the substrate at zero actuation cycles. (d) Example of a final position of the needle inside the gelatin phantom. Variable  $x_n(C)$  is the measured distance of the needle in the substrate after  $C$  number of actuation cycles and  $d_c(C)$  is the measured displacement of the cart with respect to the air track.

the ruler on the air track (Figures 11.7c,d).

- $x_n(0)$  [mm]: initial needle insertion distance
- $x_n(C)$  [mm]: needle insertion distance
- $d_n(C)$  [mm]: traveled distance of the needle tip in the substrate
- $d_c(C)$  [mm]: traveled distance of the cart with respect to the air track

The distance over which the advance mechanisms advance the needle segments equals  $d_n(C) + d_c(C)$ . The expected traveled distance,  $d_e(C)$ , of the needle tip was computed by averaging the distance traveled by the needle tip with respect to the air track per actuation cycle in the air (i.e., the needle stroke distance) and multiplying it by  $C$ .

- $d_e(C)$  [mm]: expected traveled distance of the needle tip

### 11.3.3 Experimental variables

In the experiments, the independent variables were  $C$ , which was set to 5, 10, 15, and 20, and the substrate through which the needle was propelled, which was either air or tissue-mimicking phantoms. The concentration of gelatin powder in the tissue-mimicking phantoms was set at weight ratios (wt) of 5 wt% or 10 wt%. These weight ratios lead to gelatin samples with moduli of elasticity of approximately 5.3 and 17 kPa, respectively [7], resembling healthy liver tissue (<6 kPa) [16] and healthy muscle tissue (12–32 kPa) [17] or healthy prostate tissue (16 kPa) [18].

The dependent variables were  $d_n(C)$  and  $d_c(C)$ . The dependent variables and  $d_e(C)$  were used to compute  $\eta_c(C)$  (Eq. 11.2),  $\eta_p(C)$  (Eq. 11.3), and  $\eta_m(C)$  (Eq. 11.4).

$$\eta_c(C) = \frac{d_n(C) + d_c(C)}{d_e(C)} \cdot 100\% \quad (11.2)$$

$$\eta_p(C) = \frac{d_n(C)}{d_n(C) + d_c(C)} \cdot 100\% \quad (11.3)$$

$$\eta_m(C) = \eta_c(C) \cdot \eta_p(C) = \frac{d_n(C)}{d_e(C)} \cdot 100\% \quad (11.4)$$

### 11.3.4 Experimental procedure

Before each experiment run, the cart was manually translated over approximately 30 mm to ensure  $x_n(0) \approx 30$  mm, establishing sufficient contact between the needle surface and the substrate for the self-propelled motion. The initial manual insertion is required to enable the needle's self-propelled motion. After the initial manual insertion, the actuation system was turned on, allowing the needle segments to move within the substrate. The actuation system was turned off when the needle segments reached an insertion distance,  $x_n(C)$ , of 110 mm or when the actuation system ran for 60 seconds. Each experimental condition was repeated six times.

### 11.3.5 Results

The means and standard deviations of  $d_n(C)$  and  $d_c(C)$ , as well as those of  $\eta_c(C)$ ,  $\eta_p(C)$ , and  $\eta_m(C)$ , for each experimental condition are presented in Table 11.2 and Figure 11.8. In the air, the needle had already reached  $x_n(C) = 110$  mm after an average of 18 actuation cycles. Hence, the traveled distances and efficiencies for more than 15 actuation cycles are provided only for the tissue-mimicking phantoms, as indicated by the gray overlay in Figure 11.8.

The data in Table 11.2 show that the mean  $\eta_c(C)$  in 5-wt% gelatin remained approximately constant and comparable to the mean  $\eta_c(C)$  in air over the 20 actuation cycles. In contrast, the mean  $\eta_c(C)$  in 10-wt% gelatin decreased over the number of actuation cycles from  $100 \pm 6\%$

**Table 11.2. Results of the experiment**, showing the substrate through which the needle traveled, number of actuation cycles, traveled distance of the needle tip in the substrate, traveled distance of the cart, clamp efficiency, propulsion efficiency, and motion efficiency, with mean values and standard deviations.

Substrate	Number of actuation cycles, $(C)$	Traveled distance needle tip [mm], $d_n(C)$ (mean $\pm$ SD)	Traveled distance cart [mm], $d_c(C)$ (mean $\pm$ SD)	Clamp efficiency [%], $\eta_c(C)$ (mean $\pm$ SD)	Propulsion efficiency [%], $\eta_p(C)$ (mean $\pm$ SD)	Motion efficiency [%], $\eta_m(C)$ (mean $\pm$ SD)
Air	5	22 $\pm$ 2	2 $\pm$ 1	100 $\pm$ 6	93 $\pm$ 5	93 $\pm$ 8
	10	44 $\pm$ 2	2 $\pm$ 1	100 $\pm$ 3	96 $\pm$ 2	96 $\pm$ 4
	15	67 $\pm$ 2	2 $\pm$ 1	100 $\pm$ 1	98 $\pm$ 2	98 $\pm$ 2
5-wt% gelatin	5	13 $\pm$ 2	10 $\pm$ 2	95 $\pm$ 2	56 $\pm$ 8	53 $\pm$ 7
	10	29 $\pm$ 3	16 $\pm$ 3	98 $\pm$ 0	64 $\pm$ 7	62 $\pm$ 6
	15	47 $\pm$ 3	21 $\pm$ 4	98 $\pm$ 1	70 $\pm$ 5	68 $\pm$ 5
	20	66 $\pm$ 3	24 $\pm$ 4	98 $\pm$ 1	74 $\pm$ 5	72 $\pm$ 3
10-wt% gelatin	5	18 $\pm$ 1	6 $\pm$ 1	100 $\pm$ 6	77 $\pm$ 3	77 $\pm$ 5
	10	32 $\pm$ 3	9 $\pm$ 1	89 $\pm$ 8	77 $\pm$ 2	68 $\pm$ 6
	15	39 $\pm$ 5	13 $\pm$ 2	76 $\pm$ 9	75 $\pm$ 2	57 $\pm$ 7
	20	45 $\pm$ 7	16 $\pm$ 2	66 $\pm$ 9	73 $\pm$ 2	49 $\pm$ 7

over the first five actuation cycles to 66  $\pm$  9% over 20 actuation cycles.

The mean  $\eta_p(C)$  in air and 5-wt% gelatin increased with the number of actuation cycles, increasing from 93  $\pm$  5% and 56  $\pm$  8%, respectively, during the first five cycles, to 98  $\pm$  2% and 70  $\pm$  5% over 15 actuation cycles. In contrast, the mean  $\eta_p(C)$  in 10-wt% gelatin remained approximately constant in the 73-77% range.

From the mean  $\eta_m(C)$ , we can see that in air and in 5-wt% gelatin, the mean percentages increased over the number of actuation cycles from respectively 93  $\pm$  8% and 53  $\pm$  7% over the first five actuation cycles to 98  $\pm$  2% and 68  $\pm$  5% over 15 actuation cycles. However, in 10-wt% gelatin, the mean  $\eta_m(C)$  decreased from 77  $\pm$  5% over the first five actuation cycles to 57  $\pm$  7% over 15 actuation cycles.

## 11.4 Discussion

### 11.4.1 Main findings

In this study, we presented the design of a stationary actuation system that can advance a wasp-inspired self-propelled needle by clamping and advancing the parallel needle segments, resulting in a theoretically unlimited insertion length. However, achieving theoretically unlimited insertion length requires at least three parallel needle segments and a corresponding driving mechanism. Based on the pencil lead advance mechanism in a mechanical pencil that advances the pencil lead over a fixed increment when the pencil button is pressed, the ONCA advances the seven needle segments that comprise our needle one by one. The actuation

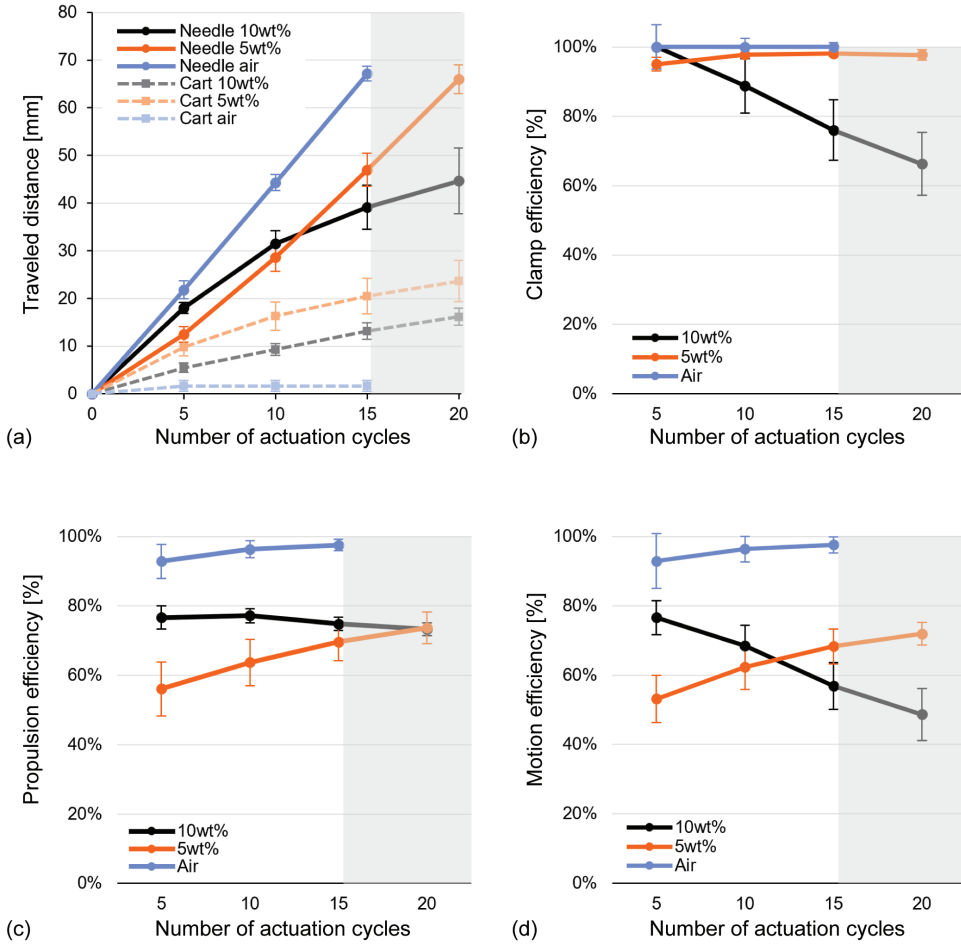


Figure 11.8. Experimental results of (a) the traveled distance for the needle tip in the substrate ( $d_n$ ) [mm] and the traveled distance of the cart ( $d_c$ ) [mm], (b) clamp efficiency ( $\eta_p$ ) [%], (c) propulsion efficiency ( $\eta_p$ ) [%], and (d) motion efficiency ( $\eta_m$ ) [%] over the number of actuation cycles ( $C$ ). The circles and solid lines are the mean values for the needle, the squares and dashed lines are the mean values for the cart, and the error bars are the standard deviation. The gray overlay indicates that the traveled distances and efficiencies for over 20 actuation cycles are provided only for the 5-wt% and 10-wt% gelatin-based tissue-mimicking phantom.

system enables the needle to propel itself through stationary tissue-mimicking phantoms by locking, advancing, releasing, and retracting the needle segment advance mechanisms while the actuation system maintains its stationary position.

In an ideal scenario,  $\eta_p(C) = 100\%$ , meaning that the needle will only self-propel and not push the substrate forward ( $d_c(C) = 0$  mm). When the advance mechanisms, in that case, operate at  $\eta_c(C) = 100\%$ , this leads to  $\eta_m(C) = 100\%$ . The results of this study suggest that for the needle operating in air, the advance mechanisms functioned at  $\eta_c(C) = 100\%$  and  $\eta_p(C)$

was nearly 100%. More specifically, the mean  $\eta_p(C)$  in air was not 100%, because of a slight movement of the cart, which was probably caused by the friction between the moving needle segments and the cart.

When  $\eta_p(C) < 100\%$ , while  $\eta_c(C) = 100\%$ ,  $d_n(C)$  is less than  $d_e(C)$ , as the cart is pushed forward and also travels a certain distance ( $d_c(C) > 0$  mm). This situation is shown in the results for the needle in 5-wt% gelatin, where the mean  $d_n(C)$  was lower than that in air, although, in both 5-wt% gelatin and in air, the mean  $\eta_c(C)$  percentages were nearly 100%. This can be attributed to slipping of the stationary needle segments in the substrate. Nevertheless, over the number of actuation cycles, the mean  $\eta_p(C)$  in 5-wt% gelatin increased; thus, the slip in the substrate decreased. This is likely due to the friction force on the needle segments, which increased with increasing insertion depth, whereas the cutting force remained constant [19].

When the advance mechanisms operate at  $\eta_c(C) < 100\%$ , they fail to move the needle segments forward by  $d_e(C)$  due to slipping within the clamps, which likely occurs during the dark green advance phase (i.e., when the collet is closed around the needle segment). This may be due to the cutting and frictional forces acting on the tip and the shaft of the advancing needle segment, which may be greater than the clamping force of the advance mechanism. This effect is shown in the experimental results for the needle in 10-wt% gelatin, where the measured mean  $\eta_c(C)$  decreased with increasing number of actuation cycles, likely due to the increasing friction force on the needle segment with increasing insertion distance, which in turn increased the required clamping force.

To compare the performance of our needle with that of state-of-the-art wasp-inspired needles, we used  $d_n(C)$  and  $d_c(C)$  to compute the slip ratio ( $s_{\text{ratio}}(C)$ ) of our needle in the substrate (Eq. 11.5).  $s_{\text{ratio}}(C)$  quantifies the slip between the stationary needle segments and the substrate, which limits the self-propulsion capabilities of the needle.

$$s_{\text{ratio}}(C) = 1 - \frac{d_n(C)}{d_n(C) + d_c(C)} \quad (11.5)$$

The mean  $s_{\text{ratio}}(20)$  values of our needle of  $0.26 \pm 0.045$  and  $0.27 \pm 0.019$  in 5-wt% and 10-wt% gelatin, respectively, are greater than the slip ratios reported in previous research on wasp-inspired needles of  $0.18 \pm 0.011$  [14] and  $0.2$  [7] in 5-wt% gelatin, and  $0.19 \pm 0.007$  [14] and  $0.3$  [7] in 10-wt% gelatin. The differences in the slip ratios can be attributed to several factors. First, an actuation system using low-friction ball splines applies a small insertion push force onto the needle segments, which helps the advancing needle segment overcome the cutting and friction forces in the stationary tissue-mimicking phantom [14]. Consequently, this approach likely resulted in a lower slip ratio than our approach did. Second, Scali *et al.* [7] used fewer needle segments (six compared with seven) with smaller diameters (0.25 mm compared with 0.3 mm) than we did, leading to an overall smaller needle diameter than our needle (0.8 mm compared with 1.0 mm). A smaller needle diameter reduces forces at the tip of the needle, resulting in a lower slip ratio. Previous research has confirmed that the peak axial needle insertion force increases with increasing needle size [20].



### 11.4.2 Limitations

Among the seven parallel needle segments comprising our needle, the segment with the heat shrink tube (i.e., the bundling segment) exhibited a shorter traveled distance than the other segments did, resulting in a lower measured mean  $\eta_c(C)$  for the bundling segment. The resultant  $\eta_c(C)$  values of the bundling segment (mean  $\pm$  SD) over the total insertion distance were  $59 \pm 13\%$  and  $15 \pm 2\%$  in the 5-wt% and 10-wt% gelatin samples, respectively. The shorter traveled distance of the bundling segment is likely caused by the increased friction and cutting forces compared with those of the other segments. These forces may overcome the clamping force of the needle segment advance mechanism, leading to the bundling segment slipping within the advance mechanism and causing a decrease in  $\eta_c(C)$ . As the bundling segment lags behind the other needle segments, the other needle segments begin to protrude while they are no longer bundled at the tip. This protrusion allows the needle segments to diverge at their tips, which increases the force required to advance the bundling segment over the other needle segments. Consequently, the lag of the bundling segment worsens with increasing insertion distance, decreasing  $\eta_c(C)$  with increasing number of actuation cycles. To address this issue, future versions of the ONCA should incorporate an internal bundling mechanism that does not interfere with the needle's wasp-inspired self-propelled motion [11].

The design of the actuation system, particularly the needle segment advance mechanisms, constrains the needle segment diameter to 0.3 mm. This diameter constraint prohibits the integration of a needle or functional segment with a different diameter into the system. Consequently, a direct experimental comparison between the wasp-inspired segmented needle and a conventional needle using the ONCA is currently not possible. Nevertheless, a previous study has shown that a wasp-inspired self-propelled motion can reduce tissue motion and deformation as compared to needle insertion of a conventional needle [5]. In future *ex vivo* experiments using the ONCA, tissue damage can be evaluated through histological analysis, similar to the approach used by Gidde *et al.* [21, 22], to enable comparison with conventional needle insertion.

### 11.4.3 Recommendations and future research

In the experiments, we evaluated the ONCA's  $\eta_c(C)$ ,  $\eta_p(C)$ , and  $\eta_m(C)$ . Our results show that in air and 5-wt% gelatin, the mean  $\eta_c(C)$  was near 100%, whereas in 10-wt% gelatin, the mean  $\eta_c(C)$  was lower.  $\eta_c(C)$  is a characteristic of the pencil lead advance mechanism used and can be increased by increasing the clamping force of the advance mechanism. We performed force measurements using a force gauge to quantify the clamping and insertion forces exerted on the needle segments by the actuation system. During actuation, the measured peak insertion force applied by the actuation system to the needle ranged from 0.5 N to 0.8 N ( $0.7 \pm 0.1$  N, mean  $\pm$  standard deviation, number of repetitions = 6). The measured peak clamping force applied to the individual locked needle segments ranged from 0.7 N to 2.9 N ( $1.6 \pm 0.8$  N, mean  $\pm$  standard deviation, number of repetitions = 6). Increasing the clamping force can help resist forces acting on the needle segment within the stiffer substrate. The clamping force



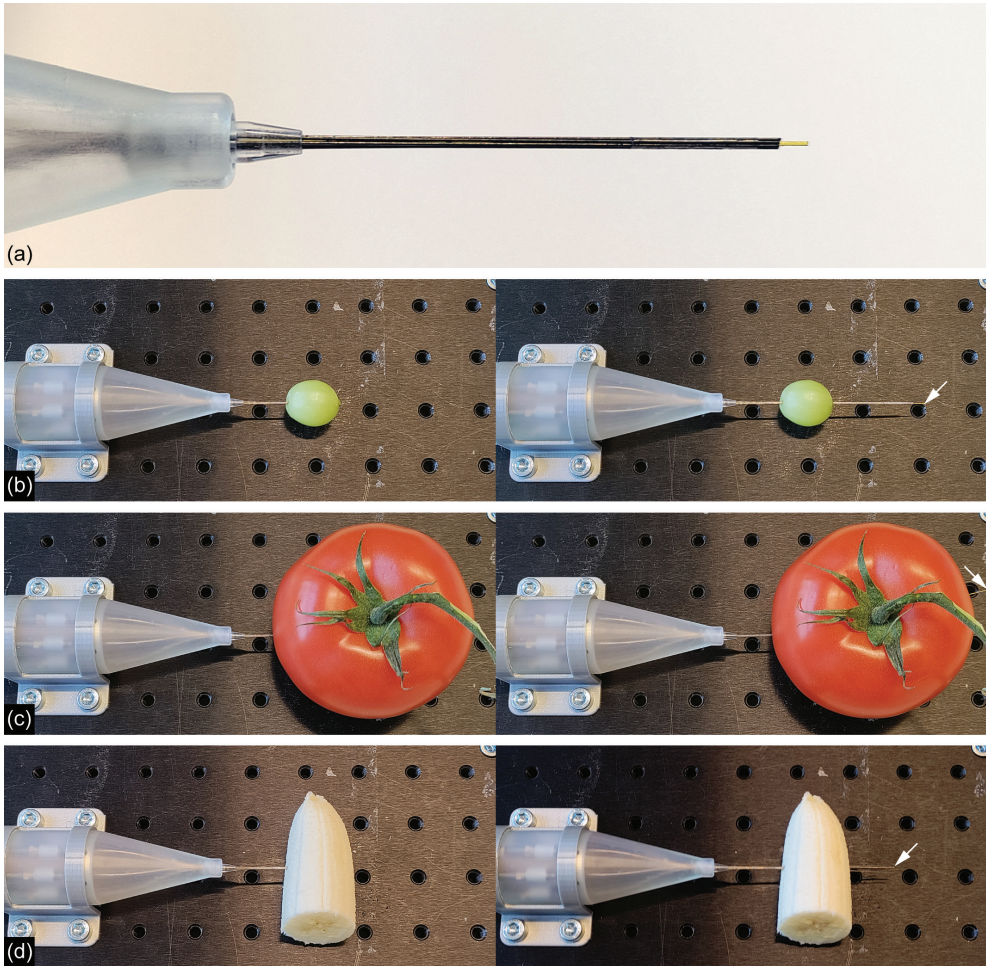
of the advance mechanism can be increased, for instance, by increasing the spring's stiffness or by reducing the taper angle of the sleeve. Nevertheless, the clamping force should not have such a high value that the needle segment deforms. This risk of deformation or damage increases when the needle segment is replaced with a functional segment, such as a hollow tube or optical fiber.

In order to enhance  $\eta_p(C)$  of the ONCA, the friction between the stationary needle segments and the surrounding substrate can be increased by incorporating a directional friction surface topography on the needle shaft, as shown by Frasson *et al.* [23], Parittotokkaporn *et al.* [24], and Fung-A-Jou *et al.* [25]. Another method to increase  $\eta_p(C)$  involves decreasing the friction and cutting forces on the advancing needle segment by, for example, sharpening the needle segment tips to lancet points [26, 27] or inserting the needle segment via a rotational or a vibratory insertion motion [28, 29]. Additionally,  $\eta_p(C)$  can be increased by preventing the separation of the needle segments by incorporating an internal bundling mechanism [11].

To clinically use the ONCA as a passageway to a target location deep within the body, a functional segment can replace the central needle segment, as illustrated in Figure 11.9a. The functional segment can be an optical fiber for prostate cancer focal laser ablation. Focal laser ablation is a prostate cancer treatment option that leads to homogeneous tissue necrosis caused by an optical fiber that is positioned near the tumor using a needle [30]. Figures 11.9b-d demonstrate the ability of the needle to successfully propel out of various fruits with differing stiffnesses and inhomogeneous anatomies, with the optical fiber serving as the central needle segment. In all cases, the needle was initially inserted halfway through the fruit and then actuated to propel itself further and out of the fruit. The self-propelled actuation enabled the needle to effectively penetrate all the fruits, including their relatively tough skins.

Besides functionalization, addressing sterilization and image guidance techniques is essential. The ONCA is a modular design that can be a so-called “reposable” device [31, 32], which integrates disposable and reusable modules. The needle segments can be easily removed from the actuation system when the advance mechanisms are in their released state. In our design, the needle that is in contact with the patient can be disposable, while the actuation system can be reusable. The main challenge that remains is the interconnection between the reusable actuation system and disposable needle segments. Research into a sterile barrier around the actuation system will be incorporated into future prototypes of our design. Furthermore, image guidance techniques can be used to visualize the trajectory of the needle inside the tissue, and implementing a feedback control system within the actuation system can enable real-time correction of this trajectory.

Our experiments were conducted in a controlled environment using tissue-mimicking phantoms made with gelatin powder. However, to assess the ONCA's functioning in a clinical setting, *ex vivo* or *in vivo* experiments are needed. These experiments will help us to investigate the effects of inhomogeneous tissue properties and the presence of different tissue layers (e.g., skin, fat, and muscle) with other mechanical properties (e.g., modulus of elasticity), as



**Figure 11.9. Demonstration of the needle with optical fiber as central needle segment propelling through fruits with varying stiffnesses.** (a) Close-up of the needle tip consisting of six stainless steel rods and a central optical fiber as the seventh central needle segment. The pictures on the left show the initial position of the needle halfway inside the fruit before actuation. The pictures on the right show the needle propelled through the fruit after actuation, where the arrow marks the needle tip. Fruits: (b) grape, (c) tomato, and (d) banana.

well as blood, on the self-propelling performance of the needle. During our evaluation, the needle was manually inserted 30 mm into the substrate before being actuated. In clinical practice, the needle must first puncture the skin of the patient before being able to self-propel through the tissue. The skin introduces a surface stiffness force due to the needle puncturing the skin until the moment of puncture [1]. To overcome this, manual insertion of the needle through the skin could be an option using an initial puncture needle, ensuring sufficient contact between the needle segments and the surrounding tissue for the self-propelled motion. The ability of a wasp-inspired self-propelled needle to advance in *ex vivo* porcine liver and

human prostate tissue has been exemplified successfully in previous studies [9, 10]. Moreover, Scali *et al.* [7] showed that a wasp-inspired self-propelled needle can advance in multilayered tissue-mimicking phantoms. These previous studies suggest that the ONCA can achieve a similar performance. To conclusively demonstrate this, evaluating the ONCA in *ex vivo* and *in vivo* experiments is necessary.

## 11.5 Conclusion

This study presents the design and evaluation of a stationary actuation system that can advance a needle through stationary tissue-mimicking phantoms. Based on the pencil lead advance mechanism in a mechanical pencil that advances the pencil lead at a fixed increment when the pencil button is pressed, our actuation system advances the seven needle segments that comprise our needle by locking, advancing, releasing, and retracting the advance mechanisms. This actuation system allows advancing a wasp-inspired self-propelled needle with a theoretically unlimited insertion length. Experimental evaluation revealed that the needle can self-propel in air, 5-wt% gelatin, and 10-wt% gelatin. The prototype's mean clamp efficiency in 5-wt% gelatin remained approximately constant and comparable to that of the needle in the air over the 20 actuation cycles. Meanwhile, in 10-wt% gelatin, the measured clamp efficiency decreased with increasing number of actuation cycles. In conclusion, the mechanical pencil-based actuation system is a step forward in developing self-propelled needles for targeting deep tissue structures.

## Supplementary material

The data underlying this study are available at doi: 10.4121/82c5b1b0-9135-4a97-85af-4931cca0c6d0.

## References

1. Okamura AM, Simone C, O'leary MD. Force modeling for needle insertion into soft tissue. *IEEE transactions on biomedical engineering*. 2004;51(10):1707-16. doi: 10.1109/TBME.2004.831542.
2. Sakes A, Dodou D, Breedveld P. Buckling prevention strategies in nature as inspiration for improving percutaneous instruments: a review. *Bioinspiration & biomimetics*. 2016;11(2):021001. doi: 10.1088/1748-3190/11/2/021001.
3. Abolhassani N, Patel RV, Ayazi F. Minimization of needle deflection in robot-assisted percutaneous therapy. *The international journal of medical Robotics and computer assisted surgery*. 2007;3(2):140-8. doi: 10.1002/rcs.136.
4. Frasson L, Ko S, Turner A, Parittotokkaporn T, Vincent JF, Rodriguez y Baena F. STING: a soft-tissue intervention and neurosurgical guide to access deep brain lesions through curved trajectories. *Proceedings of the Institution of Mechanical Engineers, Part H: Journal of Engineering in Medicine*. 2010;224(6):775-88. doi: 10.1243/09544119JEIM663.
5. Leibinger A, Oldfield MJ, Rodriguez y Baena F. Minimally disruptive needle insertion: a biologically inspired solution. *Interface focus*. 2016;6(3):20150107. doi: 10.1098/rsfs.2015.0107.
6. Scali M, Kreeft D, Breedveld P, Dodou D. Design and evaluation of a wasp-inspired steerable needle. *Proceedings of SPIE; Portland, Oregon, United States: International Society for Optics and*

Photonics; 2017. p. 1016207.

7. Scali M, Breedveld P, Dodou D. Experimental evaluation of a self-propelling bio-inspired needle in single-and multi-layered phantoms. *Scientific reports*. 2019;9(1):1-13. doi: 10.1038/s41598-019-56403-0.
8. Scali M, Pusch T, Breedveld P, Dodou D. Ovipositor-inspired steerable needle: design and preliminary experimental evaluation. *Bioinspiration & Biomimetics*. 2017;13(1):016006. doi: 10.1088/1748-3190/aa92b9.
9. Bloemberg J, Hoppener B, Coolen B, Sakes A, Breedveld P. Design and evaluation of a pneumatic actuation unit for a wasp-inspired self-propelled needle. *PLoS ONE*. 2024;19(7):e0306411. doi: 10.1371/journal.pone.0306411.
10. Bloemberg J, Trauzettel F, Coolen B, Dodou D, Breedveld P. Design and evaluation of an MRI-ready, self-propelled needle for prostate interventions. *PLoS ONE*. 2022;17(9):e0274063. doi: 10.1371/journal.pone.0274063.
11. Bloemberg J, van Wees S, Kortman VG, Sakes A. Design of a wasp-inspired biopsy needle capable of self-propulsion and friction-based tissue transport. *Frontiers in Bioengineering and Biotechnology*. 2025;12:1497221. doi: 10.3389/fbioe.2024.1497221
12. Ng KW, Goh JQ, Foo SL, Ting PH, Lee TK, Esuvaranathan K, et al. Needle deflection studies for optimal insertion modeling. *International Journal of Bioscience, Biochemistry and Bioinformatics*. 2013;3(6):570. doi: 10.7763/IJBBS.2013.V3.278.
13. Parittotokkaporn T, Frasson L, Schneider A, Huq SE, Davies BL, Degenaar P, et al. Soft tissue traversal with zero net force: Feasibility study of a biologically inspired design based on reciprocal motion. 2008 IEEE International Conference on Robotics and Biomimetics; 2009: IEEE. doi: 10.1109/ROBIO.2009.4912983.
14. Bloemberg J, Fung-A-Jou Z, Breedveld P, Sakes A. Design and evaluation of a ball spline wasp-inspired needle. *Frontiers in Bioengineering and Biotechnology*. 2024;12:1468605. doi: 10.3389/fbioe.2024.1468605.
15. Cerkvenik U, Van de Straat B, Gussekloo SW, Van Leeuwen JL. Mechanisms of ovipositor insertion and steering of a parasitic wasp. *Proceedings of the National Academy of Sciences*. 2017;114(37):E7822-E31. doi: 10.1073/pnas.1706162114.
16. Mueller S, Sandrin L. Liver stiffness: a novel parameter for the diagnosis of liver disease. *Hepatic medicine: evidence and research*. 2010;49-67. doi: 10.2147/HMER.S7394.
17. Kot BCW, Zhang ZJ, Lee AWC, Leung VYF, Fu SN. Elastic modulus of muscle and tendon with shear wave ultrasound elastography: variations with different technical settings. *PLoS ONE*. 2012. doi: 10.1371/journal.pone.0044348.
18. Zhang M, Nigwekar P, Castaneda B, Hoyt K, Joseph JV, di Sant'Agnese A, et al. Quantitative characterization of viscoelastic properties of human prostate correlated with histology. *Ultrasound in medicine & biology*. 2008;34(7):1033-42. doi: 10.1016/j.ultrasmedbio.2007.11.024.
19. Hing JT, Brooks AD, Desai JP. Reality-based needle insertion simulation for haptic feedback in prostate brachytherapy. *IEEE International Conference on Robotics and Automation (ICRA)*; 2006: IEEE. doi: 10.1109/ROBOT.2006.1641779.
20. van Gerwen DJ, Dankelman J, van den Dobbelsteen JJ. Needle-tissue interaction forces—A survey of experimental data. *Medical engineering & physics*. 2012;34(6):665-80. doi: 10.1016/j.medengphys.2012.04.007.
21. Gidde STR, Acharya SR, Kandel S, Pleshko N, Hutapea P. Assessment of tissue damage from mosquito-inspired surgical needle. *Minimally Invasive Therapy & Allied Technologies*. 2022;31(7):1112-21. doi: 10.1080/13645706.2022.2051718.
22. Gidde STR, Islam S, Kim A, Hutapea P. Experimental study of mosquito-inspired needle to minimize insertion force and tissue deformation. *Proceedings of the Institution of Mechanical Engineers, Part H: Journal of Engineering in Medicine*. 2023;237(1):113-23. doi: 10.1177/09544119221137133.
23. Frasson L, Parittotokkaporn T, Schneider A, Davies B, Vincent J, Huq S, et al. Biologically

- inspired microtexturing: Investigation into the surface topography of next-generation neurosurgical probes. 30th Annual International Conference of the IEEE Engineering in Medicine and Biology Society: IEEE; 2008. p. 5611-4.
24. Parittotokkaporn T, Frasson L, Schneider A, Davies B, Degenaar P, y Baena FR. Insertion experiments of a biologically inspired microtextured and multi-part probe based on reciprocal motion. Annual International Conference of the IEEE Engineering in Medicine and Biology; 2010: IEEE. doi: 10.1109/IEMBS.2010.5627410.
  25. Fung-A-Jou Z, Bloembergen J, Breedveld P. Bioinspired medical needles: a review of the scientific literature. *Bioinspiration & Biomimetics*. 2023. doi: 10.1088/1748-3190/acd905.
  26. Wang Y, Tai BL, Chen RK, Shih AJ. The needle with lancet point: geometry for needle tip grinding and tissue insertion force. *Journal of Manufacturing Science and Engineering*. 2013;135(4):041010. doi: 10.1115/1.4023718.
  27. Wang Y, Mei D. Five-plane lancet needle design for soft PVC phantom tissue cutting. *Bio-Design and Manufacturing*. 2018;1:195-202. doi: 10.1007/s42242-018-0022-1.
  28. Lin C-L, Huang Y-A. Simultaneously reducing cutting force and tissue damage in needle insertion with rotation. *IEEE Transactions on Biomedical Engineering*. 2020;67(11):3195-202. doi: 10.1109/TBME.2020.2979463.
  29. Barnett AC, Wolkowicz K, Moore JZ. Vibrating needle cutting force. *International Manufacturing Science and Engineering Conference*; 2014: American Society of Mechanical Engineers. doi: 10.1115/MSEC2014-4049.
  30. Oto A, Sethi I, Karczmar G, McNichols R, Ivancevic MK, Stadler WM, et al. MR imaging-guided focal laser ablation for prostate cancer: phase I trial. *Radiology*. 2013;267(3):932-40. doi: 10.1148/radiol.13121652.
  31. Malchesky PS, Chamberlain VC, Scott-Conner C, Salis B, Wallace C. Reprocessing of reusable medical devices. *ASAIO journal*. 1995;41(2):146-51.
  32. Abreu EL, Haire DM, Malchesky PS, Wolf-Bloom DF, Cornhill JF. Development of a program model to evaluate the potential for reuse of single-use medical devices: results of a pilot test study. *Biomedical instrumentation & technology*. 2002;36(6):389-404. doi: 10.2345/0899-8205(2002)36[389%3ADO-APMT]2.0.CO%3B2.

# 12

## Discussion





## 12.1 Findings of this thesis

TransPerineal Laser Ablation (TPLA) is a localized prostate cancer treatment that relies on needle control. For TPLA applications, parasitic wasp-inspired needles are particularly interesting due to their abilities to self-propel, transport, and steer, thus enabling trajectory adjustments. The aim of this thesis was to present and evaluate new wasp-inspired needle designs developed to enhance needle trajectory control for TPLA treatment. In order to achieve this goal, we have developed two wasp-inspired needles and five actuation systems. Our main findings can be summarized in the following research contributions:

In **Chapter 2**, we investigated the main challenges associated with needle positioning during therapeutic interventions for prostate cancer. These challenges include (1) access restrictions to the prostate gland caused by the pubic arch, known as Pubic Arch Interference (PAI), and (2) needle positioning errors. Current clinical guidelines addressing PAI and needle positioning errors are ambiguous, and compliance in the clinical setting varies across institutions. This lack of clarity complicates the differentiation between acceptable and unacceptable levels of PAI and needle positioning errors. We discovered that needle positioning errors are generally considered unacceptable when they exceed 2-4 mm for off-axis errors and 2-15 mm for longitudinal errors. For measuring PAI, various methods are reported, including assessing the overlap distance from the inner surface of the pubic arch to the border of the prostate. PAI is considered unacceptable at overlap distances of 4-10 mm in the lithotomy position and 10-11 mm in the supine position of the patient.

Given that novel needles can improve trajectory control, **Chapter 3** provided an overview of the state-of-the-art in bioinspired needle designs. Designing medical needles using bioinspiration is a relatively new field, with the first article on the topic published in 2002 [1]. Bioinspiration for needle design was initially mainly limited to the parasitic wasp and the mosquito. However, to date, a variety of over 25 biological species has been investigated. We classified existing bioinspired needle designs based on their needle-tissue interaction and propulsion strategies. Most needle designs use friction-reduction strategies and are inserted using a free-hand technique.

To identify future directions of the technologies applied by the instruments for localized cancer treatment, **Chapter 4** gave a comprehensive overview of the patent literature on minimally- and non-invasive focal therapy instruments to treat localized cancer. We developed a classification based on the treatment target (cancer cell or network of cancer cells), treatment purpose (destroy the cancerous structure or disable its function), and treatment means (energy, matter, or a combination of both). Most instruments in the patent literature apply a mechanism that destroys the cell structure using energy or combined energy and matter, or disables the cell function using energy.

Female parasitic wasps use their ovipositors to transport and deposit eggs into hosts. In order to reach the host in solid substrates such as wood without buckling the ovipositor, these wasps can self-propel their ovipositors. This is achieved by relying on the friction

force between the ovipositor's parallel valves and the surrounding substrate. In the scientific literature, it is hypothesized that parasitic wasps use a similar friction-based principle to transport eggs through their ovipositors, relying on the friction force between the egg and the valves. In **Chapter 5**, these wasp-inspired transport and self-propulsion capabilities were, for the first time, integrated into a *Transport Needle* design. The resulting needle consists of six parallel needle segments interconnected by an internal ring, which passes through slots along the length of the needle segments. The needle prototype, constructed from nitinol rods and internal stainless steel rings, measures 3 mm in outer diameter and 1 mm in inner diameter. The evaluation demonstrated successful friction-based self-propulsion and transport of tissue-mimicking phantoms. The self-propelling motion and the lateral compressive forces applied by the tissue on the needle segments resulted in the needle moving forward with a zero net push force on the needle, making it less prone to buckling as it propagated through the tissue-mimicking phantom.

In addition to self-propulsion and transport, the wasp can curve and steer its ovipositor to reach the desired target location. In the scientific literature, it is hypothesized that steering is achieved through asymmetry at the tip and pretension in the ovipositor's valves. In **Chapter 6**, we investigated how to apply these steering mechanisms in a multi-segmented self-propelled needle called the *Prebent Ovipositor Needle*. In order to avoid separation of the needle segments, we developed a new interlocking mechanism consisting of an external hexagonal ring and six outer needle segments with an indent arranged in a circle around a central needle segment. The result is a sub-millimeter needle containing a central needle segment with a bevel-shaped prebent tip. We developed an actuation system consisting of six electric linear actuators that drive the six outer needle segments in the required wasp-inspired motion sequence. In an experimental evaluation in tissue-mimicking phantoms with a stiffness similar to healthy liver tissue ( $\sim 5$  kPa), we demonstrated that the *Prebent Ovipositor Needle* self-propelled in forward and steering motions. The needle steered successfully with a mean radius of curvature of 44 mm and was able to change its steering direction during insertion.

For the application of wasp-inspired needles in TPLA treatment, it is essential to ensure compatibility with the used image guidance technology, specifically Magnetic Resonance Imaging (MRI). In order to enable MR guidance, the needle must be actuated using a technology that does not incorporate metallic, magnetic, or conductive materials. Consequently, two MRI-compatible actuation systems were developed and evaluated in an MR environment. In **Chapter 7**, we presented the *Ovipositor MRI Needle*, which comprises a click-pen-inspired manual actuation system for a self-propelled needle. The manual actuation system solely consists of MR-safe 3D-printed parts, and the needle consists of six parallel 0.25-mm diameter Nitinol rods bundled using a heat shrink tube, resulting in a needle with an outer diameter of 0.84 mm. The evaluation within a preclinical 7-Tesla MRI system resulted in the first wasp-inspired needle shown to achieve successful self-propulsion through *ex vivo* human prostate tissue. The needle was visible in the MR images and self-propelled through the tissue with a

slip ratio of 0.82-0.96, indicating less effective propulsion than demonstrated by the *Prebent Ovipositor Needle* (Chapter 6), which can be explained by the higher stiffness of the prostate tissue as compared to the liver-mimicking phantom.

In **Chapter 8**, we enhanced the *Ovipositor MRI Needle* by integrating a steering system into the manual actuation system and accommodating an optical fiber for TPLA applications. To allow for steering, the housing of the handle can be rotated relative to the cone that converges the needle segments, similar to a 2-degrees-of-freedom joystick. Rotating the housing pushes and pulls the needle segments into and out of the cone, thereby shifting the needle segments in a controlled manner, resulting in a discrete bevel-shaped tip. We demonstrated that the needle prototype was able to self-propel and steer with a maximum deflection-to-insertion ratio of -0.088 in tissue-mimicking phantoms with a stiffness similar to prostate tissue (~17 kPa). This shows that a discrete bevel-shaped tip is less effective for steering than a prebent bevel-shaped tip, as used in the *Prebent Ovipositor Needle* (Chapter 6).

**Chapter 9** introduced the *Pneumatic Ovipositor Needle*, which is composed of a pneumatic actuation system and a self-propelled needle, enabling urologists to operate the needle under MR guidance without the need for manual actuation within the confined space of the MRI bore. The pneumatic actuation system consists of MR-safe 3D-printed resin parts and off-the-shelf plastic screws and uses pressurized air and a control system to actuate the needle segments. The needle consists of six parallel 0.25-mm diameter Nitinol rods bundled using a heat shrink tube, resulting in a needle with an outer diameter of 0.84 mm. We demonstrated that the prototype was able to self-propel through *ex vivo* porcine liver tissue under MR guidance with a slip ratio of 0.88, similar to the *Ovipositor MRI Needle* in human prostate tissue (Chapter 7).

In addition to ensuring MRI compatibility, it is essential for TPLA applications that the needle can extend to the required length to reach the prostate. Current prototypes of wasp-inspired needles in the scientific literature were designed as needle holders, with the actuation system directly coupled to the needle. As a result, inserting the needle into the tissue requires moving the tissue or the entire actuation system. In the confined space of the MRI bore, the needle must be able to self-propel inside the patient while the actuation system should remain in place. Therefore, we explored two design strategies to extend the needle to its required length, decoupling the needle and the actuation system.

**Chapter 10** presented the *Splinositor*, which uses a low-friction ball-spline mechanism that sequentially moves the needle segments in their self-propelled sequence while telescopically extending them from the actuation system. In this design, the low mass of the moving components of the needle and its connection to the actuation system via a ball spline introduces a small friction force, generating a small net push force on the needle that facilitates propulsion into tissue while still preventing buckling. We demonstrated that the needle prototype self-propelled with mean slip ratios of 0.18, 0.19, and 0.35 in tissue-mimicking phantoms with a stiffness similar to healthy liver tissue (~5 kPa), healthy prostate tissue (~17 kPa), and

cancerous prostate tissue ( $\sim 31$  kPa), respectively. This indicates that the small net push force reduces the slip ratio, thereby enhancing the efficiency of needle advancement.

While the insertion distance of the Splinositor is limited to 100 mm by the length of the ball spline, **Chapter 11** introduced a universal actuation system with a theoretically unlimited insertion length, named *Ovipositor Needle Clamp Actuator (ONCA)*. The ONCA is based on the lead advance mechanism in mechanical pencils. In the ONCA, this mechanism was used to advance needle segments at fixed increments. The actuation system moves the seven needle segments that comprise our needle by clamping, advancing, and releasing them sequentially. We demonstrated that the ONCA self-propelled needle segments through tissue-mimicking phantoms with a stiffness similar to healthy liver tissue ( $\sim 5$  kPa) and healthy prostate tissue ( $\sim 17$  kPa) with mean motion efficiencies of 68% and 57%, respectively. These motion efficiencies are similar to those achieved with the *Prebent Ovipositor Needle* but lower than those achieved with the *Splinositor*, which can be explained by slipping of the needle segments within the advance mechanisms during insertion through stiff tissues. After replacing one of the needle segments with a TPLA fiber, the ONCA was still able to self-propel them through fruits with differing stiffnesses and inhomogeneous anatomies.

## 12.2 Needle and actuation: Toward clinical implementation

### *Technical challenges*

This thesis presents various designs of wasp-inspired needles and actuation systems. Developing a complete needle design for clinical use requires the integration of a wasp-inspired needle with an actuation system optimized for clinical practice. Our findings from Chapters 6 and 8 indicate that the ideal wasp-inspired needle design for TPLA can self-propel and steer while allowing for optical fiber placement in the needle's central lumen.

The thesis presented two omnidirectional steering methods inspired by prevalent hypotheses on how the wasp achieves ovipositor steering: asymmetry (i.e., a bevel-shaped tip) and prebending. In terms of both self-propulsion and steering efficiencies, the combination of a bevel-shaped tip and prebending was the preferred steering method, enabling lateral steering of up to 20 mm over an insertion distance of approximately 40 mm (Chapter 6), demonstrating its potential to overcome excessive PAI and correct needle positioning errors during TPLA treatment. However, to critically evaluate the needle's trajectory control performance in a clinical setting, future research should focus on assessing the endpoint error [2]. Additionally, this needle design does not allow for steering when a straight optical fiber replaces the prebent central needle segment.

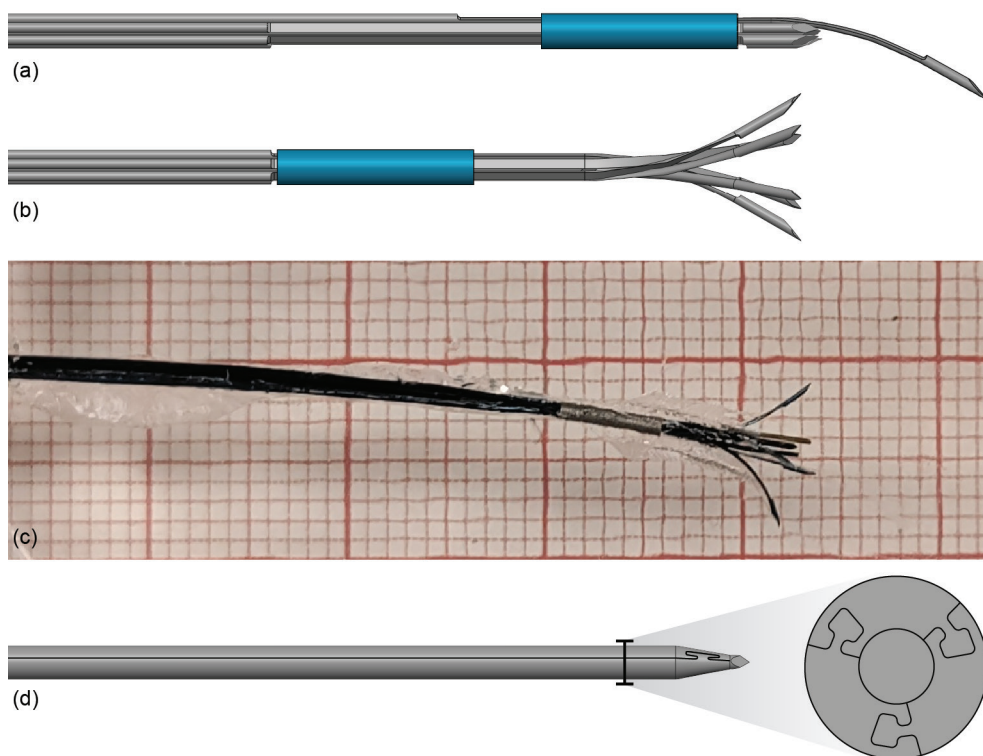
To solve this challenge, the needle can be steered to the target location using the prebent central needle segment, which is then removed and replaced by an optical fiber. This approach is similar to using a guidewire to guide a catheter through a vascular network. However, the current external interlocking ring fails to maintain the hexagonal arrangement of the outer needle segments once the central needle segment is removed. In contrast, the internal

interlocking ring described in Chapter 5 does preserve this hexagonal arrangement, but its miniaturization is challenging with the current manufacturing technique.

An alternative approach would be to incorporate the prebending in the outer needle segments instead of the central needle segment, similar to the prebending method exhibited in a wasp ovipositor [3]. When the ovipositor valves are aligned with their tips, the pretensions in the valves counteract each other, resulting in a straight structure. In contrast, when a valve protrudes, its tip curves inward toward the other valves. In order to incorporate prebending in our outer needle segments, we can prebend the outer needle segments inward at the tip (Figure 12.1a). When the needle segments are aligned tip-to-tip and the interlocking ring is positioned at the tip, the prebendings within the needle segments, in principle, counterbalance each other, thereby ensuring a straight needle. When an outer needle segment protrudes, its tip curves inward for a curved trajectory.

A disadvantage of prebent outer needle segments combined with a stiff interlocking ring is that the prebends increase the friction force with the interlocking ring as the needle segments advance. This increases the axial force on the advancing needle segments and causes buckling of their shafts. Moreover, it can cause an unstable situation in which the interlocking ring moves into the backward position, causing unwanted twisting of the needle segment tips, making them all point outward, as we observed in explorative tests (Figures 12.1b,c). This creates so much resistance with the tissue that it causes unwanted tissue damage and effectively blocks the forward motion. The explorative tests were conducted using the control and actuation system described in Chapter 6 and were performed in tissue-mimicking phantoms with a stiffness similar to healthy prostate tissue ( $\sim 17$  kPa).

In order to overcome these interlocking challenges, the stiff interlocking ring can be replaced by a solution closer to biology: an interlocking structure along the entire length of the needle all the way to its tip (Figure 12.1d), inspired by the olistheter mechanism of the wasp's ovipositor. Creating complex shapes with a high aspect ratio, similar to the olistheter mechanism, is challenging. Recently, a thermal fiber drawing process has emerged to produce complex high-aspect-ratio geometries out of polycarbonate and polypropylene [4-6]. The process begins with a macroscopic preform created using 3D printing or conventional machining [7], typically several centimeters in diameter and tens of centimeters in length. Subsequently, the preform is softened at elevated temperatures and drawn into a thin fiber with a diameter down to 1.3 millimeters while preserving the complex cross-sectional geometry throughout the length of the fiber [4-6]. The thermal fiber drawing process has successfully been applied in catheter prototypes for medical applications such as cardiovascular interventions and neurosurgery [4-6]. However, the current prototypes are unsuitable for deep percutaneous interventions such as TPLA because the thermally drawn polymer fibers cannot cut through the tissue and are prone to buckling, bending, and breaking under axial loads resulting from the tissue. In the near future, we expect that advancements in manufacturing techniques will enable the development of interlocking mechanisms made from materials that are both suffi-



**Figure 12.1. Illustration of technical challenges in applying ovipositor-inspired steering.** (a) Needle with prebent outer needle segments (gray), containing indentations and bundled with an interlocking ring (blue) at the needle tip. When the needle segments are aligned at their tips, the prebendings in the segments counteract each other, resulting in a straight needle. When a needle segment protrudes, its tip curves inward, enabling steering. (b) Unwanted unstable twisting and outward bending of the needle segment tips when the interlocking ring is pushed backward by the substrate during the self-propelled motion, illustrated by a photo (c) of an explorative test with this steering system in a tissue-mimicking phantom ( $\sim 17$  kPa). (d) Needle with olistheter-inspired interlocking structure. The needle consists of four segments (gray): three outer needle segments with an olistheter-like interlocking structure and a central cylindrical needle segment that can be removed for tissue transport and replaced by a functional element, such as an optical fiber. Drawback of this needle design is that it is hard to manufacture at a very small scale.

ciently drawable to very thin dimensions and stiff enough to cut through and be advanced into tissue without buckling. To further optimize the wasp-inspired needle designs, future research should focus on developing needle-tissue interaction models that incorporate cutting forces at the needle tip, buckling behavior, insertion velocity, and the effects of Coulomb, viscoelastic, and adhesive friction. These models should be calibrated using experimental *in vivo* data to ensure predictive accuracy.

Our insights from the designs presented in Chapters 7-11 suggest that the ideal actuation system is compatible with MR guidance and facilitates universal actuation. In order to achieve MRI compatibility in the universal actuation system presented in Chapter 11, the components of the universal actuation system should be made MRI compatible. This would



involve manufacturing the lead advance mechanisms of the mechanical pencil and the other actuation system components from MR-safe materials, like those presented in Chapters 7-9, or paramagnetic metals such as titanium. Furthermore, the motor of the actuation system should be replaced with, for example, a pneumatic actuator.

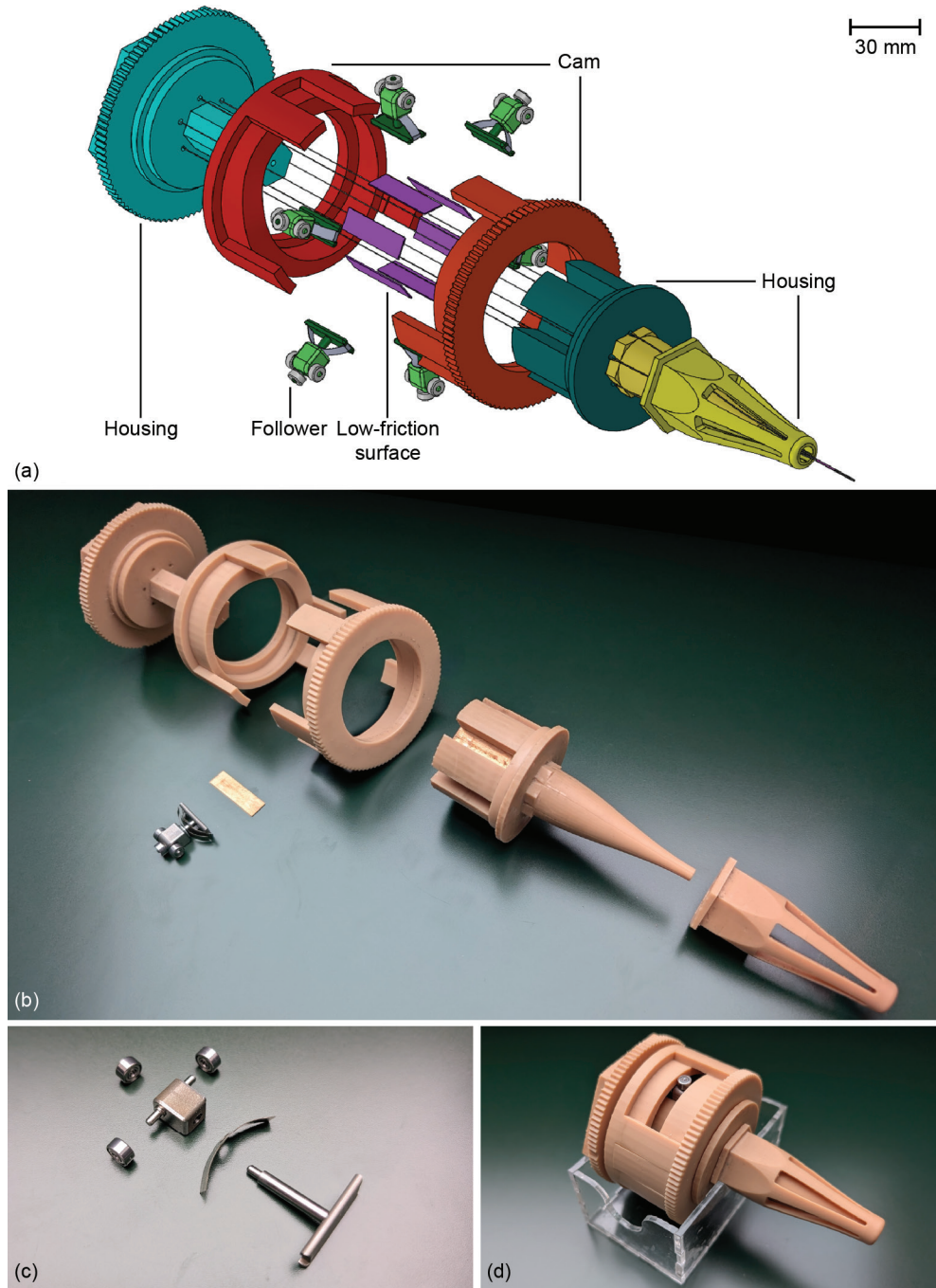
An alternative approach is to substitute the lead advance mechanisms with different universal advance mechanisms that are MRI compatible. In a side project of this research, van der Helm [8] developed a universal actuation system that does not rely on the lead advance mechanism of a mechanical pencil; instead, it uses a friction-based advance system (Figure 12.2). The system contains a cam mechanism that functions in two directions: (1) the cam path varies in radial direction to clamp the needle segments and (2) the cam path varies in axial direction to advance the needle segments. Clamping is performed by leaf-spring-driven cam followers, which apply a normal force to the needle segments, resulting in a friction force between the followers and the needle segments. When this friction force overcomes the friction force between the needle segment and the low-friction surface in the housing, the needle segment is successfully advanced. The actuation system prototype consists primarily of MR-safe 3D-printed resin parts, with only the follower components and the low-friction surfaces made from MR-unsafe materials. These components can be replaced with substitutes constructed from MR-safe materials or paramagnetic metals such as titanium. Evaluation of the prototype showed self-propulsion through tissue-mimicking phantoms with a stiffness similar to healthy liver tissue (~5 kPa) and healthy prostate tissue (~17 kPa) with a high slip ratio as compared to the universal actuation system presented in Chapter 11, which can be explained by slipping of the needle segments within the friction-based advance mechanisms during insertion through tissues.

#### *Toward clinical implementation*

Technology Readiness Levels (TRLs) ranging from 1 to 9 are a method to assess the maturity of new technologies, with TRL 1 representing a technology of which the basic principles are observed and reported and TRL 9 representing a commercially ready technology that has been proven to work in an operational environment [9]. The needles and actuation systems developed in this thesis are at TRL 3, which in the medical field involves *ex vivo* evaluation but does not yet include *in vivo* testing [10]. TRL 3 is, therefore, exempt from regulatory approval, such as compliance with the Medical Device Regulation 2017/745 (MDR) in Europe. However, when moving toward *in vivo* evaluation (TRL 4), some crucial aspects, such as user-system interaction and sterilization techniques, should be addressed (MDR: Chapter I, 2.1, Annex VIII) [11].

First, the actuation system should have an ergonomic design that facilitates needle actuation and steering within the confined space of the MRI bore. Important design challenges remain regarding the interaction between the clinician positioned outside the MRI bore and the actuation system inside it. Consequently, the needles will likely require manual teleoperation (i.e., remote control by the clinician from outside the MRI bore), similar to the MR-guided





**Figure 12.2. Friction-based universal actuation system [8].** (a) Exploded view. Prototype photos: (a) exploded view (the complete prototype contains six followers and six low-friction surfaces, one for each of the six needle segments), (c) detailed exploded view of one of the followers, and (d) assembly view.

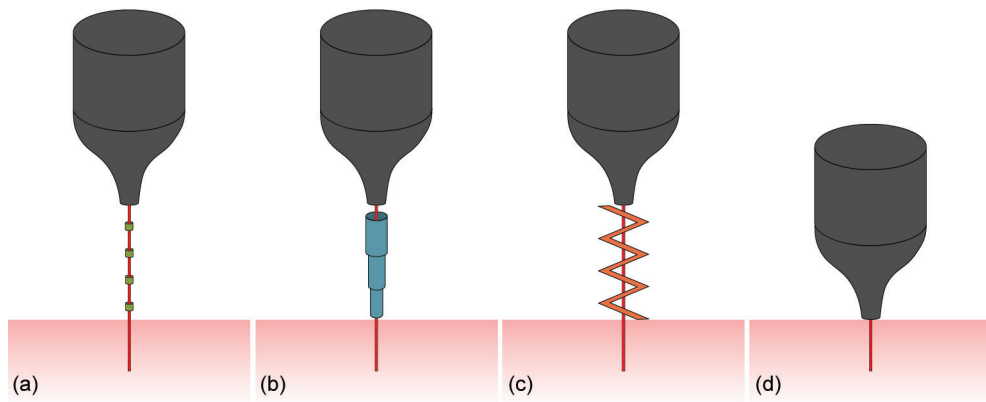
teleoperated needles presented by de Vries *et al.* [12], Franco *et al.* [13], and Krieger *et al.* [14].

Additionally, addressing sterilization techniques is essential. Common sterilization methods are heat or steam sterilization (i.e., autoclave), chemical sterilization, and gamma irradiation [15]. All sterilization methods impose challenges in ensuring the functionality of the components post-sterilization [16, 17]. A solution to consider is developing a modular wasp-inspired needle that integrates disposable and reusable modules, a so-called “reposable” device [18, 19]. The disposable modules only need to be used once and, therefore, only require one sterilization cycle, which can be incorporated into the production process. In this case, the needle that is in contact with the patient can be disposable, while the actuation system can be reusable. The main challenge that remains is the interconnection between the reusable and disposable modules. A sterile cover can create a sterile barrier around the actuation system. Detachable needle clamps can transfer the actuation motion from the actuation system to the disposable needle through the sterile cover. These clamps can be similar to the needle guides presented by Stoianovici *et al.* [20] and can be either disposable and delivered with the disposable needle or reusable and meet the requirements for cleaning, disinfection, and sterilization of medical devices, such as having smooth and flat surfaces and featuring easily accessible lumens for brushing and rinsing [21]. This reposable design approach can enhance safety and efficiency in clinical settings while promoting sustainability by minimizing waste associated with single-use devices.

### 12.3 Nature and engineering: A future outlook

The design of the ovipositor in parasitic wasps presents inherent challenges due to its high aspect ratio, which results in a low critical buckling load, making it susceptible to buckling during the oviposition process. In order to address this challenge, parasitic wasps have developed several solutions, such as the self-propelled motion inside the substrate and reducing the effective length or increasing the diameter and second moment of area of their ovipositors outside the substrate.

In this thesis, we have explored the application of wasp-inspired mechanisms for self-propulsion, transport, and steering. To prevent buckling of the individual needle segments outside the substrate, several strategies have been implemented in our designs, including: (1) supporting the needle with additional structures outside the substrate, such as rings around the needle prototype presented by Scali *et al.* [22] (Figure 12.3a), telescopic tubes in the *Prebent Ovipositor Needle* (Figure 12.3b) and a Miura-origami structure in the *Splinositor* (Figure 12.3c), and (2) disconnecting the actuation system from the needle in the *ONCA* (Figure 12.3d), allowing placement of the actuation system directly against the skin, thereby reducing the needle length outside the substrate to 0 mm. Nevertheless, the potential application of wasp-inspired mechanisms to prevent buckling outside a substrate remains an area for future exploration. Given the wide range of hosts and host-associated substrates, different parasitic wasp species have evolved unique anatomical modifications to support their

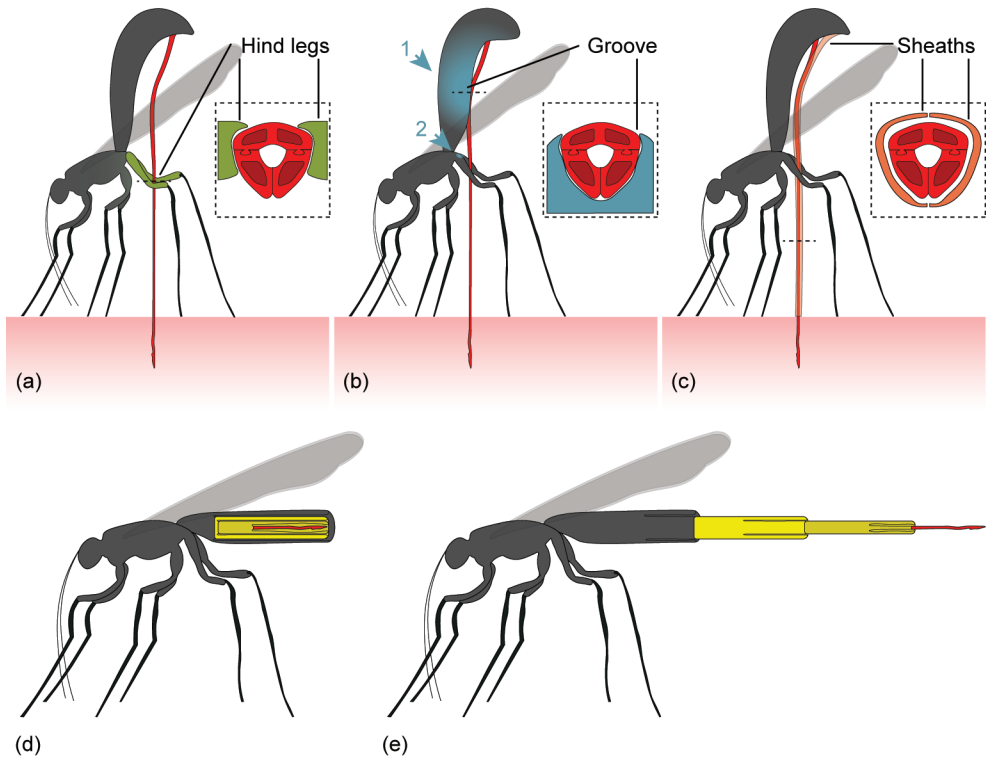


**Figure 12.3.** Schematic representation of applied strategies to prevent buckling of individual needle segments (red) between the actuation system (gray) and the substrate (pink). The needle is supported by (a) rings (green), (b) telescopic tubes (blue), or (c) a Miura-origami structure (orange). (d) The needle is directly extended from the actuation system, which allows the actuation system to be positioned directly against the substrate, reducing the effective length of the needle outside the substrate to 0 mm.

ovipositor. These modifications include supporting the ovipositor with additional structures outside the substrate, such as their hind legs (Figure 12.4a) [23], a groove inside the abdomen (Figure 12.4b) [24, 25], or specialized sheaths (Figure 12.4c) [3, 26–28], and telescopically extending the ovipositor from their abdomen (Figures 12.4d,e) [29].

Specialized sheaths (Figure 12.4c) are, for example, seen in *Diachasmimorpha longicaudata* Ashmead (Hymenoptera: Braconidae) and are flexible appendages that originate at the ventral side of the wasp's abdomen similar to the ovipositor [26]. These sheaths are not inserted into the substrate the ovipositor is probing in, but gradually peel away over their entire length in an arc-like shape with increased insertion [3]. Moreover, the tips of the sheaths are hypothesized to help anchor the tip of the ovipositor during the initial phase of the oviposition process [26].

The telescopically extendable ovipositor (Figure 12.4d,e), possessed by the *Scelio fulgidus* Crawford (Hymenoptera: Scelionidae) and related genera, is positioned inside the abdomen at rest, whereas for the oviposition process, the ovipositor telescopically extends from the abdomen by an increase in hydrostatic pressure caused by muscle contraction [29]. The distance that the ovipositor can be extended is limited by the number of telescopic sections that can be stored within the abdomen in the retracted state and successfully extended by the hydrostatic extension system. The number of telescopic sections in the Scelinoid genus *Scelio* is two or three, resulting in an extension ratio of two to four [29]. An in-depth understanding of how different parasitic wasp species reduce the functional length or increase the diameter and second moment of area of their ovipositors may serve as a source of inspiration for enhancing the actuation system of our wasp-inspired needles, as well as other bioinspired engineering designs.



**Figure 12.4.** Schematic representation of parasitic wasp anatomy modifications to reduce the effective length or increase the diameter and second moment of area of the ovipositor (red) outside the substrate (pink) to increase the penetration force that the wasp can apply without buckling the ovipositor. (a) The ovipositor (red) is held between the hind legs (green) in the wasp species *Apocrypta westwoodi* Grandi (Hymenoptera: Pteromalidae) [23]. (b) The ovipositor (red) lays in a groove (blue) on the ventral side of the abdomen (arrow 1) in the wasp species *Megarhyssa atrata* Fabricius (Hymenoptera: Ichneumonidae) [24] or in a groove between the bases of the hind legs (arrow 2) in the wasp species *Pristaulacus comptipennis* Enderlein (Hymenoptera: Aulacidae) [25]. (c) The ovipositor (red) is enveloped by sheaths (orange) that originate from the ventral side of the abdomen in wasp species such as the *Diachasmimorpha longicaudata* Ashmead (Hymenoptera: Braconidae) [28] and *Watshamiella* Wiebes (Hymenoptera: Pteromalidae) [27]. The sheaths detach and arch away during insertion when a considerable length of the ovipositor has been inserted into the substrate. (d) The ovipositor (red) shown in its retracted state is connected using telescopic tubes (yellow) to the abdomen in the wasp species *Scelio fulgidus* Crawford (Hymenoptera: Scelionidae) and related genera [29]. (e) The ovipositor in the extended state results in an extension ratio of  $\pm 3.5$  [29].

“Bioinspired design” is a well-known design approach that draws inspiration from the forms, functions, processes, and strategies found in biological organisms, which have developed themselves over millions of years of evolution, to solve engineering challenges [30, 31]. In its most effective form, bioinspired design is not based on simple imitation of biological organisms but, instead, on uncovering fundamental mechanisms and working principles underlying desirable traits of biological organisms and applying these mechanisms and working principles in new engineering designs [32]. Such designs adopt some of the features of the biological model after suitable adaptation to fulfill the different contexts of biology and engineering [32]. There are many examples of bioinspired designs, including Velcro, which

was invented by Georges de Mestral, who was inspired by the burdocks caught in his dog's fur [33], self-cleaning paints inspired by the lotus leaf [34], and the wasp-inspired needle designs presented in this thesis. Biology offers infinite resources of forms, functions, processes, and strategies, and it is up to us to understand and translate these to solve future engineering challenges.

So far, we have explored bioinspired design as a one-sided approach, where biology is a source of inspiration for engineering challenges. However, what if we shift our focus to the reciprocal interaction between engineering and biology by exploring the concept of “engineering-inspired biology”? Engineering-inspired biology refers to applying engineering principles to influence evolutionary processes or validate existing biological mechanisms [35]. For example, engineering-inspired biology is exemplified in synthetic biology, which uses engineering concepts to modify genetic structures and create organisms with specific traits (e.g., Clustered Regularly Interspaced Short Palindromic Repeats (CRISPR) technology) [36]. However, this form of engineering-inspired biology requires human intervention to apply engineering concepts. This raises philosophical questions: To what extent can human engineering practices be considered part of biological evolution? What if human intervention were unnecessary? What if biology could directly draw inspiration from engineering? Imagine a scenario in which parasitic wasps autonomously evolve by drawing inspiration from our designs to develop an ovipositor capable of being inserted over unlimited lengths, such as the ONCA (Chapter 11). The reciprocal interaction between biology and engineering opens a future full of shared ideas, where even biology might start taking notes from our designs.

## 12.4 Conclusions

This thesis demonstrates that wasp-inspired, self-propelled, and steerable needles contribute to a new generation of devices that enhance needle trajectory control, primarily for TPLA in prostate cancer treatment. To be able to actuate these needles in a clinical setting, we developed modular extension mechanisms and MRI-compatible actuation systems tested under MRI guidance. Although the focus was on TPLA, these needle designs have the potential to be applied across a broad range of percutaneous interventions in soft tissues. Steerable and self-propelled needles offer physicians greater accessibility and controllability of the needle trajectory and its final position in the patient's body, leading to improved outcomes and reduced risks of adverse effects. The needles could be used for ablation procedures or other focal therapies and minimally invasive procedures in difficult-to-reach soft tissues, such as the liver, pancreas, lungs, kidneys, and brain [37, 38]. Furthermore, steering and self-propulsion capabilities can improve the sampling accuracy in biopsy procedures, reducing procedure time and increasing diagnostic accuracy. Simple modifications to the material, shape (e.g., solid rod or hollow tube), diameter, length, and number of needle segments allow the needles to be adapted to a wide range of clinical applications, thereby broadening their impact in percutaneous interventions.

## References

1. Oka K, Aoyagi S, Arai Y, Isono Y, Hashiguchi G, Fujita H. Fabrication of a micro needle for a trace blood test. *Sensors and Actuators A: Physical*. 2002;97:478-85. doi: 10.1016/S0924-4247(01)00872-X.
2. de Vries M, Sikorski J, Misra S, van den Dobbelsteen JJ. Axially rigid steerable needle with compliant active tip control. *PLoS ONE*. 2021;16(12):e0261089. doi: 10.1371/journal.pone.0261089.
3. Cerkvenik U, Van de Straat B, Gussekloo SW, Van Leeuwen JL. Mechanisms of ovipositor insertion and steering of a parasitic wasp. *Proceedings of the National Academy of Sciences*. 2017;114(37):E7822-E31. doi: 10.1073/pnas.1706162114.
4. Abdelaziz ME, Tian L, Lottner T, Reiss S, Heidt T, Maier A, et al. Thermally Drawn Polymeric Catheters for MR-Guided Cardiovascular Intervention. *Advanced Science*. 2024;11(45):2407704. doi: 10.1002/advs.202407704.
5. Aktas A, Demircali AA, Secoli R, Temelkuran B, Rodriguez y Baena F. Towards a procedure-optimised steerable catheter for deep-seated neurosurgery. *Biomedicine*. 2023;11(7):2008. doi: 10.3390/biomedicine11072008.
6. Demircali AA, Zhao J, Aktas A, Abdelaziz ME, Temelkuran B. Fabrication of Fibers with Complex Features Using Thermal Drawing of 3D-Printed Preforms. *arXiv preprint arXiv:250200741*. 2025.
7. van der Elst L, Faccini de Lima C, Gokce Kurtoglu M, Koraganji VN, Zheng M, Gumennik A. 3D printing in fiber-device technology. *Advanced Fiber Materials*. 2021;3:59-75. doi: 10.1007/s42765-020-00056-6.
8. van der Helm M. FRON: A Friction-based Ovipositor-inspired Needle actuation system. Master thesis: Delft University of Technology; 2025.
9. Mankins JC. Technology readiness levels. White Paper. 1995.
10. Seva RR, Tan ALS, Tejero LMS, Salvacion MLDS. Multi-dimensional readiness assessment of medical devices. *Theoretical Issues in Ergonomics Science*. 2023;24(2):189-205. doi: 10.1080/1463922X.2022.2064934.
11. Medical Device Regulation (EU) 2017/745 of the European Parliament and of the Council, (2017).
12. de Vries M, Wijntjes M, Sikorski J, Moreira P, van de Berg NJ, van den Dobbelsteen J, Misra S. MR-guided HDR prostate brachytherapy with teleoperated steerable needles. *Journal of robotic surgery*. 2023;17(5):2461-9. doi: 10.1007/s11701-023-01676-x.
13. Franco E, Aurisicchio M, Ristic M. Design and control of 3-DOF needle positioner for MRI-guided laser ablation of liver tumours. *International Journal of Biomechanics and Biomedical Robotics*. 2015;3(3):145-58.
14. Krieger A, Susil RC, Ménard C, Coleman JA, Fichtinger G, Atalar E, Whitcomb LL. Design of a novel MRI compatible manipulator for image guided prostate interventions. *IEEE Transactions on Biomedical Engineering*. 2005;52(2):306-13. doi: 10.1109/TBME.2004.840497.
15. Rutala WA, Weber DJ. Guideline for disinfection and sterilization in healthcare facilities 2008. Update: June 2024: [Available from: <https://www.cdc.gov/infection-control/media/pdfs/guideline-disinfection-h.pdf>].
16. Harrell CR, Djonov V, Fellabaum C, Volarevic V. Risks of using sterilization by gamma radiation: the other side of the coin. *International journal of medical sciences*. 2018;15(3):274. doi: 10.7150/ijms.22644.
17. Massey LK. The effect of sterilization methods on plastics and elastomers: William Andrew; 2004.
18. Malchesky PS, Chamberlain VC, Scott-Conner C, Salis B, Wallace C. Reprocessing of reusable medical devices. *ASAIO journal*. 1995;41(2):146-51.
19. Abreu EL, Haire DM, Malchesky PS, Wolf-Bloom DE, Cornhill JE. Development of a program model to evaluate the potential for reuse of single-use medical devices: results of a pilot test study. *Biomed-*



- ical instrumentation & technology. 2002;36(6):389-404. doi: 10.2345/0899-8205(2002)36[389%3ADO-APMT]2.0.CO;3B2.
20. Stoianovici D, Jun C, Lim S, Li P, Petrisor D, Fricke S, et al. Multi-imager compatible, MR safe, remote center of motion needle-guide robot. *IEEE Transactions on Biomedical Engineering*. 2017;65(1):165-77. doi: 10.1109/TBME.2017.2697766.
  21. Horeman T, Schilder F, Aguirre M, Kerkhoffs G, Tuijthof G. Design and preliminary evaluation of a stiff steerable cutter for arthroscopic procedures. *Journal of Medical Devices*. 2015;9(4):044503. doi: 10.1115/1.4030506.
  22. Scali M, Pusch T, Breedveld P, Dodou D. Ovipositor-inspired steerable needle: design and preliminary experimental evaluation. *Bioinspiration & Biomimetics*. 2017;13(1):016006. doi: 10.1088/1748-3190/aa92b9.
  23. Kundanati L, Gundiah N. Biomechanics of substrate boring by fig wasps. *Journal of Experimental Biology*. 2014;217(11):1946-54. doi: 10.1242/jeb.098228.
  24. Heatwole H, Davis DM, Wenner AM. The Behaviour of *Megarhyssa*, a Genus of Parasitic Hymenopterans (Ichneumonidae: Ephialtinae) 1. *Zeitschrift für Tierpsychologie*. 1962;19(6):652-64. doi: 10.1111/j.1439-0310.1962.tb00796.x.
  25. Vilhelmsen L, Turrissi GF. Per arborem ad astra: Morphological adaptations to exploiting the woody habitat in the early evolution of Hymenoptera. *Arthropod structure & development*. 2011;40(1):2-20. doi: 10.1016/j.asd.2010.10.001.
  26. Vilhelmsen L. Flexible ovipositor sheaths in parasitoid Hymenoptera (Insecta). *Arthropod Structure & Development*. 2003;32(2-3):277-87. doi: 10.1016/S1467-8039(03)00045-8.
  27. Compton SG, Van Noort S, McLeish M, Deeble M, Stone V. Sneaky African fig wasps that oviposit through holes drilled by other species. *African Natural History*. 2009;5:9-15.
  28. van Meer NM, Cerkvenik U, Schlepütz CM, van Leeuwen JL, Gussekloo SW. The ovipositor actuation mechanism of a parasitic wasp and its functional implications. *Journal of anatomy*. 2020;237(4):689-703. doi: 10.1111/joa.13216.
  29. Field S, Austin A. Anatomy and mechanics of the telescopic ovipositor system of *Scelio Latreille* (Hymenoptera: Scelionidae) and related genera. *International Journal of Insect Morphology and Embryology*. 1994;23(2):135-58. doi: 10.1016/0020-7322(94)90007-8.
  30. Breedveld P, Herder J, Tomiyama T, editors. Teaching creativity in mechanical design. Diversity and Unity Proceedings of IASDR2011, the 4th World Conference on Design Research; 2011.
  31. Glier MW, Tsenn J, Linsey JS, McAdams DA, editors. Methods for supporting bioinspired design. ASME International Mechanical Engineering Congress and Exposition; 2011.
  32. Perera AS, Coppens M-O. Re-designing materials for biomedical applications: from biomimicry to nature-inspired chemical engineering. *Philosophical Transactions of the Royal Society A*. 2019;377(2138):20180268. doi: 10.1098/rsta.2018.0268.
  33. Budde R. The story of Velcro. *Physics World*. 1995;8(1):22.
  34. Zhang M, Feng S, Wang L, Zheng Y. Lotus effect in wetting and self-cleaning. *Biotribology*. 2016;5:31-43. doi: 10.1016/j.biotri.2015.08.002.
  35. Braun J-M, Manoonpong P, Xiong X. Biology-Inspired Engineering and Engineering-Inspired Biology. *Frontiers Media SA*; 2020. p. 614683.
  36. Lander ES. The heroes of CRISPR. *Cell*. 2016;164(1):18-28. doi: 10.1016/j.cell.2015.12.041.
  37. De Jong TL, Van De Berg NJ, Tas L, Moelker A, Dankelman J, Van Den Dobbelsteen JJ. Needle placement errors: do we need steerable needles in interventional radiology? *Medical Devices: Evidence and Research*. 2018;259-65. doi: 10.2147/MDER.S160444.
  38. Secoli R, Matheson E, Pinzi M, Galvan S, Donder A, Watts T, et al. Modular robotic platform for precision neurosurgery with a bio-inspired needle: System overview and first in-vivo deployment. *PLoS ONE*. 2022;17(10):e0275686. doi: 10.1371/journal.pone.0275686.







# Acknowledgements

In my experience, science is a collective effort and a PhD project is impossible to undertake alone. Therefore, it feels a little odd that a PhD thesis is individual. I would like to thank everyone who has contributed, supported, encouraged, and in a way been part of this journey.

First of all, I would like to thank my promotors and supervisors, Paul and Aimée. **Paul**, thank you for convincing me to start this PhD project, even though it wasn't my plan when I started my master thesis. Thank you for your guidance and enthusiasm for the project, for the creative brainstorm sessions, for your brilliance in medical device design, and for the constant source of new ideas. **Aimée**, thank you for your support and listening ear when I needed it, your punctual feedback, your genuine concern for my well-being, and your mentorship in science communication.

To the members of my thesis committee, **Prof. dr. J. Dankelman**, **Prof. dr. ir. J.L. Herder**, **Prof. dr. ir. F.T. Muijres**, **Dr. S. Graziosi**, and **Dr. D.M. de Bruin**, thank you for taking the time to read my dissertation, providing insightful feedback on my work, for participating in the defense, and for being part of this important moment. I would also like to take this opportunity to thank other inspiring professors that I have collaborated with for some of the works published in this thesis: **Prof. Dr. J.J. van den Dobbelsteen**, **Dr. D. Dodou**, and **Dr. T. de Reijke**.

I want to thank all the partners and fellow researchers from the national **MEDPHOT consortium** for the nice collaborations and inspiring talks during the consortium meetings and for the fun we had during the dinners.

During my PhD, I had the privilege to collaborate with multiple researchers from the Amsterdam UMC. Thank you **Paul**, **Mitra**, **Luigi**, **Rob**, **Katelijne**, **Martijn**, **Theo**, and **Jorg** for the fruitful Thursday afternoon discussions and for providing useful insights into the clinical aspects of the project. A big thanks to **Bram** for your help performing the MRI experiments, without which some of the projects in this thesis would never have succeeded.

The prototypes I have presented in this thesis could not work without the help of my colleagues at DEMO. With a particularly warm special thanks to **David**, **Remi**, **Mario**, and **Danny**, this thesis wouldn't have been possible without your practical advice, steady hands, and manufacturing and coding skills. I always enjoyed working with you. When I visited you, there was always room for a joke and a good conversation about how to bring the designs of this thesis to life.

During the last graduate school course I attended, I had to make a mindmap of all the things I love about my PhD. The first thing I wrote down, where the people. I feel lucky that I did my PhD in such a great department as BMEchE. That is why I want to start by thanking my amazing office mates. First up, **Vera**: Thank for always being there for me, right from the start of our Bachelor's in Industrial Design Engineering all the way to the end of my PhD. It

was great to be in the BITE group and the office together with such a good friend. I would never have enjoyed my time here as much without you. I admire your creativity, optimism and always making time for a good coffee and an even better chat. I will miss collaborating with you on design projects. Whether for IDE, ME, or student supervision during our PhD, it was always more fun when we could work together. **Merle**, I loved being in the early office club together with you, you are truly the best holiday planner I know, always finding the most amazing and delicious spots. **Esther**, thank you for always offering a listening ear for both personal and professional topics. Job hunting is a lot more enjoyable when we do it together! **Kirsten**, you have been such a great mentor in the office, your advice was always spot-on and helpful. **Mostafa**, you are a great friend, always ready for a deep conversation, taking group pictures (yes, they really are great memories), and reminding all of us to be proud of our accomplishments. **Karin**, thank you for your advice and the great distractions, they were always fun and I would not have want to miss them! **Fabian**, as my MSc thesis supervisor, you were my first point of contact from the office, thanks for our conversations and for sharing your 3D printing wisdom. **Giacomo**, you are the definition of a social butterfly who always makes people smile. **Indra**, your creativity gives color to our office. **Nynke**, I enjoyed opening the dancefloor at the BME conference with you and all the after-lunch walks. **Dina**, you are a true chef and are always looking out for everyone in our office. **Haymi**, I enjoyed our conversations and learning new words from you. **Jean**, you are great supporter and storyteller.

It is almost impossible to walk around the lunch spot or coffee machines on the first and third floor corridors without talking to someone. I want to thank all my past and present colleagues who made the BMechE department such a great place to work in: **Abdulrahman**, **Abhijeet**, **Anton**, **Arjo**, **Bart**, **Chun-Feng**, **Christoph**, **Daniel**, **Dirk**, **Edwin**, **Eline**, **Emanuele**, **Federica**, **Gabri**, **Gavin**, **Gerwin**, **Giannis**, **Giovanni**, **Hassan**, **Ioannis**, **Jan**, **Jan-Willem**, **Jenna**, **Jiahui**, **Jie**, **Jinlai**, **Jon**, **Jonathan**, **Jorik**, **Jose**, **Judith**, **Jules**, **Karien**, **Kasra**, **Keyu**, **Khashayar**, **Kim**, **Koen**, **Lennart**, **Lorenzo**, **Ludovica**, **Marin**, **Maria**, **Martijn**, **Mauricio**, **Morteza**, **Nasim**, **Nazli**, **Nick**, **Nianlei**, **Pier**, **Pritesh**, **Rick**, **Roos**, **Rogier**, **Sabrina**, **Sander**, **Sara**, **Shibo**, **Suzanne**, **Tamas**, **Teddy**, **Thomas**, **Tim**, **Vahid**, and everyone I may be forgetting. **Anneke**, I enjoyed our lunch conversations and our Norway-in-a-nutshell trip after the conference in Oslo. **Suzanne** and **Katerina**, it was great organizing the Pirates of the CariBME event together with you, you were among the first ones I got to know from the BMechE department when I started my PhD at home during covid times. And **Ebi**, you saved the day (and our stomachs) during the boat outing by being the barbecue chef! **Nianlei**, **Mohammed**, and **Bob**, thank you for adopting me in the basement crew during my noisy experiments. The coffee moments, lunches, and badminton workshops provided by badminton-pro Nianlei were a welcome break from the work. **Benjamin**, thank you for kicking off the after-lunch walking club together with your co-leader **Nynke**. **Marit**, **Monika**, **Vera**, **Niko**, thanks for the great modern dance classes we attended together. **Niko** and **Momo**, the two of you are the best pushers of the X ticket hours. Thanks for always making the sport

---

classes more fun together. **Robin**, thank you for always being there, since the introduction week of our Bachelor's, to the ME bridging program, the Master's, and the PhD. Working with you and Vera in a project group always felt like the dream team. Thanks for all the tea breaks, talks, lunches, cakes, and dinners together. I look forward to the day I get to call you Professor Robin!

Thanks to all the staff in this department that make things run smoothly. Thanks to **Angelique, Amanda, and Marjolijn** for always being there for support and a chat.

I also want to thank **José, Iris, Robin, Bob, Vishal, Pieter, Paulina, Suriya, Kate, Mariano, Yujie, Annabel, Alice, Karien, Jenna, Nasim, Steven, Martin, Aswin, Gilles, Nick, Anna, Andrea, Sietske, Hugo, Francesco**, and all the other past and present members of the (3)ME PhD Council for all the wonderful meetings and events. You helped me better understand what doing a PhD in our faculty implies, what challenges there still are, and how we can tackle them. Together with **Paul** and **Mascha**, you are doing an incredible job for our colleagues. **Mascha**, thank you for your encouragement and trust in the PhD Council, for your commitment to the PhD community, and for all the nice conversations.

I also had the opportunity to work together with a lot of great bachelor and master students. **Güven, Bruce, Sjoerd, Zola, Martijn, Suzet, David, Suzanne, Jakov, Jules, David, Kasper, Boris, Mats, Iris, Benjamin, and Robbert**: Thanks for the trust you gave me to supervise your thesis or internship. I really enjoyed our scientific discussions and I appreciate your hard work. I learned a lot from you, both personally and professionally.

And of course, a big thank you for my family and friends. Thank you for showing interest in my work, offering a listening ear, and for being the life part of my work-life balance. **Akshat** and **Sonali**, thank you for the great conversations and dinners together. **Loulou**, bedankt voor het samen lachen, sporten en de fijne gesprekken. **Anouk, Sharda, Evianne** en **Tess**, bedankt voor het daar zijn sinds de start van mijn tijd in Delft, de gesprekken, wandelingen, herinneringen en natuurlijk het creatieve advies. **Celine**, bedankt dat je er altijd bent om te praten over persoonlijke en professionele onderwerpen. Ik ben trots op hoe je nu je eigen PhD traject aflegt! **Erik, Lisanne, Nikki, Mart, Mats**, bedankt voor onze lange vriendschap en de gezelligheid. **Leonie** en **Ires**, bedankt dat jullie er altijd voor mij zijn en dat het altijd voelt als thuiskomen en 'gewoon zoals altijd' als we samen zijn. **Mama, papa, Anna** en **Toon**, bedankt voor de interesse die jullie tonen in mijn project en voor het proeflezen. Jullie zijn allemaal op jullie eigen manier een voorbeeld en een rots in de branding geweest met wie ik mijn stress en blijdschap en alles daar tussenin kon delen. Heel erg bedankt daarvoor. Ten slotte wil ik graag **Luuk** bedanken. Bedankt dat je er altijd voor me bent, voor de discussies, voor je interesse in mijn project, voor het helpen herinneren om pauzes te nemen, voor het luisteren en voor het vieren van elke kleine en grote mijlpaal.



# Curriculum Vitae

**Jette Bloemberg**, born 21-11-1995 in Winterswijk, The Netherlands

## Work Experience

2021-2025	<i>PhD researcher</i> Biomechanical Engineering department, TU Delft, Delft, The Netherlands
2017-2025	<i>Industrial and graphic designer</i> Jette Bloemberg, Schiedam, The Netherlands
2022-2024	<i>PhD council member</i> Faculty of Mechanical Engineering, TU Delft, Delft, The Netherlands
2019	<i>Research intern</i> The BioRobotics Institute, Sant'Anna, Pisa, Italy

## Education

2018-2021	<i>Master of Science in Mechanical Engineering</i> (cum laude) Faculty of Mechanical Engineering, TU Delft, The Netherlands
2017-2018	<i>Bridging Program</i> Faculty of Mechanical Engineering, TU Delft, The Netherlands
2014-2017	<i>Bachelor of Science in Industrial Design Engineering</i> (cum laude, honours) Faculty of Industrial Design Engineering, TU Delft, The Netherlands
2008-2014	<i>Voorbereidend Wetenschappelijk Onderwijs (VWO)</i> Assink Lyceum, Haaksbergen, The Netherlands

## Awards

2021	<i>Young Talent Pitch Award</i> , Precisiebeurs
2022	<i>Young Investigator Award</i> , 33rd Conference of International Society for Medical Innovation and Technology (iSMIT)



# List of Publications

## Publications as part of this thesis

- **Bloemberg J.**, Jager D.J., Breedveld P., Sakes A. (2025). Steering strategies for wasp inspired self propelled needles. *Scientific Reports*, 15:31018. doi: 10.1038/s41598-025-15031-7.
- **Bloemberg J.**, van der Wel M., Sakes A., Breedveld P. (2025). Design and evaluation of a mechanical pencil-based actuator for a wasp-inspired needle. *PLoS ONE*, 20(7): e0326584. doi: 10.1371/journal.pone.0326584.
- **Bloemberg J.\***, van Wees S.\*, Kortman V.G., Sakes A. (2025). Design of a wasp-inspired biopsy needle capable of self-propulsion and friction-based tissue transport. *Frontiers in Bioengineering and Biotechnology*, 12:1497221. doi: 10.3389/fbioe.2024.1497221 (\*these authors have contributed equally to this work).
- **Bloemberg J.**, Sakes A., Breedveld P. (2024). Wasp-inspired steerable needle for transperineal focal laser ablation. *Proceedings of the 16th Hamlyn Symposium on Medical Robotics held in London, United Kingdom, 25-28 June 2024*.
- **Bloemberg J.\***, Fung-A-Jou Z.\*, Breedveld P., Sakes A. (2024) Design and evaluation of a ball spline wasp-inspired needle. *Frontiers in Bioengineering and Biotechnology*, 12:1468605. doi: 10.3389/fbioe.2024.1468605 (\*these authors have contributed equally to this work).
- **Bloemberg J.\***, de Vries M.\*, van Riel L., de Reijke T., Sakes A., Breedveld P., van den Dobbelsteen J. (2024). Therapeutic prostate cancer interventions: a systematic review on pubic arch interference and needle positioning errors. *Expert Reviews on Medical Devices*, 21(7):625-641. doi: 10.1080/17434440.2024.2374761 (\*these authors have contributed equally to this work).
- **Bloemberg J.**, Hoppener B., Coolen B., Sakes A., Breedveld P. (2024). Design and evaluation of a pneumatic actuation unit for a wasp-inspired self-propelled needle. *PLoS ONE*, 19(7):e0306411. doi: 10.1371/journal.pone.0306411.
- Fung-A-Jou Z., **Bloemberg J.**, Breedveld P. (2023). Bioinspired medical needles: a review of the scientific literature. *Bioinspiration & Biomimetics*, 18(4):041002. doi: 10.1088/1748-3190/acd905.
- **Bloemberg J.**, Trauzettel F., Coolen B., Dodou D., Breedveld P. (2022). Design and evaluation of an MRI-ready, self-propelled needle for prostate interventions. *PLoS ONE*, 17(9):e0274063. doi: 10.1371/journal.pone.0274063.
- **Bloemberg J.**, van Riel L., Dodou D., Breedveld P. (2021). Focal therapy for localized cancer: a patent review. *Expert Review of Medical Devices*, 18(8):751-769. doi: 10.1080/17434440.2021.1943360.

## Other publications

- Hinnen K. A., Kuitens I., Den Butter R., Arnods B., De Reijke T., Van Kesteren Z., **Bloemberg J.**, Breedveld P., Pieters B. (2023). PO78: Improving HDR prostate

- brachytherapy catheter fixation with a self-fixating double helix screw thread design. *Brachytherapy*, 22(5):S107-S108. doi: 10.1016/j.brachy.2023.06.179.
- Kater E.P. de, Sakes A., **Bloemberg J.**, Jager D.J., Breedveld P. (2021). Design of a flexible wasp-inspired tissue transport mechanism. *Frontiers in Bioengineering and Biotechnology*, 9:782037. doi: 10.3389/fbioe.2021.782037.
  - **Bloemberg J.**, Stefanini C., Romano D. (2021). The role of insects in medical engineering and bionics: towards entomomedical engineering. *IEEE Transactions on Medical Robotics and Bionics*, 3(4):909-918. doi: 10.1109/TMRB.2021.3101693.
  - Romano D., **Bloemberg J.**, McGloughlin T., Dario P., Stefanini C. (2020). Insect ultra-structures as effective physical-based bactericidal surfaces. *IEEE Transactions on Medical Robotics and Bionics*, 2(3):425-436. doi: 10.1109/TMRB.2020.3000584.
  - Romano D., **Bloemberg J.**, Tannous M., Stefanini C. (2020). Impact of aging and cognitive mechanisms on high-speed motor activation patterns: evidence from an orthoptera-robot interaction. *IEEE Transactions on Medical Robotics and Bionics*, 2(2):292-296. doi: 10.1109/TMRB.2020.2977003.

### Conference contributions

- **Bloemberg J.**, Sakes A., Breedveld P. (2025). Wasp-inspired needles for prostate cancer treatment – Ball spline actuation. Proc. 10th Dutch Conference of Bio-Medical Engineering, Jan. 30-31, Egmond aan Zee, The Netherlands. (oral presentation)
- **Bloemberg J.**, Sakes A., Breedveld P. (2024). Wasp-inspired steerable needle for transperineal laser ablation. Hamlyn Symposium on Medical Robotics, June 25-28, London, United Kingdom. (oral presentation)
- **Bloemberg J.**, Sakes A., Breedveld P. (2023). Stinging success: drawing parallels between wasps and needles. 35th Nederlandse Entomologische Vereniging (NEV) Entomology Day, 15 December, Ede, The Netherlands. (oral presentation)
- **Bloemberg J.**, Trauzettel F., Dodou D., Sakes A., Breedveld P. (2023). Wasp-inspired needle: How can wasps improve prostate cancer treatment? 5th Dutch Society of Precision Engineering (DSPE) conference on precision mechatronics, Sep. 26-27, Sint Michielgestel, The Netherlands. (poster)
- **Bloemberg J.**, Trauzettel F., Dodou D., Breedveld P. (2023). Design and ex-vivo evaluation of a wasp-inspired needle for prostate cancer treatment. Proc. 9th Dutch Conference of Bio-Medical Engineering, Jan. 26-27, Egmond aan Zee, The Netherlands. (oral presentation)
- **Bloemberg J.**, Kortman V. G., Sakes A. (2022). Development of a soft suction cup for tissue stabilization during percutaneous prostate interventions. 44th International Engineering in Medicine and Biology Conference (EMBC), July 11-15, Glasgow, Scotland. (poster)
- **Bloemberg J.**, Sakes A., Breedveld P. (2022). A wasp-inspired, self-propelling steerable needle for MRI-guided procedures. 33rd Conference of International Society for Medical Innovation and Technology (iSMIT), May 30-31, Oslo, Norway. (oral presentation)

# PhD Portfolio

## Education

- **Integrated mechanical systems**, exam, Bachelor Werktuigbouwkunde, TU Delft, 2021-2024
- **Bio-inspired design**, lectures and assignments, Master Mechanical Engineering, TU Delft, 2021-2024
- **Lecture: ‘Finding biological information,’** Master Mechanical Engineering, TU Delft, 2023
- **General introduction to biomedical engineering**, assignments, Minor Biomedical Engineering, TU Delft, 2023
- **Fundamentals in biomedical engineering**, assignments, Master Biomedical Engineering, TU Delft, 2023

## Organization and Outreach

- **Soft Robotics Summerschool**, PhD candidates, TU Delft, 2022
- **Nacht van Ontdekkingen**, Hortus Botanicus, Leiden, 2023
- **How wasps can improve needle designs for prostate cancer treatment**, The PLOS Research Showcase on Kudos, 2023
- **Girls day**, High school students, TU Delft, 2022-2024
- **Summer lecture: ‘Wil jij een octopus of wesp in de operatiekamer?’** Children aged 8-12, Rijksmuseum Boerhaave, Leiden, 2025

## Supervision

### Master students

- **Güven Aydin**. *The ProSTATIC – a Suction-based Stabilisation Instrument for the Prostate*. Mechanical Engineering, TU Delft.
- **Bruce Hoppener**. *MRI-Compatible Pneumatic Actuation Unit for a Self-Propelling Needle*. Mechanical Engineering, TU Delft.
- **Sjoerd van der Voort**. *Suction Stabilising Device for Breast Biopsies*. Mechanical Engineering, TU Delft.
- **Zola Fung-A-Jou**. *WASP: a Wasp-Inspired Surgery Needle for Prostate Cancer Procedures*. Mechanical Engineering, TU Delft.
- **Martijn van der Helm**. *FrON: The Design and Experimental Evaluation of a Friction-Based Ovipositor-Inspired Needle Actuation System*. Mechanical Engineering, TU Delft.
- **Suzet Giltay**. *The Ovipositor Maximator: A Novel Follow-the-Leader Mechanism*. Mechanical Engineering, TU Delft.
- **David Vainer**. *MR-Conditional Wasp-Inspired Needle with Integrated Laser Functionality for TransPerineal Laser Ablation*. Biomedical Engineering, TU Delft.
- **Suzanne van Wees**. *Wasp-Inspired Biopsy Needle: Integrating Self-Propulsion and Tissue Transport for Enhanced Pancreatic Tissue Sampling*. Biomedical Engineering, RU Groningen.
- **Jakov Jukić**. *Development and Evaluation of an MRI-Compatible Control System for Pneumatically Powered Wasp-Inspired Needles*. Mechanical Engineering, TU Delft.

- **Jules de Ruiter.** *Stroke Adjustment for Wasp-Inspired Needles.* Mechanical Engineering, TU Delft.

#### **Bachelor students**

- **David Wolfrat, Kasper Stavenga, Boris Ullrich, and Mats Kerver.** *Design of a Novel Stable Needle Insertion Device for Laparoscopic Liver Surgery.* Werktuigbouwkunde, TU Delft.

#### **Internship students**

- **Iris Kuiteims, Benjamin Arnods, and Robbert den Butter.** *Increasing HDR Prostate Brachytherapy Catheter Fixation due to a Self-Fixating Double Helix Screw Thread Design.* Mechanical Engineering and Biomedical Engineering, TU Delft.

#### **Courses and Workshops**

- Hypothesis testing in public health (2 GS) - 2021
- Safe by design (2 GS) - 2021
- In vivo NMR course (5 GS) - 2021
- Practical data analysis for researchers (5 GS) - 2021
- PhD video competition (1 GS) - 2021
- Speedreading and mindmapping (1.5 GS) - 2021
- The informed researcher: information and data skills (1.5 GS) - 2021
- PhD start-up module A, B & C (2 GS) - 2021
- Scientific text processing with LaTeX (1.5 GS) - 2021
- Teamwork, leadership, and group dynamics (1.5 GS) - 2021
- Achieving your goals and performing more successfully in your PhD (3 GS) - 2021
- Foundations of educational design (1 GS) - 2021
- Cross-cultural communication skills in academia (1 GS) - 2021
- Data management plan training (1 GS) - 2022
- Structuring your design-oriented PhD project (5 GS) - 2022
- Medical device regulations (5 GS) - 2022
- Basic problem solving and decision making (1.5 GS) - 2022
- Voice training (1 GS) - 2022
- Coaching individual students and project groups (1.5 GS) - 2022
- Assessing students and master thesis projects (1 GS) - 2022
- English pronunciation (2 GS) - 2022
- Career development – exploring a research career outside academia (0.5 GS) - 2023
- Career development – personality matters (0.5 GS) - 2023





